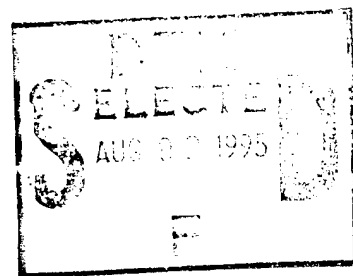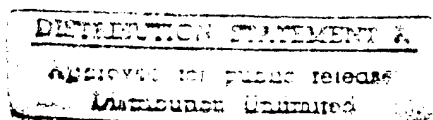# PROCEEDINGS

1993 U.S. WORKSHOP
ON THE PHYSICS AND CHEMISTRY
OF MERCURY CADMIUM TELLURIDE
AND OTHER IR MATERIALS

Edited by
James R. Waterman

TMS
Minerals · Metals · Materials

Proceedings of the

1993 U.S. Workshop on the Physics and Chemistry of Mercury Cadmium Telluride and Other IR Materials

N00014-94-1-G002

Proceedings of the

1993 U.S. Workshop on the Physics and Chemistry of Mercury Cadmium Telluride and Other IR Materials

19-21 October 1993

Seattle, Washington

Special Editor for the Proceedings:

James R. Waterman

19950731 007

TMS
Minerals • Metals • Materials

Proceedings of the
1993 U.S. Workshop on the Physics and Chemistry of Mercury Cadmium Telluride and Other IR Materials

(Continued)

(Continued)

(Continued)

Foreword

The 1993 U.S. Workshop on the Physics and Chemistry of Mercury Cadmium Telluride and Other IR Materials was held in Seattle, Washington, on October 19–21, 1993. This workshop was the twelfth in a series which began in October 1981. Over that time, it has become the preeminent forum for open interdisciplinary discussion of scientific and technological issues concerning HgCdTe. Its scope includes the discussion of other materials which are important to the development of technology based on HgCdTe, e.g., CdZnTe substrates for epitaxial growth and other materials addressing applications for which HgCdTe is the leading contender, e.g., III-V strained-layer superlattices and quantum wells for infrared detectors.

Subject areas discussed in the 1993 workshop include material growth processes, bulk and thin-film substrates, defects, III-V materials, diffusion, devices, and optical characterization. This special issue is arranged by topical area, as presented at the workshop. Forty of the 58 papers presented at the workshop appear in this publication. The editor thanks the referees for their careful and prompt review of the manuscripts and the program committee for having selected such high-quality work for presentation.

The program committee members were S.M. Johnson (Santa Barbara Research Center), C.J. Summers (Georgia Tech Research Institute), R.L. Aggarwal (Massachusetts Institute of Technology), J.M. Arias (Rockwell International), R.S. Balcerak (Advanced Research Projects Agency), I.B. Bhat (Rensselaer Polytechnic Institute), L.E. Brown (Wright Laboratory), T.N. Casselman (Lockheed Missiles and Space Co.), J.P. Faurie (University of Illinois at Chicago), J.K. Furdyna (Notre Dame University), C.R. Helms (Stanford University), M. Martinka (U.S. Army CECOM Night Vision and Electronic Sensors Directorate), T.C. McGill (California Institute of Technology), P.W. Norton (Loral IR and Imaging Systems), H.F. Schaake (Texas Instruments), D.G. Seiler (National Institute of Standards and Technology), A. Sher (SRI International), H.R. Vydyanath (Aerojet Electronic Systems), and J.R. Waterman (Naval Research Laboratory). Special thanks go to Scott Johnson and Chris Summers, cochairmen of the workshop, and Jay Morreale (Palisades Institute for Research Services, Inc.), workshop coordinator.

The workshop was cosponsored by the U.S. Army CECOM Night Vision and Electronic Sensors Directorate, U.S. Air Force Wright Laboratory, and the U.S. Office of Naval Technology.

The editor is grateful to Theodore C. Harman, editor of *Journal of Electronic Materials* (*JEM*), Robert Makowski, Director of Publishing Services of The Minerals, Metals, and Materials Society, and members of the *JEM* Editorial Oversight Committee for their cooperation in publishing this special edition.

James R. Waterman
Naval Research Laboratory
Washington, DC

Special Issue Editor

HgCdTe Molecular Beam Epitaxy Technology: A Focus On Material Properties

OWEN K. WU, D.M. JAMBA, and G.S. KAMATH

Hughes Research Laboratories, Malibu, CA 90265

G.R. CHAPMAN, S.M. JOHNSON, J.M. PETERSON, K. KOSAI, and
C.A. COCKRUM

Santa Barbara Research Center, Goleta, CA 93117

HgCdTe MBE technology is becoming a mature growth technology for flexible manufacturing of short-wave, medium-wave, long-wave, and very long-wave infrared focal plane arrays. The main reason that this technology is getting more mature for device applications is the progress made in controlling the dopants (both n-type and p-type in-situ) and the success in lowering the defect density to less than $2 \times 10^5/cm^2$ in the base layer. In this paper, we will discuss the unique approach that we have developed for growing As-doped HgCdTe alloys with cadmium arsenide compound. Material properties including composition, crystallinity, dopant activation, minority carrier lifetime, and morphology are also discussed. In addition, we have fabricated several infrared focal plane arrays using device quality double layers and the device results are approaching that of the state-of-the-art liquid phase epitaxy technology.

Key words: HgCdTe, infrared detectors, molecular beam epitaxy (MBE)

INTRODUCTION

HgCdTe is the material of choice for infrared (IR) detectors because of its variable bandgap, its high quantum efficiency, its capability for operation above liquid nitrogen temperatures,[1] and its potential for enhanced device performance through superlattice and quantum well based structures.[2] HgCdTe detectors sensitive to wavelengths of 1–16 micron have been demonstrated in several laboratories, and many are now in use for sensing or imaging applications, both civilian and military.[3]

Various growth techniques, such as liquid phase epitaxy (LPE), metalorganic chemical vapor deposition (MOCVD), and molecular beam epitaxy (MBE), have been researched and developed to grow a number of detector structures including photovoltaic double-layer heterojunction devices. By far, LPE is the most developed and mature growth technique for focal plane array (FPA) applications.[4]

However, progress on MBE over the last two years, in electrical doping, has shown that the vapor phase growth technique has become mature and important for the growth of advanced structures, such as P/N double layers and triple layers for two-color detectors.[5-9] The major advantage of this growth technique is its flexibility for the growth of various compositions in the same system. The advantage of growing a multi-layer structure in the same growth system is that it greatly reduces the contaminants at the junction interfaces. In addition, an advantage of MBE over LPE is its controllability of composition at the junction interface, enabling it to take advantage of heterojunction effects for optimal device performance. As the defense industry continues to downsize, there is an even greater need for a more flexible and cost-effective manufacturing technology for IRFPAs for both military and commercial applications. HgCdTe MBE technology offers these possibilities.

In this paper, we will first describe the experimental process and status of HgCdTe MBE growth for various wavelength applications; then discuss key

material features such as crystallinity, electrical properties of n-type and p-type doping with indium and arsenic, minority carrier lifetime and etch pit density (EPD). In addition, issues relating to uniformities of thickness and composition will be discussed. Finally, several 64 × 64 diode array results obtained from MBE-grown double layer heterojunction (DLHJ) structures will be briefly presented.

EXPERIMENTAL

Our MBE system is a modified V-80H MBE system manufactured by Vacuum Generators, a division of
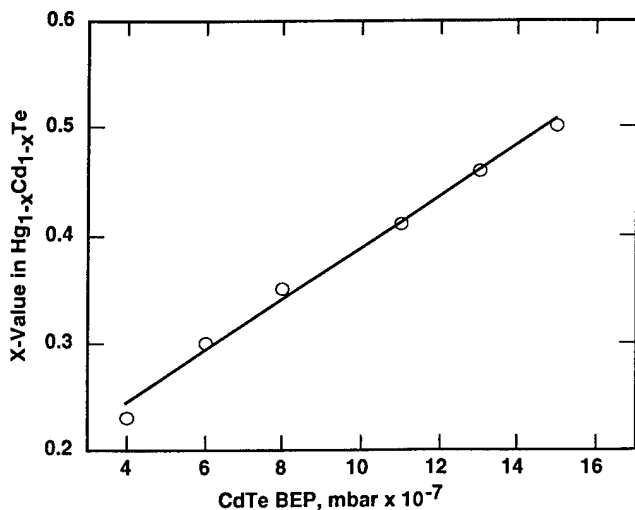
Fig. 1. HgCdTe alloy compositions (x value) as a function of CdTe flux during MBE growth.

Fison Instruments. This system has two interconnected V-80H growth chambers with integrated surface analysis and ion etching capabilities. Each growth chamber is equipped with dual Hg reservoirs, eight effusion cells and load locks for Te cracker and extended CdTe effusion cells, to enable recharging the materials without breaking the vacuum. This system can accommodate sample sizes up to 3 inches in diameter, but the majority of our growth experience has been with smaller sizes because available high quality (211) CdZnTe substrates are usually less than 3 × 3 cm.

Growth runs were carried out at 160–190°C on (211) CdZnTe substrates using Hg, CdTe, and Te sources. Typically, the (211) CdZnTe substrates were 2.5 × 2.5 cm in size and heat-cleaned at 350°C for 15–20 min under vacuum prior to the MBE growth of HgCdTe. The growth rate of HgCdTe ranged from 1–2 μm per hour depending upon the composition. The extrinsic dopants of choice were In for n-type and cadmium arsenic compounds for p-type dopants.[9]

Regarding material properties, the composition (x value) of HgCdTe was determined by infrared transmission and photoflectance techniques.[10] The crystallinity was measured by the x-ray rocking-curve measurement using $CuK_{\alpha1}$ x-rays from a Ge four-crystal monochromator. The concentration of In and As dopants was determined by secondary ion mass spectrometry (SIMS) and their electrical properties were determined by Hall measurements. Morphology and microstructure were investigated with optical and electron microscopies.
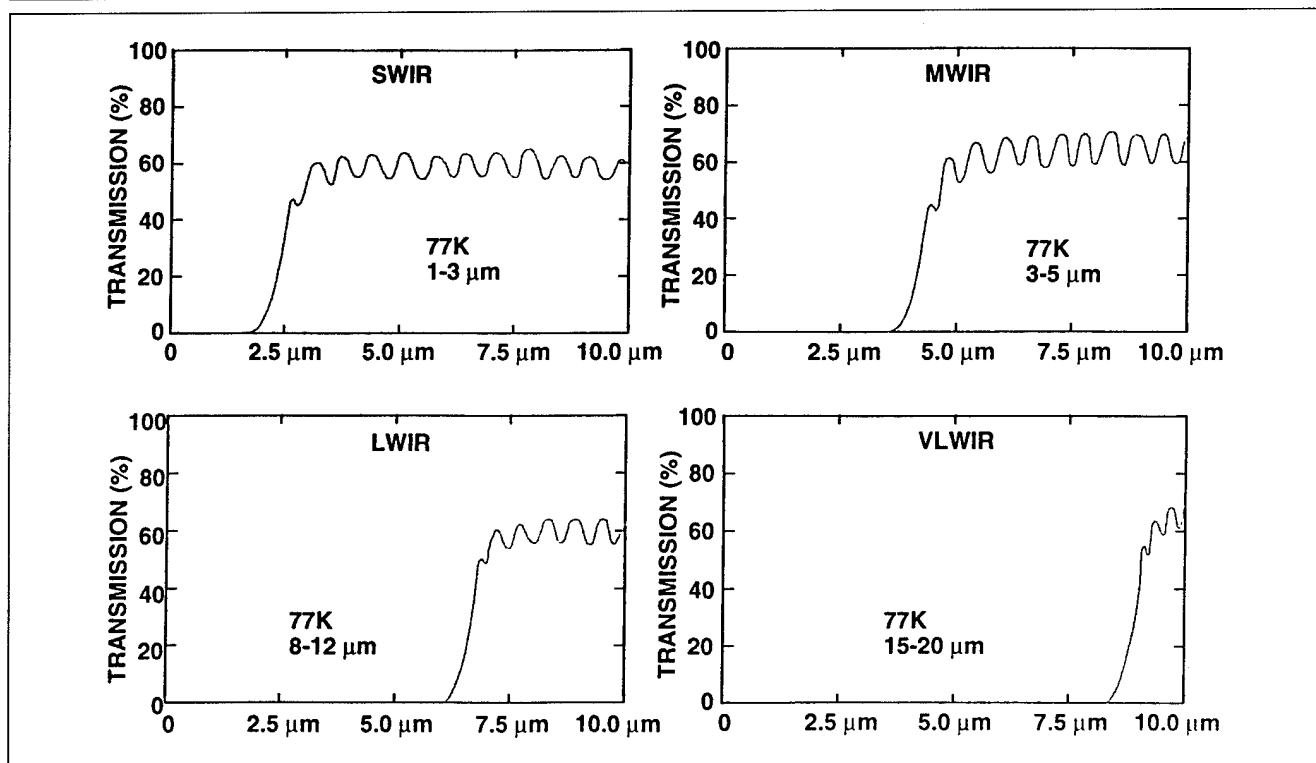
Fig. 2. Room temperature IR transmission data for various MBE-grown HgCdTe double-layer heterojunction structures. These structures can be used for SWIR, MWIR, LWIR, and VLWIR applications at 77K.

SPOT	THICKNESS, μm	X-VALUE	I_{max}, μm
A1	7.2	0.258	6.96
A2	7.2	0.257	6.99
A3	7.2	0.258	7.03
A4	7.1	0.263	6.95
B1	7.2	0.256	6.9
B2	7.2	0.256	6.86
B3	7.2	0.256	6.94
B4	7.2	0.26	6.95
C1	7.2	0.257	6.93
C2	7.3	0.255	6.97
C3	7.2	0.258	7.07
C4	7.1	0.262	6.84
D1	7.2	0.258	7.09
D2	7.2	0.258	7.04
D3	7.2	0.261	7.02
D4	7.1	0.266	6.94
AVE	7.2	0.259	6.97
MIN	7.1	0.255	6.84
MAX	7.3	0.266	7.09
MED	7.2	0.258	6.96
STD DEV	0.05	0.003	0.06

A_1	A_2	A_3	A_4
B_1	B_2	B_3	B_4
C_1	C_2	C_3	C_4
D_1	D_2	D_3	D_4

2.5 cm (vertical) — 2.5 cm (horizontal)

Fig. 3. Thickness, x value, and transmission maximum for a 2.5 × 2.5 cm HgCdTe DLHJ specimen. Data are measured and calculated from FTIR.

RESULTS AND DISCUSSIONS

Growth of HgCdTe Alloys for Short, Medium, Long, and Very Long Wave Infrared Applications

The growth of high quality $Hg_{1-x}Cd_xTe$ alloys has been demonstrated over the range of interest for short wave infrared (SWIR)–very long wave infrared (VLWIR) detector applications. The composition of HgCdTe alloys can be varied readily by choosing appropriate beam flux ratios. We have shown that over the range from x = 0.22 to x = 0.50, excellent control of composition can be achieved by varying the CdTe source flux with a constant flux of Hg at 3×10^{-4} mbar and Te at 8×10^{-7} mbar during the MBE growth, as shown in Fig. 1. For x-values outside this range, only an additional simple adjustment of Hg and Te fluxes is required.

Figure 2 shows room temperature IR transmission data for various MBE-grown HgCdTe double-layer heterojunction structures. The basic structure consists of a 1.5–2 μm As-doped p-type HgCdTe cap layer on top of a 7–8 μm In-doped n-type HgCdTe base layer. The data show that the room temperature cutoffs are extremely abrupt, which is indicative of high degree in-depth compositional uniformity. It should be noted that these structures can be used for short-wavelength infrared (1–3 μm), medium-wavelength infrared (MWIR, 3–5 μm), long-wavelength infrared (LWIR, 8–12 μm) and very long-wavelength infrared (>16 μm) applications at 77K. Thus, flexibility is a number one characteristic of MBE technology, which makes it ideal for IRFPA applications.

Figure 3 lists the thickness, composition (x value)

and wavelength of maximum transmission for a 2.5 × 2.5 cm DLHJ structure. The results were obtained from a computer-automated Fourier transform infrared spectrometer (FTIR) system, which measured 16 spots across the sample. The thickness and x-value were determined from the interference fringes and cutoffs of the transmission spectra. The data show that average total thickness was 7.2 μm with a standard deviation of 0.05 μm for this sample; the average x-value for the base layer was 0.259 with a standard deviation of 0.003 (x/x is about 1.16%); and the transmission maximum peak average value[10] was 6.97 μm with a standard deviation of 0.06 μm. This initial set of data suggests that MBE technology is able to provide HgCdTe alloys with uniform compositions for IRFPA applications. One main reason is that the sample is rotated during the MBE growth. It should be noted that we have not optimized for the purpose of uniformity yet. We anticipate achieving even better uniformity by enlarging and/or doubling the effusion cells.

Morphology and Crystallinity of MBE-Grown DLHJ Materials

The surface morphology of the HgCdTe materials is important from the device fabrication point of view, especially as (now that array size is getting larger) the requirements are becoming more stringent. Figures 4a and 4b show the scanning electron micrographs (SEM) for HgCdTe DLHJ structures. Note that the scale is 50 μm. Both samples have very smooth surface morphology suitable for device applications, except for the undulations on the left sample. It is believed that these ripples have something to do with the surface finish on the CdZnTe substrates and the

a   **b**
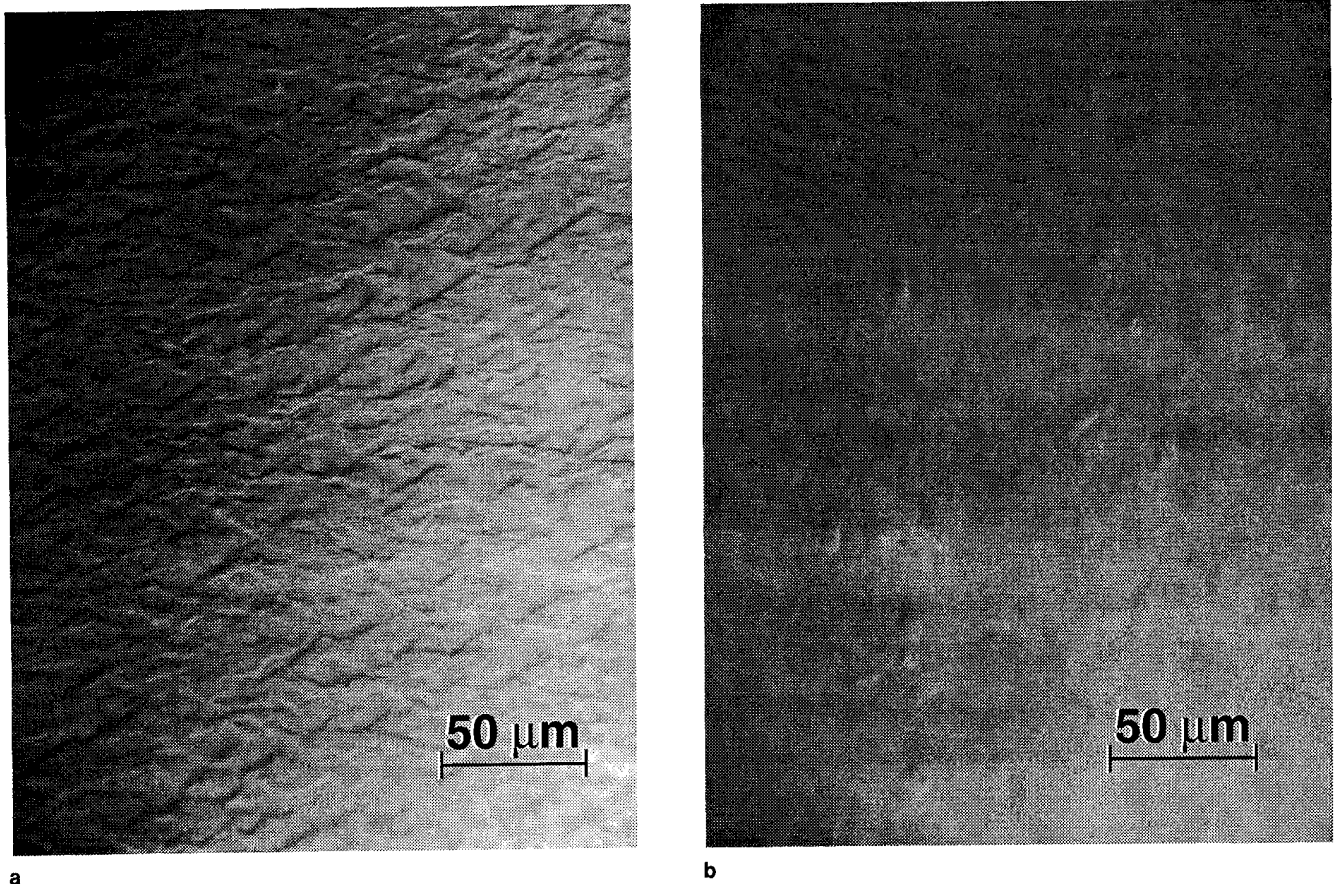
Fig. 4. (a) and (b) Scanning electron micrographs for HgCdTe DLHJ structures. Both samples have smooth surface morphology for device fabrication.

heat treatment performed prior to the MBE growth.

The excellent crystal quality of HgCdTe layers grown by MBE is illustrated in Fig. 5, where x-ray rocking curve data are presented for a p-on-n LWIR double layer heterojunction structure. The In-doped n-type (about 8 μm) base layer peak has a width of <25 arc-s and is indistinguishable from the CdZnTe substrate, to which it is exactly lattice-matched. Because the As-doped p-type cap layer is much thinner (about 2 μm) and has a different alloy composition, its peak is shifted slightly and is broader (45 arc-s), but the x-ray full width at half maximum (FWHM) is still indicative of high quality. Figure 5 also shows the x-ray FWHM data map for nine spots across the 2.5×2.5 cm specimen. It demonstrates that the FWHM for the base layer ranges from 25–30 arc-s, and that the FWHM for the cap layer ranges from 45–50 arc-s. These results indicate that the uniformity of crystallinity is excellent for IRFPA applications.

Electrical Properties of N- and P-Type HgCdTe Alloys

Indium is the most widely used n-type dopant for HgCdTe alloys during MBE. The n-type doping of HgCdTe with In by MBE was first reported in 1988[13] and later studied and improved at several other laboratories.[8,14] Most recently, we have shown that In concentration can be varied from 1×10^{15}/cm³ to 5×10^{18}/cm³ by varying the In cell temperature in the range from 450 to 700°C with no evidence of a memory effect. This is of interest because a memory effect had been reported previously[8] due to contamination from the substrate which was mounted with indium. In these recent experiments, the Hall mobility of In-doped n-type HgCdTe was studied as a function of Cd composition and carrier concentration. For a typical HgCdTe alloy with a 22% Cd composition and doping of 1.5×10^{15}/cm³ for long wavelength applications, the Hall mobility was greater than 9×10^4 and 2×10^5 cm²/v.s. for 77 and 30K, respectively. This temperature dependence of the Hall data indicates that n-type carrier concentrations which are constant are independent of temperature, in turn suggesting that the In-donor energy level is near the conduction band edge. It should be noted that the doping efficiency of In was almost 100% as evidenced from the Hall measurement and secondary ion mass spectroscopy (SIMS) data for a carrier concentration that was less than 2×10^{18}/cm³. Also, where the In concentration was greater than 5×10^{18}/cm³, the morphology of the alloys became rough. All the results indicate that n-type doping of HgCdTe is easier to achieve than p-type, because In incorporation in the group II sublattice is facilitated by the vacancies in the HgCdTe materials.

So far, two approaches have been investigated for

DLHJ STRUCTURE: $Hg_{0.74}Cd_{0.26}Te$ (As DOPED, 2 μm)/$Hg_{0.78}Cd_{0.22}Te$ (In DOPED, 8 μm)/CdZnTe (211) SUBSTRATE
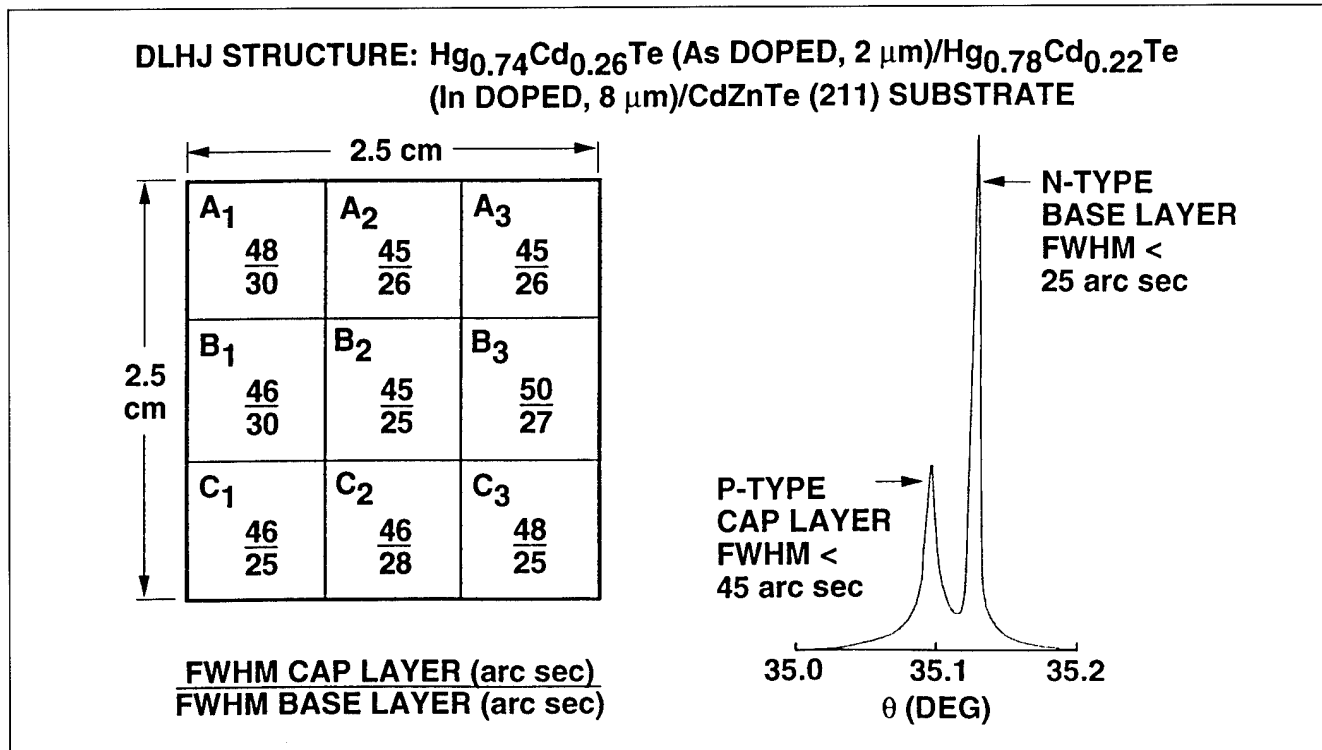
Fig. 5. X-ray rocking curve data for HgCeTe DLHJ structure. The results indicate that the uniformity of crystallinity of base and cap layers is excellent.

the MBE growth of As-doped HgCdTe. The first approach is based on the success of photo-assisted MBE in enabling high levels of p-type As doping of CdTe.[14,15] For As doping, during compositionally modulated structure growth, only the CdTe layers in a CdTe-HgTe combination are doped by As. Since the CdTe does not contain Hg vacancies, and is grown under cation-rich conditions, the As is properly incorporated in the Te site and its concentration is proportional to the As flux. The structure then interdiffuses after annealing at high temperature to remove residual Hg vacancies, resulting in p-type, homogeneous HgCdTe. The disadvantage of this approach is that it requires a high temperature anneal that results in reduced junction and interface control.

In contrast, our approach is to use cadmium arsenide compound and tellurium from a cracker effusion cell in order to enhance the sticking coefficient of the Hg and hence to minimize Hg vacancies.[8,9,12] As a result of our approach, the As is directed to the group VI sublattice to promote efficient p-type doping. Today, using this approach, many layers of p-type HgCdTe alloys have been successfully grown and characterized. The SIMS data indicate that an As doping concentration ranging from 10^{16}/cm^3 to 10^{18}/cm^3 can be achieved. Based on the Hall data and SIMS measurements, the doping efficiency of As is estimated to be about 50%. In this study, some of these samples were annealed under Hg ambient to avoid Hg vacancies, and temperature dependence Hall measurements were carried out to determine the activation energy of As. The data show that the activation energy for As is about 7–8 meV above the valence
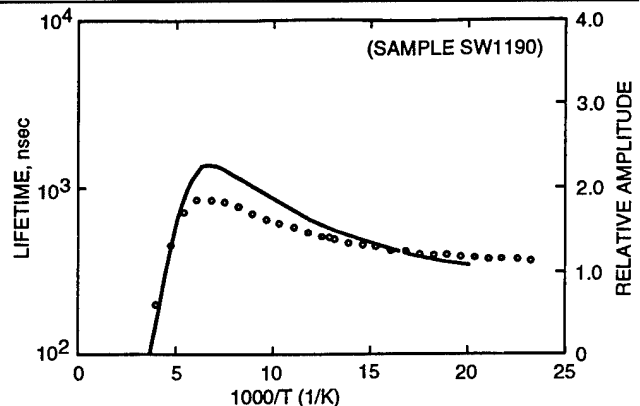
Fig. 6. Comparison of the theoretical Auger lifetime compared to the measured photoconductive decay lifetime for sample SW1190.

band, which is consistent with the reported literature values from LPE materials.[16] The mobilities of these samples are on the order of 100–300 cm^2/v.s at 77K. Key growth parameters that determine the properties of As-doped p-type HgCdTe are the growth temperature and Hg/Te flux ratio.

Minority Carrier Lifetime and Etch Pit Density

Other material properties such as minority carrier lifetime and etch pit density of the material are all very important for device performance. Especially, the lifetime of the photoexcited carrier is among the most important parameters for a detector material, since it governs the diode leakage current and quantum efficiency of detector operations. In short, the ultimate performances of infrared detectors depend critically on the lifetimes of their optically excited

SPECTRAL RESPONSE

SHORT CIRCUIT CURRENT
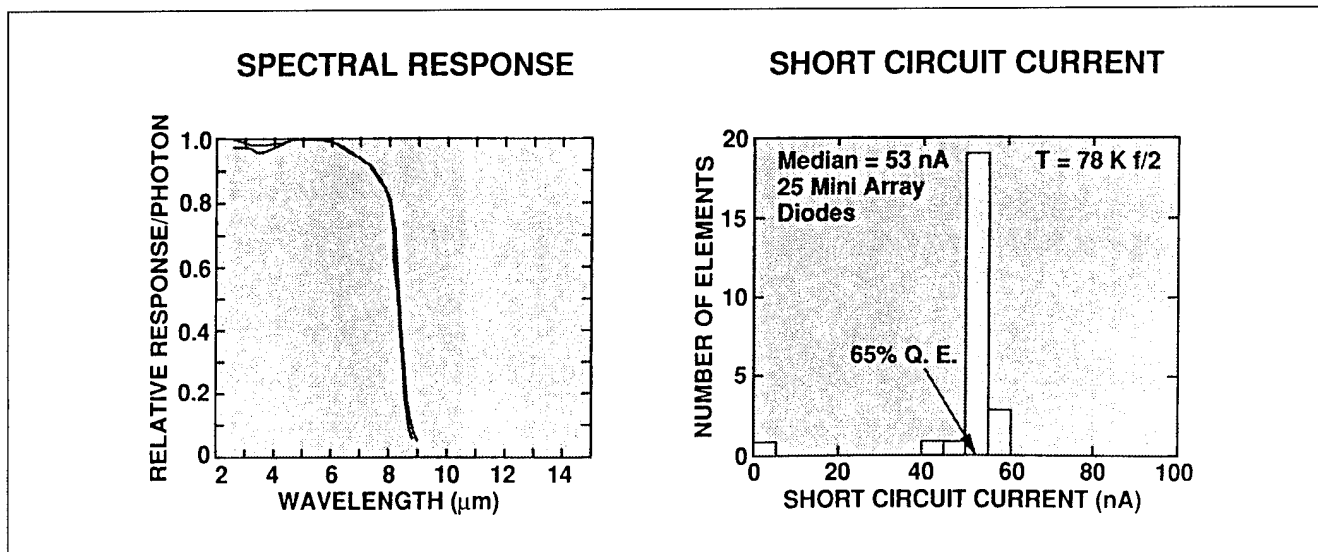
Fig. 7 (a) and (b) spectral resonse and short circuit current data for a MBE grown DLHJ diode array, showing abrupt cutoff at 8.3 μm.
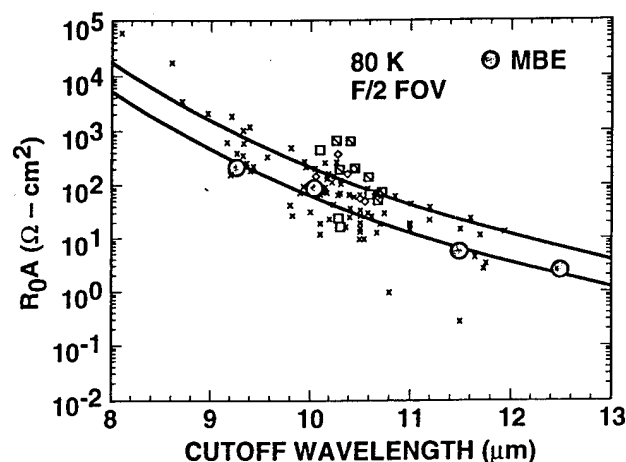
Fig. 8. R_oA data for several LWIR detector results in comparison with the LPE-grown device performance trend line.

carriers. Here, we have used photoconductive decay measurements to determine the minority carrier lifetime of several MBE-grown In-doped n-type HgCdTe (x = 0.2–0.3) materials. The results show that the lifetime ranges from 0.3–1.2 μs depending upon the x value and carrier concentration. For example, Fig. 6 shows a comparison of the theoretical Auger lifetime compared to the measured photoconductive decay lifetime for sample 1190. This sample (SW1190) has a cutoff at 10 μm and N_d = 1.5 × 10^{15}/cm^3 at 77K. The measured lifetime is about 500 ns or 80% of the theoretical lifetime limit and is comparable with LPE grown HgCdTe alloys.[17]

Material defects can be classifed into extended defects or point defects. Extended defects include dislocations, pinholes, particulates, inclusion, microtwins, precipitates, and inhomogeneities. They can extend over lengths of several microns and are often observable by appropriate techniques of selective etching and microscopy.[18] For example, we have used CrO_3/HCl/H_2O etchant to reveal the extended defects on the (211) HgCdTe alloys grown by MBE.[11]

Optical microscopy studies of several etched MBE grown HgCdTe base layers indicate that the EPD of device-quality alloys is on the order of 2 × 10^5/cm^2, which is in good agreement with the lifetime data discussed previously and comparable to the best LPE materials for device applications. We have also found that EPD is sensitive to the Hg/Te flux ratio and growth temperature used during the MBE growth.

Device and Array Results from MBE-Grown P/N DLHJ

We have used the above-described growth parameters to grow a number of p/n double layer heterojunctions for MWIR and LWIR applications. Processing and testing of several 64 × 64 arrays were carried out at Santa Barbara Research Center. High-performance device results were achieved. For example, a typical LWIR DLHJ structure will consist of a 1.5 μm As-doped p-type (>5 × 10^{17}/cm^3, x = 0.26) HgCdTe cap layer on top of an 8 μm In-doped n-type (2 × 10^{15}/cm^3, x = 0.22) HgCdTe base layer. Figure 7a shows the spectral response of diodes which have uniform cutoff wavelengths at 8.3 μm while Fig. 7b shows the short circuit current of a miniarray with 65% quantum efficiency. Figure 8 shows the R_oA for several LWIR detector results in comparison with the LPE-grown device performance trend line. The data indicate that the detectors have R_oA of 2.5 × 10^2, 1.1 × 10^2, 7 × 10^1, and 1.5 × 10^0 ohm-cm^2 at 80K for 9.4, 10.2, 11.5, and 12.5 μm cutoffs, respectively. The results indicate that diode performance is approaching that of state-of-the-art LPE detectors. Further improvement is expected as the technology becomes more mature in the near future.

FUTURE DIRECTIONS AND CONCLUSION

Efforts in research and development of HgCdTe MBE technology during the last decade have laid the solid foundation necessary for successful application of MBE in the realization of HgCdTe multilayer

structures for IR detectors and other optoelectronic devices. However, additional development of temperature and flux sensors, larger (211) CdZnTe substrates, purer source materials and/or alternative substrates is anticipated. These will be necessary (along with improved in-situ processing for dry-etching, selective area epi growth and passivation integrated with flexible MBE growth) to ensure a cost-effective and flexible manufacturing technology for IRFPA in both military and commercial applications.

ACKNOWLEDGMENTS

REFERENCES

1. A. Rogalski and J. Piotrowski, *Progress in Quantum Electronics* 12, (2/3), 205 (1988).
2. P.N. Norton, *Optical Engineering* 30 (Nov) 1649 (1991).
3. A. Stout, *R&D Mag.* Feb. 46 (1992).
4. (a) T. Tung, *J. Cryst. Growth* 86, 161 (1988); (b) T. Tung, L. DeArmond, R. Herald, P. Herning, M. Kalisher, D. Olson, R. Risser, A. Stevens and S. Tighe, *SPIE Vol. 1735* 109 (1992).
5. R. Zucca, M. Zandian, J.M. Arias and R.V. Gil, *J. Vac. Sci. Technol. B* 10 (4), 1587 (1992).
6. J.M. Arias, J.G. Pasko, M. Zandian, S.H. Shin, G.M. Williams, L.O. Bubulac, R.E. DeWarmes and W.E. Tennant, *Appl. Phys. Lett.* 62 (9), 1 March 976 (1993).
7. O. Wu and G. Kamath, *J. Vac. Sci. Technol.* A8 (2), 1034 (1990).
8. O. Wu, D. Jamba and G. Kamath, *J. Cryst. Growth* 127, 365 (1993).
9. G. Kamath and O. Wu, U.S. Patent Number 5,028,561, July 1, (1991).
10. S.L. Price and P.R. Boyd, *Semiconductor Sci. & Technol.* 8 No. 6S, 842 (1993).
11. J.H. Tregilgas, T.L. Polgreen and M.C. Chen, *J. Cryst. Growth* 86, 460 (1988).
12. O.K. Wu, Spring MRS Mtg. Abs. (1993) San Francisco, April 12–16, 1993, p. 76.
13. M. Boukerche, P.S. Wijewarnasuriya, S. Sivananthan, I. Sou, Y. Kim, K. Mahavadi and J. Faurie, *J. Vac. Sci. Technol. A* (6) 4, 2830 (1988).
14. J. Arias, S. Shin, D. Copper, M. Zandian, J. Pasko, E. Gertner, R. Dewames and J. Singh, *J. Vac. Sci. Technol. A* 8 (2), 1025 (1990).
15. J. Schetzina, J. Han, Y. Lansari, N. Giles, Z. Yang, S. Hwang and J. Cook, Jr., *J. Cryst. Growth* 101, 23 (1990).
16. W. Radford and C. Jones, *Proc. IRIS Detector Specialty Conf.,* Seattle, WA August, 1984.
17. V.C. Lopes, A.J. Syllaios and M.C. Chen, *Semicond. Sci. Technol.* 8, 824 (1993).
18. S.M. Johnson, D.R. Rhiger, J.P. Rosebeck, J.M. Peterson, S.M. Tayor and M.E. Boyd, *J. Vac. Sci. Tech. B* 10, 1499 (1992).

Precise Control of HgCdTe Growth Conditions for Molecular Beam Epitaxy

MASAYA KAWANO, TOKUHITO SASAKI, and NAOKI ODA

Material Development Center, NEC Corporation, Kawasaki, Kanagawa 216, Japan

A $Hg_{1-x}Cd_xTe$ growth method is presented for molecular beam epitaxy, which precisely controls growth conditions to routinely obtain device quality epilayers at a certain specific composition. This method corrects the fluctuation in composition x for run-to-run growth by feedback from the x value for the former growth to the fluxes from CdTe and Te cells. We achieved standard deviation $\Delta x/\bar{x}$ of 3.3% for 13 samples grown consecutively. A substrate temperature drop was found during growth, which considerably degrades the crystal quality of epilayers. In this method, this drop is greatly diminished by covering the holder surface with a heavily doped Si wafer. Finally, etch pit density of 4×10^4 cm^{-2} and full width at half-maximum of 12 arc-s for the x-ray double-crystal rocking curve were obtained as the best values.

Key words: Control of composition, HgCdTe, infrared detectors, molecular beam epitaxy (MBE)

INTRODUCTION

Considerable efforts have been expended to accomplish HgCdTe epilayer growth on CdZnTe substrates by molecular beam epitaxy (MBE). It is, however, still difficult to routinely obtain device quality HgCdTe epilayers at a certain specific composition. Main reasons are
- Difficulty in maintaining optimal growth conditions, and
- Lack of reproducibility for CdZnTe substrate quality and/or Zn concentration.

The latter issue will be solved by substrates suppliers.

The growth conditions consist of fluxes, namely the fluxes from CdTe, Te, and Hg cells, and the surface temperature at the growth front. There are two problems to be considered. One is the fluctuation in the fluxes from CdTe and Te cells for run-to-run growth,

which is caused by shape changes of source materials. This is not the case for Hg flux, because constant flux can be achieved by maintaining the liquid level in the Hg cell. The Te/Hg and Te/CdTe flux ratios mainly affect crystal quality and composition of HgCdTe epilayers, respectively, so it is necessary to keep the fluxes from the CdTe and Te cells constant.

Another problem is temperature change at the substrate surface during growth. The substrate temperature is usually monitored by a thermocouple located in the back of the substrate holder. If the thermocouple reading is kept constant, then a drop in the substrate-surface temperature is observed. Several groups have reported on this for the III-V group MBE[1,2] and for the HgCdTe MBE.[3,4] This is a crucial problem especially for HgCdTe growth, because of its narrow optimal-temperature range. It considerably degrades the crystal quality of epilayers.

This paper gives a growth method which accurately controls the fluxes from the CdTe and Te cells, and the

substate-surface temperature. With this method, we achieved routine growths of high quality HgCdTe epilayers at a certain specific composition.

GENERAL EXPERIMENTAL PROCEDURE

$Hg_{1-x}Cd_xTe$ (x = 0.2–0.3) epilayers were grown on $Cd_{1-y}Zn_yTe(\bar{1}\,\bar{1}\,2)B$ (y = 0.03–0.05) substrates in a Riber 32P MBE system. The substrates were etched in a Br_2-methanol solution and thermally annealed at 310°C for 10 min before the growth. The substrate temperature was 180°C, which was measured with a Chromel-Alumel thermocouple in contact with the back surface of the molybdenum substrate holder. The thermocouple reading was calibrated with the melting point of tin and/or indium placed on the holder. Source materials were Hg, CdTe, and Te. The reflection high energy electron diffraction (RHEED) pattern was monitored during growth. The epilayers were characterized by Nomarski microscopy, x-ray double-crystal rocking curves (DCRCs), and etching technique. The full width at half-maximum (FWHM) of DCRCs was measured with $(\bar{2}\,\bar{2}\,4)$ reflections, using a Si(001) reference crystal with (004) reflections. The epilayer dislocations were investigated with etch pit density (EPD) technique[5] on the $(\bar{1}\,\bar{1}\,2)B$ surface.

FLUX CONTROL

The growth conditions, namely the fluxes and the growth temperature, determine growth rate r in Å·s^{-1}, Cd composition x for $Hg_{1-x}Cd_xTe$ epilayers. These parameters can be approximately expressed as a function of Cd flux J_{Cd} and Te_2 flux J_{Te_2} in molecules m^{-2}·s^{-1},

$$r = \frac{d^3}{2 \times 10^{20}} s_{Te_2} J_{Te_2}, \qquad (1)$$

$$x = \frac{s_{Cd} J_{Cd}}{2 s_{Te_2} J_{Te_2}}, \qquad (2)$$

where d is HgCdTe lattice constant in Å and s_i is sticking coefficient for species i. The Cd atoms are supplied from a CdTe cell and Te_2 molecules are supplied from both Te and CdTe cells. The flux from CdTe cell $J_{CdTe\,cell}$ are expressed as $2J_{Cd}/3$, because Cd atoms and Te_2 molecules evaporate from CdTe at a ratio of 2:1.[6] So, Eq. (1) and Eq. (2) can be rewritten by using fluxes from Te and CdTe cells,

Table I. The Sticking Coefficient Ratio for Several Pairs of Growths

Sample No.	x	j	s_{Cd}/s_{Te_2}
34	0.274	1.374	0.66
36	0.225		
57	0.241	1.071	0.62
58	0.231		
81	0.273	1.251	0.72
82	0.236		

$$r = \frac{d^3}{2 \times 10^{20}} s_{Te_2} \left(J_{Te\,cell} + \frac{J_{CdTe\,cell}}{3} \right), \qquad (3)$$

$$x = \frac{s_{Cd}}{s_{Te_2}} \cdot \frac{1}{1 + 3\dfrac{J_{Te\,cell}}{J_{CdTe\,cell}}}. \qquad (4)$$

The $J_{CdTe\,cell}$ and $J_{Te\,cell}$ fluxes were measured by placing a movable Bayard-Alpert (B-A) ion gauge in the substrate position. The pressure readings p in Pa were calibrated to get the fluxes as follows:

$$J_{Te\,cell} = \frac{N_A p_{Te\,cell}}{\sqrt{3RT_{Te\,cell} M_{Te_2}}\, I\left(z_{Te_2}\right)}, \qquad (5)$$

$$J_{CdTe\,cell} = \frac{\sqrt{3}\, N_A p_{CdTe\,cell}}{\sqrt{RT_{CdTe\,cell}}\left(2\sqrt{M_{Cd}}\, I\left(z_{Cd}\right) + \sqrt{M_{Te_2}}\, I\left(z_{Te_2}\right)\right)}, \qquad (6)$$

where N_A is the Avogadro number in molecules, mol^{-1}, M_i is the molecular mass of species i in kg-mol^{-1}, R is the gas constant in J·K^{-1}·mol^{-1}, and $I(z_i)$ is the ionization coefficient of species i. It is known that I(z) depends on atomic number z_i of species i and $I(z_i) = [0.4z_i/14 + 0.6]$, when compared with that of nitrogen.[7] The unknown parameters in Eq. (3) and Eq. (4) are the sticking coefficients s_{Cd} and s_{Te_2}. They can be determined from growth rate, composition, and the fluxes. There is, however, one problem, in that the absolute flux value is difficult to measure from B-A ion gauge, because of sensitivity changing in the B-A ion gauge, molecular-beam inhomogeneity over the size of ion gauge, or molecular-beam reflection around the gauge. For this reason, only the sticking-coefficients ratio s_{Cd}/s_{Te_2} was measured from x value change when the $J_{Te\,cell}/J_{CdTe\,cell}$ ratio was changed. The sticking-coefficient ratio can be estimated by growing a pair of epilayers as follows:

$$\frac{s_{Cd}}{s_{Te_2}} = \frac{1 - j}{1/x - j/x'}, \qquad (7)$$

$$j = \frac{J_{Te\,cell} J'_{CdTe\,cell}}{J_{CdTe\,cell} J'_{Te\,cell}}, \qquad (8)$$

where the primed values mean the values for the former growth. The s_{Cd}/s_{Te} ratio of 0.7 was obtained experimentally in the compositional range from 0.22 to 0.27, as is shown in Table I. This value has good agreement with Monterrat et al.'s value of 0.7 when CdTe were grown on CdZnTe(001) substrates under Hg flux at 180°C.[8] Although they called this value as sticking coefficient of Cd in their paper, this is true only when the sticking coefficient of Te_2 is unity. One can also compare with the value of 0.8 obtained from HgTe incorporation in a film grown on $CdTe(\bar{1}\,\bar{1}\,2)B$ substrates at 180°C under fluxes from CdTe and Hg cells.[9]

With this sticking coefficient ratio, composition can be controlled in principle using Eq. (4). Assuming that the sticking coefficient of Te_2 is unity, growth rate can be also controlled using Eq. (3). The flux control,

however, for run-to-run growth using Eq. (3) and Eq, (4) requires flux measurements before each growth. In addition, there is a difficulty involved in the absolute flux measurement, as mentioned above, especially for growth rate control. For these reasons, it is practical to control fluxes by correcting individual cell temperatures on the basis of the composition x′ and the growth rate r′ of the former growth. In order to grow epilayers at specific composition x and growth rate r, we used the following equations which give the CdTe cell temperature $T_{CdTe\ cell}$ and the Te cell temperature $T_{Te\ cell}$.

$$J_{CdTe\,cell} = \frac{xr}{x'r'}J'_{CdTe\,cell},\qquad(9)$$

$$J_{Te\,cell} = \frac{(1-x)r}{(1-x')r'}J'_{Te\,cell},\qquad(10)$$

$$J_i \propto \exp\left(-\frac{H_i}{kT_i}\right)T_i^{-\frac{1}{2}},\qquad(11)$$

where H_i is the enthalpy for evaporation in eV, and k is the Boltzmann constant in eV·K⁻¹. The enthalpy values of 1.97 eV for CdTe and 1.65 eV for Te were used.[10] Using above equations, standard deviation Δx/$\bar{x}$ of 3.3% (x = 0.224 ± 0.007) was obtained for 13 samples grown consecutively, excluding the first run (Fig. 1). It was found recently that a small difference in substrate position for each growth can change the composition. Thus, the compositional fluctuation can be reduced by placing substrates at the same position as possible.

SURFACE TEMPERATURE DROP

It is a real challenge to maintain the surface temperature at the growth front during HgCdTe growth. As has been reported,[1-4] the growth temperature could not be kept constant, when the thermocouple reading at the back surface of the substrate holder was kept constant. If the temperature was set at an optimal value at the initial growth stage, twin formation occurs in the middle of growth, which was observed with RHEED pattern. The twin formation indicates that temperature drop occurs during the growth.

Infrared images of a substrate and a molybdenum holder, before growth and just after growth initiation, show that emissivity of the holder surface abruptly increases (Fig. 2). The heater power change of 7.5 W was observed, when 10 μm HgCdTe was deposited on a 15 × 15 mm substrate and a 2 inch holder. On the other hand, the thermal loss change of 6 W, between before growth started and at the growth end, was roughly estimated, assuming that the emissivity of the molybdenum bare surface changes from zero to unity by coating with HgCdTe. The temperature drop, therefore, was found to be predominantly caused by emissivity change at the molybdenum bare surface.

As a result, the temperature drop strongly depends on the area of the holder bare surface. It changes with the substrate size, number of substrates grown simultaneously, the holder size, etc. In the case of 10 μm HgCdTe growth on a 15 × 15 mm substrate, the drop amount is about 15°C for a 2 inch holder, and over 40°C for a 3 inch holder. Especially, in the latter case,
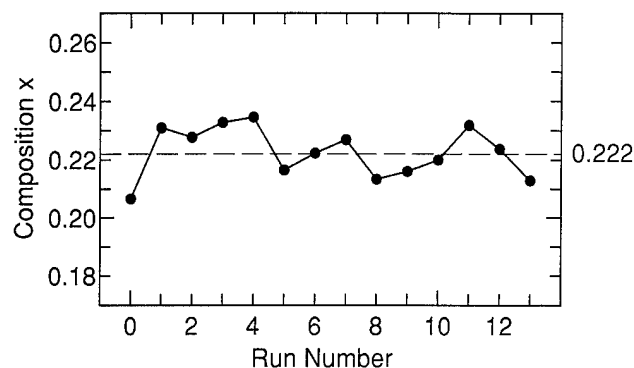
Fig. 1. Composition fluctuation of $Hg_{1-x}Cd_xTe$ epilayers grown consecutively.
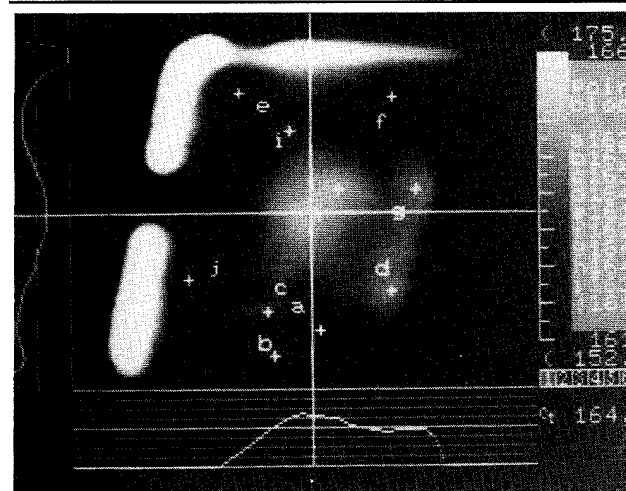
a
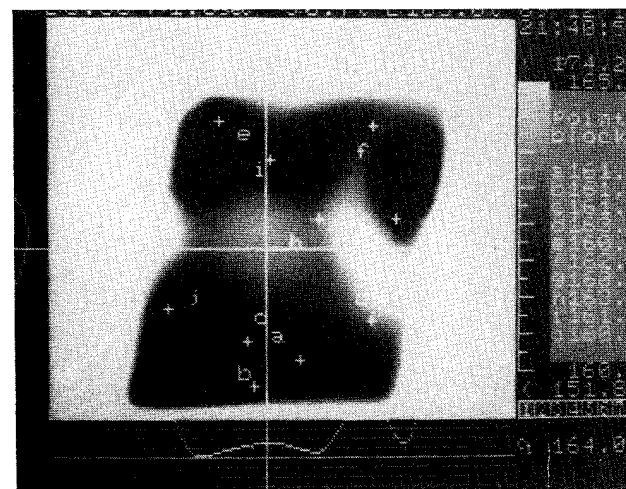
b

Fig. 2. Infrared images of a substrate and a molybdenum holder before growth (a), and just after growth initiation (b).
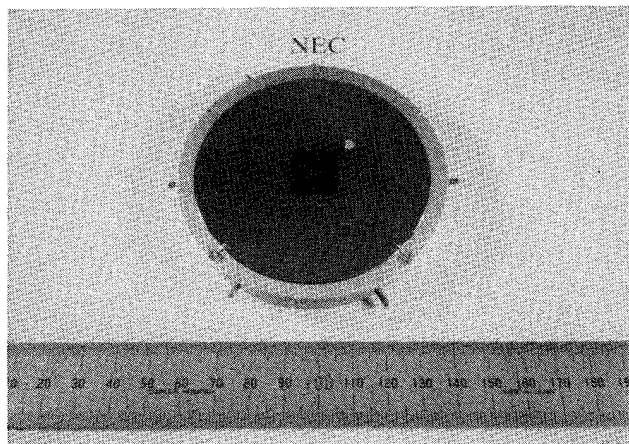
Fig. 3. Substrate holder and CdZnTe substrate described in this paper. Almost area of the holder was covered with a Si wafer to reduce the emissivity change of the holder surface during growth. A tip of tin is placed on the Si wafer to calibrate the temperature.

Fig. 5. Etch pit density histogram for HgCdTe epilayers using the new 3 inch holder.
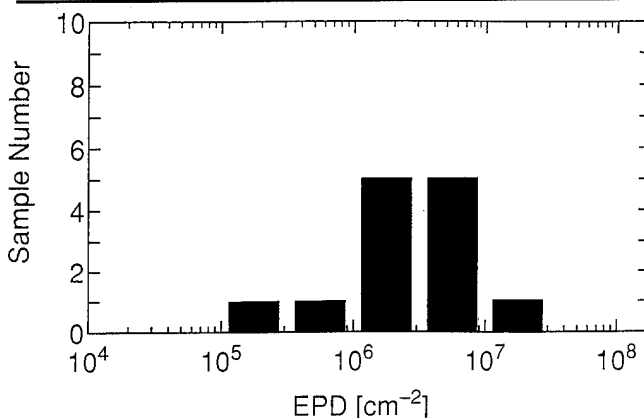
Fig. 6. Etch pit density histogram for HgCdTe epilayers using the conventional 2 inch holder. The thermocouple reading was compensated for the temperature drop during growth.

Fig. 4. Pyrometer temperature profiles after growth initiation as a function of time. Each profile is shifted for clarity. The values indicate the resistivities of Si wafers. The temperature readings in the beginning of the growth do not indicate real temperature change.

the temperature drop speed is too large to grow single crystal epilayers.

NEW SUBSTRATE HOLDER

For obtaining the same growth condition no matter what the substrates or the holder sizes were, we developed a new substrate holder for 3 inch wafers (Fig. 3), in which most of the molybdenum bare surface is covered with a Si wafer. Then we investigated the temperature-drop dependency on the resis-

tivity, namely emissivity of the Si wafer.

A 3 inch Si wafer is mounted onto this holder using gallium for good thermal contact. A 15×15 mm CdZnTe substrate is also mounted using gallium, and a tip of tin is placed onto the Si wafer. The surface temperature of the growth front was monitored during growth by a pyrometer for 2 μm wavelength and RHEED pattern. The resistivities of the Si wafers employed were 10–20, 1–3, 0.01–0.05, and <0.02 in Ω·cm. The dopants for these wafers were boron for the former two wafers, phosphorous, and arsenic, respectively. The emissivity ε values of the Si wafers were roughly estimated from the infrared reflectance r_f and transmittance t at the 6.5 μm wavelength, using Kirchhoff's law $\varepsilon = \alpha = 1 - r_f - t$, where α is absorptance. The incident and viewed fluxes were normal to the wafers. A gold thin film deposited on a sapphire wafer was used as reference for the reflectance measurements.

Figure 4 shows the temperature profiles measured by the pyrometer, when the thermocouple reading was kept constant. In the beginning of the growth, the temperature reading changes do not indicate real temperature change, because of the interference between the surface and the interface of the epilayer. It was found that the temperature drop was dramati-

a **b** **c**
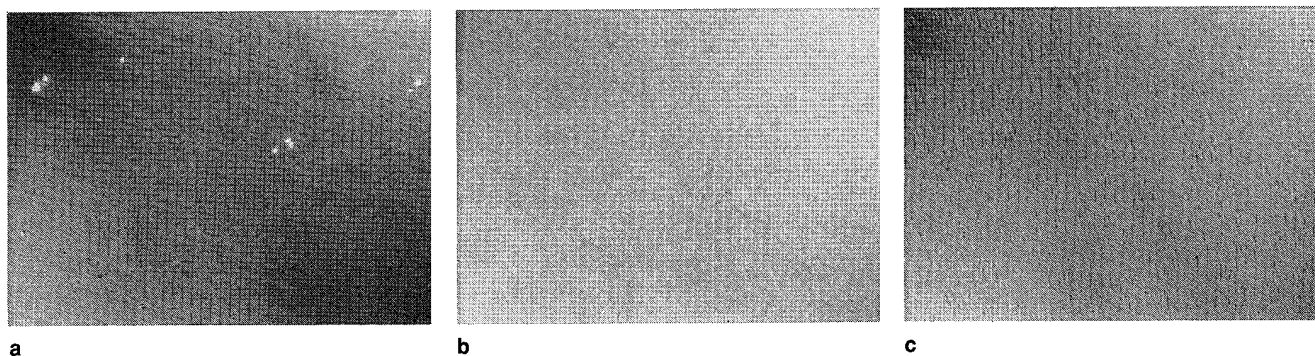
Fig. 7. Nomarski micrographs of epilayer surfaces; (a) $d_{epi} < d_{sub}$, FWHM = 25.3″, EPD = 1.3 × 10^5 cm^{-2}; (b) $d_{epi} \leq d_{sub}$, FWHM = 11.8″, EPD = 4.3 × 10^4 cm^{-2}; (c) $d_{epi} \geq d_{sub}$, FWHM = 16.2″, EPD = 3.9 × 10^5 cm^{-2}. Marker represents 20 μm.

cally reduced when using this holder, and strongly depends on resistivity ρ of the Si wafers. Constant surface temperature during growth was achieved with a heavily doped Si wafer ($\rho < 0.02$ Ω·cm).

The reason why the 6.5 μm wavelength was used for the emissivity measurements is that this wavelength matches the peak wavelength of black body emittance around the growth temperature (~180°C). The measured values were <0.1 for 10–20 and 1–3 Ω·cm wafers, 0.45 for the 0.01–0.05 Ω·cm wafer, and 0.85 for the <0.02 Ω·cm wafer. Although these values include some error, due to infrared scattering at the as-rapped back surface of the wafers, they have good agreement with reported data, such as $\varepsilon = 0.026$ for an n-type 30–60 Ω·cm sample and 0.808 for a sample which is heavily doped with arsenic (8.5 × 10^{19} cm^{-3} which is corresponding to $\rho \sim 0.001$ Ω·cm).[11] The reduction in the temperature drop is explained as the reduction in emissivity change for the holder surface during growth. The emissivity of HgCdTe epilayer was measured as 0.70, which was smaller than that of heavily doped Si wafer. That of polycrystalline HgCdTe layer on the Si wafer, however, is considered to be higher than that, so the heavily doped Si wafer was thought to mostly diminish the emissivity change on the holder surface.

QUALITY OF EPILAYERS

The crystal quality of epilayers is affected by both fluxes and growth temperature. The flux contribution, i.e. the contribution from growth rate and Hg flux, to the DCRCs has been investigated and results reported by Faurie et al.[12] In this section, we report the effect of the stability of the growth temperature on the EPDs of epilayers when using the new substrate holder.

The HgCdTe epilayers were grown with the new 3 inch holder and conventional holders for 2 and 3 inch sizes, respectively. Typical growth rate was 5Å/s. During the initial stage of each growth (~60 min), the thermocouple reading was kept constant for the new holder, and was compensated for to maintain the surface temperature for the conventional holders. After that, the pyrometer reading was kept constant for both holders.

The run-to-run EPD distributions are shown in Fig.

5 and Fig. 6 for the new holder and the conventional 2 inch holder. The EPD at the maximum of distribution clearly shifts to about one-fifth the small value for the new holder. In spite of the compensation for the thermocouple reading for the conventional holder, the epilayer crystal quality was degraded. It is considered that a small amount of fluctuation in growth rate can change temperature drop amount enough to degrade epilayers. In the case of the conventional 3 inch holder, no single-crystal epilayer was obtained.

The EPD distribution for the new holder has two peaks. It was found recently that substrate polishing strongly affects the EPD for MBE grown epilayers, and that the substrate-surface conditions vary from lot to lot. Some substrate lots always produce high EPDs of epilayers. Thus, most of the epilayers with EPDs over 1 × 10^6 cm^{-2} can be eliminated by screening such substrate lots. This problem was solved by repolishing these substrates.

The variation in zinc concentration is also a problem for CdZnTe substrates. The zinc concentration determines the amount of misfit $\Delta d/d$. The cross-hatched surface morphology was observed for low zinc concentration (Fig. 7a). On the other hand, many short lines, about 5 μm in length, were observed along the <110> direction for higher zinc concentration (Fig. 7c). The best morphology and the best EPD were obtained for the mostly lattice matched substrate, as shown in Fig. 7b. Needless to say, the dislocation density of substrates strongly affects the EPDs of epilayers. Since the EPDs of the CdZnTe substrates were in the range of 1 × 10^4 ~ 1 × 10^5 cm^{-2}, measured by Nakagawa etch on the side ($\bar{1}\,\bar{1}\,\bar{1}$)A surfaces of the substrates, EPDs of epilayers are limited by substrates.

Finally, etch pit density of 4 × 10^4 cm^{-2} and x-ray FWHM of 12 arc-s were obtained as the best values by the growth method presented in this paper. Although the crystal quality of epilayers strongly depends on that of the substrates used, the EPDs of 10^5 cm^{-2} range were constantly obtained. In most recent growths, low 10^5 cm^{-2} was obtained as a typical value for EPDs.

SUMMARY

High quality $Hg_{1-x}Cd_xTe$ epilayers at a certain specific composition were obtained by precise control of

fluxes for run-to-run growth and surface temperature of the growth front during growth. It is shown that growth rate and composition of epilayers were controlled on the basis of fluxes from CdTe and Te cells, or the growth rate and the composition for the former growth. The sticking-coefficient ratio s_{Cd}/s_{Te_2} was obtained as 0.7 experimentally. Standard deviation $\Delta x/x$ of 3.3% was achieved for 13 samples grown consecutively. A substrate temperature drop during growth was found to be caused predominantly by emissivity change in molybdenum bare surface of the substrate holder. A heavily doped Si water mounted on a substrate holder dramatically reduced the temperature drop. As a result, etch pit density of 4×10^4 cm^{-2} and full width at half-maximum of 12 arc-s for the x-ray double-crystal rocking curve were obtained as the best values. The crystal quality of epilayers, however, was limited by that of CdZnTe substrates.

REFERENCES

1. M. Heiblum, E.E. Mendez and L. Osterling, *J. Appl. Phys.* 54, 6982 (1983).
2. W.E. Hoke, P.S. Lyman and W.H. Labossier, *J. Vac. Sci. Technol.* B5, 734 (1987).
3. J.P. Faurie, R. Sporken, S. Sivananthan and M.D. Lange, *J. Cryst. Growth* 111, 698 (1991).
4. S. Sivananthan and J.P. Faurie, *Ext. Abs. 1992 U.S. Workshop on MCT.*
5. J.S. Chen, U.S. Patent, No. 4,897,152 (Jan. 30, 1990).
6. R.F.C. Farrow, G.R. Jones, G.M. Williams and I.M. Young, *Appl. Phys. Lett.* 39, 954 (1981).
7. C.E.C. Wood, D. Desimone, K. Singer and G.W. Wicks, *J. Appl. Phys.* 53, 4230 (1982).
8. E. Monterrat, L. Ulmer, R. Mallard, N. Magnea, J.L. Pautrat and H. Mariette, *J. Appl. Phys.* 71, 1774 (1992).
9. M.A. Reed, R.J. Koestner, M.W. Goodwin and H.F. Schaake, *J. Vac. Sci. Technol.* A5, 3147 (1987).
10. K. Takahashi, *Molecular Beam Epitaxy Technology,* Kougyou-chousakai Co., written in Japanease, 173 (1984).
11. Y.S. Touloukian and D.P. DeWitt, ed., *Thermophysical Properties of Matter,* Vol. 8, (IFI/Plenum, 1972).
12. J.P. Faurie, S. Sivananthan and P.S. Wijewarnasuriya, *SPIE 1735*, 141 (1992).

Metalorganic Vapor Phase Epitaxy *In-Situ* Growth of p-on-n and n-on-p $Hg_{1-x}Cd_xTe$ Junction Photodiodes Using Tertiarybutylarsine as the Acceptor Source

V. RAO, H. EHSANI, and I.B. BHAT

Electrical, Computer, and Systems Engineering Department, Rensselaer Polytechnic Institute, Troy, NY 12180

M. KESTIGIAN, R. STARR, M.H. WEILER, and M.B. REINE

Loral Infrared Imaging Systems, Lexington, MA 02173

We report arsenic doping of $Hg_{1-x}Cd_xTe$ (0.2 < x < 0.3) grown using metalorganic vapor phase epitaxy (MOVPE) by the direct alloy growth (DAG) technique. Tertiarybutylarsine (TBAs) was used as a precursor for As doping. Several epilayers were grown at different Hg partial pressures and TBAs bubbler temperatures in order to study the doping characteristics. The amount of As incorporated in the layer as well as the acceptor concentration were found to be a strong function of the Hg pressure. Secondary ion mass spectrometric studies on heterostructures showed that the compositional interdiffusion is less than the diffusion of As during growth. P-N junctions were grown using TBAs for the first time and several of these layers were processed to fabricate photodiodes. A p-on-n grown junction photodiode with a cutoff wavelength of 8.2 μm had an R_oA value of 241 ohm-cm^2 at 80K and is the highest reported value for p-on-n DAG-MOVPE devices. Methods to improve the device R_oA of the grown junctions are also proposed.

Key words: As-doping, direct alloy growth, HgCdTe, infrared detectors, metalorganic vapor phase epitaxy (MOVPE)

INTRODUCTION

Photodiodes fabricated using mercury cadmium telluride (HgCdTe) have found wide applications for infrared detection in the 3–5 μm and 8–14 μm regimes. These p-n junctions have been fabricated using mercury vacancies (p-type intrinsic defects), as well as using impurity doping. Doping is commonly achieved either by ion implantation or by the addition of impurities during growth. The most common method of fabricating these devices is by the liquid phase epitaxial (LPE) technique.[1-3] Other methods, such as molecular beam epitaxy (MBE)[4,5] and metalorganic vapor phase epitaxial methods (MOVPE),[6,7] are also being actively pursued. With vapor phase epitaxial methods such as MOVPE and MBE, p-on-n and n-on-p homojunctions and heterojunctions, as well as more advanced multilayer devices such as dual-band detec-

tors,[8] can be grown *in situ* in a single run. In this paper, we will concentrate on these structures grown insitu by MOVPE.

As-grown layers by MOVPE are p-type due to the presence of Hg vacancies which are acceptors and films usually convert to n-type with the carrier concentrations in the high 10^{14} cm^{-3} after annealing under Hg-saturated conditions. Hence, undoped films can be used for the n-type layers. P-type layers can be obtained in MOVPE by extrinsic doping using arsenic. Arsenic doping using AsH_3 as the precursor[9,10] has been demonstrated before. But it is highly toxic and is dangerous because it is generally used from a high pressure cylinder. Hence, there is interest in the use of an alternative source for As. Tertiarybutylarsine (TBAs), an organometallic precursor, seems to be an attractive alternative since it is a liquid at room temperature and is less toxic than AsH_3. It is commercially available in high purity form. Arsenic doping of HgCdTe using TBAs has been reported when layers
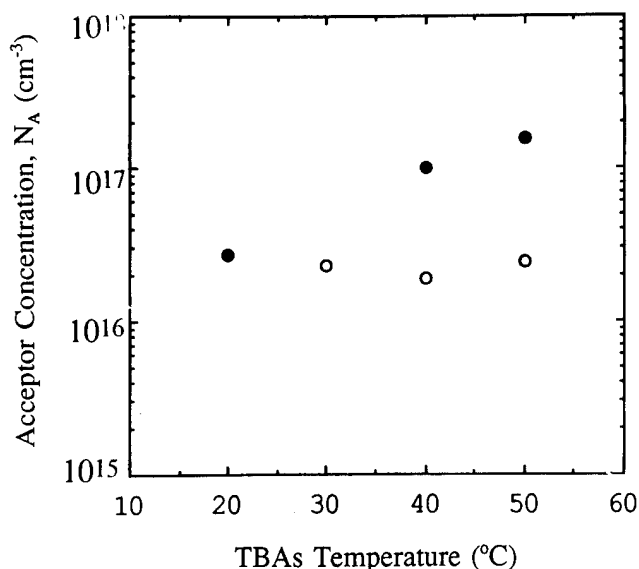
Fig. 1. Acceptor concentration (measured from variable temperature Hall data) as a function of TBAs bubbler temperature in As-doped films. (o): Hg Pressure = 0.07 atm; (●): Hg Pressure = 0.09 atm.
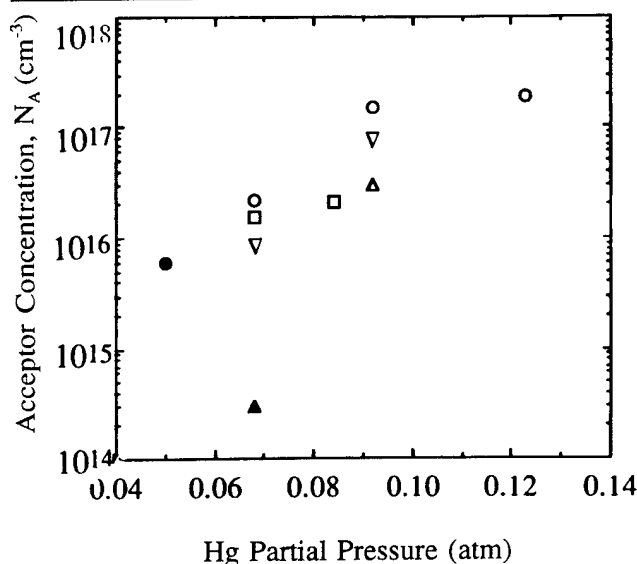
Fig. 2. Acceptor concentration as a function of Hg partial pressure in As-doped films. Closed symbols are n-type and open symbols are p-type. ($\triangle$): TBAs = 20°C; ($\square$): TBAs = 30°C; ($\triangledown$): TBAs = 40°C and (o):TBAs = 50°C.

are grown by the interdiffused multilayer process (IMP)[11] and direct alloy growth (DAG) process.[12] In this paper, we report on a detailed growth study using TBAs as the dopant source and report for the first time on the *in-situ* grown device structures using this source.

EXPERIMENTAL PROCEDURE

HgCdTe layers were grown at 370°C in a vertical flow warm wall reactor at a pressure of 380 Torr. Substrates used were 1 × 1 cm in size, chem-mechanically polished (100) oriented CdTe or CdZnTe, misoriented four degrees toward (110), obtained from II-VI incorporated. Before growth, as received substrates were degreased and etched in Br-methanol

solution to remove about 1 μm thick surface layer. Growth was carried out using the DAG process, involving simultaneous pyrolysis of dimethylcadmium (DMCd), diisopropyltelluride (DIPTe) and elemental mercury. Doping was achieved by the simultaneous introduction of TBAs into the reaction chamber during growth, with TBAs bubbler connected in the "effuser" mode. In this mode, only the outlet of the bubbler is connected to a hydrogen stream leading to the reactor. Typical partial pressures of mercury were between 0.04 and 0.13 atm, calculated using the flow rates of hydrogen through the Hg reservoir. The pressures of DMCd and DIPTe were 5×10^{-5} and 2×10^{-4} atm, respectively. The partial pressure of TBAs was controlled from 2×10^{-6} to 8×10^{-6} atm by controlling the bubbler temperature between 20 and 50°C. The DMCd flow was adjusted in the above growth runs to keep the alloy composition of the epilayers between 0.25–0.33. All layers have an undoped CdTe cap layer of 0.3 μm in thickness. This was grown to prevent unintentional annealing of the layer during cool down after growth.

Fourier transform infrared (FTIR) transmission measurement was used to determine the thickness and alloy composition of these layers. As-grown layers were annealed under Hg saturated conditions to annihilate the Hg vacancies as described in Ref. 13. After annealing, samples were briefly etched in a 1% Br-methanol solution to remove any surface degradation due to annealing. Van der Pauw patterns were then etched on these layers and ohmic contacts were made by evaporating gold. Variable temperature Hall measurements between 20 and 300K were carried out at a magnetic field of 2 kG on most of these samples. These results were analyzed in terms of a three carrier conduction model involving holes, bulk electrons and surface electrons,[13] to determine the acceptor concentration. Secondary ion mass spectroscopy (SIMS) measurements were also carried out at Charles Evans and Associates on several layers to determine the As concentration and $Hg_{1-x}Cd_xTe$ alloy composition profile.

RESULTS

Layer Characteristics

Several undoped layers were grown on CdTe substrates under a Hg pressure of 0.04 atm and annealed under Hg saturated conditions. Most of these layers converted to high mobility n-type with carrier concentrations lower than 1×10^{15} cm^{-3} at 30K. The electrical and structural characteristics of these undoped layers were similar to the results presented elsewhere.[14] However, some of the undoped layers, even though converted to n-type after annealing, had lower electron mobility by a factor of 2–4 compared to the typical bulk value. The reasons for lower mobility in some of these layers are not clear at present.

P-type layers were grown by introducing TBAs during growth. The partial pressure of TBAs in the reactor was controlled by controlling the bubbler

MOVPE *In-Situ* Growth of p-on-n and n-on-p $Hg_{1-x}Cd_xTe$ Junction
Photodiodes Using Tertiarybutylarsine as the Acceptor Source

439

temperature since TBAs was connected in an effuser mode. Control of TBAs partial pressure in the range $2-8 \times 10^{-6}$ atm was possible by varying the bubbler temperature from 20 to 50°C. Figure 1 shows the acceptor concentration obtained from the variable temperature Hall measurements as a function of TBAs temperature. Measurements were made on layers grown at two different mercury partial pressures of 0.07 and 0.09 atm. As shown in the figure, the doping level increased with increasing TBAs temperature and finally saturated when a higher mercury pressure was used, but no change in the doping level was observed at the lower Hg pressure. This indicates that the saturation in the doping depends on the Hg pressure used and the doping efficiency is better at higher mercury pressures.

The effect of Hg partial pressure is more clearly seen in Fig. 2, where the acceptor concentration is plotted as a function of Hg partial pressure. Here, the Hg pressure was varied from 0.05 to 0.13 atm and at each Hg pressure, the layers were grown at various TBAs bubbler temperatures. As can be seen, with increasing Hg pressure, there is a significant increase in the acceptor concentration. At low Hg pressure (<0.06 atm), the doped layers on annealing converted to low mobility n-type. For example, film #549 (x = 0.34) converted to n-type with 77K mobility of 1200 cm²/Vs, whereas film #550 (x = 0.22) showed a mobility of 17000 cm²/Vs at 77K. Both of these were grown with TBAs temperature of 20°C. Another layer grown under the same conditions as above but with a Hg pressure of 0.09 atm remained p-type, with a 77K measured carrier concentration of $3.5 \times 10^{16}/cm^3$.

Secondary ion mass spectroscopy measurements were carried out on As-doped layers to determine the total amount of As incorporated. Figure 3 shows a typical As profile on a doped layer (#525). The higher As concentration seen in the SIMS profile near the surface is believed to be due to SIMS artifacts caused by surface contamination. The As concentrations measured from SIMS are compared to the 80K Hall data measured on several samples. The results are shown in Table I. Note that at higher doping concentrations, close to 100% activation is observed, whereas at lower doping concentration, the activation of As is found to be only 50%. This is in fact contrary to what one would expect, because higher compensation is expected as the doping concentration is increased. The reason for this difference may lie in the accuracy
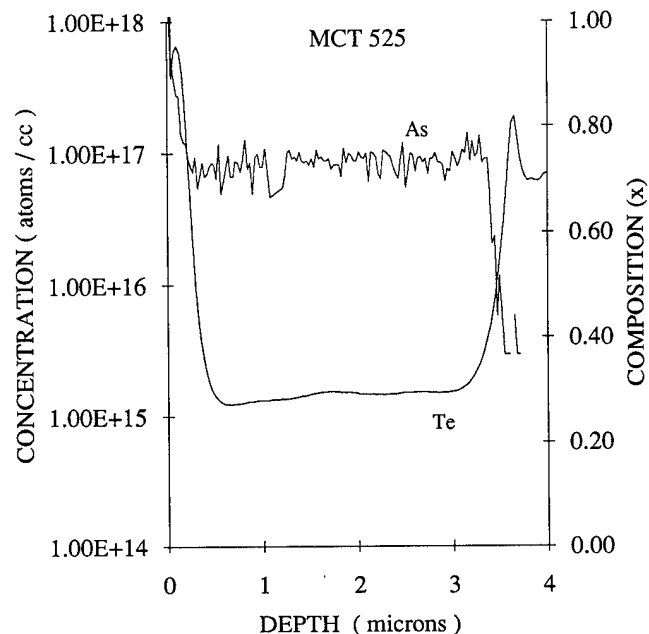
Fig. 3. Secondary ion mass spectrosocpy profile of typical As doped sample (film #525).
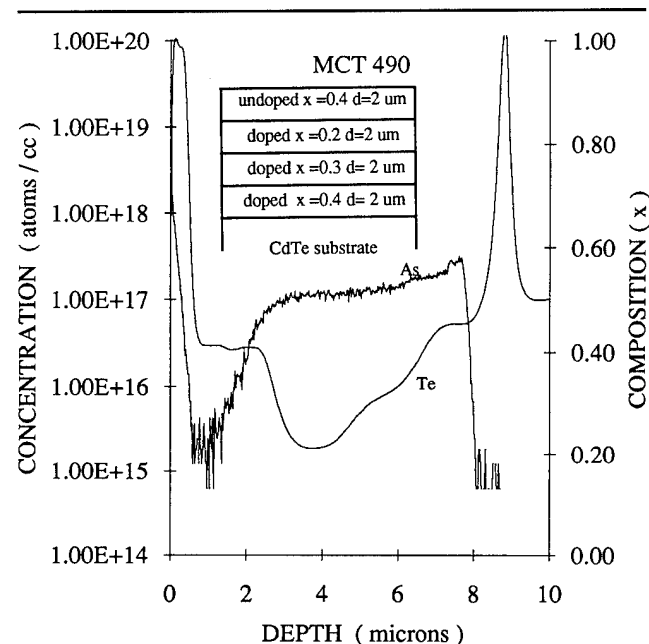
Fig. 4. Secondary ion mass spectroscopy profile of a multilayer structure (film #490) where the composition was changed intentionally from x = 0.4 to 0.2, while keeping all other parameters constant.

Table I. Comparison of Carrier Concentration Measured at 80K and As Concentration Measured by SIMS

Hall Sample	t (μm)	x	Hall (80K) 1/eR$_H$ at 2kG	SIMS as (cm⁻³)	TBAs (°C)	P$_{Hg}$ (atm.)
459	6.6	0.26	2.67×10^{16}	$5-8 \times 10^{16}$	30	.07
460	7.4	0.224	2.11×10^{16}	$3-5 \times 10^{16}$	40	.07
461	5.5	0.223	9.45×10^{16}	$1.3-2.1 \times 10^{17}$	40	.09
525	3.4	0.28	1×10^{17}	1×10^{17}	46	.07

Note: Also shown are the TBAs temperatures and the Hg pressures used during growth.
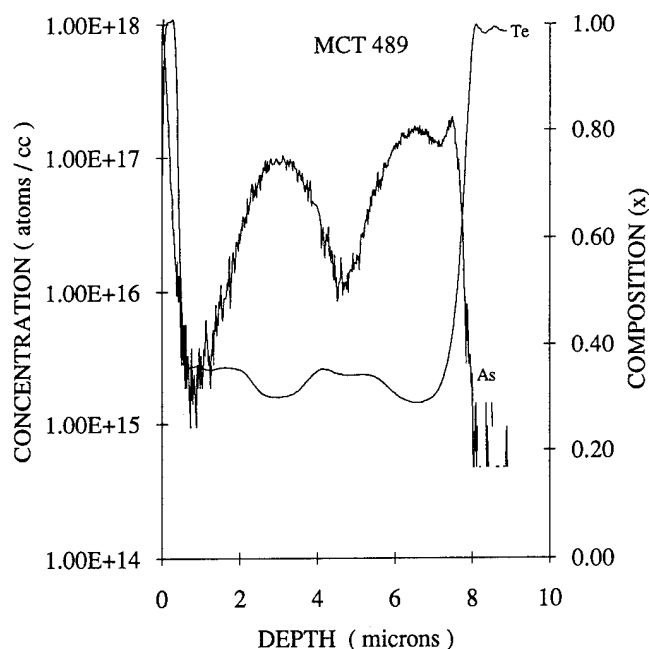
Fig. 5. Secondary ion mass spectroscopy profile of a multilayer film #489 where the TBAs flow was switched on and off alternately.
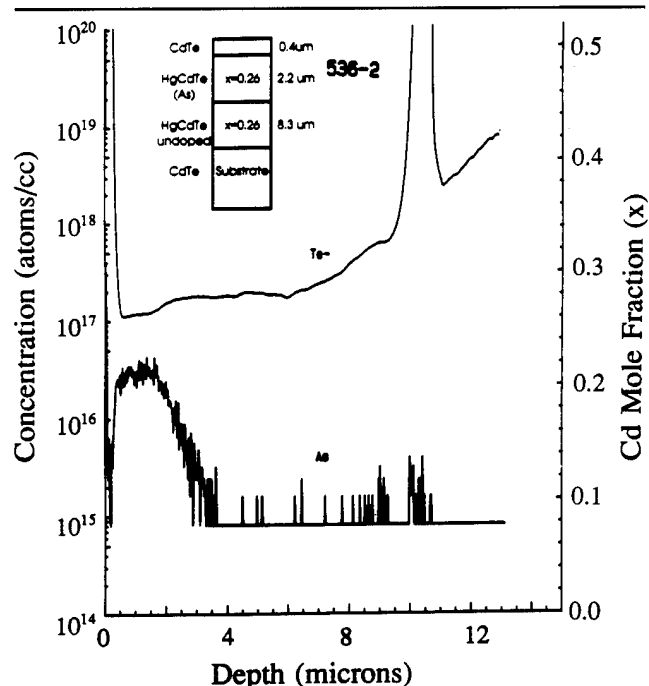
Fig. 6. Secondary ion mass spectroscopy profile of As in doped/ undoped (p-on-n) grown junction.

Fig. 7. Secondary ion mass spectroscopy profile of As in undoped/ doped (n-on-p) grown junction.

of SIMS when the As concentration is below $1 \times 10^{17} cm^{-3}$.

We have also studied the effect of x value on the incorporated As in the layer. This was done by making SIMS measurements on a multilayer structure consisting of several layers grown successively in a single growth run with different x values, followed by an undoped layer. All the reactor conditions except DMCd flow were kept constant. Secondary ion mass spectroscopy profile of this layer (#490) is shown in Fig. 4, with the inset showing the layer structure. The As

incorporation is seen to decrease only slightly when the x value is decreased from 0.4 to 0.2. Since the TBAs pressure used is more than a decade lower compared to DMCd pressure, small changes in the DMCd flow does not seem to have any appreciable effect on the As incorporation. Note that the fall off in the As profile is gradual when TBAs was turned off. We believe this gradual fall off is due to the diffusion of As occurring during the growth of undoped layer. The composition of the undoped layer was found to be much higher than the top most doped layer even though we did not change the DMCd flows when TBAs was turned off.

To study the effect of TBAs flow on the composition, we carried out the following experiment. Keeping all the flows constant, we turned TBAs flow on and off as shown in the inset in Fig. 5. As can be seen from the SIMS data from film #489, the x value drops when TBAs is introduced, and the fall in the x value is greater for heavily doped layers. Once again, we observed a gradual fall off and rise in the As concentration when TBAs was switched off and on.

We grew several p-on-n and n-on-p device structures by growing a doped layer on an undoped layer and vice versa for device fabrication. Figures 6 and 7 show the SIMS profiles with the grown structures shown in the inset. In all cases, significant diffusion of As was observed and we can estimate the diffusion coefficient at the growth temperature using the single Gaussian profile. The value we get is 10^{-13} cm^2/s and this value closely agrees with the diffusion coefficient reported earlier for As in HgCdTe.[15,16] The diffusion coefficient depends on the Hg pressure as well and the value quoted here is at our growth conditions. A similar tail in the As profile was observed when a doped layer was grown on undoped layer indicating that the profile is clearly not due to any "memory

MOVPE *In-Situ* Growth of p-on-n and n-on-p $Hg_{1-x}Cd_xTe$ Junction
Photodiodes Using Tertiarybutylarsine as the Acceptor Source

441

**Table II. Characteristics at T = 80K of Variable-Area HgCdTe Photodiode Arrays, Fabricated
from n-on-p and p-on-n Films Grown *in situ* by DAG MOCVD**

Film	Device Configuration	Substrate	λ_{co} (μm)	$\Delta\lambda_{co}$ (%)	Best R_oA (ohm-cm²)	QE(1D) (%)	L_{OPT} (μm)
493	n-on-p	CdTe(100)4°→(110)	10.3	10	54	14	1
535-1	p-on-n	CdTe(100)4°→(111)B	8.23	5.7	241	41	16
535-2	p-on-n	CdTe(100)4°→(111)B	8.84	1.6	48	51	23

effect" of TBAs in the reactor and is due to the As diffusion at the growth temperature. From SIMS data, we can also see that the alloy interdiffusion rate is lower than the As diffusion rate under our growth conditions. This is beneficial in a p-on-n heterojunction device because the junction will be located in the low x region and not near the graded region where the composition changes from low to high x. This kind of structure is suitable for a high quantum efficiency and a high zero bias resistance device.[15]

Photodiode Characteristics

Characteristics of n-on-p and p-on-n variable-area arrays of ZnS-passivated circular mesa photodiodes fabricated from the DAG MOVPE films described in previous sections of this paper are summarized in Table II. The radius of the diodes varied from 20 to 175 μm. These arrays were bump-interconnected to fanout boards and tested in the backside-illuminated configuration, with the radiation incident on the CdTe substrate surface. The CdTe surface was not anti-reflection coated.

Table II lists the film number, the substrate orientation, the average cutoff wavelength λ_{co} at 80K, the total variation (maximum minus minimum) in percent of λ_{co} over the array, the R_oA at 80K of the best element of the array, the one-dimensional quantum efficiency QE(1D), and the optical collection length L_{OPT}. The latter two quantities were deduced from the dependence of quantum efficiency at 80K on junction area in the variable-area photodiode arrays, as described in Ref. 17.

The spectral response at 80K and I-V curves and R_DA data at 80 and 70K for one element of the n-on-p array from film #493 are shown in Fig. 8. These are the first reported data for an n-on-p HgCdTe junction grown *in situ* by the DAG MOVPE method. The best R_oA product of 54 ohm-cm² is quite respectable, only down by a factor of two from the LPE p-on-n heterojunction state-of-the-art (see Fig. 10). However, reverse bias current increases rapidly with increasing reverse bias voltage, indicative of a defect-generated current mechanism. The quantum efficiency is low and the optical collection length is quite short. These are both consistent with the peak nature of the spectral response shown in Fig. 8, which may be due to floating p-n junctions formed at the interface between the CdTe substrate and the p-type HgCdTe film. Alternatively, they may be due to a short diffusion length in the heavily doped p-type layer, in which SIMS data showed the arsenic concentration to be at
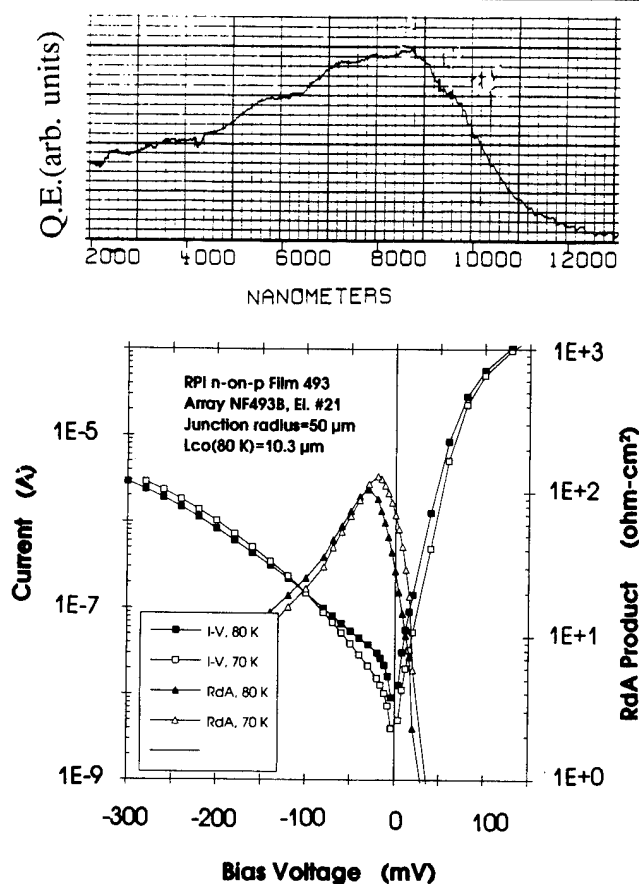
Fig. 8. Relative quantum efficiency spectrum at 80K, and I-V curves and R_DA product data at 80 and 70K, for Element #21 of an n-on-p HgCdTe photodiode array from DAG MOVPE film #493.

1×10^{17} cm⁻³.

The spectral response at 80K and I-V curves and R_DA data at 80 and 70K for one element of a p-on-n array from film #535-1 are shown in Fig. 9. Here the spectral response curves for the p-on-n film is nearly classical in shape, and the quantum efficiency is high, particularly when compared to the maximum quantum efficiency of 80% achievable for a CdTe substrate with no antireflection coating. The optical collection length of 16 μm is generally consistent with the minority carrier diffusion lengths expected for n-type HgCdTe with doping in the 0.5–2 × 10¹⁵ cm⁻³ range. The reverse bias current rapidly increases with reverse bias voltage, indicative of defect-dominated current mechanism. Still it is noteworthy that these are the highest reported R_oA products for *in situ* grown p-on-n HgCdTe junctions by DAG MOVPE.
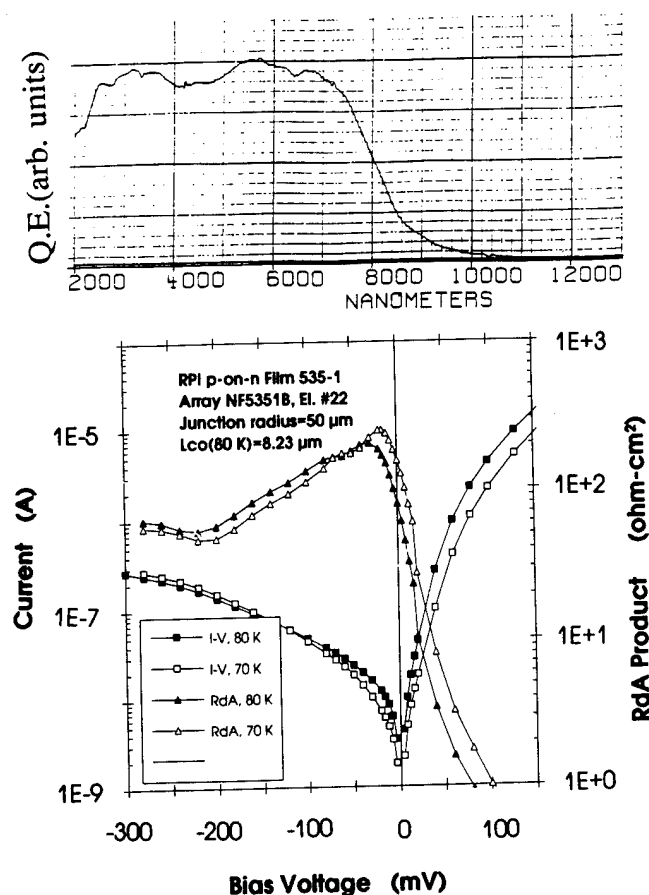
Fig. 9. Relative quantum efficiency spectrum at 80K, and I-V curves and R_0A product data at 80 and 70K, for Element #22 of a p-on-n HgCdTe photodiode array from DAG MOVPE film #535-1.

Fig. 10. Comparison of R_0A data at 80K for n-on-p and p-on-n HgCdTe photodiodes grown *in situ* by DAG MOVPE with the state-of-the-art for p-on-n LPE heterojunctions. The LPE trend line is taken from Ref. 17.

The only previously reported p-on-n HgCdTe photodiodes grown *in-situ* by DAG MOVPE were from the Raytheon group,[18] who quote a R_0A value of 50 ohm-cm^2 at 77K for a cutoff wavelength of 8.1 µm.

The "best element" R_0A data at 80K in Table II for the n-on-p and p-on-n arrays grown *in-situ* by DAG MOVPE are plotted vs cutoff wavelength in Fig. 10. For comparison, the state-of-the-art R_0A values for p-on-n LPE two-layer heterojunctions is indicated by the heavy dashed line. The solid line in Fig. 10 is the calculated R_0A due to diffusion current from the n-layer only, for a thickness of 15 µm and a lifetime determined by the Auger–1 mechanism. The dashed line is the calculated R_0A product due to depletion layer g-r current, for doping levels of 1×10^{15} and 1×10^{16} cm^{-3} on the n-side and p-side, respectively, and for a depleted surface recombination velocity S_0 of 1×10^4 cm/s. The calculated g-r limited R_0A values increase proportionally to the assumed value for S_0. For typical LPE p-on-n heterojunction photodiodes, S_0 is 1000 cm/s or less.

DISCUSSIONS

The effect of Hg pressure seen here is similar to the behavior observed earlier when arsine was used for doping.[19] At higher Hg pressure, Te vacancies present will be high and hence higher amounts of active As

can be incorporated. Thus, the number of active sites available for As incorporation is higher, which means we can dope to higher levels. In addition, from SIMS results, we see that the higher doping level observed is not due to decreased compensation, but due to higher levels of arsenic incorporation in the layer. This can be seen from the results shown in Table I. Layers MCT #460 and MCT #461 were grown under the same TBAs pressure conditions but at different Hg partial pressures of 0.07 atm and 0.09 atm, respectively. The As concentration seen in layer #461 is higher than in layer #460. Hence, Hg partial pressure also affects the total incorporation of As, instead of changing only the compensation ratio.

One conclusion we draw from this study is that the mechanism by which As incorporates into HgCdTe is similar whether TBAs or arsine is used. Similar to the model outlined before,[19] we speculate that DMCd and TBAs could form an adduct in the gas phase. This will reduce the amount of DMCd available for incorporation in the layer, thus lowering the x value when TBAs is introduced. A small percentage of this adduct may land on the surface and decompose into Cd-As. Now, when Cd incorporates into the lattice, As can incorporate into the Te lattice sites. This can explain why As is incorporated mainly in Te sites (where it behaves as an acceptor) in spite of the fact that large concentration of Hg vacancies (V_{Hg}) exist during growth. Also, increasing the Hg pressure will increase the concentration of Te vacancies (V_{Te}), thus increasing the As incorporation. Based on the above model, As will not be incorporated in Hg sites. However, layers doped under low Hg pressure conditions converted to poor quality (low mobility) n-type on annealing (see Results section). Other workers have also reported poor

MOVPE *In-Situ* Growth of p-on-n and n-on-p $Hg_{1-x}Cd_xTe$ Junction
Photodiodes Using Tertiarybutylarsine as the Acceptor Source

443

quality n-type layers when As was used as the p-type dopant in MBE[20] and Te-rich LPE.[21] We speculate that As may incorporate preferentially in Hg sites under very low Hg pressure conditions, owing to the presence of high concentrations of V_{Hg} (in comparison to V_{Te}). These inactive As may be responsible for the poor quality of the material when doped under low Hg pressure. Secondary ion mass spectroscopy measurements should be carried out to confirm whether As is present in these layers. The Hg pressure at which p-to-n type transition occurs may depend on the TBAs pressure as well.

The R_oA values of the devices reported here are at least a factor of two lower compared to those made from the best quality LPE layers. We believe there are two reasons for the poor quality of the devices. First, these layers have higher density of defects (low 10^6 cm^{-2} vs low 10^5 cm^{-2}) compared to LPE layers. Another important reason we speculate is that the diffused As present near the junction is inactive or n-type. Since the tail in the As profile, we have seen is due to diffusion under low Hg pressure condition, most of these As are in Hg sites rather than in active Te sites. Generally, an activation anneal at higher temperature (>400°C) is required to activate these diffused As. Hence, a higher temperature Hg-rich activation anneal followed by a low temperature stoichiometric anneal may improve the junction characteristics.

CONCLUSIONS

We have demonstrated that TBAs in the effuser mode can be used as an arsenic source for direct alloy growth of MOVPE HgCdTe p-on-n and n-on-p in-situ grown junctions. The acceptor level could be controlled in the range $1.2 \times 10^{16}/cm^3$ to $2.2 \times 10^{17}/cm^3$, by either increasing the TBAs partial pressure or by increasing the Hg partial pressure. We have found that As incorporation is a stronger function of Hg partial pressure than that of TBAs pressure. Layer grown at a low Hg pressure of ≤0.06 atm showed n-type behavior, possibly caused by the incorporation of As in Hg sites. From Hall and SIMS data, we estimate that more than 50% of incorporated As is active. From SIMS profiles, the diffusion coefficient of arsenic for x = 0.24 material was calculated to be 10^{13} cm^2/s at 370°C, under our growth conditions. Both p-on-n and n-on-p grown junctions were processed to fabricate devices and the results show that DAG MOVPE can be used to fabricate advanced device structures. Further improvements will be necessary to fully exploit this technology.

REFERENCES

1. T. Tung, M.H. Kalisher, A.P. Stevens and P.E. Herning, *Mat. Res. Soc. Symp. Proc.* 90, 321 (1987).
2. C.C. Wang, *J. Vac. Sci. Technol.* B9, 1740 (1991).
3. G.N. Pultz, P.W. Norton, E.E. Krueger and M.B. Reine, *J. Vac. Sci. Technol.* B9, 1724 (1991).
4. O.K. Wu, G.S. Kamath, G.R. Chapman, S.M. Johnson, J.M. Peterson, B.A. Baumgratz, J.W. Wilson and C.A. Cockrum, *J. Electron. Mater.* 24, 423 (199).
5. J.M. Arias, J.G. Pasko, M. Zanadian, S.H. Shin, G.M. Williams, L.O. Bubulac, R.E. DeWames and W.E. Tennant, *Appl. Phys. Lett.* 62, 976 (1993).
6. P. Mitra, T.R. Schimert, F.C. Case, R. Starr, M.H. Weiler, M. Kestigian and M.B. Reine, *J. Electron. Mater.* 24, 663 (1995).
7. R. Korenstein, P.H. Hallock, D.L. Lee, E. Sullivan, R.W. Gedridge, and K.T. Higa, *J. Electron. Mater.* 22, 853 (1993).
8. M.B. Reine, P.W. Norton, R. Starr, M.H. Weiler, M. Kestigian, B.L. Musicant, P. Mitra, T. Schimert, F.C. Case, I.B. Bhat, H. Ehsani and V. Rao, *J. Electron. Mater.* 24, 671 (1995).
9. N.R. Taskar, I.B. Bhat, K.K. Parat and S.K. Ghandhi, *J. Vac. Sci. Technol.* B9, 1705 (1991).
10. P. Capper, C.D. Maxey, P. Whiffin and B.C. Easton, *J. Cryst. Growth* 97, 833 (1989).
11. D.D. Edwall, J.S. Chen and L.O. Bubulac, *J. Vac. Sci. Technol.* B9, 1691 (1991).
12. J. Elliot and V.G. Kreismanis, *J. Vac. Sci. Technol.* B10, 1428 (1992).
13. K.K. Parat, N.R. Taskar, I.B. Bhat and S.K. Ghandhi, *J. Cryst. Growth* 106, 513 (1990).
14. I. Bhat, *J. Cryst. Growth* 117, 1 (1992).
15. D. Chandra, M.W. Goodwin, M.C. Chen and J.A. Dodge, *J. Electron. Mater.* 22, 1033 (1993).
16. L.O. Bubulac, D.D. Edwall, E.R. Gertner, S.J.C. Irvine and S.H. Shin, *J. Electron. Mater.* 24, 617 (1995).
17. M.B. Reine, K.R. Maschhoff, S.P. Tobin, P.W. Norton, J.A. Mrozkowski and E.E. Krueger, *Semicond. Sci. Technol.* 8, 788 (1993).
18. S. Oguz, R.J. Olson, D.L. Lee, L.T. Specht and V.G. Kreismanis, *Proc. SPIE* 1307, 560 (1990).
19. N.R. Taskar, I.B. Bhat, K.K. Parat, S.K. Ghandhi and G.J. Scilla, *J. Cryst. Growth* 110, 692 (1991).
20. M. Boukerche, P.S. Wijewanasuriya, S. Sivananthan, I.K. Sou, Y.J. Kim, K. Mahavedi and J.P. Faurie, *J. Vac. Sci. Technol.* A6, 2830 (1988).
21. H.R. Vydyanath, J.A. Ellsworth and C.M. Devaney, *J. Electron. Mater.* 16, 13 (1987).

Application of Spectroscopic Ellipsometry for Real-Time Control of CdTe and HgCdTe Growth in an OMCVD System

S. DAKSHINA MURTHY and I.B. BHAT

Electrical, Computer, and Systems Engineering, Rensselaer Polytechnic Institute, Troy, NY 12180

B. JOHS, S. PITTAL, and P. HE

J.A. Woollam Company, 650 J Street, #39, Lincoln, NE 68508

A multi-wavelength *in-situ* spectroscopic ellipsometer system is described. The hardware can acquire accurate ellipsometric data at 44 wavelengths in less than one second, is simple and compact, and is well suited for *in-situ* monitoring of chemical vapor deposition. The software used for data analysis is capable of determining the growth rate and composition of the growing layer in real time. These tools were used to study the organometallic chemical vapor deposition of CdTe, HgTe, and HgCdTe on GaAs. We could obtain the dielectric constants of these materials at the growth temperature and also the growth rate and composition of the layers in real time. Feedback control of CdTe growth was performed by connecting an analog control voltage line from the data acquisition/ analysis computer to the dimethylcadmium mass flow controller. Using dielectric constants of HgCdTe for two different compositions at the growth temperature, composition control of HgCdTe was attempted in a similar manner.

INTRODUCTION

Many compound semiconductors, such as HgCdTe (MCT) are now grown by the chemical vapor deposition (CVD) process. During the growth, various parameters such as layer thickness, composition, interface quality, dopant incorporation, and quality of the (hetero) epitaxial layer need to be monitored and controlled. The growth mechanism also needs to be well understood. An *in-situ*, noninvasive, real-time monitoring technique will be well suited for this task.

Reflection high energy electron diffraction (RHEED) is the usual technique employed in high-vacuum growth environments such as molecular beam epitaxy (MBE), but by its very nature is unsuitable for general CVD systems. However, optical monitoring techniques such as reflectance difference spectros-

copy (RDS), laser reflectance, and spectroscopic ellipsometry have been used to study growth in CVD systems.

Reflectance difference spectroscopy[1] is the optical analog of RHEED and is surface sensitive. By measuring the polarization anisotropy of near-normal incident light, the nature and time evolution of changes at the surface may be monitored. Since it is mainly a surface sensitive technique, it is not suited for controlling bulk properties like layer thickness and composition. Laser reflectometry[2] monitors the near-normal reflectance intensity and is mainly sensitive only to the thickness of the growing layer. Spectroscopic ellipsometry[3] is both bulk and surface sensitive and can resolve both thickness and composition and also yield information on surface roughness. However, this is a highly computational intensive technique and only recently, with advances in computer hardware and software, can the data be acquired and
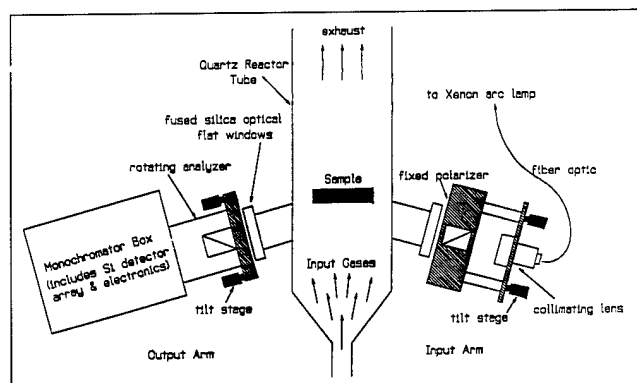
Fig. 1. Spectroscopic ellipsometer mounted on CVD system.

processed within a fraction of a second. This has made possible the use of this technique in a real-time environment. The usefulness of this technique has been demonstrated previously,[4–6] both in MBE and CVD systems.

HARDWARE

Figure 1 shows the main components of ellipsometer hardware positioned around a modified reactor tube to allow *in-situ* measurements during chemical vapor deposition growth.[7] The fused silica optical flat windows were flushed with H_2 to prevent window fogging. The ellipsometer was employed in the standard rotating analyzer configuration, which is well suited for acquiring data in growth environments.[8] A Xenon arc lamp acts as a wide spectral source. Spectral resolution is obtained using a diffraction grating monochromator placed after the rotating analyzer. Normally, doing this would introduce large errors due to the polarization dependent sensitivity of the monochromator. These errors are eliminated using a correction formula derived by Russev[9] and by the use of a regression calibration method to calibrate the ellipsometer.[10] The monochromator contains a 46 element Si photodiode array. Filtering and multiplexing electronics are connected to 44 of these elements, allowing the signal to be digitized at 44 wavelengths (ranging from 404 to 740 nm) within a single analyzer revolution (0.05 s). Data can be acquired and analyzed within a fraction of a second, but highly accurate ellipsometric data can be obtained by averaging data over 20 analyzer revolutions, which takes about one second.

An Intel 80486 based computer, running Microsoft Windows™ was used for instrument control, data acquisition, data analysis, and process control feedback.

DATA ANALYSIS

A Fourier analysis is performed on the intensity signal of all 44 wavelengths sampled sequentially. The coefficients of the second harmonics of the analyzer rotation frequency are obtained and the ellipsometric parameters Ψ and Δ are extracted from them. These are linked to the growth behavior using three different methods of data analysis. In all meth-

ods, exact Fresnel expressions are used to calculate the model and the Levenberg-Marquadt regression algorithm[11] is used to fit the model to the data.

Prior to attempting feedback control, we need the dielectric constants of the material at the growth temperature (and at different compositions, if an alloy). We used the following modeling techniques to obtain them.

We denote the first method as the "Standard Model" method. Here, a user-defined model for the various layers is fit to ellipsometric data at one particular instant. This is the typical analysis method for ellipsometric data, and may be used to obtain the dielectric constants of the substrate, temperature of the substrate, film thickness, and surface roughness. The desired material can be grown optically thick, treated as a substrate and its optical constants obtained at the growth temperature.

We denote the second method as the "Growth Rate" method. The time evolution of the ellipsometric data acquired during growth can be used to determine the optical constants and the growth rate. A model is constructed where the film, with unknown dielectric constants, grows at a certain rate on a substrate whose dielectric constants are known. The ellipsometric data generated by this model, as a function of time, is then fit to the experimental ellipsometric data measured during deposition. We can use this method to determine the average growth rate and dielectric constants of an unknown epilayer. This is based on the same principles as a multiple sample analysis method described by McGahan et al.[12]

In order to perform control, we also need the growth rate and/or composition in real time. For this, we use the third method, namely the "Virtual Interface" method, first proposed by Aspnes.[13] This makes use of Aspnes' common pseudo-substrate approximation, but the analysis proceeds in a slightly different manner. In this method, two sets of ellipsometric data, acquired at consecutive sampling times, are used to determine the film growth rate and/or composition within that time interval. The ellipsometric data at the first sampling time, when transformed into pseudo-dielectric functions, defines a "Virtual Interface" which is assumed to contain the entire growth history of the sample. This is not exact, but works well for the growth of semiconductors on semiconductors. A model consisting of the virtual interface with an overlayer is then fit to the ellipsometric data acquired at the second sampling time by suitably adjusting the overlayers thickness and/or composition. This method is used here to determine the instantaneous growth rate and composition of the layers, and also used for the closed loop control.

EXPERIMENTAL RESULTS

CdTe Growth Monitoring and Control

Our system was first used for *in-situ* monitoring of CdTe grown on GaAs substrates. GaAs dielectric constants at 350°C were determined using "Standard

Model" analysis prior to growth. CdTe was then grown on (100) GaAs, misoriented 6 or 10° toward 110 at 350°C in an atmospheric pressure reactor with a partial pressure of 1×10^{-4} atm for dimethylcadmium (DMCd) and 3×10^{-4} atm for diisopropyltelluride (DIPTe). Owing to the reduced capability of our instrument at the time, ellipsometric Ψ and Δ data at 12 wavelengths (from 404 to 740 nm) were acquired every three seconds. The CdTe optical constants at 350°C were then determined by "Growth Rate" analysis using only data taken between 4 and 20 min. The growth rate was determined to be 2.48Å/s which agreed with the post-deposition analysis. Using the dielectric constants obtained above, a "Standard Model" fit was performed for CdTe layers grown during the first 20 min. It was necessary to include a "surface roughness" layer consisting of a 50% mixture (by volume) of CdTe and void (using the Bruggeman's effective medium approximation),[14] along with the GaAs substrate and CdTe epilayer, to accurately model the growth. Figure 2 shows the film roughness as a function of time. A large roughness layer is seen in the initial phase of growth which may be explained by the process of CdTe film nucleation on the bare substrate. The ellipsometric Ψ data measured during deposition and analyzed using standard model is shown in Fig. 3.

Having characterized the growth of CdTe on GaAs using the post-deposition analysis of *in-situ* data, an attempt was made to perform real-time monitoring and feedback control. The determination of the dynamic growth rate of CdTe was done using the previously determined CdTe optical constants and the real-time "Virtual Interface" method.

CdTe was grown on GaAs under similar conditions as described previously. Feedback control of growth was then attempted as follows: for the first four minutes of growth, the DMCd mass flow controller was set at 65%, resulting in an average growth rate of 4.8Å/s. At t = 4 min, the computer was given control of the DMCd MFC via an analog (0–5 V) line and instructed to reduce the growth rate to 2.8Å/s. As can be seen from Fig. 4, the CdTe growth rate subsequently dropped, undershot the desired value, and stabilized at a rate of about 2.8Å/s. The processing time required was insignificant, since the ellipsometric data at 12 wavelengths were acquired, analyzed, and feedback voltage provided every 3.15 s. A simple proportional control algorithm was used, which resulted in undershoot. Post-deposition "Standard Model" analysis of this run yielded the thickness vs time curve in Fig. 5. The kink in the growth rate around t = 4 min confirms the demonstration of feedback control.

Growth of Optically Thick HgTe and CdTe

The next step was to monitor the growth of both the constituents of HgCdTe, namely HgTe and CdTe, before an attempt was made on the control of HgCdTe. Alternate layers of CdTe and HgTe were grown on (100) GaAs misoriented 10° toward (110) at 350°C. The partial pressures of DMCd and Hg were 4.5×10^{-5} atm and 0.02 atm, respectively. A partial pressure of 4.7×10^{-4} atm for DIPTe was used for both materials.

Fig. 2. Roughness layer on CdTe during deposition.
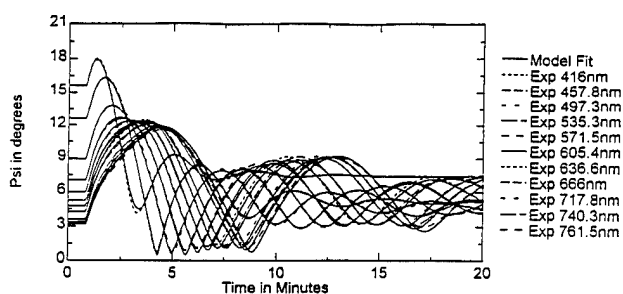
Fig. 3. Ellipsometric Ψ data obtained during growth of CdTe on GaAs.
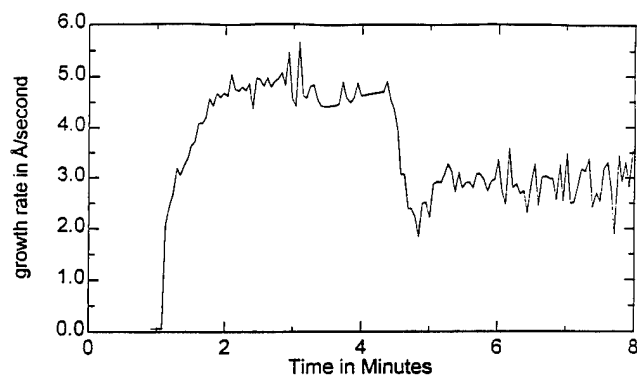
Fig. 4. Growth rate of CdTe determined in real-time during feedback control experiment.
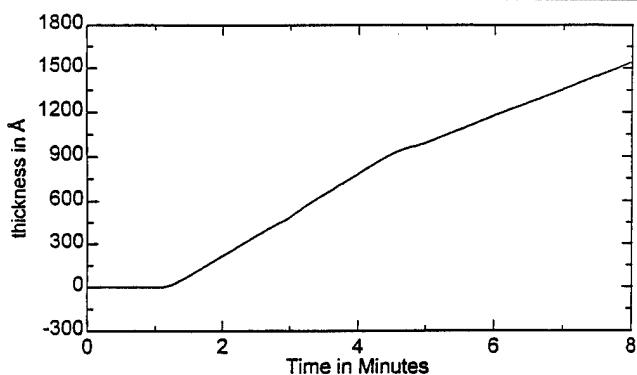
Fig. 5. CdTe film thickness as a function of time during feedback control deposition.

a

b
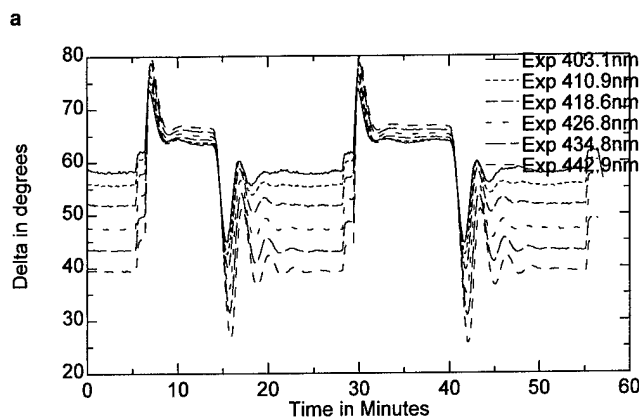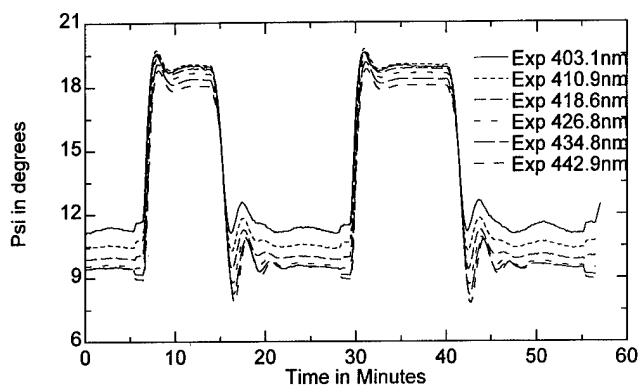
Fig. 6. Ellipsometric Ψ and Δ data for alternate layers of optically thick HgTe and CdTe grown on GaAs.

The portion of the reactor wall before the susceptor was heated to 165°C and the Hg source was maintained at 275°C.

Ellipsometric data was acquired throughout the growth (Fig. 6). As can be seen from Fig. 6, the ellipsometric data for optically thick CdTe and HgTe are the same in their respective layers for the wavelengths of interest. The trajectories for the data for each material as a function of time show excellent correspondence in all their respective layers. This shows that both the material grown and the data acquired and processed by the ellipsometer are quite reliable. We can, therefore, attempt to monitor the growth of HgCdTe with some confidence.

Monitoring of Direct Alloy Grown HgCdTe

HgCdTe was grown on GaAs using the direct alloy growth technique at 350°C. A CdTe buffer was first grown, followed by a HgCdTe layer and a CdTe cap at the end. The partial pressures of DMCd, DIPTe, and Hg used in all cases were 4.5×10^{-5} atm, 4.7×10^{-4} atm, and 0.02 atm, respectively. The wall was kept at 165°C. The objective was to obtain the optical constants for the optically thick HgCdTe layer at the growth temperature. Repeating this at different compositions would permit the compilation of a library of optical constants at different compositions. These could then be suitably incorporated for feedback control.
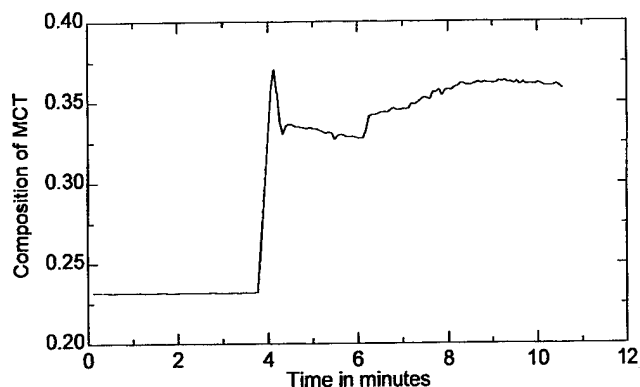
Fig. 7. Composition of $Hg_{1-x}Cd_xTe$ determined in real time during control experiment.

Control of DAG Growth of HgCdTe

Having obtained optical constants for HgCdTe at the growth temperature at two compositions, an attempt was made to control the composition. The computer was given control of the DMCd MFC and optically thick HgCdTe of composition x = 0.23 was first grown. A step in the composition was then fed to the computer, which tried to control it to reach x = 0.35. As can be seen from the dynamic composition data shown in Fig. 7, the target composition is reached. We observe an abrupt change in the composition at around t = 6 min, the cause of which could not be explained. The control voltage was generated using a proportional control algorithm. In order to obtain the optical constants of HgCdTe at compositions other than those measured, a critical point dependent spectrum shifting weighted algorithm (from Snyder)[15] was used.

CONCLUSIONS

We have demonstrated the control of CVD growth using an integrated multi-wavelength, *in-situ* ellipsometer system with fast data acquisition, analysis, and real-time feedback capability. The ellipsometer was used for real-time monitoring and control of CdTe, HgTe, and HgCdTe growth on GaAs by OMCVD. In order to perform very reliable and accurate control of HgCdTe growth, the following steps are required: an extensive library of growth temperature optical constants as a function of composition is needed; system identification from a control viewpoint is needed to ensure proper and fast response. These efforts are now underway. The system is versatile so that the method outlined is applicable to any CVD system.

ACKNOWLEDGMENT

REFERENCES

1. D.E. Aspnes, R. Bhat, C. Caneau, E. Colas, L.T. Florez, S.

Gregory, J.P. Harbison, I. Kamiya, V.G. Keramidas, M.A. Koza, M.A.A. Pudensi, W.E. Quinn, S.A. Schwarz, M.C. Tamargo and H. Tanaka, *J. Cryst. Growth* 120, 71 (1992).

2. S.J.C Irvine, J. Bajaj, H.O. Sankur and S.A. Svoronos, *J. Electron. Mater.* 22, 899 (1993).

3. R.M.A. Azzam and N. M. Bashara, *Ellipsometry and Polarized Light,* (Amsterdam: North-Holland, 1977).

4. J.B. Theeten, F. Hottier and J. Hallais, *J. Cryst. Growth* 46, 245 (1979).

5. D.E. Aspnes, W.E. Quinn and S. Gregory, *Appl. Phys. Lett.* 57, 2707 (1990).

6. D.R. Rhiger, *J. Electron. Mater.* 22, 887 (1993) (and references therein).

7. B. Johs, S. Pittal, D. Doerr, I. Bhat and S. Dakshina Murthy, *Thin Solid Films* 234, 293 (1993).

8. R.W. Collins, *Rev. Sci. Instru.* 61, 2029 (1990).

9. S.H. Russev, *Appl. Opt.* 28, 1504 (1989).

10. B. Johs, *Thin Solid Films* 234, 395 (1993).

11. W.H. Press, B.P. Flannery, S.A. Teukolsky and W.T. Vetterling, *Numerical Recipes in C* (Cambridge University Press, 1988).

12. W.A. McGahan, B. Johs and J.A. Woollam, *Thin Solid Films* 234, 443 (1993).

13. D.E. Aspnes, *Appl. Phys. Lett.* 62, (4), May (1993).

14. D.A.G. Bruggeman, *Ann. Phys.* (Leipzig), 24, 636 (1935).

15. P.G. Snyder, J.A. Woollam, S.A. Alterovitz and B. Johs, *J. Appl. Phys.* 68, 5925 (1990).

Growth of High Quality CdTe and ZnTe on Si Substrates Using Organometallic Vapor Phase Epitaxy

WEN-SHENG WANG and ISHWARA BHAT

Electrical, Computer, and Systems Engineering Department, Rensselaer Polytechnic Institute, Troy, NY 12180

Epitaxial (100) CdTe and ZnTe layers with high crystalline quality have been grown on Si substrates by atmospheric pressure organometallic vapor phase epitaxy (OMVPE). A thin Ge interfacial layer grown at low temperature was used as a buffer layer prior to ZnTe and CdTe growth. The layers were characterized by Nomarski optical microscopy and double crystal x-ray diffraction. Double crystal rocking curves with full width at half maximum of about 110 and 250 arc-sec have been obtained for a 7 μm thick ZnTe layer and a 4 μm thick CdTe layer, respectively. The results presented demonstrate a novel method of *in-situ* Si cleaning step without a high temperature deoxidation process to grow high quality CdTe and ZnTe on Si in a single OMVPE reactor.

Key words: CdTe/Si, Ge/Si, heteroepitaxy, organometallic vapor phase epitaxy (OMVPE)

INTRODUCTION

Heteroepitaxy of CdTe on foreign substrates has been carried out for several years, since CdTe is not available in large area wafer form. These substrates are to be used for eventual growth of HgCdTe. Silicon substrates are the best choice for heteroepitaxy of CdTe and HgCdTe, since the thermal mismatch problems can be reduced when Si signal processing electronics is In-bonded to detector arrays in hybrid infrared focal plane array fabrication. In addition, it is possible to integrate the HgCdTe infrared sensors and signal processing electronics in the same wafer, if high quality HgCdTe can be grown on Si.

The principal difficulties for growing high quality CdTe arise from the presence of strong native oxide on Si, and the problems associated with lattice and thermal mismatch between CdTe and Si. Several reports in the literature[1,2] claim that hydrogen passivated Si surface can be prepared by etching Si in a dilute HF solution and this passivated Si is stable up to several minutes in air. If loaded quickly into an ultra high vacuum (UHV) chamber, an oxide free surface can be obtained. However, presence of sub-monolayer oxide cannot be ruled out because of variations in processing conditions. In addition, the strong Si-H bonds may prevent single crystal CdTe growth unless hydrogen is desorbed from Si. Absence of epitaxy caused by hydrogen has been observed in Si homoepitaxy,[3] and similar problems associated with Si-H bonds can be expected in CdTe growth on Si by organometallic vapor phase epitaxy (OMVPE).

There are two approaches to achieve CdTe growth on Si. In molecular beam epitaxy (MBE)[4] and UHV[5] systems, Si substrates are heated to high temperature (>850°C) to remove Si surface oxide, and CdTe is
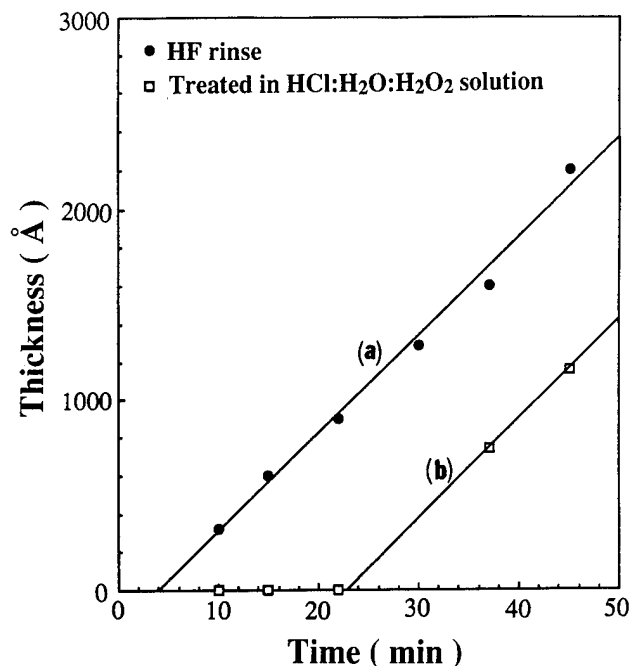
Fig. 1. The Ge layer thickness as a function of growth time. (a) Si substrate was dipped in dilute HF:methanol solution prior to Ge growth. (b) Si substrate treated in $HCl:H_2O_2:H_2O$ (4:1:1 by volume) at 90°C for 10 min before Ge growth.
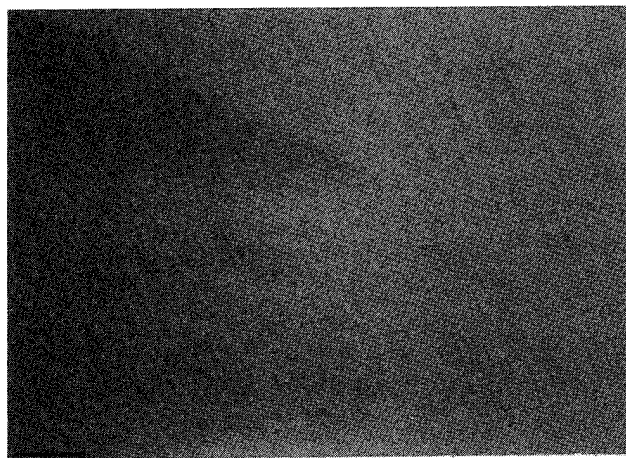
Fig. 2. Surface morphology of a 7 μm thick ZnTe layer grown on (100)Si, misoriented nine degrees toward [011]. The marker represents 25 μm.

deposited on these cleaned surfaces. However, this high temperature baking step is not preferred in OMVPE because Te reacts with Si.[6] Therefore, any adsorbed Te in the reactor from a previous run, or if the reactor is not fully cleaned of Te, may react with Si resulting in "pitted" Si surface. In addition, this high temperature deoxidation step should be avoided completely if signal processing electronics are already present in the wafer. Another approach is to use commercially available GaAs/Si substrate in OMVPE.[7] Since both Ga and As are dopant impurities in CdTe and HgCdTe, the complete structure (HgCdTe/CdTe/GaAs/Si) cannot be grown in a single reactor. Moreover, use of GaAs/Si substrate significantly increases the starting substrate cost.

Most of the reported CdTe layers grown on Si (100) substrate are of (111) orientation. This orientation suffers from high density of twin defect formation, which does not occur in (100) oriented epitaxy. Hence, it is important to study the growth of (100) oriented CdTe on (100) Si for the subsequent growth of HgCdTe. This orientation can also be used for Hg-rich liquid phase epitaxy (LPE) growth of HgCdTe. In this paper, a novel method to grow high quality (100) ZnTe and CdTe on (100) Si substrates by OMVPE without using high temperature deoxidation, namely by growing a Ge interfacial layer on Si before ZnTe and CdTe growth, will be reported.

EXPERIMENTAL DETAILS

All the studies reported here were carried out in a 2″ diameter reactor operated under atmospheric pressure. No load lock or glove box was used. Hence, the system and the susceptor were exposed to air during sample loading. The graphite susceptor was heated using a radio frequency generator. (100)Si wafers, misoriented nine degrees toward [011] direction, were used. The substrates were cleaned by using the process similar to that of Ishizaka et al.[8] Finally, the native oxide was removed by dilute hydrofluoric acid (HF) solution before the substrates were loaded into the reactor. Ge growth on Si was carried out by the decomposition of GeH_4 gas at a temperature range from 420 to 700°C. ZnTe and CdTe films were grown in the same reactor on Ge/Si substrates using dimethylcadmium (DMCd), dimethylzinc (DMZn), and diethyltellurium (DETe) as the precursors. The ZnTe growth temperature was 420°C and that of CdTe was 360°C. The surface morphology of layers was examined by Nomarski optical microscopy. The crystal quality of films was measured by single and double crystal x-ray diffraction.

RESULTS AND DISCUSSIONS

It has been reported by Takahasi et al.[9] that germane gas reacts with native oxide (SiO_x) to form volatile GeO resulting in clean Si surface coated with a thin layer of Ge. Their studies were carried out in a UHV chemical vapor deposition (CVD) system in the 350 to 500°C range. To investigate Si surface deoxidation at atmospheric pressure, Ge growth on Si was studied at 450°C. Figure 1 shows the Ge thickness grown on Si at 450°C as a function of time. For curve (a), there is a delay time of about 4 min before growth starts. For curve (b), the Si substrates were treated with a $HCl:H_2O:H_2O_2$ solution which leaves about 8Å thick native oxide.[8] A 23 min delay time occured when this intentional oxide layer was grown. When thermal 1000Å thick SiO_2 covered Si was used, no Ge growth was observed even after one hour of growth. The delay time observed was thought to be caused by the time required to reduce the native oxide by adsorbed germane molecules. It was speculated that Ge growth starts when all the SiO_x is desorbed. However, a quantitative secondary ion mass spectroscopy (SIMS) measurement is required to ascertain the role of

GeH$_4$. Using a two-step growth process, a high quality Ge layer on Si was obtained, with featureless surface morphology.[10] First, a 300Å thick Ge layer was grown at 450°C, followed by a thicker layer at 650°C. The x-ray full width at half maximum (FWHM) of a 1 μm thick Ge epilayer was about 140 arc-sec.

CdTe growth on Ge/Si was carried out at temperatures from 360 to 450°C. For a growth temperature of 360°C, the CdTe layer was (111) dominated with a small fraction of (100) phase. When the growth temperature was increased, the orientation of the layer changed from (111) to (100). At 420°C or higher, the CdTe layers become (100) single crystalline. This result is similar to the result reported earlier for CdTe growth on Ge substrate.[11] The change of CdTe orientation from (111) to (100) at about 400°C may be attributed to the formation of Ge-Te interfacial layers which promote (100) growth. However, when a thin layer of ZnTe was deposited prior to CdTe growth, only (100) CdTe was obtained at all growth temperatures. Hence, the growth of ZnTe on Ge/Si was investigated to control the CdTe orientation. Single crystal (100) ZnTe with high crystal quality could be grown on Ge/Si substrates at a temperature range from 360 to 450°C, with the optimum layers at 420°C. The surface morphology and the double crystal x-ray diffraction data for a 7 μm thick ZnTe layer are shown in Fig. 2 and Fig. 3. To our knowledge, the x-ray FWHM of 110 arc-sec is the best reported result for ZnTe grown on Si substrate.

Figures 4 and 5 show the Nomarski contrast micrograph and the double crystal xray diffraction of a 4 μm thick CdTe layer grown on Si with the ZnTe/Ge interfacial layer, demonstrating the excellent surface morphology and high crystalline quality. These results represent the highest crystalline quality ever obtained for CdTe on Si substrates grown in a single OMVPE reactor, and are comparable in quality to the recent results of CdTe grown on ZnTe/Si substrate using MBE.[12] The thickness of the Ge layer is not critical, and the results are the same for Ge layer of 300Å or 1 μm.[13] One concern we have when a polar semiconductor is grown on a nonpolar semiconductor is the likelihood of having antiphase domains (APD). We investigated this using a selective etching solution, E-Ag1 (0.5 mg AgNO$_3$ + 10cc E-solution, E-solution: 10cc HNO$_3$ + 20cc H$_2$O + 4g K$_2$Cr$_2$O$_7$).[14] Figures 6a and 6b show the etched surfaces of CdTe grown on (100) Si and (100) Si which had a misori-
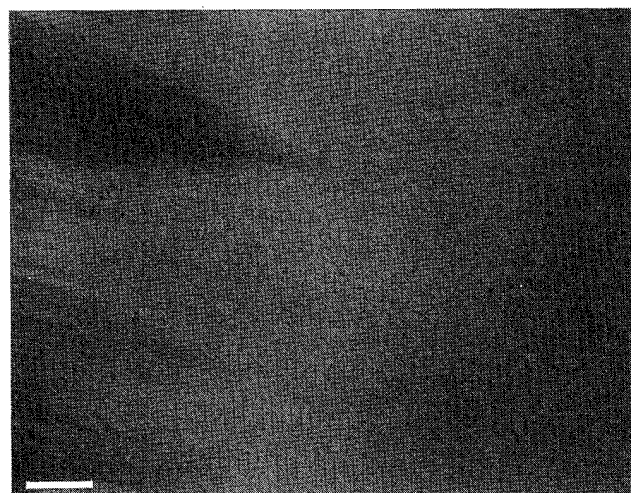
Fig. 4. Surface morphology of a 4 μm thick CdTe layer grown on (100)Si, misoriented nine degrees toward [011]. The marker represents 25 μm.
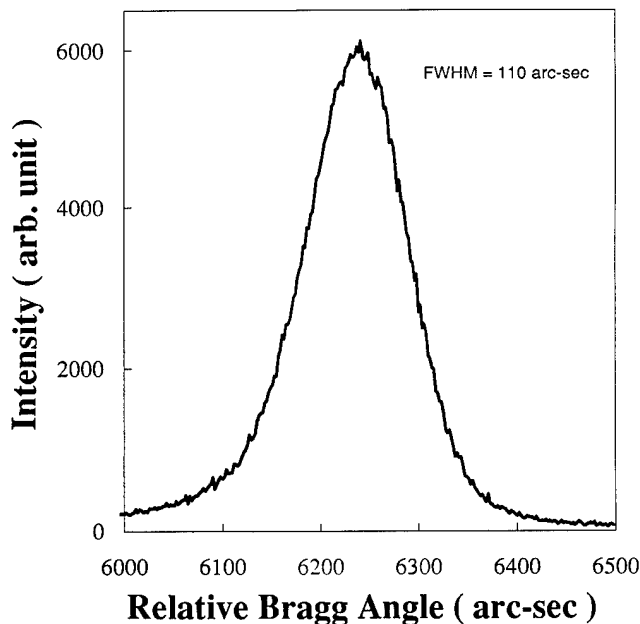
Fig. 3. Double crystal x-ray rocking curve of a 7 μm thick ZnTe grown on (100) Si, misoriented nine degrees toward [011]. The FWHM is 110 arc-sec.
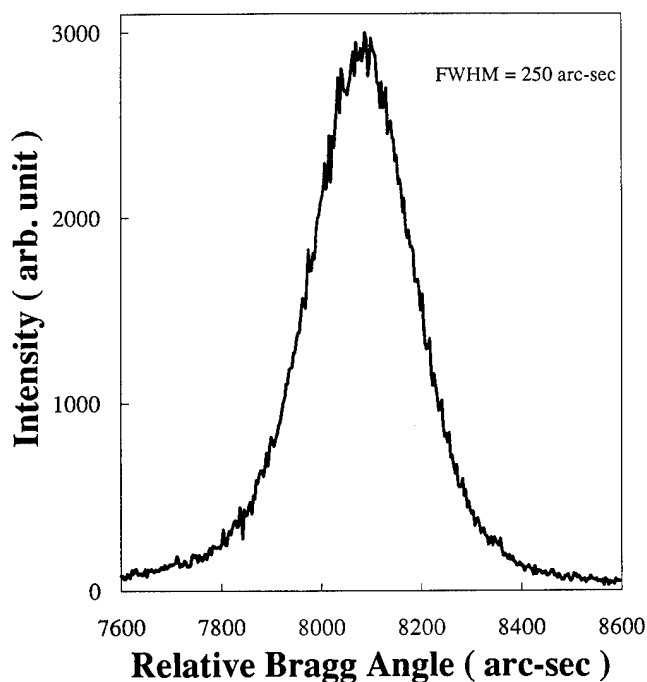
Fig. 5. Double crystal x-ray rocking curve of a 4 μm CdTe grown on (100) Si, misoriented nine degrees toward [011]. The FWHM is 250 arc-sec.

a

b
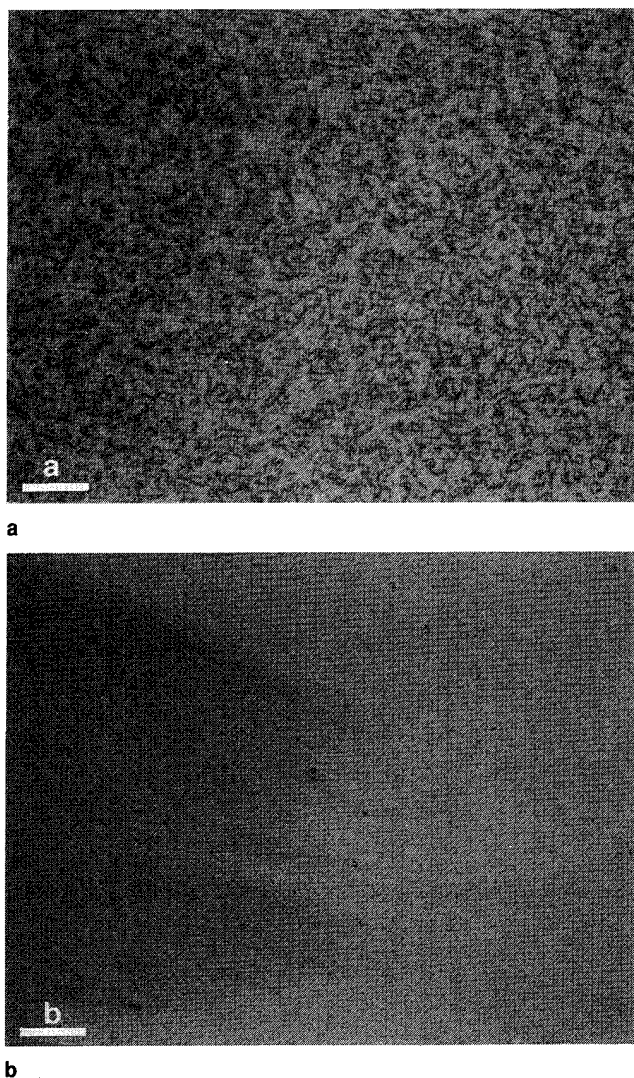
Fig. 6. The surface morphology of CdTe layers grown on Si substrate after etched E-Ag1 solution. (a) CdTe layer grown on (100) oriented Si. (b) CdTe layer grown on (100)Si,misoriented nine degrees toward [011]. The marker represents 25 μm. Note the absence of APDs in misoriented substrate.

entation of nine degrees toward [011], respectively. For CdTe grown on (100) oriented Si, many APDs were observed. Each domain is approximately 100 μm² in size. However, such domains were not seen in CdTe layers grown on nine degrees misoriented Si. Similar results are obtained when GaAs is grown on misoriented Si, and the same mechanism may be operating here.[15,16] The etch pit density (about 3×10^5 cm^{-2}) for CdTe grown on nine degrees misoriented (100) Si, however, is rather low compared to x-ray diffraction data. It is reported that etch pits of (100) CdTe cannot be fully revealed by etching in E-Ag1 solution.[17] Hence, real etch pit counts will be possibly higher than the value reported here.

To understand the role of germane, direct growth of CdTe on Si was conducted under various growth conditions. We always got oriented (111) polycrystals when the growth temperatures were in the range of 300 to 450°C.[6] The absence of epitaxial growth may be caused by the presence of submonolayer native oxide on Si even after the HF etch. Also, the Si surface oxidation during heat-up is very likely from the adsorbed O_2 and moisture on the reactor wall for an atmospheric pressure reactor without a loadlock. Germane gas can scavenge oxygen from the reactor wall as well. Another reason for the polycrystalline CdTe growth may be from the presence of strong Si-H bonds which are stable up to about 500°C. Since the bond strength difference of Si-O (191 kcal/mol)[18] and Ge-O (160 kcaVmol)[18] are comparable, it is likely that the reaction of the type

$$Ge + Si\text{-}O \leftrightarrow Ge\text{-}O + Si$$
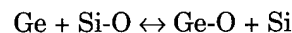
will go from left to right if Ge-O is continuely desorbed. So, reduction of SiO to Si is possible in a gemane gas flowing ambient. Similar reaction had also been observed by Morar et al.[19] On the other hand, the Si-H bonds can be replaced by Si-Ge bond, since Si-Ge bond (75 kcaUmol)[18] is stronger than Si-H bond (<71.5 kcaVmol).[18] In addition, Ge-H bond is weaker than Si-H bond, hence the presence of the hydrogen does not affect the CdTe growth on Ge.

CONCLUSIONS

In this paper, we outlined a novel technique to grow high quality CdTe layers on Si substrates in a single atmospheric pressure OMVPE reactor without using high temperature deoxidation step. The growth was carried out in a very simple atmospheric pressure horizontal reactor without any load-lock system. Prior to ZnTe and CdTe growth, a thin interfacial Ge layer was grown using germane gas, which is found to be responsible for Si native oxide desorption at low temperature. High quality ZnTe and CdTe layers was grown on Si using a Ge interfacial layers. The thickness of this Ge layer was found to be not critical. It should be possible to grow a complete HgCdTe/CdTe/Ge/Si structure in a single OMVPE reactor.

ACKNOWLEDGMENT

REFERENCES

1. B.S. Meyerson, F.J. Himpsel and K.J. Uram, *Appl. Phys. Lett.* 57, 1034 (1990).
2. D.J. Eaglesham, G.S. Higashi and M. Cerullo, *Appl. Phys. Lett.* 68, 59 (1991).
3. S.H. Wolff. S. Wagner, J.C. Bean, R. Hall and J.M. Gibson, *Appl. Phys. Lett.* 55, 2017 (1989).
4. R. Spoken, S. Sivanathan, K.K. Maharadi, G. Boukerche and J.P. Faurie, *Appl. Phys. Lett.* 55, 1879 (1989).
5. R. Korenstein, P. Madison and P. Hallock, *J. Vac. Sci. Technol.* B10, 1370 (1992).
6. W.S. Wang, H. Ehsani and I. Bhat, *J. Electron. Mater.* 22, 873 (1993).
7. S.M. Johnson, J.A. Vigil, J.B. James, C.A. Cockrum, W.H. Konkel, M.H. Kalisher, R.F. Sisser, T. Tung, W.J. Hamilton, W.A. Ahlgren and J.M. Myrosznys, *J. Electron. Mater.* 22, 835 (1993).

8. A. Ishizaka and Y. Shiraki, *J. Electron. Soc.* 133, 666 (1986).

9. Y. Takahasi, H. Ishii and K. Fujiuaga, *Appl. Phys. Lett.* 57, 599 (1990).

10. I. Bhat and W.S. Wang, *Appl. Phys. Lett.* 64, 566 (1994).

11. N. Matsumura, T. Ohshima, J. Saraie and Y. Yodogawa, *J. Cryst. Growth* 71, 361 (1985).

12. T.J. DeLyon, J.A. Roth, O.K. Wu, S.M. Johnson and C.A. Cockrum, *Appl. Phys. Lett.* 63, 818 (1993).

13. W.S. Wang and I. Bhat, presented at the 6th Intl. Conf. on II-VI Compounds, Newport, RI, Sept. 13–15, 1993.

14. M. Inoue, I. Teramoto and S. Takayanagi, *J. Appl. Phys.* 33, 2578 (1962).

15. R. Kaplan, *Surf. Sci.* 93, 145 (1980).

16. S. Strite, D. Biswas, N.S. Kumar, H. Fradkin and H. Morkoç, *Appl. Phys. Lett.* 56, 244 (1990).

17. I. Hahnert and M. Schenk, *J. Cryst. Growth* 101, 251 (1990).

18. A.G. Gaydon, *Dissociate Energies and Spectra of Diatomic Molecules,* 3rd ed., (London: Chapman & Hall, 1968).

19. J.F. Morar, B.S. Meyerson, U.O. Karisseu, F.J. Himpsel, F.M. McFeely, D.R. Rieger, A. Taleb-lbrahimi and J A. Yarmoff, *Appl. Phys. Lett.* 50, 463 (1987).

Integrated *In Situ* Wafer and System Monitoring for the Growth of CdTe/ZnTe/GaAs/Si for Mercury Cadmium Telluride Epitaxy

S.J.C. IRVINE, J. BAJAJ, and R.V. GIL

Rockwell International Science Center, Thousand Oaks, CA 91360

H. GLASS

Rockwell International, Electro Optical Center, Anaheim, CA

Reproducible improvements in the metalorganic vapor phase epitaxy (MOVPE) grown CdTe buffer quality have been demonstrated in a horizontal rectangular duct silica reactor by the use of integrated *in situ* monitoring that includes laser reflectometry, pyrometry, and Epison concentration monitoring. Specular He-Ne laser reflectance was used to *in situ* monitor the growth rates, layer thickness, and morphology for both ZnTe and CdTe. The substrate surface temperature was monitored using a pyrometer which was sensitive to the 2–2.6 μm waveband and accurate to ±1°C. The group II and group VI precursor concentrations entering the reactor cell were measured simultaneously using two Epison ultrasonic monitors and significant variations were observed with time, in particular for DIPTe. The surface morphology and growth rates were studied as a function of VI/II ratio for temperatures between 380 and 460°C. The background morphology was the smoothest for VI/II ratio in the vicinity of 1.5–1.75 and could be maintained using Epison monitors. Regularly shaped morphological defects were found to be associated with morphological defects in the GaAs/Si substrate. The x-ray rocking curve widths for CuK_α (531) reflections were in the range of 2.3–3.6 arc-min, with no clear trend with changing VI/II ratio. X-ray topography images of CdTe buffer layers on GaAs/Si showed a mosaic structure that is similar to CdTe/sapphire substrates. The etch pit density in $Hg_{1-x}Cd_xTe$ layers grown onto improved buffer layers was as low as 6×10^6 cm^{-2} for low temperature MOVPE growth using the interdiffused multilayer process.

Key words: CdTe/ZnTe/GaAs/Si, *insitu* monitoring, laser reflectrometry, metalorganic vapor phase epitaxy (MOVPE), pyrometer

INTRODUCTION

The use of silicon as the substrate material for large format $Hg_{1-x}Cd_xTe$ IR focal plane arrays (FPAs) eliminates the problems associated with the differential thermal expansion mismatch between II-VI materials and the silicon multiplexer.[1] The large lattice mismatch (19%) between Si and $Hg_{1-x}Cd_xTe$ creates many structural defects that can affect diode performance.[2] The epitaxial quality of the buffer layer, which accommodates the lattice mismatch, is critical in attaining high quality of the epitaxial $Hg_{1-x}Cd_xTe$ grown onto these substrates. Several approaches to overcome the adverse effects of large lattice mismatch between CdTe and Si have been followed. These include the use of GaAs[3–5] and CaF_2/BaF_2[6] nucleation layers on Si. Direct growth of CdTe onto Si has been reported[7] using molecular beam epitaxy (MBE). Two-dimensional focal plane arrays on liquid phase epitaxy (LPE) HgCdTe grown on CdTe/GaAs/Si substrates,[8] and all *in situ* growth of mercury cadmium telluride (MCT)/CdTe/ZnTe onto GaAs/Si for 256×256 array fabrication[1] have been demonstrated. However, reduction of dislocation density remains a challenge for the CdTe buffer layers grown onto Si based substrates.

This paper reports on recent progress made in the quality of buffer CdTe layers grown by metalorganic
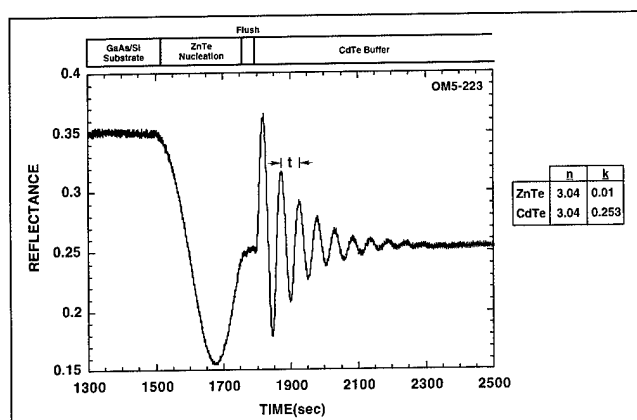
Fig. 1. *In situ* measured reflectance signal during growth of ZnTe nucleation and CdTe buffer layer growth.

vapor phase epitaxy (MOVPE) on 3″ GaAs/Si substrates. The characteristics of CdTe and $Cd_{1-x}Zn_xTe$ grown onto GaAs/Si for different growth conditions provide insights into the mechanisms that limit its morphology, structural, and optical quality.[9,10] The strength of the present work comes from an integrated *in situ* monitoring capability that has enabled better understanding of the growth dynamics and offers the potential for better growth control.[11] *In situ* monitoring in real time implies that if a change occurs during growth it can be corrected, leading to better reproducibility of material properties.

The monitors used in the present work can be divided into two groups: wafer monitors and system monitors. The objective of wafer monitoring is to measure the properties of the epitaxial layer, while system monitoring looks at the parameters that determine the layer properties (such as morphology, growth rate, composition, and structure). Both wafer and system monitoring are required to build a complete picture of the growth process; combining the two is what constitutes an *in situ* integrated monitoring capability.

The relatively high pressure of the reaction chamber in MOVPE (0.1–1 atm) precludes the use of *in situ* wafer monitoring techniques that require electrons for excitation or detection.[12] Therefore, *in situ* wafer monitoring techniques are based on photon excitation and detection. The wafer monitoring for the present work has concentrated on laser reflectometry for real-time feedback on growth rate, thickness, and morphology,[13,14] to improve the quality of CdTe buffer layers on GaAs/Si substrates.

EXPERIMENTAL DETAILS

A horizontal rectangular duct silica reactor was modified to accommodate laser reflectance monitoring and has been described in detail.[13,14] As reported earlier,[13] these reactor modifications did not affect the temperature and the gas flow conditions over the substrate, thereby maintaining the growth rate and lateral uniformity. A polarized He-Ne laser (2mW at 632.8 nm) was mounted such that the light enters the window and reaches the wafer at near normal inci-

dence. The reflected light was monitored as a function of time using a Si detector followed by standard phase sensitive detection using a lock-in amplifier. A portion of the incident beam was reflected off a glass plate and detected by another detector to monitor the incident laser intensity. Signals corresponding to both the incident and the reflected light intensities were fed into an IBM PC for data storage, retrieval, and analysis. Typically, two data points per second were measured and stored.[14]

The metalorganic vapor phase epitaxy reactor was designed with two independent feed manifolds; one dedicated to group II and the other to group VI compounds. Two Epison ultrasonic monitors (supplied by Thomas Swan Ltd.), were installed to simultaneously measure the concentration of group II and group VI organometallic precursors entering the reactor.[11,15] The molecular weight and ratio of the principal specific heats were stored for each of the organometallics. These monitors measure (and display) the concentration continuously and can be used as a feedback to the MOVPE reactor control. The Epison monitors have been instrumental in addressing issues such as condensation of organometallics in the feed lines, complete flushing of lines before introduction of the organometallics, and steady flow of organometallics throughout the growth cycle.

An IRCON Modline Plus Pyrometer was installed on the reactor to monitor the surface temperature. This pyrometer was sensitive to a narrow band of radiation from 2 to 2.5 μm. At this wavelength, the substrate and the CdTe buffer are transparent, so the detector was sensitive to radiation coming from the graphite substrate holder. However, for MCT growth, the emission was from the MCT surface and a different emissivity correction was required. The initial experiments were designed to look at the substrate holder during substrate heat clean and buffer growth. The emissivity was calibrated by ramping up the temperature until a fragment of Te melted, then corrected the emissivity to read a temperature of 450°C. This pyrometer constantly monitored the temperature/emissivity throughout the run. Flow of gases was controlled by commercial mass flow controllers which offered ±1% full-scale accuracy and 0.1% full-scale reproducibility.

Dimethylzinc (DMZn) plus dimethyltellurium (DMTe) were used for the ZnTe nucleation layer which was typically 1000Å thick. This layer will ensure (100)//(100) epitaxial orientation and help to grade the lattice parameter misfit. Dimethylcadmium (DMCd) plus DMTe or diisopropyltellurium (DIPTe) were used for CdTe buffer growth which is typically 6–8 μm thick. The substrate temperature was maintained by heating with a pyrolytic boron nitride (PBN) resistance heater placed directly below the substrate.

The bulk GaAs/Si substrates, purchased from Kopin, were 2–3 inches in diameter and oriented (100)10°→(111). Prior to loading in the reactor, these substrates were etched in a 5:1:1 mixture of $H_2SO_4{:}H_2O,H_2O_2$ for 15 s.
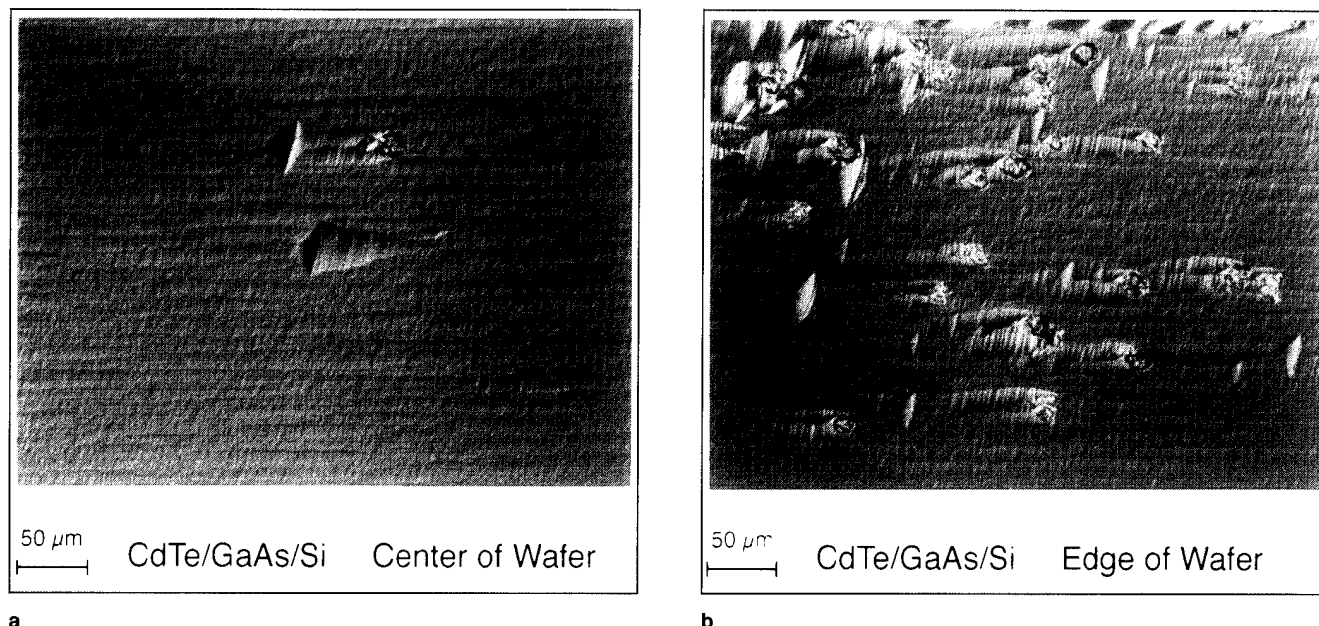
Fig. 2. Nomarski contrast micrographs showing the morphology and the "bell" shaped defects at (a) the center and (b) near the edges of MOVPE CdTe grown on 3″ GaAs/Si substrate.

EXPERIMENTAL RESULTS AND DISCUSSION

In situ Monitored Reflectance for Growth Rate and Thickness Determination

Figure 1 shows a typical *in situ* reflectance-time profile measured during the growth of the double layer structure; ZnTe nucleation layer followed by CdTe buffer layer. Different phases of growth are identified on the top. The reflectance is plotted in arbitrary units as a function of time. To obtain the absolute values of reflectivity, the entire reflectance profile was normalized so that the reflectance from GaAs matches the theoretically expected value calculated using a known value of the refractive index.

The thickness of ZnTe nucleation and CdTe buffer, which influence the quality and crystallinity of the subsequently grown structure, can be precisely determined.[14] The effect of ZnTe thickness on the x-ray rocking curve widths measured in CdTe buffer layers has been reported[13] for GaAs substrates. A clear trend was observed, with increasing rocking curve broadening for ZnTe thicknesses greater than 1000Å. In the example given in Fig. 1, the ZnTe thickness was 760Å. The growth rates of the ZnTe and CdTe layers, measured by the spacing of these oscillations, was monitored and related to the system monitors.

Surface Morphology and its Dependence on Temperature and II:VI Ratio

The surface morphology of CdTe grown on GaAs/Si differed significantly from that of CdTe grown on bulk GaAs and has been reported as being a major cause of compositional inhomogeneities.[16] Growth conditions optimized for smooth mirror-like morphology of CdTe/bulk GaAs, when applied to CdTe/GaAs/Si yielded a rough, faceted surface; replacing DMTe with DIPTe
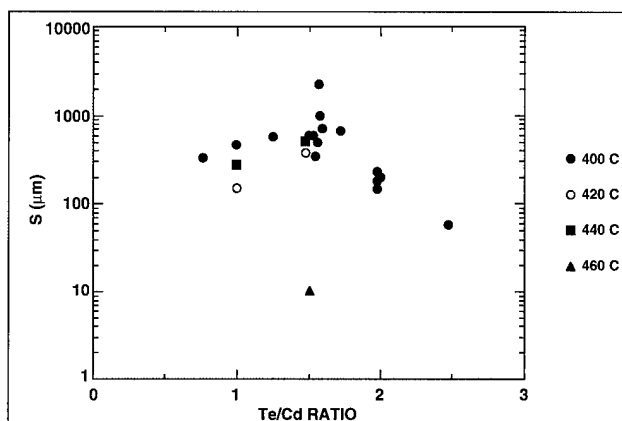
Fig. 3. Smoothness length of MOVPE CdTe grown on GaAs/Si as a function of the VI/II ratio and temperature. This length is defined (see text) as the thickness of the layer at which the extrapolated *in situ* monitored reflectance signal goes to zero.

as the tellurium precursor and growing under Te-rich conditions yielded a smooth surface.[14]

The standard orientation of $(100)10°{\rightarrow}(111)$ showed significant variation in the surface morphology of CdTe grown on GaAs/Si wafers, particularly at the edges. The same surface features were visible in wafers etched and unetched prior to growth and propagated into the CdTe buffer layers as "bell" shaped morphological defects shown in Fig. 2a. The density of these defects is higher near the wafer edges as shown in Fig. 2b. In extreme cases, their density caused extensive faceting in the subsequently grown MOVPE HgCdTe, and the individual features were no longer distinguishable. The cause of the "bell" defects was attributed to morphological defects in the GaAs epitaxial layer on silicon.

A detailed study was made of the relationship between surface morphology and VI:II ratio. Epison

T$_G$ = 400°C

(a)
VI/II = 0.763

(b)
VI/II = 0.994

(c)
VI/II = 1.25

(d)
VI/II = 1.50

(e)
VI/II = 1.98

(d)
VI/II = 2.47

50 µm
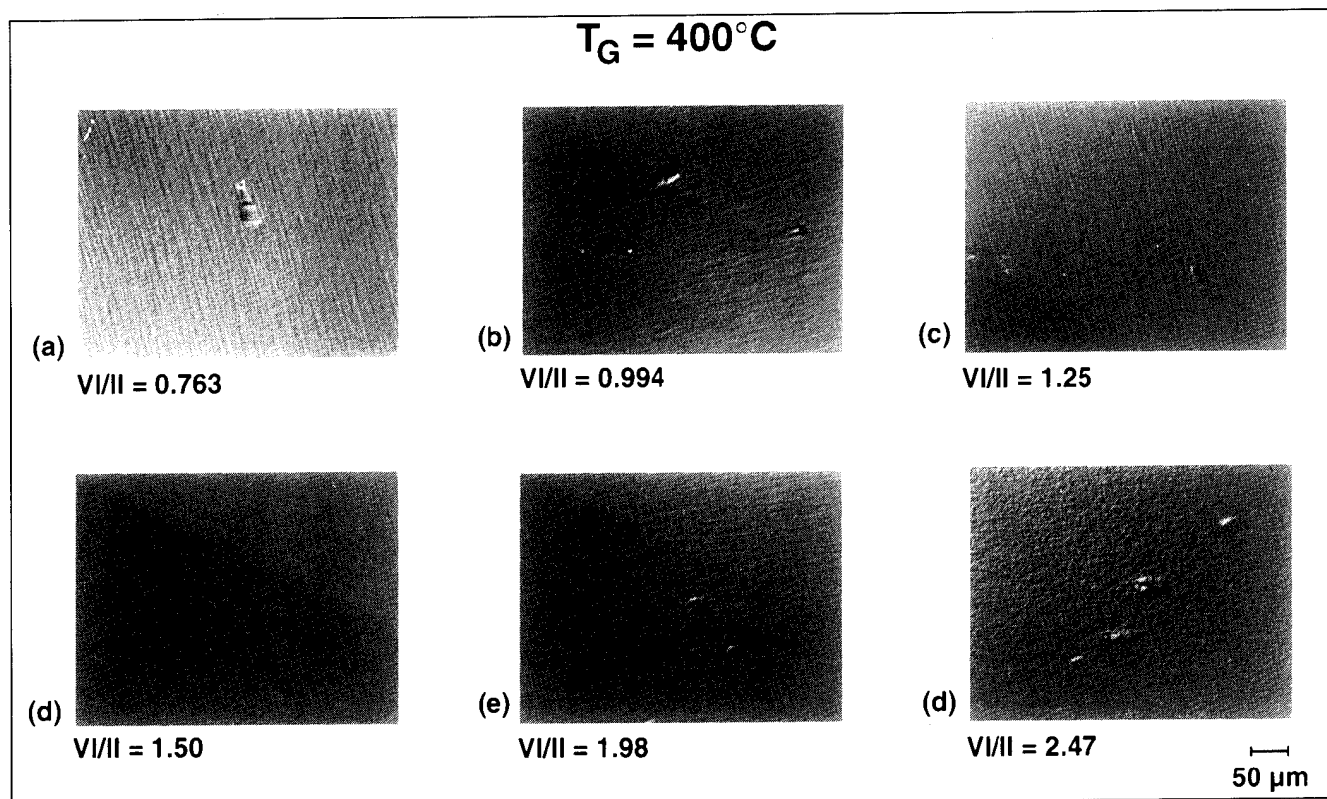
Fig. 4. Nomarski contrast micrographs showing surface morphology with varying VI/II ratio. All these layers are 8±1 µm thick.
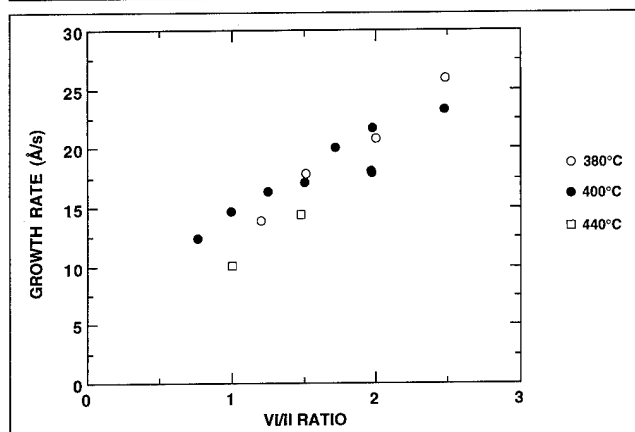
Fig. 5. Growth rate of CdTe on GaAs/Si(100)10°→(111) as a function of the VI/II ratio at different growth temperatures.

monitors allowed controlled variations in the DMCd to DIPTe concentration ratios entering the reactor cell. A smoothness length was defined using laser reflectance monitoring to compare the rate of surface roughening under different growth conditions. The decrease in specularly reflected light is ascribed to scattering of light from the surface due to the formation of facets. The smoothness length (S) is defined as the thickness of epilayer where the extrapolated reflectance goes to zero. The highly faceted surfaces resulted in S~1 µm.

The results over a number of growth runs, at 400°C, are shown in Fig. 4. Looking at the minimum resolvable decrease in reflectivity for a 10 µm thick CdTe layer, it was not possible to resolve S to better than

500 µm. Figure 3 shows that S peaks around VI/II = 1.6 and decreases more rapidly for higher ratios (more DIPTe rich) than for lower ratios. Optimization of this ratio would be difficult without the direct measurement of concentration given by the Epison monitor.

The structure contributing to the surface roughening is revealed in the Nomarski contrast micrographs in Fig. 4. Each field of view was chosen to include a typical macrodefect to determine if the shape changes with the VI:II ratio. Starting from the highest VI/II ratio of 2.47, the background morphology had an orange-peel appearance; and the macrodefects were rounded, with no distinct shape other than their elongation. Decreasing the VI:II ratio made the background more terraced and the macrodefects smaller. The terracing for VI:II ratio of 1.5 is very slight and the macrodefects are very shallow. Some increase in the terracing is seen for further decreases in VI:II ratio, and the macrodefects become more angular and larger.

Temperatures up to 460°C were also investigated; the results are shown in Fig. 3. For the VI:II ratio of 1.5, the surface smoothness was maintained up to 440°C but rapidly deteriorated to an orange-peel morphology at higher temperatures. Lowering the VI:II ratio to 1.0 appeared to make the morphology more sensitive to temperature, with some decrease in S at 420 and 440°C compared with 400°C. The macrodefect density also increased for T>400°C. These defects were mostly of the bell shape or faceted type rather than the polycrystalline forms associated with dust.

Growth Rate and its Dependence on Temperature and VI/II Ratio

The function of growth rate with VI/II ratio and temperature can give vital information about growth mechanisms and provide insights to the development of surface morphology. Figure 5 shows the growth rate measured by laser reflectometry for different VI/II ratios and temperatures where the DMCd concentration was kept constant at 2×10^{-4} atm. The temperature range covered by this data is 380 to 440°C (pyrometer calibration of surface temperatures are displaced by -17C compared with these thermocouple temperatures). For this temperature range, the growth rate increased sublinearly up to the maximum VI/II ratio of 2.5. The higher growth rates may play a part in the roughening of the surface at high VI/II ratios. The behavior with increasing DMCd concentration is quite different with saturation in growth rate as soon as the DMCd concentration exceeds that of the DIPTe concentration, as shown in Fig. 6. A similar behavior was observed by Tasker et al.[17] using DETe. The results in Fig. 6 were obtained before the Epison monitors were installed, but the DMCd and DIPTe flows given in the figure have been calibrated subsequently, using the Epison monitors.

The stoichiometric concentrations are shown in Fig. 6. As the DIPTe concentration is increased, so the growth rate saturates at higher DMCd concentrations and at a higher growth rate. These results show two different plots for DIPTe flow of 295 SCCM, unsaturated and saturated. A problem was identified with condensation of DIPTe in the feed line, above the bubbler, which reduced the vapor pressure of DIPTe at the reactor inlet to below the expected partial pressure based on a calculation of saturation of the DIPTe flow in the bubbler. These results show a lower growth rate and an apparent saturation of growth rate at a lower DIPTe flow than expected. After solving this problem by heating the feed lines above the bubbler, the DIPTe flow became saturated at the

bubbler temperature of 27°C, and the CdTe growth rate showed the expected behavior as shown in Fig. 6. The apparent nonsaturation of growth rate with increasing concentration, indicates that DIPTe is either not pyrolyzing efficiently on the surface or the sticking coefficient is lower than for DMCd. The correct interpretation of these results has implications for the change of morphology, and possibly defect structure, with VI/II ratio.

Control of VI/II Ratio and Temperature with *In Situ* Monitoring

An application where the Epison monitors have helped to improve growth control was in monitoring run-to-run variations of organometallic concentrations. These changes were tracked by calculating the saturated vapor pressure in the bubbler from the Epison measurement of concentration in the inlet manifold and the dilution flow rates. The organometallic concentration in the reactor is related to the flows as follows:

$$C_i = \frac{p_i F_i}{p_T \sum_{m=1}^{n} F_m} \tag{1}$$
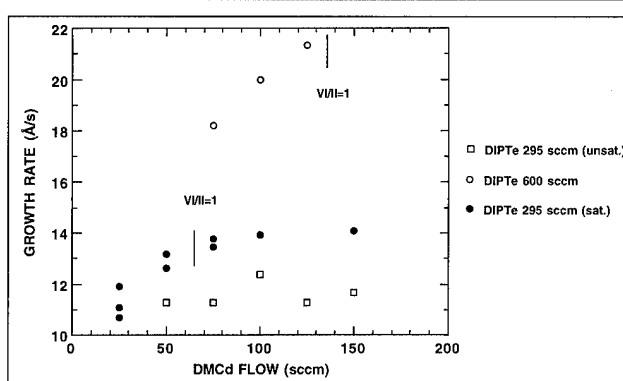
Fig. 6. Growth rate of CdTe on GaAs/Si(100)10°→(111) as a function of DMCd flow for different DIPTe flows; the stoichiometric ratios are indicated.
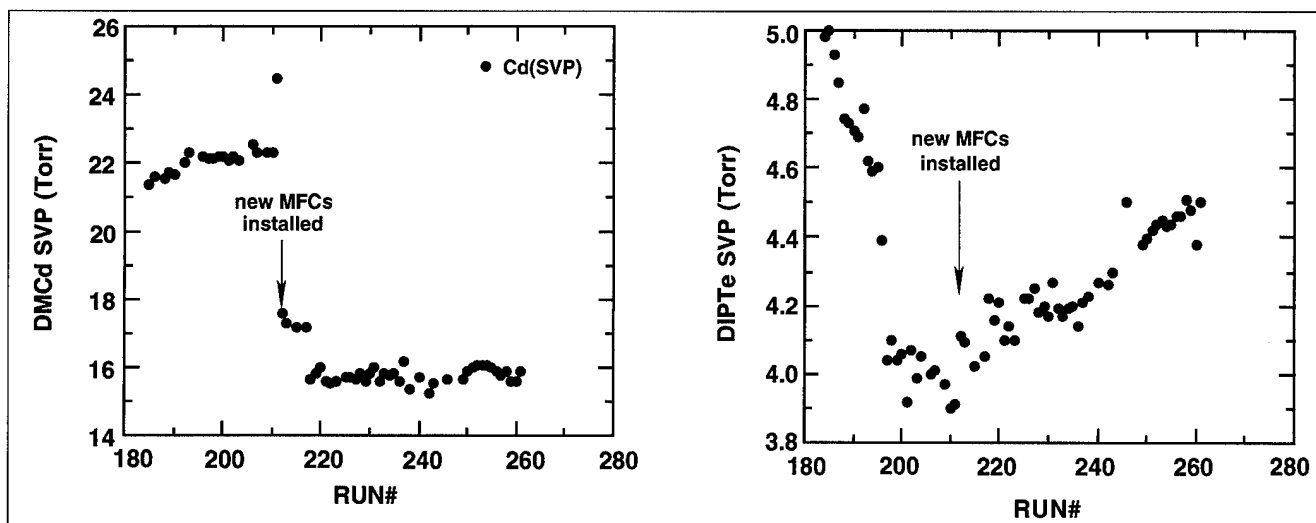
Fig. 7. Run-to-run variations in the bubbler SVP of (a) DMCd and (b) DIPTe calculated from concentrations as measured by the Epison monitors.
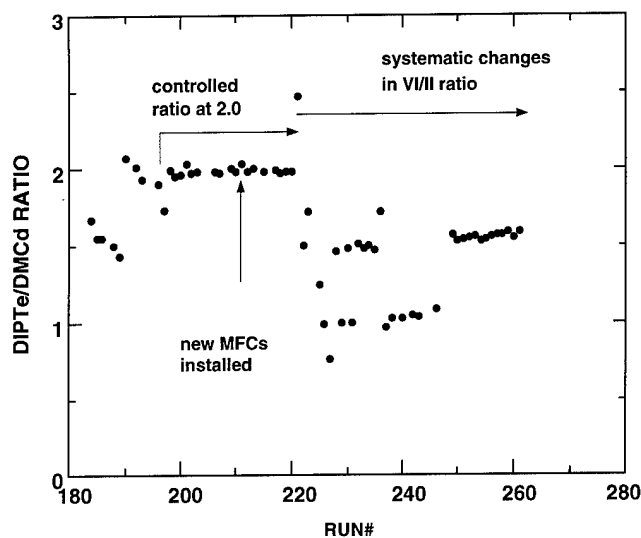
Fig. 8. VI/II concentration ratio as a function of growth run showing increased control achieved by *in situ* monitoring.
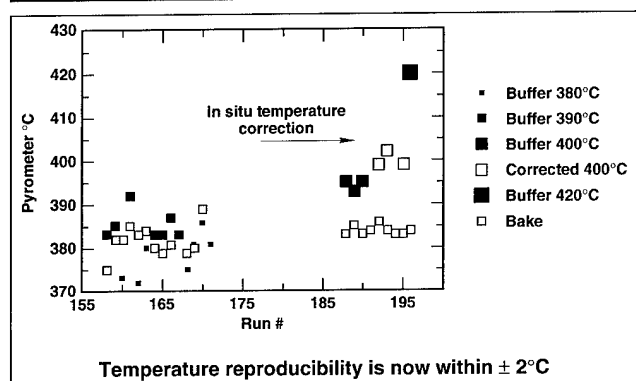
Fig. 9. Temperature, as measured by the infrared pyrometer during substrate bake prior to growth, as a function of growth run. Feedback from the measured temperature to adjust the set temperature resulted in a reduced variance.

where C_i is the concentration of the ith organometallic component in the diluted stream, p_i is the saturated vapor pressure (SVP) in the bubbler, p_T is the total reactor pressure, F_i is the hydrogen flow through the ith bubbler, n is the maximum number of bubblers. Equation (1) can also apply to the concentration in the inlet manifold, where the concentration (C_i) is independently measured by the Epison monitor. The SVP of the ith organometallic (p_i) can then be calculated by rearranging Eq. (1) and substituting for the flows and total pressure, which are all measured independently. These results, from over 80 runs, are shown in Fig. 7. Both DMCd and DIPTe show significant changes that could cause unaccounted changes in growth rate or layer properties. The largest instabilities occur for DIPTe, falling from a SVP of 5.0 to 4.0 Torr. Between runs 195 and 205, the changes for both DMCd and DIPTe flatten. High stability mass flow controllers (Precision Flow Devices 501) were fitted between runs 211 and 212 to reduce variance in bulk flow rate of the organometallics.

From the viewpoint of growth stability, it is sufficient to measure these concentrations and make appropriate corrections to the flow to maintain organometallic bulk flow rate. After installation of the PFD 501 MFCs, as seen in Fig. 8, the SVP was very stable between runs 218 to 260. The higher SVP for runs 211 to 216 was probably caused by a higher DMCd bubbler temperature. The large change in apparent SVP between the new and old MFCs is consistent with a large zero error on the removed MFCs. Figure 8 also shows a long-term drift in the apparent SVP, which is attributed to poor flow control. No long-term drift has been seen in the DMCd concentration since replacing the MFCs. The calculated SVP for a source temperature of 12°C is 18.7 Torr, significantly higher than the SVP determined from Epison measurement. This could be due to either (a) errors in the thermodynamic constants used for this calculation (supplied by Morton International), or (b) the ratio of principal specific heats, γ, of 1.1 used in the Epison measurement may be in error.

The DIPTe SVP showed a different behavior to that described above for DMCd, where the changes in DIPTe SVP do not seem to be connected with the replacement of MFCs or any other observation of changes in the reactor variables. The most significant feature is the steady rise in SVP from run 210 to 261. These drifts may in fact be genuine changes in SVP, which could be attributed to chemical changes in the DIPTe bubbler. Corrections have been made in the DIPTe flow rate to maintain its concentration in the reactor chamber. These long-term drift studies are providing new insights into the behavior of the organometallic sources and are clearly essential for accurate control and good run-to-run growth stability.

The VI/II ratio has been identified as a critical parameter in maintaining good morphology on GaAs/Si substrates. The first series of 28 runs had a nominal ratio of 2.0 but gave measured ratios as low as 1.4, which was unacceptable. After observing the variance in this parameter over the first 11 runs, corrections were applied for subsequent runs to keep the ratio on target. Figure 8 shows clearly that this was very successful in maintaining the ratio close to the target value, even after the change to new MFCs. Some experimental growths were performed where the VI/II ratio was intentionally changed within a growth run with target values between 0.7 to 2.5 for runs 221 to 231. For runs above 249, a new set-point of 1.5 gave better surface morphology.

Temperature Measurement by IR Pyrometer

Figure 9 shows the run-to-run variations in measured temperatures for 14 runs. The set temperature for the bake was 400°C and two different temperatures were used for buffer growth, 380 and 390°C, as indicated. The measured bake temperature was between 380 and 385°C for most of these runs, but one was as low as 375°C and another as high as 389°C, for the same thermocouple set-point. The buffer temperature also shows significant run-to-run variations with the measured temperature in some cases being higher for a set temperature of 380°C than for 390°C.

The reasons for these run-to-run variations are possibly slight movements in the control thermocouple position or alignment of the substrate and heater assembly prior to each run. Efforts were made to make these more reproducible, and temperature calibration corrections were made at the start of each run.

In general, the surface temperature was lower than the control thermocouple temperature by 15 to 20°C. Monitoring the surface temperature during the substrate bake phase (set temperature of 400°C) showed a run-to-run variation of up to 15°C. Similar variations in surface temperature were also observed during the CdTe buffer growth and are shown in Fig. 9. More recent experiments have corrected this variation by determining a ΔT correction factor in the bake phase and correcting all subsequent growth phases (runs 188 to 196) by that amount. The buffer layer was grown at different temperatures; and these intentional changes are now clearly reflected in the surface temperature, whereas the uncorrected growths did not show a clear difference.

Ex Situ Characterization of CdTe/GaAs/Si Layers

Double Crystal X-Ray Diffraction

X-ray diffraction rocking curves, complemented by x-ray topographs, were used routinely to measure the crystal quality of the grown CdTe layers. For the near-(100) oriented buffer layers reported here, a double crystal diffractometer was set up with CuK_α x-rays and a symmetric (333) Ge reflection as the first crystal. With the sample set as the second crystal and oriented for a {531} CdTe reflection, there is negligible instrumental contribution to the rocking curve. Rocking curves of GaAs layers on Si were measured using the same configuration but with a {511} GaAs reflection. The full width at half the maximum (FWHM) intensity is measured and used as a simple indicator of crystal quality.

A large area detector captures the entire diffracted beam, so the rocking curve is integrated over the sample area that is illuminated by the incident beam. If, however, a photographic plate is used to intercept and record the diffracted beam at a fixed incidence angle, a map is obtained of diffracted intensity over the illuminated area. This map constitutes a topograph. If the sample is a perfect crystal, then all regions will diffract with the same intensity and the topographic image will be uniform. On the other hand, if the sample has defects, there will be variations in diffracted intensity and the defective regions will be imaged as contrast variations in the topograph. The value of combining topography with rocking curve measurements lies in the fact that similar samples having similar rocking curves can have significantly different defect structures. Topographs help to identify the origin of rocking curve broadening by imaging the defects.

Figure 10 shows how rocking curve width varied with layer thickness for 17 CdTe buffer layers grown

on GaAs/Si. This figure also contains the effects of growth temperature and VI:II ratio on buffer layer quality. Different symbols are used for the three different growth temperatures: 400, 420, and 440°C. The figure shows very clearly that rocking curve width decreases with increasing layer thickness, but there is no apparent dependence of rocking curve width on growth temperature.

Similarly, there was no observable dependence of rocking curve width on VI:II ratio over the range from 0.76:1 to 2.47:1. The insensitivity of rocking curve width to growth temperature and VI:II ratio means that these two growth parameters may be selected to optimize other qualities, such as surface morphology, without compromising crystal quality. A similar variation of CdTe rocking curve width with thickness has been seen in (111)B CdTe/Sapphire (PACE-I) substrates that have been grown to different thicknesses or that have been grown thick and then etched back in several steps. Full width at half maximum decreases fairly rapidly as CdTe thickness increases up to about 6 μm, then there is a more gradual decrease. For PACE-I wafers which have CdTe layers about 8 μm thick, FWHM is typically in the range of 1.0 to 1.3 arc-
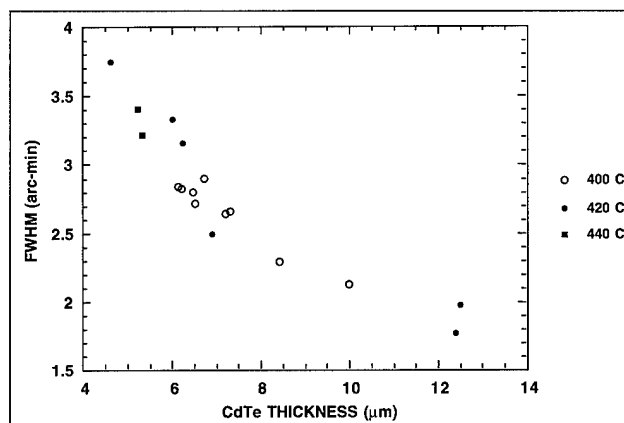
Fig. 10. X-ray rocking curve FWHM of MOVPE CdTe on GaAs/Si(100)10°→(111) as a function of CdTe layer thickness.
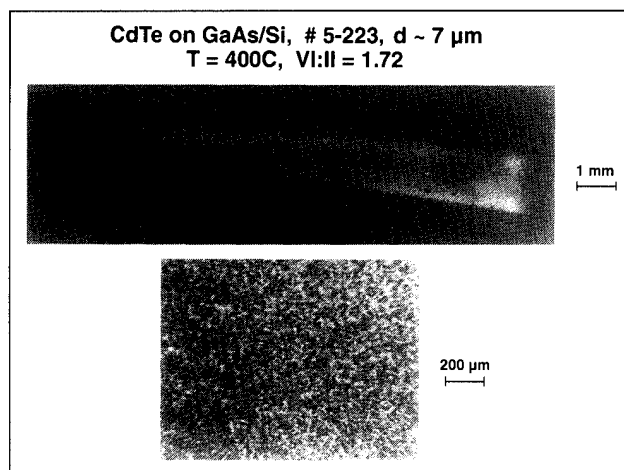
Fig. 11. X-ray topograph of (a) typical MOVPE grown CdTe on GaAs/Si, and (b) magnified image from a small region showing mosaic structure.

min. The smallest FWHM in Fig. 11 is 1.8 arc-min.

Figure 11a shows the x-ray topograph of a typical CdTe layer grown on GaAs/Si. The "graininess" of the topographic image is magnified in Fig. 11b, which show mosaic blocks on the order of 10 μm in diameter. Rocking curve width in these CdTe layers is broadened by the small misorientations between mosaic blocks. In view of these topographs, the reduction in rocking curve width with layer thickness can be interpreted as a reduction in the range of mosaic block tilts. Accompanying the reduction in FWHM is an increase in mosaic block size with increasing CdTe thickness, block size being roughly equal to layer thickness. Again, similar effects are seen for PACE-I substrates. A notable difference is that PACE-I has (111)B oriented CdTe which exhibits a strongly faceted matt surface, easily seen by interference contrast optical microscopy.

In addition to the mosaic structure, the topographs show several other features. The bands which run the length of the image arise from overlap of the CuK$_\alpha$ doublet beams and do not correspond to features in the CdTe. Apart from this banding, the image should show a uniformly intense mosaic structure if no other defects were present. This uniformity is difficult to achieve, especially if the topographs are recorded at incidence angles corresponding to positions off the rocking curve peak. These double crystal topographs are extremely sensitive to small variations (fractions of FWHM) in orientation. Topographs also exhibit smaller, high contrast features; generally <100 μm in diameter. Most often these appear as nondiffracting spots (dark spots in Fig. 11a) in contrast to the bright areas corresponding to high diffracted intensity. Similar features are seen in CdTe on sapphire, although at lower densities. It is difficult to identify the origin of such features directly. A possible source is a small particle on the substrate or a pinhole in the GaAs layer.

The use of deliberately misoriented substrates may also contribute to long-range contrast variations. The Si substrates used for the present work were typically oriented (100) 10°→ (111). The orientations of CdTe layers grown on these substrates show appreciable tilts between the epitaxial layers and the Si substrate, typically 0.5° for the GaAs and 3° for the CdTe.

The direction of these tilts reduces the misorientation of the epitaxial layers from (100). These tilts arise from the interfacial defects that accommodate the misfit. Clearly, small variations in the interfacial defect structure could easily produce strong contrast variations in the double crystal topographs and present a major obstacle to defect reduction in large lattice mismatched systems.

Since substrate quality strongly influences buffer layer quality, some rocking curves and topographs of GaAs/Si were obtained. Generalizing from a few samples, the GaAs also exhibits a mosaic structure, FWHM is about 3 arc-min or more and the GaAs is strained under in-plane tension consistent with the known thermal expansion difference between GaAs and Si.

Growth of HgCdTe on CdTe/GaAs/Si

Growth and characterization of HgCdTe by MOVPE and LPE were used to assess the CdTe buffer layer quality. The results on LPE evaluation are given in another paper in this proceedings.[18]

Metalorganic vapor phase epitaxy $Hg_{1-x}Cd_xTe$ was grown using the interdiffused multilayer process (IMP).[19] These layers were grown in situ following the growth of the CdTe buffer layer onto GaAs/Si. DMCd and DiPTe were used for the CdTe phase and DiPTe and Hg vapor were used for the HgTe phase of the IMP cycles. The IMP $Hg_{1-x}Cd_xTe$ growth took place at 380°C and was monitored in situ[14] for parameters such as composition, thickness, and morphology. The HgCdTe morphology and dislocation density were some of the characteristics measured and were taken as an indication of the quality of underlying substrate.

The lowest dislocation density measured in metalorganic vapor phase epitaxy HgCdTe grown onto CdTe/GaAs/Si was measured at 6×10^6 cm^{-2} for layer 233 which was 8 μm thick (with x = 0.278) with an 8.5 μm thick CdTe buffer layer. This is now similar to etch pit densities (EPDs) measured in MCT grown onto bulk GaAs substrates. The CdTe buffer layer was grown with a VI/II ratio of 1.49 and a substrate temperature of 422°C.

SUMMARY AND CONCLUSIONS

The surface morphology of CdTe buffer layers has improved from a very poor faceted surface with surface smoothness factor, S = 1 μm, to highly specular epilayers with S >500 μm. The factors that have been identified as being crucial in determining the quality of CdTe are VI/II ratio, substrate temperature, type of organometallic precursor, quality of GaAs/Si, orientation, and surface preparation. The best conditions were found for VI/II ratio of 1.5–1.6, using DIPTe in place of DMTe, temperature of 400°C and substrate orientation of (100)10°→(111). Some surface defects have been attributed to features in the surface morphology of the GaAs/Si substrates. Further progress in the CdTe buffer layer quality will require improvements in the quality of GaAs/Si substrates, including atomic layer epitaxy (ALE) grown GaAs which has an excellent surface smoothness.

Integrated in situ monitoring, including laser reflectometry, pyrometry, and Epison concentration monitoring, were used to establish the key growth parameters and find optimum growth conditions. Specular He-Ne laser reflectance, measured using a silicon detector and standard lock-in techniques, was used to in-situ monitor the growth rates, layer thickness, and morphology for both ZnTe and CdTe. The substrate surface temperature was monitored using a pyrometer which was sensitive to the 2–2.6 μm waveband and accurate to ±1°C. The group II and group VI precursor concentrations entering the reactor cell were measured simultaneously using two Epison ultrasonic monitors.

The surface morphology and growth rates were studied as a function of VI/II ratio for temperatures between 380 and 460°C. The background morphology was the smoothest for VI/II ratio in the vicinity of 1.5–1.75. This smooth morphology could be obtained reproducibly by maintaining the VI/II ratio close to the desired value using Epison monitors. Regularly shaped morphological defects were associated with morphological defects in the GaAs/Si substrate. The density of the irregularly shaped macrodefects, related to dust, was as low as 50 cm^{-2}. The growth rate at fixed temperatures (380–400°C) increased monotonically with increasing DIPTe concentration. For fixed VI/II ratio of 1.5, the growth rate decreased with increasing temperature above 400°C, decreasing from 6.2 µm/h at 400°C to 2.7 µm/h at 460°C. These results highlight the complex surface chemistry and the need to monitor system and wafer parameters. The x-ray rocking curve widths for CuK$_\alpha$ (531) reflections were in the range of 2.3–3.6 arc-min, with no clear trend with changing VI/II ratio. X-ray topography of CdTe buffer layers on GaAs/Si showed a mosaic structure that is similar to CdTe/sapphire substrates. The EPD in HgCdTe layers grown onto improved buffer layers was as low as 6×10^6 cm^{-2} for low temperature MOVPE growth and low 10^5 cm^{-2} in the near surface region of the higher temperature grown Hg-melt LPE layers.[18]

The CdTe buffer layers grown onto GaAs/Si (PACE-III) are generally similar to CdTe grown onto sapphire (PACE-I). Both are characterized by a mosaic structure. Rocking curve width is primarily determined by the misorientation spread of the mosaic blocks. The mosaic block dimensions are comparable to the layer thickness. For thicker layers, the blocks are larger and the rocking curve width decreases. For buffer layer about 10 µm thick, rocking curves are 1.5 to 2.0 times broader for PACE-III than PACE-I. The crystal quality as measured by rocking curves and topographs is insensitive to MOVPE growth temperature and VI/II ratio for the case of CdTe/GaAs/Si. This means that these parameters can be chosen within fairly broad limits to optimize properties, such as surface morphology, which are more sensitive to them.

REFERENCES

1. S.J.C. Irvine, E.R. Gertner, L.O. Bubulac, R.V. Gil and D.D. Edwall, *Semicond. Sci. Technol.* 6, C15 (1991).
2. S.M. Johnson, D.R. Rhiger, J.P. Rosbeck, J.M. Peterson, S.M. Taylor and M.E. Boyd, *J. Vac. Sci. Technol. B* 10, 1499 (1992).
3. S.M. Johnston, J.B. James, C.A. Cockrum, J. Vigil, W.H. Konkel, W.J. Hamilton and W.L. Ahlgren, *J. Electron. Mater.*
4. J. Bajaj, S.J.C. Irvine, H.O. Sankur and S.A. Svoronos, *J. Electron. Mater.* 22, 899 (1993).
5. D.D. Edwall, J. Bajaj and E.R. Gertner, *J. Vac. Sci. Technol. A8*, 1045 (1990).
6. A.N. Tiwari, H. Zoog and S. Blunier, *Nucl. Instr. and Methods in Phys. Research* A322, 352 (1992).
7. S. Sporken, Y.P. Chen, S. Sivanathan, M.D. Lange and J.P. Faurie, *J. Vac Sci Technol.* B10, 1405 (1992).
8. S.M. Johnson, M.H. Kalisher, W.L. Ahlgren, J.B. James and C.A. Cockrum, *Appl. Phys. Lett.* 56, 946 (1990).
9. R. Bean, K. Zanio and J. Ziegler, *J. Vac. Sci. Technol. A* 7, 343 (1989).
10. W.L. Ahlgren, S.M. Johnson, E.J. Smith, R.P. Ruth, B.C. Johnston, M.H. Kalisher, C.A. Cockrum, T.W. James and D.L. Arney, *J. Vac. Sci. Technol. A* 7, 331 (1989).
11. S.J.C. Irvine, J. Bajaj and R.V. Gil, Proc. Sixth Biennial Workshop on OMVPE, to appear in *J. Electron. Mater.*
12. S.J.C. Irvine and J. Bajaj, *Semicond. Sci. Technol.* 8, 860 (1993).
13. S.J.C. Irvine, J. Bajaj and H.O. Sankur, *J. Cryst. Growth* 124, 654 (1992).
14. J. Bajaj, S.J.C. Irvine, H.O. Sankur and S.A. Svoronos, Proc. 1992 MCT Workshop, to appear in *J. Electron. Mater.*
15. J.P. Stagg, J. Christer, E.J. Thrush and J. Crawley, *J. Cryst. Growth* 120, 98 (1992).
16. S.J.C. Irvine, D.D. Edwall, L.O. Bubulac, R.V. Gil and E.R. Gertner, *J. Vac. Sci. Technol. B* 10, 1392 (1992).
17. N.R. Tasker, I.B. Bhat, J.M. Borrego and S.K. Ghandhi, *J. Electron. Mater.* 15, 165 (1986).
18. S.H. Shin, J. Bajaj, S.J.C. Irvine, M. Zandian, E.R. Gertner, H. Glass and S. Sivanathan, *J. Electron. Mater.* 24, (1995).
19. J. Tunnicliffe, S.J.C. Irvine, O.D. Dosser, and J. B. Mullin, *J. Cryst. Growth* 68, 245 (1984).

Direct Growth of CdZnTe/Si Substrates for Large-Area HgCdTe Infrared Focal Plane Arrays

S.M. JOHNSON, T.J. de LYON,* C.A. COCKRUM, W.J. HAMILTON, T. TUNG, F.I. GESSWEIN, B.A. BAUMGRATZ, L.M. RUZICKA, O.K. WU,* and J.A. ROTH*

Santa Barbara Research Center, Goleta, CA 93117
*Hughes Research Laboratory, Malibu, CA 90265

Direct epitaxial growth of high-quality {100}CdZnTe on 3 inch diameter vicinal {100}Si substrates has been achieved using molecular beam epitaxy (MBE); a ZnTe initial layer was used to maintain the {100}Si substrate orientation. The properties of these substrates and associated HgCdTe layers grown by liquid phase epitaxy (LPE) and subsequently processed long wavelength infrared (LWIR) detectors were compared directly with our related efforts using CdZnTe/GaAs/Si substrates grown by metalorganic chemical vapor deposition (MOCVD). The MBE-grown CdZnTe layers are highly specular and have both excellent thickness and compositional uniformity. The x-ray full-width at half-maximum (FWHM) of the MBE-grown CdZnTe/Si increases with composition, which is a characteristic of CdZnTe grown by vapor phase epitaxy, and is essentially equivalent to our results obtained on CdZnTe/GaAs/Si. As we have previously observed, the x-ray FWHM of LPE-grown HgCdTe decreases, particularly for CdZnTe compositions near the lattice matching condition to HgCdTe; so far the best value we have achieved is 54 arc-s. Using these MBE-grown substrates, we have fabricated the first high-performance LWIR HgCdTe detectors and 256 × 256 arrays using substrates consisting of CdZnTe grown directly on Si without the use of an intermediate GaAs buffer layer. We find first that there is no significant difference between arrays fabricated on either CdZnTe/Si or CdZnTe/GaAs/Si and second that the results on these Si-based substrates are comparable with results on bulk CdZnTe substrates at 78K. Further improvements in detector performance on Si-based substrates require a decrease in the dislocation density.

INTRODUCTION

HgCdTe hybrid infrared focal plane arrays (IRFPAs) consisting of two-dimensional detector arrays that are hybridized to Si readout chips using In-bumps are the dominant technology for second generation photovoltaic long wavelength infrared (LWIR) imaging applications. The detectors are predominantly fabricated using HgCdTe layers grown using liquid phase epitaxy (LPE) on lattice-matched bulk CdZnTe sub-

strates.[1] As the size of the hybrid IRFPAs increases, it becomes more important to create a thermal-expansion-matched hybrid structure to ensure long-term thermal cycle reliability. One attractive approach is to grow the HgCdTe on a Si-based substrate rather than a bulk CdZnTe substrate. Additional benefits of using a Si-based substrate include lower cost, increased strength, and larger dimensions than bulk CdZnTe substrates.

We have previously reported the status of achieving a thermal-expansion-matched IRFPA using CdZnTe/GaAs/Si alternative substrates grown by
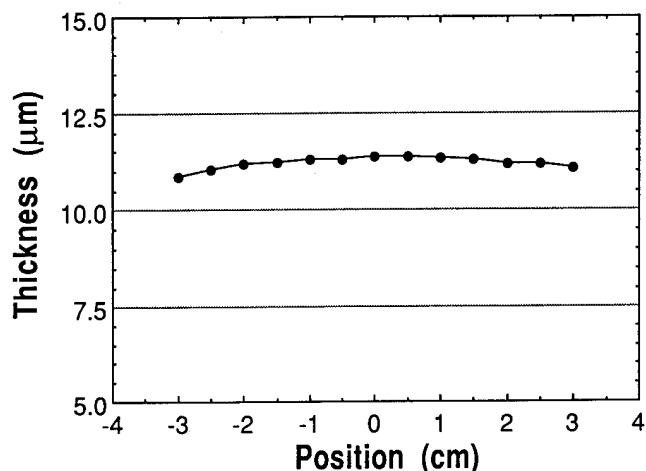
Fig. 1. $Cd_{0.96}Zn_{0.04}Te$/Si thickness uniformity across 3 inch diameter wafer (mean = 11.2 μm, standard deviation = 0.15 μm, standard deviation/mean = 1.35%).
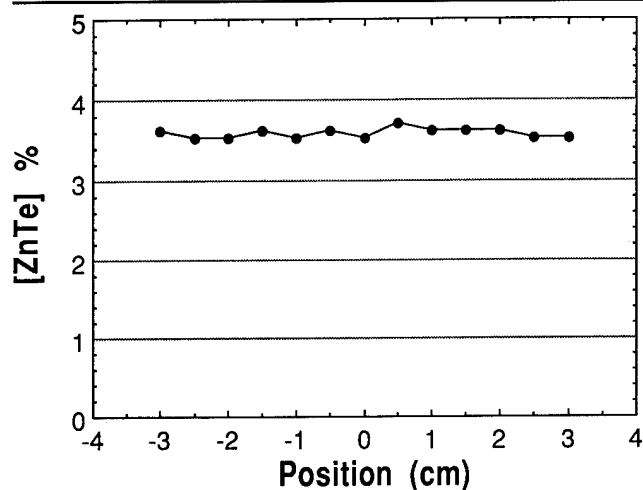
Fig. 2. $Cd_{0.96}Zn_{0.04}Te$/Si composition uniformity across 3 inch diameter wafer (mean [ZnTe] = 3.58%, standard deviation = 0.062%).

metalorganic chemical vapor deposition (MOCVD) for the growth of p-on-n double-layer heterojunction structures by controllably doped, mercury-rich LPE; arrays as large as 480 × 640 have been demonstrated.[2] As previously summarized,[2] (also see references in these proceedings)[3,4] most of the efforts on Si-based substrates have utilized MOCVD to grow CdTe or CdZnTe on GaAs/Si substrates because of the relative ease of obtaining II-VI epitaxy on a GaAs surface in comparison with directly on Si. However, the use of a GaAs intermediate layer is undesirable since it adds to the wafer cost and introduces contamination risk in the LPE HgCdTe growth process since Ga and As are both effective dopants in HgCdTe.

More recently, direct growth of CdTe on Si has been achieved by MOCVD using atomic-layer epitaxy (ALE)[5] and by using an *in situ* grown Ge buffer layer.[6] Historically, most of the work on direct growth of CdTe on Si has been done using molecular beam epitaxy (MBE) and has focused on achieving {111}CdTe/{100}Si.[7,8] The purpose of the work reported here was to use MBE for the direct growth of {100}CdZnTe/{100}Si to achieve a Si-based substrate

that is lattice-matched to HgCdTe, by utilizing a CdZnTe epitaxial layer, and to maintain a {100} layer orientation to avoid the problem of twinning which is common in {111}CdTe and {111}HgCdTe grown by vapor phase epitaxy techniques.

This paper will first describe the MBE growth of CdZnTe/Si and the LPE growth of HgCdTe followed by the results of material characterization measurements made on these epitaxial layers. The performance characteristics of LWIR HgCdTe detectors fabricated on CdZnTe/Si substrates will be discussed next followed by results obtained for the first demonstration of an LWIR HgCdTe 256 × 256 focal plane array using a substrate consisting of CdZnTe grown directly on Si without the use of an intermediate GaAs buffer layer. Throughout the paper, the material characteristics of the CdZnTe/Si substrates and their associated detector performance will be compared with our results for CdZnTe/GaAs/Si substrates.

MATERIAL GROWTH

A more detailed discussion of the direct growth of $Cd_{1-y}Zn_yTe$ epitaxial layers on {100}Si and {112}Si substrates by MBE was previously published[9-12] and is briefly summarized below. CdTe, ZnTe, and CdZnTe epitaxial layers were grown in a VG Model 80 MBE system using Cd, Zn, CdTe, and ZnTe sources. Three-inch diam {100}Si substrates that were misoriented either 4 or 8° toward <111> were cleaned using HF-based, low-temperature cleaning procedures. $Cd_{1-y}Zn_yTe$ layers were grown under Group II stabilized conditions with growth temperatures of 300–360°C and growth rates of 1.0–1.2 μm/h. An initial layer of ZnTe with a thickness of 1 μm was used to maintain the {100}Si orientation; ZnTe nucleation layers are commonly used for this same purpose for growth of CdTe and CdZnTe on GaAs/Si substrates.[2-4] CdZnTe layers were typically grown to a thickness of 10 μm which, including the 1 μm ZnTe layer, resulted in a nominal total layer thickness of 11 μm on the Si substrate.

Long wavelength infrared $Hg_{0.77}Cd_{0.23}Te$ double-layer heterojunctions were grown by vertical LPE from infinite melt mercury-rich solutions. The n-type base layer was doped with indium and the p-type wider bandgap layer was doped with arsenic. Several excellent reviews describing this technology have been published.[1,13,14]

MATERIAL PROPERTIES

The thickness uniformity of the CdZnTe layers was determined from the spacing of interference fringes in the transmission vs wavenumber spectrum measured at room temperature using a Fourier transform infrared (FTIR) spectrometer. Note that this technique measures the combined thickness of the ZnTe and CdZnTe layers since the indices of refraction for these materials are nearly identical. X-ray rocking curve full-width at half-maximum (FWHM) measurements were determined from symmetric (400) reflections using a high-resolution x-ray diffractometer having a

Si four-crystal monochromator to produce CuKα$_1$ radiation and having an optically encoded angular readout for precise angle measurements. Cd$_{1-y}$Zn$_y$Te composition and its uniformity across the wafer surface was determined from 77K photoluminescence (PL) measurements.[15]

Figure 1 shows a plot of the CdZnTe thickness uniformity measured across the 3 inch diameter wafer. The thickness uniformity is excellent with a mean of 11.2 μm and a standard deviation/mean of 1.35%. The wafer is rotated about the center during growth and Fig. 1 shows the slight decrease in thickness from the center to edge which is unimportant for this application. Figure 2 shows a similar plot of the y = [ZnTe] composition measured across this same wafer. The composition is extremely uniform with a mean value of [ZnTe] = 3.58% and a standard deviation of 0.062%. Unlike the thickness plot in Fig. 1, the composition profile has no systematic variation from the center to edge of the wafer and is within the resolution of the PL measurements used to determine the composition. This composition uniformity is better than our previous results for MOCVD-grown CdZnTe/GaAs/Si.[2] Figure 3 shows the {400} x-ray FWHM measured at various locations on this same wafer. The average FWHM is 193 arc-s with a standard deviation/mean of 6%. This is typical of what is observed for CdZnTe of this same composition grown on GaAs/Si substrates. For comparison, we have grown [100]CdTe/Si having x-ray FWHM values as low as 78 arc-s which is the best reported value for growth directly on Si without the use of a GaAs intermediate layer.[12]

Figure 4 shows a plot of the {400} x-ray FWHM of a large number of Cd$_{1-y}$Zn$_y$Te layers grown directly on Si substrates by MBE (this work) compared with results of MOCVD-grown CdZnTe/GaAs/Si.[2] The MOCVD-grown CdZnTe layers shown in Fig. 4 have a nominal thickness of 8 μm. Figure 4 shows that the CdZnTe layers grown by either technique are comparable in quality and the FWHM increases with increased [ZnTe] alloy content. This FWHM broadening is a characteristic that is peculiar to ternary CdZnTe alloys (but not CdTe or ZnTe binary compounds) grown by vapor phase epitaxial techniques and has been attributed to phase separation[16,17] and is discussed in more detail elsewhere.[2] The data points for the MBE CdZnTe layers in Fig. 4 that exceed approximately 250 arc-s are associated with early process development experiments and are not indicative of the current process reproducibility.

Hg$_{0.77}$Cd$_{0.23}$Te baselayers having a nominal thickness of 15 μm were grown on the CdZnTe/Si substrates using LPE and compared with similar growths done earlier on CdZnTe/GaAs/Si substrates grown by MOCVD.[2] We have always found that the x-ray FWHM of the HgCdTe layer grown on a Si-based substrate is substantially better than the FWHM of the starting Cd$_{1-y}$Zn$_y$Te epitaxial layer. This FWHM reduction is attributed to dislocation annihilation which occurs both as the thickness of the CdZnTe and HgCdTe layers increase and to thermal annealing, which increases the mobility of dislocations, during the HgCdTe LPE growth.

The reduction in x-ray FWHM in the LPE-grown HgCdTe layers is also related to the composition of the CdZnTe/Si substrates as shown in Fig. 5. Figure 5 is a plot of the x-ray FWHM of HgCdTe layers vs the composition of the CdZnTe/Si substrate grown by MBE (this work) compared with our results using MOCVD-grown CdZnTe/GaAs/Si substrates. Figure 5 shows that the use of ternary Cd$_{1-y}$Zn$_y$Te grown either directly on Si or on GaAs/Si substrates, particularly y ≈ 0.03–0.05, results in a smaller x-ray FWHM in the HgCdTe layer compared with using a CdTe buffer layer. The most obvious explanation is to attribute this effect to closer lattice-matching of the CdZnTe buffer layer to the HgCdTe layer, but it is interesting to observe that this near lattice matching results in a lower x-ray FWHM in the HgCdTe despite
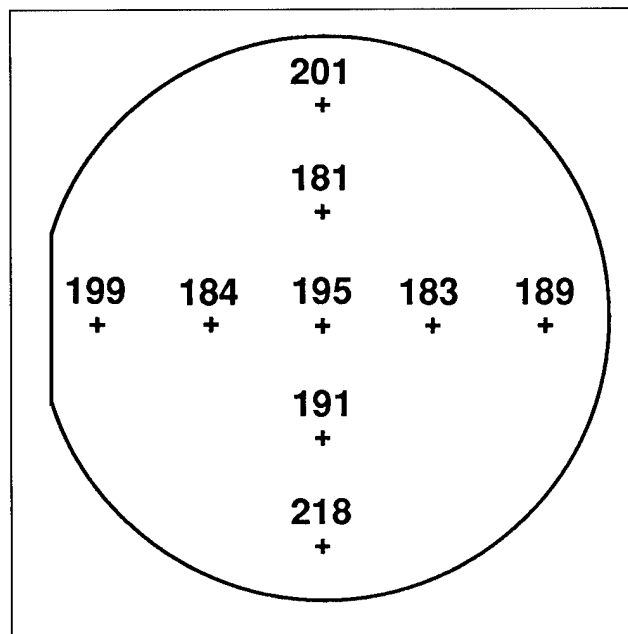
Fig. 3. {400} x-ray FWHM measured over a 3 inch Cd$_{0.96}$Zn$_{0.04}$Te/Si wafer (mean = 193 arc-s, standard deviation = 11.6 arc-s).
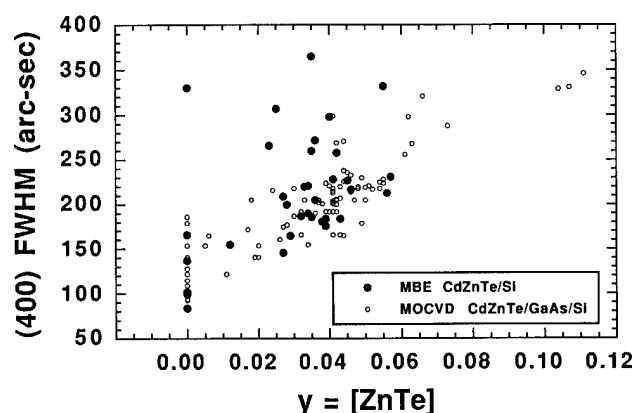
Fig. 4. Plot of the {400} x-ray FWHM of Cd$_{1-y}$Zn$_y$Te layers grown directly on Si substrates by MBE (this work) compared with results of MOCVD-grown CdZnTe/GaAs/Si as a function of y = [ZnTe] substrate composition.

the fact that the ternary CdZnTe layers have a much broader x-ray FWHM compared with CdTe. Figure 5 also shows that excellent quality HgCdTe can be grown by LPE on CdZnTe/Si substrates and that several of these layers have FWHM values that are better than those achieved on CdZnTe/GaAs/Si substrates; so far the best value we have achieved is 54 arc-s.

Similar to our earlier observations on CdZnTe/GaAs/Si,[2] a further benefit of using the ternary CdZnTe buffer layers is seen by the improvement in the surface morphology of HgCdTe grown by LPE on these substrates compared with HgCdTe layers grown on either CdTe/Si or CdTe/GaAs/Si. Figures 6a and 6b compare the surface morphology, accentuated using Nomarski optical microscopy, of MBE-grown $Cd_{0.96}Zn_{0.04}Te/Si$ and $Hg_{0.77}Cd_{0.23}Te$ grown on $Cd_{0.96}Zn_{0.04}Te/Si$, respectively. Using a surface profilometer, the peak-to-peak roughness of the CdZnTe buffer layer (Fig. 6a) is approximately 25Å while that of the HgCdTe (Fig. 6b) grown on a CdZnTe buffer

Fig. 5. Plot of the {400} x-ray FWHM of LPE-grown LWIR $Hg_{0.77}Cd_{0.23}Te$ layers vs the composition of the CdZnTe/Si substrate grown by MBE (this work) compared with our results using MOCVD-grown CdZnTe/GaAs/Si substrates.

layer is approximately 0.25 µm. The MBE-grown CdZnTe/Si surface morphology is substantially smoother than our previous results on MOCVD-grown CdZnTe/GaAs/Si which had a peak-to-peak roughness of approximately 0.1 µm.[2] However, in both cases, the LPE-grown HgCdTe had a surface roughness of approximately 0.25 µm and is apparently independent of the roughness of the initial CdZnTe layer (at least in the range we have measured). This HgCdTe surface morphology is adequate to fabricate high density focal-plane arrays as discussed in the next section.

LWIR HgCdTe 256 × 256 ARRAYS ON CdZnTe/Si SUBSTRATES

Long wavelength infrared HgCdTe 256 × 256 hybrid arrays and test structures were fabricated from p-on-n double-layer heterojunctions grown by LPE on the MBE-grown CdZnTe/Si substrates by defining and etching mesas to isolate the individual detectors. The center-to-center spacing of the individual elements was 30 µm in the 266 × 256 array and 50 µm in the miniarray on the test structure. Figure 7a shows a histogram of the resistance-area product at zero bias (R_oA_o; optical area, $A_o = 2.5 \times 10^{-5}$ cm^2) of 23 diodes in a miniarray from the test structure, accessed from a fanout, measured at T = 78K under f/2 field of view (FOV, 300K) background and Fig. 7b shows the spectral response of two of these detectors measured at zero bias at T = 78K. The mean R_oA_o product is 613 Ω-cm^2 for detectors having a cutoff wavelength of 9.4 µm and a mean quantum efficiency of 64% (no anti-reflection coating) which demonstrates that high-quality LWIR HgCdTe detectors can be fabricated directly on Si substrates.

To help determine the mechanisms which limit the performance of these detectors, the R_oA_j product (junction area, $A_j = 1.1 \times 10^{-5}$ cm^2) was measured as a function of temperature at zero FOV for one of the miniarray diodes in Fig. 7 which has a cutoff wave-

a   b
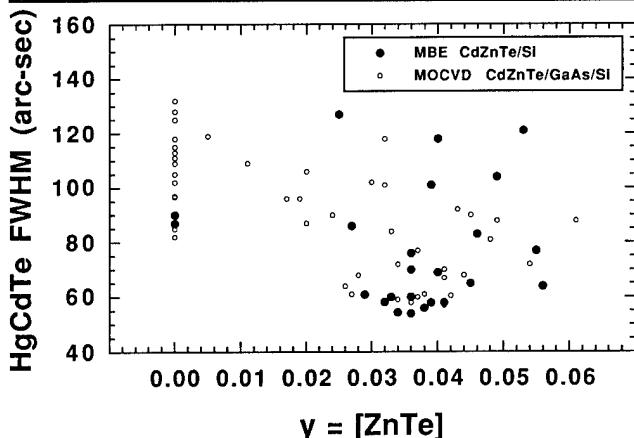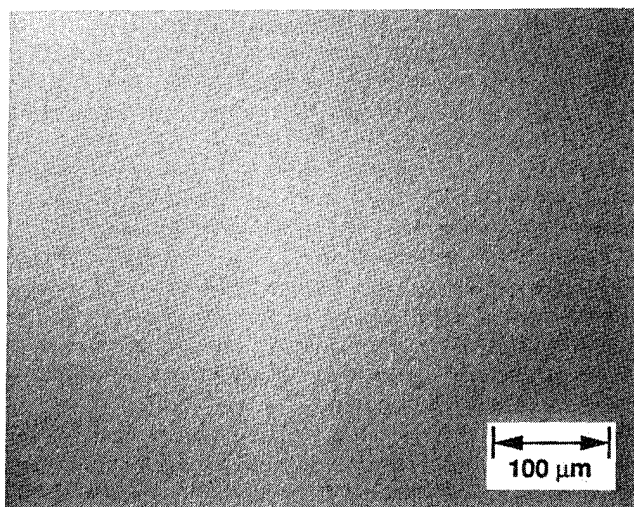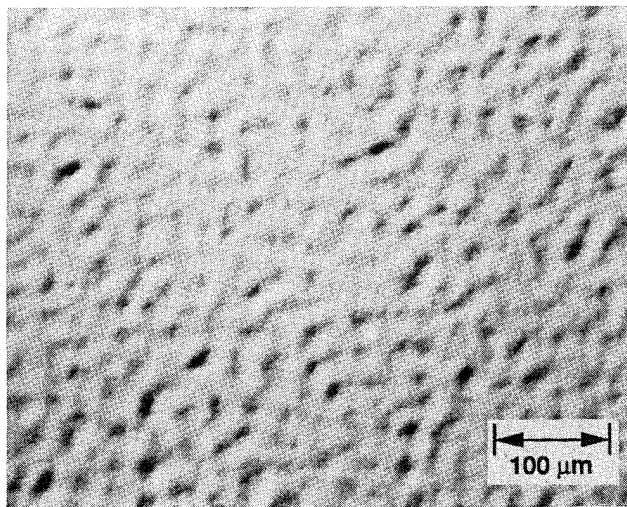
Fig. 6. Nomarski micrographs comparing the surface morphology of (a) MBE-grown $Cd_{0.96}Zn_{0.04}Te/Si$, and (b) $Hg_{0.77}Cd_{0.23}Te$ grown by LPE on $Cd_{0.96}Zn_{0.04}Te/Si$.
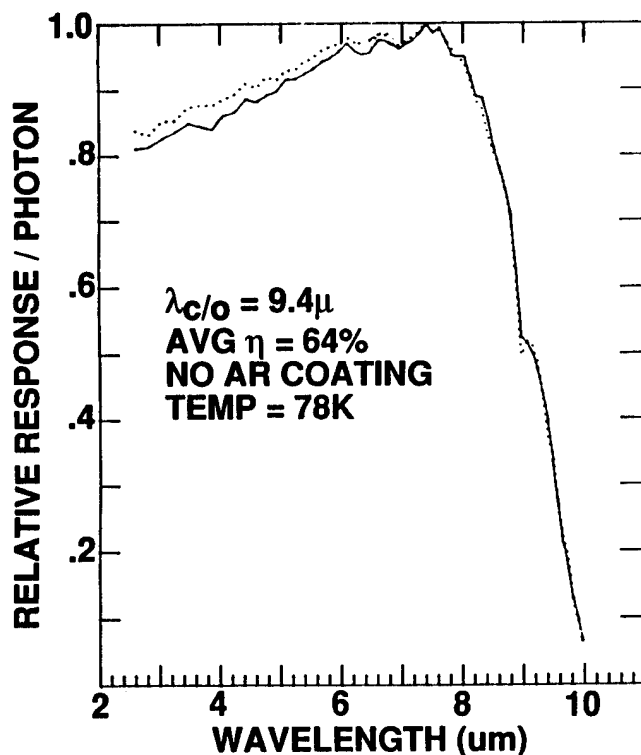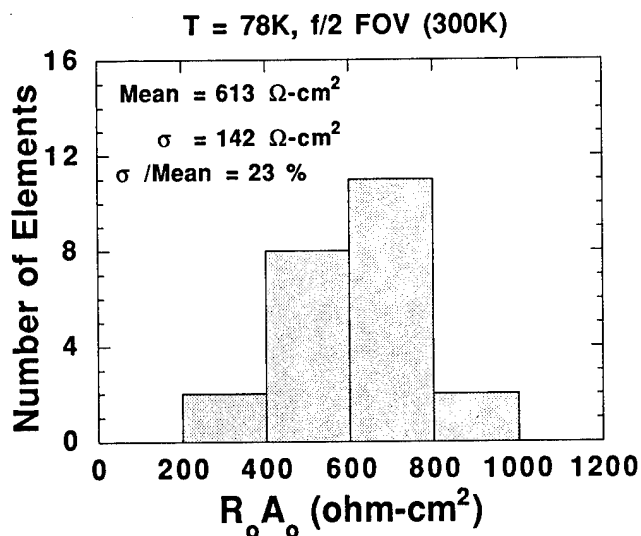
Fig. 7. (a) R_oA_o histogram of 23 diodes in a HgCdTe test structure miniarray fabricated on CdZnTe/Si substrates measured at T = 78K under f/2 FOV (300K) background, and (b) spectral response of two of these detectors measured at zero bias at T = 78K.

Fig. 8. R_oA_j product measured at zero FOV vs inverse temperature for a HgCdTe miniarray diode fabricated on CdZnTe/Si.
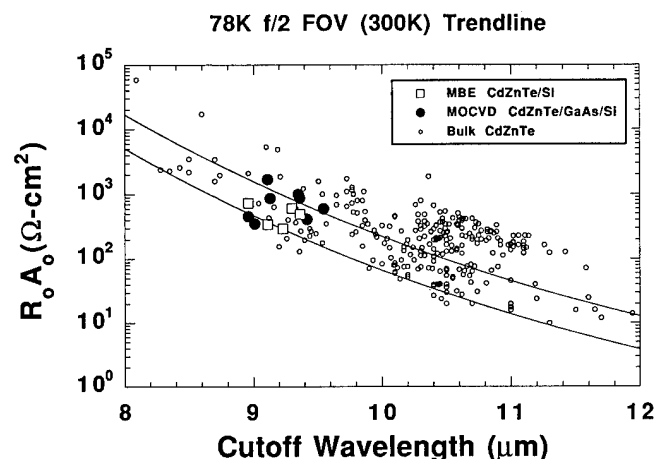
Fig. 9. Comparison of recent results of LWIR HgCdTe arrays fabricated on MBE-grown CdZnTe/Si and MOCVD-grown CdZnTe/GaAs/Si with a historical trendline of arrays fabricated on bulk CdZnTe for a wide variety of applications at different cutoff wavelengths; each data point represents the array average R_oA_o product measured at f/2 FOV (300K) background at a temperature of 78K.

length of 9.4 µm at 78K. Figure 8 shows a plot of R_oA_j vs 1/T for this diode. A line with a slope that corresponds to the diffusion-limited R_oA_j product and is representative of detectors fabricated on bulk CdZnTe substrates is also shown in Fig. 8. Figure 8 shows that the R_oA_j product of the diode fabricated on CdZnTe/Si is diffusion-limited for temperatures exceeding approximately 100K; below about 100K, the R_oA_j product is affected by both excess generation-recombination (g-r) and tunneling currents. At 40K, the R_oA_j product is nearly 10^5 Ω-cm^2 which is excellent for a Si-based substrate; a detector fabricated on bulk CdZnTe with this same cutoff wavelength would have a R_oA_j prod-

uct exceeding 10^7 Ω-cm^2 when cooled to 40K.

These results are entirely consistent with our previous findings for HgCdTe MWIR[18] and LWIR[2] detectors fabricated on CdZnTe/GaAs/Si substrates. We believe that the excess g-r and tunneling currents are associated with the increased density of threading dislocations, determined from the etch-pit density, in the HgCdTe which are typically in the mid-10^6 cm^{-2} range for Si-based substrates compared with about 10^5 cm^{-2} for bulk CdZnTe substrates. This higher dislocation density only weakly affects the diffusion current, spectral response, and quantum efficiency while it can dramatically affect the R_oA product, particularly at temperatures below 78K.[19,20]

Figure 9 compares the recent results of LWIR HgCdTe arrays fabricated on MBE-grown CdZnTe/Si and MOCVD-grown CdZnTe/GaAs/Si with a historical trendline of arrays fabricated on bulk CdZnTe for

AVG = 1.0×10^{-12}

σ = 14%

RESPONSIVITY @ 78K
$(\times 10^{-13})$ (mV/ph/cm^2-sec)

a

AVG = 56mK

σ = 13mK

AVG D*
= 2.6×10^{11}
(cm Hz$^{1/2}$/W)

NEΔT @ 78K (mK)

b
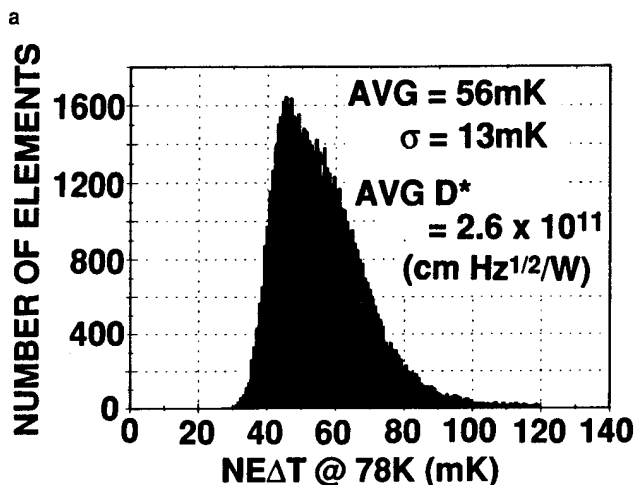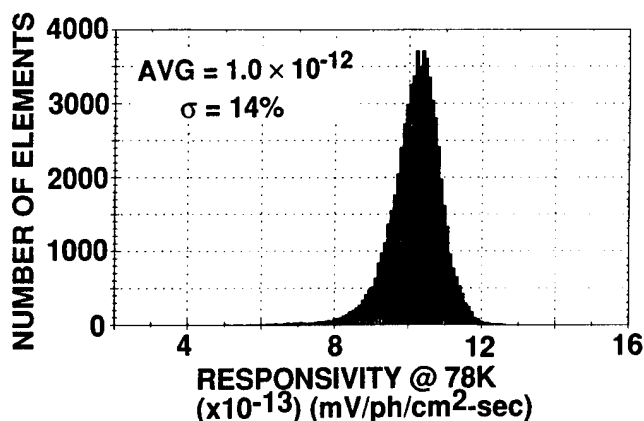
Fig. 10. Performance of HgCdTe LWIR 256×256 array fabricated on CdZnTe/Si substrate showing histogram of (a) responsivity and (b) NEΔT measured at 78K.

a wide variety of applications at different cutoff wavelengths; each data point represents the array average R_oA_o product measured at f/2 FOV (300K) background at a temperature of 78K. The two continuous curves shown in Fig. 9 were calculated to indicate diffusion-limited behavior and are only shown as a guide to the eye. Figure 9 shows first that there is no significant difference between arrays fabricated on either CdZnTe/Si or CdZnTe/GaAs/Si and second that the results on these Si-based substrates are comparable with results on bulk CdZnTe substrates at 78K. A further reduction in the dislocation density for HgCdTe grown on Si-based substrates is needed to improve the detector performance margin and reverse-bias characteristics at 78K and to improve detector performance at lower temperatures in comparison with bulk CdZnTe substrates.

One of the LWIR HgCdTe 256 x 256 arrays fabricated on the MBE-grown CdZnTe/Si substrates was hybridized to a Si readout circuit and tested at 78K under a background flux of 1.6×10^{15} ph/cm^2-s and a 600 μs integration time. The readout includes a standard direct injection input circuit with a large integration capacitor for large charge storage capacity. Other features include dynamic adjustment of the integration period in a range from 20 μs to 8 ms and

frame rates as high as 120 Hz. Figure 10a shows a histogram of the responsivity which has an average of 1.0×10^{-12} mV/ph/cm^2-s and a standard deviation/mean of 14%; Fig. 10b shows the NEΔT histogram which has an average of 56mK and standard deviation of 13mK. Average D* under these conditions was 2.6×10^{11} Jones, a value which is in good agreement with a BLIP-limited D* of 6.6×10^{11} Jones, for a detector with 64% quantum efficiency. These results represent the first demonstration of an LWIR HgCdTe 256×256 focal plane array using a substrate consisting of CdZnTe grown directly on Si without the use of an intermediate GaAs buffer layer.

SUMMARY AND CONCLUSIONS

Direct epitaxial growth of high-quality {100}CdZnTe on 3 inch diam vicinal {100}Si substrates has been achieved using MBE; a ZnTe initial layer was used to maintain the {100}Si substrate orientation. The properties of these substrates and associated LPE-grown HgCdTe layers and LWIR detectors were compared directly with our related efforts using MOCVD-grown CdZnTe/GaAs/Si substrates. The MBE-grown CdZnTe layers are highly specular and have both excellent thickness uniformity, determined from FTIR measurements, and compositional uniformity, determined from 77K PL measurements. The x-ray FWHM of the MBE-grown CdZnTe/Si increases with composition, which is a characteristic of CdZnTe grown by vapor phase epitaxy, and is essentially equivalent to our results obtained on CdZnTe/GaAs/Si. As we have previously observed, the LPE-grown HgCdTe x-ray FWHM decreases, particularly for CdZnTe compositions near the lattice matching condition to HgCdTe. Several of these HgCdTe layers grown on CdZnTe/Si have x-ray FWHM values that are better than those achieved on CdZnTe/GaAs/Si substrates; so far the best value we have achieved is 54 arc-s.

Using these CdZnTe/Si substrates, we have fabricated the first high-performance LWIR HgCdTe detectors and 256 × 256 arrays. We find first that there is no significant difference between arrays fabricated on either CdZnTe/Si or CdZnTe/GaAs/Si and second that the results on these Si-based substrates are comparable with results on bulk CdZnTe substrates at 78K. A further reduction in the dislocation density for HgCdTe grown on Si-based substrates is needed to improve the detector performance margin and reverse-bias characteristics at 78K and to improve detector performance at lower temperatures in comparison with bulk CdZnTe substrates. Finally, these Si-based thermal-expansion-matched substrates are compatible with our mature LPE HgCdTe photovoltaic detector process and the recent achievement[11,12] of high-quality {112}CdZnTe/Si holds promise for all-MBE grown HgCdTe detectors on Si-based substrates.

REFERENCES

1. T. Tung, L.V. DeArmond, R.F. Herald, P.E. Herning, M.H. Kalisher, D.A. Olson, R.F. Risser, A.P. Stevens and S.J. Tighe, *Infrared Detectors: State of the Art,* ed. W.H. Makky, (Bellingham, WA: Soc. Phot. Opt. Inst. Eng., 1992), 1735, p.109.
2. S.M. Johnson, J.A. Vigil, J.B. James, C.A. Cockrum, W.H. Konkel, M.H. Kalisher, R.F. Risser, T. Tung, W.J. Hamilton, W.L. Ahlgren and J.M. Myrosznyk, *J. Electron. Mater.* 22, 835 (1993).
3. S.J.C. Irvine, J. Bajaj, R.V. Gil, H. Glass and L.O. Bubulac, *J. Electron. Mater.* 24, 457 (1995).
4. N.H. Karam, R. Sudharsanan, A. Mastrovito, M.M. Sanfacon and F. Smith, *J. Electron. Mater.* 24, 483 (1995).
5. W.-S. Wang, H. Ehsani and I. Bhat, *J. Electron. Mater.* 22, 873 (1993).
6. W.-S. Wang and I. Bhat, *J. Electron. Mater.* 24, 451 (1995).
7. R. Sporken, S. Sivananthan, K.K. Mahavadi, G. Monfroy, M. Boukerche and J.P. Faurie, *Appl. Phys. Lett.* 55, 1879 (1989).
8. Y.P. Chen, J.P. Faurie, S. Sivananthan, G.C. Hua and N. Otsuka, *J. Electron. Mater.* 24, 475 (1995).
9. T.J. deLyon, J.A. Roth, O.K. Wu, S.M. Johnson and C.A. Cockrum, *Appl. Phys. Lett.* 63, 818 (1993).
10. T.J. deLyon, S.M. Johnson, C.A. Cockrum, O.K. Wu and J.A. Roth, *Infrared Detectors—Materials, Processing, and Devices,* eds. A. Appelbaum and L.R. Dawson (Pittsburgh, PA: Mater. Res. Soc., 1993), Vol. 302, p. 445.
11. T.J. deLyon, S.M. Johnson, C.A. Cockrum, W.J. Hamilton and O.K. Wu, *Growth and Characterization of Materials for Infrared Detectors,* (Bellingham, WA: Soc. Phot. Opt. Inst. Eng., 1993), SPIE 2021, in print.
12. T.J. deLyon, S.M. Johnson, C.A. Cockrum, O.K. Wu, W.J. Hamilton and G.S. Kamath, *First International Symposium on Long Wavelength Infrared Detectors and Arrays: Physics and Applications,* (Electrochem. Soc. Symp.), in print.
13. T. Tung, M.H. Kalisher, A.P. Stevens and P.E. Herning, *Materials for Infrared Detectors and Sources,* eds. R.F.C. Farrow, J.F. Schetzina and J.T. Cheung (Pittsburgh, PA: Mater. Res. Soc., 1987), Vol. 90, p. 321.
14. T. Tung, *J. Cryst. Growth* 86, 161 (1988).
15. S.M. Johnson, S. Sen, W.H. Konkel and M.H. Kalisher, *J. Vac. Sci. Technol.* B 9, 1897 (1991).
16. R.D. Feldman, R.F. Austin, A.H. Dayem and E.H. Westerwick, *Appl. Phys. Lett.* 49, 797 (1986).
17. R.D. Feldman, R.F. Austin, P.H. Fuoss, A.H. Dayem, E.H. Westerwick, S. Nakahara, T. Boone, H. Menéndez, A. Pinczuk, H.P. Valladares and S. Brennan, *J. Vac. Sci. Technol.* B 5, 690 (1987).
18. S.M. Johnson, M.H. Kalisher, W.L. Ahlgren, J.B. James and C.A. Cockrum, *Appl. Phys. Lett.* 56, 946 (1990).
19. S.M. Johnson, D.R. Rhiger, J.P. Rosbeck, J.M. Peterson, S.M. Taylor and M.E. Boyd, *J. Vac. Sci. Technol.* B 10, 1499 (1992).
20. R.S. List, *J. Electron. Mater.* 22, 1017 (1993).

Suppression of Twin Formation in CdTe(111)B Epilayers Grown by Molecular Beam Epitaxy on Misoriented Si(001)

Y.P. CHEN, J.P. FAURIE, and S. SIVANANTHAN

University of Illinois at Chicago, Microphysics Laboratory, Physics Department (M/C 273), 845 W. Taylor St. Room # 2236, Chicago IL 60607-7059

G.C. HUA and N. OTSUKA

School of Materials Engineering, Purdue University, West Lafayette, IN 47907

CdTe(111)B layers have been grown on misoriented Si(001). Twin formation inside CdTe(111)B layer is very sensitive to the substrate tilt direction. When Si(001) is tilted toward [110] or [100], a fully twinned layer is obtained. When Si(001) is tilted toward a direction significantly away from [110], a twin-free layer is obtained. Microtwins inside the CdTe(111)B layers are overwhelmingly dominated by the lamellar twins. CdTe(111)B layers always start with heavily lamellar twinning. For twin-free layers, the lamellar twins are gradually suppressed and give way to twin-free CdTe(111)B layer. The major driving forces for suppressing the lamellar twinning are the preferential orientation of CdTe[$11\bar{2}$] along Si[$1\bar{1}0$] and lattice relaxation. Such preferential orientation is found to exist for the CdTe(111)B layers grown on Si(001) tilted toward a direction between [110] and [100].

Keywords: CdTe/Si, heteroepitaxy, molecular beam epitaxy (MBE), twinning

INTRODUCTION

Before CdTe(111)B grown on Si(001) can be considered as an alternative substrate for the growth of HgCdTe, there are several obstacles to be eliminated. Foremost of those is formation of double-domain and twin in CdTe(111)B layers grown on Si(001), since CdTe[$11\bar{2}$] can align with any one of Si⟨001⟩ axes.[1] Such structural defects are nicely revealed by transmission electron microscopy (TEM) pictures.[2] In our previous publication,[1] we have also shown that the double-domain defect can be effectively eliminated by using the misoriented Si(001) tilted toward [110], which lifts the 90°-rotation symmetry of the Si(001) surface. In this paper, we present our investigation toward understanding and suppressing the formation of twinning.

Microtwins are known to be the common defects in CdTe(111) layers. Along the [111] orientation, the

crystal with zinc-blende structure, like the CdTe, can be visualized as being continuously piled up close packed planes. Each plane contains two sheets of atoms. There are two possible packing sequences, which are almost energetically identical. One is ABCABC · · ·. The other is ACBACB · · ·. The twin is presented when both types of sequences coexist inside the crystal. Basically, there are two types of twins, as shown in Fig. 1. The lamellar twin is formed with a coherent twin boundary parallel to the (111) plane, when layers in different sequences are packed on top of each other. The double-positioning twin is formed with an incoherent boundary perpendicular to the (111) plane, when layers in different sequences are packed side by side. Both twin configurations possess 180° rotation symmetry.

In order to prevent the formation of twinning in CdTe(111)B layer grown on Si(001) substrate, we have to avoid at least the 180° rotation symmetry of the Si(001) surface. This can be achieved by using the misoriented Si(001) with tilt parameters (θ,φ), as

Chen, Faurie, Sivananthan,
Hua, and Otsuka
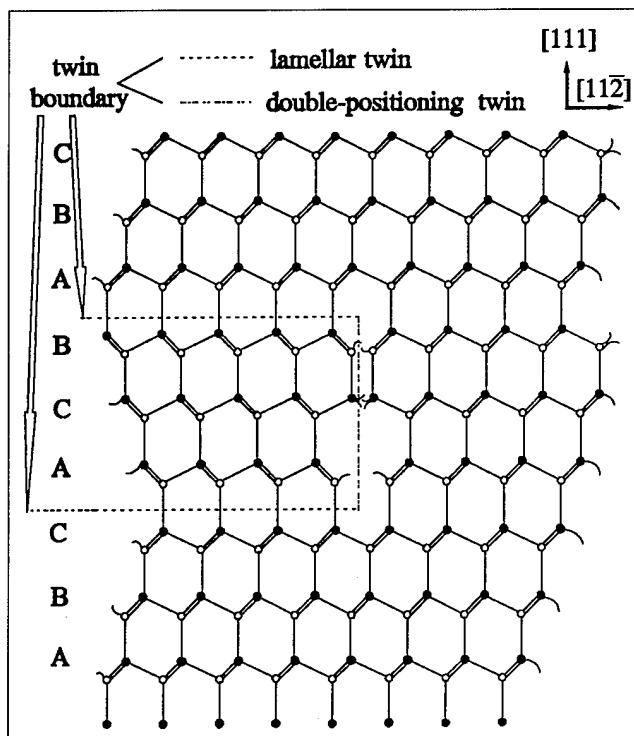
Fig. 1. Two types of microtwin structures in CdTe(111) layer.
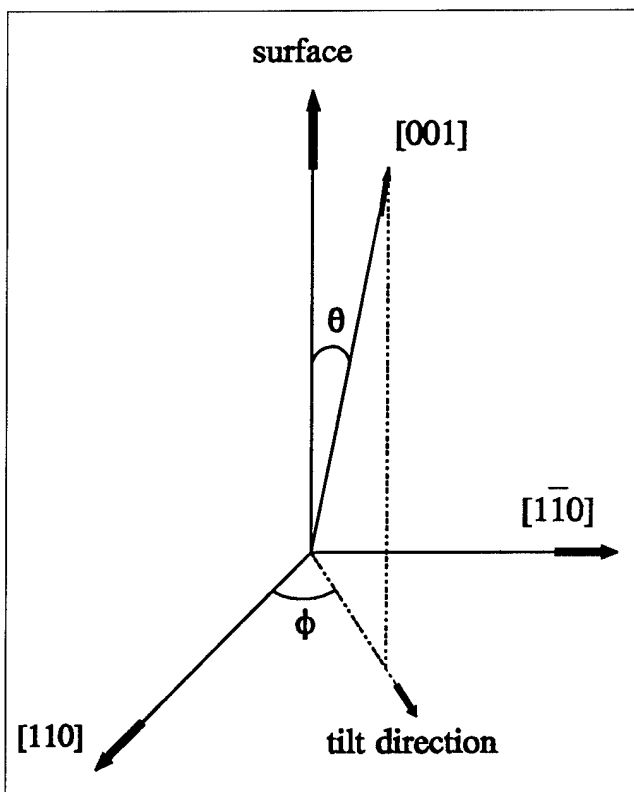
Fig. 2. Schematic illustration of substrate tilt and its tilt parameters.

defined in Fig. 2.

In this paper, we present our experimental results on the growth of CdTe(111)B on misoriented Si(001) with varying tilt parameters (θ, ϕ). The microtwin structure is revealed by TEM. The microtwin content

is detected by x-ray double crystal diffractometer (DCD).

EXPERIMENT

The substrates used for this research are 2 inch diam misoriented Si(001) wafers with varying tilt parameters (θ, ϕ). All the CdTe(111)B layers are grown in an OPUS 45 which is a multiwafer molecular beam epitaxy (MBE) system manufactured by ISA-Riber. This system can handle up to three 2 inch diam or one 5 inch diam wafer. In each run, CdTe(111)B layers are grown simultaneously on three 2 inch diam Si(001) substrates with same θ and different ϕ values, or vice versa. From run to run, we also use the same growth conditions, so that the experimental results are compatible.

The substrates used for the MBE growth of CdTe(111)B first go through a routine chemical cleaning procedure just before they are loaded into the MBE chamber. This chemical cleaning procedure is developed from both the RCA method,[3] and the method described by Ishizaka and Shiraki.[4] The procedure includes a degreasing step, a wet chemical etching, and an oxidation step. Between each step, the wafer is thoroughly rinsed with deionized water. As a result, at the end of the process, the wafer is covered by a protective thin oxide film. Immediately before deposition of CdTe, the oxide film is removed in-situ by heating up the wafer over 850°C.

CdTe(111)B layers are grown on Si(001) by using a two-step method which is similar to the method used routinely for the growth of GaAs on Si. CdTe is first grown at about 220°C for several minutes, then grown at about 260°C for about 10 min. The as-grown layer is then annealed at about 360°C under Te flux for 10 min. The remainder of the CdTe layer is grown at about 310°C. At the end of the growth, the layer is annealed in-situ at 360°C under Te flux for about 30 min. During the annealing, no surface re-evaporation is observed by reflection high energy electron diffraction (RHEED). The typical growth rate is about 2Å/S.

The as-grown layers are then evaluated by x-ray DCD for the layer quality and twin content. The layer quality is indicated by the line width which is defined as the full width at half maximum (FWHM) of the x-ray rocking curves. The twin content of the layers can be detected by x-ray diffraction. This was done in a similar way as the twin content of HgCdTe(111) was detected.[5] For a CdTe single crystal (111) orientation posses a threefold symmetry, which can be identified by a set of planes such as {224}, {335} etc. For a twinned CdTe layer, the twin counterpart is rotated around [111] axis by 180°. These are illustrated in Fig. 3.

In present work, we use the symmetry of {224} diffraction to study the twin content of the CdTe(111)B layers. The experimental setup for detecting the twin content in CdTe layers is demonstrated in Fig. 4a. When a sample is rotated around its surface normal, we expect to obtain three peaks of the rocking curves corresponding to {224} reflection for a twin-free layer.

Additional minor peaks, however, are recorded in between the two principal peaks. These are shown in Fig. 4b. The twin content is defined as following:

$$\text{twin content} = \frac{I_m}{I_m + I_p} \times 100\%,$$

where I_m and I_p are the intensities of minor peak and principal peak, respectively. In such a definition, the 50% twin content stands for a fully twinned CdTe(111)B layer.

Some CdTe(111)B layers are also examined by TEM. A cross-section bright field image can clearly reveal the microtwin structure inside the CdTe(111)B layers. This work is done in Purdue University.

RESULTS AND DISCUSSIONS

CdTe(111)B layers have been grown on Si(001) substrates with different tilt parameters (θ, ϕ). The twin contents of the layers are assessed by x-ray diffraction. Figure 5 shows the twin contents of the as-grown layers vs the substrate tilt directions (ϕ) with two sets of tilt angle (θ). When CdTe(111)B was grown on Si(001) tilted toward [110] ($\phi = 0$), the as-grown layers are plagued by heavy twinning. As the substrate tilt direction turns away from [110] or ϕ value increases, the twin content of the epilayers decreases. The twin content reaches its minimum when ϕ values fall between 30 and 36°. Then the twin content increases again as the ϕ value approaches 45°. These results indicate that the twin content is very sensitive to the substrate tilt direction.

In order to find out the contribution of the substrate tilt angle to the formation of the twin, we also grow CdTe(111)B on Si(001) with similar tilt direction and different tilt angle. In Fig. 6, we show the twin contents of the epilayers vs the substrate tilt angle with two sets of tilt directions. The results exhibit that the twin content tends to increase as the tilt angle increases. In other words, the increase of the tilt angle does not enhance suppression of the twin formation at all.

Since the x-ray diffraction can only provide the average twin content of the epilayer, the results give us no hint about the microtwin structure and its evolution as the layer thickness increases. Therefore, we also examine the epilayers by TEM. Figure 7 shows the cross-section bright field TEM images taken

a

b
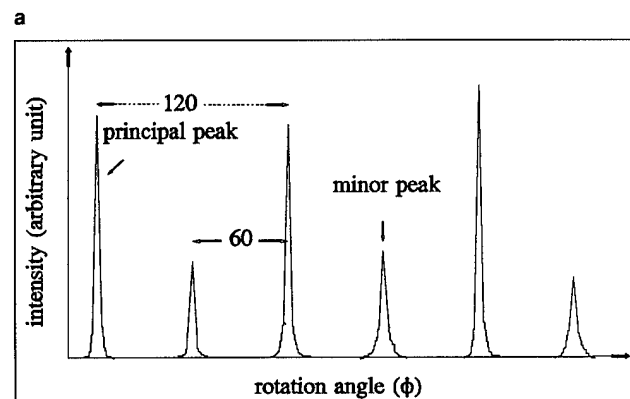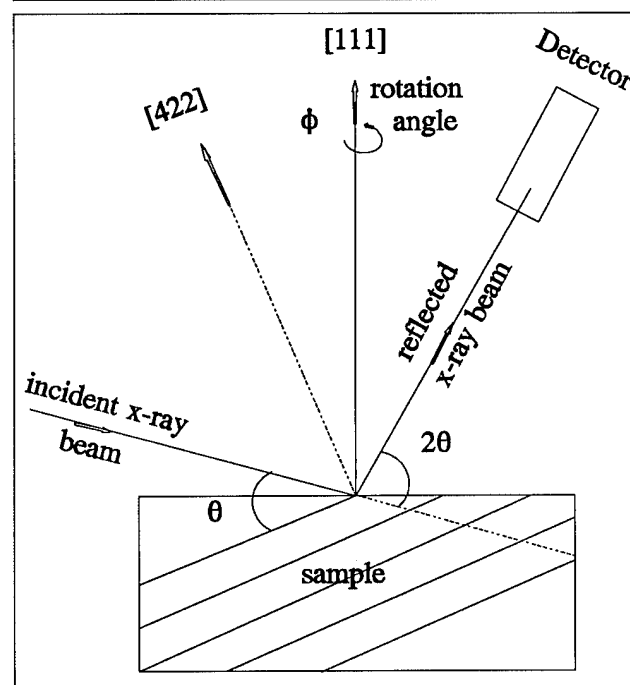
Fig. 4. (a) Experimental setup for measuring twin content in CdTe(111)B layers by x-ray diffraction, where θ is Bragg angle for (422) refraction and ϕ is rotation angle of the sample around its surface normal. (b) Schematic illustration of x-ray rocking curves of CdTe(111)B layer measured by the setup shown in (a). Present of minor peaks indicates a twinned layer.

Fig. 3. Schematic illustration of part of stereographic (111) projection, the projection in dash line shows presentation of twin as a result of 180° rotation around [111] axis.
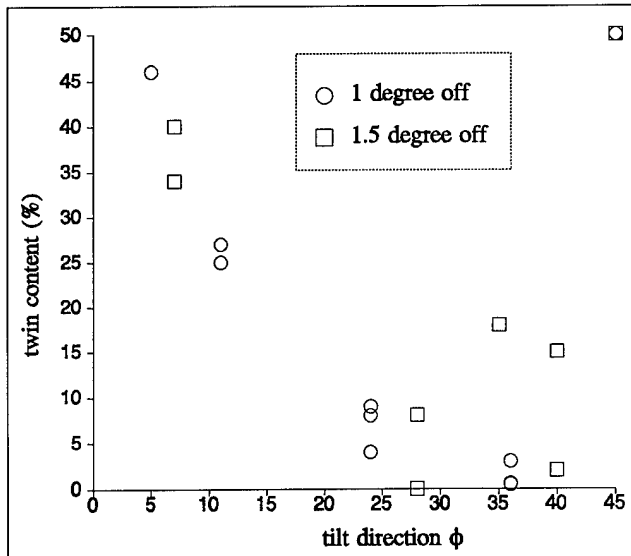
Fig. 5. Twin content of CdTe(111)B layers vs substrate tilt direction (θ) for two sets of tilt angles (θ).
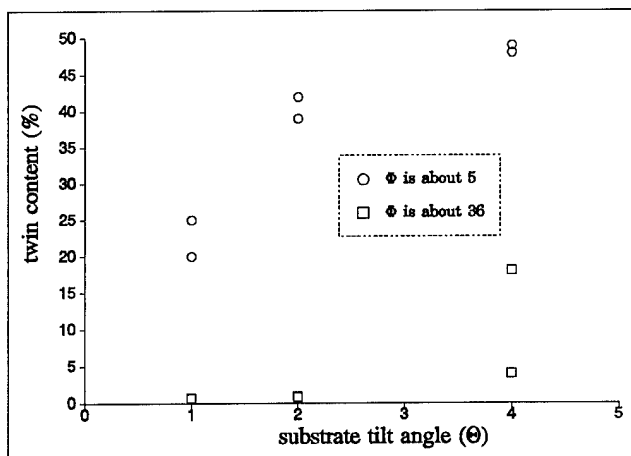
Fig. 6. Twin content of CdTe(111)B layers vs substrate tilt angle (θ) for two sets of tilt directions (φ).

from different parts of the CdTe(111)B layer at increasing distance from the CdTe/Si interface. The layer are grown on Si(001) tilted 1° toward [170] which is about 35° rotated from [110]. The pictures clearly indicate that the microtwins of the CdTe(111)B grown on Si(001) are overwhelmingly dominated by the lamellar twins, which is quite similar to the microtwin structures of the CdTe(111)B grown on GaAs(001), GaAs(111)B, and CdTe(111)B.[6,7] But, in our case, the lamellar twin does not extend throughout the whole layer. The heavy twinning is confined in a region within 2 μm from the interface. Then a few scattering twins present in the next 3 μm region. Beyond that the twins completely die out and give way to twin-free region of the CdTe(111)B layer. The twin content of the same layer measured by x-ray diffraction is about 0.6%. This is due to large penetration depth of the probing x-ray which is about 5 μm. The thickness of the CdTe layer is about 9 μm. Therefore, the x-ray diffraction can still detect the twin structure deep inside the CdTe layer, even though
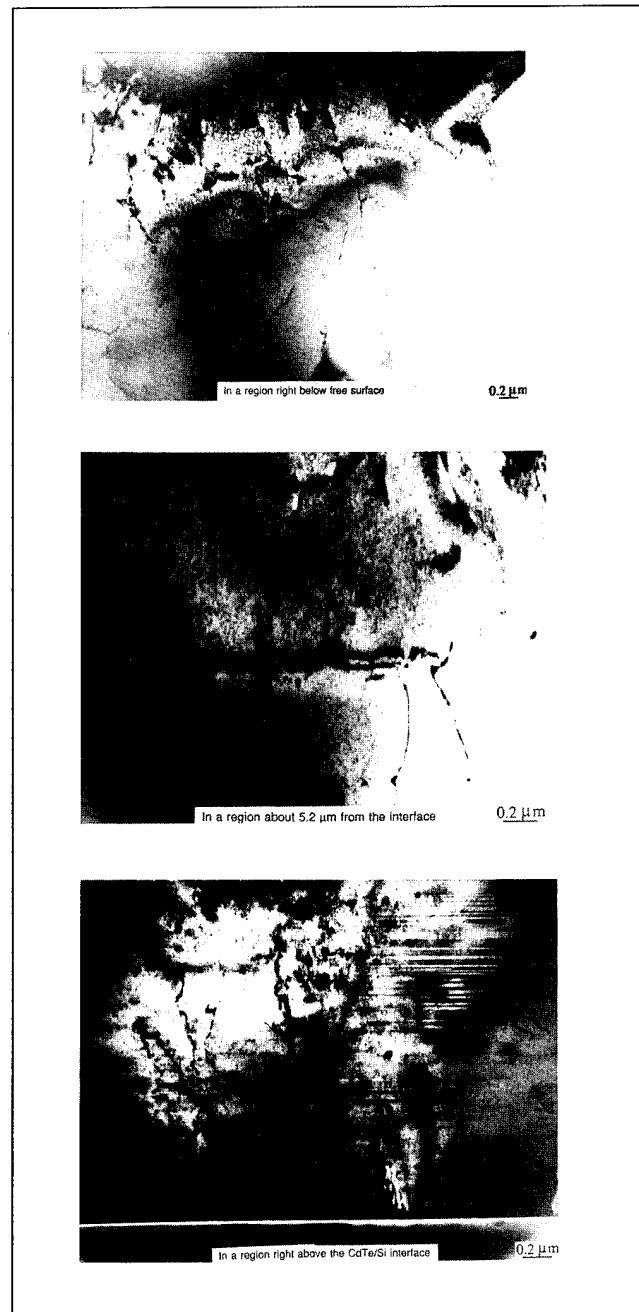
Fig. 7. Cross-section bright field TEM images of CdTe(111)B layer taken from different regions inside the layer, bright and dark contrast in the picture shows presentation of twins.

the top portion of the layer is twin-free. The x-ray double crystal rocking curve (DCRC) is also performed on this layer. The full width at half maximum (FWHM) of the rocking curve is 140 arc-s which, to our knowledge, represents the best CdTe(111)B layer grown directly on Si(001). Similar microtwinning evolution is also observed by A. Hobbs et al. on the CdTe(111)B grown by hot wall epitaxy (HWE) on GaAs(111)B.[8] In that case, the lamellar twins stop at about 6 μm from the interface and give way to a sixfold symmetric pattern of twinned sectors found at the layer surface. They attribute such a microtwinning evolution to the curvature growth front which pro-

duces a series of surface steps in the radiant direction. In the case of CdTe(111)B on Si(001), however, we do not observe such a symmetric twinned sector on the layer surface. The twin content on the CdTe(111)B surface is uniformly distributed over the whole wafer. The thickness of the layer is also very uniform over the whole wafer. Therefore, the diminishing of the lamellar twins in CdTe(111)B layer grown on Si(001) cannot be explained by the argument which seems to explain the development of microtwinning in the CdTe(111)B grown by HWE on GaAs(111)B.

Based on our experimental results, we have developed a model which may explain the development of the microtwinning in CdTe(111)B grown on Si(001) by MBE. Since the twin content is very sensitive to the substrate tilt direction which in turn determines the Si(001) surface step structure, the surface structure of the substrate must play some role in suppressing the microtwinning in CdTe(111)B layers. Figures 8a and 8b show schematic surface structure of misoriented Si(001) with $\phi = 0$ and $\phi > 0$, respectively. The only difference is the dense kinks which are introduced when Si(001) is tilted toward a direction away from [110].

In Fig. 8a, Si(001) is tilted toward [110]. The step edge is rather flat, except for some thermally excited random kinks. Still the symmetry relative to (110) plane remains on such a surface. Therefore,

CdTe(111)B layer has equal probability to be grown with its [11$\bar{2}$] aligned with either one of Si<1$\bar{1}$0> axes, which leads to the formation of twins.

In Fig. 8b, the Si(001) is tilted toward a direction with ϕ value significantly greater than zero. The same kind of dense kinks are introduced at the step edges, which, as a consequence, destroys the symmetry of the Si(001) surface structure relative to (110) plane. Therefore, CdTe(111)B layer has an unequal probability to be grown with its [11$\bar{2}$] aligned with Si[1$\bar{1}$0] or Si[$\bar{1}$10]. In fact, there is a preferential orientation of the CdTe[11$\bar{2}$] along Si[1$\bar{1}$0] axis. Such a preferential orientation of the CdTe[11$\bar{2}$] has been confirmed by our experimental observation. We have measured numerous CdTe(111)B layers with x-ray diffraction. With no exception, the CdTe[11$\bar{2}$] axis is always aligned with Si[1$\bar{1}$0], as shown in Fig. 8b. Even for a twinned CdTe(111)B layer, the domain of the CdTe(111)B with its [11$\bar{2}$]∥Si[1$\bar{1}$0] always gives large (422) x-ray diffraction intensity. In other words, the CdTe(111)B layers tend to be grown with its [11$\bar{2}$] aligned with Si[1$\bar{1}$0] or upward direction of the steps running along the Si[1$\bar{1}$0]. When the substrate tilt direction is reversed, the CdTe[11$\bar{2}$] is also reversed. Therefore, the kinks on the Si(001) surface do induce the preferential growth of CdTe(111)B, which can effectively prevent the formation of massive double-positioning twins at the interface as well as inside the
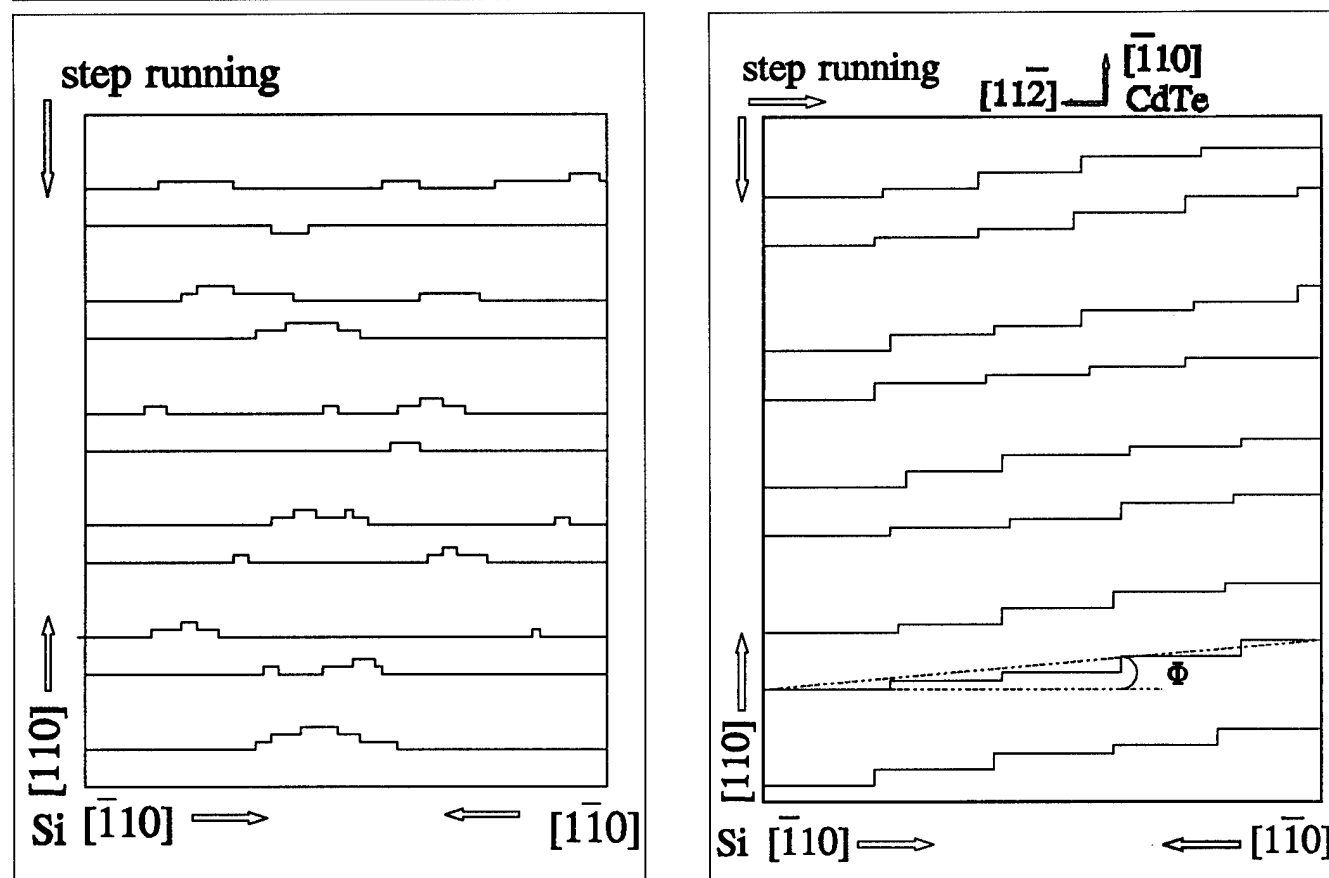
Fig. 8. Schematic step structure of Si(001) surface, (a) Si(001) is tilted toward [110], (b) Si(001) is tilted toward a direction rotated from [110] by an angle ϕ, and orientation of CdTe(111)B grown on such Si(001) substrate is also shown in up-right corner.
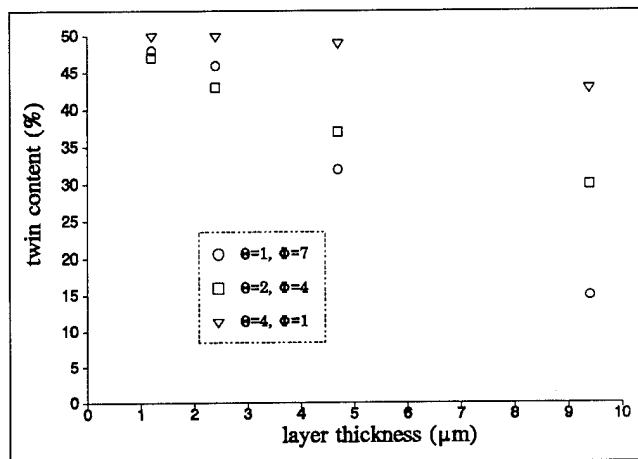
Fig. 9. Twin content of CdTe(111)B layers vs the layer thickness with three sets of tilt parameters.
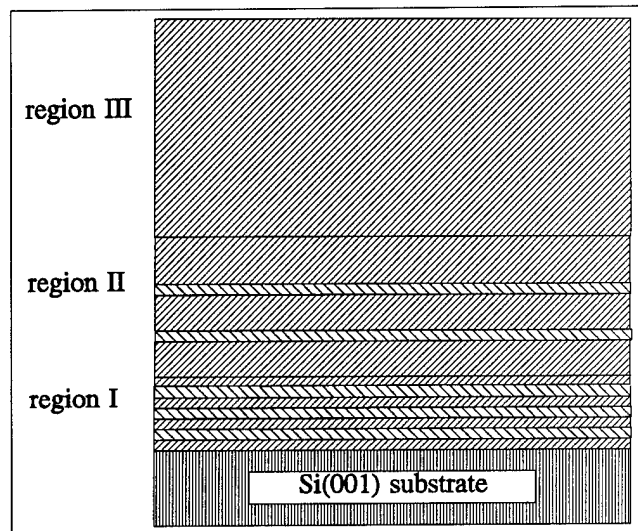
Fig. 10. Schematic cross-section illustration of evolution of twin structure in CdTe(111)B layers (for details see text).

CdTe layer. However, the microtwinning can happen in the other type of twin, namely lamellar twins. Since the lamellar twin boundary preserves the bonding between Cd and Te as shown in Fig. 1, we can expect the formation energy for a lamellar twin is very small. After the CdTe(111)B is initiated on the Si(001) substrate, there is still a finite probability to form the lamellar twins.

For the CdTe/Si system, the huge lattice mismatches both in horizontal and vertical directions make the initial growth of CdTe(111)B especially turbulent. In other words, the system is in a very energetic state. Therefore, it is not surprising to see the dense lamellar twins crowded in the region close to the interface. As the layer thickness increases, the strain caused by the lattice mismatches is being relaxed. The growth of CdTe(111)B is approaching the equilibrium state. The tendency to form lamellar twins is diminishing. This was also observed by our experiments. We have measured by x-ray diffraction the twin content of CdTe(111)B layers, grown on misoriented Si(001), with different layer thicknesses.

We found that twin content decreases steadily as the layer thickness increases, when the layers are grown on the Si(001) with ϕ greater than zero. On the other hand, the twin content virtually remains constant as the layer thickness increases, when the layers are grown on Si(001) tilted toward [110]. The results are shown in Fig. 9. Another important fact is the preferential orientation of CdTe[11$\bar{2}$] axis. Experimentally, we have found the CdTe(111)B preserves the tilt of Si(001) substrate. That means that the CdTe(111)B has the similar step structure to that of the misoriented Si(001). Therefore, one domain of the CdTe(111)B, with its [11$\bar{2}$] aligned with Si[1$\bar{1}$0] has higher probability to be grown than its twin counterpart. Above are mentioned two factors which will enhance the suppression of the formation of the lamellar twins. At a certain point, the domain with its [11$\bar{2}$] aligned with Si[1$\bar{1}$0] completely dominates the CdTe(111)B growth, and the twin-free layer is established.

Under such a model, a twin-free CdTe(111)B layer can be divided into three regions, as shown in Fig. 10. In region I, heavily lamellar twinning is presented due to turbulent initial growth of CdTe(111)B on Si(001). The typical thickness of this region is about 2 to 3 μm. In region II, only a few scattering lamellar twins are presented. The suppression of twin is attributed to the preferential orientation of CdTe[11$\bar{2}$] axis and relaxation of crystal lattice. The typical thickness of the region is about 2 to 4 μm. Finally, in region III, twin-free layer is obtained as the domain of CdTe(111)B layer with its [11$\bar{2}$] axis aligned with Si[1$\bar{1}$0] completely dominates the growth. It is also interesting to note that a fully twinned layer is obtained when substrate tilt direction is approaching [100] (ϕ = 45°). This is understandable when we notice that Si(001) surface regains its 90° rotation symmetry. Then the as-grown CdTe(111)B layer is plagued by double-domain defect as well as twins. Therefore, substrate tilt direction must be carefully chosen so that a twin-free layer can be obtained.

For CdTe(111)B layers grown on misoriented Si(001) with ϕ = 0, the results are quite different. Although the system is being relaxed as the layer thickness increases, the lamellar twins are still likely to happen since there is no preferential orientation of the CdTe[11$\bar{2}$] axis. That is what we observed in our experiments. When Si(001) substrate is tilted toward [110], even with tilt angle as large as 4°, a twinned CdTe(111)B layer is always obtained. It is also interesting to note that the substrate tilt angle plays little role in suppressing the microtwinning.

It is so even for the substrate with ϕ greater than zero. As we pointed out in our previous publication,[1] the step density on the surface is large for large tilt angle. Since at the step edge CdTe(111)B lattice suffers from huge distortion due to the large vertical lattice mismatch between the two materials, it is, in general, more difficult for the system to recover from such large distortion. As a result, it is easier to stimulate the formation of the lamellar twins.

CONCLUSIONS

We have reported that twin-free CdTe(111)B layers can be grown on misoriented Si(001). Suppression of twin formation is very sensitive to the substrate tilt direction (ϕ). Twinned layers are obtained when ϕ value is about 0 or 45°. Twin-free layers are obtained when ϕ is around 30 to 36°. The microtwins inside the CdTe(111)B layer are overwhelmingly dominated by the lamellar twins. Dense lamellar twins are always found in the region close to CdTe/Si interface. For a twin-free layer density of lamellar twin diminishes very fast as the layer thickness increases. Then a twin-free layer is established on such a twinned region. The major motive forces for suppression of twins are the preferential orientation of the CdTe [11$\bar{2}$] axis, which is introduced when the substrate is tilted toward a direction with ϕ significantly greater than zero, and the lattice relaxation as the layer thickness increases.

REFERENCES

1. Y.P. Chen, S. Sivananthan and J.P. Faurie, *J. Electron. Mater.* 22, 951 (1993).
2. R. Sporken, M.D. Lange, J.P. Faurie and J. Petruzzello, *J. Vac. Sci. Technol. B* 9, 1651 (1991).
3. W. Kern and D.A. Puotinen, *RCA Rev.* 31, 187 (1970).
4. A. Ishizaka and Y. Shiraki, *J. Electrochem. Soc.* 1333, 666 (1986).
5. R. Koestner, V. Lopes, R. Korenstein, S. Oguz, V. Kreismanis, H. Ehsani and I. Bhat, *J. Vac. Sci. Technol. B* 10, 1643 (1992).
6. P.D. Brown, J.E. Hails, G.J. Russell and J. Woods, *Appl. Phys. Lett.* 50, 1144 (1987).
7. I.V. Sabinina, A.K. Gutakovskii, Yu.G. Sidorov and V.D. Kuzmin, *Phys. Stat. Solidi* (a) 126, 181 (1991).
8. A. Hobbs, O. Ueda, Y. Nishijima, K. Shinohara and I. Umebu, *J. Cryst. Growth* 126, 605 (1993).

Large Area Depositon of Cd$_{1-x}$Zn$_x$Te on GaAs and Si Substrates by Metalorganic Chemical Vapor Deposition

N.H. KARAM, R. SUDHARSANAN, A. MASTROVITO, and M.M. SANFACON

Spire Corporation, One Patriots Park, Bedford, MA 01730

F.T.J. SMITH

Loral Infrared & Imaging Systems, Lexington, MA 02173

M. LEONARD and N.A. EL-MASRY

North Carolina State University, Raleigh, NC 27695

Results of large-area (up to 1000 cm²/run) Cd$_{1-x}$Zn$_x$Te heteroepitaxy on both GaAs and GaAs/Si substrates by metalorganic chemical vapor deposition (MOCVD) are presented. Cd$_{1-x}$Zn$_x$Te (x = 0–0.1) films exhibited specular surface morphology, 1% thickness uniformity (standard deviation), and compositional uniformity (Δx) of ±0.002 over 100 mm diam substrates. For selected substrate orientations and deposition conditions, the only planar defects exhibited by (111)B Cd$_{1-x}$Zn$_x$Te/GaAs/Si films were lamella twins parallel to the CdTe/GaAs interface; these do not propagate through either the Cd$_{1-x}$Zn$_x$Te layer or subsequently deposited liquid phase epitaxy (LPE) HgCdTe layer(s). Background Ga and As-impurity levels for Cd$_{1-x}$Zn$_x$Te on GaAs/Si substrates were below the secondary ion mass spectroscopy detection limit. Preliminary results of HgCdTe liquid phase epitaxy using a Te-rich melt on Si-based substrates resulted in x-ray rocking curve linewidths as narrow as 72 arc-sec and etch-pit densities in the range 1 to 3 × 10⁶ cm².

Key words: CdZnTe/GaAs, CdZnTe/GaAs/Si, GaAs/Si, CdZnTe, heteroepitaxy, HgCdTe, liquid phase epitaxy (LPE), metalorganic chemical vapor deposition (MOCVD)

INTRODUCTION

The growth of heteroepitaxial Cd$_{1-x}$Zn$_x$Te on sapphire, GaAs, and Si-based alternative substrates has attracted significant interest in recent years due to its potential for the fabrication of large-area HgCdTe infrared focal plane arrays (IRFPAs).[1-13] To date, the best IRFPAs are fabricated using liquid phase epitaxy (LPE) on bulk Cd$_{1-x}$Zn$_x$Te substrates.[1,2] However, Si-based substrates have several advantages over these including availability in large diameters at lower cost, higher mechanical strength, thermal expansion match to Si-readout circuitry, and the prospect for monolithic integration of IRFPAs with Si-based integrated circuits (ICs). Successful deposition of Cd$_{1-x}$Zn$_x$Te on GaAs and Si-based substrates has been demonstrated using metalorganic chemical vapor deposition (MOCVD),[7,8] hot wall epitaxy,[4] atomic layer epitaxy,[5,6] and molecular beam epitaxy (MBE).[9] The main hindrances to the progress of this alternative substrate technology are the high density of defects (5 × 10⁶ to 1 × 10⁷ cm⁻²) resulting from the large lattice mismatch between CdZnTe and Si, and the thermal-expansion-coefficient mismatch which leaves the heteroepitaxial film under a residual bi-axial tensile stress. For this technology to reach its desired goals, large area Cd$_{1-x}$Zn$_x$Te on Si-based substrates with defect densities lower by one to two orders of magnitude than have been achieved to date are required.

Although high defect density has been shown to degrade the low-temperature performance of IR-detectors, respectable high-temperature performance has been reported for IRFPAs fabricated using LPE-HgCdTe on MOCVD-Cd$_{1-x}$Zn$_x$Te/ GaAs/Si alternative

substrates.[7,10] Heteroepitaxy of [111]B $Cd_{1-x}Zn_xTe$ on GaAs and Si-based substrates has been plagued with a high density of twins[12,13] which propagated into subsequently deposited LPE films, degrading their properties. This prompted researchers to develop LPE of HgCdTe on (100) $Cd_{1-x}Zn_xTe$ where twins are unstable. However, recent results for (111)B CdTe-on-sapphire showed that twin formation can be suppressed by proper selection of the deposition parameters, heat treatment, and wafer orientation.[14] In this paper, we report the first demonstration of large-area (18, 75 mm or ten, 100 mm wafers per run, a total area of 1000 cm²) MOCVD of $Cd_{1-x}Zn_xTe$ on GaAs and GaAs/Si substrates resulting in excellent thickness and compositional uniformity. We also report initial results for LPE of HgCdTe on (111)B $Cd_{1-x}Zn_xTe$/GaAs/Si alternative substrates.

Fig. 1. Spire's dual-chamber production-scale SPI-MOCVDT™ 3000G reactor for III-V and II-VI compounds.

Avg. = 41997Å
Range = 1494Å
% Range = ±1.8%
Std. Dev. = 424Å
% Std. Dev. = 1.0%

Fig. 2. Thickness uniformity contour map for (111) $Cd_{1-x}Zn_xTe$ deposited on a 100 mm GaAs wafers in SPI-MOCVD 3000G.

EXPERIMENTAL

Large-area MOCVD of (111) $Cd_{1-x}Zn_xTe$ has been achieved on (100) GaAs and (100) GaAs-on-Si substrates in a dual chamber, low-pressure MOCVD reactor, the SPI-MOCVD™ 3000G, which has a capacity of up to 18, 75 mm wafers or ten, 100 mm wafers per run. Figure 1 shows the dual-chamber reactor which is equipped with two independent gas handling systems for the separate deposition of III-V (e.g., GaAs) and II-VI compounds with no cross contamination. The GaAs-on-Si films were deposited using the conventional two-step process, reported earlier,[15] to thicknesses in the range of 0.5 to 2.5 µm. Dimethyl-cadmium (DMCd), dimethyltellurium (DMTe), and diethylzinc (DEZn) were used for Cd, Te, and Zn sources, respectively. In a typical deposition experiment for [111]B $Cd_{1-x}Zn_xTe$ on GaAs/Si, the substrate is first exposed to a short pre-growth bake to remove the native oxide and provide a Ga-rich surface. This is followed by a two-step deposition of CdZnTe at temperatures in the range 390 to 450°C, reactor pressures in the range 300 to 650 Torr, VI/II in the range 5 to 0.4, and a growth rate in the range 4 to 8Å/s.

The $Cd_{1-x}Zn_xTe$ films were characterized using Nomarski optical microscopy for surface morphology, optical reflectance spectroscopy (ORS)[16] for thickness measurement, and photoluminescence (PL) at 77K and room temperature for compositional measurement and uniformity. Secondary ion mass spectroscopy (SIMS) was used for impurity level determination. Double crystal x-ray diffraction (DXRD), Laué x-ray back reflection, cross-sectional transmission electron microscopy (XTEM), and selective-area electron diffraction (SAD) were used for structural characterization and determination of film orientation. Cross-sectional TEM samples were prepared using standard mechanical thinning followed by Ar⁺-ion milling at 77K to achieve foil thicknesses in the range 0.2 to 0.5 µm. Samples were examined using a Hitachi-800 TEM operated at 200 kV acceleration voltage.

RESULTS AND DISCUSSION

Successful fabrication of $Cd_{1-x}Zn_xTe$ on Si-based alternative substrates requires addressing the following issues: thickness and compositional unifor-
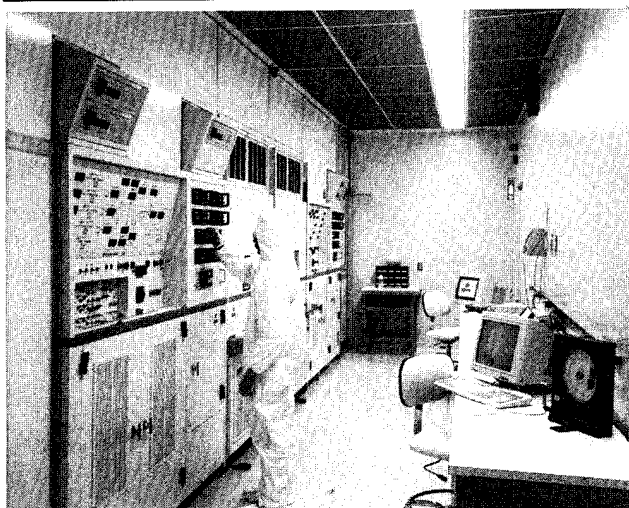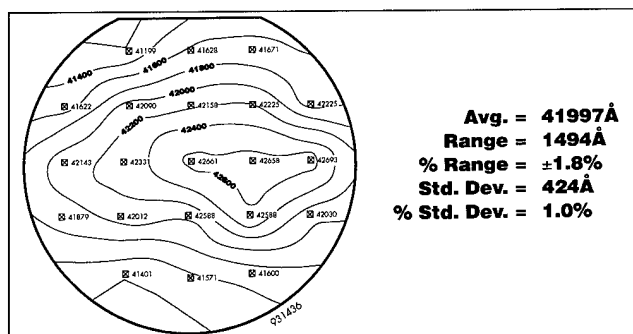
Table I. Thickness Uniformity Data of $Cd_{1-x}Zn_xTe$ Films Grown on GaAs Substrates

Wafer No.	Size (Inches)	Average (Å)	Range (Å)	% Range	Standard Deviation	% Standard Deviation
G26-77-1	4	42472	1063	±1.3	330	0.8
G26-77-2	3	43358	1698	±2.0	433	1.0
G26-77-3	4	42914	1428	±1.7	443	1.0
G26-77-4	4	41997	1494	±1.8	424	1.0
G26-77-5	3	42547	978	±1.1	261	0.6
G26-77-6	4	42345	1432	±1.7	427	1.0
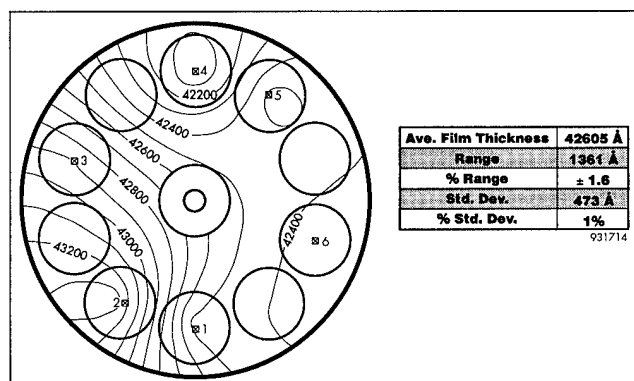
Fig. 3. Wafer-to-wafer thickness uniformity contour map for $Cd_{1-x}Zn_xTe$ films grown on GaAs substrates.

mity, background impurity level, surface morphology, film orientation, and defect density. In this paper, we discuss these issues with specific emphasis on the (111)B orientation of $Cd_{1-x}Zn_xTe$.

Thickness and Compositional Uniformity of $Cd_{1-x}Zn_xTe$

The thickness and compositional uniformity of $Cd_{1-x}Zn_xTe$ films grown in Spire's production-scale, SPI-MOCVD 3000G reactor were measured on 75 and 100 mm diam GaAs wafers oriented 2° off (100) → [110]. The GaAs wafers were positioned in such a way that uniformity across the entire susceptor could be mapped. Thickness uniformity mapping used ORS, a nondestructive tool that can reliably measure $Cd_{1-x}Zn_xTe$/GaAs film thickness with an accuracy of ±5 nm. Thirteen-point and 21-point thickness measurement mapping was performed on 75 and 100 mm wafers, respectively. Figure 2 shows the thickness uniformity of a $Cd_{1-x}Zn_xTe$ film on a 100 mm GaAs substrate. Table I shows thickness uniformity data for all the wafers in a six-wafer growth lot which yielded 1% standard deviation (see Fig. 3).

The composition of $Cd_{1-x}Zn_xTe$ films was routinely estimated using 77K PL,[10] and was found to be in good agreement with DXRD measurements. Room temperature PL mapping was used to determine compositional uniformity of $Cd_{1-x}Zn_xTe$ films grown on 100 mm GaAs substrates. These measurements were done at the SCANTEK company in France. Line-scan peak-wavelength measurements were performed at 42 points across the 100 mm wafer and composition variation across the wafer was determined by converting the peak wavelength to $Cd_{1-x}Zn_xTe$ composition.[11] Figure 4 shows typical variation of the peak wavelength across a 100 mm $Cd_{1-x}Zn_xTe$/GaAs wafer. Using data from Fig. 4 and the calibration given in Ref. 11, the average composition is 0.027 and ±0.002, respectively.

Impurity Level

Ga and As impurity levels in CdZnTe films on GaAs and GaAs/Si substrates have been measured by SIMS. The measurements employed an O_2+ beam with a net impact energy of 8 keV and a sputter rate of 9 nm/s.
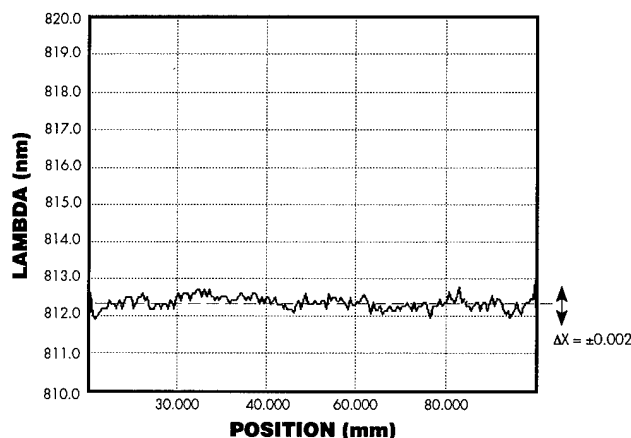
Fig. 4. Compositional uniformity mapping across 100 mm $Cd_{1-x}Zn_xTe$/GaAs using high resolution photoluminescence.
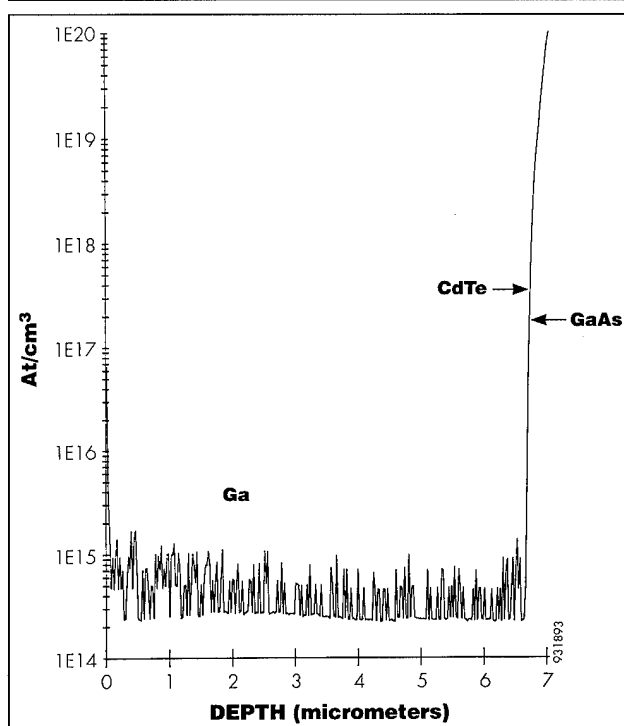
Fig. 5. Secondary ion mass spectroscopy profile for Ga impurity level in CdTe/GaAs/Si structure.

Figure 5 shows the Ga concentration as a function of film depth for a 6.5 μm thick CdTe/GaAs/Si film. The average Ga concentration was 5×10^{14} cm^{-3}, which is approximately the SIMS detection limit. No arsenic was detected in these films (the As detection limit is approximately 3×10^{16} cm^{-3}). These results indicate that Ga and As diffusion at our baseline growth conditions is very limited. We have not observed a significant difference in impurity levels between CdTe and $Cd_{1-x}Zn_xTe$ films on GaAs coated Si substrates. However, the Ga impurity level in CdTe on GaAs substrates is an order of magnitude higher, which could be due to autodoping from the GaAs wafer.

Surface Morphology and Film Orientation

To achieve (111)B $Cd_{1-x}Zn_xTe$ films with the im-

proved surface morphology and reduced defect density that are needed for LPE of HgCdTe, we have investigated a number of Si and GaAs wafer orientations and deposition conditions. The GaAs wafer orientations investigated were exact (100) and 2° off (100) toward the [110], while the Si wafer orientations investigated were 0, 2, 4, 7, and 10° off (100) toward the [111]. For the initial screening experiments, 1 µm thick GaAs-on-Si films with typical x-ray rocking curve FWHM in the range 200 to 400 arc-sec and surface roughness of ±30 nm were used. The deposition parameters for optimal compositional and thickness uniformity of $Cd_{1-x}Zn_xTe$ (x = 0.04) on GaAs were initially used, although the VI/II ratio had to be optimized for each orientation to achieve specular surface morphology. Figure 6 shows typical surface morphology for 5–10 µm thick films grown on GaAs and GaAs/Si substrates of various orientations. In general, all films exhibited specular mirror-like surface morphology. Films deposited on substrates with low off-axis misorientation (<2°) had smoother surfaces, while those deposited on substrates with higher off-axis misorientation (up to 10°) had regular fine features that were stable as a function of film thickness.

The orientation of the heteroepitaxial $Cd_{1-x}Zn_xTe$ films was determined using Laué x-ray back reflec-

tion measurements and confirmed by SAD patterns on XTEM samples. The accuracy of Laué x-ray back reflection measurements is ±0.5°. The dependence of $Cd_{1-x}Zn_xTe$ film orientation on that of the starting substrate is summarized in Table II.

For wafers misoriented off the (100) Si toward the [111] Si pole, $Cd_{1-x}Zn_xTe$ films were found to be misoriented off the CdTe (111)B direction toward the same [111] Si pole. The degree of misorientation of the $Cd_{1-x}Zn_xTe$ film off the (111) $Cd_{1-x}Zn_xTe$ direction was greater than that of the Si substrate surface normal off the (100) Si direction. Moreover, CdTe films deposited on direct (100) GaAs had an exact (111) orientation. Finally, $Cd_{1-x}Zn_xTe$ films deposited on 2° off (100) toward [110] GaAs were misoriented by the same degree off the (111)B $Cd_{1-x}Zn_xTe$ toward the [110] GaAs.

Cross-sectional TEM was used to investigate the effect of substrate misorientation on defect formation and twin propagation. By adjusting growth conditions, similar defect features have been observed in $Cd_{1-x}Zn_xTe$ films deposited on Si substrates oriented 2, 4, and 7° off (100) toward the [111]. Figure 7 shows a typical XTEM bright field image (g = 220) for CdTe/GaAs/Si 2° off (100) toward [111]. These measurements clearly indicate that thin lamella twins exist parallel to the CdTe/GaAs interface. The twins form

CdZnTe/GaAs
2° off (100)→[110]

CdZnTe/GaAs/Si
Si: Direct (100)

CdZnTe/GaAs/Si
Si: 2° off (100)→[111]

CdZnTe/GaAs/Si
Si: 4° off (100)→[111]

CdZnTe/GaAs/Si
Si: 7° off (100)→[111]

CdZnTe/GaAs/Si
Si: 10° off (100)→[111]

942033*

50 µm
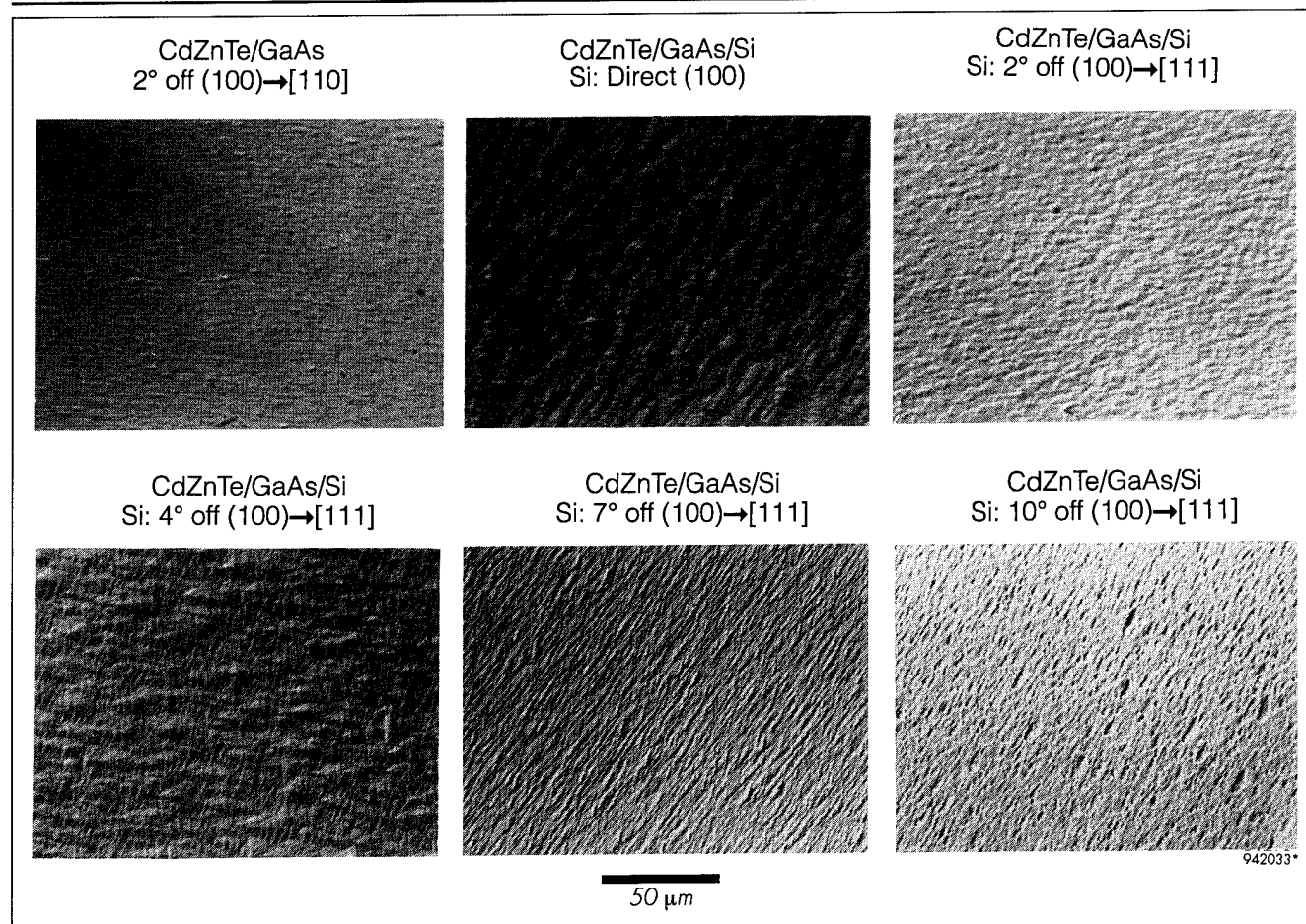
Fig. 6. Surface morphology of $Cd_{1-x}Zn_xTe$ films deposited on GaAs and GaAs/Si substrates with different orientations.

Table II. Dependence of Cd$_{1-x}$Zn$_x$Te Film Orientation on GaAs and GaAs/Si Substrate Misorientation

Sample No.	Structure	Substrate Orientation (Laué)	Cd$_{1-x}$Zn$_x$Te Film Orientation
G26-0035-4	CdTe/GaAs/Si	(100) off 2° → [111]	(111) off 3° → [111]Si
G26-0027-2	CdTe/GaAs/Si	(100) off 4° → [111]	(111) off 5° → [111]Si
G26-0035-2	CdTe/GaAs/Si	(100) off 7° → [111]	(111) off 9° → [111]Si
G26-0091-5	CdTe/GaAs/Si	(100) off 10° → [111]	(111) off 12° → [111]Si
G26-0006-1	CdTe/GaAs	exact (100)	exact (111)
G26-0013-1	CdTe/GaAs	(100) off 2° → [110]	(111) off 2° → [110]Si
C26-0064-2	Cd$_{1-x}$Zn$_x$Te/GaAs	(100) off 2° → [110]	(111) off 2° → [110]Si

in the early stages of growth and are confined near the CdTe/GaAs interface. Further, these twins seem to block the propagation of threading dislocations into the epitaxial layer. Figure 8 shows an XTEM for CdTe/GaAs/Si 4° off (100) toward [111]; the inset electron diffraction (SAD) pattern close to the CdTe/GaAs interface shows the extra diffraction spots due to the presence of twins near the interface, while the SAD pattern near the surface shows that the film is twin-free. Further deposition and characterization by etch-pit measurements of the HgCdTe films by LPE on these substrates showed that the twins do not propagate into the HgCdTe film.

Figure 9 is a XTEM bright field image (g = 220) of (111)B Cd$_{1-x}$Zn$_x$Te (x = 0.03)/CdTe/GaAs (100) off 2° → [110]. This orientation is of special interest since no twinning has been observed by TEM. The same deposition conditions were used to grow 6.7 μm thick Cd$_{1-x}$Zn$_x$Te on 100 mm GaAs of the same orientation (sample G26-0088, Table III). X-ray analysis on this wafer by Rockwell[14] indicated that twinning is below the detection limit (<1%). Another interesting feature of Fig. 9 is the bending of dislocations at the Cd$_{1-x}$Zn$_x$Te/CdTe interface, suggesting that a Cd$_{1-x}$Zn$_x$Te strained layer can effectively reduce the dislocation density in the film.

LPE of HgCdTe/Cd$_{1-x}$Zn$_x$Te/GaAs/Si

Preliminary results of HgCdTe deposition on (111)B CdZnTe/GaAs/Si substrates using Te-rich LPE slider are very promising. Figure 10 compares the surface morphologies of GaAs/Si, Cd$_{1-x}$Zn$_x$Te/GaAs/Si, and LPE HgCdTe/CdTe/ GaAs/Si. The morphology of the GaAs/Si film is typical for a 1 μm film, corresponding to a surface roughness of approximately ±30 nm. In comparison, typical surface roughnesses for CdTe (6 μm thick), Cd$_{1-x}$Zn$_x$Te (6 μm thick), and HgCdTe (20 μm thick) films on these GaAs/Si substrates are 65, 60, and 900 nm, respectively. The HgCdTe film (AS002R) is approximately 46 μm thick, as measured by FTIR, and is characterized by a wavy, cross-hatched surface.

Table III shows the x-ray rocking curve characteristics, film thickness, and cut-on wavelength for HgCdTe deposited on both CdTe/GaAs/Si and Cd$_{1-x}$Zn$_x$Te/GaAs/Si substrates. All of the HgCdTe results reported here are on (111) CdZnTe on GaAs on Si (100) off 4° → [111]. Defect densities in the LPE
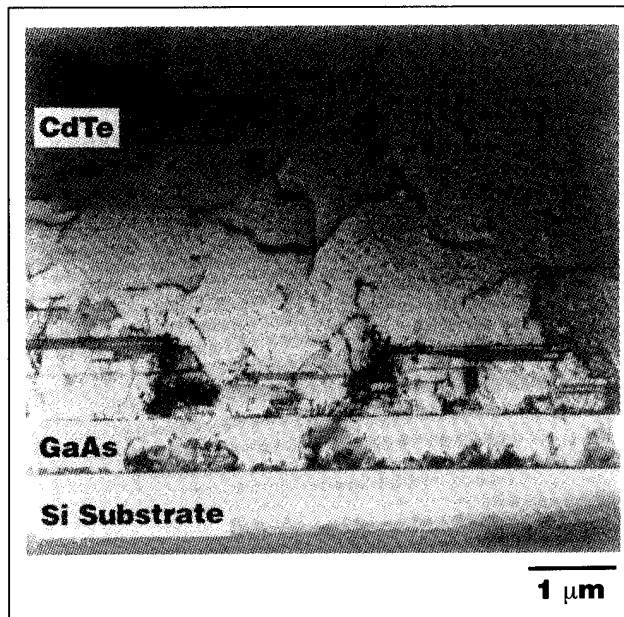
Fig. 7. Cross-sectional TEM of (111) oriented CdTe films on GaAs/Si substrate with (100) off 2° →[111] misorientation.
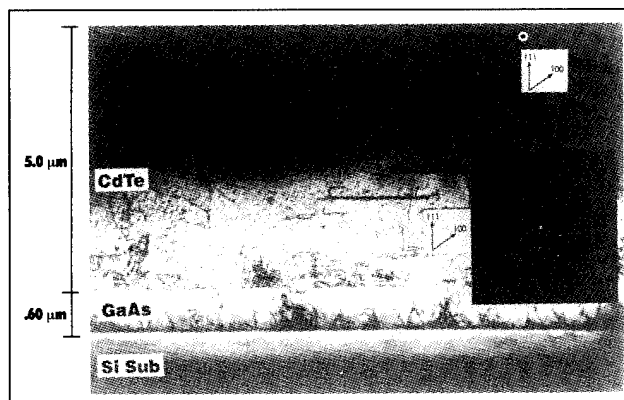
Fig. 8. Cross-sectional TEM of (111) oriented CdTe films on GaAs/Si substrate with (100) off 4° → [111] misorientation. Insets show selected area electron diffraction (SAD) pattern taken near CdTe/GaAs interface and at CdTe film.

HgCdTe films have been measured, using the recently reported etchant by I. Hahnert and M. Schenk,[17] and found to be in the range 1 to 3 × 10^6 cm^{-2}. Latest results indicate that specular HgCdTe surface morphologies are achievable for selected Si-wafer orientations and Cd$_{1-x}$Zn$_x$Te/GaAs/Si growth conditions.

Effects of misorientation off the (111)B axis on surface morphology, crystalline perfection, and electrical properties of LPE-HgCdTe films are currently under investigation. The narrowest x-ray rocking curve FWHM achieved to date is 72 arc-sec for sample AS007R, a 19.5 μm HgCdTe film (cut-on wavelength of 6.5 μm), deposited on CdTe/GaAs/Si.
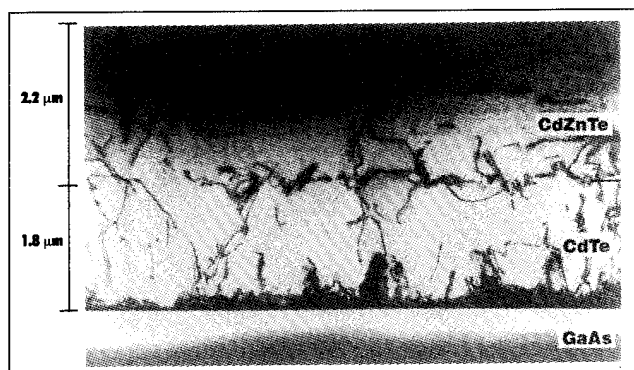
Fig. 9. Cross-sectional TEM of (111) oriented CdTe films on GaAs substrate with misorientation (100) off 2° → [110] showing no twins.

CONCLUSIONS

We have demonstrated large-area uniform MOCVD of $Cd_{1-x}Zn_xTe$ with excellent thickness and compositional uniformity in a production scale SPI-MOCVD 3000G reactor. It has further been shown that (111)B $Cd_{1-x}Zn_xTe$/GaAs/Si alternative substrates are suitable for LPE, MOCVD, or MBE deposition of HgCdTe. Specular morphology of CdZnTe films on GaAs and GaAs-on-Si substrates has been achieved. For optimized deposition conditions, thickness uniformity in the range 0.6 to 0.8% is typical for growths on multiple three and four inch diameter wafers per run. A 1% standard deviation wafer-to-wafer thickness uniformity is obtained for $Cd_{1-x}Zn_xTe$/GaAs (x = 0.04) over the entire susceptor. Typical composition uniformity of $\Delta x = \pm 0.002$ across a 100 mm substrate has been achieved for $Cd_{1-x}Zn_xTe$ in the production scale reactor. Secondary ion mass spectroscopy shows that Ga and As impurities are below the detection limit (5×10^{14} cm^{-3}) in films deposited on GaAs-on-Si substrates. For selected wafer orientations and deposition conditions, transmission electron microscopy

Table III. Typical X-Ray FWHM for CdZnTe and HgCdTe of Different Thicknesses

Wafer ID No.	Structure	CdZnTe MOCVD Growth Temp (°C)	Cut-On λ (μm)	Thickness (μm)	X-Ray FWHM (arc-sec)
G26-073-1	CdTe/GaAs	420	—	3.0	144
G26-0120-8	CdTe/GaAs/Si	420	—	4.9	144
AS002R	HgCdTe/CdTe/GaAs/Si	—	8.3	46	86
AS007R	HgCdTe/CdTe/GaAs/Si	—	6.5	19.5	72
G26-088-7	$Cd_{1-x}Zn_xTe$/GaAs	420	—	6.7	135
G26-0121-7	$Cd_{1-x}Zn_xTe$/GaAs/Si	420	—	9.5	237
AS004R	HgCdTe/ $Cd_{1-x}Zn_xTe$/GaAs/Si	—	6.7	20	100

Note: GaAs wafer orientation: 2° off (100) toward [110]; Si wafer orientation: 4° off (100) toward [111].

MOCVD (100)
GaAs on Si

MOCVD (111)B
$Cd_{1-x}Zn_xTe$/GaAs/Si,
x = 0.04

LPE
$Hg_{1-x}Cd_xTe$/CdTe/GaAs/Si,
x = 0.22

50 μm
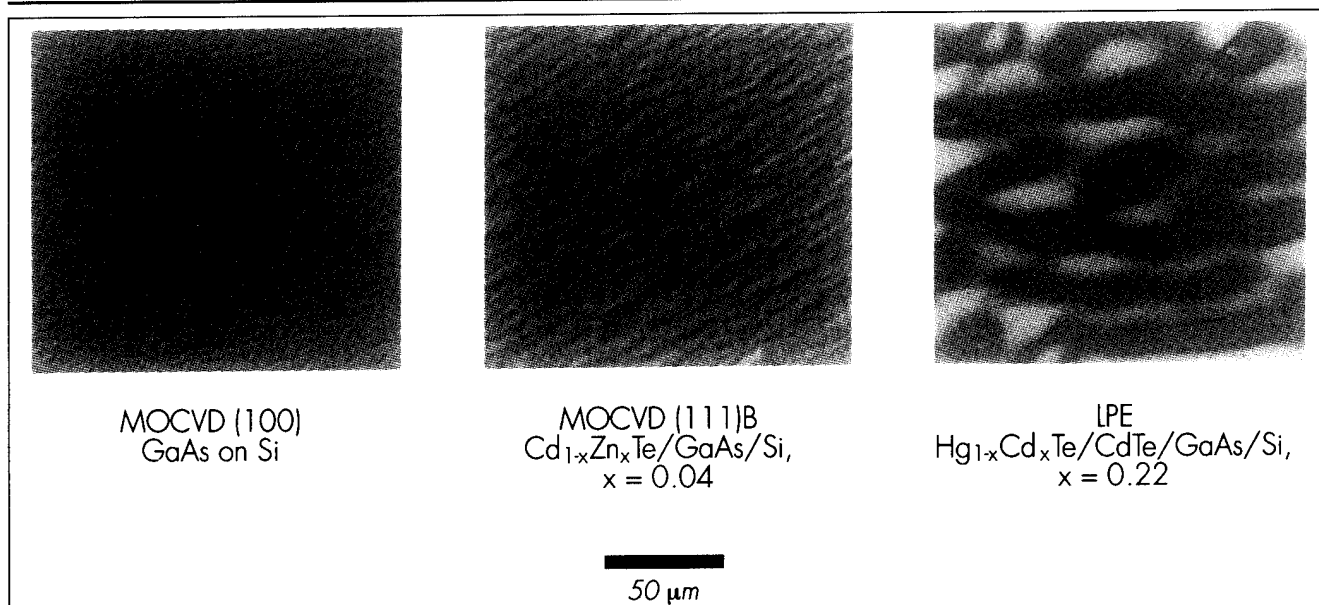
Fig. 10. A comparison of the surface morphology for GaAs on Si, $Cd_{1-x}Zn_xTe$/GaAs/Si and HgCdTe/$Cd_{1-x}Zn_xTe$/GaAslSi. The Si-substrate orientation is (100) off 4° → [111].

shows that only lamella twins parallel to the CdTe/
GaAs interface form, while inclined twins are suppressed. The lamella twins do not propagate through
subsequently deposited LPE HgCdTe layer(s). The
surface morphology of these films is comparable to
LPE HgCdTe films deposited on bulk $Cd_{1-x}Zn_xTe$
substrates. Etch-pit density measured for as-deposited Te-rich LPE-HgCdTe films on [111]B $Cd_{1-x}Zn_xTe$/
GaAs/Si is typically in the range 1 to 3 × 10^6 cm^{-2}.
Metalorganic chemical vapor deposition of $Cd_{1-x}Zn_xTe$
on GaAs on Si promises low-cost production of alternative substrates to the IRFPA community.

ACKNOWLEDGMENTS

REFERENCES

1. See for example Proc. U.S. Workshop on the Physics and
Chemistry of Mercury Cadmium Telluride and Novel Infrared Detector Materials, *J. Vac. Sci. and Tech. B* 9 (3), (1991);
J. Vac. Sci. and Tech. B 10 (4), (1992).

2. Proc. U.S. Workshop on the Physics and Chemistry of Mercury Cadmium Telluride and Novel Infrared Detector Materials, *J. of Electron. Mater.* 22 (8), (1993).

3. K. Zanio, R. Bean, R. Matson, P. Vu, S. Taylor, D. McIntyre,
C. Ito and M. Chu, *Appl. Phys. Lett.* 56, 1207 (1990).

4. R. Korenstein, P. Madison and P. Hallock, *J. Vac. Sci.
Technol. B* 10, 1370 (1992).

5. N.H. Karam, R. Wolfson, I.B. Bhat, H. Ehsani and S.K.
Ghandhi, *Thin Solid Films* 225, 261 (1993).

6. I.B. Bhat, H. Ehsani, W.-S. Wang and S.K. Ghandhi, and
N.H. Karam, *J. Vac. Sci. and Tech. B* 10 (4), 1376 (1992).

7. S.M. Johnson, J.A. Vigil, J.B. James, C.A. Cockrum, W.H.
Konkel, M.H. Kalisher, R.F. Risser, T. Tung, W.J. Hamilton,
W.L. Ahlgren and J.M. Myrosznyk, *J. Electron. Mater.* 22 (8),
835 (1993).

8. S.M. Johnson, W.L. Ahlgren, M.H. Kalisher, J.B. James, and
W.J. Hamilton, *Mater. Res. Soc. Symp. Proc.*, eds. F.J. Bartoli,
H.F. Schaake and J.F. Schetzina (Pittsburgh, PA: Mater.
Res. Soc., 1990), Vol. 161, p.351; S.M. Johnson, M.H. Kalisher,
W.L. Ahlgren, J.B. James and C.A. Cockrum, *Appl. Phys.
Lett.* 56 (10), 946 (1990).

9. D. Rajavel and J.J. Zinck, *Appl. Phys. Lett.* 63 (3), 322 (1993).

10. S.M. Johnson, S. Sen, W.H. Konkel and M.H. Kalisher, *J.
Vac. Sci. Technol. B* 9 (3), 1897 (1991).

11. D.J. Olego, J.P. Faurie, S. Sivananthan and P.M. Raccah,
Appl. Phys. Lett. 47 (11), 1172 (1985).

12. G. Patriarche, R. Triboulet, Y. Marfaing, and J. Castaing, *J.
Cryst. Growth* 129, 375 (1993).

13. A. Raizman, M. Oron, G. Cinader and Hadas Shtrikman, *J.
Appl. Phys.* 67 (3), 1554 (1990).

14. H.L. Glass, M.R. Appleby Woods, M.L. Buehnerkemper, D.L.
Varnum and T.P. Weismuller, *J. Cryst. Growth,* 128, 617
(1993); H.L. Glass and M.R. Appleby Woods, *Appl. Phys. Lett.*
60 (21), 2619 (1992).

15. N.H. Karam, V. Haven, S.M. Vernon, N. El-Masry, E.H.
Lingunis, and N. Haegel, *J. Cryst. Growth* 107, 129 (1991).

16. S.N. Bunker, P. Sioshansi, M.M. Sanfacon and S.P. Tobin,
Appl. Phys. Lett. 50, 1900 (1987).

17. I. Hahnert and M. Schenk, *J. Cryst. Growth* 101, 251 (1990).

Monitoring Vertical Bridgman-Stockbarger Growth of Cadmium Telluride by an Eddy Current Technique

GARY J. ROSEN, FREDERICK M. CARLSON, JEFFREY E. THOMPSON, and WILLIAM R. WILCOX

Department of Mechanical and Aeronautical Engineering, Clarkson University, Potsdam, NY 13699-5729

JOHN P. WALLACE

Casting Analysis Corporation, Route 2, Box 113, Weyers Cave, VA 24486

The electric conductivity of indium-doped cadmium telluride (CdTe) in the temperature range 600–1080°C was 163 to 1203 $\Omega^{-1}\text{m}^{-1}$. *In-situ* monitoring of vertical Bridgman-Stockbarger growth showed an unexpected step change in the voltage response vs height. Differential thermal analysis of CdTe showed both Cd and Te melting peaks as well as an exothermic reaction above 790°C.

Key words: CdTe, eddy current, vertical Bridgman

INTRODUCTION

Cadmium telluride (CdTe) is a semiconductor material that belongs to the family derived from the group IIA and VIB elements. Cadmium telluride has a wide range of applications including x-ray and gamma-ray detection, electro and acousto-optic modulation and as a substrate for the growth of mercury cadmium telluride, an infrared detector material. The infrared transmission range of 0.85–30 μm and low absorption coefficient makes it useful in the production of infrared windows.

Although considerable research has been conducted over the past 30 years, CdTe growth continues to be plagued by various problems. Twinning is the most common problem cited by industrial bulk CdTe growers. Dislocations, precipitates, voids and bubbles, impurities, nonstoichiometry, and polycrystallinity are also commonly cited problems.

A variety of techniques have been tried for growing CdTe crystals. These methods include growth from solution, vapor and near-stoichiometric melt. Growth from the melt, via the Bridgman method, is the most popular because of the faster growth rates and the ability to produce large ingots. Currently, commercial CdTe is grown by the vertical Bridgman-Stockbarger (VBS) and horizontal Bridgman methods. The resulting ingots typically contain several grains, twins, and precipitates. Considerable post-growth processing such as single crystal mining and annealing must be done to obtain wafers of suitable quality and proper orientation.

The VBS technique is a method of directional solidification that has been widely used to grow a variety of materials. In this technique, the growth charge is sealed in a fused silica ampoule and placed in the upper portion of a multi-zone furnace. The growth charge is melted and translated through a temperature gradient created by a higher temperature zone on top of a lower temperature zone.
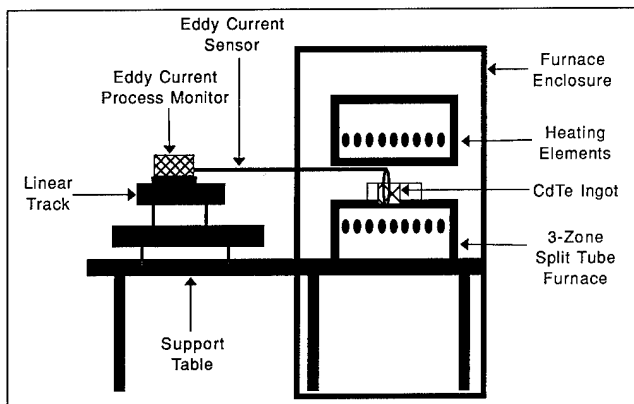
Fig. 1. Experimental setup used to determine the electric conductivity-temperature relationship for indium doped CdTe.
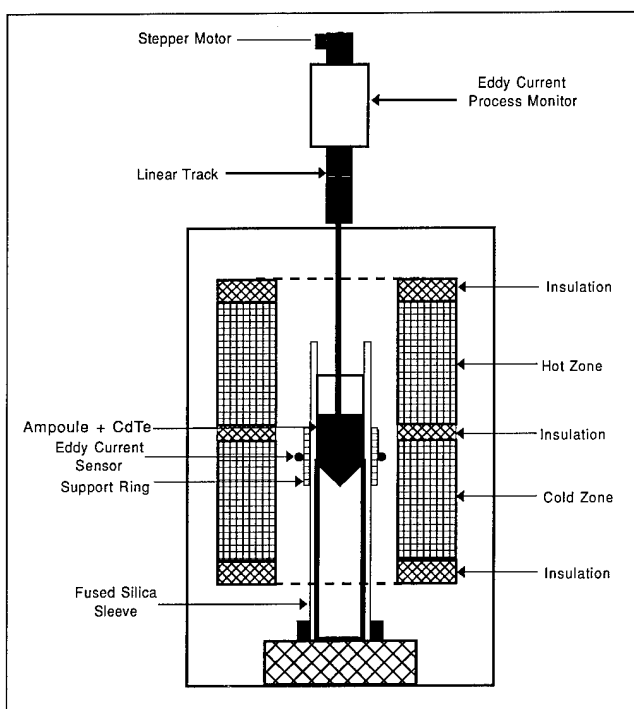
Fig. 2. Schematic of vertical Bridgman-Stockbarger experimental setup used for *in situ* eddy current growth monitoring.

Fig. 3. Phase angle response during one scan along an indium doped CdTe ingot. Region 1: vapor space; region 2: solid ingot.
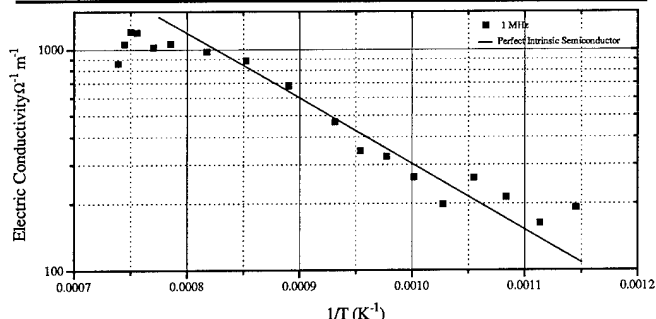
Fig. 4. Electric conductivity of indium doped CdTe calculated by linear interpolation from a 952 $\Omega^{-1}m^{-1}$ silicon standard.

There are a few large problems associated with VBS growth of cadmium telluride. Cadmium telluride is a weakly bonded material with a high ionicity. The weak bonding combined with thermo-mechanical stresses which can be induced during VBS growth may cause a large number of associated defects. Some of the stresses are thought to arise primarily from adhesion between the ampoule and crystal combined with differential thermal contraction. Additional stresses arise from the non-constant temperature gradients present during growth. Contamination originating in the ampoule is an additional problem that has been difficult to quantify.

Rosch[1] identified adhesion between the ampoule and crystal as the major source of stress during VBS growth. Subsequent work by Shetty,[2] reduced adhesion by coating quartz ampoules with pyrolytic boron nitride.

The high melting point and vapor pressure of CdTe require complex handling methods. Also, the high temperature environment of a VBS furnace combined with the coatings used on the fused silica ampoules limit the possible process monitoring techniques. Eddy current techniques provide an alternative to more standard process monitoring methods.

Eddy current diagnostics is an electromagnetic technique sensitive to changes in electric conductivity. Eddy current measurements are nondestructive, noncontact, and remote. They can be applied where more conventional methods such as thermocouples or infrared pyrometers are not feasible. Eddy current signals can potentially provide information on a wide variety of growth related parameters. The liquid-solid interface, segregation, and condensation are features capable of being measured by this technique.

In this study, eddy current techniques were applied to the vertical Bridgman-Stockbarger growth of indium-doped cadmium telluride. The results are presented from experiments on the electric conductivity-temperature relationship, *in-situ* monitoring of vertical Bridgman-Stockbarger growth, and differential thermal analysis of material obtained from growth experiments.

EDDY CURRENT MONITORING

Basic Eddy Current Principles

The basic theory behind eddy current measurements comes from the electromagnetic equations formalized by Maxwell. Stefani[3] explained the application of this theory to eddy current measurements. A sinusoidally varying voltage is applied to a coil to

create a varying magnetic field within the coil. This magnetic field, known as the primary field, causes currents to flow within any conductor placed in the vicinity of the coil. These currents create another magnetic field. This magnetic field, known as the secondary field, modifies the primary field. The amount by which the original field is modified yields information on the electromagnetic properties of the conductor. The modification is determined by monitoring the induced complex voltages in a sensor. The induced voltages are indicative of the conductor's electric conductivity at the depth at which the current was induced.

Application to Crystal Growth

Stefani et al.,[3] Choe et al.,[4] and Tien et al.[5] conducted a variety of experiments on the Czochralski growth of silicon. Both axial and radial temperature profiles were calculated from the electric conductivity data obtained from eddy current diagnostics. The work completed in these studies provided an excellent basis for the application of eddy current diagnostics to VBS solidification of CdTe. Many of the techniques used in these studies were directly applicable to the VBS process.

EXPERIMENTS

Three different experiments were conducted during the course of this study. First, a series of solid state experiments were conducted to determine the variation of the electric conductivity with temperature. Then, *in-situ* monitoring experiments were performed during VBS solidification of indium-doped CdTe. Finally, a differential thermal analysis of the material grown during the monitoring experiments was performed.

Solid-State Experiments

In order to determine the electric conductivity-temperature (σ-T) relationship for indium-doped CdTe, a 24 mm diameter cylindrical ingot was first formed by directional solidification in a vertical Bridgman-Stockbarger furnace. The first and last to freeze sections were removed with a diamond wire saw. The ingot was chemically polished in a 5% bromine-methanol solution. The ampoule was evacuated and sealed in a 24 × 27 mm fused silica tube.

A pellet of 99.999% cadmium was placed in the vapor space above the ingot prior to sealing. This provided an overpressure that varied with temperature and prevented condensation. This ampoule was placed in the center of the three-zone isothermal horizontal furnace depicted in Fig. 1. A type R thermocouple along with a 35 mm diameter, single-turn, parallel feed eddy current probe was inserted in the furnace so that its coil encircled the ampoule.

Prior to installing the cadmium telluride ampoule assembly, a scan was performed along a 25 mm diameter silicon crystal with an electric conductivity of 952 $\Omega^{-1}m^{-1}$. The scan was performed at frequencies of 1, 11, 15, and 19 MHz which were also used for the

subsequent CdTe scans. Since there was no prior work with eddy current signals of CdTe over the temperature range in this experiment, a wide range was selected. The signal obtained from this experiment was used as an electric conductivity calibration standard.

The experiment was performed by first adjusting the furnace zones for the desired temperature. The thermocouple and sensor assembly was then scanned along the length of the ampoule to verify that a constant temperature existed across the ingot. The eddy current monitor was zeroed at a position approximately 3 cm ahead of the ingot. A scan that
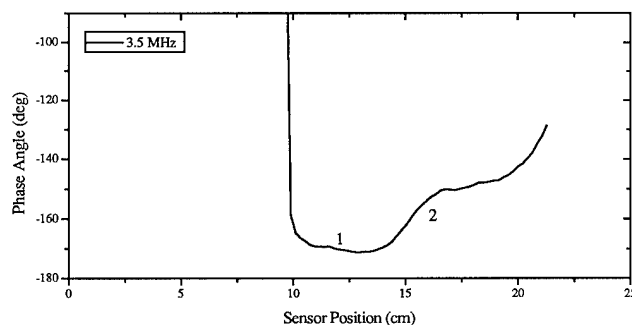
Fig. 5. Phase angle response during one scan along an indium doped cadmium telluride growth ampoule. Region 1: liquid; region 2: liquid-solid transition.
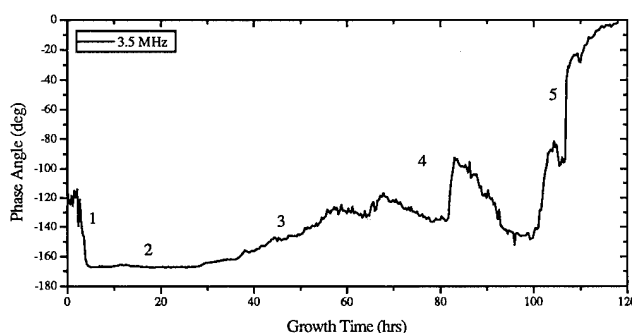
Fig. 6. Growth history of an indium doped CdTe ingot. Region 1: heat-up from room temperature; region 2: liquid; region 3: liquid-solid transition; region 4: solid; region 5: cool-down to room temperature.
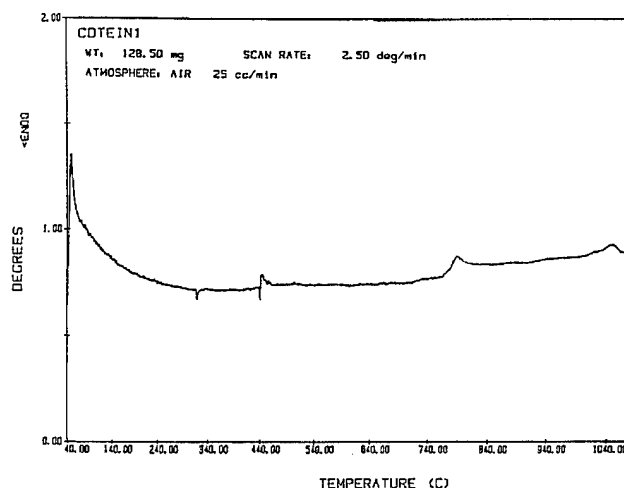
Fig. 7. A differential thermal anlaysis curve for indium doped CdTe.

contained 550 data points was then performed along the length of the ingot.

Figure 3 shows a typical scan taken at 1050°C on which the vapor space and ingot regions are both indicated. The temperatures were incrementally increased from 600–1080°C repeating the temperature verification and scanning procedure at each increment. The same procedures were then performed on cooling from 1080–600°C.

Monitoring VBS Solidification

Continuous scanning of a 52 mm diameter ingot in a VBS furnace was carried out at frequencies of 0.35, 0.9, 2.1, and 3.5 MHz using the apparatus shown schematically in Fig. 2. The ampoules were first coated with either carbon or boron nitride using the process developed by Shetty.[2] Pre-compounded CdTe doped with 6 ppm (atomic) indium was chemically polished in a 5% bromine-methanol solution for 2 min. The ingot was broken into pieces and loaded in a 52 mm I.D. × 55 mm O.D. ampoule. The ampoule was then flushed three times with ultra-high purity argon, evacuated in a cryogenic pump, and sealed at 10^{-6} Torr. The ampoule was then placed in the VBS furnace depicted in Fig. 6. A 70 mm diameter, single-turn, parallel feed eddy current probe was inserted from the top of the furnace as indicated.

The furnace control program and probe scanning were started simultaneously. The probe automatically scanned from a point approximately 3 cm above the ampoule to a position 1 cm below the conical tip of the ampoule. The ingots were solidified with a furnace gradient at the melting point (1092°C) of 7°C/cm. A furnace translation rate of 2 mm/h was used. The eddy current probe scanned the axis of the ampoule between three and four times per hour. This yielded approximately 400 scans per growth experiment. Each scan contained 100 data points that corresponded to 100 axial sensor locations. A representative phase angle response from one scan is shown in Fig. 5. The liquid and liquid-solid transition region are both indicated in the plot.

Differential Thermal Analysis

A differential thermal analysis (DTA) was performed on the indium doped CdTe grown as a result of the monitoring experiments. A Perkin-Elmer differential thermal analyzer was used for these experiments. A 3 mm I.D. × 5 mm O.D. fused silica ampoule was first coated with carbon by pyrolysis of methane. A 128 mg sample of CdTe was cut from an ingot and chemically polished in a 5% bromine-methanol solution for 2 min. After a thorough rinse in electronic grade methanol, the sample was loaded into the ampoule. The ampoule was then evacuated to greater than 10^{-6} Torr and sealed. A reference sample was fabricated from 3 × 5 mm fused silica. The reference sample was also coated with carbon and then evacuated and sealed. The DTA was performed over the temperature range 40–1085°C with a heating rate of 2.5°C/min.

RESULTS AND DISCUSSION

Electric Conductivity-Temperature Relationship

The electric conductivity at each temperature increment was calculated by a linear interpolation from the complex voltages obtained on the 952 $\Omega^{-1}m^{-1}$ silicon standard at 1 MHz. The validity of this calculation was verified by calculating the expected complex voltages at 1 MHz. The resulting phase angle and amplitude vs electric conductivity curves showed linear relationships for the geometries and frequency used in the interpolation. Therefore, a single calibration point was adequate for the interpolation.

As shown in Fig. 4, the electric conductivity-temperature data depicts a complex behavior. The straight line is a schematic representation of the relationship for a perfect intrinsic semiconductor. The data obtained for CdTe contained three distinct features. Two transitions occurred, one between 675 and 700°C and another between 1025 and 1050°C on both heating and cooling. These transitions are not understood although several possible explanations have been proposed. The transitions may indicate a p-n conversion, the dissolution of tellurium precipitates into the lattice or an allotropic phase transition. The third feature of this curve is the sharp drop in conductivity that occurred between 1050 and 1080°C. This has not been explained.

In-Situ Monitoring

To better view the large data sets obtained from the monitoring experiments, a procedure was developed to compile and extract the necessary information. First, the individual scans were appended to one large data file. The phase angle and amplitude signals for fixed axial locations along the ampoule were then extracted from the data file. The resulting plot presented in Fig. 6 is a representation of the entire growth history for a point approximately 8 cm below the top free surface of CdTe ingot. The heat-up room temperature liquid, liquid-solid transition, solid, and cool-down regions are indicated.

Two step changes in the phase angle response occurred between 65 and 80 h. These changes were observed on experiments performed in carbon and boron nitride coated ampoules. The corresponding temperature range for this axial location was between 1070 and 1050°C. This correlated to the sharp drop in electric conductivity previously discussed. While these step changes are not well understood, they may indicate an allotropic phase transition as previously suggested by Triboulet[6] and Kendall.[7]

Differential Thermal Analysis

A differential thermal analysis was performed to test for the possibility of an allotropic phase transformation in indium-doped CdTe. The heating curve from a differential thermal analysis is presented in Fig. 7. Two endothermic peaks that correspond to the

melting points of Cd (321.9°C) and Te (419.5°C) appear. The tellurium peak is immediately followed by an exothermic peak which may indicate the formation of CdTe. The material used to perform the analysis contained Te precipitates. This may explain the presence of a Te melting endotherm. Also, CdTe may have evaporated during heating and separate Cd and Te condensed out from the vapor and subsequently reacted. The exothermic peak indicated at approximately 790°C is unexplained.

CONCLUDING REMARKS

The work completed to date raised several important questions. The presence of a sharp drop in electric conductivity above 1050°C coupled with the step change in eddy current response during the actual growth may have indicated an allotropic phase transformation. The differential thermal analysis did not confirm the existence of a transformation. More DTA runs are required to further explore this question.

REFERENCES

1. W.R. Rosch and F.M. Carlson, *J. Cryst. Growth* 109, 75 (1991).
2. R. Shetty, *Directional Solidification of Cadmium Telluride,* Ph.D. Dissertation, Clarkson University, Potsdam, New York, June 1993.
3. J.A. Stefani, J.K. Tien, K.S. Choe and J.P. Wallace, *J. Cryst. Growth* 88, 30 (1988).
4. K.S. Choe, J.A. Stefani, J.K. Tien and J.P. Wallace, *J. Cryst. Growth* 88, 39 (1988).
5. J.K. Tien, J.P. Wallace, J. Kobayashi, B.C. Hendrix and Birmingham, *Intelligent Processsing of Materials* ed. H.P. Wang, (ASME, 1990), Book# G00560.
6. R. Triboulet, *Materials Forum,* 15, 30 (1991).
7. E.J.M. Kendall, *Phys. Lett.* 84, 237 (1964).

CdZnTe Substrate Impurities and Their Effects on Liquid Phase Epitaxy HgCdTe

J.P. TOWER, S.P. TOBIN, M. KESTIGIAN, and P.W. NORTON

Loral Infrared & Imaging Systems, Lexington, MA 02173

A.B. BOLLONG

Johnson Matthey Electronics, Spokane, WA 99216

H.F. SCHAAKE

Texas Instruments Incorporated, Dallas, TX 75265

C.K. ARD

II-VI Incorporated, Saxonburg, PA 16056

Impurity levels were tracked through the stages of substrate and liquid phase epitaxy (LPE) layer processing to identify sources of elements which degrade infrared photodetector performance. Chemical analysis by glow discharge mass spectrometry and Zeeman corrected graphite furnace atomic absorption effectively showed the levels of impurities introduced into CdZnTe substrate material from the raw materials and the crystal growth processes. A new purification process (*in situ* distillation zone refining) for raw materials was developed, resulting in improved CdZnTe substrate purity. Substrate copper contamination was found to degrade the LPE layer and device electrical properties, in the case of lightly doped HgCdTe. Anomalous HgCdTe carrier type conversion was correlated to certain CdZnTe and CdTe substrate ingots.

Key words: CdZnTe, glow discharge mass spectrometry (GDMS), HgCdTe, impurities, infrared detectors, liquid phase epitaxy (LPE), purification

INTRODUCTION

Epitaxial films of HgCdTe have become important for the fabrication of infrared detector focal plane arrays (FPAs). Much work has been concentrated on liquid phase epitaxial (LPE) growth technology using CdTe and CdZnTe substrate material. CdZnTe has the advantage of lattice matching to HgCdTe and thus, reduction of misfit dislocations. Various substrate properties can affect the quality of the LPE HgCdTe films and the resulting process yield greatly affects the economics of FPA production. In order to reduce overall production costs, effective substrate screening and improved substrate yield are necessary. Since the purity of HgCdTe is critical to its electrical properties, the effects of substrate purity have received considerable attention.[1,2] The electrical prop-

erties of HgCdTe result from the net effects of the active impurities, native defects, and intrinsic carriers. Native defects (such as Hg vacancies) can generally be controlled through proper growth and annealing conditions, while the intrinsic carrier concentration is determined by the HgCdTe composition (bandgap) and temperature. Electrically active impurities consist of intentional and unintentional dopant elements. In order to meet the requirements of FPA production, the electrical properties must achieve a high degree of uniformity and reproducibility. Commonly desired n-type carrier concentrations (10^{14}–10^{15}/cc) require consistently low levels of impurities in the HgCdTe layers.

Substrate impurities can migrate into LPE layers by diffusion (during LPE growth or post-growth annealing) or through melt segregation (resulting from meltback at the onset of LPE). For n-type HgCdTe, acceptor impurities are especially problematic be-

Table I. SIMS and GDMS Sensitivity Limits in HgCdTe

	Element	SIMS Detection Limit (cm⁻³)	GDMS Detection Limit (cm⁻³)	Doping Type	Group
O_2^+ Beam	Li	mid E12	low E14	P (Hg)	I
	Na	mid E12	low E13	P(Hg)	I
	Al	low E13	low E13	N(Hg)	III
	In	mid E12	mid E14	N(Hg)	III
	Mg	low E13	low E13	—	II
	Ca	low E13	low E14	—	II
	Fe	mid E15	low E13	—	VIII
	Ni	high E15	low E13	—	VIII
Cs⁺ Beam	Cu	low E16	mid E13	P(Hg)	I
	P	low E14	low E13	P(Te)	V
	Cl	low E15	low E13	N(Te)	VII
	Br	high E13	—	N(Te)	VII
	C	low E16	low E16	—	IV
	Si	low E15	low E13	—	IV
	O	low E16	low E16	—	VI
	S	mid E14	high E13	—	VI

Note: These limits vary by about a factor of three depending on the sample and instrument conditions.
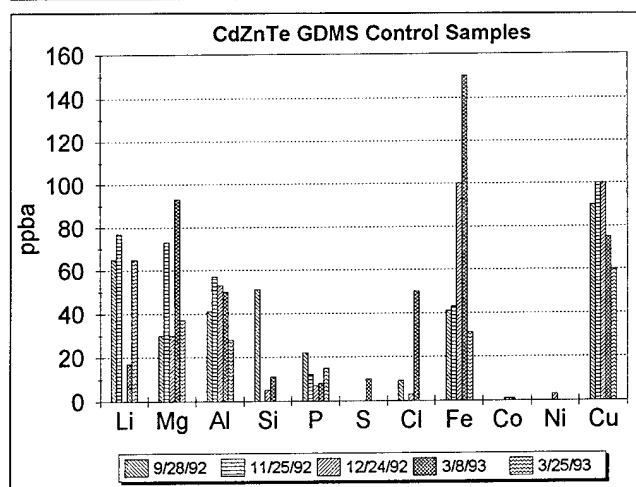
Fig. 1. Glow discharge mass spectrometry results for CdZnTe control samples measured over six months indicate the measurement uncertainty. Each control sample was cut from the same substrate.

cause they compensate the intentional dopant (typically indium), resulting in reduced carrier concentration and mobility. In extreme cases, this compensation effect results in complete carrier type conversion. Some impurities are also minority carrier lifetime "killers" which reduce photodetector response. In HgCdTe, common acceptor impurities are from group I (Li, Na, K, Cu, Ag) which incorporate on the metal lattice sites or group V (N, P, As, Sb) which incorporate on the tellurium lattice site. Of these, the Group I elements have been found to diffuse readily in Cd(Zn)Te and HgCdTe at elevated growth and annealing temperatures and might be expected to move from the substrate into the LPE layer during these processes. For this reason, they merit special attention. In particular, copper has been found to migrate from substrate material into MBE grown HgCdTe, producing unacceptable electrical properties.[3]

The work presented here was performed as part of the ARPA sponsored Infrared Materials Producibility (IRMP) program. The IRMP program objective is to lower the cost of FPA production by improving substrate quality and yield. The program is based on an industrial partnership between end users [Loral Infrared & Imaging Systems (LIRIS) and Texas Instruments (TI)] and substrate growers [Johnson Matthey Electronics (JME), II-VI Incorporated (II-VI), and TI]. The particular goal of the IRMP impurity work is to achieve improved substrate quality through reduction of the impurities which degrade HgCdTe photodetector performance. The technical approach is to identify which substrate impurities alter LPE layer electrical properties and to revise crystal growth processing to eliminate such impurities. In order to determine the sources of impurities and their effects on eventual HgCdTe LPE layer properties, impurity levels were tracked through the initial raw materials, substrate crystals, and LPE layers. Because of the range of materials being studied and the spectrum of elements being tested for, several complementary chemical analysis techniques were investigated to obtain the necessary parts-per-billion (ppb) sensitivity. A comparison of techniques was made and the effectiveness of each was determined. Baseline CdZnTe crystals were produced at each grower site using pre-existing processes, providing a benchmark against which to gauge process modifications. Improved purity raw materials were developed using a new technique which integrates low-pressure distillation and zone refining. These new raw materials were fed into the CdZnTe crystal growth processes for improved substrate purity.

EXPERIMENTAL

Each of the IRMP program substrate growers (TI, II-VI, and JME) produced five baseline $Cd_{1-x}Zn_xTe$ (x ≈ 0.04) ingots by their standard processes, the hori-

zontal (HB) and vertical Bridgman (VB) methods. Additional crystals were grown at each site using raw materials that were prepared by a new purification technique, *in situ* distillation zone refining (ISDZR). In ISDZR purification, distillation and zone refining are integrated into a single process which eliminates extra handling associated with the original two-step process. A controlled "liquid to liquid" distillation is first performed to remove impurities using differences in vapor pressure. This is followed by zone refining, in which impurities are removed using segregation. By combining the two purification mechanisms into one process with no handling between, ultra-high purity Te, Cd, and Zn are produced. Substrates from each CdZnTe crystal were used in the standard LPE HgCdTe growth processes at TI and LIRIS. Photodetector test devices were fabricated using a p-on-n heterojunction diode structure at LIRIS and a metal-insulator semiconductor (MIS) structure at TI.[4,5]

Impurity concentrations were measured in the raw materials and substrate crystals using glow discharge mass spectrometry (GDMS) and Zeeman corrected graphite furnace atomic absorption (ZCGFAA). Samples for chemical analysis were cut from the first-to-freeze (head) and last-to-freeze (tail) ends of all CdZnTe baseline and improved crystals. Glow discharge mass spectrometry provides a survey of elemental impurities in solid samples with sensitivity limits for all elements generally at the low ppb level or better. In this work, GDMS analysis was performed at the National Research Council of Canada using a VG 9000 instrument. Inhomogeneous impurity distributions in the test samples can cause the GDMS measurements to differ from the true average concentrations because only 1/2 micron depth of material is sputtered off and sampled for each element. The reproducibility of GDMS for analysis of CdZnTe was tested by sending a control sample along with each batch of CdZnTe test samples, over a six month period of time. The control samples were cut adjacent to each other from a single slice of CdZnTe. Results for the five control samples are shown in Fig. 1, indicating the GDMS measurement uncertainty for each element in CdZnTe. For example, Cu, P, Al, and Mg show good reproducibility, within a factor of three, while Li, Si, Cl, and Fe were more scattered. S, Co, Na, and Ni were near the GDMS detection limit and were only detected in one or two samples each. Variations in the control sample results are attributed mostly to sample inhomogeneity since the GDMS instrumental precision is typically better then 5%, except near the detection limits where it is limited by count rate or detector noise.[6] Nonuniform impurity distributions in CdZnTe are due to macroscopic segregation effects and microscopic gettering by crystalline defects such as inclusions and dislocations.

In ZCGFAA impurity testing, the solid samples are dissolved in acids, and thus, inhomogeneities within the samples are averaged out. The ZCGFAA instrument uses a separate lamp and different testing

parameters for each analyte element and testing parameters must be optimized for each sample matrix. Therefore, ZCGFAA is not intended to provide a comprehensive survey of elements. For identified "problem" elements, however, ZCGFAA is a cost effective technique for quick on-line testing. In addition, ZCGFAA offers lower detection limits than GDMS for certain elements, such as Ag (in CdZnTe). In this work, ZCGFAA was performed at LIRIS using a Perkin-Elmer 5100 PC instrument. The graphite furnace tubes were pyrolytically coated and used stabilized temperature (L'vov) platforms. Calculations were based on the integrated absorbence (peak area). Spectroscopic grade nitric acid was used for sample dissolution and all of the labware was made out of PFA Teflon or semiconductor grade quartz. Despite these procedures, occasional contamination of the blank solutions was found. Therefore, in order to verify their cleanliness, every sample solution was tested for the

Table II. ZCGFAA Reproducibility Tests Results for CdZnTe

		Test 1	Test 2	Test 3	Test 4	GDMS
Cu	Head	28	30	30	42	29
	Tail	1181	741	632	1090	550
Ag	Head	5	2	1		<20
	Tail	70	75	50		<30
Na	Head	78	10	164		84
	Tail	93	223	66		210
Fe	Head	38	17	8		7
	Tail	153	183	206		200
Li	Head	<70	19			64
	Tail	870	800			4000

Note: Repeat measurements were made using different pieces from two sample slices. Results are in ppb atomic.
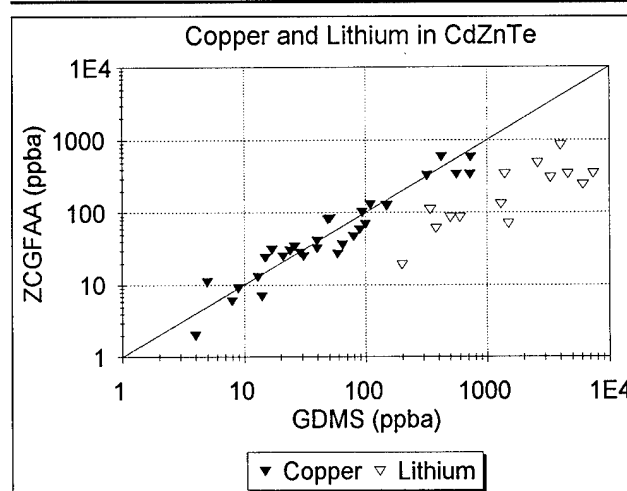
Fig. 2. Zeeman corrected graphite furnace atomic absoprtion measurements of baseline CdZnTe plotted against GDMS for Cu and Li. Good agreement was found for Cu over three orders of magnitude. For Li, ZCGFAA measurements were consistently lower than GDMS.

Tower, Tobin, Kestigian, Norton,
Bollong, Schaake, and Ard
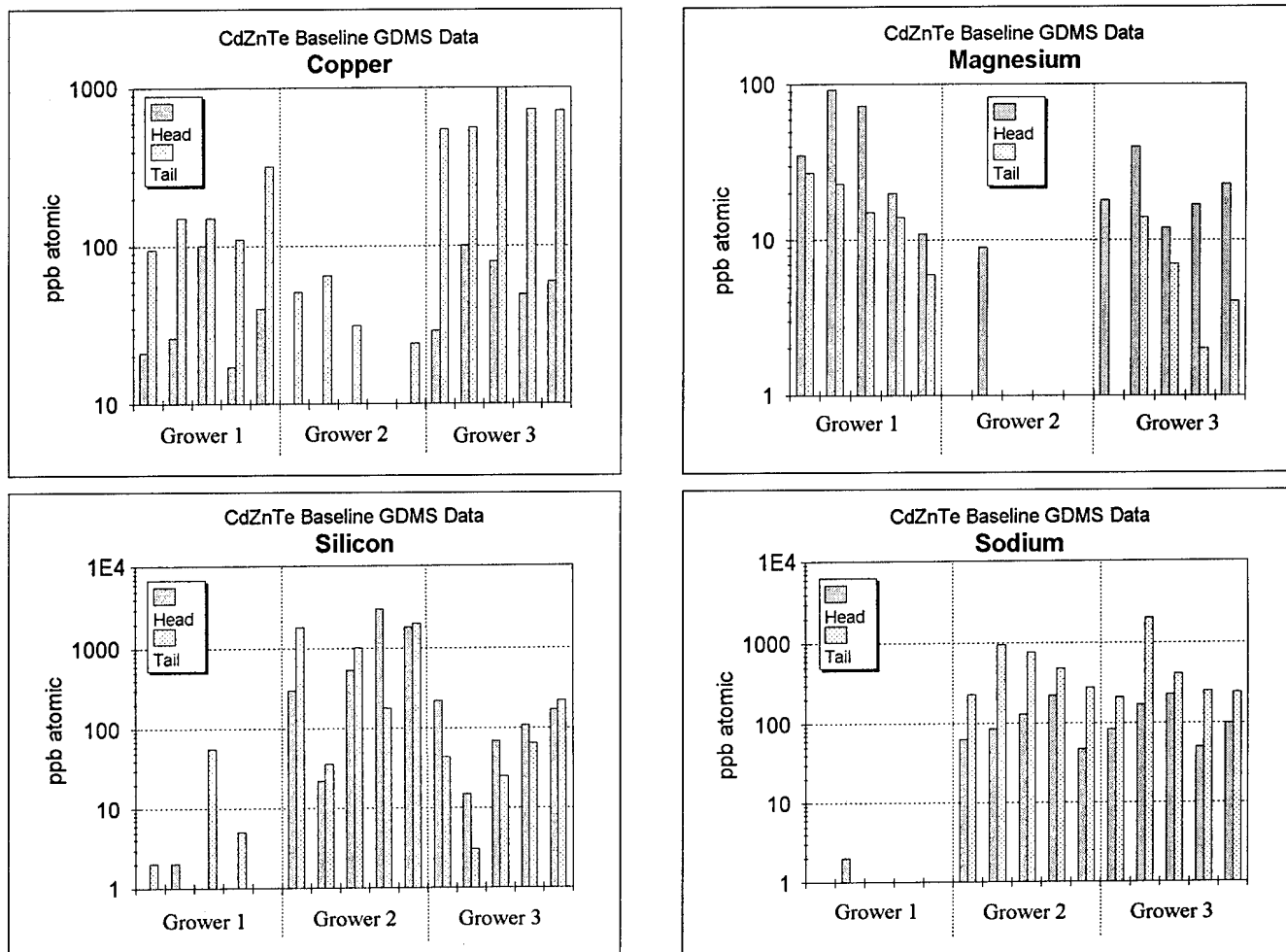
Fig. 3. Head and tail impurity concentrations are plotted for each baseline crystal. Large differences between grower sites are evident. Effective segregation is toward the tails for Cu and Na, toward the heads for Mg, and mixed for Si.

elements of interest prior to dissolving the samples. Calibration of the ZCGFAA data was done using the method of standard additions with aqueous standard solutions. Standard additions are necessary because the high concentration of CdZnTe matrix in the sample solutions make them dissimilar to the available standard solutions.

The distribution of impurities in the HgCdTe LPE layers were measured by secondary ion mass spectrometry (SIMS) depth profiling at Charles Evans and Associates using a Cameca instrument. For these samples, an oxygen primary beam was used for Li, In, Na, Mg, Al, Ca, Fe, and Ni and a cesium primary beam was used for Cu, O, C, Si, P, S, Cl, and Br. The primary ion beams were rastered over an area $(300 \ \mu m)^2$ and the detected secondary ions extracted from the central 85 μm diam of the crater. This limited sampling volume makes SIMS sensitive to microscopic sample inhomogeneity. The SIMS profiles extend through the entire thickness of the LPE layers and several microns into the substrates. Secondary ion mass spectrometry data are not accurate at the surfaces of the samples because of a "surface effect" that occurs before the sputtering process reaches equilibrium. This artifact disappears after the first several points

in the depth profile. The data are quantified using relative sensitivity factors determined from ion implant standards of known dose into HgCdTe and should be accurate to within a factor of two. Secondary ion mass spectrometry detection limits for HgCdTe vary widely for each element, as shown in Table I. These are approximate values which vary by about a factor of three depending on the sample and instrument conditions. For comparison, Table I also lists the GDMS detection limits in HgCdTe. The detection limits in CdZnTe should be similar to HgCdTe for both SIMS and GDMS. Secondary ion mass spectrometry is more sensitive for some elements (Li, In, Ca) while GDMS is more sensitive for others (Cu, Fe, Ni, P, Cl, Si).

RESULTS AND DISCUSSION

The reproducibility of ZCGFAA for testing CdZnTe was determined through a series of repeat tests, each using different pieces from the same two sample slices. These results are shown in Table II along with corresponding GDMS data. As in the case of GDMS testing, variations for a given sample can be due to sample inhomogeneity or instrumental precision. However, microscopic inhomogeneity is reduced in

ZCGFAA because of the larger sample volume. Instrumental precision was typically better than 10% in repeat measurements of the same sample solutions. In ZCGFAA, the problem of anomalous contamination in the sample solutions also contributes to the measured differences. Table II shows reproducible results for Cu, Ag, Fe, and Li, but not for sodium, since the later is always present as a variable background in the blank solutions. Zeeman corrected graphite furnace atomic absorption and GDMS results in Table I are in close agreement for Cu and Fe. Silver was below the GDMS detection limit in both samples but was easily detected by ZCGFAA. Lithium was lower by ZCGFAA, but both techniques found the tail sample to be much higher than the head. Figure 2 compares ZCGFAA to GDMS for Cu and Li in most of the baseline head and tail samples. This graph shows good agreement between the two analytical techniques over three orders of magnitude of Cu concentration. The ZCGFAA Li concentrations are 5–10 times lower than the GDMS for a wide range of concentrations, indicating a systematic offset in calibration between the two techniques. The origins of this offset are not known, but they could be caused by unaccounted loss of Li during the ZCGFAA char step or by inaccuracy in the GDMS calibration.

The purity of initial elemental raw materials is clearly important to the eventual CdZnTe substrate impurity levels. Baseline crystals were grown using various grades of raw materials depending on the grower site and, not surprisingly, the resulting substrate impurity levels were dependent on the grower site. Some of the differences, however, have been attributed to the different crystal growth procedures. In Fig. 3, the head and tail concentrations of Cu, Si, Mg, and Na in each of the baseline crystals illustrate differences in impurity concentrations between the grower sites as well as the effective segregation of these elements during growth. Five different boules are shown for each grower. For Cu and Na, the effective segregation is clearly toward the tail ends of the crystals, while Mg is consistently higher in the heads. Silicon does not follow any consistent segregation trend and there is significant fluctuation between the crystals. We believe that Si leaches out of the quartz ampoules during crystal growth depending on the carbonization quality, causing inconsistent Si incorporation in the CdZnTe. Effective segregation coefficients for the elements detected in the baseline CdZnTe are listed in Table III. Interestingly, most of the impurities that are electrically active in HgCdTe preferentially segregate toward the tail ends of the crystals, suggesting that substrates cut from near the tails may be more problematic for HgCdTe layer dopant control.

The baseline impurity averages for each grower site are shown for all detected elements in Table IV. Elements not listed in Table IV were tested for but not detected by GDMS. The differences between grower sites were investigated in order to differentiate between the contributions of the raw materials and the

crystal growth processes. To provide a direct comparison between the growth processes, equivalent purity lots of ISDZR grade raw materials (Cd, Zn, and Te) were used at each grower site. The average impurity concentrations in ISDZR CdZnTe are shown in Table V, along with averages for the Cd, Zn, and Te raw lots. Since the ISDZR raw materials are almost entirely impurity-free, most of the elements detected in the resultant CdZnTe are attributed to the crystal growth processes. These include Li, Na, Mg, Al, Si, Cl, and Cu. The only major exception is Se, which originates in the raw Te and shows up in each crystal at about the same concentrations. However, as a group VI element, selenium is generally thought to be electrically inactive in HgCdTe. In general, differences between grower sites were greatly reduced and overall purity was improved when ISDZR raw materials were used. Figure 4 shows the excellent overall improvement in CdZnTe purity achieved from the baseline to the ISDZR crystals. The dramatic increase in Fe at Grower #1 (compare Tables IV and V) was not included in Fig. 4 because it was due to an identified growth process change which is not due to the ISDZR raw material purity. Since most of the remaining impurities in the ISDZR crystals originated from crystal growth, fur-

Table III. Effective Segregation Coefficients in CdZnTe Baseline Crystals

	K<1		K>1	K Mixed
Li	S	V	Mg	Si
Na	Cl	Cr	Zn	Ni
Al	Ca	Fe		Se
P	Ti	Co		
		Cu		

Table IV. GDMS Results of CdZnTe Baseline Crystals Averaged for Each Grower Site

	Grower #1		Grower #2		Grower #3	
	Head	Tail	Head	Tail	Head	Tail
Li	284	5080	329	142	303	857
Na	127	622	<1	<1	101	434
Mg	22	5	44	17	3	4
Al	52	239	91	104	47	53
Si	117	71	9	13	1015	858
P	4	38	15	29	<1	1
S	41	284	3	2	<4	<4
Cl	27	968	2	14	7	16
Ca	8	142	<5	<5	<5	<5
Ti	<0.2	4	<0.2	10	1	<0.2
V	1	31	<0.2	<0.2	1	<0.2
Cr	4	27	<1	<1	<1	1
Fe	9	142	43	77	1	8
Co	<0.3	2	<0.3	<0.3	<0.3	<0.3
Ni	95	26	<1	5	<1	<1
Cu	63	732	49	165	<5	24
Zn	2.2%	1.0%	2.0%	1.5%	2.1%	1.6%
Se	164	228	4848	4428	4	2

Note: In parts per billion atomic.

Table V. Impurity Averages for CdZnTe Grown Using ISDZR Raw Materials

| | Grower #1 CdZnTe | | Grower #2 CdZnTe | | Grower #3 CdZnTe | | ISDZR Te | ISDZR Cd | ISDZR Zn |
	Head	Tail	Head	Tail	Head	Tail	Tail	Tail	Tail
Li	12	13	<3	100	73	547	<5	<0.6	<0.3
Na	14	16	130	74	51	393	<2	<0.4	<0.2
Mg	5	5	11	7	7	<2	<2	<0.3	<0.1
Al	38	43	130	32	40	47	6	<0.2	<0.2
Si	92	42	86	9	3342	148	20	<0.8	1
P	2	1	2	5	<1	<1	<1	<0.2	<0.1
S	<4	<4	15	<7	<4	3	<2	<2	<3
Cl	5	11	8	7	7	32	<1	1	<2
Ti	<0.2	<0.2	2	0.6	1	<0.2	<0.3	<1	<0.03
V	1	<0.2	<0.2	<0.2	<0.2	<0.2	<0.6	<0.1	<0.05
Cr	<1	2	<3	16	1	9	<1	<0.2	<0.6
Fe	1000	1080	<4	<6	5	2	1	<4	8
Ni	<1	5	<2	<2	<1	1	<0.7	1	<0.1
Cu	10	14	17	30	6	33	<2	<0.4	<34
Se	875	895	840	1000	580	817	3433	<5	<0.1

Note: ISDZR raw material process averages are also listed. Comparison to Table IV shows substantially improved CdZnTe purity when ISDZR raw materials are used. Measurements were made by GDMS and values are reported in ppba.
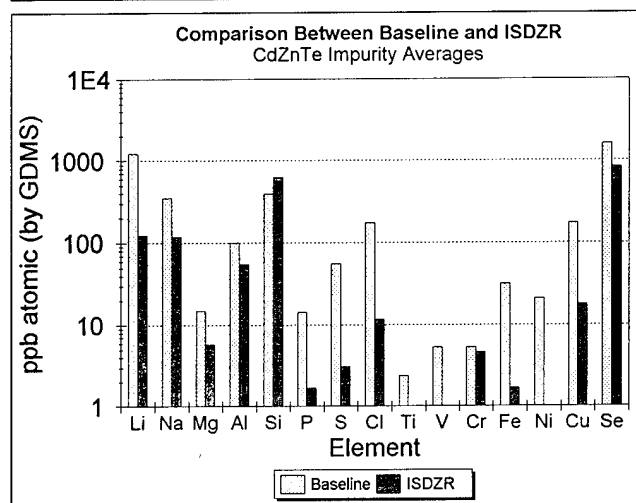
Fig. 4. Overall process averages are plotted for comparison between the baseline and ISDZR crystal growth processes.

ther improvements in CdZnTe purity will require modifications of the crystal growth procedures rather than additional raw materials purification.

Liquid phase epitaxy films were grown at TI on 75 substrates provided by the IRMP program using TI's large tellurium melt dipping process. The films were grown in one of two reactors: Reactor 10 is doped nominally to 2×10^{14}/cc with indium, while reactor 11 is doped to 4×10^{14}/cc indium. Low doping was intentionally done to exacerbate any effects which impurities in the substrate have on epitaxial films. After post-growth annealing, the 77K cutoff predicted by room temperature Fourier transform infrared was measured. Two pieces were cut from each film. One was used to measure the Hall properties, while the other was used to fabricate MIS test structures. The chief parameter of interest in the MIS devices is Q_{400},

which is the nodal capacitance (in nC/cm^2) measured under bias conditions which result in a dark current of 400 uA/cm^2 averaged over the first 5 μsec integration time. The Q_{400} is thus the well capacity under conditions which produce a given dark current, and is analogous to the voltage to which a diode can be reverse biased to produce a given dark current. Under the conditions which occur when an MIS capacitor is pulsed into depletion, the main source of dark current is via tunneling through bandgap states. "Good" values for Q_{400} are 20 nC/cm^2 and above for material with a cutoff of 10 μm.

These data were analyzed in conjunction with GDMS impurity data measured on the first and last to freeze portions of the ingots. The only correlations which could be discerned are with the copper concentrations in the ingots. Figure 5 shows the relationship between the Hall mobility measured at 77K with the copper concentrations measured in the first to freeze portions of the ingots. In this figure, the mobility has been normalized to a cutoff of 10 μm using the theoretical behavior of mobility as a function of cutoff.[7] The mobility data have been averaged over all substrates from each ingot. A strong negative correlation exists, with the mobility decreasing as the copper concentration increases. Indeed, LPE films grown on an ingot with a first to freeze copper concentration of 100 ppba (not shown in Fig. 5) were p-type after post-anneal. The same kind of correlation with substrate copper exists in the behavior of MIS test structures, as is shown in Fig. 5. The data in this figure have been normalized to a cutoff of 10 μm using an empirical relationship between cutoff and Q_{400} observed in previous work. The well capacity is greatly reduced as the copper concentration in the substrate rises. The highest performing devices are on substrates with the lowest copper concentration. These data are the first

solid demonstration of the link between MIS performance and substrate copper concentrations.

The p-on-n heterojunction diodes were found to be far less affected by the substrate impurity concentrations than were the MIS devices. This is presumably due to the higher indium doping level (1.5×10^{15}) used in the heterojunction baselayers. In fact, there was no consistent correlation found between the device or LPE layer properties and any of the measured substrate impurities in the baseline boules used for this study. However, in the overall LPE heterojunction production process at LIRIS, a small fraction (~10% over the last three years) of the substrate boules produce compensation and even p-type conversion in the n-type baselayers. Among the 15 IRMP baseline boules used for LPE growth, one such boule (#54) was found. All LPE baselayers grown on substrates from this boule were found to have lowered mobility. It is suspected that out-diffusion of impurities from the substrates is responsible for this effect. The measured copper concentration in boule #54 is about average when compared to the other baseline boules, implying that there may be some additional property (besides just the measured Cu concentration) that contributed to the degradation of HgCdTe layer properties. The incompletely understood role of substrate Te inclusions in gettering Cu may be responsible for such anomalous compensation effects. Under Phase 2 of the IRMP program, we are undertaking experiments to better understand the interactions between impurities and substrate defects, such as Te precipitates. Methods to control precipitate size and density by stoichiometry control during boule growth or by post-growth annealing are now fairly well understood.[8] Therefore, substrates can be prepared with differing precipitate and impurity levels. We will evaluate sets of nominally identical substrates (adjacent slices of the same boules) which have undergone different post-growth thermal treatments. These will include substrates from a copper spiked boule, in which copper has been intentionally added at a high enough level to easily detect and evaluate in terms of its effects on HgCdTe layers.

Secondary ion mass spectroscopy depth profiling was used to track impurities from the substrates into the LPE layers. The SIMS data were analyzed in conjunction with the measured LPE electrical properties and the GDMS ingot concentrations. Samples selected for SIMS consisted of heterojunction baselayers on substrates from each grower site, including two layers grown on boule #54. Electrical properties of all the SIMS samples were good except for the two from boule #54. As described in the Experimental section, the sensitivity of SIMS depends very strongly on the analyte element. For some elements, such as Cu, Fe, Ni, Si, and Cl, concentrations could be present in sufficient quantities to affect the HgCdTe electrical properties, yet go undetected by SIMS. Although the SIMS detection limit for Cu is higher than the electrical compensation level in the IRMP samples, SIMS has been able to measure Cu in

a separate case of extraordinarily high contamination. This is shown in Fig. 6 for an LPE layer with a Hall carrier concentration of 6.5×10^{16}/cc p-type. This layer was grown on a substrate from a boule that consistently produced p-type LPE layers (after isothermal Hg vapor anneal at 250°C). For other elements, such as Al, Mg, Li, Na, P, Ca, and S, the SIMS measurements have much better sensitivity. However, these elements were not detected in high enough concentrations to account for the measured p-type electrical compensation (up to about 2×10^{15}/cc). The suspected p-type impurities, Li, Na, and P, were measured below 10^{14}/cc in all of the LPE layers. Sulfur was measured at 2×10^{15}/cc in two of the LPE layers, while the others were near the detection limit in the high 10^{14}/cc range. However, the two samples with high S were among the good electrical samples, indicating that these levels of S do not adversely affect HgCdTe properties. In summary, we were not able to detect the elements responsible for the degraded
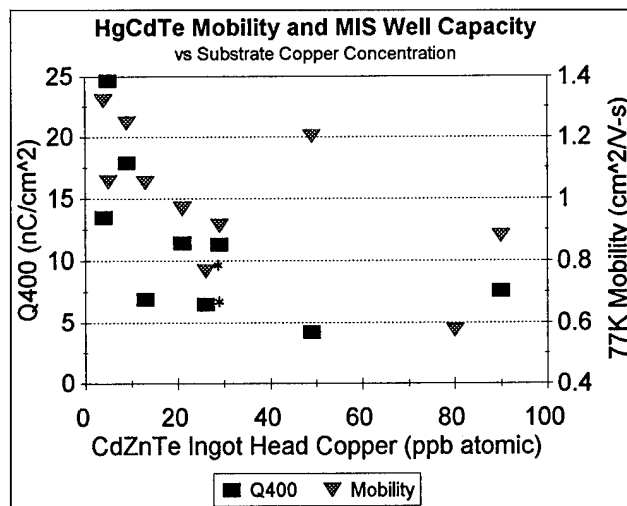
Fig. 5. HgCdTe layer mobility and MIS well capacity are averaged over all substrates from each ingot and plotted against the copper concentration in the first to freeze a portion of the ingots. The * marks an ingot that gave poor results in the p-on-on heterojunction growth process.
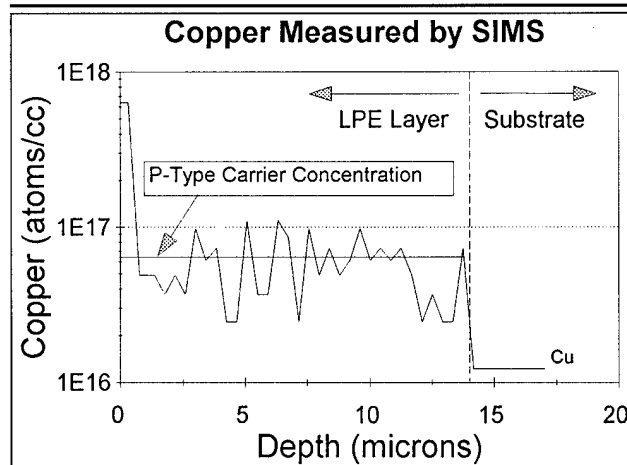
Fig. 6. Secondary ion mass spectrometry depth profile measurement shows copper at the same level as the p-type carrier concentration. The SIMS measurement was made on the actual Hall sample.

electrical properties in some HgCdTe layers. If copper plays a role, it is below the SIMS detection limit. In Phase 2 of the IRMP program, we will investigate other analytical techniques to directly measure copper in HgCdTe layers. The newly developed technique of sputter initiated resonance ionization spectroscopy (SIRIS) holds much promise for depth profiling and small scale spatial imaging of copper at low levels in HgCdTe.[9]

CONCLUSION

Several analytical measurement techniques were used to track the levels of impurities through the various processing stages from the initial raw materials to the CdZnTe substrates and the eventual HgCdTe LPE layers. A baseline was established for CdZnTe purity, against which the effectiveness of process modifications were gauged. The origins of impurities and their effective segregation in CdZnTe crystal growth were determined. A novel technique of raw materials purification was developed and greatly improved substrate purity was achieved using this technique. However, several elements were still found in the improved purity substrates and were attributed to the crystal growth processes. Further substrate purification will require modifications to the crystal growth processes or post-growth impurity extraction.

HgCdTe LPE layers were grown and test devices were fabricated on IRMP baseline substrates. These were evaluated in conjunction with the measured substrate and LPE layer purity levels. In lightly doped LPE layers used for MIS devices, the HgCdTe Hall mobility and MIS well capacitance were strongly dependent on the substrate copper concentration. However, in the more heavily doped LPE layers used for p-on-n heterojunction diodes, the LPE layer and test device properties were far less affected by the substrate purity. Secondary ion mass spectrometry depth profile measurements were made to identify impurities in HgCdTe LPE layers that may be responsible for electrical compensation. Several common p-type impurities (Li, Na, and P) were found in concentrations far too low to account for the observed compensation. However, the SIMS detection limits for certain other elements (particularly Cu) are not sensitive enough to detect concentrations which can adversely affect HgCdTe electrical properties.

ACKNOWLEDGMENT

REFERENCES

1. M.G. Astles, H. Hill, G. Blackmore, S. Courtney and N. Shaw, *J. Cryst. Growth* 91, 1 (1988).
2. P. Rudolph, M. Muhlberg, M. Neubert, T. Boeck, P. Mock, L. Parthier, K. Jacobs and E. Kropp, *J. Cryst. Growth* 118, 204 (1992).
3. T.H. Myers, K.A. Harris, R.W. Yanka, L.M. Mohnkern, R.J. Williams and G.K. Dudoff, *J. Vac. Sci. Technol. B* 10, 1438 (1992).
4. G.N. Pultz, P.W. Norton, E.E. Krueger and M.B. Reine, *J. Vac. Sci. Technol. B* 9, 1724 (1991).
5. J.D. Beck, M.A. Kinch, E.J. Esposito and R.A. Chapman, *J. Vac. Sci. Technol.* 21, 172 (1982).
6. J.C. Huneke and W. Vieth, *Encyclopedia of Materials Characterization,* eds. C.R. Brundle, C.A. Evans and S. Wilson, (Boston: Butterworth-Heinemann, 1992).
7. M.C. Chen and L. Columbo, *J. Appl. Phys.* 73, 2916 (1993).
8. H.R. Vydyanath, J. Ellsworth, J.J. Kennedy, B. Dean, C.J. Johnson, G.T. Neugebauer, J. Sepich and P.-K. Liao, *J. Vac. Sci. Technol. B* 10, 1476 (1992).
9. S. Sen, J.E. Stannard, S.M. Johnson, H.F. Arlinghaus and G.I. Bekov, Proc. 1993 U.S. Workshop on the Physics and Chemistry of Mercury Cadmium Telluride and Other IR Materials, Seattle. *J. Electron Mater.* 24, 515 (1995).

Etch Pit Characterization of CdTe and CdZnTe Substrates for Use in Mercury Cadmium Telluride Epitaxy

W.J. EVERSON, C.K. ARD, J.L. SEPICH, B.E. DEAN, and
G.T. NEUGEBAUER

II-VI Incorporated, Saxonburg, PA 16056

H.F. SCHAAKE

Texas Instruments, Dallas, TX 75265

A new etch system is described which produces pits on the technologically important B face of (111) and (211) CdTe and CdZnTe which are commonly used in mercury cadmium telluride (MCT) epitaxy. A ratio of approximately 10 wide:1 deep is achieved with this etch allowing its use without removing excessive material. Examples of the use of this etch are given and a comparison is made with the Nakagawa, A face etch system which is in common use to characterize this family of materials. A screening protocol is discussed which integrates the use of etch pitting into the manufacture of substrates for use in epitaxial MCT applications. Comparisons are made between CdZnTe substrates grown using the horizontal and vertical Bridgman techniques.

Key words: CdTe, CdZnTe, defects, etch pit, HgCdTe

INTRODUCTION

Mercury cadmium telluride (MCT) is the most important material currently in use for the manufacture of high performance infrared (IR) detectors.[1] Many factors contribute to the overall performance of detectors manufactured from MCT and much work has been carried out to elucidate what these factors are. Considerable advances have been made in the understanding of MCT materials science and device physics over the past decade and the dominant mechanisms which lead to low performance or poor uniformity of devices and arrays are now fairly well understood.

Bulk grown MCT was the primary material used for *first generation*[2] infrared detectors; this produced photoconductive devices with adequate performance, although there have been reports of significant savings in cost and improvements in yield by switching to epitaxially grown material. For *second generation*

devices, which typically consist of arrays of photodiodes, it quickly became apparent that the dislocation structure in bulk grown material led to fixed pattern noise from nonconforming elements in the arrays. A typical, state-of-the-art, high performance array would consist of a p-on-n diode structure, sensitive to long wavelength IR (typically >10 µm), and bump bonded to a silicon multiplexer for readout into the system electronics.

One key aspect which determines the performance of a photovoltaic (PV) IR detector is the leakage path which exists across the p-n junction, this is particularly important in the performance of long wavelength detectors when operated at temperatures significantly below 77K. Dislocations in the material which intersect the p-n junction are an example of current leakage paths; this has been quantified by Johnson et al.,[3] leading to a potential specification for the maximum permissible dislocation density which is acceptable in a given application.

It has been reported that the minimum dislocation

density which can be achieved in MCT material grown by liquid phase epitaxy (LPE) is close to that which is measured in the CdTe or the CdZnTe substrate.[4] It is clear, therefore, that nonuniformities in dislocation density in substrates will lead to nonuniformity in MCT layers and subsequently to defective arrays of detectors. The growth of highly perfect CdTe family materials for use as substrates is not currently reproducible. Many authors quote average dislocation densities for these materials and do not address the issue that significant fluctuations in dislocation density within an ingot and even within a wafer exist. Table I shows the average and the range of dislocation densities which are typically seen in Bridgman grown CdTe family substrate materials. It is clearly important to minimize the range of dislocation densities in wafers which are to be used as substrates for MCT growth.

A key tool in the measurement and identification of areas of high dislocation density is the use of etch pitting solutions; many such solutions have been reported for use on CdTe family materials. In particular, the Nakagawa etch[5] which became the industry standard, whereas the Inoue[6] (E, E-Ag1, and E-Ag2) and Hähnert/Schenk[7] etches find limited application. Each of these etches has particular strengths and weaknesses on the various crystallographic orientations which are in common use for MCT epitaxy. The polarity as well as the orientation of faces for epitaxial growth is important in determining the properties of MCT epitaxial layers. The "B" face in this system is the Te-rich face, conversely, the "A" face is the Cd or metal-rich face.

Table II shows the orientations which are most commonly specified for substrates; the most common is the (111)B orientation which is used in Te-rich, sliding boat LPE. The checks in Table II indicate that the orientation is in common use for the particular MCT growth technique, the crosses indicate that the

orientation is not in common use and the queries indicate that no data is available to indicate that the orientation is commonly used. A reliable B face defect revealing etch could be an important tool for improving Te-rich MCT epitaxial processing.

It can be seen from Table II that the most key orientations for substrates are (111)A and B, (211)B, and (100) misoriented in various numbers of degrees to (110). To date, no reliable, *effective* etch for the (111)B or the (211)B has been available. Bagai et al.[8] have reported a version of the Nakagawa solution to work on B face CdTe, but this cannot be reproduced in the authors' laboratories. Lack of an etch has encumbered the screening of materials for use on these orientations although the reverse side of (111)B substrates can be effectively screened with the Nakagawa solution.

EXPERIMENTAL PROCEDURES AND RESULTS

Requirements of the B Face Etch

A number of possible etch systems were explored in an attempt to find a pitting solution which met the criteria defining an *effective* etch, those criteria were as follows:

- The etch must be effective at producing pits on the (111)B face of CdTe and CdZnTe.
- The etch must be effective at producing pits on the (211)B face of CdTe and CdZnTe.
- The pits produced by the etch must be comparable in terms of pits per cm² with the Nakagawa solution i.e. they must be related to dislocations.
- The etch must produce pits which can be used to discriminate areas of high EPD from a low background EPD with the *unaided* eye.
- The etch must be easy to use and reproducible in a production environment.

Development and Characterization of the B Face Etch

The etch which was developed meets all of the above criteria and is described below.

Composition of the solution:

6 cm³ of 48% HF:24 cm³ of HNO$_3$:150 cm³ of Lactic Acid (1:4:25)

Table I. Average and Typical EPDs Reported on CdTe Family Materials

Material	CdTe	CdZnTe	CdTeSe
Average EPD/cm^{-2}	25×10^4	6×10^4	4×10^4
Typical range of EPD/cm^{-2}	$10–100 \times 10^4$	$1–50 \times 10^4$	$0.5–50 \times 10^4$

Table II. Orientations of Substrates

	Te Slider LPE	Te Dipper/ Tipper LPE	Hg Dipper LPE	MOCVD	MBE
(111)B	✓	✓	?	Twins *	Twins *
(111)A	x	?	✓	Twins *	Twins *
(211)B	x	?	?	✓	✓
(211)A	x	?	?	x	x
(100) > (110)	x	?	?	✓	✓
Other Orientations	x	?	?	✓	✓

*Some reports of twin free growth.
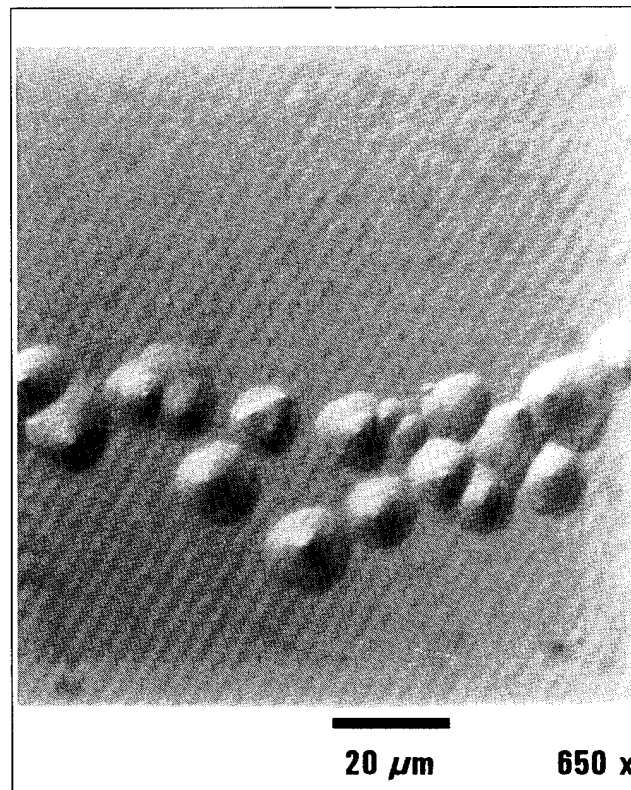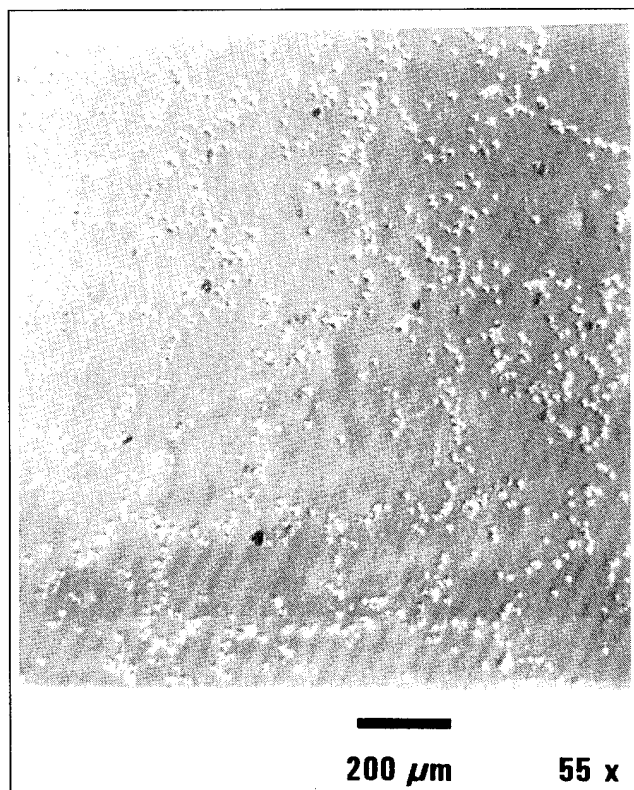
Fig. 1. Pits formed on (111)B by the B face etch.
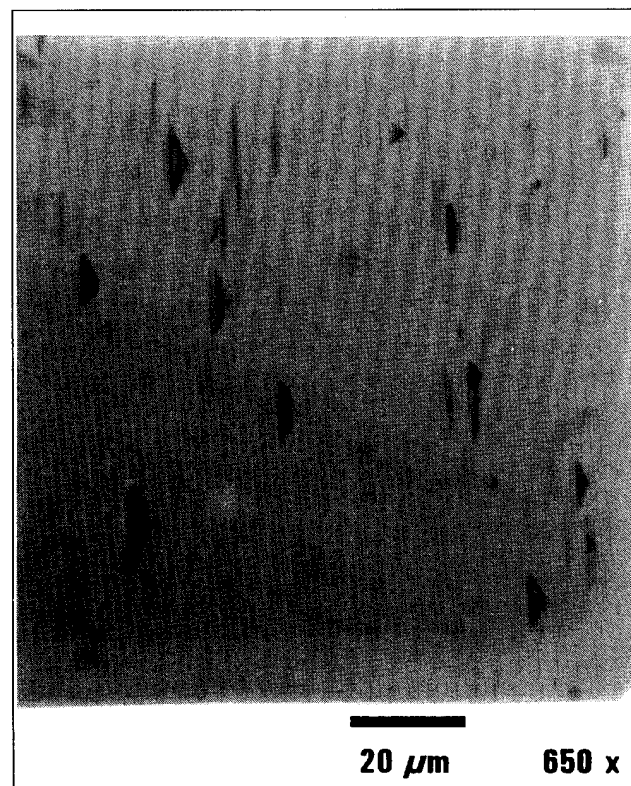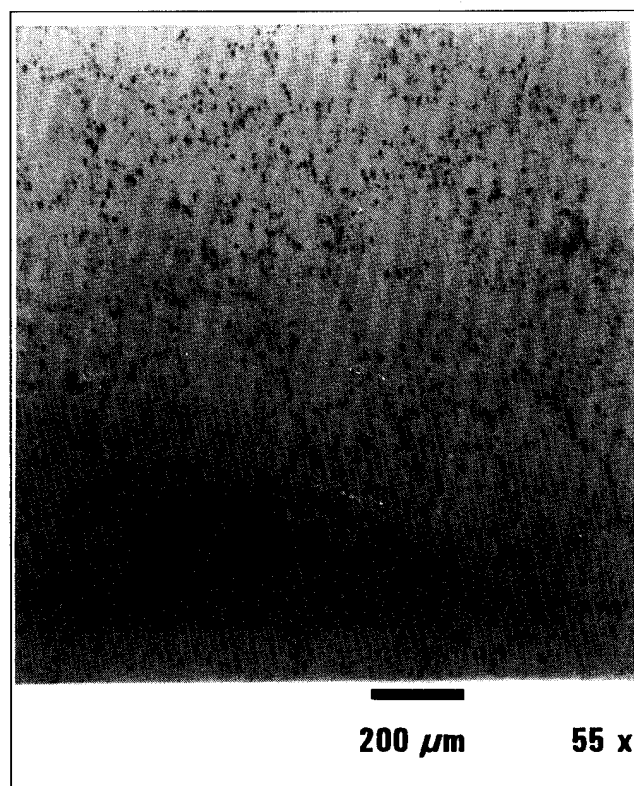
Fig. 2. Pits formed on (211)B by the B face etch.
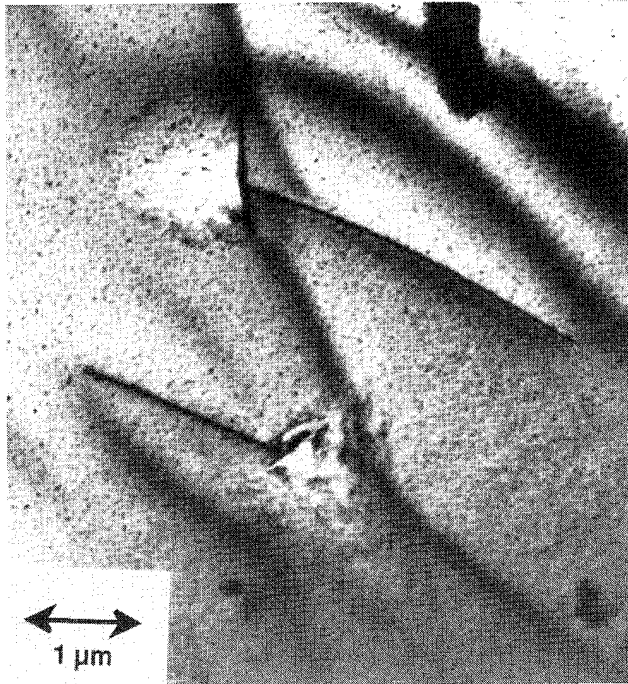
Fig. 3. TEM of pits formed on dislocations.
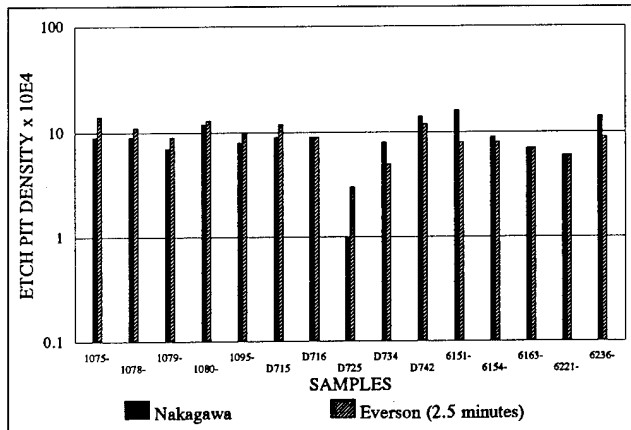
Fig. 4. Bar graph comparing EPDs on A and B faces of (111).

The condition for producing pits with this solution on CdTe or CdZnTe substrates was found to be immersion for 2.5 min with moderate agitation at room temperature.

The etch produces triangular, well defined pits on the (111)B face of CdTe and CdZnTe. The pits formed typically display a ratio of 10:1 width:depth which makes groups of pits easy to see with the unaided eye. Figure 1 shows the pits produced on the (111)B face of CdZnTe. For the (211)B orientation, the pits formed are elongated triangles; Fig. 2 shows the microstructure of these pits formed on a CdZnTe wafer.

We refer to this etch and etching procedure as the "Everson etch" as it was W.J. Everson who first noted its effectiveness and has subsequently helped to develop its application.

Validation of the Etch

It is clearly important not only to have an etch

Table III. EPDs for Single Crystal Block of CdTe

	Nakagawa	Everson
(111)A	44×10^4 cm^{-2}	N/A
(111)B	N/A	35×10^4 cm^{-2}
(211)A	N/A	N/A
(211)B	N/A	20×10^4 cm^{-2}

which produces pits on the B face of CdTe, but also to validate that the etch measures the dislocation density of the material. Four approaches to validate the dislocation revealing capability of the etch described here were used.

Firstly, transmission electron microscopy was used to determine that an etch pit was formed due to a dislocation. A high dislocation density sample which had been pitted with the Everson etch was carefully thinned to the point where the tips of the etch pits almost perforated the foil and then examined. Figure 3 shows a micrograph which shows two such etch pits with a dislocation line clearly visible at the tip of each pit.

Secondly, a cross reference with the current industry standard Nakagawa etch was used as the benchmark for the B face etch by etching both faces of a statistically significant sample of (111) orientated wafers. The results for this set of 15 measurements are graphed below in Fig. 4 and the correlation coefficients are shown.

Thirdly, detailed comparisons were made between the pits formed on each face of a (111) oriented 2×3 cm CdTe wafer by macro photography and by EPD mapping on a Cambridge instruments "Quantimet" system. The results on the (111)A Nakagawa etched face and the equivalent on the (111)B Everson etched face were very comparable in both the counts and the structure of the defects seen.

Finally, a single crystal block of CdTe was oriented such that (111) and (211) A and B faces were all visible and counts were made on the faces to cross correlate the results. Table III shows the result of these correlations. A micro twin was revealed on all etched faces of the block.

A summary is shown in Table IV of the usefulness of the various etches which are in common use on CdTe family materials including the B face "Everson" etch described in this paper. An additional etch, included in the table which the authors have found to be useful in delineating defects on all orientations of CdTe and CdZnTe is included since it was one of the prime candidate etches which, it was hoped would provide a universal screening etch. The etch, which consists of dilute bromine in methanol under bright white light[9] reveals certain features but the pits formed are very small, precluding its use as a screening etch.

SCREENING PROTOCOL

The establishment of etches which are effective at

Table IV. Usefulness of Etches in Common Use on CdTe Family Materials

	Nakagawa	Everson	Inoue E, E-Ag	Hähnert & Schenk	0.1% Bromine / Methanol
(111)B	No pits	Good pits	Good pits; not dislocation related	Small pits	Small pits; not dislocation related
(111)A	Good pits	No pits	Good pits; not dislocation related	Fair pits	Small pits; not dislocation related
(211)B	No pits	Fair pits [elongated]	Good pits; not dislocation related	Small pits	Small pits; not dislocation related
(100) >(110)	No pits	No pits	Good pits; not dislocation related	?	Small pits; not dislocation related
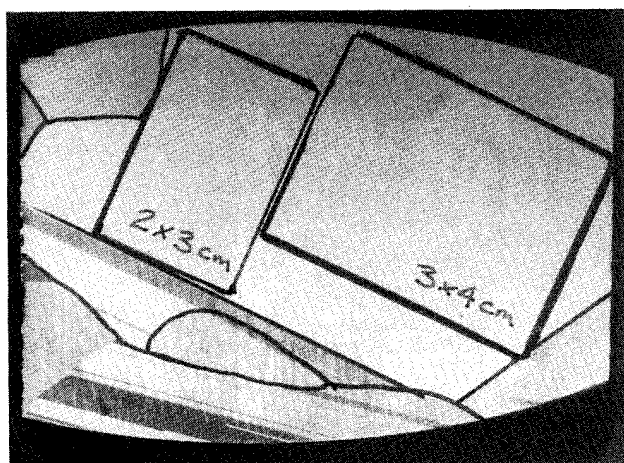
Fig. 5. As-sawn wafer of VB grown CdZnTe.
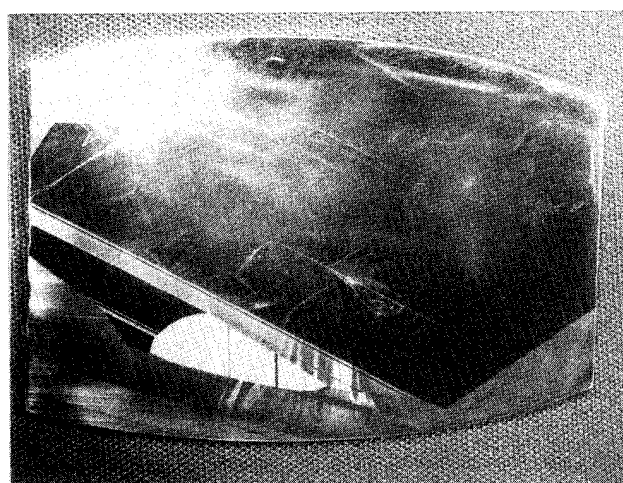
Fig. 6. Wafer pitted using the Everson etch.

revealing dislocations on the most important crystallographic faces in common use with CdTe family materials enables an important step forward in establishing quality tools for the manufacture of substrates which are used in the manufacture of high performance epitaxial MCT material and diode arrays.

The substrate screening technique which has been developed, minimizes the effect of threading dislocations on the MCT diode arrays. This is achieved by ensuring that areas of high EPD and micro twinning are not included in the clear aperture of a substrate which is used for epitaxial MCT growth.

Figure 5 shows an as-sawn CdZnTe wafer, grown by the vertical Bridgman technique, which has been marked with potential substrates. It can be seen that, at this stage, a 3 × 4 cm substrate and a 2 × 3 cm substrate could be physically manufactured from this wafer. Figure 6 shows that this same wafer, with its microstructure revealed using the Everson B face etch described in this paper, would not yield any high quality (EPD < 1 × 10^5 cm^{-2}) substrates. The wafer clearly shows areas of high dislocation density and micro twinning which were not apparent prior to etching. In this case, etch screening indicates that this particular wafer would be of little value as a substrate to produce high performance MCT material and subsequent IR detector arrays.

Figure 7 shows large area (111) as-sawn single
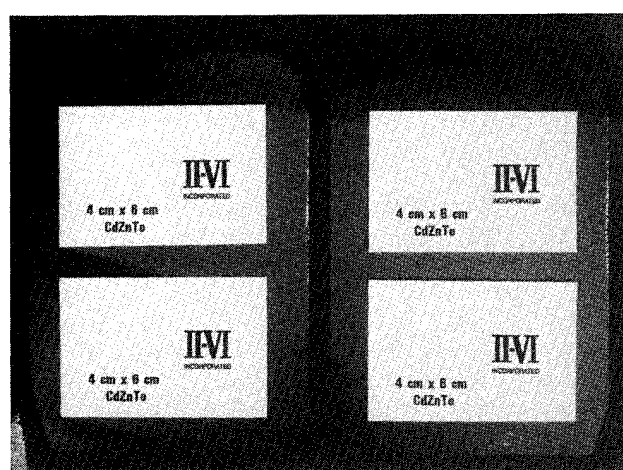
Fig. 7. Single crystal HB wafers showing two 4 × 6 cm substrates on each.

crystal wafers produced by the horizontal Bridgman technique; these wafers, when etched, showed a very uniform dislocation density averaging 3–5 × 10^4 cm^{-2}. Figure 8 shows the polished and defect etched surface of the ingot, which was parallel to the (111) plane in the as-grown condition, showing highly uniform EPD with no twins or lines of defects over the majority of the 7.5 × 10 cm single crystal area.

An initial comparison between the wafers produced using the vertical Bridgman (VB) process (which
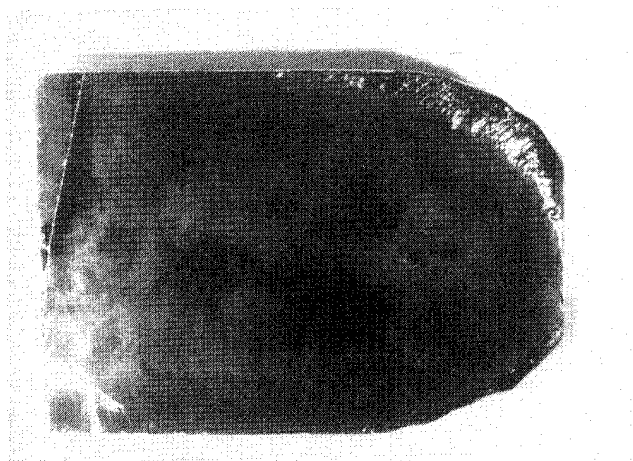
Fig. 8. HB ingot section with the (111)B surface pitted with the Everson etch.

typically shows two or three large grains) and the horizontal Bridgman (HB) process recently put into production at II-VI suggests that the lack of intruding grains in the single crystal surface layer, intrinsic to HB growth,[10] may lead to a reduced incidence of lines of defects and micro twinning.

The protocol which has been developed requires that every third to fifth as-sawn slice is screened by "view polishing" and defect etching prior to manufacturing final sized substrates.

CONCLUSION

A defect etch has been developed which is effective at forming pits on the (111)B and (211)B faces of CdTe and CdZnTe. The etch pits features formed using this etch can be seen with the unaided eye and can therefore be used in routine production to determine pass/fail criteria for wafers. This step forward enables B face screening of wafers to maximize downstream yields of material and devices on B face substrates.

The etch has been shown to compare well in terms of the density and reproducibility of pits which are produced with the industry standard Nakagawa etch, which pits only the (111)A face of CdTe family materials. Transmission electron microscopy and statistically significant sampling has confirmed that pits are formed at the intersection of dislocations with the B face, Te rich surface.

ACKNOWLEDGMENTS

REFERENCES

1. R. Balcerak and L. Brown, *J. Vac. Sci. Technol.* B 10, 1353 (1992).
2. C.F. Freeman, *J. Vac. Sci. Technol.* B9 ,1613 (1991).
3. S.M. Johnson, D.R Rhiger, J.P. Rosbeck, J.M. Peterson, S.M. Taylor and M.E. Boyd, *J. Vac. Sci. Technol.* B10, 1499 (1992).
4. M. Yoshikawa, *J. Appl. Phys.* 63 1533 (1988).
5. K. Nakagawa, K. Naeda and S. Takeuchi, *Appl. Phys. Lett.* 34, 574 (1979).
6. M. Inoue, I. Teramoto and S. Takayanagi, *J. Appl. Phys.* 33, 2578 (1962).
7. I. Hähnert and M. Schenk, *J. Cryst. Growth* 101 ,251 (1990).
8. R.K. Bagai, G. Mohan, G.L. Seth and W.N. Borle, *J. Cryst. Growth* 85, 386 (1987).
9. Private communication, D.J. Williams.
10. P.-K. Liao, G. Westphal, H.F. Schaake, B.E. Dean and C.K. Ard, *Proc. 1993 Meeting of the IRIS Specialty Group on Infrared Materials,* paper A-3.

Copper Outdiffusion from CdZnTe Substrates and its Effect on the Properties of Metalorganic Chemical Vapor Deposition-Grown HgCdTe

R. KORENSTEIN, R.J. OLSON, Jr., and D. LEE

Raytheon Company, Research Division, Lexington, MA 02173

P.K. LIAO and C.A. CASTRO

Texas Instruments, Central Research Laboratories, Dallas, TX 75265

We report that HgCdTe (MCT) epilayers grown by metalorganic chemical vapor deposition can be doped by copper outdiffusing from CdZnTe substrates. The copper content in the substrates was determined by the choice of the purity of the starting raw materials. Copper diffusion could be controlled by adjusting the tellurium precipitate density in the substrates. Growing on substrates with a high concentration of tellurium precipitates resulted in low doped MCT epilayers whereas a high copper concentration was found in MCT grown on substrates with a lower concentration of tellurium precipitates. A mechanism whereby tellurium precipitates getter copper during the post-growth cooldown of CdZnTe boules and trap copper in the substrates is proposed.

Key words: CdZnTe, HgCdTe, impurities, metalorganic chemical vapor deposition (MOCVD), Te precipitates

INTRODUCTION

Impurities in HgCdTe (MCT) can affect material properties such as carrier concentration, mobility, and minority carrier lifetime. Copper is one such impurity whose adverse effects on the transport properties of MCT are well documented.[1,2] An important source of copper contamination is the substrate used in MCT epitaxy. Myers et al. have shown that copper from CdZnTe substrates can diffuse into the MCT epilayer during MBE growth and/or post growth annealing resulting in anomalous electrical behavior.[3] Similar results have been observed in liquid phase epitaxy (LPE)-grown MCT layers.[4] Since copper may be present to some extent in most CdTe or CdZnTe substrates (in this study, the copper concentration in the substrate was determined by the choice of the starting raw materials), it is important to understand

the process of copper outdiffusion in order to minimize its effect on the material properties of epitaxially grown MCT. Here we show that metalorganic chemical vapor deposition (MOCVD)-grown MCT layers can also be doped with copper diffusing from CdZnTe substrates. We report a correlation between substrate post growth treatment, the density of tellurium precipitates, and the quantity of copper that segregates into MOCVD-grown MCT.

EXPERIMENTAL

This work was carried out both at Texas Instruments and Raytheon. Texas Instruments grew the CdZnTe boules from starting raw materials of different purity and performed substrate annealing experiments. Raytheon grew the MCT epilayers by MOCVD on Texas Instruments' substrates and characterized the material properties of the epilayers.

CdZnTe single crystals were grown by the horizontal Bridgman technique. The growth furnace con-

sisted of six independently controlled zones with a bore of 4.5 inches. Typical ingots weighed 4 Kg with nominal ZnTe mole fraction of 5%. Several purity grades of raw materials, especially elemental cadmium, were used in this study to purposely vary the impurity content and to correlate electrical properties of MCT epitaxial layers with substrate purity. The ingots were grown from pre-reacted charges placed in a graphite boat which was sealed off in an evacuated quartz ampoule. Typical growth rates were 8 mm/h. Once the growth was completed, the ingot was allowed to cool either by turning the furnace off and letting the ingot cool fairly quickly to room temperature (furnace cool) or by cooling slowly at 4°C/h (programmed cooling) to 600°C and then shutting the furnace off. Large single crystal grains extracted from the ingots were oriented to <111> or <100> and then sawed into 2 × 3 cm substrates. The CdZnTe substrates were characterized by infrared transmission measurements. An infrared microscope was used to measure the size and density of tellurium precipitates.

Mercury-cadmium-telluride was grown on both (111)B and (100) CdZnTe substrates by the MOCVD direct alloy growth process in a vertical reactor at 360°C using diisopropyltellurium, dimethylcadmium, and elementary mercury.[5] The composition of the grown layers was determined from infrared transmission and thickness measurements. Samples were annealed at 220°C for 15 h in a mercury ambient to reduce Hg vacancies before doing any electrical measurements. Carrier concentration and mobility were determined from van der Pauw measurements. The minority carrier lifetime was measured by the photoconductive decay technique using a GaAs laser

operating at 0.85 μm. Copper concentrations were determined at VHG Labs, Manchester, NH, using Zeeman corrected graphite furnace atomic absorption spectroscopy (ZCGFAAS) analysis. This technique is capable of measuring copper concentration in MCT with an accuracy of ± 50% and precision of ± 50%. The epitaxial MCT layer was separated from its substrate by means of polishing and selective etching which resulted in a free standing MCT epitaxial layer. The MCT layer and the CdZnTe substrate were then each analyzed separately.

RESULTS AND DISCUSSION

Table I summarizes the results of the two different CdZnTe ingot cooling schemes. As can be seen, fast cooldown (furnace cool) results in a high density (10^5 cm^{-3}) of large (5–8 μm) tellurium precipitates while programmed cooling results in a two orders of magnitude reduction in tellurium precipitate density as well as a reduction in precipitate size. Slow cooling allows cadmium, which has a higher vapor pressure than tellurium, to reenter the crystal lattice and reduce the size and quantity of tellurium precipitates.

Table II shows the material characteristics of some MCT epilayers grown for this study. The designation "epi" refers to the MCT epitaxial layer and the term "sub" refers to its CdZnTe substrate. Samples SR151-epi and SR158-epi are examples of low doped high quality n-type material. The measured low carrier concentration and high electron mobility at 77K are consistent with the x value.[6] Figure 1 displays the carrier concentration, n_H, and electron mobility for sample SR158-epi as a function of temperature. The classical n-type behavior (net donor level, $N_D - N_A$, of 4.5×10^{14} cm^{-3} and electron mobility, μ_H, in excess of 10^5 cm^2/V-s at low temperature) are indications of high quality low doped n-type material. The relatively high minority carrier lifetimes reported in Table II are also consistent with good n-type material.[7]

The tellurium precipitate concentration in the substrate (Table II) correlates well with the transport properties and the quantity of copper in the epilayers. For example, sample SR151-epi has a low copper concentration (<0.03 ppma). In fact, the copper con-

Table I. Tellurium Precipitate Size and Density as a Function of Growth Conditions

Cooldown	Tellurium Precipitate Size (μm)	Tellurium Precipitate Density (cm^{-3})
Fast	5–8	10^5
Programmed Cool	1–3	10^3

Table II. Material Characteristics of MOCVD-Grown HgCdTe

Sample	x	n_H^{77K} (cm^{-3})	μ_H^{77K} (cm^2/V–s)	τ^{77K} (μs)	$Te_{precipitate}$ Density	[Cu] (ppma)
SR151-epi	0.242	-5.0×10^{14}	102,600	3.3		<0.03
SR151-sub					High	<0.02
SR158-epi	0.204	-4.5×10^{14}	133,600	2.3		0.05
SR158-sub					Low	<0.02
SR155-epi	0.236	$+2.0 \times 10^{16}$	297			0.33
SR155-sub					Low	—
SR156-epi	0.215	$+9.0 \times 10^{15}$	644			0.73
SR156-sub					Low	0.02

Note: Negative carrier concentration indicates n-type material; positive carrier concentration indicates p-type material.

centration in the layer is approximately equal to that in the corresponding substrate (SR151-sub). SR151-sub was taken from an ingot that was furnaced cooled to room temperature and therefore contains a high density of tellurium precipitates (10^5 cm^{-3}). On the other hand, SR155-sub and SR156-sub were taken from ingots which were programmed cooled. Hence, these substrates have a lower density of tellurium precipitates (10^3 cm^{-3}). Note that the copper concentration in SR155-epi and SR156-epi is considerably higher (0.33 and 0.73 ppma, respectively) even though the copper concentration in the representative substrate (SR156-sub) is low (0.02 ppma). These two layers remained p-type even after a Hg vacancy filling anneal which is consistent with the high concentration of copper present in these layers. On the other hand, sample SR158-epi has a low density of tellurium precipitates (Table II) and yet it contains little copper (0.05 ppma). This inconsistency will be explained later in the discussion.

A possible explanation for the correlation between the tellurium precipitate density in the substrate and the transport properties of the epilayers is that tellurium precipitates may be gettering copper during the post-growth cooldown of the ingots from which substrates are manufactured. Hence, MCT grown on substrates whose ingots were fast cooled have good transport properties because the high concentration of tellurium precipitates in the substrate getters copper which stays in the substrate. In contrast, substrates from ingots which have been slowly cooled have significantly less tellurium precipitates. There are fewer precipitates to getter copper which can then diffuse from the substrate to the growing MCT and degrade the transport properties of the layer. A similar effect has been observed at Texas Instruments in the growth of MCT by LPE using substrates with varying densities of tellurium precipitates.[4]

As expected, the purity of the raw materials (specifically elemental cadmium) was found to make a difference in the copper content of the substrates and ultimately the properties of MCT epilayers. For example, SR158-sub came from an ingot synthesized from elemental cadmium with a copper content of less than 50 ppba (measured by glow discharge mass spectroscopy at the Canadian Research Council), whereas for the rest of the samples in Table II, the copper content in the elemental cadmium, used to synthesize the ingots, was in excess of 50 ppba. For samples SR151, SR155, and SR156, the tellurium precipitate gettering mechanism is applicable (a high density of tellurium precipitates in the substrate leads to a low copper concentration in the MCT layer). It is interesting to note, however, that sample SR158-epi had a low copper concentration (0.05 ppma) even though its substrate had a low tellurium precipitate density (Table II). This means that if one starts with sufficiently low copper concentration in the raw materials, it is possible to have a low copper concentration in the MCT layer as well as a low density of tellurium precipitates in the substrate.
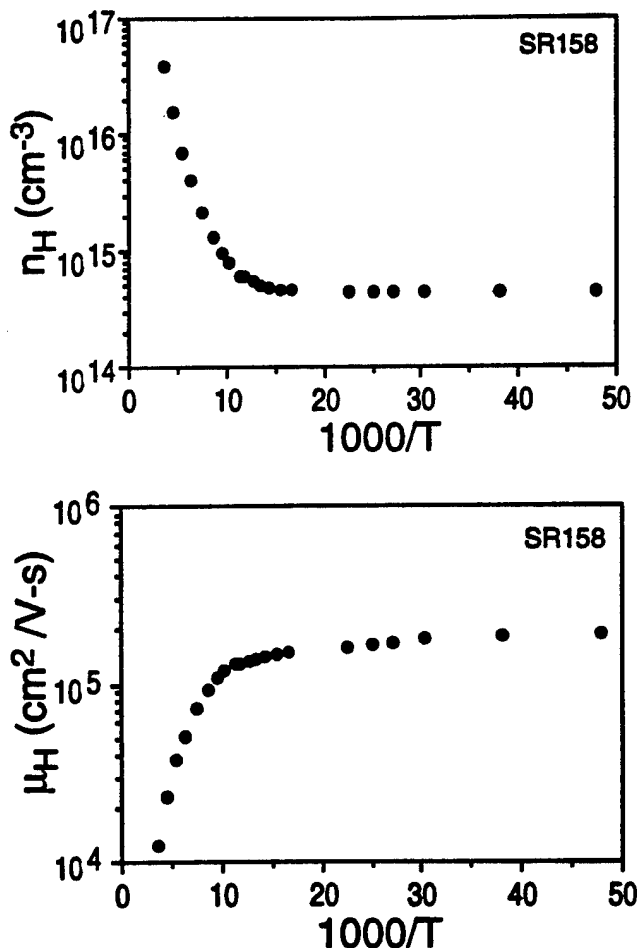
Fig. 1. Temperature dependence of the carrier concentration, n_H, and mobility, μ_H, for x = 0.204 HgCdTe epilayer.

Table III. Material Characteristics of HgCdTe as a Function of Annealing Temperature

Sample	T_{anneal} (°C)	n_H^{77K} (cm^{-3})	μ_H^{77K} ($cm^2/V\text{-}s$)	τ^{77K} (μs)
SR158-epi	220	-4.5×10^{14}	133,600	2.3
	440	-3.0×10^{15}	50,200	0.16
SR159-epi	220	-2.3×10^{14}	154,600	2.3
	440	-2.8×10^{15}	76,000	0.20
SR200-epi	220	-3.5×10^{14}	102,000	3.0
	440	-6.0×10^{14}	22,900	0.5

To gain further insight into the diffusion of copper in CdZnTe and MCT, portions of several epilayers were annealed at 440°C for 1 h in a Hg ambient followed by the standard 15 h anneal at 220°C. The results reported in Table III compare the transport properties of these layers after the conventional 220°C anneal and after the high temperature anneal. Samples SR159-epi and SR200-epi were grown on the same type of substrate as SR151-epi (these substrates contain a high density of large tellurium precipitates). It can be seen that the high quality n-type material has deteriorated as a result of the high temperature anneal and now exhibit anomalous Hall

effect behavior. The term anomalous refers to reduced mobilities at lower temperatures and this behavior is usually associated with a network of interconnected p-type regions in the n-type matrix.[8] The minority carrier lifetime of each sample in Table III also decreases substantially as a result of the high temperature annealing.

The anomalous Hall effect behavior and the decrease in minority carrier lifetime suggests an increase in the copper content of the epilayers. Indeed, Myers et al. reported the outdiffusion of copper from a CdTe substrate and its accumulation in an MBE-grown MCT layer after a 2 h 400°C anneal.[3] The outdiffusion of copper from substrates during high temperature annealing could present a problem in the high temperature processing of MCT materials since even substrates synthesized from the purest raw materials may contain quantities of copper which can segregate in the MCT epilayers.

SUMMARY

We have shown that MCT layers can be doped with copper during the MOCVD growth process. The quantity of copper which accumulates in the MCT epilayer and originates in the CdZnTe substrates could be controlled in two ways.

First, the purity of the raw materials used to synthesize the CdZnTe substrates, particularly the cadmium, was found to affect the copper content of the substrates and consequently the quantity that segregates in the MCT epilayers. Secondly, copper

outdiffusion could also be minimized by growing on substrates with a high density of tellurium precipitates. A mechanism whereby tellurium precipitates getter copper impurities during the CdZnTe boule post-growth cooldown and trap them in the substrate is proposed.

The density and size of tellurium precipitates in CdZnTe crystals can be controlled by means of the post-growth cooldown scheme. Fast cooldown results in a high density of precipitates, whereas the density can be reduced by cooling slowly.

Finally, high temperature annealing was found to deteriorate the transport properties of MCT epilayers resulting from the possible incorporation of copper in the epilayers.

REFERENCES

1. J.H. Tregilgas, J.D. Beck and B.E. Gnade, *J. Vac. Sci. Technol.* A3, 143 (1985).
2. L.F. Lou and W.H. Frye, *J. Appl. Phys.* 56, 2253 (1984).
3. T.H. Myers, K.A. Harris, R.W. Yanka, L.M. Mohnkern, R.J. Williams and G.K. Dudoff, *J. Vac. Sci. Technol.* B10, 438 (1992).
4. L. Colombo and P.K. Liao, Texas Instruments, private communication.
5. S. Oguz, R.J. Olson, Jr., D.L. Lee, L.T. Specht and V.G. Kreismanis, *Electro-Optical Materials for Switches, Coatings, Sensor Optics, and Detectors, SPIE Proc.* 1307, 560 (1990).
6. W. M. Higgins, G.N. Pultz, R.G. Roy, R.A. Lancaster and J.L. Schmit, *J. Vac. Sci. Technol.* A7, 271 (1989).
7. M.B. Reine, K.R. Maschoff, S.P. Tobin, P.W. Norton, J.A. Mroczkowski and E.E. Kruger, *Semicond. Sci. Technol.* 8, 788 (1993).
8. M.C. Chen, *Appl. Phys. Lett.* 51, 1836 (1987).

Resonance Ionization Spectroscopy for Quantitative and Sensitive Surface and Bulk Measurements of Impurities in II-VI Materials

S. SEN, J.E. STANNARD, and S.M. JOHNSON

Santa Barbara Research Center, Goleta, CA 93117

H.F. ARLINGHAUS and G.I. BEKOV

Atom Sciences, Inc., Oak Ridge, TN 37830

We have applied resonance ionization spectroscopy for the first time on II-VI materials, Cd, Te, CdZnTe, and HgCdTe for the measurement of trace impurities. It is an analytical technique with extremely high sensitivity, selectivity, dynamic range, and quantitation accuracy. The technique provides virtual freedom from matrix effects and minimizes isobaric and other mass interferences, known to be the shortcomings in secondary ion mass spectroscopy and other mass spectroscopic measurements. Quantitative analysis of Cu in bulk CdZnTe boules has shown Cu concentration in the range low 10^{14} to low 10^{15} cm^{-3} with an average copper content in four different boules near 2×10^{14} cm^{-3}. High Cu concentration (1–2×10^{17} cm^{-3}) measured in some HgCdTe epitaxial layers correlated with lower Hall mobility in the layer, and in one case the intentionally In-doped, n-type HgCdTe layer turned p-type.

Key words: Cd, CdZnTe, HgCdTe, impurities, resonance ionization spectroscopy (RIS), secondary ion mass spectroscopy (SIMS), Te

INTRODUCTION

Resonance ionization spectroscopy (RIS) is an emerging laser-based analytical technique for quantitative and sensitive measurements of impurities and doping profiles in semiconductors.[1] Resonance ionization spectroscopy analysis requires free atoms (neutrals, usually in the ground state) in the gas phase, with the atomization and ionization occuring in two separate steps.[2,3] The technique consists of atomization of the sample by either sputtering with an energetic ion beam (SIRIS), laser beam (LARIS), or thermally heating in a graphite furnace (TARIS), suppression of the secondary ions formed in the sputtering/atomization process, selective ionization of the neutrals by pulsed tunable lasers, and mass analysis of the ions by magnetic-sector or time-of-flight (TOF) mass spectrometer. Through precise tuning of the

wavelengths of the RIS lasers, only atoms of a selected element are resonantly excited, ionized, and counted in the mass spectrometer. The transitions between discrete excited states are unique to each element; therefore, resonance ionization is extremely selective. Resonance ionization spectroscopy is specially valuable for trace element analysis in materials where molecular ions, isobars, or ions from the major constituents of the sample are serious sources of interferences, e.g. Fe in Si or Cu and Fe in HgCdTe and CdZnTe. The ionization efficiency for the selected element can be as much as 10^9 times higher than for the other elements in the sample.[4] The high selectivity of the RIS process also helps maintain linearity in the mass spectrometer ion extraction region by reducing space charge effects that would otherwise be present due to ionization of the major constituents of the sample. Since the isotope shifts of most elements are small in comparison to the bandwidth of the RIS lasers used in our experiments (7–12 GHz), all iso-
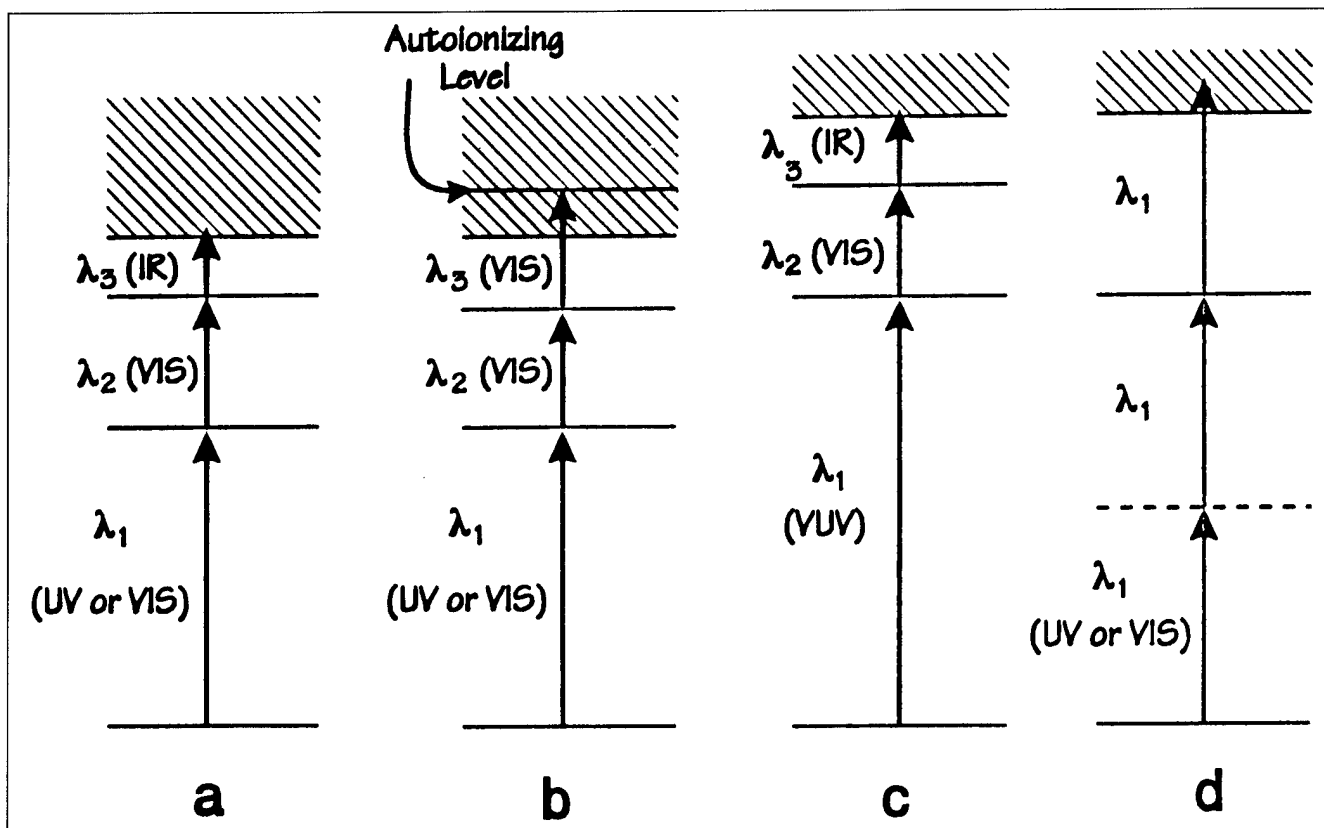
Fig. 1. Simplified energy level diagrams illustrating the photoionization of neutral atoms: (a) resonance ionization by the absorption of two resonant photons and a low-energy IR photon. (b) photoionization by resonant excitation of an autoionization state. (c) vacuum ultra-violet (VUV) resonance ionization, required for elements with a large energy gap to the first excited state (elements of the upper right-hand corner of the periodic table), and (d) two-photon resonance ionization, an alternative for VUV, but at the loss of sensitivity and selectivity.

topes of a chosen element will be ionized with almost equal sensitivity. If a time-of-flight mass spectrometer is used, all isotopes of an element can be detected simultaneously. The mass spectrometer requirements are, therefore, reduced to the resolution of neighboring isotopes of a single element. High ionization selectivity and the suppression of the secondary ions virtually eliminates interferences from molecular ions, isobars, or ions from the major constituents of the sample.

Resonance ionization spectrsocpy is also extremely sensitive and efficient. The radiation intensity of modern pulsed dye lasers is sufficient to saturate both the bound to bound transitions and the ionization step, thereby assuring near unit probability of ionizing all atoms of the selected element that are in the volume intersected by the RIS laser beams.

The efficiency of RIS is independent of many of the properties, such as electronegativity, that are important in secondary ion mass spectroscopy (SIMS). The applicability of RIS to a particular element depends upon the accessibility of electronic transitions by tunable lasers. Laser RIS schemes have been proposed for all elements except He and Ne. Simple RIS schemes, such as U(ultraviolet) + VIS(visible) + IR(infrared)(Fig. 1a), U + U + IR, VIS + VIS + IR, and UV + IR, yield near-uniform sensitivity down to the few atom level for 80% of the elements in the periodic system,[4] and can be accomplished by a single Nd:YAG

laser pumping two tunable dye lasers. Ionization via autoionization states (Fig. 1b) requires lower laser intensity in the photoionization step, thereby reducing interference from nonresonant processes. Selective ionization in elements of the upper right hand corner of the periodic table requires more complex laser arrangements to generate vacuum ultraviolet radiation (Fig. 1c). These elements can also be ionized with simple laser schemes by the absorption of two photons to reach a two-photon resonance, with consequent ionization from the absorption of a third photon (Fig. 1d). Although this process is less selective and sensitive than the previous ones, shown in Figs. 1a, 1b, and 1c, it still has a significant advantage over conventional ionization and nonresonant photoionization methods.

DESCRIPTION OF TECHNIQUES

The main components of the SIRIS system are a microfocus ion gun (incident angle = 60° from normal), a pulsed flood electron gun, a RIS laser system consisting of a pulsed Nd:YAG laser (repetition rate 30 Hz) pumping two dye lasers, a computer-controlled high-resolution sample manipulator, a sample introduction system, and a mass spectrometer detection system. For quantitative analysis of samples with high vapor pressure such as HgCdTe, samples are cooled to 100K. In the SIRIS experiments, the sample is bombarded with a pulsed Ar$^+$ ion beam (up to 10^7

ions/500 ns pulse) (Fig. 2). The expanding cloud of sputtered material consists of excited state and ground state neutral atoms, molecular fragments, and ions, The ions are removed by timed extraction voltage switching (positive ions are retarded, negative ions are accelerated) and electrostatic energy analysis. The remaining neutral particles are then selectively ionized by the RIS laser beams. Efficient overlap of the laser beams with the cloud of desorbed material is achieved by choosing the appropriate delay time between firing the ion gun and firing the RIS lasers, and carefully positioning the RIS laser beams with regard to the ion beam/sample surface intersection. The ionized atoms are extracted into a mass spectrometer. SIRIS depth profile measurements involve two steps:

- scanning the sample with a continuous ion beam to etch the sample to a specific depth, and
- taking data with a pulsed ion beam in the center of the crater.

Trace element concentrations can be monitored as a function of depth with less than 0.1 nm depth intervals because the high efficiency of the SIRIS technique enables detection at the ppb level while consuming less than one monolayer of material in an area of 1×10^{-4} cm^2. Imaging is achieved by either scanning the ion beam over the sample or by changing the x and y target positions while the RIS laser beams and the bombarding ion beam positions remain fixed. If a liquid metal ion gun is used, spatial resolution down to 100 nm is achievable.[5]

The efficiency of the SIRIS process of ionizing and detecting a selected element in a atomized cloud depends on the temporal and spatial overlap of the resonance laser beam with the atomized cloud (20–50%), the ionization efficiency (~100%), the total transmission of the mass spectrometer (50–80%), and the detector efficiency (50–80%). For most elements, useful yields (atoms detected/atoms sputtered), between 2–10 % can be achieved and sub-parts-per billion detection limits are possible.[3,6,7] So far, the highest reported useful yield is ~26 % for indium in silicon.[3] Since the SIRIS sensitivity between most of the elements is approximately the same, (variation is less than a factor of two), the absolute concentration in many cases can be approximately determined without standards.

SIRIS RESULTS

SIRIS depth profiles of Cu and Fe in five Hg$_{1-x}$Cd$_x$Te epitaxial layers (A, B, C, D, and E) grown by liquid phase epitaxy (LPE) on CdZnTe substrates are shown in Fig. 3 and Fig. 4, respectively. The legend shows the sample numbers. Sample A, B, and C are double layers, consisting of a 2 μm thick Hg$_{0.70}$Cd$_{0.30}$Te layer on top of a 15 μm thick Hg$_{0.80}$Cd$_{0.20}$Te base layer. Samples D and E are single layers of Hg$_{0.80}$Cd$_{0.20}$Te of thickness 15 μm. The base layers and the single layers were intentionally doped n-type with In (mid 10^{15} cm^{-3}). All depth profiles were taken under cooled condition. Cu signal from a bulk CdTe sample which was intentionally doped with a Cu concentration of

1×10^{17} cm^{-3}, was used as a calibration standard for these measurements. The signal was used to determine the absolute Cu concentration in the layers. The change in the sputter yield between Cd$_{0.96}$Zn$_{0.04}$Te (substrate) and Hg$_{0.80}$Cd$_{0.20}$Te was not taken into account in the expressed signal. The Fe signal was calibrated by assuming the same Cu sensitivity factor for Fe. None of the tail signal values should be construed as detection limits, since detuning of the RIS lasers caused the signal to disappear, indicating that the lower signals seen were indeed coming from the samples. Figure 3 shows low copper concentrations in the range 4–5 × 10^{15} cm^{-3} in samples A, B, C, and E, whereas in sample D the copper concentration is high (1–2 × 10^{17} cm^{-3}) by more than a factor of ten. The high copper concentration in sample D agrees with the
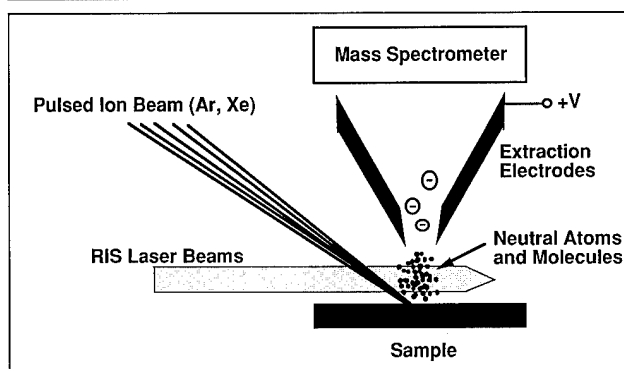
Fig. 2. Schematic diagram of the sputter-initiated resonance ionization spectroscopy system.
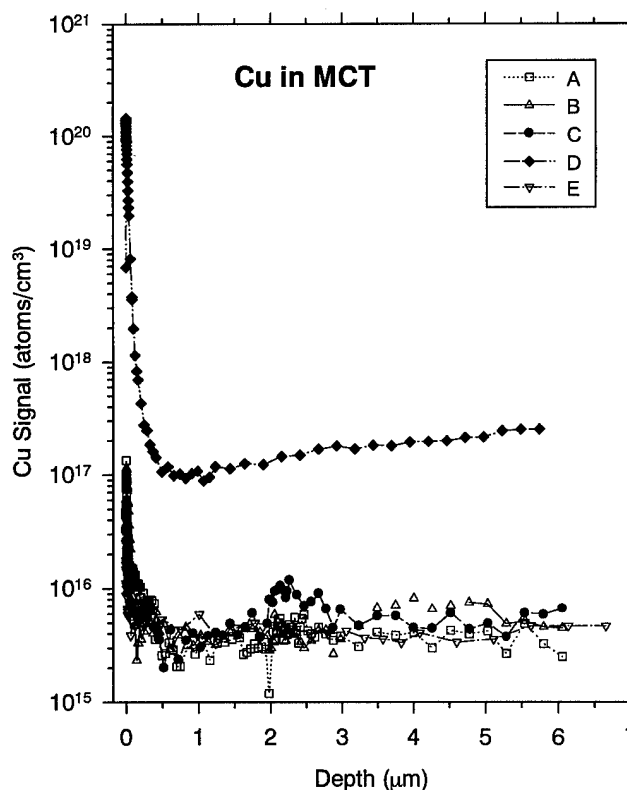
Fig. 3. Sputter-initiated resonance ionization spectroscopy depth profiles of Cu in HgCdTe epitaxial layers.

carrier concentration value of 2.5×10^{17} cm^{-3} as measured by Hall effect at 77K. The underlying substrate in this sample also had a high copper concentration (1×10^{18} cm^{-3}) as measured separately by SIRIS. It is believed that copper outdiffused from the CdZnTe substrate into the HgCdTe layer during epitaxial growth. Hall effect measurements in samples A, B, C, and E have shown normal n-type behavior with high Hall mobilities, consistent with the intentionally introduced In concentrations. Figure 4 shows higher
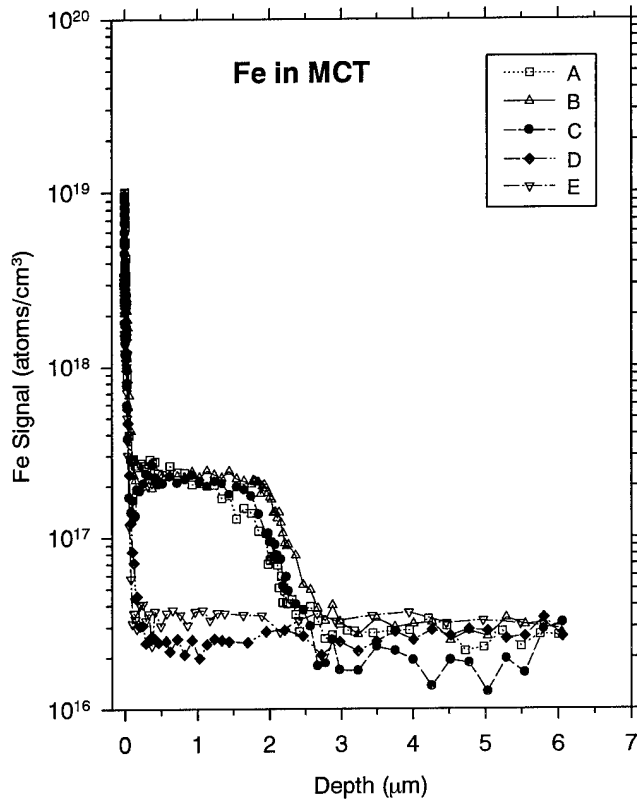
Fig. 4. Sputter-initiated resonance ionization spectroscopy depth profiles of Fe in HgCdTe epitaxial layers.

concentration of Fe (2×10^{17} cm^{-3}) in the top layers of the double layer samples A, B, and C and a factor of ten lower Fe signal in the base layers. However, tail concentrations (lowest measured signals) of both copper (4×10^{15} cm^{-3}) and Fe (2–3×10^{16} cm^{-3}) were somewhat higher than expected. The lowest measured signal in CdZnTe was also in this range for Cu and Fe. Particularly, if Cu concentrations in the range of 4–5×10^{15} cm^{-3} were present in these n-type HgCdTe samples, it would have shown to have reduced Hall mobilities in these layers. It was, therefore, suspected that the high background signal was caused by contamination in the ion beam used for sputtering. This was verified recently by remeasuring sample C with a newly installed mass filtered ion gun in the SIRIS system. The tail concentration of both Cu and Fe dropped down to 1–2×10^{14} cm^{-3}.

TARIS RESULTS

The TARIS technique is similar to SIRIS, except in TARIS the sample is vaporized and atomized in a graphite crucible heated by a graphite furnace. The atomized substance forms an atomic beam which is irradiated by the RIS laser beams at right angles to the atomic flow between two electrodes. The resulting ions are then extracted by an electric field pulse and are detected by a time-of-flight mass spectrometer.[8,9] We applied TARIS for the analysis of Cu in bulk $Cd_{0.96}Zn_{0.04}Te$ substrates. Two compounded charges of $Cd_{0.96}Zn_{0.04}Te$ doped with 1×10^{17} cm^{-3} and 1×10^{18} cm^{-3} copper were used as standards for these measurements. Use of two standards with a known ratio of copper concentration permitted a check on the linearity of the technique. Materials to be analyzed were broken into pieces of less than 20 mg in mass, and the individual pieces were used for direct analysis. Each weighed piece was placed in the graphite crucible which was then inserted in the thermal atomizer. After pumping out the atomizer, a valve separating the analytical chamber from the atomizer was opened

Table I. Copper Concentration (1×10^{14} cm^{-3}) in $Cd_{0.96}Zn_{0.04}Te$ Samples by TARIS

Sample	Number of Measurements	Mass (mg)	Average Cu (1×10^{14} cm^{-3})	Std. Dev. 1×10^{14} cm^{-3}
A (tail)	4	15	9.6	3.7
A (tail)	4	13	1.5	1.0
A (tip)	1	10	6	—
A (tip)	2	16	1	0.5
B (mid)	2	8	1.1	0.5
B (mid)	3	10	1.3	1.0
C (tail)	4	15	1.3	0.5
C (tip)	3	11	7.2	5.9
D (tail)	2	10	12.2	0.3
D (tip)	3	11	4.5	3.0
E (tail)	3	9	1.5	0.7
E (mid)	3	10	1.7	0.6
E (tip)	3	11	3	1.5
Doped CdZnTe (1×10^{18} cm^{-3})	3	4	5.4×10^{17} cm^{-3}	1.7×10^{17} cm^{-3}

and the crucible and sample were heated to 800°C. It was found that the vaporization rate of CdZnTe at this temperature was about 2 mg/min with no significant vaporization of copper impurities.

After the sample vaporization was completed, the crucible temperature was increased to 1800°C in a stepped manner. The copper signal first appeared at a temperature of 1000°C and the signal was integrated through the temperature range 1000 to 1800°C for both isotopic masses 63 and 65 of copper. In order to clean the crucible for the next analysis, the temperature was increased to 2100°C for 30 s. No residual copper signal was detected after this heating procedure. Results of the TARIS analysis are shown in Table I. Samples from tip, middle, and tail sections of five CdZnTe boules were analyzed, along with the samples from the two doped boules. The data does not indicate a higher concentration of copper in the tail as would be expected for its reported segregation constant of 0.23.[10] If segregation follows the normal freezing law, however, copper concentration should increase strongly only in the last 14% of the boule length. Within the variation seen here, it is possible the variation due to segregation would not be apparent. The standard deviation seen is believed to be due to inhomogeneity in copper distribution. Additional data are needed to determine the true variability. The data does indicate average copper content in four different boules is near 2×10^{14} cm^{-3} (13 ppb atomic). A possible source of contamination present in the ion beam of SIRIS is not present in TARIS, because the samples are vaporized and atomized in a graphite furnace and not by sputtering with an ion beam.

CONCLUSIONS

We have applied resonance ionization spectroscopy for trace impurity analysis of II-VI materials, with both SIRIS (mainly for epitaxial layers) and TARIS (only for bulk materials) in an effort to minimize matrix effects and mass interferences. These initial results on HgCdTe and related II-VI materials demonstrate the high selectivity of both techniques (SIRIS and TARIS), which allows virtually interference-free trace element analysis of bulk and epitaxial layered structures. High sensitivity of RIS reduces the sample size required for analysis by orders of magnitude compared to other techniques. Thus, depth profile data in SIRIS technique can be taken with depth increments of only 0.1 nm or less, yielding unprecedented resolution for surface or near surface analysis. In combination with a scanning submicron ion beam, SIRIS will be able to image trace elements both with high spatial resolution and with extremely high sensitivity and selectivity. It is estimated there is an error of factor of two in the present calibration factors used for the SIRIS measurements of Cu and Fe. Calibration standards in HgCdTe and CdZnTe for various elements will be made in the near future, for determination of absolute sputter yield in these matrices which will further improve quantitative analysis in these materials. It was suspected that the lowest measured Cu and Fe signals (4×10^{15} cm^{-3} Cu and $2-3 \times 10^{16}$ cm^{-3} Fe) by SIRIS was caused by contamination in the ion beam; as this was not seen with TARIS. This was verified recently by remeasuring sample C with a newly installed mass filtered ion gun in the SIRIS system. The tail concentration of both Cu and Fe dropped down to $1-2 \times 10^{14}$ cm^{-3}. Additional measurements in the future will establish the detection limits for Cu, Fe and other impurity species in HgCdTe and CdZnTe.

REFERENCES

1. H.F. Arlinghaus, M.T. Spaar, N. Thonnard, A.W. McMahon, T. Tanigaki, H. Shichi and P.H. Holloway, *J. Vac. Sci. Technol.* A11, 2317 (1993).
2. H.F. Arlinghaus, M.T. Spaar and N. Thonnard, *J. Vac. Sci. Technol.* A8, 2318 (1990).
3. H.F. Arlinghaus, M.T. Spaar, N. Thonnard, A,W. McMahon and K.B. Jacobson, *Optical Methods for Ultrasensitive Detection and Analysis: Techniques and Applications,* ed. B.L.Fearey, SPIE, 1435, 26 (1991).
4. N. Thonnard, J.E. Parks, R.D. Willis, L.J. Moore and H.F. Arlinghaus, *Surf. Interface Anal.* 14, 751 (1989).
5. N. Winograd, Y. Zhou, M. Wood and S. Lakiszak, *Inst. Phys. Conf. Ser. No. 128* Section 7, RIS 92, Santa Fe, NM, USA, 29 May 1992.
6. D.L. Pappas, D.M. Hrubowchak, M.H. Ervin and N. Winograd, *Science* 243, 64 (1989).
7. M.J. Pellin, C.E. Young, W.F. Calaway, J.E. Whitten, D.M. Gruen, J.B. Blum, I.D. Hutcheon and G.J. Wasserburg, *Phil. Trans. R. Soc. Lond.* A 333 (1990).
8. G.I. Bekov and V.S. Letokhov, *Laser Analytical Spectrochemistry,* ed. V.S. Letokhov (Bristol: Adam Hilger, 1986), p. 98.
9. G.I. Bekov, V.S. Letokhov and V.N. Radaev, *Spectrochim. Acta,* 43B, 491 (1988).
10. K. Zanio, *Semiconductors and Semimetals,* ed. R.K. Willardson and A.C. Beer, (New York: Academic Press, 1978), p. 13.

Molecular Beam Epitaxy HgCdTe Growth-Induced Void Defects and Their Effect on Infrared Photodiodes

J.M. ARIAS, M. ZANDIAN. J. BAJAJ, J.G.PASKO, L.O. BUBULAC, S.H. SHIN, and R.E. DE WAMES

Rockwell Science Center, Thousand Oaks, CA 91360

We have carried out a study and identified that MBE HgCdTe growth-induced void defects are detrimental to long wavelength infrared photodiode performance. These defects were induced during nucleation by having surface growth conditions deficient in Hg. Precise control and reproducibility of the CdZnTe surface temperature and beam fluxes are required to minimize such defects. Device quality material with void defect concentration values in the low 10^2 cm^{-2} range were demonstrated.

Key words: Defects, HgCdTe, infrared detectors, molecular beam epitaxy (MBE)

INTRODUCTION

A greater understanding of the type and nature of defects limiting HgCdTe photovoltaic device performance and array operability and their relationships with the various growth and device processing steps is needed.[1,2] Currently, MBE HgCdTe material is used to make photovoltaic devices and infrared (IR) focal plane arrays (FPA).[3] For certain long wavelength infrared (LWIR) applications, we have reported device operability values as high as 97%.[4,5] When growing HgCdTe material on lattice-matched CdZnTe wafers under growth conditions that gave high performance MBE LWIR devices, using optical microscopy, we identified a particular growth induced void defect on the surface of the HgCdTe epilayer. The concentration of these defects is in the 10^2–10^3 cm^{-2} range. Using these values, we estimate that a typical 128 × 128 FPA made with this material could have as much as five percent and as little as 0.5 percent of pixels with this kind of defect. The purpose of this paper is to present device data that show that MBE growth-induced void defects are detrimental to HgCdTe photovoltaic devices and likely account for the drop in FPA operability.

A detailed discussion of MBE HgCdTe growth and device fabrication procedures used here can be found in Refs. 4 and 5. The LWIR HgCdTe heterostructures used to fabricate devices in this study were grown on near lattice-matched (211) $Cd_{0.96}Zn_{0.04}Te$ substrates to minimize the dislocation density in the HgCdTe epilayers. Growth was carried out with effusive sources that contain Hg, Te_2, and CdTe. Nominal beam fluxes for these sources were in the 10^{-5}, 10^{-6}, and 10^{-7} Torr beam equivalent pressure (BEP) ranges, as measured with a nude ion gauge in the growth position, and corrected for atomic and molecular weight and ionization efficiency. Under these conditions, growth rates are in the range of 3–4 μm/h. The optimum Hg/Te$_2$ flux ratio necessary to maintain monocrystalline HgCdTe
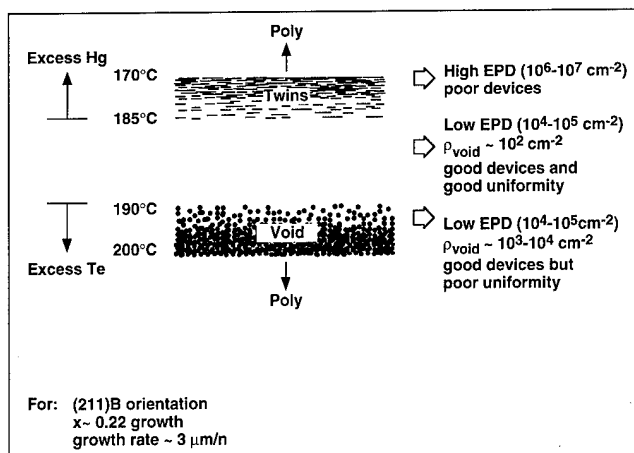
Fig. 1. Schematic growth representation of MBE HgCdTe epilayers grown on (211)B lattice-matched CdZnTe substrates.
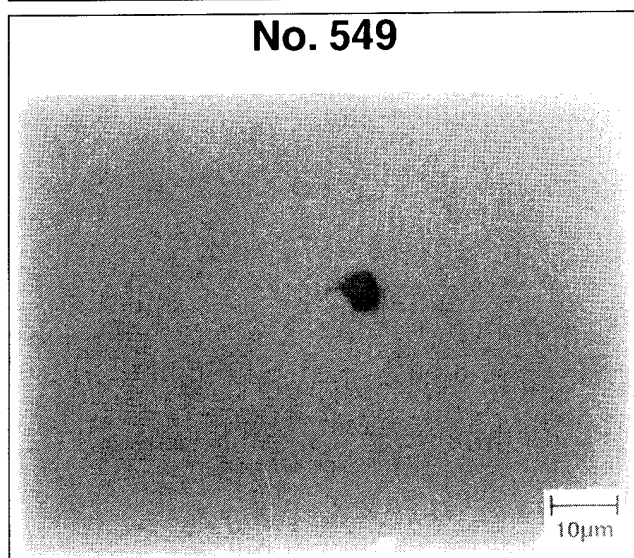
Fig. 2. Top view photograph of a void defect induced during the MBE growth of HgCdTe on a (211)B CdZnTe substrate.

Fig. 3. Atomic force microscopy three-dimensional scan photograph of the surface of a MBE HgCdTe epilayer grown under deficiency of Hg and which had a high (10^4 cm^{-2} range) concentration of void defects.

Fig. 4. Cross-sectional SEM photograph of a void defect induced during the MBE growth of HgCdTe.

growth is determined by using *in situ* reflection high-energy electron diffraction (RHEED) analysis.[6]

DISCUSSION

Because MBE is a far from equilibrium technique in which the growth is being controlled by surface kinetics, the surface growth temperature is critical to the introduction of defects. This is schematically illustrated in Fig. 1, which shows that the optimized HgCdTe growth temperature, under the previously mentioned flux conditions, is in the range of 185–190°C as measured by an IR pyrometer. Good device performance and high (98%) operability values have been reported using material grown under these conditions.[4,5] If surface growth temperature, under the same conditions, is raised above 190°C, then a deficiency of Hg (due to a drop in the sticking coefficient)[7] is obtained at the surface and a high concentration (10^3–10^4 cm^{-2}) of defects is formed, as indicated in the figure. These results indicate that the introduction of such defects is due to a lack of Hg (or an excess Te) at

the surface. A top view photograph of one of these particular defects is illustrated in Fig. 2. Their void size at the surface depends on the epilayer thickness; for a 10 µm thick layer, void sizes of 5 µm are frequently observed. We have also observed that dislocations tend to cluster around these defects

We have used atomic force microscopy (AFM) and scanning electron microscopy (SEM) to probe the microscopic shape of the defects. Shown in Fig. 3 is an AFM scan photograph of an epilayer which had a high (10^4 cm^{-2}) concentration of these particular defects. As clearly shown in the figure, the defects are of the void kind. The depth of the void extends about 1.5 µm from the surface into the material. A cross-sectional SEM photograph of a void defect is shown in Fig. 4. As illustrated in the figure, the defect was generated at the CdZnTe interface during the first stages of nucleation. From this photo, it is also clear that there is HgCdTe material inside the void; this material has a polycrystalline structure as determined by RHEED. The composition of the HgCdTe material inside the void has not been determined.

Currently, under the best optimized Hg/Te$_2$ flux growth conditions for a growth temperature in the

No. 508

30μm x 30μm Diodes

Pin 54

Pin 42

Void defects/diode = 0
77K R_oA = 270 Ω - cm^2

Void defects/diode = 1
77K R_oA = 0.2 Ω - cm^2
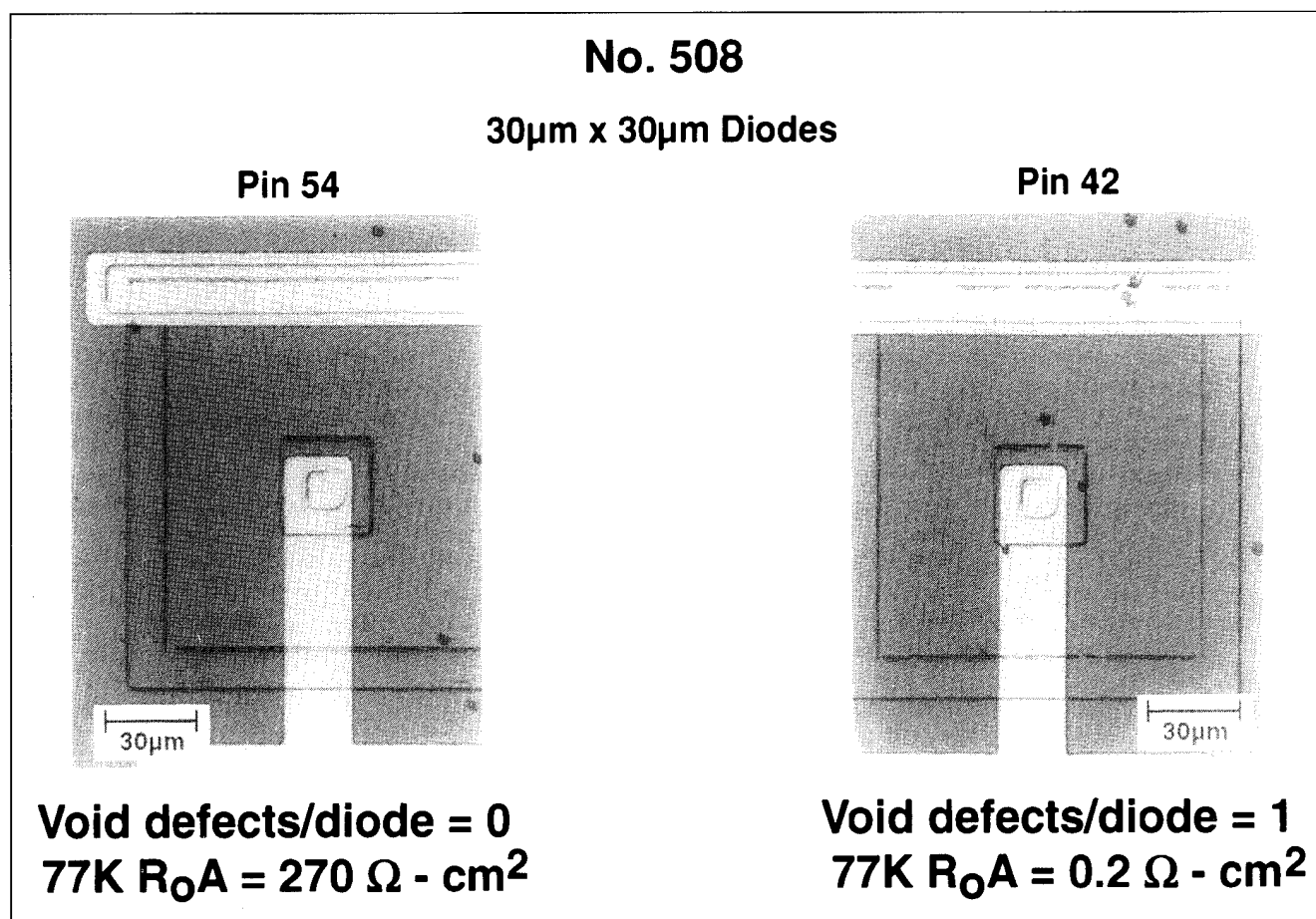
Fig. 5. Top view photograph of the surface of two 30 × 30 μm planar LWIR (λ_{co} = 10 μm) detectors, present on the same test chip. Void defects are clearly visible; one of the detectors has one void defect while the other has none. Also indicated are their 77K R_oA products.

185–190°C range, the lowest content of void defects at the surface that we have achieved is around 100 cm^{-2}. Etch pit density values for epilayers grown under these conditions are low (10^4–10^5 cm^{-2} range) and adequate for device fabrication.[4] Sub-micron size defects generated by dust particulates present on the wafer after sample preparation etching may account for the low concentration of void defects because the particulates can act as localized sites where the sticking coefficient of Hg during nucleation is reduced.[8] The sample preparation etching step is carried out to clean the surface using a 0.5% chemical solution of bromine methanol to remove about 4 μm of material before loading the substrate into the MBE chamber. Another possibility could be tellurium precipitate defects present on the surface of the CdZnTe substrates.

At lower (below 185°C) growth temperatures, under the same flux conditions (Fig. 1), an excess of Hg is obtained at the surface because the sticking coefficient of Hg increases as the temperature is reduced.[7] The excess Hg produces microtwin defects that are easily detected by RHEED during growth. These defects are detrimental to the electrical properties of the epilayer and devices. The EPD values of material grown under these conditions are very high (10^6–10^7 cm^{-2} range). It is interesting to point out that material

grown under these conditions has a surface morphology which is free of void defects even though it is not adequate for device fabrication.

Planar LWIR p-on-n heterostructure detector mini-arrays with variable area (30 × 30, 50 × 50, 125 × 125 and 500 × 500 μm^2) diodes were made with HgCdTe material with low and high void defect concentrations to test their effect on device performance. After the diodes were measured at 77K to determine their R_oA products as a function of device area, they were analyzed under a microscope to correlate R_oA values for devices with and without defects. A one-to-one correlation between devices which have a void defect and poor R_oA device performance was established as illustrated in Fig. 5. The figure shows a top view photograph of two 30 × 30 μm planar LWIR (λ_{co} = 10 μm) detectors present on the same test chip, also indicated are their 77K R_oA products. R_oA data were measured under zero background and the area (A) used was the device junction area. Void defects are clearly visible; one of the detectors has one void defect while the other has none. The photodiode that had no defect on it had a normal R_oA value of 270 Ω-cm^2 at 77K, while the one that had a defect had an extremely low R_oA value of 0.2 Ω-cm^2 (almost a short).

To further illustrate the effect of the void defects on photodiodes, in Fig. 6 we have plotted R_oA distributions
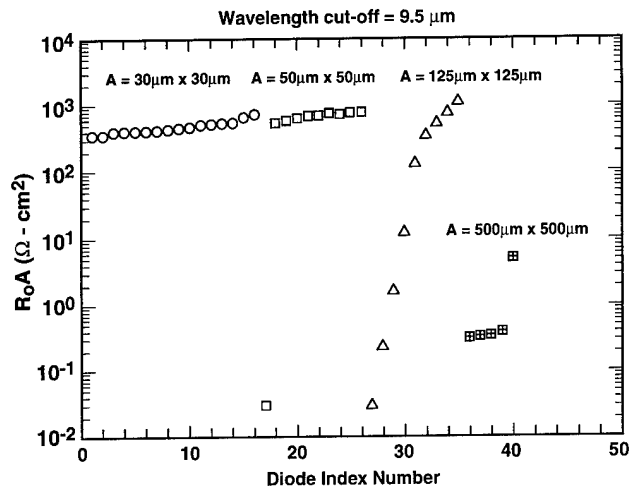
Fig. 6. Area dependence R_oA values at 77K of LWIR (λ_{co} = 9.5 µm) detectors made with a MBE HgCdTe layer which had a growth-induced void concentration of 1×10^3 cm^{-2}. R_oA data were measured under zero background and the area (A) used was the device junction area.

at 77K for the various device areas of an LWIR (λ_{co} = 9.5 µm) miniarray made using a HgCdTe sample that had a void concentration of 1×10^3 cm^{-2}. As seen in the figure, small devices (30 × 30 and 50 × 50 µm^2) have high R_oA values and good uniformity and operability. Only one of the 50 × 50 µm^2 devices had a poor R_oA value; when analyzed under the microscope, it was the only one of that area that had a void defect. On the other hand, larger (125 × 125 and 500 × 500 µm^2) detectors have lower R_oA values and mediocre uniformity and operability because the majority of the 125 × 125 devices have at least one defect, while all of the 500 × 500 ones had more than one.

SUMMARY

In summary, we have carried out a study and identified that MBE HgCdTe growth-induced void defects are detrimental to photodiode performance and likely account for the reported drop in MBE LWIR FPA operability. We showed that these defects were induced during nucleation by having surface growth conditions which were deficient in Hg. Precise control and reproducibility of the CdZnTe surface temperature, as well as of the beam fluxes, are required to minimize such defects. Device quality material with void defect concentration values in the low 10^2 cm^{-2} range were demonstrated.

ACKNOWLEDGMENT

REFERENCES

1. R. Balcerak and L. Brown, *J. Vac. Sci. Technol.* B 10, 1353 (1992).
2. W.E. Tennant, C.A. Cockrum, J.B. Gilpin, M.A. Kinch, M.B. Reine and R.P. Ruth, *J. Vac. Sci. Technol.* B 10, 1359 (1992).
3. R.E. DeWames, J.M. Arias, L.J. Kozlowski and G.M. Williams, *Infrared Detectors: State of the Art,* SPIE Conf. Proc. 1735, 2 (1992).
4. J.M. Arias, J.G. Pasko, M. Zandian, S.H. Shin, L.O. Bubulac, R.E. DeWames and W.E. Tennant, *J. Electron. Mater.* 22, 1049 (1993).
5. J.M. Arias, J.G. Pasko, M. Zandian, L.J. Kozlowski and R.E. DeWames, *Optical Engineering,* 33, 1422 (1994).
6. S. Sivananthan, X. Chu, J. Reno and J.P. Faurie, *J. Appl. Phys.* 40, 1359 (1986).
7. J.P. Faurie, R. Sporken, S. Sivananthan and M.D. Lange, *J. Cryst. Growth* 111, 698 (1991).
8. M. Zandian, J.M. Arias, J. Bajaj, J.G. Pasko, L.O. Bubulac and R.E. DeWames, presented at the 1994 U.S. Workshop on the Physics and Chemistry of Mercury Cadmium Telluride and Other IR Materials, October 1994, San Antonio, TX.

How Dislocations Affect Transport

A.T. PAXTON

Department of Materials, University of Oxford, OX1 3PH, U.K.

A. SHER, M. BERDING, M. VAN SCHILFGAARDE

SRI International, Menlo Park, CA 94025

M.W. MULLER

Washington University, St. Louis, MO 63130

Dislocations crossing a junction in HgCdTe have little effect on detector responsivity, but are known to reduce the zero bias impedance R_0A and increase the leakage current, especially at low temperatures where R_0A is dominated by tunneling and generation/recombination processes. We have calculated the Coulomb and piezoelectric fields associated with dislocations in an attempt to interpret their effect on the junction's transport properties. Dislocation electric fields can affect transport since they are superimposed on the built-in and applied junction fields which control the currents. The screening of the fields in the neutral region is consistent with the dislocations' small effect on responsivity. Their impact in the space charge region is found to be significant and consistent with the nonlinear dependence of performance on dislocation density. The piezoelectric potential of the typical 60° dislocation in a sphalerite crystal, and the Coulomb potential of a dislocation crossing the junction plane other than normally, are angularly varying in the junction plane. Angular variation of the potentials can be qualitatively interpreted as an angular modulation of the potential barrier. Because of the nonlinear dependence of junction currents on the barrier (or the junction potential), the angular variation of the currents does not vanish upon averaging. We find that the range of the Coulomb potential is too small to account for a major portion of the experimentally reported performance degradation but may be responsible for the reduction of R_0A at cryogenic temperatures and low dislocation density, and that the longer range piezoelectric potential may be important. We also find that superposing the potentials of neighboring dislocations, because of the nonlinear dependence of junction leakage currents on junction potentials may account for the observed nonlinearity of performance degradation with dislocation density as measured by etch pit density.

Key words: Dislocations, HgCdTe, piezoelectric, transport properties

INTRODUCTION

The p-on-n $Hg_{1-x}Cd_xTe$ (MCT) double layer heterojunction (DLHJ) mesa-diode-based focal plane arrays (FPAs) shown in Fig. 1 are currently leading the art in long-wave infrared (LWIR) applications. The most effective structures to date are those grown by liquid-phase epitaxy (LPE) on lattice-matched CdZnTe substrates. Typical values of active (n layer) and cap (p layer) compositions are x = 0.224[1] and x ≥ 0.28, respectively. The n layers are typically indium-doped in the growth process, with carrier concentrations as low as permitted by series resistance and capacitance concerns, but usually realized at > 2×10^{15} cm^{-3}. The cap p$^+$ layers are typically arsenic doped with p ≅ 2×10^{17} cm^{-3}. The metallurgical p-n junction
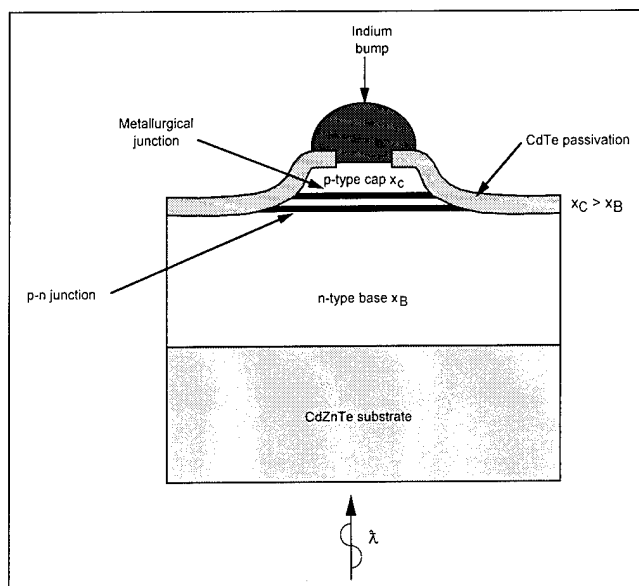
Fig. 1. Cross-sectional view of DLHJ mesa diode.

is positioned on the narrowgap side of the hetero-junction, and the grading width is chosen to minimize the barrier in the valence band that occurs in such structures, as the barrier reduces the collection efficiency of photon-induced minority carriers (holes) in the n-layer from the back-lit array.

The virtues of the DLHJ are that the major absorption occurs in the n-type base layer where the photon-induced minority carriers are holes. The minority carrier lifetimes of holes in n-type materials are much longer than those of electrons in p-type material, which compensates for the mobility difference between electrons and holes. As a result, high quantum efficiencies are possible, and lower n-type carrier concentrations can be obtained. In addition, at least in principle, the generation-recombination (G-R) and tunneling dark currents are decreased in the heterojunction compared with those of homojunctions, and therefore the device noise is less. However, even if there is no tunneling current reduction, the wider bandgap still prevents interface-assisted recombinations from occurring at the metal contact with the p-cap layer.

There is ample experimental evidence[2–5] that dislocations degrade the performance of MCT IR detectors; dislocations may be the most deleterious of the defects limiting the capabilities of the material. The measurements that lead to these conclusions relate various material parameters pertinent to detector performance to dislocation density. The important, interrelated parameters in the thin epitaxial layers suitable for the fabrication of LWIR photovoltaic devices are minority carrier lifetime, zero-bias junction impedance (R_0A product), and 1/f noise.

Dislocations are thought to influence the electronic properties of semiconductors primarily through their electric field. In this paper, we report the results of analyses of the space charge (Coulomb) and of the piezoelectric fields associated with dislocations in an

attempt to understand the mechanism through which they affect the responsivity and dark currents at low temperature.

SUMMARY OF EXPERIMENTAL RESULTS

In the work to be discussed, dislocation densities are measured by etch pit densities (EPDs). The etch pits on the film surface are associated with threading dislocations that are assumed to penetrate the films.

Shin et al.[2] have studied the relationship between dislocation density and minority carrier lifetime in epitaxial MCT films grown by LPE, metalorganic chemical vapor deposition (MOCVD), and molecular beam epitaxy (MBE). At small dislocation densities, minority carrier lifetime is not affected by the presence of dislocations, and the temperature and carrier concentration dependence of the lifetime suggests Auger recombination at high temperature (above 150K) and Shockley-Read recombination for T<150K. However, even in samples with very low EPDs (down to pixels with no etch pits), the lifetime and the R_0A product exhibit great variability, sometimes exceeding an order of magnitude.

In these high-quality samples, the transition from Auger to trap-assisted recombination can occur a T as low as 60K[3]. We take this observation as evidence that the ultimate device performance limits are imposed by recombination centers not associated with threading dislocations. In the low temperature range of interest for IR detectors, for EPD densities above the mid-10[5] range minority carrier lifetime decreases with dislocation density at an EPD$^{-2/3}$ to EPD$^{-3/4}$ rate. The observed behavior is consistent with dislocations acting as Shockley-Read recombination centers with a trap level 60 meV above the valence band edge and a trap density proportional to EPD$^{-3/4}$. Although not explicitly stated, the results reported suggest that dislocations active as recombination centers are likely to carry a core charge. Similar results have been reported by Baranskii et al.[4] who find that mobile dislocations introduced in bulk MCT by indentation give rise to a trapping level at $E_v + 50$ meV and act as impurity getters. Johnson et al.[5] have measured the dependence of R_0A in arrays of photovoltaic (PV) diodes on dislocation density by deliberately using plastic deformation to introduce dislocations in localized regions and carrying out the measurement on both high and low EPD diodes of the same array. They find that the resistance is relatively insensitive to EPD or decreases linearly at low densities, and quadratically at high densities. The nonlinear behavior sets in at small dislocation densities (mid-10[5] cm^{-2} or less) at low temperature (40K), at higher densities (>10[6] cm^{-2}) at 78 and 120K.

Measurements of the temperature dependence of the leakage current of diodes with different dislocation densities show that the high temperature (diffusion regime) R_0A is not affected by the presence of dislocations, but that as the temperature is reduced below 150K, the R_0A values diverge, differing by several orders of magnitude at 40K and below. The

authors interpret the low temperature leakage current as G-R current. They adopt a model[6] for estimating the reduction of the minority carrier diffusion length by recombination at dislocations, and then account for the inverse quadratic increase of the *dark* current at high dislocation densities by the *ad hoc* assumption that closely spaced dislocation pairs contribute a conductance that exceeds the sum of the conductances of two individual dislocations. We shall point out below that such nonlinear behavior may be a feature of tunneling currents associated with dislocations.

CHARGED DISLOCATIONS

The Coulomb fields associated with electrically charged dislocation cores can act as scattering and recombination centers and may attract or repel charged point defects. The presence and amount of charge on a dislocation core depends on the distribution of localized levels in the bandgap in the core and on the Fermi level in the semiconductor. Once the core structure of the dislocation has been determined, we can take a phenomenological view and consider only the electric field and potential generated by a given core charge. The effective radius of the field is taken to be that distance from the dislocation core within which the field is large enough to move a carrier the distance between dislocations in a minority-carrier lifetime as measured in dislocation-free material. In this way, we define a volume within which the lifetime and mobility are affected by the presence of a charged dislocation. If the affected volume surrounding all the dislocations is a significant fraction of the total volume, then their presence can affect lifetime and mobility and hence R_0A. This relates the depletion radius R or screening radius l to a threshold dislocation density n_D. The results of the calculation to follow, relating dislocation density, effective volume, and temperature, are summarized in Fig. 2.

The bandgap of the material sets the boundary condition for the potential at the core radius. We assume, conservatively, a core radius of 5Å and a core edge potential of 0.1 eV. The core edge potential is limited to the bandgap by free carrier accumulation. It may of course be smaller, in which case the volume over which the dislocation's Coulomb potential can affect performance is reduced. We shall find that, except in the vicinity of the metallurgical junction as discussed below, the Coulomb potential is not a major factor affecting performance. Therefore, this conservative assumption is justified for providing a limit. We represent the dislocation core by a cylindrical charge density –p in a cylinder of radius a in n-type material with donor density N_D.

We calculate the Coulomb field both using the depletion approximation and the exact space charge equation, which takes into account the thermal agitation of the carriers. The exact equation must be used if the screening radius is larger than the depletion radius. In the depletion approximation, the charge density is assumed to be equal to the donor density out

to a depletion radius R and zero outside. The potential, depletion radius, and core charge are determined by integrating the Poisson equation with the core edge potential as boundary condition. Using the values given above results in a plot of R as a function of carrier density shown in Fig. 2. It turns out that the radius is close enough to the Debye length to make the depletion approximation questionable at low temperatures, where the intrinsic carrier density is small.

The exact space charge equation is

$$\frac{1}{r}\frac{d}{dr}r\frac{d\varphi}{dr} = \frac{2}{L^2}\left[\sinh(\varphi - \varphi_F) - \sinh\varphi_F\right]$$

where

$$\varphi = \frac{e\phi}{kT}, L^2 = \frac{\varepsilon kT}{e^2 n_i}, \varphi_F = \frac{E_F - E_i}{kT} = \sinh^{-1}\frac{N_D - N_A}{n_i}.$$

For φ small this is

$$\frac{1}{r}\frac{d}{dr}r\frac{d\varphi}{dr} \cong \left(\frac{2}{L^2}\cosh\varphi_F\right)\varphi = \frac{2}{L_D^2}\varphi$$

with the extrinsic Debye length

$$L_D^2 = \frac{L^2}{\cosh\varphi_F} \cong \frac{\varepsilon kT}{e^2 N_D} = \frac{2.77 \times 10^5}{N_D}, N_D \text{ in cm}^{-3}.$$

Then with $x = r/L_D$, we have $(1/x)(d/dx)x(d\varphi/dx) = \varphi$, the zero order modified Bessel equation. The solution of interest is the decreasing Hankel function $K_0(x)$.

The depletion approximation is only valid for $r < R - L_D$. Since R and L_D are comparable, the exact expression must be used. We let $\varphi = CK_0(x)$ and evaluate C from $\phi(a)$ at $x = a/L_D$.

The electric field is

$$E = \frac{d\phi}{dr} = \frac{kT}{e}\frac{d\varphi}{dr} = \frac{kT}{eL_D}\frac{d\varphi}{dx} = \sqrt{\frac{nkT}{\varepsilon}}CK_1(x)$$

where n is the carrier density.

During its lifetime τ a carrier moves a distance l, the
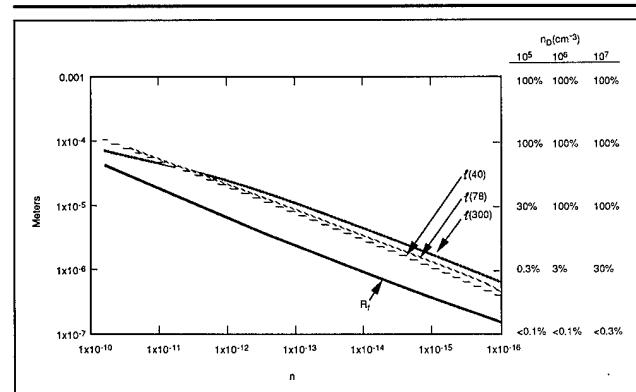
Fig. 2. Depletion radius R and screening radius l (meters) at 40, 70, and 300K as functions of carrier density in cm^{-3}. The table to the right of the figure converts the screening radius of the left-hand-axis to the percent volume of the material which is within the screening volume of a dislocation of various dislocation densities.

Table I. Mobility and Lifetime Values for Screening Radius l as a Function of n

T, K	μ, cm²/Vs	τ,s
40	1.9×10^5	1×10^{-6}
78	9×10^4	3×10^{-7}
300	1×10^4	1×10^{-7}

mean free path in the Coulomb field, given by

$$\tau = \int_0^l \frac{dr}{v} = \int_0^l \frac{dr}{\mu E} = \int_0^l \frac{dr}{\mu\sqrt{\frac{nkT}{\varepsilon}}CK_1\left(\frac{r}{L_D}\right)}$$

where v is the carrier's velocity and μ its mobility. Given the lifetime and mobility, this expression can be solved for the free path l, that is to say, the distance the carrier drifts before recombining. We equate this distance with the effective range of the dislocation's field, which we identify with the screening radius. The screening radius should be distinguished from the smaller diffusion length an electron travels in a field free region in a lifetime. We show a plot of the screening radius l as a function of n for T = 40, 77, and 300K in Fig. 2. To compute this plot, we have used the values of mobility and lifetime in Table I.

As expected, l turns out to be larger than the depletion radius, confirming the need for the more accurate screening theory. With the parameters we use, the calculation of the screening radius over five orders of magnitude of the carrier density, and over the temperature range from 40 to 300K, results in values of l that range from about 5 L_D at n = 10^{10} cm⁻³ to 10 L_D at n = 10^{15} cm⁻³, resulting in a rate of decrease of l with carrier density at a rate slightly slower than $L_D^{-1/2}$. At the higher temperatures, the intrinsic carrier densities exceed N_D and the screening radius would be smaller.

The carrier density in the neutral region of the device material generally equals or exceeds 10^{14} cm⁻³. The screening length at this carrier density, even at room temperature, is less than 6 μm, and it is only about 3 μm at 40K. Therefore, we can conclude that in the presence of mobile carriers, especially at cryogenic temperatures, the core charge fields have a limited range. This is also consistent with the observations of Johnson et al.[5] that the responsivity of p on n heterojunction devices (dependent on diffusion in the neutral region) is little affected even by high dislocation densities.

The situation is less clear in the vicinity of the metallurgical junction of the p-n diode detector. In this region, the carrier density is reduced to the intrinsic value n_i under zero bias, and below that with reverse bias. We estimate a value of n_i about 5×10^{11} cm⁻³ for $Hg_{0.8}Cd_{0.2}Te$ at 40K, with a decrease of about a factor of two for every 5 mV of reverse bias. This reduction of the carrier density is confined to a small region, and an assessment of its quantitative effect will require detailed computation. Nonetheless, it is worth observing that we estimate a screening radius of 45 μm for this carrier density. This is consistent with the experimental finding[5] that R_0A at this temperature is already decreasing with dislocation densities in the 10^5 cm⁻² range, corresponding to this order of separation between dislocation lines. The literature values of $n_i = 1.2 \times 10^{14}$ cm⁻³ at 77 K and $n_i = 4.0 \times 10^{16}$ cm⁻³ at 300K[7] correspond to progressively shorter screening lengths, which is also consistent with the experimental observation that the decrease in R_0A with dislocation density has a higher threshold at the higher temperature.

Because its form is geometrically simpler and more readily visualizable in this context, we have discussed screening entirely in connection with the effect of core charges. It should be kept in mind that similar, although quantitatively different, considerations apply to the screening of the piezoelecitrically induced potentials, to be discussed next.

DISLOCATION STRAIN FIELDS AND PIEZOELECTRIC POTENTIALS

The MCT crystal structure lacks inversion symmetry and it, therefore, is piezoelectric. In a piezoelectric crystal, the strain field around a dislocation may generate an electric field. Conversely, an electric field applied to a piezoelectric crystal can produce a stress that may deform the crystal. This self-consistent field problem has been treated rigorously for a straight dislocation in a homogeneous insulating crystal (intrinsic wide gap semiconductor) by Saada.[8] The general analysis was extended by Faivre and Saada[9] to include the effects of screening by free carriers. Several qualitatively significant conclusions can be drawn from this work:

- The strains are only slightly affected by the electric field; that is, the inverse piezoelectric effect is small, and the electric field can be calculated directly without imposing the requirement of self-consistency.
- The electric field in the vicinity of the dislocation core can be quite large, and the dislocation can interact strongly with charges (point defects or mobile carriers) in its vicinity.
- In a semiconductor, the dislocation preferentially traps carriers of a particular sign.
- The estimated screening distance is of the order of several Debye lengths.

Booyens and Vermaak[10] have applied Saada's analysis to ⟨110⟩/(111) dislocations in zinc-blende III-V semiconductors and Booyens and Basson[11] to CdTe and MCT. They do not explicitly include the effects of screening as analyzed by Faivre and Saada[8] in these calculations. As a result, they find that an uncharged dislocation, in the absence of screening, generates a net radial field. They then suggest that the dislocation core is likely to acquire a charge that compensates for the radial field and so minimizes the total energy of the dislocation.

We have extended the analysis to the commonly observed 60° dislocations in intrinsic MCT. The dislocation lies along $[\bar{1}01]$ and has a Burgers vector **b** at 60° to the dislocation line ξ. The edge component b of the Burgers vector is chosen as x_1; x_2 is the normal to the slip plane; and x_3 is ξ. The transformation matrix from principal axis coordinates is

$$T_{ij} = \frac{1}{\sqrt{6}} \begin{pmatrix} 1 & -2 & 1 \\ \sqrt{2} & \sqrt{2} & \sqrt{2} \\ \sqrt{3} & 0 & \sqrt{3} \end{pmatrix}$$

The transformation of the piezoelectric tensor is

$$d'_{ijk} = T_{ip} T_{jq} T_{kr} d_{pqr}.$$

In cubic symmetry and principal axis coordinates, all the nonzero components of the piezoelectric tensor are equal: $d_{123} = d_{132} = d_{231} = d_{213} = d_{312} = d_{321} = d$. The nonzero components of the transformed tensor (d') are

$$d'_{133} = d'_{313} = d'_{331} = -d'_{111} = \frac{2d}{\sqrt{6}},$$

$$d'_{112} = d'_{121} = d'_{211} = d'_{233} = d'_{323} = d'_{332} = \frac{d}{\sqrt{3}},$$

$$d'_{222} = \frac{2d}{\sqrt{3}}. \tag{1}$$

The piezoelectrically induced bound charge density is[12]

$$\rho(r) = \frac{1}{\varepsilon} d_{ijk} e_{jk,i} \quad \text{with} \quad e_{jk,i} \equiv \frac{\partial}{\partial x_i} e_{jk} \tag{2}$$

where ε is the isotropic dielectric constant, e_{jk} is the jk component of the strain tensor, and summation over repeated indexes is implied.

For a screw dislocation in linear anisotropic theory, the displacements are

$$u_1 = u_2 = 0, \quad u_3 = -\frac{b_3}{2\pi} \tan^{-1} A\left(\frac{x_1}{x_2}\right)$$

where b_3 is the screw component of the Burgers vector, and

$$A = \frac{\sqrt{c'_{44} c'_{55}}}{c'_{44}}; \quad c'_{44} = c_{44} - \frac{1}{3} H;$$

$$c'_{55} = c_{44} - \frac{1}{6} H; \quad H = 2c_{44} + c_{12} - c_{11}.$$

Here c_{ij} and c'_{ij} are the components of the elastic tensor in the principal axis and transformed coordinate systems, respectively. The nonzero components of the strain tensor are, using

$$e_{ij} = \frac{1}{2}\left(u_{i,j} + u_{j,i}\right): \quad e_{13} = e_{31} \text{ and } e_{23} = e_{32};$$

all others zero.

Using Eq. (1) and Eq. (2) shows immediately that for this case $\rho = 0$.

Even in anisotropic linear elasticity (assuming the dielectric constant isotropic), the screw component of the 60° dislocation induces no piezoelectric effect. Therefore, pure screw <110> dislocations will also show no piezoelectric activity even if they are dissociated. We now proceed to consider the edge component. In order to arrive at a transparent expression, we will make the isotropic elastic approximation. This will not affect the order of magnitude calculations that follow.

For an edge dislocation, with ν Poisson's ratio

$$u_1 = \frac{b}{2\pi}\left[\tan^{-1}\frac{x_2}{x_1} + \frac{x_1 x_2}{2(1-\nu)(x_1^2 + x_2^2)}\right],$$

$$u_2 = -\frac{b}{2\pi}\left[\frac{1-2\nu}{4(1-\nu)}\ln(x_1^2 + x_2^2) + \frac{x_1^2 - x_2^2}{4(1-\nu)(x_1^2 + x_2^2)}\right],$$

$$u_3 = 0.$$

The nonzero strain components are

$$e_{11} = \frac{b}{2\pi}\frac{(1-2\nu)x_2^3 + (3-2\nu)x_1^2 x_2}{2(\nu-1)(x_1^2 + x_2^2)^2},$$

$$e_{22} = \frac{b}{2\pi}\frac{(1-2\nu)x_2^3 - (1+2\nu)x_1^2 x_2}{2(\nu-1)(x_1^2 + x_2^2)^2},$$

$$e_{12} = \frac{b}{2\pi}\frac{x_1 x_2^2 - x_1^3}{2(\nu-1)(x_1^2 + x_2^2)^2}.$$

From Eq. (2) and Eq. (1),

$$\rho(r) = \frac{1}{\varepsilon}(d'_{111}e_{11,1} + 2d'_{112}e_{12,1}$$

$$+ d'_{211}e_{11,2} + d'_{222}e_{22,2})$$

so, substituting the components of the piezoelectric tensor from Eq. (1) and evaluating the strain tensor gradient, we find

$$\rho(x_1, x_2) = \frac{d}{\sqrt{3}\varepsilon}\left(-\sqrt{2}e_{11,1} - 2e_{12,1} - e_{11,2} + 2e_{22,2}\right)$$

$$= \frac{bd}{2\pi\sqrt{3}\varepsilon}\left[\frac{(2\nu-3)x_2^4 - 2\sqrt{2}(2\nu+1)x_1 x_2^3}{2(\nu-1)(x_1^2 + x_2^2)^3}\right.$$

$$\left. + \frac{30x_1^2 x_2^2 + 2\sqrt{2}(3-2\nu)x_1^3 x_2 - (2\nu+7)x_1^4}{2(\nu-1)(x_1^2 + x_2^2)^3}\right].$$

When this expression is converted to polar coordinates in the $x_1 x_2$ plane (xy plane), it becomes a somewhat simpler expression with angular terms having quadrupole and hexadecapole form:

$$\rho = \frac{bd}{2\pi\sqrt{3}\varepsilon}(\rho_1 + \rho_2 + \rho_3 + \rho_4 + \rho_5)$$

with

$$\rho_1 = \frac{(2v-3)}{2(v-1)}\frac{\cos 4\theta - 4\cos 2\theta + 3}{8r^2},$$

$$\rho_2 = -\frac{2\sqrt{2}(2v+1)}{2(v-1)}\frac{\sin 4\theta - 2\sin 2\theta}{8r^2},$$

$$\rho_3 = \frac{30}{2(v-1)}\frac{1-\cos 4\theta}{8r^2},$$

$$\rho_4 = \frac{2\sqrt{2}(3-2v)}{2(v-1)}\frac{\sin 4\theta + 2\sin 2\theta}{8r^2},$$

$$\rho_5 = -\frac{(2v+7)}{2(v-1)}\frac{\cos 4\theta + 4\cos 2\theta + 3}{8r^2}$$

so

$$\rho = \frac{bd}{4\pi\sqrt{3}\varepsilon(1-v)}\frac{1}{r^2} \cdot$$

$$\left[5\cos 4\theta - \sqrt{2}\sin 4\theta + 2(1+v)\cos 2\theta - \sqrt{2}(1-2v)\sin 2\theta\right]$$

$$\equiv \frac{C}{r^2}\sum_{n=2,4}\left[a_n \cos(n\theta) + b_n \sin(n\theta)\right]$$

which defines a useful constant C, and four parameters depending only on Poisson's ratio.

This simple expression reveals the charge density to have an inverse square decay and quadrupole and hexadecapole terms only. Note in particular that there is no monopole term and hence no net piezoelectric charge induced on the dislocation line. This rather transparent expression has not been revealed in previous work (Refs. 10, 11).

To obtain the piezoelectric potential, we need to solve the Poisson equation $\nabla^2\Phi = -4\pi\rho/\varepsilon$ with this charge distribution as the source. In two dimensions, the formal solution of the Poisson equation is

$$\Phi(r,\theta) =$$

$$\frac{1}{\pi}\int_0^\infty r'dr'\int_0^{2\pi}d\theta'\left[\ln\frac{1}{r_>} + \sum_{m=1}^\infty \frac{1}{m}\left(\frac{r_<}{r_>}\right)^m \cos m(\theta-\theta')\right]\rho(r')$$

$$= \frac{C}{\pi}\sum_{m=1}^\infty \frac{1}{m}\int_0^{2\pi}d\theta'[\sin(m\theta)\sin(m\theta') + \cos(m\theta)\cos(m\theta')]$$

$$\times \sum_{n=2,4}\left[a_n \cos(n\theta') + b_n \sin(n\theta')\right]\int_0^\infty \frac{r'dr'}{r'^2}\left(\frac{r_<}{r_>}\right)^m$$

where $r_>$ and $r_<$ are the greater and lesser, respectively, of r and r'. In analogy with the solution for the elastic field, the integral diverges at the origin because of the r^{-2} dependence of ρ. To deal with this difficulty, we adopt the same procedure that is used to avoid the

divergence of the elastic energy of a dislocation at the origin in continuum theory. We set cutoffs at an inner radius, R_1, and an outer radius, R_2. The cutoff at R_1 removes the core singularity and the cutoff at R_2 allows ρ to be expanded in multipoles. Later, we will identify R_1 as the core radius and we will let $R_2 \to \infty$. We now have

$$\Phi(r,\theta) = \frac{C}{\pi}\sum_{n=2,4}\frac{\pi}{n} \cdot$$

$$\left[a_n \cos(n\theta) + b_n(n\theta)\left(\frac{1}{r^n}\int_{R_1}^r (r')^{n-1}dr' + r^n\int_r^{R_2}(r')^{-n-1}dr'\right)\right]$$

$$= C\left\{\frac{1}{4}[a_4\cos(4\theta) + b_4\sin(4\theta)]\left[\frac{1}{2} - \frac{1}{4}\left(\frac{R_1}{r}\right)^4 - \frac{1}{4}\left(\frac{r}{R_2}\right)^4\right]\right.$$

$$\left. + \frac{1}{2}[a_2\cos(2\theta) + b_2\sin(2\theta)]\left[1 - \frac{1}{2}\left(\frac{R_1}{r}\right)^2 - \frac{1}{2}\left(\frac{r}{R_2}\right)^2\right]\right\}$$

for $r < R_2$. For $r > R_2$, we have

$$\Phi(r,\theta) = C\left\{\frac{1}{4}[a_4\cos(4\theta) + b_4\sin(4\theta)]\frac{1}{4}\left[\left(\frac{R_2}{r}\right)^4 - \left(\frac{R_1}{r}\right)^4\right]\right.$$

$$\left. + \frac{1}{2}[a_2\cos(2\theta) + b_2\sin(2\theta)]\frac{1}{2}\left[\left(\frac{R_2}{r}\right)^2 - \left(\frac{R_1}{r}\right)^2\right]\right\}$$

which is a multipole potential. The two solutions are matched at R_2. We can now let $R_2 \to \infty$ and neglect the terms in R_1, which amount to a small correction near the core, to get a potential valid for $r \gg R_1$

$$\Phi(r,\theta) =$$

$$C\left\{\frac{1}{8}[a_4\cos(4\theta) + b_4\sin(4\theta)] + \frac{1}{2}[a_2\cos(2\theta) + b_2\sin(2\theta)]\right\}$$

which is independent of r.

This rather surprising behavior is a consequence if the inverse square decay of the charge density. In this connection, we can pursue the analogy with the well-known elastic solution for an edge dislocation by pointing out that while the elastic energy per unit length is given by

$$\frac{\mu b^2}{4\pi(1-v)}\left(\ln\frac{R_2}{R_1} - \frac{1}{2}\right)$$

(where μ is the isotropic shear modulus), the piezoelectric energy per unit length is (taking $v = 0.3$)

$$\frac{9\pi^2 C^2}{1.6}\left(\ln\frac{R_2}{R_1} - \frac{1}{8}\right)$$

which is six orders of magnitude smaller, justifying our neglecting the reverse piezoelectric effect. In both cases, the first term comes from the energy in an
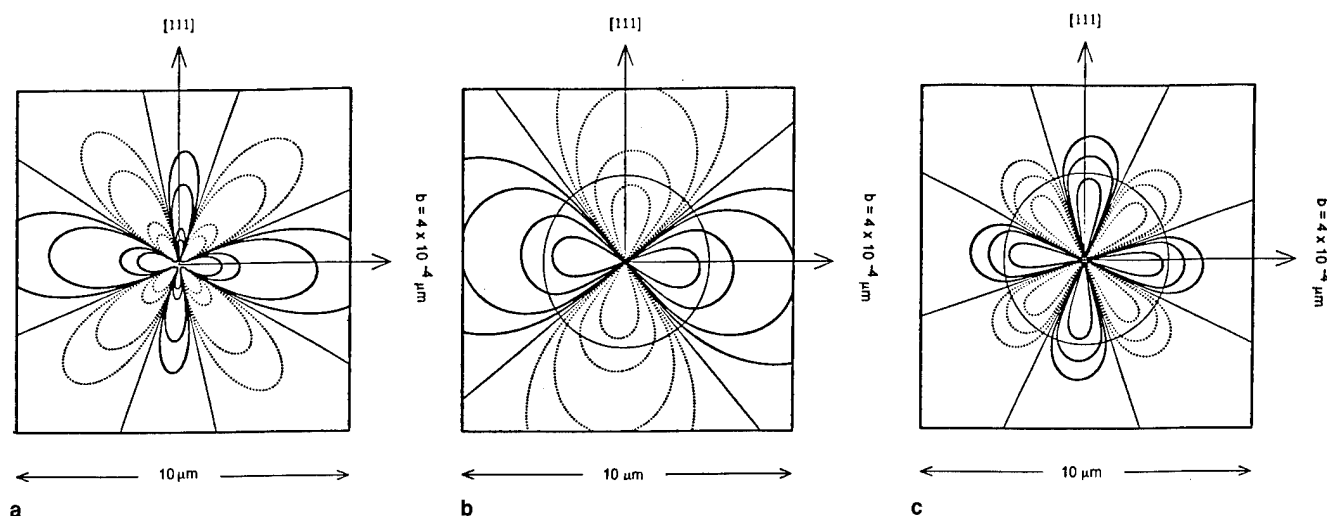
Fig. 3. Piezoelectric properties of a 60° dislocation in $Hg_{0.8}Cd_{0.2}Te$: (a) Piezoelectric charge normal to the dislocation line. Solid contours are 1, 0.5, 0.1, and 0.05×10^{12} e/cm³ going out radially; dotted contours are the negative of thse; (b) quadrupole component of the piezoelectric potential, and (c) hexadecapole component of the piezoelectric potential.

infinite cylinder integrated to R_2 which diverges logarithmically, and the second term is the effect of the cylindrical surface bounding the dislocation in a finite crystal (the image term).

For a good numerical calculation, we would need the piezoelectric constant of the alloy, which has not been determined. For an order-of-magnitude estimate, we can use the piezoelectric constant of CdTe, 3×10^{-6} coul cm⁻². The Burgers vector is 4×10^{-8} cm, and Poisson's ratio can be taken as 0.3. Using these values, we have computed the charge, potential, and field plots of Figs. 3a–3c.

It should be understood that because of the symmetry of the strain field associated with a straight dislocation, several of the possible sources of the piezoelectric potential are identically zero. In the reduced symmetry of curved dislocations, kinks, and jogs, these components of the potential do not vanish and may be significant.

AVERAGING NONLINEAR EFFECTS

The results we have obtained afford a qualitative insight into the effect of the piezoelectric potential on the characteristics of a pn junction threaded by a dislocation. The angular variation of the potential will alternately add to and subtract from the built-in potential of the junction, so that the barrier seen by a carrier crossing the junction will depend on its trajectory. The modification of the built-in potential due to the angularly varying piezoelectric potential can increase or lower the barrier seen by a carrier crossing the junction in a direction other than perpendicularly. Because of the strongly nonlinear dependence of both diffusion and tunneling currents on the barrier, the effect of such a barrier variation does not average to zero and the currents can be enhanced by a large factor. To illustrate the principle, we choose as an example the average tunneling probability for carriers crossing a narrow semiconductor junction.

The band-to-band tunneling probability has the
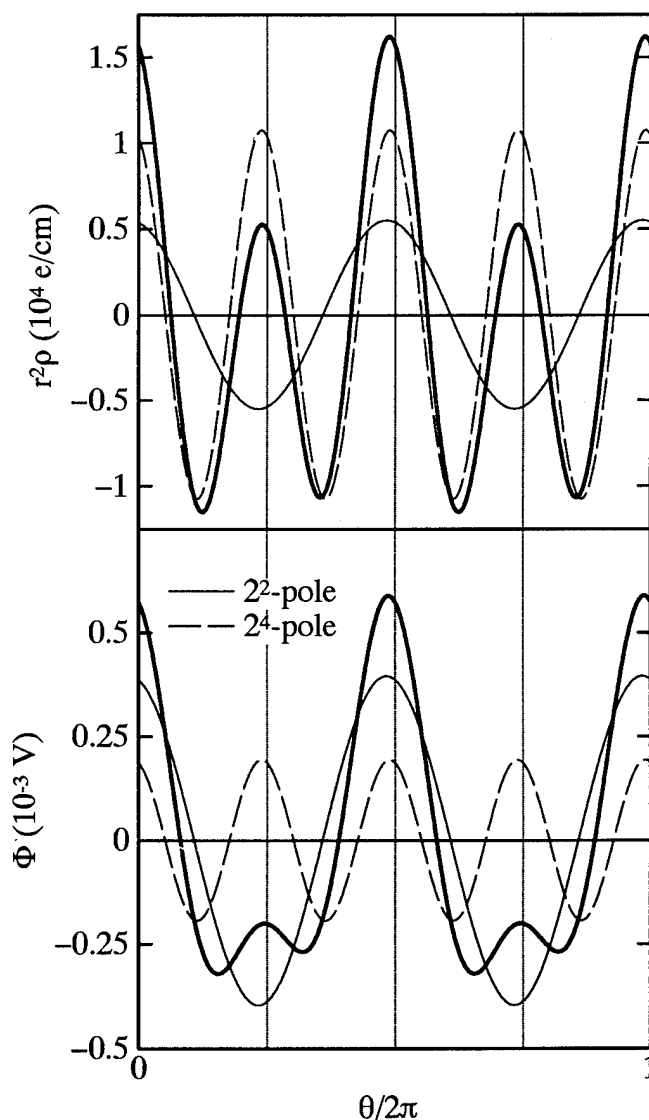
Fig. 4. Angular variation of the piezoelectric charge and potential normal to a 60° dislocation line.

form p = exp($-CB^{3/2}$) where B is the barrier and where C is a constant containing all the other material parameters.

We crudely represent the effect of the dislocation potential, which makes the tunneling barrier a function of the carrier's trajectory, as an angular variation of the barrier of the form $B = B_0(1 + \Delta\sin\theta)$ (it will be apparent presently that the detailed form of the angular variation is irrelevant for this argument). It is likely that this representation of the piezoelectric potential introduced by a dislocation can be justified by a WKB calculation.

If Δ is small compared with unity, we have $B^{3/2} = B_0^{3/2}[1 + (3/2)\Delta\sin\theta]$ (this approximation is taken purely to simplify the arithmetic and has no effect on the argument). We can now compute an average of p

$$< p >=$$

$$\frac{1}{2\pi}\int_0^{2\pi}\exp\left[-CB_0^{3/2}\left(1+\frac{3}{2}\Delta\sin\theta\right)\right]d\theta =$$

$$\frac{p_0}{2\pi}\int_0^{2\pi}\exp\left[-\frac{3}{2}CB_0\Delta\sin\theta\right]d\theta = p_0 I_0\left(\frac{3}{2}CB_0\Delta\right)$$

where $I_0(x)$ is the modified zero order Bessel function and p_0 is the tunneling probability in the absence of any dislocations. From this last form, it is apparent that the average tunneling probability could have been written as

$$< p >= p_0 I_0\left(\frac{3}{2}\Delta\ln|p_0|\right).$$

It is apparent that although the fractional barrier "angular modulation" Δ is small, the argument of the Bessel function need not be, and the factor multiplying the unmodulated barrier transition probability can be quite large. It is also evident that any other angular variation would lead to very similar results. The angular variation Δ can be estimated from the angular potential plots of Fig. 4 to be roughly 0.05–0.1. The parameters determining p_0 (effective mass, doping, temperature, etc.) cover a wide range. For typical values of these parameters, the multiplying

Bessel function ranges from near unity to about ten.

As another consequence of the type of nonlinearity examined here, the effect of overlapping piezoelectric potentials of neighboring dislocations is expected to be enhanced over what might be expected from linear superposition. This may be a possible clue to the observed inverse faster than linear falloff of R_0A with dislocation density.

CONCLUSIONS

We have evaluated the electric fields associated with dislocation charges and strain fields and estimated their effects on junction performance. We conclude that the fields associated with core charges alone are not likely to account for the observed degradation of junction performance. The longer range piezoelectric potentials, which we have calculated explicitly for the common 60° dislocation, are likely to have a larger effect, especially on R_0A through the tunneling leakage current. The effect of the nonlinearity of the junction characteristic on R_0A is examined and is proposed as a mechanism to account for observed nonlinear behavior.

ACKNOWLEDGMENT

REFERENCES

1. G.L. Hansen, J.L. Schmit and T.N. Casselman, *J. Appl. Phys.* 53, 7099 (1982).
2. S.H. Shin, J.M. Arias, D.D. Edwall, M. Zandian, J.G. Pasko and R.E. DeWames, *J. Vac. Sci. Technol.* B 10, 1492 (1992).
3. R.E. DeWames, private communication 1993.
4. P.I. Baranskii, A.E. Belyaev, O.P. Gorodnicheii and S.M. Komirenko, *Sov. Phys. Semicond.* 24, 73 (1990).
5. S.M. Johnson, R. Righer, J.P. Rosbeck, J.M. Peterson, S.M. Tailor and M.E. Boyd, *J. Vac. Sci. Technol.* B 10, 1499 (1992).
6. J.C. Zolper and A.M. Barnett, *IEEE Trans. Elect. Dev.* 37, 478 (1990).
7. J. Brice and P. Capper, eds., *The Properties of Mercury Cadmium Telluride, EMIS Data Reviews*, Series No. 3, (New York: INSPEC, 1987).
8. G. Saada, *Phys. Stat. Sol.* (B) 44, 717 (1971).
9. G. Faivre and G Saada, *Phys. Stat. Solidi.* (B) 52, 127 (1972).
10. H. Booyens and J.S. Vermaak, *J. Appl. Phys.* 50, 4302 (1979).
11. H. Booyens and J.H. Basson, *Phys. Stat. Solidi* (A) 85, 243 (1984).
12. P.A. Fedders, *J. Appl. Phys.* 54, 1804 (1983).

Dislocation Profiles in HgCdTe(100) on GaAs(100) Grown by Metalorganic Chemical Vapor Deposition

H. NISHINO, S. MURAKAMI, T. SAITO, Y. NISHIJIMA, and H. TAKIGAWA

Fujitsu Laboratories Ltd., 10-1 Morinosato-Wakamiya, Atsugi 243-01, Japan

We studied dislocation etch pit density (EPD) profiles in HgCdTe(100) layers grown on GaAs(100) by metalorganic chemical vapor deposition. Dislocation profiles in HgCdTe(111)B and HgCdTe(100) layers differ as follows: Misfit dislocations in HgCdTe(111)B layers are concentrated near the HgCdTe/CdTe interfaces because of slip planes parallel to the interfaces. Away from the HgCdTe/CdTe interface, the HgCdTe(111)B dislocation density remains almost constant. In HgCdTe(100) layers, however, the dislocations propagate monotonically to the surface and the dislocation density decreases gradually as dislocations are incorporated with increasing HgCdTe(100) layer thicknesses. The dislocation reduction was small in HgCdTe(100) layers more than 10 μm from the HgCdTe/CdTe interface. The CdTe(100) buffer thickness and dislocation density were similarly related. Since dislocations glide to accommodate the lattice distortion and this movement increases the probability of dislocation incorporation, incorporation proceeds in limited regions from each interface where the lattice distortion and strain are sufficient. We obtained the minimum EPD in HgCdTe(100) of 1 to 3×10^6 cm^{-2} by growing both the epitaxial layers more than 8 μm thick.

INTRODUCTION

Heteroepitaxial growth of CdTe or HgCdTe on GaAs has been studied tor use in fabricating large-area infrared focal plane arrays. Metalorganic chemical vapor deposition (MOCVD) is one of the most promising techniques for growing HgCdTe, because of its high throughput and suitability for large-area substrates.

Direct alloy growth (DAG)[1,2] and the interdiffused multilayer process (IMP)[3,4] were developed to prepare HgCdTe layers by MOCVD. In DAG, an epitaxial layer of the alloy is grown by supplying all the sources simultaneously. In IMP, thin epitaxial layers of CdTe and HgTe are grown alternately and interdiffused completely to form the alloy by annealing. Direct alloy growth produces a poorer compositional uniformity than IMP[5,6] because of the very different formation

energies of CdTe and HgTe. But recent advances such as using a multinozzle injector[7] or a wide reaction cell[8] can solve this problem. Historically, DAG has been expected to produce a lower dislocation density than IMP[8] because the IMP layers contain many interfaces with growth interruptions which increase misfit dislocations.

Metalorganic chemical vapor deposition forms both HgCdTe(100)[2,9] and HgCdTe(111)B[10,11] epitaxial layers on GaAs(100) substrates because of the large lattice mismatch (14.6%) between GaAs and CdTe buffer layers. HgCdTe(100) layers have a higher arsenic doping efficiency than HgCdTe(111)B layers.[12] Since arsenic is a commonly used acceptor which diffuses slowly in HgCdTe[13] and donor doping is easy for both orientations,[14,15] HgCdTe(100) is an attractive plane for constructing abrupt pn junctions for infrared photodiodes.

High-quality long-wavelength infrared detectors require HgCdTe(100) layers with a low dislocation

Nishino, Murakami, Saito,
Nishijima, and Takigawa
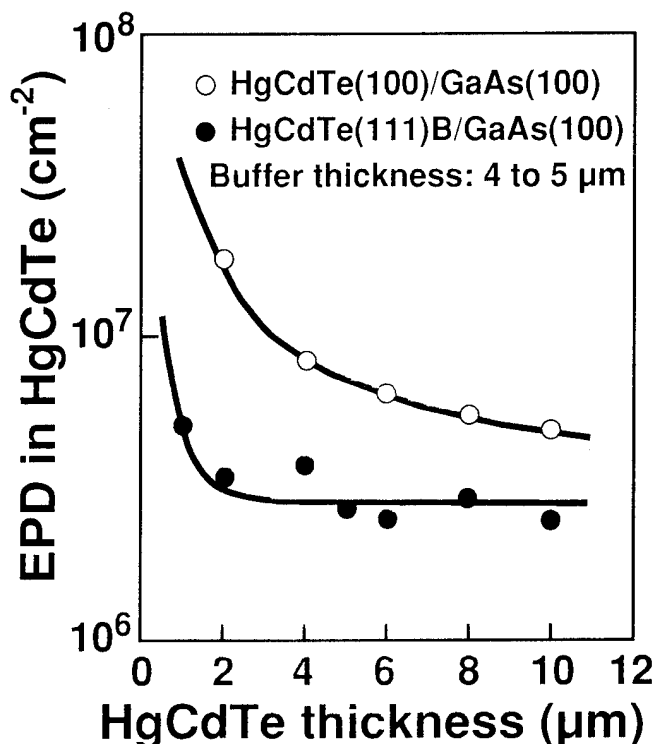
Fig. 1. Etch pit density thickness profiles in HgCdTe(111)B and HgCdTe(100) layers CdTe buffer thickness for both layers is 4 to 5 µm.
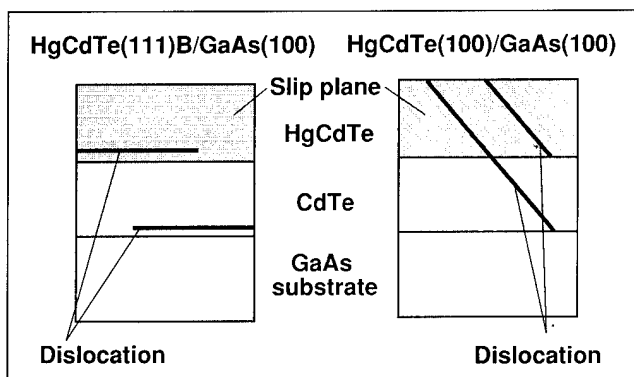
Fig. 2. Propagation of misfit dislocations in HgCdTe/CdTe/GaAs(100) with two epitaxial orientations (111)B and (100). Dislocations are generated at each interface and propagate along {111} slip planes.

density,[16] but the dislocation density in HgCdTe layers grown on GaAs substrates is high because of the large lattice mismatch. Dislocations in HgCdTe(111)B on CdZnTe(111)B grown by liquid phase epitaxy (LPE) have been well studied[17,18] but, to our knowledge a study of MOCVD-grown HgCdTe layers has not been published. We studied the dislocation profiles in HgCdTe(100) on GaAs(100) grown by MOCVD (DAG). We considered the dependence of the dislocation density on the thickness of both the HgCdTe and CdTe buffer layers and the dislocation reduction mechanism in these layers.

EXPERIMENTAL

We did the epitaxial growth in a horizontal reactor with multiple nozzles and a rotatiing graphite susceptor heated by radio frequency induction.[19] We
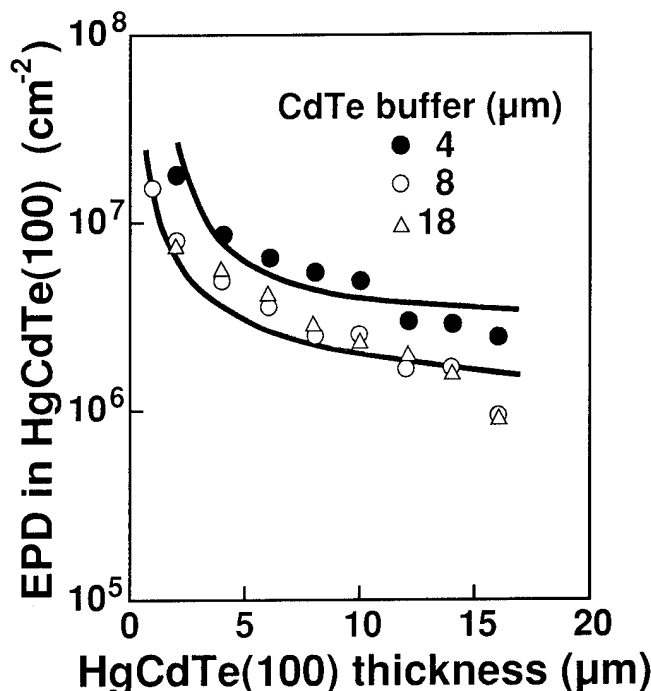
Fig. 3. Etch pit density thickness profiles in HgCdTe(100) layers grown on different thick CdTe(100) buffer layers.

used 3 inch GaAs substrates (100) misoriented 2° toward the nearest (110). To improve the compositional uniformity, we simultaneously injected the three precursors, dimethylcadmium (DMCd), diiso-propyltelluride (DIPTe), and elemental mercury (Hg) into the reactor from different nozzles.

We preheated the GaAs substrates at 600°C for 20 min and grew the CdTe buffer layers at 410°C under low pressure (150 Torr) to improve thickness uniformity. Since we grew both (100) and (111)B oriented layers to compare dislocation profiles, before buffer growth, we treated the substrates as follows. To obtain the CdTe(111)B layer, we first introduced DIPTe into the reactor at 410°C, which formed a relatively Te-poor Ga-As-Te interfacial phase and caused (111)B growth.[20,21] To form the CdTe(100) layer, we supplied DMCd and DIPTe simultaneously. We also deposited the CdTe buffer layers for each orientation under different VI/II source gas ratios and growth rates a relatively high VI/II ratio[22] and a growth rate of 2 µm/h for the (111)B layer and a relatively low VI/II ratio[23] and a growth rate of 3 µm/ h for the (100) layer.

We grew the HgCdTe layers at 360°C under atmospheric pressure. After growing the CdTe(100) buffers, we cleaved the substrates into small pieces and loaded several samples with different buffer thicknesses (4 to 18 µm) together into the reactor. We deposited HgCdTe(100) layers on the substrates at the same time to prevent unintentional differences in the run affecting the dislocation profiles. We grew the HgCdTe(111)B layers on full 3 inch substrates in another growth run because the optimum growth conditions, such as Hg partial pressure, differ from those for HgCdTe(100) growth. The HgCdTe growth

rate was 2.5 μm/h.

We evaluated the HgCdTe layers dislocation density from the defect etch-pit density (EPD)[17] by step-etching the samples. We determined the HgCdTe layers thicknesses by controlling the step-etching rate with a bromine (Br) methanol solution. The $Hg_{1-x}Cd_xTe$ layer composition (x-value) which we determined by room-temperature infrared transmission was x = 0.20 to 0.25.

RESULTS

EPD Profiles in HgCdTe (100) and (111)B

The HgCdTe(111)B layer's EPD remained almost constant except near the HgCdTe/CdTe interface where misfit dislocations were generated (Fig. 1). This profile is similar to that in HgCdTe(111)B layers grown by LPE[17] but the EPD values are higher due to the large lattice mismatch at the CdTe/GaAs interface. In contrast, dislocations spread into the HgCdTe(100) layer and the EPD gradually decreases. The EPD values in the HgCdTe(100) layer were higher than those in the HgCdTe(111)B layer when the CdTe buffer thicknesses were the same (4 to 5 μm). The dislocation profiles in the CdTe buffer layers are probably similar to those in the HgCdTe layers for both (100) and (111)B orientations.

The difference in the EPD profiles is due to the different angles between the interfaces and the slip planes where dislocation lines are most easily generated (Fig. 2). In CdTe and HgCdTe, the {111} planes are the slip planes. The interfaces in (111)B layers are parallel to the (111) slip planes and most misfit dislocations from the interfaces propagate along the slip plane through the epitaxial layers. Since dislocation lines terminate at the side of epitaxial layers, the high EPD values in (111)B layers near the interfaces decrease rapidly. In contrast, misfit dislocations generated at the interfaces in (100) layers propagate monotonically to the growth surface because the {111} slip planes are not parallel to the (100) interfaces. The dislocation density in (100) layers decreaes gradually as dislocation lines approach each other and make dislocation loops that incorporate dislocations.

Dependence of EPD on (100) Layer Thickness

We measured the EPD profiles in the HgCdTe(100) layers with three different buffer thicknesses (Fig. 3). Each HgCdTe(100) layer's EPD decreased as the HgCdTe layer thickiness increased, although the rate of decrease was very slow in the region more than 10 μm from the HgCdTe/CdTe interface. The minimum EPD value, obtained by increasing the HgCdTe layer thickness, was governed by the CdTe buffer layer thickness. Although the EPD in HgCdTe with a 4 μm buffer reached 3 to 5 × 10⁶ cm⁻², we obtained an EPD below 2 × 10⁶ cm⁻² for an 8 μm buffer. Most residual dislocations in the HgCdTe(100) layers were, therefore, threading dislocations from the butfer layers. Misfit dislocations generated at the HgCdTe/CdTe interface did not significantly affect the dislocation

density away from the interface.

We plotted the dependence of the HgCdTe(100) layer's EPD on the thickness of the CdTe(100) buffer layers (Fig. 4). The HgCdTe layer's EPD decreased with increasing CdTe buffer thickness; however, the EPD of the layers with 8 μm and with 18 μm thick buffers were almost the same. This suggests that the dislocation density in the CdTe(100) buffer layers did not decrease in the region more than 8 μm from the CdTe/GaAs interface. This is similar to the relationship between the EPD and the HgCdTe(100) thickness.

By growing both HgCdTe and CdTe layers more than 8 μm thick, we obtained a reproducible EPD value of 1 to 3 × 10⁶ cm⁻² (Table I). This is comparable to the dislocation reduction which Shin et al. achieved in MOCVD-grown HgCdTe(100) layers using thermal cycle annealing.[24] To our knowledge, our best value of
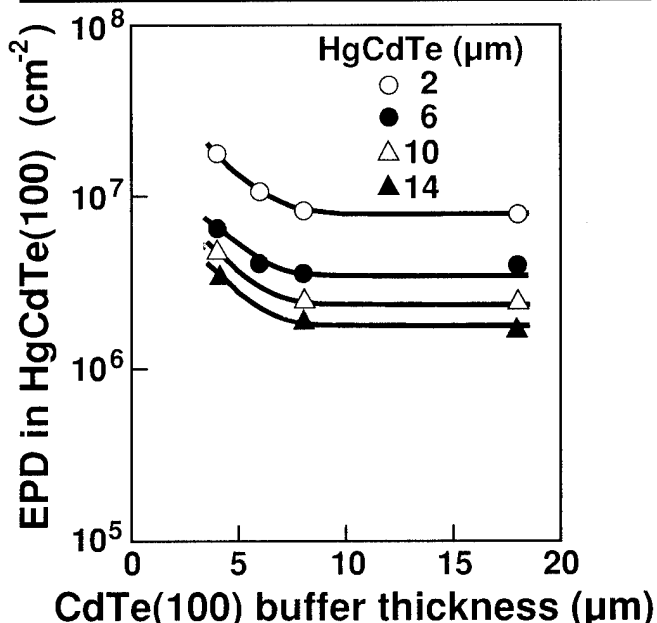
Fig. 4. Dependence of EPD at several depths in HgCdTe(100) layers on CdTe(100) buffer layers.

Table I. Reproducibility of Low-EPD HgCdTe(100) Layers with HgCdTe and CdTe Buffer Thicknesses Greater than 8 μm

Layer Index	Thickness (μm) CdTe	Thickness (μm) HgCdTe	EPD × 10⁶ (cm⁻²)
101	9	10	2.1
102	8	8	3.4
103A	9	12	1.7
103B	18	12	1.5
104A	8	16	0.9
104B	18	16	0.9
201	8	12	3.0
305	8	13	2.4
307	8	13	2.2

Note: We prepared layers 103A,B and 104A,B in the same HgCdTe growth runs. We grew layers 201 and 307 on full 3 inch wafers.
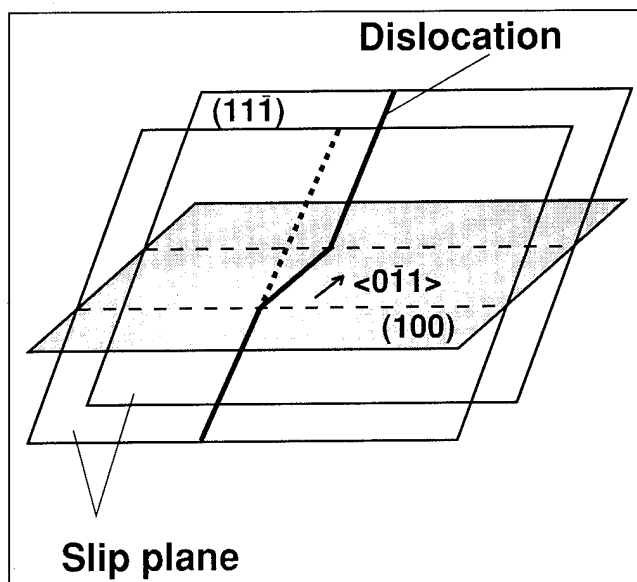
Fig. 5. Dislocation gliding in epitaxial layers.
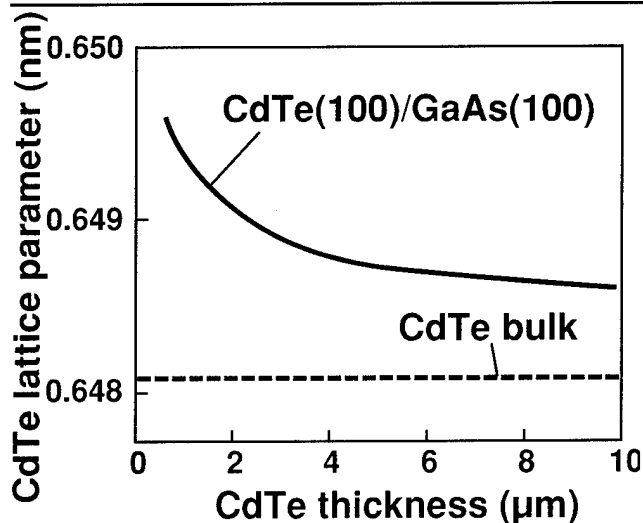
Fig. 6. CdTe lattice parameter calculated for CdTe(100)/GaAs(100). Lattice parameter is determined in the <100> direction, perpendicular to interface, and decreases with increasing CdTe thickness.

9.2×10^5 cm^{-2} is the lowest EPD reported to date for as-grown HgCdTe layers on GaAs substrates.

DISCUSSION

We think that dislocation lines on slip planes glide along the [011] direction in the epitaxial layers (Fig. 5), because the residual strain caused by the lattice mismatch at each interface acts as the dislocation motive force. This gliding increases the probability of the dislocation incorporation.

To explain the saturation of the EPD reduction with increasing layer thickness, we estimated the lattice distortion and mismatch strain. We plotted the dependence of the lattice parameter calculated[25,26] for CdTe(100)/GaAs(100) on the CdTe layer thickness (Fig. 6). The lattice parameter is defined as a value perpendicular to the interface. For the calculation, we assumed that the difference in length between the

seven lattices of CdTe and the eight lattices of GaAs caused the compressive strain. The lattice mismatch strain is proportional to the difference between the calculated and measured bulk lattice parameters and the large strain $(3 \times 10^{-3}$ dyn) near the interface decreases to a steady value $(4 \times 10^{-4}$ dyn) away from the interface.

To accommodate CdTe lattice distortion, dislocations move and are incorporated more frequently near the interface where the lattice parameter's rate of change is fast. The speed of movement depends on the change in strain. Far from the interface, however, the probability of incorporation is small because dislocations do not move when the lattice distortion and strain are almost uniform. The dislocation reduction, therefore, saturates with increasing layer thickness.

CONCLUSION

We studied the EPD profiles in HgCdTe(100) layers grown by MOCVD (DAG) on GaAs(100) substrates. We compared the profiles to those in HgCdTe(111)B layers, and measured the profiles' dependence on the HgCdTe(100) and CdTe(100) buffer thicknesses. Unlike dislocations in (111)B layers, dislocations in (100) layers propagate in the growth direction due to the difference in the angles between the interfaces and slip planes. The EPD in HgCdTe(100) decreases gradually as the thicknesses of the HgCdTe and the CdTe buffer layers increase; however, the EPD reduction proceeds only in a limited area within 10 μm of each interface. The dislocation reduction mechanism we propose is that the lattice mismatch strain at each interface enhances the incorporation of dislocations. Using this model, we can explain the saturation of EPD reduction by considering the lattice distortion and mismatch strain. We obtained an EPD of 1 to 3 $\times$ 10^6 cm^{-2}, which is the lowest reported value for HgCdTe(100) on GaAs(100) to our knowledge.

It is possible to grow low-EPD HgCdTe(100) layers on large-area substrates. This will contribute to the development of large-scale long-wavelength infrared focal plane arrays.

REFERENCES

1. J.B. Mullin and S.J.C. Irvine, *J. Phys. D: Appl. Phys.* 14, 149 (1981).
2. S.K. Ghandhi, I.B. Bhat and N.R. Tasker, *J. Appl. Phys.* 59, 2253 (1986).
3. S.J.C. Irvine, J. Tunnicliffe and J.B. Mullin, *Mater. Lett.* 2, 305 (1984).
4. J. Tunnicliffe, S.J.C. Irvine, O.D. Dosser and J.B. Mullin, *J. Cryst. Growth* 68, 245 (1984).
5. S.K. Ghandhi, I.B. Bhat and H. Fardi, *Appl. Phys. Lett.* 52, 392 (1988).
6. D.D. Edwall, J. Bajaj and E.R. Gertner, *J. Vac. Sci. Technol.* A8, 1045 (1990).
7. S. Murakami, Y, Sakachi, H. Nishino, T. Saito, K. Shinohara and H. Takigawa, *J. Vac. Sci. Technol.* B10, 1380 (1992).

8. D.D. Edwall, *J. Electron. Mater.* 22, 847 (1993).
9. W.E. Hoke, P.J. Lemonias and R. Traczewki, *Appl. Phys. Lett.* 44, 1046 (1984).
10. H.A. Mar, K.T. Chee and N. Salansky, *Appl. Phys. Lett.* 44, 237 (1984).
11. R. Korenstein, P. Hallock, B. MacLeod, W. Hoke and S. Oguz, *J. Appl. Phys.* 62, 4929 (1987).
12. J. Elliott and V.G. Kreismanis, *J. Vac. Sci. Technol.* B 10, 1429 (1992).
13. C.D. Maxey, P. Capper, P.A.C. Whiffin, B.C. Easton, I. Gale, J.B. Clegg and A. Harker, *Mater. Lett.* 8, 385 (1989).
14. S.K. Ghandhi, N.R. Taslier, K.K. Parat and I.B. Bhat, *Appl. Phys. Lett.* 57, 252 (1990).
15. R. Korenstein, P. Hallock, B. MacLeod, W. Hoke and S. Oguz, *J. Vac. Sci. Technol.* A8, 1039 (1990).
16. S.M. Johnson, D.R. Rhiger, J.P. Rosbeck, J.M. Peterson, S.M. Taylor and M.E. Boyd, *J. Vac. Sci. Technol.* B10, 1499 (1992).

17. M. Yoshikawa, K. Maruyama, T. Saito, T. Maekawa and H. Takigawa, *J. Vac. Sci. Technol.* A5, 3052 (1987).
18. H. Takigawa, M. Yoshikawa and T. Maekawa, *J. Cryst. Growth* 86, 446 (1988).
19. H. Takigawa, *Ext. Abs. 1992 U.S. Workshop on the Physics and Chemistry of Mercury Cadmium Telluride and Other IR Materials,* (1992), p. 111.
20. R.D. Feldman, R.F. Austin, D.W. Kisker, K.S. Jeffers and P.M. Bridenbaugh, *Appl. Phys. Lett.* 48, 248 (1986).
21. R. Srinivasa, M.B. Panish and H. Temkin, *Appl. Phys. Lett.* 50, 1441 (1987).
22. H. Takigawa, H. Nishino, T. Saito, S. Murakami and K. Shinohara, *J. Cryst. Growth* 117, 28 (1992).
23. P.L. Anderson, *J. Vac. Sci. Technol.* A4, 2162 (1986).
24. S.H. Shin, J.M. Arias, D.D. Edwall, M. Zandian, J.G. Pasko and R.E. DeWames, *J. Vac. Sci. Technol.* B10, 1492 (1992).
25. Z. Feng and H. Liu, *J. Appl. Phys.* 54, 83 (1983).
26. S.N.G. Chu, A.T. Macrander, K.E. Strege and W.D. Johnston, Jr., *J. Appl. Phys.* 57, 249 (1985).

The Minority Carrier Lifetime in Doped and Undoped p-Type Hg$_{0.78}$Cd$_{0.22}$Te Liquid Phase Epitaxy Films

M.C. CHEN, L. COLOMBO, J.A. DODGE, and J.H. TREGILGAS

Texas Instruments Incorporated, Corporate Research and Development, Dallas, TX 75265

This paper will describe: (1) the first comparative study of recombination mechanisms between doped and undoped p-type Hg$_{1-x}$Cd$_x$Te liquid phase epitaxy films with an x value of about 0.22, and (2) the first determination of τ^i_{A7}/τ^i_{A1} ratio by lifetime's dependence on both carrier concentration and temperature. The doped films were either copper- or gold-doped with the carrier concentration ranging from 2×10^{15} to 1.5×10^{17} cm^{-3}, and the lifetime varied from 2 μs to 8 ns. The undoped (Hg-vacancy) films had a carrier concentration range between 3×10^{15} and 8×10^{16} cm^{-3}, and the lifetime changed from 150 to 3 ns. It was found that for the same carrier concentration, the doped films had lifetimes several times longer than those of the undoped films, limited mostly by Auger 7 and radiative recombination processes. The ineffectiveness of Shockley-Read-Hall (SRH) recombination process in the doped films was also demonstrated in lifetime vs temperature curves. The important ratio of intrinsic Auger 7 lifetime to intrinsic Auger 1 lifetime, τ^i_{A7}/τ^i_{A1}, was determined to be about 20 from fitting both concentration and temperature curves. The reduction of minority carrier lifetime in undoped films can be explained by an effective SRH recombination center associated with the Hg vacancy. Indeed, a donor-like SRH recombination center located at midgap (E$_v$+60 meV) with a capture cross section for minority carriers much larger than that for majority carriers was deduced from fitting lifetime vs temperature curves of undoped films.

Key words: HgCdTe, impurity doped, minority carrier lifetime, photoconductivity decay

INTRODUCTION

The minority carrier lifetime of p-type Hg$_{1-x}$Cd$_x$Te is fundamentally important in the performance of n-on-p photovoltaic infrared detectors. Past studies of recombination mechanisms in p-type materials with an x value of about 0.2, suitable for detectors with a cutoff wavelength of 10–12 μm at 77K, are briefly summarized as follows. Polla et al.[1] reported a Shockley-Read-Hall (SRH) recombination center at about E$_v$+56 meV in undoped bulk n$^+$/p diodes using the reverse recovery method to measure the lifetime. Schacham and Finkman[2] obtained a value of 20 for the important ratio of intrinsic Auger 7 lifetime to intrinsic Auger 1 lifetime, τ^i_{A7}/τ^i_{A1}, from fitting the temperature dependence of lifetimes in undoped (Hg vacancy) bulk materials. Chen et al.[3] measured life-

times over a hole concentration range from 1×10^{15} to 5×10^{15} cm^{-3} in undoped liquid phase epitaxy (LPE) films. Tung et al.[4] reported lifetimes with the hole concentration ranging between 5×10^{15} and 2×10^{17} cm^{-3} in arsenic-doped LPE films. Lacklison and Capper[5] measured lifetimes over a wide concentration range between 3×10^{15} and 2×10^{17} cm^{-3}, and found no significant difference between doped and undoped bulk materials. Fastow and Nemirovsky[6] identified a SRH recombination center at E$_v$+15 meV in undoped bulk materials by fitting the temperature dependence of lifetimes. Souza et al.[7] measured undoped molecular beam epitaxy (MBE) films over an x value range from 0.2 to 0.3, and found that the lifetime is limited by a SRH recombination center at midgap. Adomaitis et al.[8] measured a lifetime as low as 53 ps in undoped LPE films, and concluded that Auger 7 process dominates at the hole concentration exceeding 4×10^{16} cm^{-3}. Tyan et al.[9] used a three-level SRH model to analyze
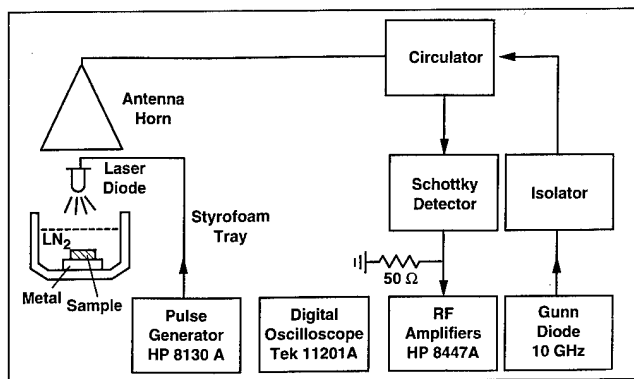
Fig. 1. The block diagram of the contactless microwave lifetime apparatus capable of measuring lifetimes as short as 3 ns.

a

b
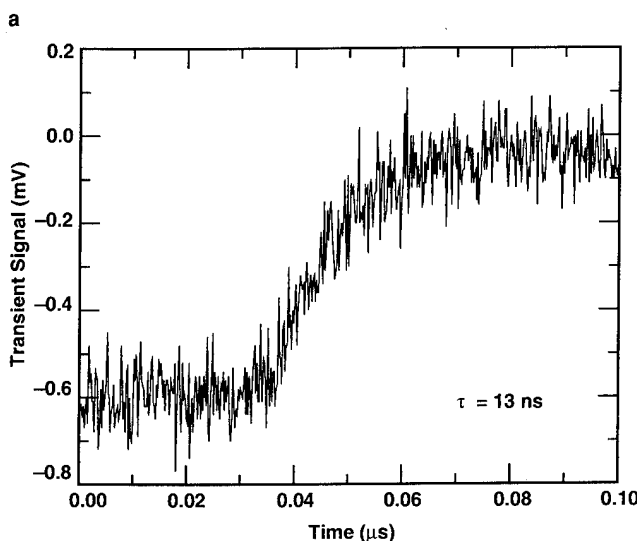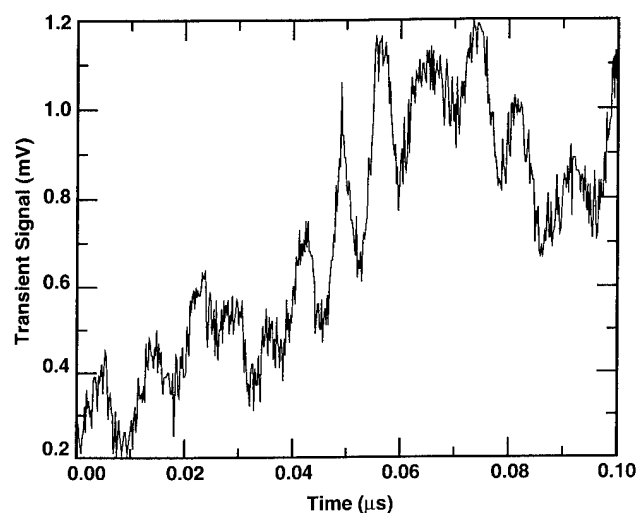
Fig. 2. The photo-induced transients of a vacancy-doped film with a lifetime of 13 ns. (a) without baseline correction (b) with baseline correction.

the temperature dependence of lifetimes in undoped LPE films. Recently, Mitra et al.[10] reported lifetimes in doped and undoped metalorganic chemical vapor deposition (MOCVD) films over a hole concentration range from 6×10^{15} to 1.5×10^{17} cm^{-3}.

Despite all these works, several issues regarding to the recombination processes in p-type $Hg_{1-x}Cd_xTe$ remains to be solved. One is the experimental value for τ^i_{A7}/τ^i_{A1} ratio which determines the effectiveness of Auger 7 recombination process in p-type $Hg_{1-x}Cd_xTe$. Another issue is whether or not there is a difference between lifetimes in doped and undoped samples. Finally, the nature of SRH centers such as the energy level seems to vary significantly from one study to another.

In this paper, we report a first comparative study on the recombination mechanisms between doped and undoped p-type $Hg_{0.78}Cd_{0.22}Te$ LPE films by measuring minority carrier lifetime's dependence on the carrier concentration and temperature. Also for the first time, the ratio of τ^i_{A7}/τ^i_{A1} has been determined by lifetime's dependence on both carrier concentration and temperature. The lifetime's dependence on the carrier concentration at 77K was measured by a contactless microwave reflection technique,[11] and its temperature dependence was obtained by the standard photoconductivity (PC) decay method from 77 to 200K. Liquid phase epitaxy films were grown on <111>B lattice-matched CdZnTe substrates from Te-rich melts in a dipping reactor. The doped films were either copper- or gold-doped with the carrier concentration ranging from 2×10^{15} to 1.5×10^{17} cm^{-3} at 77K. Post-growth anneal in Hg-saturated atmosphere at 220°C eliminated most of Hg vacancies in doped films. The undoped films were post-annealed in Hg-saturated atmosphere between 400 and 550°C to achieve different levels of Hg vacancies. They had a carrier concentration range between 3×10^{15} and 8×10^{16} cm^{-3} at 77K. The van der Pauw Hall measurements were conducted at 2 and 7 kG to not only determine the carrier concentration but also screen out films exhibiting effects of mixed conduction. The hole mobility was, depending on the carrier concentration, between 300 and 600 cm^2/V-s at 77K. The x value (Cd mole fraction) of these films ranged from 0.218 to 0.232.

EXPERIMENTAL

The lifetime measurement apparatus (Fig. 1) consists of a fast Oki laser diode emitting 1.3 μm light with an optical power of 100 mW driven by a HP8130A pulse generator with 1 ns rise/fall time, two 400 MHz HP8447A amplifiers with a combined gain of 1000, and a Tek11201A 400 MHz digital oscilloscope capable of averaging 4096 traces. The shortest lifetime that can be measurable by our current contactless microwave lifetime measurement apparatus is about 3 ns, limited mainly by the x-band microwave Schottky detector terminated with a 50 ohm resistor.

Due to the high carrier concentration of the films under this study, the photo-induced transient signals were usually weak. This can be seen from the following equation for measurements using the PC decay method under a constant current bias:

$$\Delta V = I_b \Delta R = -\frac{\Delta n}{n} V_b \qquad (1)$$

where ΔV and ΔR are light-induced voltage and resistance respectively, and I_b is the constant current bias, and V_b the resulting dark voltage bias. When the pulse width of the excitation light is longer than the lifetime, the concentration of excess electrons, Δn, is given by:

$$\Delta n = \eta \Phi \tau_n \qquad (2)$$

where η is the quantum efficiency and Φ is the photon flux. The lifetime, τ_n, also decreases with increasing carrier concentration. As a result, the photo-induced transient signal decreases with at least the square of the carrier concentration. A similar but more complex situation holds for measurements using the contactless microwave reflection technique.

One way to solve the measurement problem due to small transient signals from samples with a high carrier concentration is to increase the power of the excitation light. However, the large electrical current pulse needed to generate the high optical power inevitably induces spurious noise in the transient signal at very short times following the pulse, such as the curve shown in Fig. 2a. It was found that, in our microwave reflection setup, this spurious interference noise is independent of the sample. Therefore, a reference baseline containing the interference noise can be generated simply by shifting the sample away from the laser diode (by pushing the Styrofoam tray, see Fig. 1). The reference baseline is stored in the data acquisition software and then subtracted out of the transient signal. This baseline correction procedure results in clean and smooth signal curves such as the one shown in Fig. 2b, which was derived from the noisy curve in Fig. 2a.

The strong dependence of the photo-induced transient signal on the carrier concentration can be illustrated by Fig. 3 where the curve (a) is from a film with copper doping at about 2.3×10^{15} cm^{-3} measured with a gain of 100 and 50 mW optical power, and the curve (b) is from a film with Hg vacancy doping at about 4.5×10^{16} cm^{-3} measured with a gain of 1000 and 100 mW optical power. Although the carrier concentration only differs by a factor of 20, the signal changes by a factor of 200. It should also be noted that, long lifetime or short, the transient signals are exponential functions with a single time constant.

ANALYSIS OF LIFETIME DATA

The lifetime of p-type HgCdTe that includes contributions from Auger 1 (two electrons and one hole), Auger 7 (one electron and two holes), radiative, and Shockley-Read-Hall recombination processes is expressed as:

$$1/\tau = 1/\tau_{Al} + 1/\tau_{A7} + 1/\tau_{Rad} + 1/\tau_{SRH} \qquad (3)$$

The expression for Auger 1 process is:

$$\tau_{Al} = \frac{2n_i^2 \tau_{Al}^i}{(n+p)n} \qquad (4)$$

And the expression for Auger 7 process is:

$$\tau_{A7} = \frac{2n_i^2 \tau_{A7}^i}{(n+p)p} \qquad (5)$$

The expressions of Eq. (4) and Eq. (5) derived using nondegenerate statistics are applicable in p-type $Hg_{0.7}8Cd_{0.22}Te$ samples with a carrier concentration up to 1×10^{18} cm^{-3} at 77K where the density of states for the valence band is about 1×10^{18} cm^{-3}. Note that Auger 1 process in p-type HgCdTe is important only at high temperatures (such as above 150K) when materials become intrinsic. Two important parameters in calculating Auger recombination processes that have to be determined experimentally are the overlap integral of Bloch functions, $|F_1 F_2|$, which was determined to be 0.15 in our previous study on the recombination mechanisms in n-type $Hg_{0.78}Cd_{0.22}Te$ LPE films,[12] and the ratio of intrinsic Auger 7 lifetime to intrinsic Auger I lifetime, τ_{A7}^i/τ_{Al}^i, which was calculated by Casselman[13] to be about 2 for $Hg_{1-x}Cd_xTe$ with $x \sim 0.2$. The detailed expressions for lifetimes of each

a

b
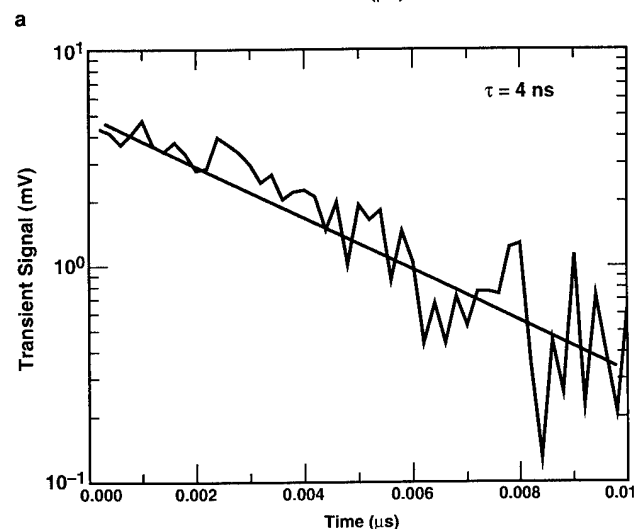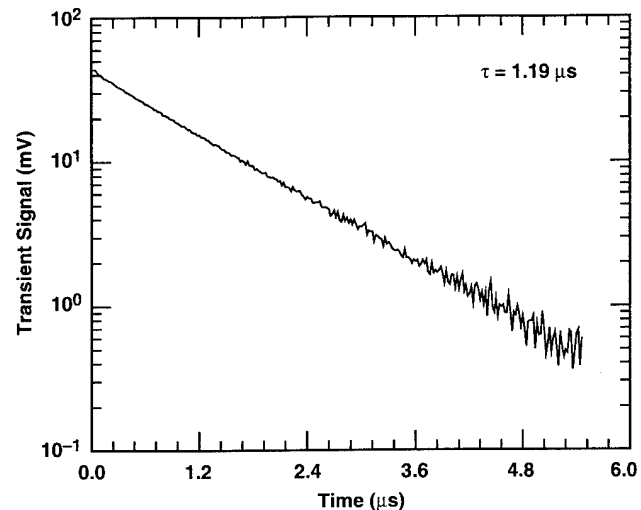
Fig. 3. The semi-logarithmic plots of photo-induced transients for (a) a copper-doped film, and (b) a vacancy-doped film.
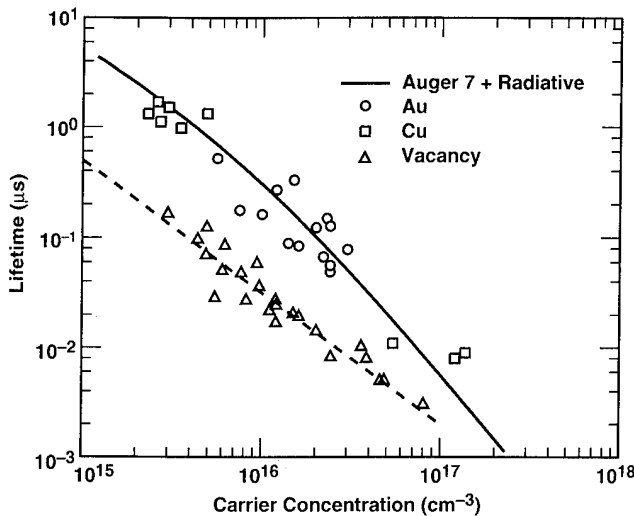
Fig. 4. Measured and calculated lifetimes as a function of carrier concentration at 77K. The solid line through the data of doped films was calculated with Auger 7 and radiative recombination processes for x = 0.225. And the dashed line through the data of undoped films is the trend line.

Fig. 6. The calculated diffusion-limited R_0A values, based on lifetimes in Fig. 4, for films with extrinsic and vacancy doping. The calculation assumes a device thickness of 6 μm.

and x = 0.225. That large ratio makes Auger 7 process relatively ineffective at low carrier concentrations. To illustrate each recombination process more clearly, the data of the doped films are replotted in Fig. 5 along with the radiative lifetime and the combined lifetime of Auger 7 and radiative processes with three τ^i_{A7}/τ^i_{A1} ratios (designated as γ): 10, 20, and 30. It can be seen that radiative process dominates the recombination until the carrier concentration exceeds 5×10^{15} cm^{-3}. Most of the scatter in the data is due to an uncertainty of about ±10 for the τ^i_{A7}/τ^i_{A1} ratio. The spread of about ±0.007 in the x value causes only ±20% deviation in the calculated lifetime. Schacham and Finkman[2] also obtained a value of 20 for the τ^i_{A7}/τ^i_{A1} ratio from fitting their temperature dependence data. The lifetimes in our doped films agree with those reported by Tung et al.[4] for the carrier concentration below 2×10^{16} cm^{-3}, and are shorter than those with the carrier concentration above 2×10^{16} cm^{-3}. The lifetimes in the doped MOCVD films reported by Mitra et al.[10] are shorter than those in our doped films.

The reduction of minority carrier lifetime in undoped films can be explained by the existence of an effective SRH recombination center whose association with Hg vacancy may be implied by a slope of about one for the dashed line through the lifetime data of undoped films in Fig. 4. As pointed out by Jones el al.,[14] this SRH center does not have to be the same defect as Hg vacancy, which acts as a shallow acceptor. It may be a complex that involves Hg vacancy. Also note that due to the dependence on the square of the carrier concentration, Auger 7 process will become dominant even in undoped films when the carrier concentration exceeds 3×10^{17} cm^{-3}. The lifetimes in our undoped films roughly agree with those measured by Lacklison and Capper,[5] but are longer than those obtained by Chen et al.[3]

From Fig. 4, one can also calculate the diffusion-limited device performance of n-on-p homojunction diodes. Assuming a thin diode approximation, the

Fig. 5. Measured and calculated lifetimes as a function of carrier concentration at 77K for the doped films. The solid line was calculated with only radiative recombination process. The combined lifetime calculated with a τ^i_{A7}/τ^i_{A1} ratio of 20 seems to be the best fit.

recombination process in Eq. (3) can be found in Ref. 2.

The Concentration Dependence

The dependence of lifetime on the carrier concentration as measured by the contactless microwave reflection method at 77K is shown in Fig. 4. The doped films had a lifetime range between 2 μs and 8 ns, and the undoped films from 150 to 3 ns. Below 1×10^{17} cm^{-3}, it is clear that the doped films had lifetimes several times longer than those of the undoped films at the same carrier concentration. Jones et al.[14] also observed a difference of about a factor of 2 in arsenic-doped and undoped $Hg_{0.7}Cd_{0.3}Te$ bulk materials. The solid line fitting the data of the doped films in Fig. 4 was calculated with Auger 7 and radiative recombination processes with a value of 20 for the τ^i_{A7}/τ^i_{A1} ratio

product of dynamic resistance and diode area, R_0A often used as the figure of merit, is given as:[15]

$$R_0\dot{A} = \frac{k_B T}{e^2} \frac{N_A}{n_i^2} \frac{\tau}{d} \qquad (6)$$

where d is the diode thickness. The calculation results are shown in Fig. 6 for both doped and undoped $Hg_{0.78}Cd_{0.22}Te$. Because the lifetime decreases slightly faster than the carrier concentration in undoped films, the R_0A curve is not flat, varying from 700 ohm-cm^2 at 1×10^{15} cm^{-3} to about 300 ohm-cm^2 at 1×10^{17} cm^{-3}. Note that this diffusion-limited R_0A values are in fact in the same range those achieved in p-on-n heterojunction diodes.[16]

The Temperature Dependence

The ineffectiveness of SRH recombination centers in copper- or gold-doped films can also be seen in lifetime vs temperature curves such as the one shown in Fig. 7a. Again a best fit dictates a value of 20 for the τ^i_{A7}/τ^i_{A1} ratio. The dashed line labeled "AUG" represents the combined Auger 1 and Auger 7 processes. The film was copper-doped to 2.6×10^{15} cm^{-3} with an x value of 0.222. Due to a low carrier concentration, radiative process dominates at low temperatures below 150K. The sensitivity of the fit to the value of the τ^i_{A7}/τ^i_{A1} ratio (designated as γ) is shown in Fig. 7b where the scatter of data leads to an uncertainty less than ±10, consistent with the result from fitting the concentration dependence of the lifetime (Fig. 5). Note that an accurate expression for the absorption coefficient is needed to calculate the temperature dependence of radiative lifetime in order to accurately deduct the τ^i_{A7}/τ^i_{A1} ratio from the fit to the temperature dependence of the lifetime. We used the expression of the absorption coefficient given by Schacham and Finkman,[2] whose accuracy has been widely demonstrated in its use in Fourier transform infrared measurements to determine the bandgap of $Hg_{1-x}Cd_xTe$ materials.

As for undoped films, Fig. 8 shows that SRH recombination process dominates the lifetime at low temperatures. In attempting a best fit, it was found that the SRH center is located at midgap (E_v+60 meV), and is donor-like since its capture cross section for minority carriers is much larger than that for majority carriers. This film has a hole concentration of 4.8×10^{15} cm^{-3} with an x value of 0.225. If one assumes a σ_n of 1×10^{-16} cm^2, then the best fit yields σ_p of 5×10^{-19} cm^2 and N_r of 8×10^{14} cm^{-3}. Our finding of a SRH center near the midgap in undoped p-type LPE films is consistent with that by Polla et al.[1] in undoped bulk samples and Souza et al.[7] in undoped MBE films.

EFFECTS OF SURFACE PASSIVATION

The measured lifetime in thin-film semiconductors is inherently sensitive to the surface properties. An improperly passivated surface gives rise to a large surface recombination velocity which obscures the bulk lifetime. Due to the short bulk lifetime in p-type
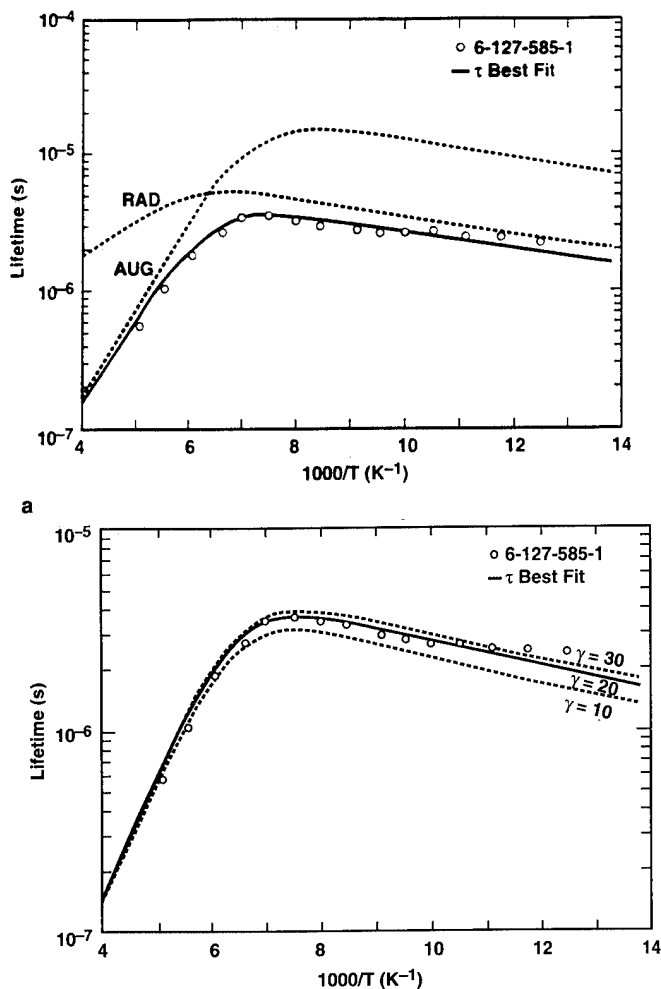
Fig. 7. (a) The temperature dependence of the lifetime for a copper-doped LPE film with p = 2.6×10^{15} cm^{-3} at 77K. The dashed lines show the individual contributions of Auger and radiative recombination mechanisms. (b) A value of 20 for the τ^i_{A7}/t^i_{A1} ratio was found to provide the best fit.
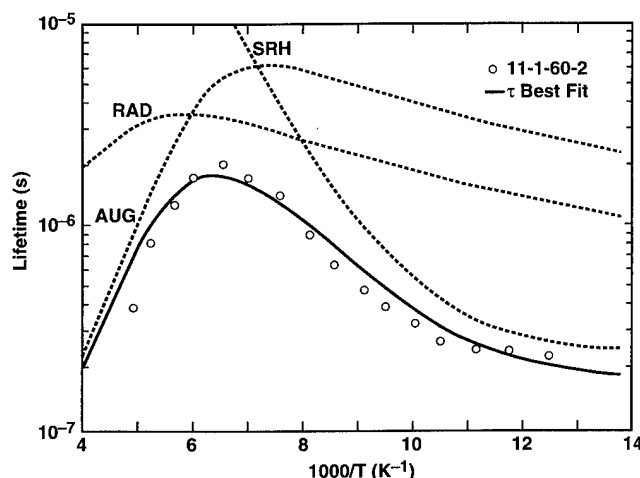
Fig. 8. The temperature dependence of the lifetime for an undoped LPE film with p = 4.8×10^{15} cm^{-3} at 77K. The dashed lines show the individual contributions from Auger, radiative, and SRH recombination mechanisms.
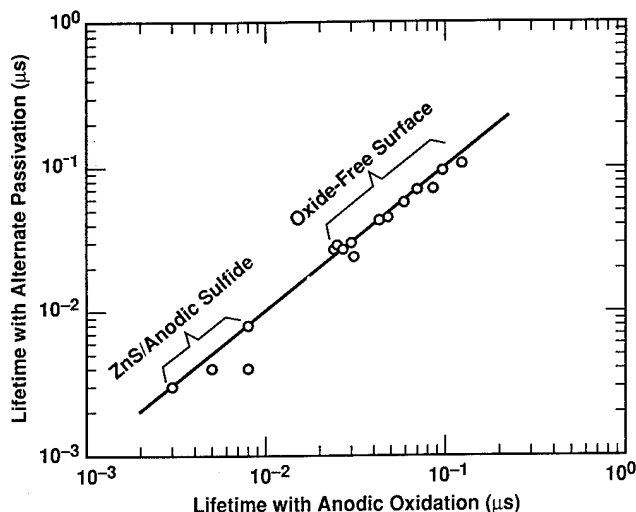
Fig. 9. The good agreement between lifetimes at 77K measured with either oxide-free or anodically sulfidized surfaces and those measured with anodically oxidized surfaces. Different surface passivation treatments were successively applied to the same set of samples.

$Hg_{0.78}Cd_{0.22}Te$, the effect of surface recombination cannot be studied using the transient decay method since the pulse width of the excitation light has to be significantly smaller than the bulk lifetime. Using photoelectromagnetic measurements, Finkman and Schacham,[17] and Sarusi et al.[18] concluded that SRH recombination process dominates the surface recombination in p-type $Hg_{0.78}Cd_{0.22}Te$ with surfaces being bare, CdTe coated, and anodically sulfidized. In these studies, both CdTe and anodic sulfide were established as good surface passivation for lifetime measurements. Note that anodic sulfide passivation yields a slightly accumulated surface in p-type $Hg_{1-x}Cd_xTe$.[19] According to theoretical calculations that have been verified experimentally in Si and Ge,[20] the surface recombination velocity as a function of surface potential has a maximum near depletion. At accumulation and strong inversion, the surface recombination velocity is at minimum.

To further support the picture of the surface recombination being dominated by SRH centers, Fig. 9 shows a comparative study between 77K lifetimes in samples with surfaces being anodically oxidized and those being anodically sulfidized or oxide-free. The lifetimes were measured, by the contactless microwave reflection method, on the same set of samples which were successively treated with different surface passivation techniques. The oxide-free surfaces are fresh surfaces produced by removing anodic oxide with lactic acid. The good correlation between lifetimes over almost two decades of magnitude shown in Fig. 9 establishes the anodic oxide as a good surface passivation for lifetime measurements, despite the

fact that anodic oxide strongly inverts the surface of p-type $Hg_{0.78}Cd_{0.22}Te$.

CONCLUSIONS

To summarize, we have presented a first detailed comparative study on the recombination mechanisms between doped and undoped p-type $Hg_{0.78}Cd_{0.22}Te$ LPE films by measuring minority carrier lifetime's dependence on the carrier concentration and temperature. Also, for the first time, the ratio of τ^i_{A7}/τ^i_{A1} has been determined to be about 20 by lifetime's dependence on both carrier concentration and temperature. It was found that the lifetime in the doped films was mostly limited by Auger 7 and radiative recombination processes. The lifetime for the undoped films with a carrier concentration below 1×10^{17} cm^{-3} was limited by an effective donor-like Shockley-Read-Hall recombination center located at midgap (E_v+60 meV).

REFERENCES

1. D.L. Polla, S.P. Tobin, M.B. Reine and A.K. Sood, *J. Appl. Phys.* 52, 5182 (1981).
2. S.E. Schacham and E. Finkman, *J. Appl. Phys.* 57, 2001 (1985).
3. J.S. Chen, J. Bajaj, W.E. Tennant, D.S. Lo, M. Brown and G. Bostrup, *Mat. Res. Soc. Symp. Proc.* V90, (Pittsburgh, PA: Mater. Res. Soc., 1987), p. 287.
4. T. Tung, M.H. Kalisher, A.P. Stevens and P.E. Herning, *Mat. Res. Soc. Symp. Proc.* V90, (Pittsburgh, PA: Mater. Res. Soc., 1987), p. 321.
5. D.E. Lacklison and P. Capper, *Semicond. Sci. Technol.* 2, 33 (1987).
6. R. Fastow and Y. Nemirovsky, *J. Appl. Phys.* 66, 1705 (1989).
7. M.E. de Souza, M. Boukerche and J. P. Faurie, *J. Appl. Phys.* 68, 5195 (1990).
8. E. Adomaitis, K. Grigoras and A. Krotkus, *Semicond. Sci. Technol.* 5, 836 (1990).
9. Y.L. Tyan, T. R. Schimert and L. T. Claiborne, *J. Vac. Sci. Technol.* B10, 1560 (1992).
10. P. Mitra, T.R. Schimert, Y.L. Tyan, A.J. Brouns and F.C. Case, *Mat. Res. Soc. Symp. Proc.* V299 (Pittsburgh, PA: Mater. Res. Soc., 1993).
11. M.C. Chen, *J. Appl. Phys.* 64, 945 (1988).
12. M.C. Chen and L. Colombo, *J. Appl. Phys.* 72, 4761 (1992).
13. T.N. Casselman, *J. Appl. Phys.* 52, 848 (1981).
14. C.E. Jones, K. James, J. Merz, R. Braunstein, M. Burd, M. Eetemadi, S. Hutton and J. Drmheller, *J. Vac. Sci. Technol.* A3, 131 (1985).
15. M.B. Reine, A.K. Sood and T.J. Tredwell, *Semiconductors and Semimetals* (New York: Academic Press, 1981) Vol. 18, p. 201.
16. R.E. DeWames, J.M. Arias, L.J. Kozlowski and G.M. Williams, *SPIE Proc.* Vol. 1735, (1992), p. 2.
17. E. Finkman and S.E. Schacham, *J. Vac. Sci. Technol.* A7, 464 (1989).
18. G. Sarusi, A Zemel, D. Eger, S. Ron and Y. Shapira, *J. Appl. Phys.* 72, 2312 (1992).
19. Y. Nemirovsky, L Burstein and I. Kidron, *J. Appl. Phys.* 58, 366 (1985).
20. A. Many, Y. Goldstein and N.B. Grover, *Seminconductor Surfaces* (Amsterdam: North-Holland, 1965) ch. 7.

Minority Carrier Lifetime in Indium-Doped HgCdTe(211)B Epitaxial Layers Grown by Molecular Beam Epitaxy

P.S. WIJEWARNASURIYA,[*†] M.D. LANGE,[†] S. SIVANANTHAN,[*] and J.P. FAURIE[*]

[*]University of Illinois at Chicago, Microphysics Laboratory, Physics Department, 845 W. Taylor St., Room 2236, Chicago, IL 60607–7059
[†]EPIR Ltd., P.O. Box 803827 - P2E, Chicago, IL 60680-3827

We have studied the minority-carrier lifetime on intentionally indium-doped (211)B molecular beam epitaxially grown $Hg_{1-x}Cd_xTe$ epilayers down to 80K with $x \approx 23.0\% \pm 2.0\%$. Measured lifetimes were explained by an Auger-limited band-to-band recombination process in this material even in the extrinsic temperature region. Layers show excellent electron mobilities as high as $\approx 2 \times 10^5$ $cm^2v^{-1}s^{-1}$ at low temperatures. When the layers are compensated with Hg vacancies, results show that the Schockley-Read recombination process becomes important in addition to the band-to-band processes. From the values of τ_{n0} and τ_{p0} of one sample, the obtained defect level is acceptor-like and is somewhat related to the Hg vacancies.

Key Words: HgCdTe, impurity doped, minority carrier lifetime, photoconductive decay

INTRODUCTION

Molecular beam epitaxially (MBE)-grown HgCdTe layers have been extensively studied over the last decade for infrared detector applications. Minority carrier lifetime (τ) of the excess photogenerated carriers is of great importance for the performance of infrared detectors.[1,2] Thus, it is essential to understand the factors that limit the recombination mechanism in MBE-grown layers. We have reported[3] previously, electron lifetime on (111)B p-type HgCdTe layers grown by MBE. The temperature dependence of the lifetime on these p-type HgCdTe layers was explained in terms of the Schockley-Read (SR) recombination mechanisms in the extrinsic temperature region and have shown a deep level closer to midgap. Lifetimes on n-type HgCdTe were studied by several investigators,[4-6] but layers were grown by different growth techniques. In the bulk grown crystals, the temperature dependence of lifetime data vs could be explained by intrinsic material properties. Compensated layers show SR recombination. Reported en-

ergy levels fall between 10 to 70 meV below the conduction band. On the other hand, on epitaxial layers, very little work has been reported in literature. We recently reported[7] lifetimes on indium-doped n-type MBE layers; and in this work, we have carried out a detailed analysis of factors that limit the recombination mechanisms.

EXPERIMENT

HgCdTe layers were grown in the (211)B growth orientation on CdZnTe(211)B substrates in an ISA Riber 2300 MBE machine which is designed to handle mercury. The detailed growth technique has been previously reported. Layers were doped *in situ* during MBE growth with indium. The Cd composition and the layer thickness were determined at room temperature by infrared transmission measurements. All of the layers investigated were annealed under Hg-saturated atmosphere at 250°C in order to reduce the Hg-vacancy concentration created during the MBE growth. The carrier concentration [extracted from the Hall coefficient $R_h(T)$] and the mobility [extracted from $R_h(T)/\rho(B=0,T)$] of the layers were measured by the van der Pauw technique[8] for temperatures rang-
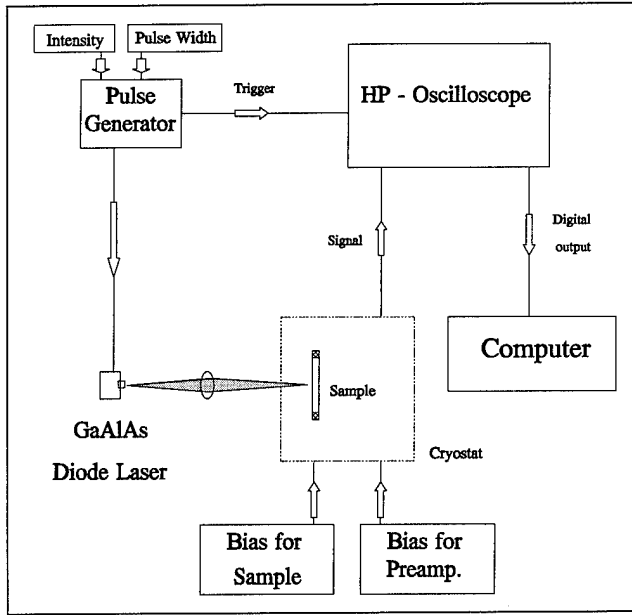
Fig. 1. Block diagram of the photoconductive apparatus for measuring the minority carrier lifetime of HgCdTe layers.
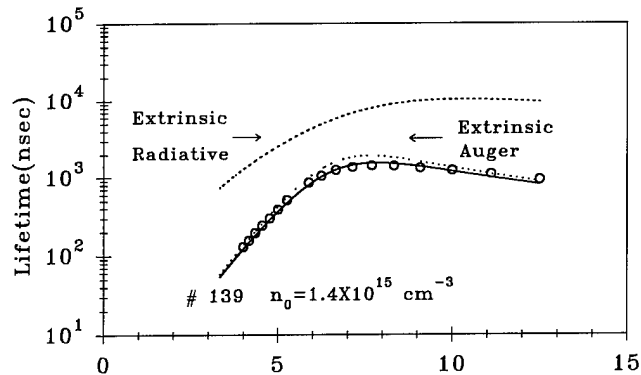
a
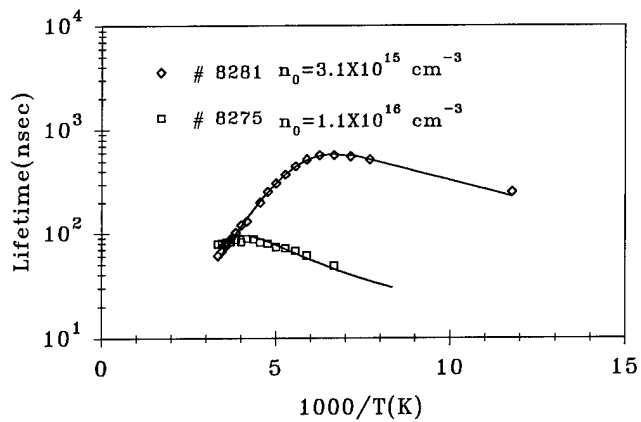
b

Fig. 2. (a) Measured (O) and theoretical (—) minority carrier lifetime on low indium-doped MBE-grown HgCdTe layer vs reciprocal temperature. Auger (···) and radiative (—) recombination processes are also shown; (b) Measured (◇, □) and theoretical (—) minority-carrier lifetime vs reciprocal temperature on moderately and high indium-doped MBE layers.

ing from 20 to 300K and magnetic fields up to 1.0 Tesla. The lifetime measurements (typical sample dimensions are $\approx 3 \times 3$ mm^2) were carried out using the photoconductive decay technique. All the samples were etched in Br-methanol solution prior to measurement, which was especially important in the latter case. Indium was used to make good ohmic contacts for n-type layers.

A block diagram of the measurement technique at the Microphysics Laboratory is shown in Fig. 1. A pulsed GaAlAs laser beam ($\lambda = 850$ nm) was focused on the sample to generate the excess carriers. The samples were mounted on the cold finger of a liquid nitrogen variable temperature dewar. Photoconductive decay signals were amplified with a low-noise cryogenic preamplifier and were obtained by a Hewlett-Packard 54100A digitizing oscilloscope. The obtained decay signals were averaged to minimize the noise, and the noise was further subtracted by taking a measurement with zero beam intensity. The biasing was kept low to avoid sweep-out effects, and the light intensity, was also kept low in order to satisfy the low injection conditions.

THEORY: RECOMBINATION MECHANISM IN N-TYPE HgCdTe

Minority carrier lifetime in n-type HgCdTe is determined by several different recombination mechanisms; namely Auger, radiative, and Schockly-Read mechanisms and these have been discussed extensively in the literature.[4,9,10] We have applied all these mechanisms earlier for MBE-grown, indium-doped, HgCdTe layers, and here we will outline briefly the relevant equations under low injection conditions.

In the case of the Auger process, recombination occurs directly between bands which involves two electrons in the conduction band and a heavy hole in the valence band. The relevant lifetime is given by,

$$\tau_A = \frac{2n_i^2 \tau_{Ai}}{(n_0 + p_0)(n_0 + \gamma p_0)} \tag{1}$$

where n_i is the intrinsic carrier concentration,[11] τ_{Ai} is the intrinsic Auger lifetime,[10] and n_0 and p_0 are the equilibrium electron and hole concentrations in the conduction band and valence band, respectively. The quantity γ is the hole-hole collision term, which we have neglected for n-type layers.

In the case of radiative process, the recombination also occurs between bands, but the excess energy is released in the form of a photon. The radiative lifetime is given by,[4]

$$\tau_R = \frac{2\tau_{Ri} n_i}{(n_0 + p_0)} \tag{2}$$

where τ_{Ri} is the radiative lifetime in the intrinsic material.

Finally, the SR lifetime is given by,[9]

**Table I. Summary of the Measured and Fitted Parameters of Annealed
MBE-Grown $Hg_{1-x}Cd_xTe$ Layers That Were Studied**

Sample Name	x (%)	t (μm)	N_d (cm^{-3}) [Extracted from R_h(T)] ($\times 10^{15}$)	μ (cm^2/V·s) ($\times 10^5$)	n_0 (cm^{-3}) [Extracted from Lifetime] ($\times 10^{15}$)	τ at 80K (ns)
139	21.7	08.7	1.4	1.6	1.3	940
8530	22.0	10.3	2.0	2.3	1.8	580
8533	22.0	10.8	2.3	2.2	2.7	410
8532	22.2	11.4	2.2	1.3	2.9	220
8281	23.7	11.5	4.0	1.6	3.1	250
9046	22.6	12.1	4.7	1.6	3.3	184
9044	22.0	12.2	4.9	1.6	3.6	140
8275	24.4	09.5	21.0	1.0	11.0	20

**Table II. Summary of the Measured and Fitted Parameters of MBE-Grown $Hg_{1-x}Cd_xTe$
Layers that Showed SR Recombination in the Extrinsic Temperature Region**

Sample Name	x (%)	N_d (cm^{-3}) [Extracted from R_h(T)] ($\times 10^{15}$)	n_0 (cm^{-3}) [Extracted from Lifetime] ($\times 10^{15}$)	τ at 80 K (ns)	E_t (meV)	τ_{p0} (ns)
8537	22.1	1.4	1.4	780	45.1	8900
8283	24.6	3.8	2.7	560	32.7	7800
6991	24.5	1.9	1.9	235	40.2	9500
8[annealed]	25.4	1.4	1.0	1490	38.6	6063
8[as-grown]	25.4	1.6	2.0	150	44	162

$$\tau_{SR} = \frac{\tau_{po}(n_0 + n_1)}{(n_0 + p_0)} + \frac{\tau_{no}(p_0 + p_1)}{(n_0 + p_0)} \qquad (3)$$

where τ_{no} and τ_{p0} are the shortest time constant for electron and hole captures; and $n_1 = n_0\exp(E_t - E_F)/KT$ and $p_1 = p_0\exp(E_F - E_t)/KT$, where E_F is the Fermi energy and E_t is the defect energy level.

Here, we have assumed that the recombination occurs through a single level E_t inside the forbidden gap, and the defect density N_t is small enough compared to n_0.

RESULTS AND DISCUSSION

Lifetime vs Temperature

Measured lifetime and material parameters of these annealed indium-doped n-type layers at 80K are summarized in Table I. As can be seen from the table, these indium-doped layers show excellent electrical properties. The expected behavior of increase in mobility with decreasing doping levels can be seen. Electron mobility at low temperature varies in the range of $(1-2) \times 10^5$ cm^{2}v^{-1}s^{-1} for doping levels in the range of $(1-10) \times 10^{15}$ cm^{-3}. N_d is the doping concentration extracted from the measured R_h(T) data at B = 0.4 Tesla.

Figure 2 shows the lifetime vs reciprocal temperature for three selected layers from Table I. Symbols represent experimental data points. It can be seen that, as the temperature decreases, the lifetime in-

creases, becomes maximum, and then decreases. In Fig. 2a, the peak lifetime reaches ≈1.4 μs at 130K; and at lower temperatures, it decreases exponentially. For sample #8275, the highest doping level, the maximum τ reaches ≈100 ns. The solid lines represent the theoretical curves, which include only Auger and radiative recombination processes. In order to achieve a good fit to the experimental data, the measured Cd composition x and the doping concentration were adjusted slightly. The value of the doping concentration (n_0) obtained from the fitting of τ data are also shown in Table I. As can be seen, there is an excellent correlation between the experimental data and the intrinsic material properties of MBE-grown HgCdTe layers. Similar behavior is obtained for higher doping levels, up to ≈1.0 × 10^{16} cm^{-3}. The Auger lifetime dominates throughout the entire temperature region down to 80K.

As previously discussed,[7] lifetime data on some of the MBE-HgCdTe layers cannot be explained by band-to-band recombination processes. Table II shows the measured lifetime, transport properties, and material parameters on these layers at 80K. Also, Table II contains the values of E_t and τ_{p0} obtained by fitting to the experimental data according to the theory. The SR energy level E_t varies between 33 and 45 meV below the conduction band on these layers, as can be seen from the table.

As an example, Fig. 3 shows lifetime vs reciprocal temperature for sample #8537, which falls into this category. It is evident that the behavior is very similar
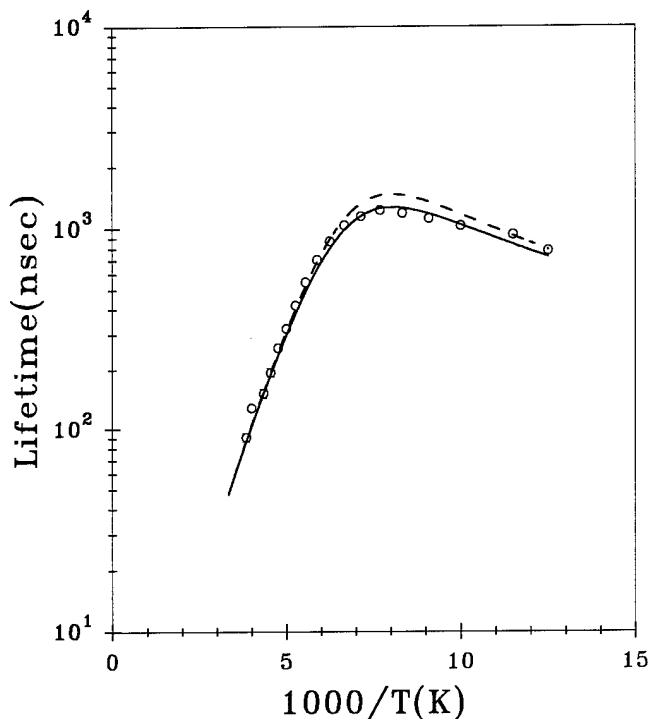
Fig. 3. Dependence of minority-carrier lifetime vs temperture on sample # 8537. Lines show various contributions; SR recombination (···), combined Auger and radiative recombination (---), and combined Auger, radiative, and SR recombination (—).

Fig. 4. Measured (O) and theoretical (—) minority-carrier lifetime vs reciprocal temperature on sample #8; (a) as-grown (parameters used: E_t = 43.8 meV, τ_{p0} = 162 ns, and τ_{n0} = 6887 ns); (b) after n-type anneal under Hg pressure at 250°C (parameters used: E_t = 38.6 meV, τ_{p0} = 6063 ns).

to those samples in Fig. 2. The combined Auger and radiative lifetimes gives good agreement with the experimental data in the intrinsic temperature region. But, in the extrinsic temperature range the data is lower by a factor of ≈1.2 than the theory. Hence, in order to obtain a good fit throughout the entire temperature range, we had to assume recombination from SR centers in addition to the combined Auger and radiative processes.

In order to find out the origin of this defect level, we carried out lifetime measurements on an as-grown, indium-doped, HgCdTe layer. The measured lifetime was again lower than the band-to-band recombination lifetime at temperatures below 200 K. At 80K, the lifetime is ≈150 ns. Figure 4b shows the lifetime data on the same sample after it was annealed at 250°C under Hg saturated conditions. Note that the lifetime improved from 150 ns to 1.4 μs at 80K. This is an almost one order of magnitude improvement. The solid line represents the best fit curve, and it was obtained with all recombination mechanisms as discussed previously. During MBE growth at a growth temperature of 185°C, it is very difficult to avoid compensation due to Hg vacancies, especially when the indium doping levels are in the range of 10^{15} cm^3 (we assume that N_d arises mainly from indium atoms). At 185°C, according to the HgCdTe P-T phase diagram, the accepter level due to Hg vacancies should be in the 10^{15} cm^{-3} range.[12] Hence, as-grown layers are very compensated. We obtained N_d = 1.6 × 10^{15} cm^{-3} and N_a = 1.5 × 10^{15} cm^{-3} from fitting of $R_h(T)$ vs temperature data. After n-type annealing under Hg

pressure, we obtained N_t = 1.4 × 10^{15} cm^{-3} and N_a = 1.4 × 10^{14} cm^{-3}. From the lifetime data, τ_{p0} increased from 162 ns to 6 μs when N_a decreased from 1.5 × 10^{15} cm^{-3} to 1.4 × 10^{14} cm^{-3}. According to Fig. 2, this SR defect level was not seen for doping levels up to 1.0 × 10^{16} cm^{-3}. Since these samples were indium-doped during the growth, it is safe to assume that the origin of this SR defect level is not related to extrinsic indium. Hence, we concluded that this SR level is somehow related to the Hg vacancies. Figure 5 shows the variation of τ_{p0} with acceptor concentrations for indium-doped layers.

Lifetime vs Electron Concentration

Figure 6 shows the behavior of the lifetime vs electron concentration of indium-doped HgCdTe layers at 80K. the lifetime decreased from ≈950 to ≈20 nsec when the doping increased from ≈1.4 × 10^{15} cm^{-3} to ≈1.0 × 10^{16} cm^{-3}. The data can be fitted according to Eq. (1). The solid line shows n_0^{-2} dependence, as expected from Eq. (1); and this further confirms that the measured lifetime is limited by Auger recombination in the extrinsic temperature region. We have taken | F_1F_2 | to be 0.22, and the Cd composition to be 22%. Since there exists an ambiguity in the exact value of | F_1F_2 | for HgCdTe in the literature,[4,5,10] we have also calculated the concentration dependence of lifetime for upper and lower limits of | F_1F_2 |. The lifetime data follows extremely well for | F_1F_2 | = 0.22, and the inverse square dependence of the electron concentration is clearly visible.

CONCLUSION

In this paper, we have studied, in detail, the minority-carrier lifetime of indium-doped, MBE-grown, HgCdTe layers with x ≈ 23.0% ± 2.0%. Lifetime data measured by the photoconductive decay method can be explained satisfactorily by the Auger-limited band-to-band recombination process in the entire temperature region down to 80K. We have observed lifetime on the order of 1 μs at 80K for the lowest doped layers that were achieved by MBE growth. Our layers show excellent electron mobilities as high as ≈2 × 10⁵ cm²v⁻¹s⁻¹ at low temperatures. Measured data fits very well with the band-to-band recombination mechanisms up to 1.0×10^{16} cm⁻³ doping levels. The overlap integral $|F_1F_2| = 0.22$ gives excellent agreement for MBE-HgCdTe layers.

Hence, the incorporation of indium during the growth of MBE HgCdTe is under control down to the doping levels of ≈(1–2) × 10¹⁵ cm⁻³, and these low doping levels are supported by the measured lifetime data, indicating the high quality of MBE-HgCdTe layers. This study shows that there has been tremendous improvement in the growth of HgCdTe by MBE.

In the second category of MBE layers, SR limited recombination was observed in the extrinsic temperature region. At higher temperatures, when the sample is intrinsic, Auger limited band-to-band recombination still dominates. A single defect level between ≈33 and 45 meV below the conduction band was necessary to explain the measured data. At present, due to lack of data in this category, we were unable to determine conclusively the origin of this defect level; but it appears that when layers are compensated due to Hg vacancies created during the low temperature of MBE growth, this level tends to dominate.

ACKNOWLEDGMENTS

REFERENCES

1. D. Lang and J.L. Schmit, *Semiconductors and Semimetals,* ed. R.K. Willardson and A.C. Beer (New York: Academic, 1970), Vol. 5.
2. D.L. Polla and C.E. Jones, *J. Appl. Phys.* 52, 5118 (1981).
3. M.E. de Souza, M. Boukerche and J.P. Faurie, *J. Appl. Phys.* 68, 5195 (1990).
4. M.A. Kinch, M.J. Brau and A. Simmons, *J. Appl. Phys.* 44, 1649 (1973).
5. M.C. Chen and L. Colombo, *J. Appl. Phys.* 72, 4261 (1992).
6. M.Y. Pines and O.M. Stafsudd, *Infrared Phys.* 20, 73 (1980).
7. P.S. Wijewarnasuriya, M.D. Lange, S. Sivananthan and J.P. Faurie, *J. Appl. Phys.* 75, 1004 (1994).
8. L.J. van der Pauw, *Philips Tech. Rev.* 20, 220 (1958).
9. J.S. Blakemore, *Semiconductor Statistics* (New York: Pergaman, 1962).
10. R.G. Pratt, J. Hewett, P. Capper, C.L. Jones and M.J. Quelch, *J. Appl. Phys.* 54, 5152 (1983).
11. G.L. Hansen and J.L. Schmit, *J. Appl. Phys.* 54, 1639 (1983).
12. J.P. Faurie, S. Sivananthan and P.S. Wijewarnasuriya, *SPIE Proc.* (July 1992).
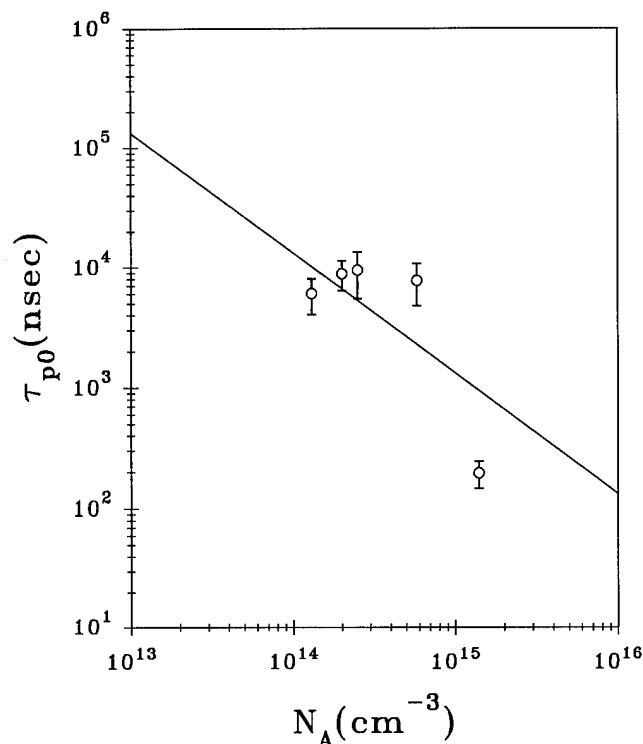
Fig. 5. Variation of τ_{p0} vs acceptor concentration for MBE layers in which SR recombination was dominant in the extrinsic temperature region.
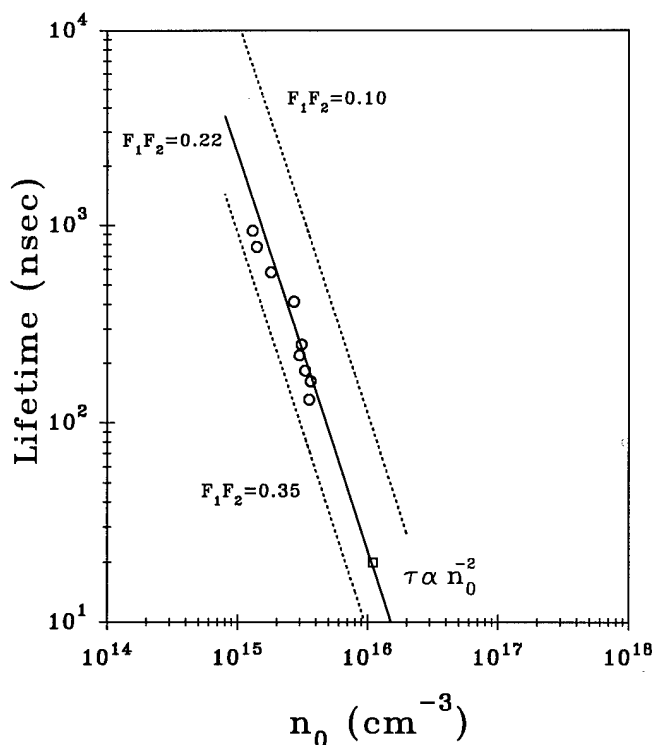
Fig. 6. Dependence of minority carrier lifetime on electron density at 80K on indium-doped, MBE-grown, HgCdTe layers. Data point □ was extrapolated at 80K from graph 2b. The dotted lines show the concentration dependence of lifetime for $|F_1F_2| = 0.35$ and $|F_1F_2| = 0.10$.

Band Structure, Magneto-Transport, and Magneto-Optical Properties of InAs-Ga$_{1-x}$In$_x$Sb Superlattices

J.R. MEYER, C.A. HOFFMAN, J.P. OMAGGIO, E.R. YOUNGDALE, and F.J. BARTOLI

Naval Research Laboratory, Washington, DC 20375

R.H. MILES and D.H. CHOW

Hughes Research Laboratories, Malibu, CA 90265

L.R. RAM-MOHAN

Worcester Polytechnic Institute, Worcester, MA 01609

We have theoretically and experimentally investigated the electronic properties of InAs-Ga$_{1-x}$In$_x$Sb superlattices. It is found that a strong repulsion between the E1 and H1 bands in superlattices with thin Ga$_{1-x}$In$_x$Sb layers leads to dispersion relations that closely resemble those in HgTe-CdTe superlattices. Temperature-dependent magneto-transport and magneto-optical measurements on samples with a range of InAs layer thicknesses confirm several of the theoretically predicted consequences, e.g., the coexistence of two electron species in semimetallic superlattices and a very light electron cyctron mass in narrow-gap semiconducting samples. The electron mobility is found to be dominated by interface roughness scattering under nearly all conditions of interest. Implications for this system as an infrared detector material are discussed.

Key word: Band structure, InAs/GaInSb superlattice, magneto-transport, magneto-optical

INTRODUCTION

Hg-based II-VI semiconductors have long been the optical materials of choice for long-wave infrared (LWIR) detectors. Hg$_{1-x}$Cd$_x$Te alloys have dominated this application for several decades, although it has been proposed that reduced tunneling noise and enhanced cutoff-wavelength uniformity may be attainable in photovoltaic (PV) devices employing HgTe-CdTe superlattices.[1,2] While recent work has demonstrated significant progress toward the achievement of an attractive superlattice detector technology,[3,4] well-known difficulties with regard to producibility and robustness remain a common concern for both alloy and heterostructure devices containing Hg.

It is generally acknowledged that the growth and processing of LWIR detector arrays would be much less demanding if narrow-gap III-V semiconductors

were available with optical and electronic properties analogous to those in the Hg-based II-VIs. Unfortunately, no bulk III-V binary compound or alloy has a cutoff wavelength extending into the LWIR at 77K. While InAs-GaSb heterostructures with relatively thick layers can be designed to have an arbitrarily small energy gap (E$_g$),[5] that system is inappropriate for detectors because the matrix elements for optical absorption near the band edge become quite small. The Type-II alignment between the conduction band minimum (the E1 band of InAs) and the valence band maximum (the H1 band of GaSb) minimizes the overlap between the electron and hole wavefunctions. The weak E1-H1 interactions also lead to other significant contrasts between the InAs-GaSb and HgTe-CdTe superlattice systems. For example, whereas a strong repulsive interaction causes E1 and H1 to invert when the semiconductor-semimetal transition point is crossed in a HgTe-CdTe superlattice (i.e., E1 becomes hole-like and H1 becomes electron-like),[6] the
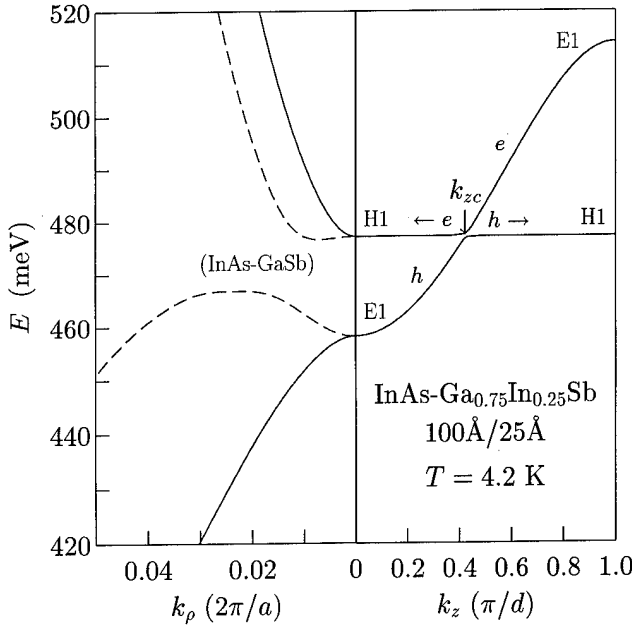
Fig. 1. Calculated in-plane (left panel) and growth-direction (right panel) dispersion relations for a semimetallic [100] InAs-Ga$_{1-x}$In$_x$Sb superlattice with the indicated layer thicknesses. The dashed curves illustrate the corresponding in-plane dispersion for a semimetallic InAs-GaSb superlattice (101–120Å) with the same negative energy gap at the zone center.
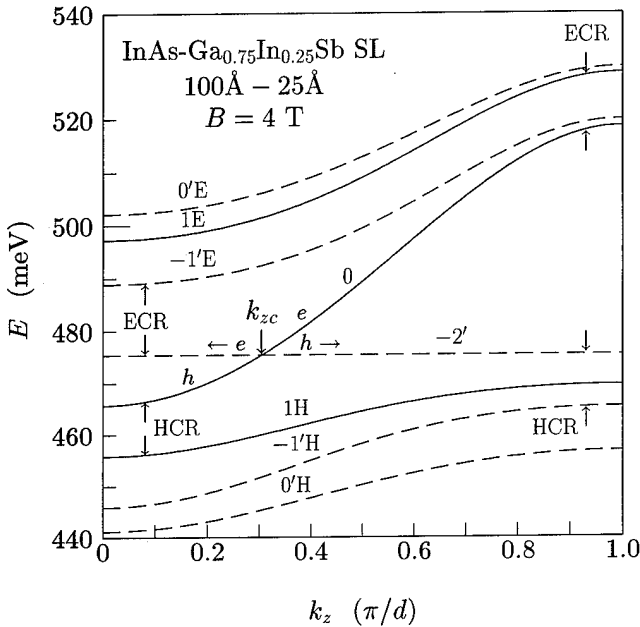
Fig. 2. Calculated Landau levels (B = 4 T) for a semimetallic [100] InAs-Ga$_{1-x}$In$_x$Sb superlatttice at T = 4.2K. Transitions corresponding to lowest-order electron and hole cyclotron resonances near k$_z$ = 0 and near k$_z$ = π/d are indicated.

in-plane dispersion relations for a semimetallic InAs-GaSb superlattice remain relatively unperturbed from those for electrons in InAs and holes in GaSb.[7–9]

Smith and Mailhiot proposed in 1987 that much larger LWIR optical matrix elements should be achievable in InAs-Ga$_{1-x}$In$_x$Sb strained-layer superlattices.[10] By taking the layer thicknesses (d$_1$ and d$_2$) to be

relatively thin, and hence assuring much greater penetration of the electron wavefunctions into the Ga$_{1-x}$In$_x$Sb and hole wavefunctions into the InAs, they obtained a theoretical absorption edge which was almost identical to that for Hg$_{0.79}$Cd$_{0.21}$Te. This prediction was subsequently confirmed experimentally,[11] and InAs-Ga$_{1-x}$In$_x$Sb superlattices have also been found to display other properties which have favorable implications for their ultimate performance in LWIR detectors.[12]

In the present work, we show that the similarities between InAs-Ga$_{1-x}$In$_x$Sb and Hg-based materials are much more extensive than had previously been recognized. In fact, the electron and hole dispersion relations in III-V strained-layer superlattices with strong E1-H1 interactions are found to closely mimic those in HgTe-CdTe superlattices, while being quite dissimilar from those in InAs-GaSb heterostructures with weak E1-H1 interactions. Many distinctive features of the HgTe-CdTe band structure, which are known to manifest themselves in observable experimental properties,[6] carry over directly into the InAs-Ga$_{1-x}$In$_x$Sb system.

It should be emphasized that whereas we will contrast the cases of InAs-Ga$_{1-x}$In$_x$Sb with thin d$_2$ and InAs-GaSb with thick d$_2$ (the limits usually considered for each system), there is clearly a continuum connecting those two limiting cases. Either decreasing d$_2$ or increasing x (which increases the strain and hence enhances the negative energy overlap of the bands) makes the InAs-Ga$_{1-x}$In$_x$Sb superlattice more HgTe-CdTe-like.

Following a discussion of calculated superlattice band structures in the next section, the derived theoretical framework will be used to interpret magneto-transport (Section on Growth and Magneto-Transport) and magneto-optical (Section on Magneto-Optics) data which display identifiable consequences of the strong E1-H1 interactions. Measurements were performed on a series of n-type samples with a range of InAs quantum well thicknesses. While a detailed analysis of the experimental mobility in terms of interface roughness scattering is discussed in detail elsewhere,[13] the present work will emphasize the semimetallic regime where the interband interactions are strongest and their effects on the experimental data are greatest.

BAND STRUCTURE THEORY

An eight-band transfer-matrix (k·p) algorithm including strain[14] has been used to calculate band structures for [100]-oriented InAs-Ga$_{1-x}$In$_x$Sb superlattices as a function of layer thicknesses. Bulk material parameters were obtained from Ref. 15, and the valence band offset was taken to be –540 meV (independent of x).[10,16] Dispersion relations for InAs-GaSb and HgTe-Hg$_{0.15}$Cd$_{0.85}$Te superlattices were also calculated for comparison.

We first consider the InAs-Ga$_{1-x}$In$_x$Sb band structure in the absence of a magnetic field. With decreasing energy gap (increasing d$_1$), the repulsion of the

strongly-interacting E1 and H1 bands leads to a rapid decrease of the in-plane electron and hole masses (see the cyclotron resonance results discussed below). With further increases of d_1, the E1 and H1 bands eventually cross at the semiconductor-semimetal transition point. Figure 1 illustrates the in-plane (k_p) and growth-direction (k_z) dispersion relations for a semimetallic InAs-Ga$_{1-x}$In$_x$Sb superlattice (d_1 = 100Å, d_2 = 25Å). Note that near the zone center the two bands have inverted, with E1 becoming hole-like along k_p and H1 electron-like. This is exactly the behavior observed in HgTe-CdTe superlattices, but not in InAs-GaSb with thicker d_2 and hence much weaker E1-H1 interactions (see the dashed curves in the left panel of the figure). In the latter case, H1 remains hole-like and E1 electron-like, except near the band anti-crossing at $k_p \approx 0.015(2\pi/a)$ (a is the lattice constant).[9]

The right panel of Fig. 1 shows that along the growth axis of the InAs-Ga$_{1-x}$In$_x$Sb superlattice, the E1 and H1 bands anti-cross at some intermediate point k_{zc}. When $k_z > k_{zc}$, E1 is the conduction band and H1 is the valence band as in a conventional semiconductor. However, for $k_z < k_{zc}$, the roles are reversed. The conduction band minimum and valence band maximum are therefore both in the H1 band, yielding an indirect energy gap whose magnitude is almost exactly zero. The strong repulsion between E1 and H1 also leads to a rough proportionality of the in-plane masses to the energy gap $E_g(k_z)$, hence electrons and holes with the same energy but a wide range of effective masses co-exist in the semimetallic superlattice (mass-broadening).[6] With further increases of d_1, k_{zc} eventually reaches the zone boundary (π/d, where $d = d_1 + d_2$), and a second semimetal-semiconductor transition occurs.[6,17,18] These qualitative features are identical to those discussed previously for HgTe-CdTe superlattices.[6]

Figure 2 illustrates the band structure for the same semimetallic InAs-Ga$_{1-x}$In$_x$Sb superlattice in the presence of a magnetic field of 4 T along the growth axis. A comparison with Fig. 1 of Ref. 19 indicates that the arrangement of the Landau levels closely resembles that for a semimetallic HgTe-CdTe superlattice. The dispersion in the plane becomes quantized into two concurrent series of discrete levels, designated primed and unprimed (dashed and solid curves), and in lowest order only magneto-optical transitions within a

given series are allowed. The bands labeled 0 and –2′ represent ground state levels for E1 and H1, and their dependences on k_z are quite similar to those in the absence of a magnetic field. The crossing at k_{zc} separates the region in which –2′ is a conduction band and 0 is a valence band from that in which their roles are reversed, mixing the usual distinctions between intraband (cyclotron resonance) and interband (across the gap) transitions. For example, the transition 1H→ 0 changes its character from hole cyclotron resonance at $k_z < k_{zc}$ to interband when $k_z > k_{zc}$. Also evident is that there is a strong dependence of the cyclotron energy (and therefore the cyclotron mass) on k_z. This may lead to the observation of multiple cyclotron resonance peaks corresponding to different portions of the Brillouin zone, and should be considered another manifestation of the mass-broadening effect discussed above.

Also noteworthy is that above a certain critical magnetic field B_{crit}, the band arrangement in Fig. 2 leads to the magnetic activation of an electron-hole plasma whose density is proportional to $B - B_{crit}$. That phenomenon was predicted theoretically for HgTe-CdTe superlattices and was confirmed experimentally by magneto-optical measurements.[6] Because InAs-Ga$_{1-x}$In$_x$Sb superlattices with a given k_{zc} remain semimetallic up to considerably higher applied fields, the present system may yield electron-hole densities which are an order of magnitude greater than those observable in HgTe-CdTe.

We emphasize that the field-dependent band structure in Fig. 1 is quite different from that for an InAs-GaSb superlattice (thick d_2) with the same negative energy gap at $k_z = 0$. In that case, –2′ is hole-like and 0 electron-like at small k_z, but both cyclotron masses are more than an order of magnitude larger than those in Fig. 2. For InAs-GaSb, multiple higher-order bands often lie *between* –2′ and 0, in contrast to both Fig. 2 and semimetallic HgTe-CdTe.

GROWTH AND MAGNETO-TRANSPORT

Magneto-transport measurements were performed on a series of five n-type superlattices with fixed Ga$_{0.75}$In$_{0.25}$Sb barrier thicknesses (d_2 = 25Å) but a range of InAs quantum well thicknesses (25Å $\leq d_1 \leq$ 86Å). The superlattices were grown onto (100) GaAs substrates by molecular beam epitaxy (MBE), in a

Table I. Well and Barrier Thicknesses, Experimental and Theoretical Energy Gaps, Low-Temperature Hall Densities and Mobilities, and Experimental and Theoretical Cyclotron Masses for Five n-Type InAs-Ga$_{0.75}$In$_{0.25}$Sb Superlattices

d_1 (Å)	d_2 (Å)	E_g^{exp} (T=0) (meV)	E_g^{th} (0) (meV)	n_0 (10^{16}cm^{-3})	μ_n(4.2K) (cm^2/Vs)	m_{CR}^{exp}/m_0	m_{CR}^{th}/m_0
25	25	187	217	1.8	3900	—	0.027
37	25	105	120	3.3	7400	—	0.024
45	25	91	87	7.6	13000	—	0.022
54	25	52	60	3.3	17000	0.017	0.019
86	25 3500	–3	0	6.3	13000	0.044–0.076	0.028–0.058
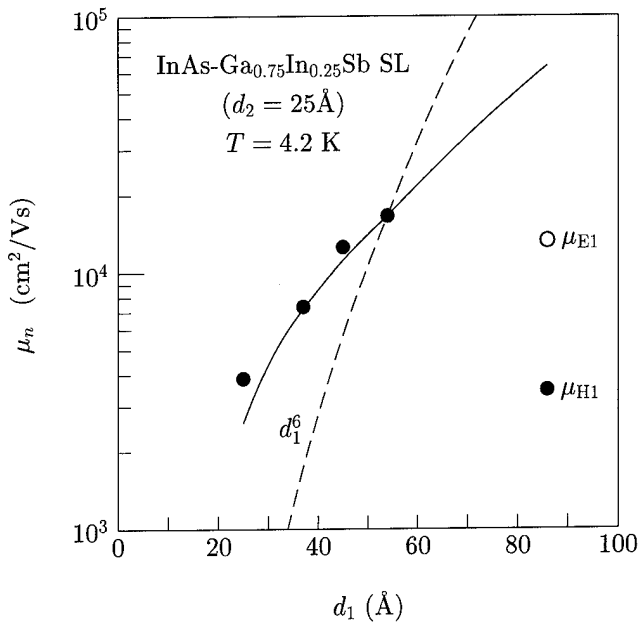
Fig. 3. Experimental (points) and theoretical (curves) low-temperature electron mobilities vs well thickness. The dashed curve represents the d_1^6 dependence generally associated with interface roughness scattering, while the solid curve was obtained by explicitly calculating $(\partial E/\partial d_1)^{-2}$ for the E1 band. Both curves are normalized to give agreement with the experimental mobility at $d_1 = 54$Å.
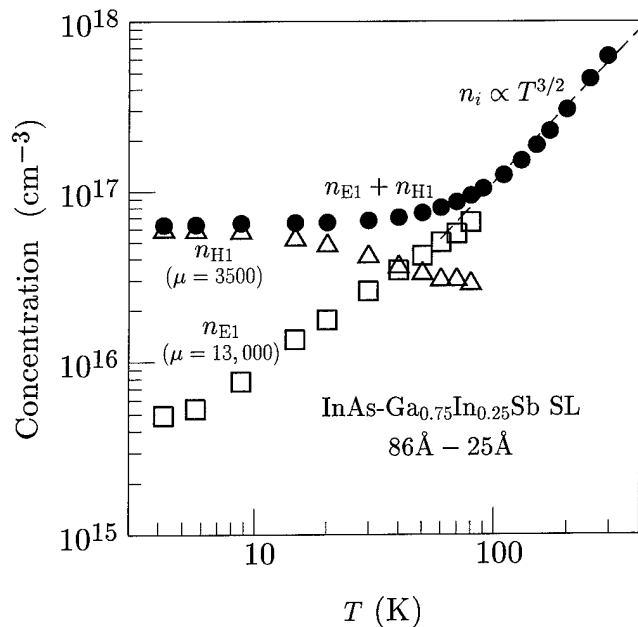
Fig. 4. Experimental densities vs temperature for the two coexisting electron species in the semimetallic superlattice. The dashed curve represents the $T^{3/2}$ dependence expected for the intrinsic regime.

system which has been described elsewhere.[20] The growth sequence consisted of a GaAs buffer layer, a two monolayer-two monolayer GaSb-GaAs super-lattice (ten periods), a GaSb buffer layer, the InAs-Ga$_{1-x}$In$_x$Sb superlattice (45–105 periods), and finally a 500Å GaSb cap layer. The Ga$_{1-x}$In$_x$Sb layers are believed to be terminated with InSb-like bonds, while the InAs layers are probably terminated with approximately equal fractions of InSb-like and

Ga$_{1-x}$In$_x$As-like bonds.[20] The middle of each InAs layer was doped with silicon, in order to assure that the superlattices had a net electron concentration in the mid-10^{16} cm^{-3} range. Layer thicknesses and compositions were determined from the growth parameters and x-ray diffraction data.

For each sample, the resistivity and Hall coefficient were measured as a function of magnetic field (B = 0 – 7 T) and temperature (T = 4.2–300K). Table I lists low-temperature electron densities and mobilities obtained from a mixed-conduction analysis of the field-dependent conductivity tensor.[21] At low temperatures, quantum oscillations were observed in the diagonal and Hall conductivities for all five samples, as will be discussed elsewhere. The table also lists the zero-temperature extrapolation of the energy gap, as determined from the temperature dependence of the intrinsic carrier concentration (n$_i$).[22] Note that the experimental values for E$_g$ agree well with the theoretical results from the eight-band calculation.

The points in Fig. 3 represent the experimental dependence of the electron mobility (μ_n) on InAs layer thickness. The variation in the four semiconducting samples is seen to be quite rapid. From a detailed analysis of the temperature-dependent and thickness-dependent data, it can be concluded that interface roughness scattering dominates the electron transport under nearly all conditions of interest for LWIR detectors (e.g., for all temperatures up to nearly 300K).[13] However, we note that $\mu_n(d_1)$ varies much more slowly than the $\mu_n \propto d_1^6$ dependence (dashed curve) calculated for an infinite square well[23] and observed experimentally in GaAs/Al$_x$Ga$_{1-x}$As,[23] HgTe-CdTe,[24] and InAs/AlSb[25] quantum wells. This is because the quantum wells are quite "leaky" due to the very thin Ga$_{1-x}$In$_x$Sb barriers in the present super-lattices. Hence, the variation of energy level with thickness fluctuation ($\partial E/\partial 9d_1$) is considerably weakened. Furthermore, we predict that the scattering rates should be sensitive to fluctuations in d$_2$ as well as those in d$_1$. The solid curve in Fig. 3 represents the results of a scaling calculation which employs $\partial E/\partial d_i$ from the band structure theory.[13] Agreement with the observed variation of $\mu_n(d_1)$ is seen to be excellent for the four semiconducting samples.

Note from Table I that theory yields a semimetallic band alignment for the superlattice with the thickest quantum wells (d$_1$ = 86Å), a prediction which is confirmed by the n$_i$(T) data. This sample differs from the others, in that the low-temperature mixed-conduction analysis indicates the presence of two different electron species. Furthermore, it is apparent from Fig. 3 that both mobilities fall far below the dependence on d$_1$ displayed by the semiconducting samples. Figure 4 plots the temperature-dependent concentrations for both species (open points), along with the total concentration (filled points). Note that while the density for the lower-mobility species is an order of magnitude greater at 4.2K, electrons are transferred to the higher-mobility species with increasing T, so that at 40K the two densities are approximately

equal. The total concentration remains essentially constant up to T ≈ 50K, after which it gradually begins to increase in a manner consistent with intrinsic generation. Eventually, the net density follows the T$^{3/2}$ dependence (dashed curve) expected for a semimetal displaying 3D dispersion.[21]

These observations are easily understood in terms of the semimetallic superlattice band structure. It was pointed out in the discussion of Fig. 1 that we actually expect the coexistence of two distinct electron populations: those occupying H1 states at $k_z < k_{zc}$ and those occupying E1 states at $k_z > k_{zc}$. The H1 states, which dominate at T → 0 because they lie at the bottom of the conduction band, should have a lower interface-roughness-limited mobility because $\partial E_{H1}/\partial d_2 > \partial E_{E1}/\partial d_1$ for the relevant layer thicknesses. However, increasing T should lead to thermal excitation of a greater fraction of the population into the higher-mobility E1 states. The total density ($n_{H1} + n_{E1}$) should naturally remain constant until the intrinsic temperature regime is reached. In the next section, it will be seen that the magneto-optical data similarly reflect the redistribution of electrons from H1 states to E1 states with increasing T.

MAGNETO-OPTICS

Two of the samples were studied by far infrared (FIR) magneto-optical experiments, in which the transmission of unpolarized radiation from a pumped gas laser source was measured in Faraday geometry (magnetic field and optical propagation both parallel to the growth axis). Figure 5 illustrates results for the semimetallic superlattice (86–25Å) at FIR photon energies of 3.28 and 17.6 meV and at several temperatures between 4.2 and 73K. At both photon energies, a single cyclotron resonance minimum is observed, which becomes shallower and broader with decreasing T. In fact, at $\hbar w = 3.28$ meV (and also at 10.4 meV), there is no distinct feature at all in the low-temperature limit. At $\hbar w = 17.6$ meV, the minimum moves to lower resonance fields (B_r) with decreasing T, particularly between 38 and 4.2 K.

These observations are qualitatively consistent with the calculated semimetallic band structure in a magnetic field (Fig. 2), and with the magneto-transport results for this superlattice discussed in the preceding section. At low temperatures, only states near the bottom of the band are occupied, i.e., the H1-like states at small k_z. (The wavefunctions for these electrons are concentrated primarily in the Ga$_{1-x}$In$_x$Sb layers!) We found from the mixed-conduction analysis that the H1-like electrons have an average mobility of only 3500 cm^2/Vs. Since one then has $\mu B_r < 1$ for the lower photon energy, it is not surprising that no distinct feature is observed at 4.2K. However, the transport results also indicated that the higher-mobility E1-like states (larger k_z) become increasingly populated as the temperature is raised. Figure 2 shows that these tend to have somewhat smaller cyclotron energies at a given field (or equivalently, larger B_r at a given $\hbar w$). Due to their higher mobility

(≈13,000 cm^2/Vs), the E1-like electrons exhibit a stronger and narrower cyclotron resonance. Note that at $\hbar w = 17.6$ meV, B_r continues to shift and sharpen as T is increased from 38K (where $n_{E1} \approx n_{H1}$) to 70K (where $n_{E1} \gg n_{H1}$). It should be pointed out, however, that even at 70K, the observed linewidth exceeds that expected from collision-broadening alone. This is probably a consequence of the mass-broadening phenomenon discussed in the section on band structure theory, since it is apparent from Fig. 2 that the cyclotron energy varies significantly with k_z (particularly for 0 → 1E transitions).

We also performed FIR magneto-transmission experiments on the semiconducting superlattice with $d_1 = 54$Å, which displayed a considerably larger electron mobility at low T (17,000 cm^2/Vs). Preliminary spectra at 4.2K yielded three distinct peaks, corresponding to cyclotron masses (m_{CR}) of 0.017, 0.028, and 0.061 m_0. While the lowest-field feature is believed to correspond to cyclotron resonance by majority electrons occupying the interior of the superlattice, the other lines have not yet been positively identified (electron mass broadening should be relatively insignificant in the semiconducting regime). Further experiments as a function of temperature, circular polarization, and field angle would clarify the interpretation.

Quantitative comparisons between the theoretical and experimental results for the electron cyclotron masses are presented in Table I. A range of values are given for the 86Å sample, since the spectra in Fig. 5 did not yield a single resonance field, and since the theoretical m_{CR} in a semimetallic superlattice varies considerably with Landau index and with k_z (see Fig. 2). Although the experimental values are approxi-
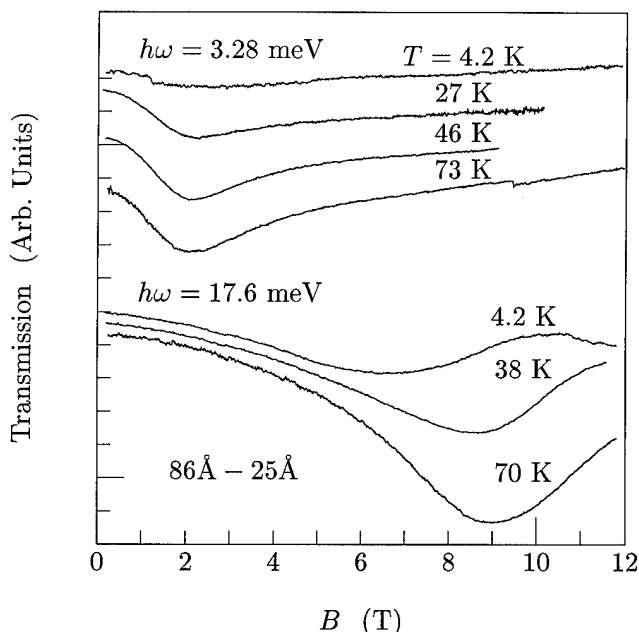
Fig. 5. Experimental magneto-transmission vs magnetic field for the semimetallic superlattice at two FIR photon energies and several temperatures.

mately 1.5 times higher than the theoretical predictions, both span ranges of roughly a factor of two. Theory and experiment also agree that at the relevant magnetic fields, m_{CR} should be smaller in the semiconducting 54Å sample than in the semimetallic sample. In fact, the measured value of 0.017 m_0 (which agrees with theory to within $\approx 10\%$) represents the first experimental confirmation that the strong E1-H1 interactions in Type-II superlattices with small positive energy gaps can lead to cyclotron masses smaller than the bulk values in either of the constituents. This would not occur in a Type-I heterostructure. The table shows that the theoretical m_{CR} monotonically increase with energy gap in the semiconducting regime. Previous experiments have yielded m_{CR} (0.030 ± 0.003)m_0 for InAs-Ga$_{1-x}$In$_x$Sb superlattices with $E_g \approx$ 120 meV.[26]

DISCUSSION

We have demonstrated that due to a significant overlap of the E1 and H1 wavefunctions in narrow-gap Type-II heterostructures with thin layers, the dispersion relations for InAs-Ga$_{1-x}$In$_x$Sb superlattices are strikingly similar to those for Hg-based heterostructures. As a consequence, one expects to reproduce a number of novel phenomena which are known to occur in the HgTe-CdTe system. On the other hand, the calculated band structures differ dramatically from results for InAs-GaSb superlattices (with thick GaSb layers), which have much more in common compositionally with InAs-Ga$_{1-x}$In$_x$Sb but are characterized by weak E1-H1 interactions.

We have further demonstrated that any meaningful interpretation of the experimental magneto-transport and magneto-optical properties must fully account for the special features of the HgTe-CdTe-like band structures. This applies particularly to the semimetallic regime, for which theory predicts the coexistence of electrons occupying both H1-like and E1-like states. We find that the field-dependent Hall and resistivity data for a semimetallic superlattice confirm the presence of two different electron species, whose temperature-dependent densities and mobilities vary as one would expect for H1 and E1 carriers. Also observed is that the slope of $\mu_n(d_1)$ changes abruptly at the transition from a semiconductor (in which all electrons occupy E1) to a semimetal (in which most occupy H1 at low T). This is related to the lower interface-roughness-limited mobility for H1-like electrons. While the magneto-transmission spectra for the semimetallic sample display at most a broad, weak cyclotron resonance feature when the electrons occupy H1-like states at 4.2K, the data indicate a thermal activation into higher-mobility E1-like states with increasing T. The experiments also confirm the tendency of the strong E1-H1 interactions to decrease the in-plane mass to a value below that in the bulk constituent materials.

While the present work has focused primarily on the similarities between III/V strained-layer superlattices and the better-known Hg-based alloys

and heterostructures, there are naturally differences between the two systems as well. It is useful to consider briefly how some of those differences may impact on the performance of InAs-Ga$_{1-x}$In$_x$Sb superlattices as LWIR detector materials. First, because the relevant d_1 and d_2 are thin, interface roughness scattering dominates the free-carrier transport under nearly all conditions of interest. The in-plane electron and hole mobilities, therefore, tend to be somewhat smaller than those in Hg-based heterostructures with the same energy gaps, although μ_p is higher than in the Hg$_{1-x}$Cd$_x$Te alloy.[22] Since it is the mobility along the vertical axis which will govern the minority-carrier collection efficiency in mesa diodes, experiments are now being initiated to study growth-direction transport. InAs-Ga$_{1-x}$In$_x$Sb and HgTe-CdTe superlattices share the advantage that the growth-direction mass is several times larger than that in LWIR Hg$_{1-x}$Cd$_x$Te, which may ultimately lead to significantly lower tunneling noise in PV detectors.[1]

We finally point out that even in terms of band structure, there is one significant difference between InAs-Ga$_{1-x}$In$_x$Sb and HgTe-CdTe superlattices: whereas the in-plane valence-band dispersion for HgTe-CdTe is extremely nonparabolic (m_p tends to become quite heavy or even negative within ≈ 20 meV of the valence band maximum),[6] m_p in InAs-Ga$_{1-x}$In$_x$Sb remains relatively parabolic over a significant energy range (compare Figs. 1 and 2 of Ref. 6 with the present Fig. 1). The nonparabolicity results primarily from interactions with the L1 band, which is close to the valence band maximum in HgTe-CdTe but lies at a much lower energy in the present system due to greater strain and quantum confinement shifts. This has the very important practical consequence of suppressing Auger recombination in InAs-Ga$_{1-x}$In$_x$Sb superlattices.[12,27] The large hole-to-electron mass ratio in Hg$_{1-x}$Cd$_x$Te alloys (≈ 100) represents a worst case, in that it optimizes the conservation of both momentum and energy in the Auger process. In a HgTe-CdTe superlattice, the situation may be improved somewhat[4] by the light in-plane hole mass near the valence band maximum, although one must take care not to introduce a resonance between the energy gap and the H1-L1 splitting.[27] However, the nearly parabolic hole mass and large H1-L1 splitting in InAs-Ga$_{1-x}$In$_x$Sb superlattices are ideal for minimizing Auger recombination. We have recently demonstrated experimentally that the Auger lifetime in an LWIR InAs-Ga$_{1-x}$In$_x$Sb superlattice at 77K is two orders of magnitude longer than that in the Hg$_{1-x}$Cd$_x$Te alloy with the same energy gap.[12] This finding is consistent with theoretical predictions by Grein et al.[27] and has favorable implications for the ultimate performance of InAs-Ga$_{1-x}$In$_x$Sb LWIR detectors.

ACKNOWLEDGMENT

REFEENCES

1. D.L. Smith. T.C. McGill and J.N. Schulman, *Appl. Phys. Lett.* 43, 180 (1983).
2. T.H. Myers, J.R. Meyer, C.A. Hoffman and L.R. Ram-Mohan, *Appl. Phys. Lett.* 61, 1814 (1992).
3. K.A. Harris, T.H. Myers, R.W. Yanka, L.M. Mohnkern and N. Otsuka, *J. Vac. Sci. Technol.* B 9, 1752 (1991).
4. A.R. Reisinger, K.A. Harris, T.H. Myers R.W. Yanks, L.M. Mohnkern and C.A. Hoffman, *Appl. Phys. Lett.* 61, 699 (1992).
5. L. Esaki, *Proc. 17th Int. Conf. Phys. Semicond.* (San Francisco, 1984), p. 473.
6. J.R. Meyer, C.A. Hoffman and F.J. Bartoli, *Phys. B* 191, 171 (1993).
7. G.A. Sai-Halasz, L. Esaki and W.A. Harrison, *Phys. Rev. B* 18, 2812 (1978).
8. M. Altarelli, *Phys. Rev. B* 28, 842 (1983).
9. G. Grosso, S. Moroni and G. Pastori Parravicini, *Phys. Rev. B* 40, 12328 (1989).
10. D.L. Smith and C. Mailhiot, *J. Appl. Phys.* 62, 2545 (1987).
11. R.H. Miles, D.H. Chow, J.N. Schulman and T.C. McGill, *Appl. Phys. Lett.* 57, 801 (1990).
12. E.R. Youngdale, J.R. Meyer, C.A. Hoffman, F.J. Bartoli, R.H. Miles and D.H. Chow, *J. Vac. Sci. Technol.* B 12, 1129 (1994).
13. C.A. Hoffman, J.R. Meyer, E.R. Youngdale, F.J. Bartoli and R.H. Miles, *Appl. Phys. Lett.* 63, 2210 (1993).
14. J.R. Meyer, R J. Wagner, F.J. Bartoli, C.A. Hoffman, M. Dobrowolska, T. Wojtowicz, J.K. Furdyna and L.R. Ram-Mohan, *Phys. Rev. B* 42, 9050 (1990).
15. *Landolt-Börnstein, Numerical Data and Functional Relationships in Science and Technology,* ed. O. Madelung, (Berlin: Springer, 1982), Gp. III, Vol. 17.
16. G.J. Gualtieri, G P. Schwartz, R.G. Nuzzo, R.J. Malik and J.F. Walker, *J. Appl. Phys.* 61, 5337 (1987).
17. N.F. Johnson, P.M. Hui and H. Ehrenreich, *Phys. Rev. Lett.* 61, 1993 (1988).
18. J. Shen, S.Y. Ren and J.D. Dow, *Phys. Rev. B* 46, 6938 (1992).
19. J.R. Meyer, R.J. Wagner, F.J. Bartoli, C.A. Hoffman and L.R. Ram-Mohan, *Phys. Rev. B* 40, 1388 (1989).
20. R.H. Miles, D.H. Chow and W.J. Hamilton, *J. Appl. Phys.* 71, 211 (1992).
21. J.R. Meyer, C.A. Hoffman, F.J. Bartoli, D.J. Arnold, S. Sivananthan and J.P. Faurie, *Semicond. Sci. Technol.* 8, 805 (1993).
22. J.P. Omaggio, J.R. Meyer, R.J. Wagner, C.A. Hoffman, D.H. Chow, R.H. Miles and M.J. Yang, *Appl. Phys. Lett.* 61, 207 (1992).
23. H. Sakaki, T. Noda, K. Hirakawa, M. Tanaka and T. Matsusue, *Appl. Phys. Lett.* 51, 1934 (1987).
24. J.R. Meyer, D.J. Arnold, C.A. Hoffman and F.J. Bartoli, *Appl. Phys. Lett.* 58, 2523 (1991).
25. C.R. Bolognesi, H. Kroemer and J.H. English, *Appl. Phys. Lett.* 61, 213 (1992).
26. J.P. Omaggio, R.J. Wagner, J.R. Meyer, C.A. Hoffman, M.J. Yang, D.H. Chow and R.H. Miles, *Semicond. Sci. Technol.* 8, S112 (1993).
27. C.H. Grein, P.M. Young and H. Ehrenreich, *Appl. Phys. Lett.* 61, 2905 (1992).

Photoresponse Study of Normal Incidence Detection in p-Type GaAs/AlGaAs Multiple Quantum Wells

G.J. BROWN

Wright Laboratory, Materials Directorate, WL/MLPO, Wright Patterson AFB, OH 45433-7707

F. SZMULOWICZ and S.M. HEGDE

University of Dayton Research Institute, Dayton, OH 45469-0178

We studied p-type GaAs/AlGaAs multiple quantum well (MQW) materials as a possible alternative to the current n-type GaAs/AlGaAs MQWs for infrared detection. The advantage of p-type MQWs is that absorption of infrared radiation at normal incidence is not selection rule forbidden as it is for the n-type. We have verified that significant photoresponse occurs at normal incidence in p-type MQWs. We studied changes in the photoresponse spectrum as a function of well width and temperature. The MQW heterostructures were designed to use bound to continuum intersubband absorption in the GaAs valence band and to have a peak photoresponse near 8 μm. The photoresponse spectrum was compared to the first theoretical model of the bound to continuum absorption in p-type GaAs/AlGaAs MQWs. The theoretical absorption curve was found to be in good qualitative agreement with the experimental results.

Key words: GaAs/AlGaAs multiple quantum well (MQW), infrared detectors, intersubband absorption, quantum well infrared photodetector (QWIP)

INTRODUCTION

Considerable progress has been made in the last ten years in the development of multiple quantum well (MQW) heterostructures for long-wavelength (8–12 μm) infrared detection.[1] In these quantum well infrared photodetectors (QWIPs), intersubband transitions are used to photo-excite an electron from a filled ground state to a higher subband state near the top of the quantum well. The III-V based QWIPs are of increasing interest due to the capability of producing large area, high uniformity, two-dimensional (2D) imaging arrays. Most previous work was focused on n-type (donor doped) GaAs/AlGaAs multiple quantum wells since the lower effective mass of the electron should lead to superior transport properties.[1,2] How-ever, for these n-type QWIPs intersubband transitions are dipole selection rule limited to couple only to infrared radiation with a polarization component perpendicular to the quantum wells (i.e. normal incidence absorption is forbidden).[3] This limitation leads to the use of gratings or 45° facets to bend the incident radiation such that it enters the quantum well stack with a polarization component in the growth direction (z polarized). Although excellent results have been obtained for n-type QWIPs with etched gratings, the gratings increase the number of process steps and add the complication of grating uniformity over a large 2D array. An alternative approach is to use p-type (acceptor doped) QWIPs for which the intersubband selection rules intrinsically allow normal incidence absorption.

In p-type GaAs/AlGaAs multiple quantum well materials, there is strong mixing of the valence bands,
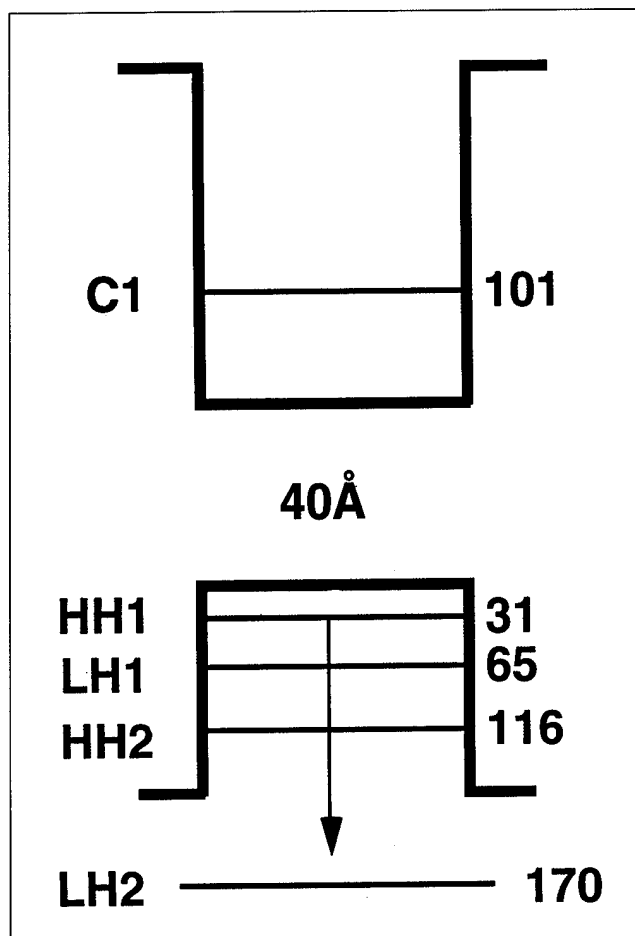
Fig. 1. Schematic energy-band diagram ($k_\parallel = 0$) for the 40Å well p-type QWIP.

especially with the conduction band, which imparts an additional s-like symmetry (at $k_\parallel \neq 0$) to the normally p-like valence band wave functions. Transitions between subbands with s-like and p-like symmetry components are not forbidden by symmetry-related quantum mechanical selection rules such that absorption of normal incidence radiation (x or y polarized) is allowed. This desirable normal incidence photo-excitation of p-type quantum well infrared photo-detectors was studied only recently.[4,5] However, the exact nature of the optical transition involved has proven difficult to model. For instance, most reports describe the photoresponse as due to a transition from the first heavy hole state to extended states in the continuum. These extended states, proposed to be just above the quantum well barrier, have been attributed to either a heavy-hole-like subband or a light-hole-like subband.[4-6] While the first heavy hole (HH1) to second light hole (LH2) transition would have a large optical matrix element, our calculations indicate that the resonant LH2 subband is too far above the top of the well to efficiently couple to the localized HH1 state for these well widths.[7] Therefore, we decided to investigate the exact nature of the intersubband transitions involved in these p-type QWIPs. As part of this study, the photoresponse was

measured as a function of well width in 5Å increments.

The p-type QWIPs reported here were made from 50 period multiple quantum well structures with either 30, 35, or 40Å well widths and 500Å barrier widths. The GaAs wells were beryllium doped to p = 1×10^{18} cm^{-3} with a 5Å offset between the dopant and the interfaces. The barrier layers were composed of undoped $Al_{0.3}Ga_{0.7}As$. This MQW stack was sandwiched between two GaAs contact layers which were also beryllium doped to p = 1×10^{18} cm^{-3}. These three MQW structures were grown by molecular beam epitaxy on three inch GaAs substrates. A schematic energy band diagram (at $k_\parallel = 0$) of the 40Å QWIP is shown in Fig. 1. The energy subbands are labeled according to the symmetry properties of the eigenstates at zone center (HH for heavy-hole-like and LH for light-hole-like states). Since the second light hole subband is about 20 meV above the top of these wells, we decided to model the transition from a bound state to the continuum of states above the barriers in addition to any resonant subband state in this continuum using a state-of-the-art 8 × 8 EFA model.

THEORY

The present calculation is the first attempt at modeling bound-to-continuum absorption in p-type quantum wells. The electronic structure, wave functions, and optical matrix elements were obtained from an 8 × 8 envelope-function approximation (EFA) calculation.[8] In this approach, the total wave function for both bound and continuum states is expanded as a linear combination of envelope functions multiplied by the Bloch wave functions at the center of the bulk Brillouin zone in the barrier and well materials. In our 8 × 8 EFA, eight bands—heavy-hole (HH), light-hole (LH), spin-orbit split off hole (SH), and conduction (C)—were taken explicitly into account in expanding the wave functions for the quantum wells, resulting in eight-component envelope functions. In particular, it was important to incorporate the coupling of the LH states to the C band because it imparts an s-like character to the nominally p-like valence band states, which makes dipole transitions between valence band subbands possible at normal incidence.

The calculation for the bound and continuum states proceed independently, owing to the different boundary conditions satisfied by these states. First, the Hermitian EFA boundary conditions are set up for the bound states as a function of the momentum parallel to the well walls. Unlike continuum states, each component of bound state wave functions decays under the barrier. Once bound state eigenvalues are identified, the corresponding wave functions are calculated and their band content is examined. At the center of the Brillouin zone, various subbands can be classified as either HH, LH, SH, or C. Away from the Brillouin zone center, the bands are coupled and acquire a mixed character. This gives rise to avoided crossings and nonparabolicities of the resulting bands. As importantly, there is an admixture of the conduc-

tion band content into the valence band subbands. Figure 2 shows the calculated band dispersions for a 35Å GaAs/Al$_{0.30}$Ga$_{0.70}$As quantum well as a function of the parallel momentum. The ground state subband is labeled as HH1 and is followed by subbands LH1 and HH2, which is located near the top of the well. Note that the bands are characterized by large nonparabolicities. In fact, the LH1 band first curves upward, resulting in an electron-like curvature.

For the range of doping used in our MQWs, only the lowest subband (HH1) is occupied by holes. In order to calculate the extent of hole filling of the ground-state subband, the density of states, Fig. 3, and the integrated density of states were obtained based on the energy bands of Fig. 2. The density of states gives the number of energy states per unit energy interval available for hole occupancy of the energy bands. Bands HH1 and HH3 produce step-like onsets at about −37 and −131 meV while the LH1 band produces the logarithmic singularity at about −73 meV which is the result of its electron-like curvature in Fig. 2. Integrating the density of states results in the integrated density of states of Fig. 4, which gives the sheet density as a function of the band filling, from which one can read off the Fermi level directly.

Continuum states are obtained in the second step of the calculation. It must be pointed out that we do not use an artificial large box to enclose the whole system in order to create two extra boundaries to confine the continuum wave functions, thus creating an extra quantization condition. By avoiding this stratagem, we are the first to treat this problem as a true continuum problem.

We do this as follows. At an energy greater than the well height, we select states that can propagate in the barrier (i.e., have real momenta and thus do not decay). For the energy range of interest to our study, these states are either heavy-hole or light-hole like. Due to Kramer's degeneracy, there are two HH and

two LH positive-going states in the barrier and the like number of negative-going states at a given energy and parallel momentum. For convenience, these states were superposed to be either even or odd with respect to the reflection in the plane through the middle of the well. Upon hitting the well, an incident state that is of either HH or LH character is partially scattered back and partially transmitted as a mixture of all eight states in the model. The exact admixture is determined by solving the appropriate boundary condition matrix for the scattering problem (further details will be the subject of a separate paper). This approach is capable of yielding not only regular continuum states but also resonant states in the continuum.

Next, the wave functions for the bound and excited states are used to obtain the requisite matrix element of momentum which governs the strength of optical transitions between the filled states in the well and the continuum states in the barrier. The required matrix elements were obtained using an extension of the formalism of Chang and James[9] to the case of finite barriers and of an 8×8 EFA (the extension will be the subject of a separate paper).[10]

The last step in the calculation is the linear absorption coefficient. The linear absorption coefficient is an integral over the initial and final states weighted by the matrix element of momentum squared be-

Fig. 3. The density of states corresponding to Fig. 2.

Fig. 2. The calculated energy bands for 35Å GaAs/Al$_{0.3}$Ga$_{0.7}$As quantum well as a function of the parallel momentum (Bohr radius = 0.529177Å). Counting from the top, the bands are HH1, LH1, and HH2. The zero of energy is at the top of the valence band of bulk GaAs. We use a 60/40 conduction-to-valence band offset ratio. The well depth is −149.6 meV.
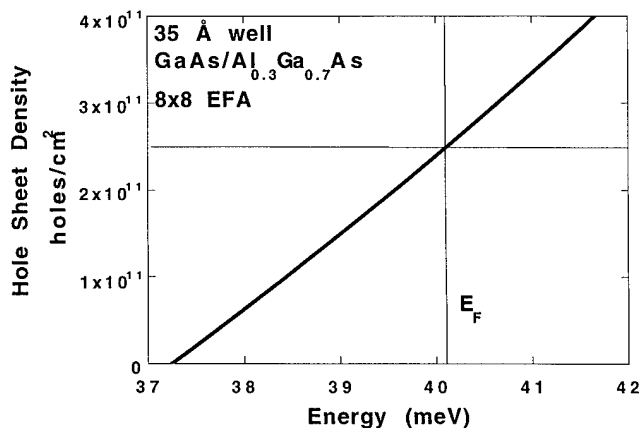
Fig. 4. Low-energy detail of the integrated density of states showing the position of the Fermi level for the sheet density used in this work.
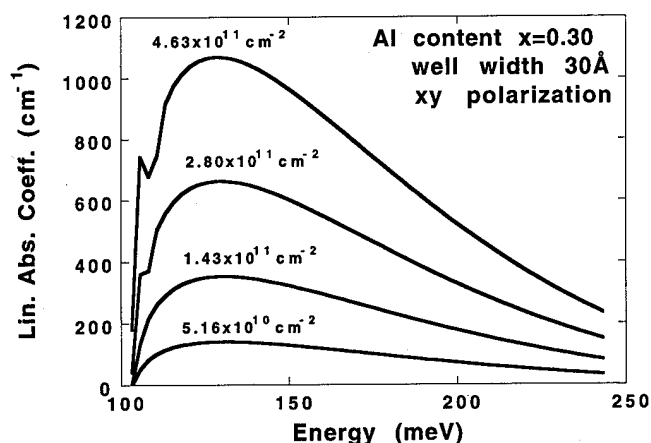
Fig. 5. The calculated linear absorption coefficient for the 30Å well as a function of energy at normal incidence (x-y polarization) for several hole sheet densities. Exchange energy corrections were not applied.
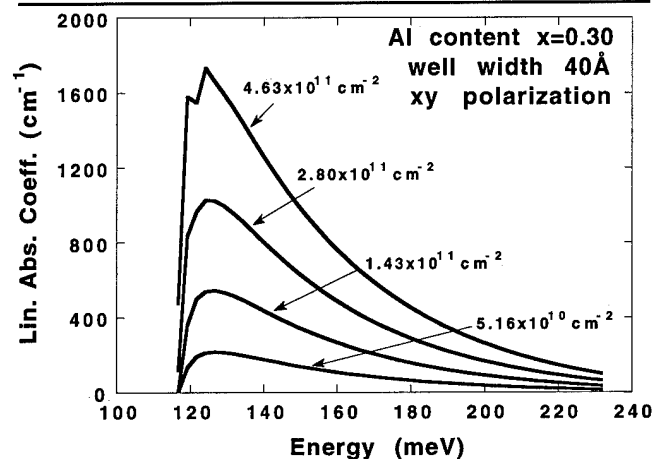
Fig. 6. The calculated linear absorption coefficient for the 40Å well as a function of energy at normal incidence (x-y polarization) for several hole sheet densities. Exchange energy corrections were not applied.

tween these states. The conservation of energy is ensured by an energy delta function and the conservation of momentum only allows transitions between bound and continuum states of the same parallel momentum. The density of final states is obtained from the derivative of the continuum state energy with respect to the incident wave momentum.

Figures 5 and 6 display the calculated linear absorption coefficient for 30 and 40Å wells, respectively, as a function of photon wavelength and doping in the well. Only absorption for x-polarized light (normal incidence) is shown (z-polarization will be the subject of a separate paper).[10] Clearly, the higher the doping, the stronger the absorption. Mathematically, higher doping necessitates integration to higher parallel momenta in the ground state band. The absorption for the 30Å well is broad and featureless. For the 40Å well, the peak absorption moves toward the long-wavelength threshold and exhibits some structure. This structure is related to the fact that at higher k-parallel values (which come in at higher doping), near the absorption threshold, the LH states are nonpropagating (that is, correspond to decaying states) and only HH states are propagating in the barrier.
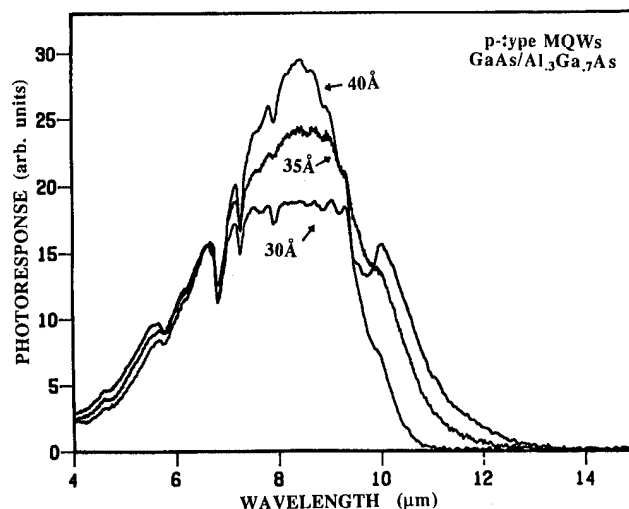
Fig. 7. Comparison of the normal incidence photoresponse spectra for the 30, 35, and 40Å well width multiple quantum well materials, at T = 9 K and V_b = +2.6 V.

We also estimated the size of possible many-body effects on the position of the peaks in the calculated spectrum. Because of the extended nature of the continuum states (which gives rise to a small overlap between the ground and continuum state wave functions), the depolarization and exciton shifts are expected to be small.[11] However, we estimate the exchange energy for the HH1 ground state to be on the order of -12.4 and -15.2 meV for the 30 and 40Å wells, respectively.[12] This would shift the long-wavelength cutoff from 11.8 to 10.6 μm for the 30Å well and from 10.5 to 9.3 μm for the 40Å well. The calculated spectra were not broadened.

RESULTS AND DISCUSSION

The photoresponse vs wavelength was measured using a Fourier transform spectrometer. The measured response is not a quantitative responsivity measurement, but it allows a qualitative comparison of different samples run under the same conditions or of the same sample run under different conditions such as temperature and bias. The measurements were made on 5 by 5 mm etched mesas using the top and bottom contact layers to vertically bias the MQW stack. It should be noted that the absorption bands on the photoresponse spectra are due to the vacuum grease that was used to mount the samples on the coldfinger of the cryostat.

Normal incidence photoresponse was verified in all three of the p-type MQW heterostructures studied (Fig. 7). The energy that corresponds to the peak response for each of these wells does not match the transition energy for a HH1 (bound) to LH2 (resonant) intersubband transition. For instance, in the 35Å well the energy of the peak response is 144 meV (λ_p = 8.6 μm) while the calculated HH1-LH2 transition energy is 202 meV. A peak response at 144 meV would correspond to transitions close to the top of the well. This agrees closely with the theoretical absorption coefficient spectrum for transitions to the con-

tinuum which similarly peak within a few meV above the top of the wells. Not only does the photoresponse peak position match closely the theoretical results but also the shape of the photoresponse spectrum. Figure 8 shows the calculated linear absorption coefficients for the 30, 35, and 40Å wells at hole sheet densities close to those used in the samples studied. The absorption in the 40Å well is stronger and narrower than for the 30Å well. The increase in the strength and in the narrowness of the absorption indicates the distant approach of the resonant state related to the LH2 band toward the top of the well. Similarly, the photoresponse study found that the 40Å response was narrower and had a higher peak intensity than the 30Å well. The shift of the photoresponse cut-off wavelength to longer wavelengths also matches the shift in the calculated absorption onsets. These shifts reflect the movement of the HH1 state to higher energies as the well width decreases.

Photoluminescence (PL) studies were also made on the three p-type MQW materials, with the top contact layer etched off. The PL peaks associated with the HH1 to C1 transitions for each of the three well widths are shown in Fig. 9. As expected, the PL peaks shift to higher energy as the well width is narrowed due to shifting of the C1 and HH1 states to higher energies. However, the double peaks for the 30 and 35Å wells were not anticipated. The cause of these double peaks is still under study. One possible explanation for these double peaks is that the interfaces are rough causing the well width to vary. This possible variation in the well widths also correlates with x-ray diffraction results which had the largest uncertainty for the 35Å well width.

To compare the photoresponse from the p-type materials to the more familiar n-type MQWs, two n-type samples were grown as part of the sample set. A comparison of the normal incidence photoresponse spectrum of a n-type MQW to that of a p-type is shown in Fig. 10. While the n-type peaked at a slightly longer

wavelength, it can still be seen that the peak photoresponse of the p-type MQW is about four times stronger than the n-type. This residual normal incidence photoresponse in n-type MQWs has been previously reported and was attributed to optical scattering and mesa edge coupling.[4] The n-type response tends to increase by an order of magnitude when a 45° facet is used to couple in the incident light.[4] Even with this order of magnitude increase in the n-type response, the p-type response at normal incidence still compares favorably. This is especially notable since the n-type samples were designed to have a C2 extended state near the top of the conduction band well.

The photoresponse spectra were also studied as a function of temperature. For all three of the p-type samples, the magnitude of the photoresponse decreased with increasing temperature from 9 to 80K (Fig. 11). This decrease in signal is more rapid than can be accounted for by significant thermionic emission of holes out of the well. Some process with a lower activation energy must be responsible. Arrhenius fits to the photoresponse peak intensity vs temperature
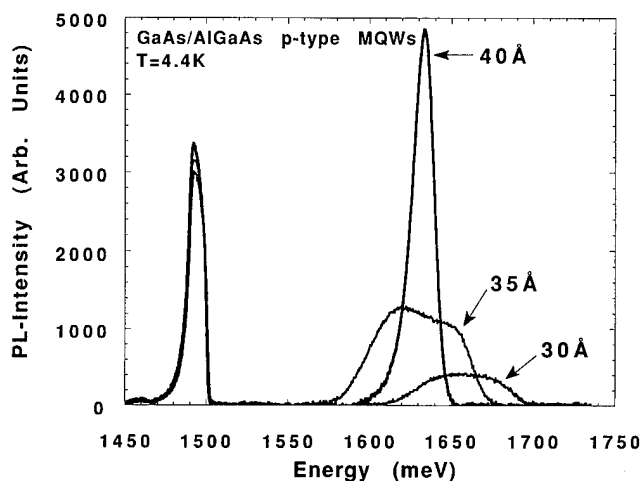
Fig. 9. A comparison of the photoluminescence spectra for the 30, 35, and 40Å MQW materials, with the top contact etched off.
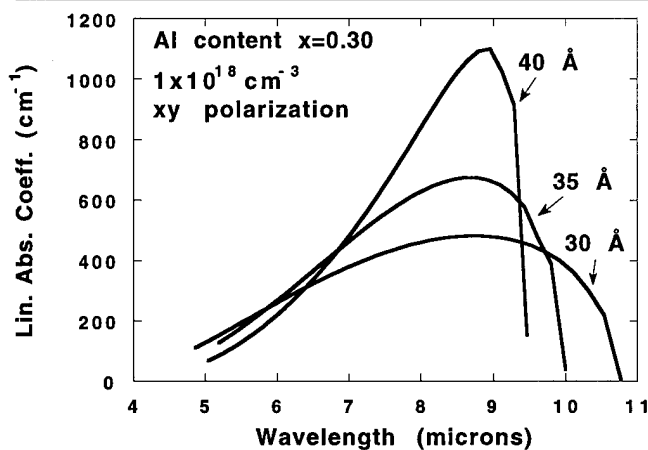
Fig. 8. The calculated linear absorption coefficient for the three well widths corresponding to the experimentally measured p-doped MQWs at normal incidence as a function of photon wavelength. The doping concentration is 10^{18} cm⁻³ and exchange energy corrections were made.
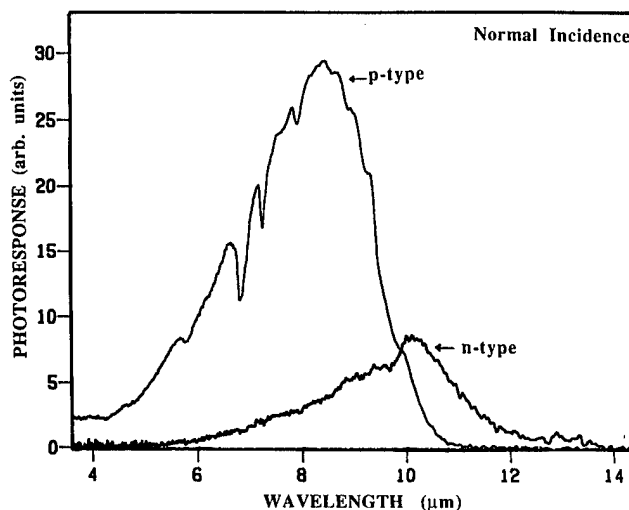
Fig. 10. Comparison of the normal incidence photoresponse spectra for a p-type and an n-type GaAs/AlGaAs MQW, at T = 9K and V_b = +2.6.
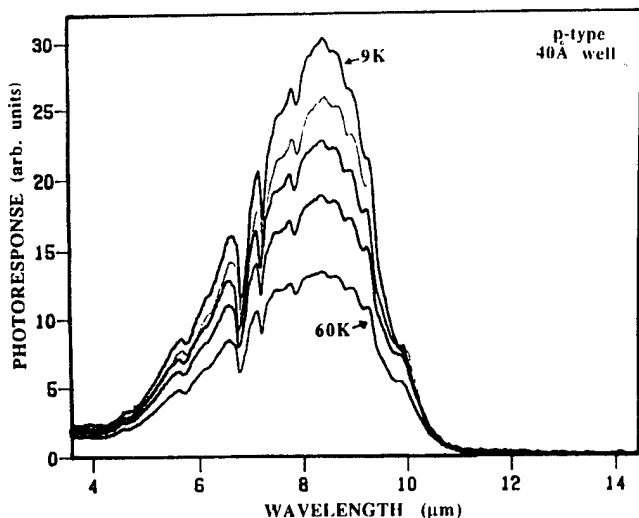
Fig. 11. The photoresponse spectra of the 40Å well MQW at various temperatures: T= 9, 30, 40, 50, and 60K.
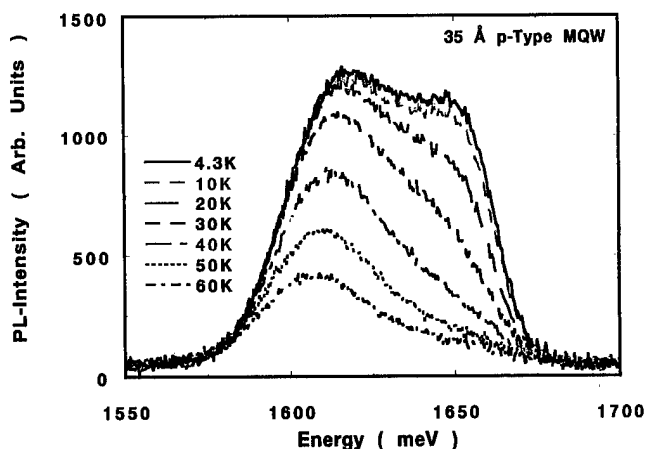
Fig. 12. Temperature dependence of the photoluminescence peak intensities for the 35Å well MQW from 4.3 to 60K.

gave an activation energy of about 25 meV. The nature of this low activation energy is still under study. Interestingly, the PL peaks show a similar rapid decrease in intensity in this temperature range (Fig. 12). Note the difference in the temperature dependence of the two PL peaks associated with the 35Å well. The higher energy peak disappears at higher temperatures and is associated with the dominant quantum well HH1-C1 transition. In any case,

the poor temperature dependence of these MQWs indicates that these materials could be further improved under more optimum growth conditions.

CONCLUSIONS

Normal incidence photoresponse was verified in the p-type GaAs/AlGaAs multiple quantum well materials studied. The p-type photoresponse was much stronger than the normal incidence photoresponse of the n-type quantum wells studied. We have determined that the p-type photoresponse for the 30 to 40Å well widths is not solely due to a transition to a resonant excited state in the continuum. We have developed the first 8×8 EFA calculation for transitions to continuum states which accurately models the bound to continuum absorption in these p-type materials. The calculated linear absorption coefficient curves are in good qualitative agreement with the experimental photoresponse results.

Although these initial results are promising, these materials could be further improved by designing a resonant excited state to be just above the top of the well. This would greatly increase the optical absorption coefficient. Also, the mechanism for the observed temperature dependence in the quantum wells needs further study in order to determine optimized growth conditions.

REFERENCES

1. B.F. Levine, J. Appl. Phys. 74, R1 (1993).
2. B.F. Levine, A. Zussman, S.D. Gunapala, M.T. Asom, J.M. Kuo and W.S. Hobson, J. Appl. Phys. 72, 4429 (1992).
3. L.C. West and S.J. Eglash, Appl. Phys. Lett. 46, 1156 (1985).
4. B.F. Levine, S.D. Gunapala, J.M. Kuo, S.S. Pei and S. Hui, Appl. Phys. Lett. 59, 1864 (1991).
5. J.M. Kuo, S.S. Pei, S. Hui, S.D. Gunapala and B.F. Levine, J. Vac. Sci. Technol. B 10, 995 (1992).
6. P. Man and D.S. Pan, Appl. Phys. Lett. 61, 2799 (1992).
7. H. C. Liu, J. Appl. Phys. 73, 3062 (1993).
8. See Gerald Bastard, Wave Mechanics Applied to Semiconductor Heterostructures (New York: Halstead, 1988).
9. Y.C. Chang and R.B. James, Phys. Rev. B39, 12672 (1989).
10. F. Szmulowicz, Phys. Rev. B 51, 1613 (1995); and F. Szmulowicz and G.J. Brown, Phys. Rev. B 51 (15 May 1995).
11. S.K. Chun, D.S. Pan, and K.L. Wang, Phys. Rev. B 47, 15, 639 (1993).
12. K.M.S.V. Bandara, D.D. Coon, O. Byungsung, Y.F. Lin and M.H. Francombe, Appl. Phys. Lett. 53, 1931 (1988); see also Erratum, Appl. Phys. Lett. 55, 206 (1989).

Process Modeling and Simulation for Hg$_{1-x}$Cd$_x$Te. Part I: Status of Stanford University Mercury Cadmium Telluride Process Simulator

JOSÉ L. MELÉNDEZ* and C.R. HELMS

Department of Electrical Engineering, Stanford University, Stanford, CA 94305

Details are provided concerning the basic point defect parameter set of the Stanford University mercury cadmium telluride process simulator (SUMerCad). The Hg interstitial and vacancy parameters are presented and justified for x = 0.2 material. In particular, values for the thermodynamic limits, diffusion coefficients, recombination rates, generation rates, and boundary conditions are specified and their determination methodology is reviewed. The parameters have been determined for overall consistency with a specific pool of experimental results which include studies of Hg self-diffusion, type-conversion, and the existence region. Our presentation will review the current state of the Hg$_{1-x}$Cd$_x$Te modeling effort, and outline the future direction of the simulator, providing examples and discussion. Finally, some issues related to the future development of SUMerCad are discussed, including electric field effects, general boundary conditions, alternative junction formation processes, extended defects, and interdiffusion.

Key words: Diffusion, HgCdTe, modeling, simulation

INTRODUCTION

The Stanford University mercury cadmium telluride process simulator (SUMerCad) is a design tool intended to facilitate the development of advanced infrared technologies by enhancing our understanding of the fundamental mechanisms involved in the formation of modern device structures and increasing the accessibility of this information. SUMerCad is based upon intuitive, physical ideas translated into a fully descriptive kinetics framework which captures the essence of the underlying mechanisms involved in the various processes required to form viable device structures. The solutions translate the mathematical descriptions into tangible information of significant value to the process engineer. Based upon sound physics, chemistry, thermodynamics, and kinetics, the modeling approach lends itself well to extension, rather than merely extrapolation, beyond the basic set of experiments necessary to establish parameter

values. SUMerCad is projected to reduce the development time of modern, sophisticated focal plane arrays, yielding substantial cost savings. In addition, a comprehensive process simulator for Hg$_{1-x}$Cd$_x$Te will be critical for cost effective development of systems for new or specialized applications, which have traditionally been cost prohibitive.

A year ago, we established the foundation for the development of a comprehensive and self-consistent modeling methodology to be applied to the Hg$_{1-x}$Cd$_x$Te system.[1] Initial, qualitative results supported the implementation of a descriptive framework based upon a reaction kinetics formalism of point-defect processes. Since our initial work, we have succeeded in determining a definitive parameter set by fits to a specific pool of experimental results.[2–11] Simulations extended beyond this experimental basis have agreed well with additional and subsequent experimental data, making no adjustments to the basic parameter set necessary. In this report, we will summarize the current status of our modeling effort, presenting examples illustrative of the power of SUMerCad as a predictive tool. The basic parameter set will be pre-

sented and justified. In addition, the future direction of development of the simulator will be discussed.

PARAMETER SET AND DEVELOPMENT

The basic reaction kinetics description is defined by point-defect diffusion coefficients, as well as thermodynamic, interaction, and boundary condition parameters.[1,12] These values have been determined as a function of temperature for consistency with a variety of experimental investigations.[2,5,9] Experiments are currently underway to extract the defining parameters for cation impurities.[7] While these results emphasize x = 0.2 material, experimental studies are available which allow the determination of some of the parameters as a function of x-value.[1,4,13–16] In fact, we have already established the framework necessary to model interdiffusion, heterostructure stability issues, and epitaxial growth, though additional development and experiments will be necessary to provide the information necessary to establish the model parameters for these complicated systems.[12] Such studies are critical for the establishment of a complete $Hg_{1-x}Cd_xTe$ simulator. In this section, some of the important parameter values representing the basic point-defect interactions and motion will be presented and the determination methodology will be discussed. The bulk parameters are defined by the set of continuity equations representing the first order reaction kinetics,

$$\frac{\partial i}{\partial t} = D_i \frac{\partial^2 i}{\partial x^2} - k_{iv} iv + g \qquad (1)$$

$$\frac{\partial v}{\partial t} = D_v \frac{\partial^2 v}{\partial x^2} - k_{iv} iv + g, \qquad (2)$$

where i and v are the concentrations of doubly ionized Hg interstitials and vacancies respectively, g is the generation rate of Hg interstitial and vacancy pairs, k_{iv} is the recombination rate constant, and the Ds are the respective diffusion coefficients.[1,12] The interrelation between these parameters and experimental studies of type-conversion, Hg self-diffusion, and interdiffusion are discussed in detail in Part II.[12] Here we have assumed that the Hg interstitials are doubly ionized, though this is not critical for the present analysis. In addition, the drift component has been neglected since its contribution is typically negligible for $Hg_{0.8}Cd_{0.2}Te$, though it may be determined when necessary from the given parameter set, through an appropriate relationship of the point-defect mobility to the diffusivity.

Thermodynamic Parameters

The limits of kinetic modeling are provided by the thermodynamic boundaries of a given system. For example, if an anneal is performed for a sufficient duration, the material will equilibrate, the resulting defect concentrations will be uniform, and their values will be given by a thermodynamic analysis of the given process conditions. For $Hg_{0.8}Cd_{0.2}Te$, the exist-

ence region of the phase diagram has been characterized in detail.[3] Pressure and temperature dependence studies have mapped out the equilibrium vacancy concentration over the regions of interest and these dependencies have been examined in the literature.[4,5] Since thorough analyses are available, only a brief summary is presented here.

The quasi-chemical reaction between the Hg in the vapor phase, Hg(g), and the neutral vacancies, v^o, is given by,

$$V^o_{Cation} + Hg(g) \leftrightarrow Hg_{Hg}. \qquad (3)$$
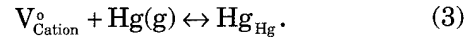
In equilibrium, Eq. (3) indicates that the charge neutral vacancy concentration will be inversely proportional to the Hg pressure. Note that the equilibrium population of neutral vacancies is not a function of the Fermi level of the material. In contrast, the doubly ionized vacancy populations, v, will vary with the Fermi energy. Consider the relationship between the neutral and doubly ionized vacancies given by,

$$V^o_{Cation} \leftrightarrow V^{--}_{Cation} + 2p^+, \qquad (4)$$

where p is the concentration of holes. In equilibrium, v is given by,

$$v = \frac{kv^o}{p^2}, \qquad (5)$$

where K is a constant. At temperatures where the material is intrinsic, v is related to the intrinsic carrier concentration, n_i, by a trivial substitution of n_i for p in Eq. (5). For anneal conditions where the material is dominated by holes due to the doubly ionized vacancies, p = 2v and Eq. (5) becomes,

$$v = \left(\frac{Kv^o}{4}\right)^{1/3}. \qquad (6)$$

Equations (5) and (6) indicate the intrinsic to extrinsic transition will be characterized by a change in the doubly ionized vacancy Hg pressure dependence from P_{Hg}^{-1} to $P_{Hg}^{-1/3}$, respectively, a result which has been reported by Vydyanath.[4,5] In fact, Eq. (6) is an oversimplification in that it neglects the dependence of the thermodynamic equilibrium constant on the Fermi energy. Above 450°C, the thermal energy (kT) is greater than 62 meV, which is a significant fraction of the bandgap even at the elevated temperatures. In addition, as the material becomes more p-type, the Fermi level moves closer to the valence band and the energy state of the doubly ionized vacancies, reducing their allowable population. Fermi-Dirac statistics must be considered to quantify this reduction and keep track of the increased concentration of the singly ionized or neutral vacancies. At temperatures below 450°C, the intrinsic limit is approximately valid over the entire existence region of the phase field for $Hg_{0.8}Cd_{0.2}Te$. In this regime, the Hg-rich equilibrium doubly ionized vacancy concentration, v_R^{--}, is given by,[3–5]

$$v_R^{--} = (2.10 \times 10^{23} cm^{-3}) \exp\left[\frac{-1.02eV}{kT}\right], \qquad (7)$$

where k is Boltzmann's constant. The Hg-rich vapor pressure curve is given by,

$$P_{HgRich} = (1.32 \times 10^5 \text{atm}) \exp\left[\frac{-0.635\text{eV}}{kT}\right], \quad (8)$$

Under Hg poor, or Te-saturated conditions, the equilibrium doubly ionized vacancy concentration, v_P^-, is given as,

$$v_P^- = (6.02 \times 10^{21} \text{cm}^{-3}) \exp\left[\frac{-0.58\text{eV}}{kT}\right], \quad (9)$$

and the corresponding Hg pressure is given by,

$$P_{HgPoor} = (4.59 \times 10^6 \text{atm}) \exp\left[\frac{-1.075\text{eV}}{kT}\right]. \quad (10)$$

Equations (7) and (9) establish the boundaries of the existence region and are consistent with Schaake's experimental results in this temperature regime. In between these limits, the doubly ionized vacancy concentration is given by,

$$v = \left(\frac{2.77 \times 10^{28} \text{cm}^{-3} \text{atm}}{P_{Hg}}\right) \exp\left[\frac{-1.66\text{eV}}{kT}\right]. \quad (11)$$

Berding et al. have given the form of Eq. (11) to be,

$$v = C_o \frac{(kT)^{5/2}}{P_{Hg}} \left(\frac{\sqrt{2\pi m_{Hg}}}{h}\right)^3 \exp\left[\frac{-S_{V_{Hg}}}{kT}\right] \exp\left[\frac{-E_{V_{Hg}}}{kT}\right], (12)$$

where C_o is the site density, $S_{V_{Hg}}$ is the entropy, and $E'_{V_{Hg}}$ is the formation energy of reaction,

$$E'_{V_{Hg}} + HgTe \leftrightarrow V_{Hg}Te + Hg(g). \quad (13)$$
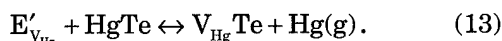
Berding et al. determined the values of the entropy and formation energy terms for neutral point defects in HgTe, assuming equilibrium conditions, and their values are shown in Table I. While Eq. (11) is for doubly ionized vacancies in $Hg_{0.8}Cd_{0.2}Te$, we would expect to obtain ball park entropy and formation energy values. Fitting Eq. (11) to Eq. (12), we obtain reasonable agreement with the calculations of Berding et al., as shown in Table I.

The value of the doubly ionized Hg interstitial concentration, i, is substantially more elusive, since it cannot be directly determined from experiment. Berding et al. have considered the reaction,

$$E'_{Hg_i} + Hg(g) \leftrightarrow Hg_i, \quad (14)$$
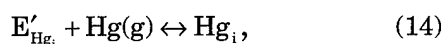
for HgTe and determined a formation energy of 1.75 eV. We have attempted to match this, but are limited by the Hg-rich self-diffusivity activation energy determined to be 1.2 eV.[9] This quantity restricts E'_{Hg_i} to values less than 0.565 eV. Otherwise, the Hg interstitial diffusion coefficient activation energy

would have to be negative. We set E'_{Hg_i} to be 0.415 eV to provide a finite activation energy of 0.15 eV for the Hg interstitial diffusivity. Experimental observations indicate that the doubly ionized Hg interstitial concentrations in equilibrium with the vapor phase, are always much less than the corresponding vacancy population. This restriction sets an upper limit on the Hg interstitial concentration pre-exponential. We have set the Hg-rich interstitial concentrations at the limit of this restriction in order to obtain a ball park entropy value. The results are summarized in Table I and the equilibrium Hg interstitial concentrations are given by,

$$i = (1.16 \times 10^{17} \text{cm}^{-3} \text{atm}^{-1}) P_{Hg} \exp\left[\frac{-0.415\text{eV}}{kT}\right]. \quad (15)$$

Recall that the equilibrium Hg interstitial and vacancy concentrations may be related to the thermodynamic equilibrium rate constant of the chemical reaction,

$$V_{Cation}^{--} + Hg_i^{++} \leftrightarrow Hg_{Hg}, \quad (16)$$

by the relationship,

$$iv = \frac{g}{k_{iv}}. \quad (17)$$

The g/k_{iv} ratio is not known experimentally, though we may determine the SUMerCad value by using Eqs. (11) and (15),

$$\frac{g}{k_{iv}} = (3.21 \times 10^{45} \text{cm}^{-6}) \exp\left[\frac{-2.075\text{eV}}{kT}\right]. \quad (18)$$

Pending further refinements in the theoretical formalism, there will remain a significant uncertainty in the actual interstitial defect concentrations.[6]

The existence regions for the doubly ionized Hg interstitials and vacancies given by Eqs. (8), (10), (11), and (15) are plotted in Fig. 1 as a function of inverse temperature. The Hg poor limits will begin to deviate from these lines above 450°C because of extrinsic effects. The absolute values of the Frenkel interaction rates, g and k_{iv}, will be discussed in a later section.

Table I. Comparison of Theoretical and SUMerCad Values for the Entropy and Formation Energy of Hg Interstitials and Vacancies

	Berding et al. Neutral, HgTe	SUMerCad Ionized, $Hg_{0.8}Cd_{0.2}Te$
$E'_{V_{Hg}}$	1.93 eV	1.66 eV
$S_{V_{Hg}}$	-66.3 to -76.4×10^{-5} eV/K	-49.4×10^{-5} eV/K
E'_{Hg_i}	1.75 eV	0.415 eV
S_{Hg_i}	72 to 82×10^{-5} eV/K	76.2×10^{-5} eV/K
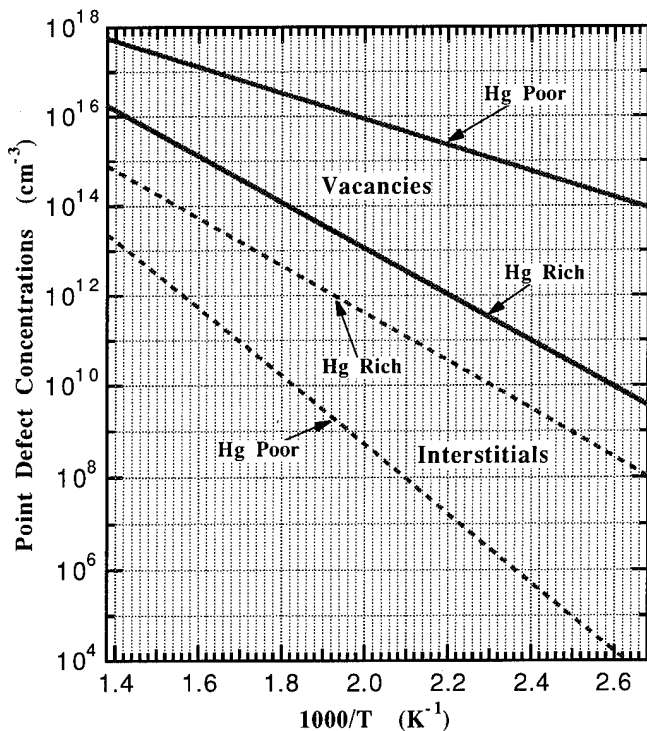
Fig. 1. Hg interstitial and cation vacancy concentration for x = 0.2 material at the phase limits, in the temperature range where the material is intrinsic at all Hg pressures.

Simplified Vapor Phase Boundary Conditions

Compared to the bulk parameters, the general boundary condition formalism is significantly more complex. Whereas the bulk coefficients are functions of the local composition and temperature, the boundary conditions must be adapted to the various types of interfaces possible. For example, the vapor phase, various insulators, and substrates may be expected to interact differently with respect to point defect transfer, generation, and recombination. The important relationships which describe the general vapor phase boundary conditions will be discussed in a later section. However, some of the most common processes are adequately modeled using the simplified vapor phase boundary conditions for Eqs. (1) and (2) given by,

$$-D_i \frac{\partial i}{\partial x}\bigg|_{surface} + v_{rec} i_{surface} = S_i P_{Hg} \qquad (19)$$

$$-D_v \frac{\partial v}{\partial x}\bigg|_{surface} = 0, \qquad (20)$$

where v_{rec} is the recombination velocity and S_i is the Hg interstitial sticking probability. In SUMerCad, the simplified boundary conditions are defined by the parameters hi_2, hi_3, hv_2, and hv_3 which may be determined by comparison of Eqs. (19) and (20) with,

$$\frac{\partial i}{\partial x}\bigg|_{surface} - (hi_2) i_{surface} = -(hi_3) \qquad (21)$$

$$\frac{\partial v}{\partial x}\bigg|_{surface} - (hv_2) v_{surface} = -(hv_3), \qquad (22)$$

where it is clear that hv_2 and hv_3 are zero. In equilibrium, the derivatives go to zero, requiring the ratio hi_3/hi_2 to be equal to the equilibrium Hg interstitial concentration set by the ambient conditions. This also sets the proper equilibrium vacancy concentration through the use of Eq. (17). The magnitudes were chosen to be sufficiently large to model the strong driving force indicated by the Hg-rich self-diffusion data and are given by use of,[9]

$$hi_3 = 1 \times 10^{17} \frac{P_{Hg}}{D_i} cm^{-4}, \qquad (23)$$

along with the equations for the Hg interstitial concentrations, where the Hg pressure in Eq. (23) is specified in atmospheres and the diffusivity is in cm^2/s.

Frenkel Interaction Rates

The exchange rate of lattice Hg with ambient Hg characterized by Hg self-diffusion studies requires large generation and recombination constants for the quasi-chemical reaction described by Eq. (16).[9] If these reaction rates are too small, the radiotracer incorporated during a Hg self-diffusion measurement will be significantly underestimated. In addition, the effective interstitial lifetime will be long, resulting in deeper incorporation of the radiotracer species into the lattice than is depicted from Hg self-diffusion investigations.[9] An example is shown in Fig. 2, for a Hg-rich self-diffusion anneal at 300°C for 16 h assuming various values of the Frenkel interaction rate constants. The SUMerCad default values yield the familiar error-function encountered for anneals of this duration. For smaller g and k_{iv}, the radiotracer surface concentration is below its equilibrium value, and the profile penetrates deeper into the material. For the smallest g and k_{iv}, the profile is clearly logarithmic. In fact, for any interaction rate values, the distribution will be logarithmic for short times, until the surface concentration reaches its equilibrium value. At such time, the distribution will start to go like an error-function. Transient effect studies should give the actual interaction rates as a function of temperature. In the absence of transient self-diffusion information, the g and k_{iv} have been set to be large enough to give error-function solutions for the time durations typically used in the literature.[9-11,17-21] The Frenkel interaction rates are given by,

$$g = (1 \times 10^{40} cm^{-3}s^{-1}) \exp\left[\frac{-2.30eV}{kT}\right] \qquad (24)$$

$$k_{iv} = (3.12 \times 10^{-6} cm^3 s^{-1}) \exp\left[\frac{-0.225eV}{kT}\right]. \qquad (25)$$

Diffusion Coefficients

A key result of our modeling has been the quantifi-

cation of vacancy and interstitial contributions to diffusivity in general. These have been determined for overall consistency with type-conversion and Hg self-diffusion data reported in the literature and the relationships are discussed in detail in Part II.[12] Since the Hg-rich self-diffusion process occurs by an interstitial mechanism below 430°C, and the interstitial concentrations may be determined by Eq. (15), the interstitial diffusivity is determined to be,

$$D_i = (2.35 \times 10^{-3} cm^2 s^{-1}) \exp\left[\frac{-0.15 eV}{kT}\right]. \quad (26)$$

Note that the results of the simulations are very sensitive to the D_i i product. This quantity is well established here, whereas the specific values of D_i and i may be further refined. The vacancy diffusion coefficient has been determined by fitting the data of Jones et al. on the type-conversion junction depth temperature dependence, with an interstitial contribution given by Hg-rich self-diffusion studies.[2,8] The vacancy diffusivity is calculated by,

$$D_v = (1.2 \times 10^5 cm^2 s^{-1}) \exp\left[\frac{-1.51 eV}{kT}\right]. \quad (27)$$

CURRENT SIMULATOR

The SUMerCad program is self-supporting and features a user friendly, menu-driven interface for both input and output operations, allowing the user the flexibility to study the end result of a multi-step anneal/diffusion process, or gain further insight by performing a step-by-step analysis. It is currently implemented on Macintosh computers and will run effectively on 68030 based machines (68040 systems provide 5X speed improvements). The output of a given simulated sequence may be easily applied as the input for the next process step. All solution profiles are displayed graphically for easy interpretation and stored in a standard format for porting to data analysis programs. The implementation of computationally efficient, process-specific algorithms in the modules allows for the realization of a fast desktop application for added convenience and portability. Built-in parameters values are used when available and may be user specified in an "expert" mode.

To perform a simulation, the user must first specify the starting material by providing essential information about the sample history in the form of the temperature of pre-equilibration along with the vapor or material on either surface, user specified profiles for the species, or the output file of a previous simulation, and the thickness of the material. The process to be simulated must be specified by the temperature, time, and specific information necessary to determine the appropriate boundary conditions. For example, in an ambient anneal, the user must specify the Hg partial pressure and the boundary conditions are determined by Eq. (23) and the relationships which provide the equilibrium intersti-

tial concentrations for the process ambient conditions.

Given the parameters presented in the previous section, we can simulate a wide variety of ambient controlled processes in order to validate SUMerCad. Since the parameter set was determined by fits to a specific pool of experimental results, extension beyond this basis will either contradict or lend further support to the models and/or parameters. Vigorous tests will be required for complete validation making certain that the material history is well documented and controlled. However, a few experimental results are available in the literature with sufficient information to specify the starting material and process with some confidence. For example, while the respective point-defect diffusion coefficients were determined from type conversion experiments on material with similar initial vacancy concentrations ($v_{init} = 2 \times 10^{17} cm^{-3}$), our models simulate junction depths accurately over a wide range of v_{init} (see Fig. 3).[2,22] Deviations at high v_{init} are expected because formation of Te precipitates reduces the effective vacancy diffusivity.[8] The resulting vacancy junction profiles will typically be broad, leading to n-on-p junction depths which may depend significantly on the n-type donor concentration.[23,24]

Low temperature junction formation processes will result in more abrupt vacancy profiles and are thus expected to be less sensitive to the donor concentration. Consider the dependence of the type-conversion junction depth on the donor concentration as determined experimentally by Dutton et al. and shown in Fig. 4.[23] The lines are the results of SUMerCad simulations based upon the process information provided in their report, with no adjustments made to the
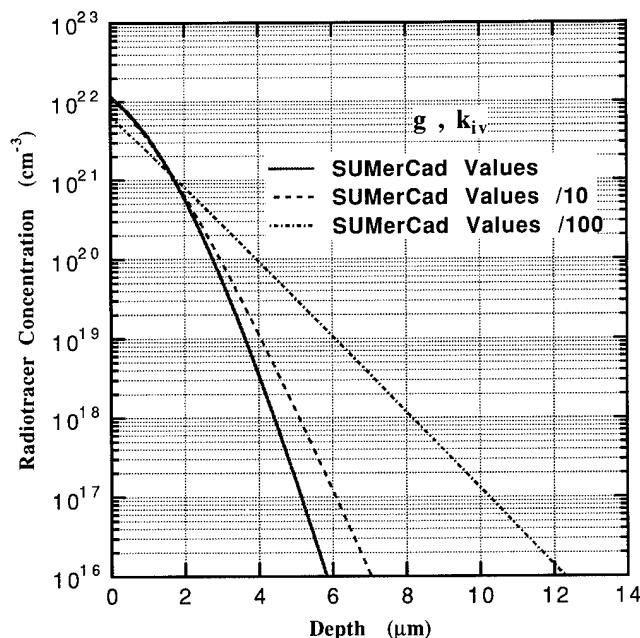
Fig. 2. Simulated Hg-rich self-diffusion profiles at 300°C for 16 h radiotracer anneal as a function of the Frenkel interaction rate magnitude.
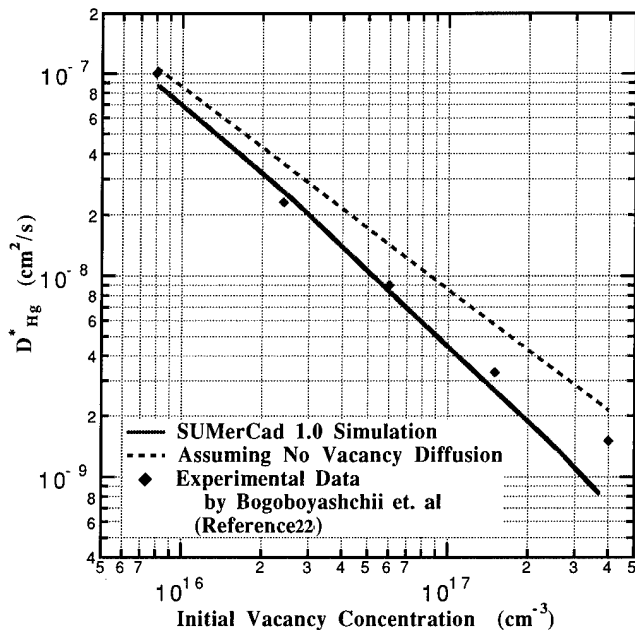
Fig. 3. Simulation of chemical diffusion coefficient (280°C) vs initial vacancy concentration for x = 0.2 material. Experimental points are taken from Ref. 22.

Fig. 5. Induced electric field at 140°C due to the distribution in the doubly ionized vacancy concentration set by a 4 h 250°C Hg-rich anneal of 325°C Te equilibrated $Hg_{0.8}Cd_{0.2}Te$.

Fig. 4. Simulated vs experimental type-conversion junction depth dependence on the background donor concentration at 200°C. Experimental points are taken from Ref. 23.

SUMerCad parameter set. While not exact, the simulation results are reasonable and indicate the proper trend. Better agreement may be obtained by using a slightly larger Hg-rich vacancy concentration at 200°C within the acceptable uncertainty range of Schaake's results, to fit, rather than simulate, the data.[3] However, these refinements do not add to the interpretation.

CURRENT AND FUTURE DIRECTIONS

There are a wide variety of processes which remain to be understood and modeled, from ion implantation to epitaxial growth. In addition, other point defects and extended defects must be tracked in the $Hg_{1-x}Cd_xTe$ and intimately associated systems such as insulators and substrates, in order to quantify primary (currents) and secondary electrical properties (noise).[25–29] In this section, a few representative issues will be discussed which are of immediate concern as well as the subject of future development. These topics are reviewed briefly, as space is limited.

Electric Field Effects

Internal electric field effects are many times neglected in process modeling and design. To the extent the materials are extrinsic at processing temperatures and the "diffusion" species are charged, determines whether or not electric field effects must be included. If so, the effects are quantified by appropriate field terms in the continuity equations and the simultaneous solution of Poisson's equation.[12] An example of the induced electric field in x = 0.2 material at 140°C is shown in Fig. 5 for the doubly ionized cation vacancy profile also shown in the figure. The intrinsic carrier concentration is about 4.4×10^{16} cm^{-3} and N_D is assumed to be much less. Such electric fields can retard or enhance ionized defect motion. Algorithms for including the effect are currently being developed. Experimental confirmation and better quantification of process temperature intrinsic carrier concentrations will be required for validation of the electric field contributions specified by the simulator.[4,12,30,31]

Boundary Conditions

The boundary conditions of the $Hg_{1-x}Cd_xTe$ system will be a function of the material or vapor at the surface. As such, a general formalism is not physically meaningful without specific information concerning the point-defect interactions at or transfer through the boundary. However, a general description of the vapor phase boundary conditions may be formulated based upon an examination of the first order interfacial interactions shown schematically in Fig. 6. In Fig.

$$J_i = S_i P_{Hg} - k_{Di}\sigma_i \rightarrow \qquad J_{GR} = g_s - k_{ivs}\sigma_i\sigma_v \qquad J_{iSB} = k_1\sigma_i - k_2 C_i \rightarrow$$

$$J_v = S_v P_{Te_2}^{1/2} - k_{Dv}\sigma_v \rightarrow \qquad \uparrow\downarrow \qquad J_{vSB} = k_3\sigma_v - k_4 C_v \rightarrow$$
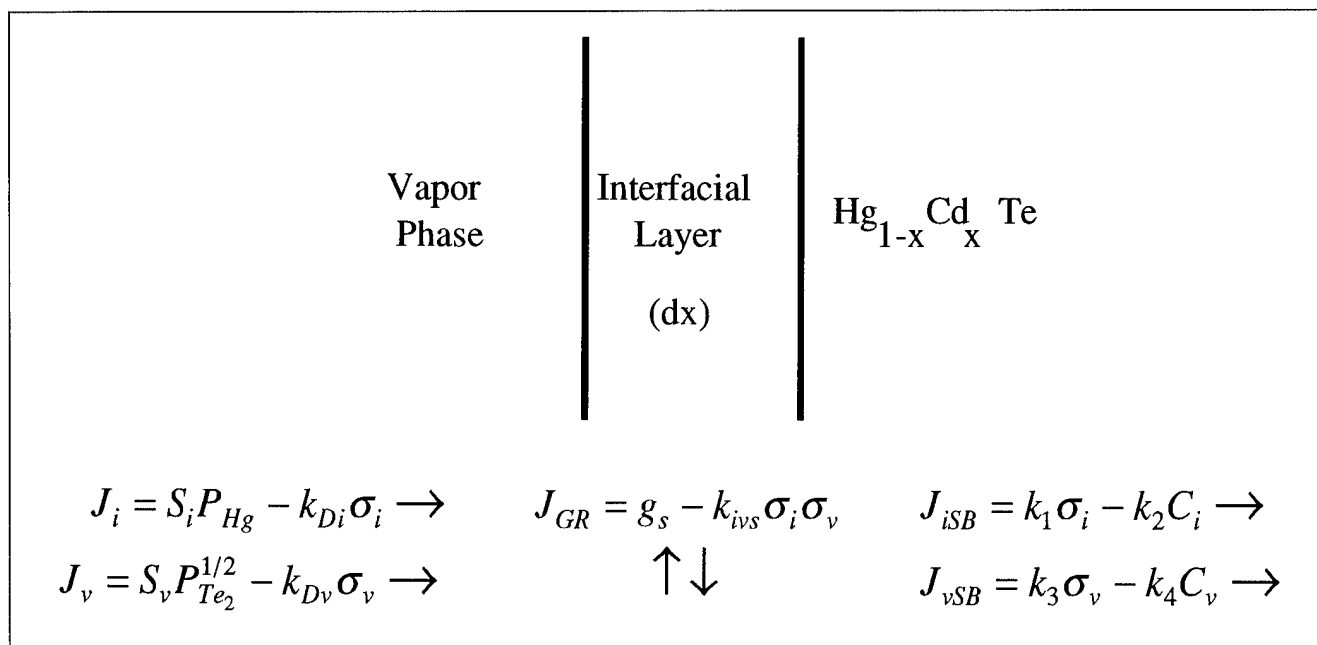
Fig. 6. Interactions for general $Hg_{1-x}Cd_xTe$ vapor phase boundary condition formulation.

6, the subscripts i and v are the Hg interstitial and vacancy concentrations respectively, J is the point defect flux, S is the sticking probability, k_D is the desorption rate constant, σ is the surface concentration, g_s and k_{ivs} are the interfacial Frenkel interaction rates, and k_{1-4} are reaction rate constants determining the transmission of the point defects from the interfacial layer to the bulk. Note that if the Hg and Te pressures are not in the $Hg_{1-x}Cd_xTe$ existence region, the $Hg_{1-x}Cd_xTe$ will not be stable. If the Te partial pressure is set to zero, the $Hg_{1-x}Cd_xTe$ will thermally etch. In fact, the interactions shown in Fig. 6 could be used to model growth processes such as molecular beam epitaxy or possibly metalorganic chemical vapor deposition for an appropriately specified vapor phase.

Alternative Junction Formation Processes

Type-conversion by Hg ambient anneals has been modeled quite effectively using the simplified vapor phase boundary conditions presented here. In fact, there are many different, technologically significant, methods by which to form n-on-p junctions by type-conversion. Ion implantation, ion milling, and anodic oxidation have all been shown to produce viable photodiodes.[32–37] In addition, these processes may be applied to intrinsicly and/or extrinsicly doped p-type material. Redistribution issues of extrinsic impurities such as As or Au must be studied carefully as a function of the junction formation process. These processes will require individual analysis and modeling specific to the respective physics dictating the relevant point defect interactions.

Extended Defects

In addition to the effects of native point defects on the material properties of $Hg_{1-x}Cd_xTe$, the formation
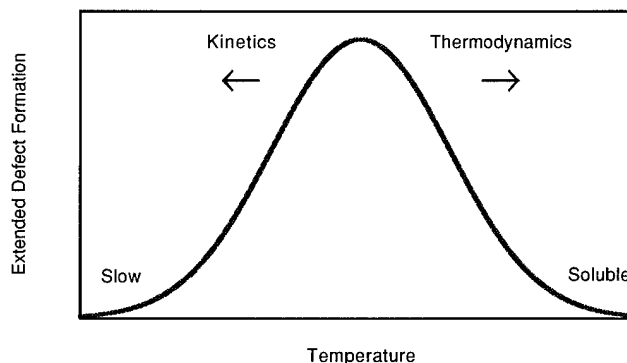
Fig. 7. Schematic diagram of extended defect formation dependence upon temperature, demonstrating a low temperature kinetic limited regime and a high temperature thermodynamic limited regime.

and presence of extended defects can dominate both the process and device physics. Because such defects are easily introduced into the material during processing, the simulator must correctly track the processing history of the material. For example, after a high temperature process, as the material is cooled, the values for the equilibrium concentrations of point defects will decrease, leading to super saturated solutions, and the possibility of the nucleation and growth of extended defects. At sufficiently low temperatures, formation of the extended defects is limited by the atomic kinetics necessary for species transport to nucleate and grow the extended defect. At high temperatures, solubility limits are greater, eliminating the thermodynamic formation driving force altogether. The "volcano plot" in Fig. 7 demonstrates the limitations on the formation of extended defects, where the tendency to nucleate and grow the extended defect will be a maximum at an intermediate temperature where both a super saturated solution exists and the kinetics of point defect diffusion are fast enough for

nucleation and growth to occur. A quantitative formulation will be based upon the kinetic process parameters and the corresponding thermodynamic limits.

Interdiffusion

The incorporation of composition dependent effects is a natural extension of our modeling approach, though it adds significant complications resulting from composition dependent thermodynamic and kinetic properties. In addition, shorter wavelength material may not be intrinsic at typical process temperatures as is normally the case for x = 0.2 material. This difference allows for internal fields which contribute through a drift term to the motion of all ionized species. The modeling approach for the general x-value system has been detailed in Part II.[12]

SUMMARY

We have discussed the framework by which a comprehensive simulator may be developed for $Hg_{1-x}Cd_xTe$ based device structures. The basic Hg interstitial and vacancy parameters have been presented and justified for x = 0.2 material. These values are incorporated into the Stanford University mercury cadmium telluride process simulator (SUMerCad) which is currently able to quantitatively model ambient anneals as a function of ambient pressures and temperature, capped or noninteractive interfaces, and the bulk $Hg_{0.8}Cd_{0.2}Te$ point-defect equilibration profiles for $CdTe/Hg_{0.8}Cd_{0.2}Te$ high temperature processes, as well as fabrication sequences composed of combinations of these processes. In this report, we have concentrated on the vapor phase processes and provided validation examples based on experimental results reported in the literature. Additional, well-defined, validation experiments will be necessary to ensure simulator accuracy. Finally, some issues related to the future development of SUMerCad were discussed, including electric field effects, general boundary conditions, alternative junction formation processes, extended defects, and interdiffusion. There are innumerable other topics of interest including epitaxial growth, heterojunction formation and stability, Te and Cd point defects, and impurities which will need to be addressed for success in developing a robust $Hg_{1-x}Cd_xTe$ simulator.

ACKNOWLEDGMENT

REFERENCES

1. J.L. Meléndez and C.R. Helms, *J. Electron. Mater.* 22, 999 (1993).
2. C.L. Jones, M.J.T. Quelch, P. Capper and J.J. Gosney, *J. Appl. Phys.* 53, (1992).
3. H.F. Schaake, *J. Electron. Mater.* 14, 513 (1985).
4. H.R. Vydyanath, *J. Electrochem. Soc.* 128, 2609 (1981).
5. H.R. Vydyanath and C.H. Hiner, *J. Appl. Phys.* 65, (1989).
6. M. Berding and A. Sher, *J. Electron. Mater.* 22, 1005 (1993).
7. H.F. Schaake, J.H. Tregilgas, J.D. Beck, M.A. Kinch and B.E. Gnade, *J. Vac. Sci. Technol. A* 3 (1985).
8. H.F. Schaake and J.H. Tregilgas, *J. Vac. Sci. Technol. A* 4 (1986).
9. N.A. Archer, H.D. Palfrey and A.F.W. Willoughby, *J. Electron. Mater.* 22, 967 (1993).
10. Mei-Fan Sung Tang, Ph.D. Thesis, Stanford University (1987).
11. John-Sea Chen, Ph.D. Thesis, University of Southern California (1985).
12. J.L. Meléndez and C.R. Helms, Part II, *J. Electron. Mater.* 24, 573 (1995).
13. H.R. Vydyanath, *J. Vac. Sci. Technol. B* 9, 1716 (1991).
14. J.L. Schmit and E.L. Stelzer, *J. Electron. Mater.* 7, 65 (1968).
15. W. Scott, E.L. Stelzer and R.J. Hager, *J. Appl. Phys.* 47, 1408 (1976).
16. E.D. Jones, V. Thanbipillai and J.B. Mullin, *J. Cryst. Growth* 118, 1 (1992).
17. N.A. Archer, H.D. Palfrey and A.F.W. Willoughby, *J. Cryst. Growth* 117, 177 (1992).
18. N. Archer and H. Palfrey, *J. Electron. Mater.* 20, 419 (1991).
19. D.A. Stevenson and M-F. S. Tang, *J. Vac. Sci. Technol. B* 9, 1615 (1991).
20. M-F. S. Tang and D.A. Stevenson, *J. Vac. Sci. Technol. A* 6, 2650 (1988).
21. M-F.S. Tang and D.A. Stevenson, *J. Vac. Sci. Technol. A* 7, 544 (1989).
22. V.V. Bogoboyashchii, A.I. Elizarov, V.I. Ivanov-Omskii and V.A. Petryakov, *Sov. Phys. Semicond.* 21, 888 (1987).
23. D.T. Dutton, E. O'Keefe, P. Capper, C.L. Jones, S. Mugfor, and C. Ard, *Semicond. Sci. Technol.* 8, S266 (1993).
24. P. Koppel and K. Owens, *J. Appl. Phys.* 67, 6886 (1990).
25. R. Fastow and Y. Nemirovsky, *J. Vac. Sci. Technol. A* 8, 1245 (1990).
26. C.L. Littler, E. Maldonado, X.N. Song, Z. Yu, J.L. Elkind, D.G. Seiler and J.R. Lowney, *J. Vac. Sci. Technol. B* 10, 1466 (1992).
27. J.L. Elkind, *J. Vac. Sci. Technol. B* 10, 1460 (1992).
28. J.L. Meléndez and J. Beck, *J. Electron. Mater.* 22, 993 (1993).
29. R.S. List, *J. Electron. Mater.* 22, 1012 (1993).
30. C.-H. Su, P.-K. Liao, and R.F. Brebrick, *J. Electron. Mater.* 12, 771 (1983).
31. R.F. Brebrick and J.P. Schwartz, *J. Electron. Mater.* 9, 771 (1980).
32. L.O. Bubulac, W.E. Tennant, D.S. Lo, D.D. Edwall, J.C. Robinson, J.S. Chen and G. Bostrup, *J. Vac. Sci. Technol. A* 5, 3166 (1987).
33. R. Kumar, M.B. Dutt, R. Nath, R. Chander and S.C. Gupta, *J. Appl. Phys.* 68, 5564 (1990).
34. M.V. Blackman, D.E. Charlton, M.D. Jenner, D.R. Purdy, J.T.M. Wotherspoon, C.T. Elliott and A.M. White, *Electron. Lett.* 23, 978 (1987).
35. G. Bahir and E. Finkman, *J. Vac. Sci. Technol. A* 7, 348 (1989).
36. P. Brogowski and J. Piotrowski, *Semicond. Sci. Technol.* 5, 530 (1990).
37. N.Kh. Talipov, V.P. Popov, V.G. Remesnik and Z.A. Nal'kina, *Sov. Phys. Semicond.* 26, 175 (1992).

Process Modeling and Simulation for $Hg_{1-x}Cd_xTe$. Part II: Self-Diffusion, Interdiffusion, and Fundamental Mechanisms of Point-Defect Interactions in $Hg_{1-x}Cd_xTe$

JOSÉ L. MELÉNDEZ* and C.R. HELMS

Department of Electrical Engineering, Stanford University, Stanford, CA 94305

The $Hg_{0.8}Cd_{0.2}Te$ type-conversion, Hg self-diffusion and interdiffusion processes are analyzed in the context of a first order reaction kinetics approach. Sets of nonlinear, stiffly coupled continuity equations are presented which describe the underlying physics, and their solutions model the observed macroscopic behavior. It is demonstrated that the Frenkel pair mechanism interactions dominated by the cation sublattice, in conjunction with basic diffusive and drift properties of the ionized point defects, comprise the basic processes which effect all macroscopic phenomena discussed. Existing experimental results are reviewed and apparent discrepancies discussed. Use is made of the Stanford University mercury cadmium telluride process simulator to provide quantitative and insightful examples of important results.

Key words: Diffusion, HgCdTe, modeling, simulation

INTRODUCTION

Thorough and detailed experimental studies of phenomena such as self-diffusion and type-conversion, available in the literature, have established the requisite database for the development of a comprehensive picture of the basic diffusion mechanisms in $Hg_{1-x}Cd_xTe$.[1-11] Archer et al., Tang et al., and Chen have provided the results of numerous self-diffusion studies.[1-6,11] Jones et al. supplied key Hg anneal type-conversion junction depth information.[7] Vydyanath et al. and Schaake have measured the ambient equilibrated vacancy concentrations as a function of temperature for a variety of Hg partial pressures.[8,9]

Parameters such as the self-diffusion or interdiffusion coefficients may be linked to the underlying, fundamental atomic level diffusion mechanisms. In this paper, the interrelations between the macroscopic phenomena and the fundamental point-defect mechanisms will be developed leading to a clear and consistent picture of the underlying mechanisms involved in self-diffusion, interdiffusion, and type-conversion processes. Existing experimental results are reviewed and apparent discrepancies discussed. Use is made of the Stanford University mercury cadmium telluride process simulator (SUMerCad) to provide quantitative and insightful examples of important results.[12]

REVIEW OF POINT-DEFECT KINETICS MODELING

The applicability of a first order reaction kinetics formalism in describing the process physics of $Hg_{1-x}Cd_xTe$ has previously been suggested.[12] This same formalism has been applied to Si and GaAs technologies.[14-19] Since our initial report, the available literature has been analyzed to determine the parameter set describing the basic interactions of the Hg interstitials and cation vacancies in $Hg_{0.8}Cd_{0.2}Te$.[20] Since a detailed development of the approach in the

context of $Hg_{1-x}Cd_xTe$ process modeling is available in the literature, only a brief summary is given here.[12,20] In particular, the modeling approach we have implemented utilizes first order reaction kinetics to describe the motion of and interactions among native point defects and foreign impurities in $Hg_{1-x}Cd_xTe$. A set of continuity equations are established with generation and recombination terms representing the important quasi-chemical reactions between the various species.

A fundamental example of the coupled diffusion modeling approach is for the case where only Hg interstitials and cation vacancies are important. For this example, only the Frenkel defect equation is considered,

$$Hg_i^{++} + V_{Cation}^{--} \leftrightarrow Hg_{Cation}. \tag{1}$$
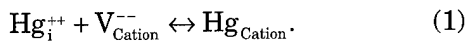
The resulting continuity equations are,

$$\frac{\partial i}{\partial t} = D_i \frac{\partial^2 i}{\partial x^2} - k_{iv} iv + g - 2i\mu_i \frac{\partial \xi}{\partial x} - 2\mu_i \xi \frac{\partial i}{\partial x} \tag{2}$$

$$\frac{\partial v}{\partial t} = D_v \frac{\partial^2 v}{\partial x^2} - k_{iv} iv + g - 2v\mu_v \frac{\partial \xi}{\partial x} - 2\mu_v \xi \frac{\partial v}{\partial x} \tag{3}$$

where i is the concentration of doubly ionized Hg interstitials, v is the doubly ionized cation vacancy concentration, ξ, is the electric field, g is the generation rate, k_{iv} is the recombination rate constant, the Ds are the respective diffusion coefficients and the μs are the point-defect mobilities which are assumed independent of the spatial coordinate for uniform x-value material.[12,13] For simplicity, we assume the interstitials are doubly ionized; for most cases this distinction is not important. For x = 0.2 material, electric field effects are usually negligible because $Hg_{0.8}Cd_{0.2}Te$ is intrinsic at most process temperatures. In cases where the material is extrinsic, Poisson's equation must be solved for the electric field.

Hg SELF-DIFFUSION

A first order reaction kinetics formalism of the Hg self-diffusion process has been developed based upon Eq. (1) and the quasi-chemical reaction,

$$RT_i^{++} + V_{Cation}^{--} \leftrightarrow RT_{Cation}, \tag{4}$$

where RT represents the Hg radiotracer. The recombination rate constant is identical to k_{iv} for Eq. (1). However, the generation rate will now be a linear function of the concentration of the substitutional radiotracer concentration. The set of continuity equations which describe the Hg self-diffusion process are given by,

$$\frac{\partial i_1}{\partial t} = D_i \frac{\partial^2 i_1}{\partial x^2} + g \frac{C_1}{C_o} - k_{iv} i_1 v \tag{5}$$

$$\frac{\partial i_2}{\partial t} = D_i \frac{\partial^2 i_2}{\partial x^2} + g \frac{C_2}{C_o} - k_{iv} i_2 v \tag{6}$$

$$\frac{\partial C_1}{\partial t} = $$
$$\frac{C_1}{C_o} D_v \frac{\partial^2 v}{\partial x^2} + \frac{v}{C_o} D_v \frac{\partial^2 C_1}{\partial x^2} - g \frac{C_1}{C_o} + k_{iv} i_1 v \tag{7}$$

$$\frac{\partial C_2}{\partial t} = $$
$$\frac{C_2}{C_o} D_v \frac{\partial^2 v}{\partial x^2} + \frac{v}{C_o} D_v \frac{\partial^2 C_2}{\partial x^2} - g \frac{C_2}{C_o} + k_{iv} i_2 v, \tag{8}$$

where C_o is the total density of Hg cation sites, and the C_i are the respective concentrations of Hg on Hg sites where the subscript 1 designates the nonradiotracer Hg species and the subscript 2 designates the Hg radiotracer species. Since the x-value remains invariant, the generation rate constant, g, in Eqs. (5) and (6) is identical to that defined in Eqs. (2) and (3). Hence, the generation rate for the radiotracer and nonradiotracer Hg interstitials is simply proportional to the fraction of their respective local cation populations.

Similarly, the recombination term is proportional to the product of the respective interstitial and vacancy concentrations. As expected, these terms show up with an opposite role in the cation Hg continuity Eqs. (7) and (8). The diffusion terms in Eqs. (7) and (8) arise from a simple flux analysis maintaining conservation of lattice sites. The vacancy diffusion coefficient, within our first-order framework, is defined by Eqs. (5) and (8) without specific regard to the matrix. Electric field effects have been neglected since x = 0.2 material is intrinsic under most Hg self-diffusion conditions. The kickout mechanism has been excluded since it is a two-step process and is not necessary to explain the available data. Comparisons of Eqs. (5)–(8) with Eqs. (2) and (3) reveal that the fundamental point-defect parameters describe the Hg self-diffusion behavior. Indeed, the self-diffusion kinetics are set by the intrinsic interactions and mobility of the native Hg interstitials and cation vacancies, underscoring the dependence of the macroscopic experimental observables upon the fundamental point-defect processes. Since these equations may be somewhat unfamiliar, a couple of analytic analyses of limiting cases are in order.

As a first example, consider the case where there is no Hg radiotracer species. Equations (6) and (8) both go to zero. Equation (5) simplifies to,

$$\frac{\partial i_1}{\partial t} = D_i \frac{\partial^2 i_1}{\partial x^2} - k_{iv} i_1 v + g, \tag{9}$$

where we have used the fact that $v \ll C_o$. Conservation of lattice sites for uniform x-value material gives,

$$C_o = C_1 + v \tag{10}$$

Substitution of Eq. (10) into Eq. (7) gives the result,

Process Modeling and Simulation for $Hg_{1-x}Cd_xTe$. Part II: Self-Diffusion, Interdiffusion, and Fundamental Mechanisms of Point-Defect Interactions in $Hg_{1-x}Cd_xTe$

575

$$\frac{\partial v}{\partial t} = D_v \frac{\partial^2 v}{\partial x^2} - k_{iv}i_1 v + g, \tag{11}$$

where we again assume $v \ll C_o$. Neglecting electric field effects, Eqs. (9) and (11) are identical to Eqs. (2) and (3), respectively, confirming that the more complicated self-diffusion equations reduce to the correct form in the limiting case.

For a second analysis of Eqs. (5)–(8), consider the simplification possible when vacancy diffusion is negligible and the material has been properly pre-equilibrated prior to a Hg self-diffusion experiment. Setting $D_v = 0$ along with all vacancy derivatives, Eqs. (7) and (8) will reduce to,

$$\frac{\partial C_1}{\partial t} = -g\frac{C_1}{C_o} + k_{iv}i_1 v \tag{12}$$

$$\frac{\partial C_2}{\partial t} = -g\frac{C_2}{C_o} + k_{iv}i_2 v. \tag{13}$$

Combination of Eqs. (5) and (12) as well as Eqs. (6) and (13) confirms that the material has been pre-equilibrated giving,

$$g = k_{iv} i_T v, \tag{14}$$

where i_T is the sum total of the radiotracer and nonradiotracer Hg interstitial concentrations. Since we know that $i_T = i_1 + i_2$ and $C_o = C_1 + C_2$, Eqs. (6) and (13) completely specify the system. Solving Eq. (13) for i_2 and substituting into Eq. (6) yields,

$$\frac{1}{k_{iv}v}\frac{\partial^2 C_2}{\partial t^2} + \frac{g}{k_{iv}vC_o}\frac{\partial C_2}{\partial t} =$$

$$\frac{D_i}{k_{iv}v}\frac{\partial}{\partial x}\left[\frac{\partial}{\partial x}\frac{\partial C_2}{\partial t} + \frac{g}{C_o}\frac{\partial C_2}{\partial x}\right] - \frac{\partial C_2}{\partial t}. \tag{15}$$

Grouping terms, substituting Eq. (14) and recognizing $i_T \ll C_o$ gives,

$$\frac{1}{k_{iv}v}\frac{\partial^2 C_2}{\partial t^2} + \frac{\partial C_2}{\partial t} = \frac{D_i i_T}{C_o}\frac{\partial^2 C_2}{\partial x^2} + \frac{D_i}{k_{iv}v}\frac{\partial^2}{\partial x^2}\frac{\partial C_2}{\partial t}. \tag{16}$$

Setting the higher order derivatives to zero, produces the final result,

$$\frac{\partial C_2}{\partial t} = \frac{D_i i_T}{C_o}\frac{\partial^2 C_2}{\partial x^2} = D_{Hg}\frac{\partial^2 C_2}{\partial x^2}, \tag{17}$$

where D_{Hg} is the Hg self-diffusion coefficient. It is clear from this example, that the Hg self-diffusion coefficient is determined by the underlying point-defect parameters. The solution of Eq. (17) for a steady state surface concentration is the familiar complementary error-function.

While in some cases Eqs. (5)–(8) may be simplified so that steady-state analytic approximations can be obtained, in general, numerical techniques are re-

quired to obtain the full spatial and temporal defect distributions as a function of the ambient temperature and Hg partial pressure for arbitrary starting material. SUMerCad utilizes modern numerical methods to solve the set of second order coupled partial differential equations which describe the Hg self-diffusion process. In addition, analyses of the experimental database available in the literature, has allowed for the determination of built-in, unique point-defect parameters.[20] The user simply specifies the starting material as an output from a previous simulation, arbitrarily as a user specified point-defect distribution file, or by specification of the conditions of equilibration. In addition, the user must specify the ambient temperature, Hg pressure, and anneal time of the Hg self-diffusion process. This information
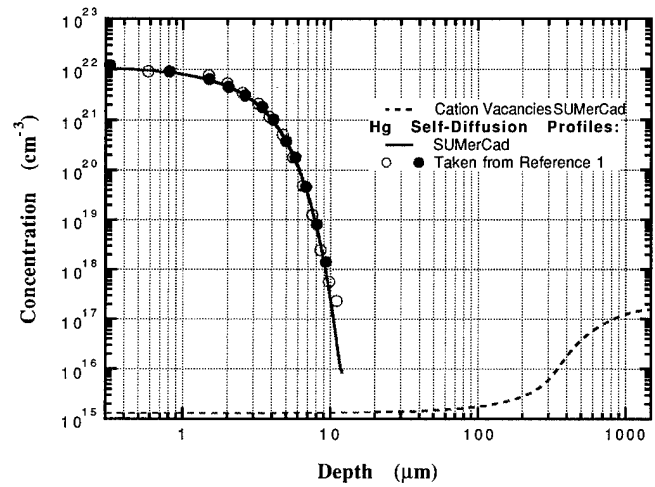

Fig. 1. Simulated cation vacancy profile compared to experimental and simulated Hg self-diffusion profile at 352°C for 11.5 h. Experimental data is taken from Ref. 1.
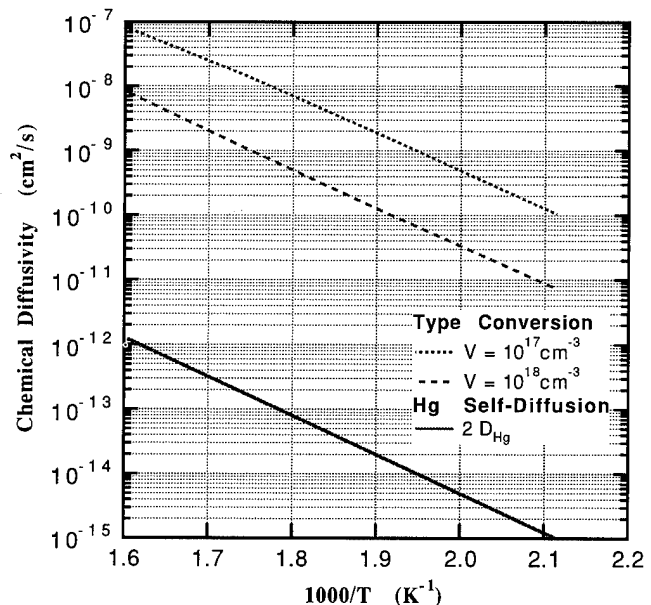

Fig. 2. Simulated type-conversion junction depths vs inverse temperature for 10^{17} cm^{-3} and 10^{18} cm^{-3} starting vacancy concentrations compared to the Hg self-diffusion junction depth.

allows the simulator to specify the bulk point-defect parameters, determine the appropriate boundary conditions, and model the process kinetics for the specified interval.

A SUMerCad simulation of Hg self-diffusion at 352°C for 11.5 h into x = 0.2 material, which was not pre-equilibrated and had a starting vacancy concentration of 2×10^{17} cm^{-3}, is shown in Fig. 1, along with experimental data taken from Ref. 1. The model parameters were previously fit to obtain the Hg self-diffusion coefficient reported in Ref. 1 based upon the radiotracer profile shown in Fig. 1, the simulator provides the vacancy distribution. The observation of the independence of Hg self-diffusion data on whether or not the starting material was pre-equilibrated is a direct consequence of the much deeper type conversion junctions which are formed on the depth and time scales of the radiotracer junction. The vacancy concentrations in the radiotracer region are forced near their Hg-rich equilibrium values far ahead of the corresponding self-diffusion front.

A series of SUMerCad simulations were utilized to establish the type conversion junction depth temperature dependence under Hg-rich anneal conditions for initial vacancy concentrations of 10^{17} cm^{-3} and 10^{18} cm^{-3}. It is assumed that the material is free of second phase Te and that it is much thicker than the simulated junction depth. The results are represented by the dashed curves shown in Fig. 2 where the chemical diffusivity (square of junction depth over time) has been plotted vs inverse temperature. The solid line represents the penetration depth of the high concentration Hg radiotracer region. It is clear that for the range of vacancy concentrations encountered in practice, pre-equilibration is not necessary.

There are generally two distinct branches observed in Hg self-diffusion studies on Hg$_{0.8}$Cd$_{0.2}$Te.[1–6,11,21–23] While there has been debate on the origin of these branches, the more recent literature seems to support the identification of the slow branch as being due to volume self-diffusion, which we describe successfully with Eqs. (5)–(8), and the fast branch as resulting from short circuit diffusion paths such as dislocations and/or (sub)grain boundaries.[1,24,25] In most cases where the fast tail has been clearly resolved, the spatial dependence appears to be exponential which is characteristic of high diffusivity paths.[1–4,11,26] Since fast diffusion down dislocations and (sub)grain boundaries are expected to manifest themselves similarly in the Hg self-diffusion analysis, a conclusive distinction is difficult, though Shaw has presented evidence slightly in favor of (sub)grain boundary diffusion as the origin of the fast tail.[24,27] Shaw and Palfrey have both analyzed the fast tail in detail and concluded that it resulted from fast diffusion down a short circuit path.[24,25] Shaw determined that the necessary dislocation densities ranged from 1.7×10^{3} cm^{-2} to 4.5×10^{5} cm^{-2}. While this lower limit appears too low based on experimental etch pit counts, all of the calculated dislocation densities in the lower range are based on the 225°C Hg self-diffusion data reported by

Brown and Willoughby in 1983.[23] These do not appear consistent with recent results from Archer, Palfrey, and Willoughby which indicate a much smaller diffusivity of the slow branch at low temperatures.[1,2,23] In addition, the appearance of a third component in the early radiotracer profiles is unusual.[23] It is likely that even the longest anneal time of 285 h is insufficient to clearly resolve the slow branch. If these points are discarded, the adjusted lower limit is 9.5×10^{4} cm^{-2}. A dislocation analysis of additional Hg self-diffusion data not considered by Shaw, also gives dislocation densities primarily in the 10^{5} cm^{-2} range.[1–3]

Tang and Stevenson have proposed a volume mechanism for both branches, though Shaw has identified significant inconsistencies in their model.[4,5,21,22,24] Chen also discounted dislocations as an explanation for the fast component, though the analysis did not include the contribution of out-diffusion from the extended defects.[11] The overall consistency in modeling a variety of experimental data based on the treatment of the slow component by Eqs. (5)–(8) supports the theory that the slow component is a result of the underlying fundamental point-defect motion and interactions. However, the observed Hg pressure dependence observed by Tang is puzzling.[4] Tang observed that the diffusion coefficient associated with the fast tail was proportional to the Hg pressure at high pressures and inversely proportional at low pressures.[4] This type of behavior is consistent with a first order quasi-chemical surface reaction by which vapor phase Hg is incorporated into the Hg$_{0.8}$Cd$_{0.2}$Te lattice and diffuses by a volume self-diffusion mechanism.[20]

However, if the fast tail is due to short circuit diffusion, it is reasonable that an error-function fit to an exponential process might give anomalous results. Both Tang and Chen determined that the slow component diffusion coefficient was largely independent of the Hg pressure which is not expected for a volume self-diffusion process.[4,11] It was on the basis of this lack of Hg pressure dependence that Tang concluded that the fast tail was due to volume self-diffusion. Pressure dependence data for a given temperature is not available from any of the groups which support the short circuit path interpretation of the fast component.[1–3,6,23–25] However, Archer et al. have used autoradiography to show conclusively that indeed Hg does diffuse rapidly down extended defect paths.[1]

Based on the time period in which the various studies were done, one possible explanation for the discrepancy is that Tang and Chen both used bulk grown material which is expected to have a high density of subgrain boundaries, while the most recent studies were performed on higher quality epitaxial material. A comparison of the radiotracer profiles reported by the various authors lends some qualitative support to this explanation.[1,2,4,11] Archer et al. clearly resolve four orders of magnitude of the slow component in their metalorganic vapor phase epitaxy studies.[1] Their liquid phase epitaxy studies yield similar results.[2] This clarity is absent from all of the

published Hg self-diffusion data of Chen and Tang with the notable exception of Fig. 25 in Chen's thesis.[11] For example, Tang states that the radiotracer profile shown in Fig. 5.5 of Ref. 4 is "typical." In fact, it is at best difficult to distinguish between two different regimes in that figure. Nevertheless, additional studies and Hg pressure dependence measurements on epitaxial material will be necessary to conclusively resolve these discrepancies.

TYPE-CONVERSION

In processing $Hg_{0.8}Cd_{0.2}Te$ material, it is common to employ a step in which as-grown material is annealed in a Hg-rich ambient to reduce the deviation from stoichiometry.[28–30] If the anneal is not performed to completion, the resulting material is typically characterized by an n-type skin on a vacancy doped p-type core (provided there are no significant extrinsic acceptors present). The transition from the n-type to p-type region is marked by the junction depth, x_j. The behavior of x_j has been studied extensively for $Hg_{0.8}Cd_{0.2}Te$ as a function of the initial concentration of excess Te in the material, temperature, time, ambient Hg pressure, and the background donor concentration.[7,8,31–34] Schaake et al. developed a detailed analytical model based on assumptions of local equilibrium and determined that at 270°C the type-conversion process occurs by a mixed interstitial vacancy mechanism.[31] Our modeling results agree with this conclusion. In fact, it can be shown that Eqs. (2) and (3) reduce to Schaake's algebraic expressions in the steady state limit.

As an example, consider the case of $Hg_{0.8}Cd_{0.2}Te$ material with an initially large, uniform vacancy concentration, v_0. A Hg-rich anneal is performed for time t at a given temperature (typically 150–350°C) to form an n-on-p junction. It is assumed that the material is free of second phase Te and that it is much thicker than the simulated junction depth. Consider the assumption that the vacancy diffusion component is insignificant in the type conversion process. Electric field effects are negligible because $Hg_{0.8}Cd_{0.2}Te$ is always intrinsic at type-conversion temperatures and Eqs. (2) and (3) reduce to,

$$\frac{\partial i}{\partial t} = D_i \frac{\partial^2 i}{\partial x^2} - k_{iv}iv + g \tag{18}$$

$$\frac{\partial v}{\partial t} = -k_{iv}iv + g. \tag{19}$$

If the interaction rate constants are sufficiently large so that the approximation of local equilibrium is valid throughout the material, the steady state approximation simplifies Eqs. (18) and (19) giving,

$$D_i \frac{\partial^2 i}{\partial x^2} = 0. \tag{20}$$

This expression may be integrated once for the interstitial flux,

$$J_i = -D_i \frac{\partial i}{\partial x} \tag{21}$$

which is a constant. Given that the interaction rate constants are large and that vacancy diffusion has been assumed negligible, the vacancy concentration will rise sharply to its core value at x_j. The total number of vacancies that were originally in the region less than x_j were annihilated by a flux of Hg interstitials given by Eq. (21) over the anneal period yielding the relationship,

$$\int D_i \frac{\partial i}{\partial x} dt = v_o x_j \tag{22}$$

In the steady state the surface interstitial concentration is assumed at its Hg-rich equilibrium value throughout the process and goes to zero at x_j where the recombination is proceeding. This gives the derivative,

$$\frac{\partial i}{\partial x} \approx \frac{i_o}{x_j} \tag{23}$$

where i_o is the Hg-rich interstitial solubility limit. Upon substituting Eq. (23) into Eq. (22), taking the derivative of both sides with respect to time, separation of variables, and integration, the resulting expression may be solved for the chemical diffusivity,

$$\frac{x_j^2}{t} = \frac{2D_i i_o}{v_o}. \tag{24}$$

If the Hg-rich self-diffusion process at the same temperature results from a Hg interstitial mechanism, then i_T in Eq. (17) is i_o and substituting into Eq. (24) gives,
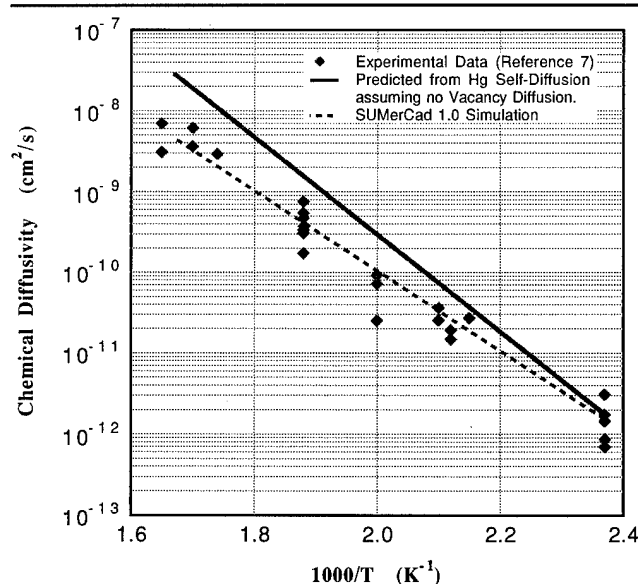

Fig. 3. Type conversion junction depth temperature dependence predicted by Hg self-diffusion data assuming no vacancy diffusion and initially 2×10^{17} cm^{-3} vacancies compared to simulated (SUMerCad) and measured (Ref. 7) values.
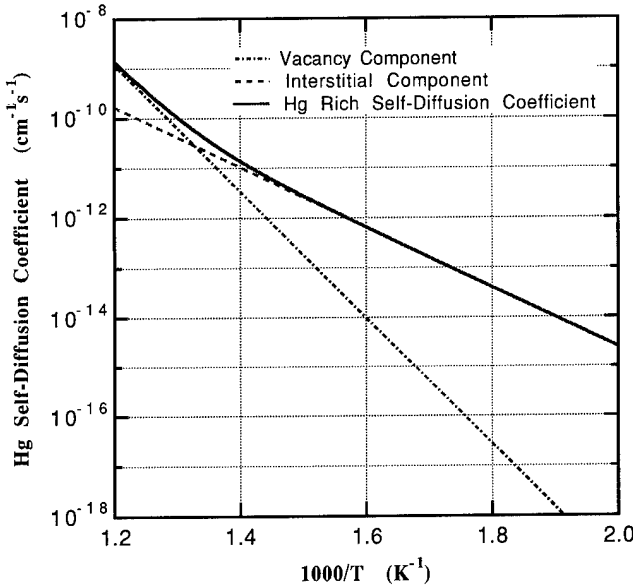
Fig. 4. A SUMerCad simulation of the Hg-rich self-diffusion coefficient as a function of temperature.

$$\frac{x_j^2}{t} = \frac{2D_{Hg}C_o}{v_o}. \tag{25}$$

The preceding expression is plotted as the solid line in Fig. 3 as a function of the Hg-rich self-diffusion expression determined by Archer et al. and taking v_o = 2×10^{17} cm^{-3}.[1] It is seen that Eq. (25) significantly overestimates the experimental data of Jones et al., getting worse at the higher temperatures.

In type-conversion, a vacancy diffusion component results in shallower electrical junctions.[31] The dashed line in Fig. 3 represents SUMerCad simulations for similar material ($N_D = 3 \times 10^{15}$ cm^{-3}) where the vacancy diffusion coefficient is given by $D_v = (1.2 \times 10^5$ cm^2/s) exp(-1.51 eV/kT) and x_j is determined by solving Eqs. (2) and (3). It is clear that the error in using Eq. (25) is a direct consequence of neglecting vacancy diffusion in type-conversion. When this vacancy diffusion coefficient is plugged back into the Hg-rich self-diffusion formalism [Eqs. (5)– (8)], it is clear that vacancy diffusion remains negligible up to 430°C (see Fig. 4). While vacancies do diffuse, they are typically not important in Hg-rich self-diffusion because their concentrations are depressed. In addition, if Hg-rich self-diffusion below 430°C were dominated by a vacancy mechanism, x_j could not be fit with a consistent D_i i_R product. The Hg-rich self-diffusion coefficients predicted by SUMerCad are shown in Fig. 4 at elevated temperatures. These results agree well with the experimental data shown in Fig. 6 of Ref. 2.

DISCUSSION

The Hg$_{0.8}$Cd$_{0.2}$Te type-conversion and Hg self-diffusion processes have been analyzed in detail in the context of a first order reaction kinetics approach. Sets of nonlinear, stiffly coupled continuity equations have been presented to describe the multiparticle, or point defect, interactions and motion. The discussion

has been centered about the Hg point defects since they tend to be more abundant.[10] In fact, the interdiffusion process can be modeled based upon a Frenkel pair mechanism interaction also dominated by the cation sublattice (including Cd).

Indeed, interdiffusion is perhaps the most interesting, if not the most complex, phenomenon to be modeled in a general Hg$_{1-x}$Cd$_x$Te simulator, because it is essentially a system comprised of a continuous set of semiconductors characterized by their Cd fraction x. Nevertheless, it is still quite easy to set up the appropriate continuity equations,

$$\frac{\partial i_H}{\partial t} = \frac{\partial}{\partial x}\left[D_{iH}\frac{\partial i_H}{\partial x}\right] +$$

$$g_H\frac{(C_T - C - v)}{C_T} - k_H i_H v - 2\frac{\partial}{\partial x}[i_H \mu_H \xi] \tag{26}$$

$$\frac{\partial i_C}{\partial t} = \frac{\partial}{\partial x}\left[D_{iC}\frac{\partial i_C}{\partial x}\right] + g_C\frac{C}{C_T} - k_C i_C v - 2\frac{\partial}{\partial x}[i_C \mu_C \xi] \tag{27}$$

$$\frac{\partial v}{\partial t} = \frac{\partial}{\partial x}\left[D_v\frac{\partial v}{\partial x}\right] + g_H\frac{(C_T - C - v)}{C_T} +$$

$$g_C\frac{C}{C_T} - v(k_H i_H + k_C i_C) + 2\frac{\partial}{\partial x}[v\mu_v \xi] \tag{28}$$

$$\frac{\partial C}{\partial t} = \frac{vD_v}{C_T}\frac{\partial^2 C}{\partial x^2} - \frac{CD_v}{C_T}\frac{\partial^2 v}{\partial x^2} +$$

$$\frac{1}{C_T}\frac{\partial D_v}{\partial x}\left[v\frac{\partial C}{\partial x} - C\frac{\partial v}{\partial x}\right] - \tag{29}$$

$$g_C\frac{C}{C_T} + k_C i_C v - 2\frac{C}{(C_T - v)}\frac{\partial}{\partial x}[v\mu_v \xi],$$

where the subscripts H and C denote Hg and Cd respectively, g_j and k_j are the Frenkel pair interaction rates, and C_T is the total density of cation sites. These should be compared to the Hg self-diffusion Eqs. (5)– (8) for additional insight. There are several simplifications of Eqs. (26)–(29) which have been done to check their accuracy in various limits, however they are too involved to go into here and so are left as an exercise for the curious reader. While these equations are unquestionably complex, numerical solutions are possible provided all of the coefficients are known as a function of x-value. Indeed, the wealth of characterization of x = 0.2 material must be repeated for a representative selection of x-values in the range x = 0 to x = 1.0. While some information for x ≠ 0.2 does exist, it is not sufficient to completely specify the model parameters.[1,9,35–38] In addition, the intrinsic carrier concentration must be better characterized at process temperatures, since this quantity sets the

transition from intrinsic to extrinsic effects or diffusion vs drift contributions.[35,39,40]

Additional investigations on higher x-value material will be necessary to determine the model parameters over the compositional range. In the absence of this data, the interdiffusion and heterostructure problems cannot be modeled quantitatively with our approach. In addition, it will be necessary to develop a similar formalism which includes the Te sublattice. While Te interstitials and vacancies are not expected to be present in significant concentrations, their existence is critical in explaining the incorporation and diffusion of anion impurities such as I and As.

Finally, it should be noted that the beauty of the kinetics formalism utilized in this paper, is that it lends itself well to extension, rather than extrapolation, beyond the existing experimental domain.

ACKNOWLEDGMENT

REFERENCES

1. N.A. Archer, H.D. Palfrey and A.F.W. Willoughby, *J. Electron. Mater.* 22, 967 (1993).
2. N.A. Archer, H.D. Palfrey and A.F.W. Willoughby, *J. Cryst. Growth* 117, 177 (1992).
3. N. Archer and H. Palfrey, *J. Electron. Mater.* 20, 419 (1991).
4. Mei-Fan Sung Tang, Ph.D. Thesis, Stanford University (1987).
5. D.A. Stevenson and M.-F.S. Tang, *J. Vac. Sci. Technol. B* 9, 1615 (1991).
6. M. Brown and A.F.W. Willoughby, *J. Cryst. Growth* 59, 27 (1982).
7. C.L. Jones, M.J.T. Quelch, P. Capper and J.J. Gosney, *J. Appl. Phys.* 53 (1992).
8. H.F. Schaake, *J. Electron. Mater.* 14, 513 (1985).
9. H.R. Vydyanath, *J. Electrochem. Soc.* 128, 2609 (1981).
10. M. Berding and A. Sher, *J. Electron. Mater.* 22, 1005 (1993).
11. John-Sea Chen, Ph.D. Thesis, University of Southern California (1985).
12. J.L. Meléndez and C.R. Helms, *J. Electron. Mater.* 22, 999 (1993).
13. Hal R. Yeager and Robert W. Dutton, *IEEE Trans. Electron Dev.* ED-32, 1964 (1985).
14. P.M. Fahey, P.B. Griffin and J.D. Plummer, *Rev. Mod. Phys.* 61, 289 (1989).
15. S.T. Dunham, *J. Electrochem. Soc.* 139, 2628 (1992).
16. S.M. Hu, *J. Appl. Phys.* 57, 1069 (1985).
17. M. Hu, *J. Appl. Phys.* 57, 4527 (1985).
18. H.G. Robinson et al., *J. Appl. Phys.* 71, 2615 (1992).
19. R.F. Lever and F.F. Morehead, *J. Appl. Phys.* 73, 1139 (1993).
20. J.L. Meléndez and C.R. Helms, Part I, *J. Electron. Mater.* 24, 565 (1995).
21. M.-F.S. Tang and D.A. Stevenson, *J. Vac. Sci. Technol. A* 6, 2650 (1988).
22. M.-F.S. Tang and D. A. Stevenson, *J. Vac. Sci. Technol. A* 7, 544 (1989).
23. M. Brown and A.F.W. Willoughby, *J. Vac. Sci. Technol. A* 1, 1641 (1983).
24. D. Shaw, *Semicond. Sci. Technol.* 7, 1230 (1992).
25. H.D. Palfrey, *J. Cryst. Growth* 94, 778 (1989).
26. Paul Shewman, *Diffusion in Solids*, (Warrendale, PA: The Minerals, Metals and Materials Society, 1989).
27. A.D. LeClaire and A. Rabinovitch, *J. Phys. C.: Solid State Phys.* 14, 3863 (1981).
28. R.K. Sharma, S.K. Mehta, V.K. Singh, G. Prasad and B.B. Sharma, Crys. *Prop. Prep.* 22-25, Part II, 885 (1989).
29. W.F.H. Micklethwaite, *Semiconductor and Semimetals,* ed. R.K. Willardson and A.C. Beer, (New York: Academic Press, 1981), p. 47.
30. B.E. Bartlett et al., *J. Cryst. Growth* 49, 600 (1980).
31. H.F. Schaake, J.H. Tregilgas, J.D. Beck, M.A. Kinch and B.E. Gnade, *J. Vac. Sci. Technol. A* 3 (1), 143 (1985).
32. H.F. Schaake, J.H. Tregilgas, A.J. Lewis and P.M. Everett, *J. Vac. Sci. Technol. A* 1 (3) 1625 (1983).
33. V.V. Bogoboyashchii, A.I. Elizarov, V.I. Ivanov-Omskii and V.A. Petryakov, *Sov. Phys. Semicond.* 21 (8), 888, (1987).
34. D.T. Dutton, E. O'Keefe, P. Capper, C.L. Jones, S. Mugford and C. Ard, *Semicond. Sci. Technol.* 8, S266 (1993).
35. H.R. Vydyanath, *J. Vac. Sci. Technol. B* 9, 1716 (1991).
36. J.L. Schmit and E.L. Stelzer, *J. Electron. Mater.* 7, 65 (1968).
37. W. Scott, E.L. Stelzer and R.J. Hager, *J. Appl. Phys.* 47, 1408 (1976).
38. E.D. Jones, V. Thanbipillai and J.B. Mullin, *J. Cryst. Growth* 118, 1 (1992).
39. C.-H. Su, P.-K. Liao and R.F. Brebrick, *J. Electron. Mater.* 12, 771 (1983).
40. R.F. Brebrick and J.P. Schwartz, *J. Electron. Mater.* 9, 771 (1980).

Studies on the Diffusion of Zinc and Iodine into CdTe

E.D. JONES, J.C. CLARK, and J. MALZBENDER

School of Natural and Environmental Sciences, Coventry University, Coventry, CVI 5FB, UK

J.B. MULLIN

Electronic Materials Consultant, The Hoo, Brockhill Road, West Malvern, Worcester, WR14 4DL, UK

N. SHAW

DRA Electronics Division, RSRE, St Andrews Road, Great Malvern Worcester, WR14 3PS, UK

A.W. BRINKMAN

Applied Physics Group, University of Durham, Durham, DH1 3LE

Studies on the diffusion of iodine and zinc into CdTe are reported. Each iodine profile was divided up into four distinct regions and described mathematically by a function consisting of the sum of four complementary error functions. When plotted on an Arrhenius graph, the diffusivities gave four straight line relationships with similar slopes and the Arrhenius parameters for the fastest component of $D_{01} = (7 \pm 3) \cdot 10^{-11} \, cm^2 \, s^{-1}$ and $E_1 = (0.21 \pm 0.05) \, eV$. When extrapolated down to 20°C this gave a diffusivity of $10^{-14} \, cm^2 \, s^{-1}$, indicating that when iodine is diffused from the vapor it is not suitable as a long term stable dopant in devices where sharp impurity profiles are required. In the case of the zinc diffusions, each profile can be divided into two parts and was fitted satisfactorily by the sum of two complementary error functions giving two values of the diffusivities: D_{slow} due to zinc diffusion into the slice from the vapor and D_{fast} due to interdiffusion between a surface layer of $Zn_xCd_{1-x}Te$ formed on the slice and the remaining CdTe.

Key words: CdTe, defects, diffusion, HgCdTe, iodine, zinc

INTRODUCTION

The II-VI semiconductor CdTe has a wide variety of applications including γ-ray detectors, solar cells, and electro-optical modulators, but the most common use is as a substrate, a barrier layer or a capping layer in the production of $Hg_xCd_{1-x}Te$ (MCT) infrared detectors. Normally bulk grown substrates of CdTe contain defects such as twins, sub-grain boundaries and tellurium precipitates which can propagate up into the growing MCT epitaxial layer and be deleterious to any devices subsequently formed. In addition, there is

poor lattice matching between the two layers and because of this alternative fabrication routes have been investigated. One of the most successful is the use of $Zn_xCd_{1-x}Te$ (ZCT) crystals as substrates on which to grow the MCT devices directly. This material possesses similar crystal imperfections to CdTe, but when x = 0.04, the ZCT substrate and the epilayer of $Hg_xCd_{1-x}Te$, with x = 0.8, are lattice matched and hence far fewer defects propagate from the interface into the epilayer. Further, the addition of zinc to CdTe to form ZCT strengthens the material, hence making the substrate more robust.

The ability to prepare doped p-n epitaxial structures is another essential requirement if some of the
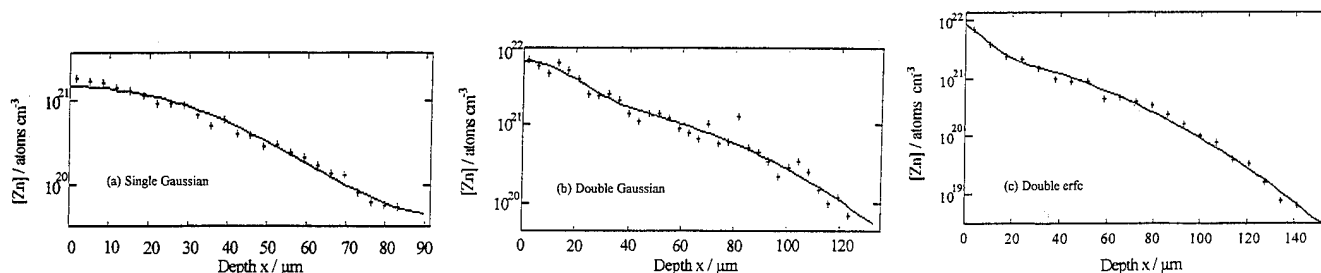
Fig. 1. Graphs showing the different types of profiles for the diffusion of zinc in CdTe.

new developments in these devices are to be realized in practice. The location of the doped region must be well defined within the structure and the concentration of the active impurities has to be controlled accurately. Currently, indium is the most widely used n-type dopant in CdTe and MCT, but it is a fairly fast diffusant.[1] Because of this, attention has been drawn to the halogens which are expected to reside on anion sites. As iodine is the largest of the halogens, it is expected to be least susceptible to diffusion and further it is the least reactive of the halogens.

In the manufacture of devices from CdTe and MCT, it is important that the rates of diffusion of both zinc and iodine in CdTe are known. Prior to this program of work, very little was known about these elements. Gorodetskii et al.[2] measured the rates of diffusion of iodine and indium in CdTe by investigating the changes in electrical conductivity of the slices which had been doped by ion bombardment and calculated the diffusion parameters for iodine at a temperature of 200°C, to give the following Arrhenius relationship:

$$D = 10^{-8} \times \exp[-(0.4 \pm 0.1 \text{ eV})/kT] \text{ cm}^2 \text{ s}^{-1}.$$

The rates of diffusion of zinc into CdTe have been measured by Aslam et al.[3] using radiotracer techniques and a scanning electron microscope with EDAX attachment.

EXPERIMENTAL TECHNIQUES

CdTe slices, of approximate size 8×8 mm and thickness 0.8 mm, grown by accelerated crucible rotation technique (ACRT) were used in this investigation along with epitaxial layers of thickness 10–15 μm grown on CdTe substrates by liquid phase epitaxy. The surfaces of the slices used for the diffusions were prepared by mechanical polishing with successively finer grades of diamond paste (6, 1, 1/4 μm) and in some cases followed by a chemical polish with 1% bromine in methanol for 10 min. This procedure removed the damaged surface layer caused by sawing the slices from the boule. A total thickness of approximately 200 μm was removed from the surface, approximately an equal thickness by each process

In the measurements reported here, each CdTe slice was sealed in an evacuated silica ampoule with sufficient radioactive tracer to give saturated vapor pressure conditions throughout each diffusion anneal which was carried out in an electric furnace under isothermal conditions. In the case of the iodine diffusions, CdI_2 containing the radioactive isotope ^{125}I, a

fission product with a half life of 60 days, was used as a diffusion source.[4] Whereas with the zinc diffusions, pure zinc which contained ^{65}Zn with a half life of 245 days, was used

The sectioning techniques used to measure the tracer concentration profiles have been described in the literature.[5]

DIFFUSION OF ZINC IN CdTe

The measurements described here are an extension of the results already reported[6] on how the diffusivity D varied with the duration of the anneal t and with the mass of zinc m placed in the capsule at 800°C. The variations in t and m were $1 < t < 140$ h and $1 < m < 43.3$ mg, respectively. The high values of m were more than sufficient to give a saturated vapor pressure of zinc metal in the capsule throughout the diffusion anneal.

It was reported in the previous paper[6] that the concentration profiles possessed two distinct components and were fitted using computer software comprising of either the sum of two Gaussian functions or two complementary error (erfc) functions. The former function gave the best fit when m was not sufficient to maintain a saturated vapor pressure over the slice throughout the diffusion whereas the latter function was used when saturated vapor pressure conditions were maintained. In certain instances where the value of m was low (< 2 mg) a single Gaussian function gave the best fit to the experimental data. Typical diffusion profiles are shown in Fig. 1.

Measurements on the variation of D with t when m = 8 mg and T = 800°C indicated that for t < 6 h, D decreased rapidly with increasing t due to the formation of the ternary compound $Zn_x Cd_{1-x} Te$ with x = 0.8 on the surface of the CdTe slice. The thickness of the layer was dependent on m. When t > 6 h, D was independent of t. For t > 6 h, the variation of D with m can be divided into two distinct parts:

a. For m < 2 mg, the thickness of the ternary layer is so thin that it does not effect the diffusion in any way, or possibly no layer is formed at all. Diffusion is due to zinc atoms diffusing from the vapor phase directly into the CdTe giving a one component profile possessing a Gaussian shape indicating that 'limited source' conditions apply.

b. For 2 mg < m < 20 mg, two component profiles are obtained which are fitted best by the sum of two Gaussian functions whereas for m > 20 mg, again two component profiles are seen but a function

composed of the sum of two erfc expressions gives the best fit.

In the former instance, both parts of the profiles are 'source limited' whereas in the second case source depletion in the capsule is negligible. In this case, it is suggested that diffusion is occurring via two different mechanisms: one from the vapor phase (D_{slow}) as proposed in (a) which is dependent on m for m < 20 mg, and a faster interdiffusion between the ZCT surface layer and the CdTe slice (D_{fast}) which is completely independent of m.

For the work reported here, further diffusion measurements were carried out in the temperature range 390–950°C. The values of m and t in these diffusions were arranged so that D was independent of these quantities and consequently only dependent on T. For the measurements carried out in the temperature range 550–950°C, two component profiles, which were fitted best by a function consisting of the sum of two erfc expressions, were obtained similar to the one shown in Fig. 1c. The corresponding Arrhenius graphs are shown in Fig. 2. Whereas the results plotted in Fig. 2 give straight line fits, the results obtained from diffusions carried out at temperatures below 550°C showed an unexpected behavior.

One diffusion carried out at 450°C resulted in a profile which was again fitted best by the sum of two erfc expressions, but it gave values of D which were 10^3 higher than expected $(D_{fast} = 2.0 \times 10^{-9}$ cm² s⁻¹ and $D_{slow} = 2.16 \times 10^{-10}$ cm² s⁻¹). This can possibly be explained by the fact that the temperature of the diffusion was very close to the melting point of tellurium which is 452°C. Tellurium precipitates, which are common in this material, may have been in the liquid phase, and could therefore have influenced the diffusion by acting as gettering centers and in addition they may have been associated with fast diffusion paths. The fact that anomalous results were found at 450°C and not at higher temperatures is because the tellurium atoms in the precipitates would have diffused out into the lattice at the higher temperatures, giving a crystal lattice with a more uniform composition. This would have resulted in an increased proportion of the zinc atoms entering the slice by volume diffusion processes rather than along short circuit paths.

A second diffusion at 390°C produced a profile that was fitted best by a single erfc expression giving a single value of D $(2.6 \times 10^{-11}$ cm² s⁻¹) which was again much higher than the value predicted from Fig. 2. Similar to the measurements at 450°C, this high value may have been associated with gettering processes in the tellurium precipitates which would have been solid in this case. If this profile is taken along with those reported earlier,[6] it implies that single component profiles are obtained for diffusions carried out at low temperatures (< 450°C) and in the diffusions where a low mass of zinc was used as the diffusion source (< 2 mg at 800°C). The slices used in these diffusions did not display any surface cracking similar to that observed in slices where two compo-

nent profiles were obtained. The implication is that either the thickness of the surface layer of ZCT was not sufficient to affect the diffusion or else no such layer was formed and that the diffusion took place by zinc atoms diffusing from the vapor directly into the CdTe slice.

The results for the activation energies quoted in Fig. 2 (0.75 eV for the slow component and 1.21 eV for the fast component) are much smaller than those for the metal self-diffusion in both CdTe and ZnTe (2.5 and 2.7 eV, respectively), however, the result for the slow component is in good agreement with the activation energy for the slow component found by Aslam et al.[3] (0.69 eV). The relatively low values of the activation energy are surprising and it is not possible to offer an explanation for this at this stage.

DIFFUSION OF IODINE INTO CdTe

An initial study on the diffusion of iodine into CdTe has been reported[7] in which four diffusion anneals were carried out at selected temperatures in the range 20–270°C. In the measurements reported here, diffusion anneals were carried out in the temperature range 20–600°C where CdI_2 was used as the diffusion source. The concentration profiles were measured using radiotracer sectioning.

The shape of each of the profiles can be divided up into four distinct regions and each profile can be described mathematically by a function consisting of the sum of four erfc expressions giving four values for the diffusivity, one for each part of the profile. A typical profile is shown in Fig. 3 and the four parts to each profile can be clearly distinguished, the slowest three components, D1–D3, are shown under high depth resolution in (a), whereas the whole concentration profile is shown in (b).

The iodine in the CdI_2 in the initial experiments possessed a low specific activity (0.01 μCi/mg), and consequently the four parts of the profile were not clearly discernible in every case. When the source strength of the iodine was increased (0.2 μCi/mg), it was possible to use a sectioning technique with an
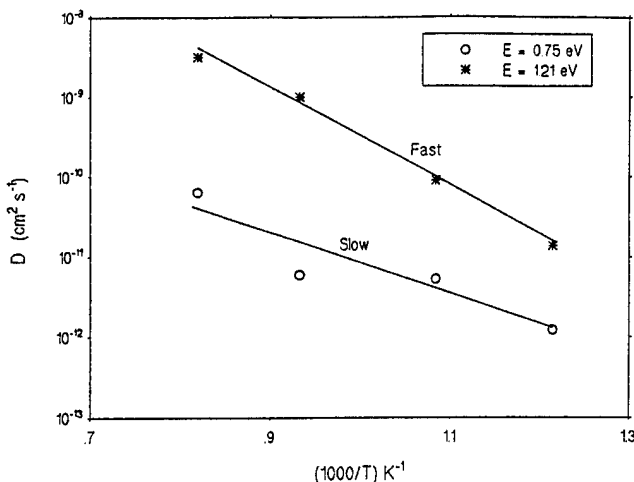
Fig. 2. An Arrhenius graph showing the diffusivities for the two componets for the diffusion of zinc in CdTe.

a

b
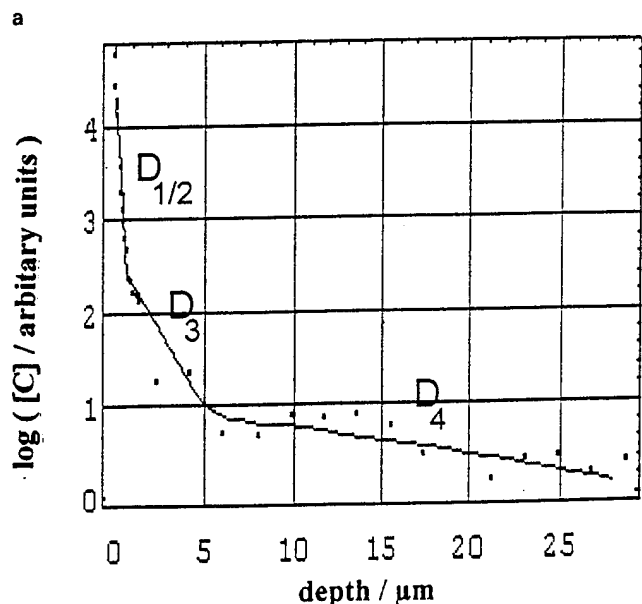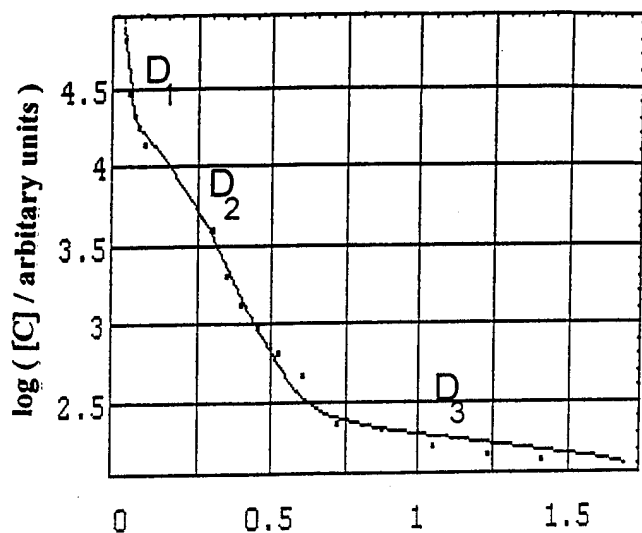
Fig. 3. A typical concentration profile for the diffusion of iodine in CdTe.

Fig. 4. An Arrhenius graph showing the diffusivities D_1–D_4 for the diffusion of iodine in CdTe.
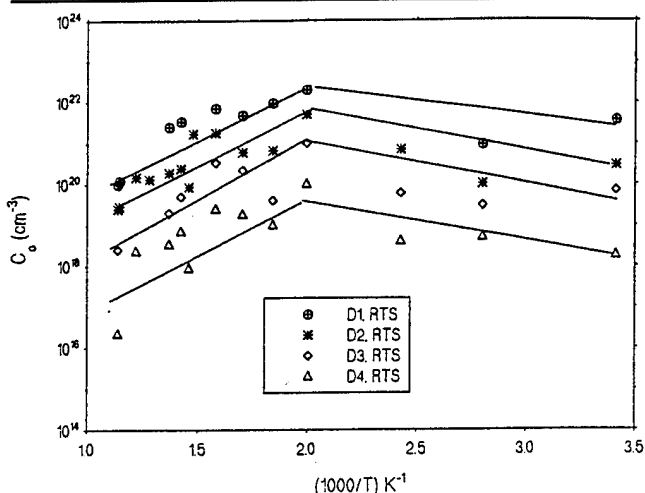
Fig. 5. An Arrhenius graph of the surface concentratons C_{01}–C_{04} for the diffusion of iondine in CdTe.

improved depth resolution and the quality of the profiles improved considerably and the four parts of the profile could be distinguished clearly.

The four values of the diffusivities D_1 to D_4 and the corresponding values of the surface concentrations C_{01} to C_{04} obtained from the profiles are plotted on an the Arrhenius graphs in Fig. 4 and Fig. 5, respectively. The diffusivities were best described by an equation of the form:

$$D = D_0 \exp (- E/kT),$$

resulting in the following Arrhenius parameters:

$E_1 = (0.21 \pm 0.05)$ eV, $D_{01} = (7 \pm 3) \cdot 10^{-11}$ cm^2 s^{-1},
$E_2 = (0.29 \pm 0.04)$ eV, $D_{02} = (2.1 \pm 0\ 8) \cdot 10^{-13}$ cm^2 s^{-1}
$E_3 = (0\ 28 \pm 0.03)$ eV, $D_{03} = (3\ 8 \pm 1.2) \cdot 10^{-14}$ cm^2 s^{-1},
$E_4 = (0.28 \pm 0.05)$ eV, $D_{04} = (2.1 \pm 1.6) \cdot 10^{15}$ cm^2 s^{-1}.

It can be seen that to within the limits of experimental error, the activation energies are equal, al-

though E_1 is slightly lower than the other activation energies. The diffusivities for the fastest component have been plotted on an Arrhenius graph in Fig. 6 along with the Arrhenius expression reported by Gorodetskii et al.[2] It can be seen that the results agree closely at 200°C, the temperature at which Gorodetskii et al.[2] made their measurements; but because of the difference in the activation energies, there is a systematic difference between the two sets of results. It must be emphasised that Gorodetskii et al.[2] only made a limited number of measurements at 200°C, whereas the measurements reported here cover the temperature range 20–600°C. In addition, it can be seen that the low activation energy for the fastest diffusing component D_1 component results in a diffusivity of 10^{-14} cm^2 s^{-1} at 20°C, indicating that when iodine is diffused into CdTe from a vapor of the compound CdI$_2$, it is not suitable as a long term stable dopant in devices where sharp impurity profiles are required.

From the values for C_0 plotted on an Arrhenius graph in Fig. 5, it can be seen that all four components increase with decreasing temperature in the range 600–230°C, whereas they decrease with decreasing

temperature in the range 230–20°C. The values for the slowest diffusing component C_{01} are very high, the highest values occurring where there is the change in slope in the graphs ($\sim 10^{22}$ cm^{-3}). This could possibly be due to a layer of a ternary compound involving iodine and CdTe possessing a high iodine concentration forming on the surface of the slice during the diffusion. It was certainly not a thin layer of CdI$_2$ which was deposited on the surface of the slice during, or at the end of the diffusion because all such deposits were removed before the sectioning commenced.

The fact that all four parts of the diffusion profile gave similar activation energies suggests that similar transport mechanisms are operating. A possible explanation of this is that diffusion is dominated by the slowest mechanism (D_1) and that in this process some iodine atoms are being trapped, possibly at defect sites. These atoms might be released after a certain time and undergo further diffusion. Trapping near the surface due to physisorption or chemisorption of the atoms could account for the high iodine concentrations near the surface of the slice. This is supported by pictures obtained of an iodine diffused slice[4] taken in the ion imaging mode of the secondary ion mass spectroscopy instrument, where small regions of high iodine concentrations were clearly distinguishable in the material (less than 10 μm across with a density of about 10^5 cm^{-2}). Similar effects have also been reported in CdTe slices doped with chlorine when grown from the melt.[8] The occurrence of two component profiles in II-VI semiconductors is common, and Shaw[9] has stated that the fast tail is due to "short circuit" diffusion, but it is difficult to draw an analogy with the work reported here.

The variation of C_0 with temperature (see Fig. 5) can be explained in terms of the Cd-Cl-Te ternary phase diagram. It has been reported that the CdTe/CdCl$_2$ pseudo binary phase diagram possesses a eutectic at 505°C[10] which indicates that complete solid solubility exists only over limited concentrations. No information has been reported for the CdTe/CdI$_2$ pseudo binary phase diagram, but a similar behavior can be expected. It is possible that the kink at 230°C in the four graphs in Fig. 4 is a part of the eutectic existing in the CdTe/CdI$_2$ pseudo binary system and is a part of an eutectic surface in the Cd-I-Te ternary system. The fact that the four lines show a similar behavior indicates that four mechanisms are operating with different solubilities.
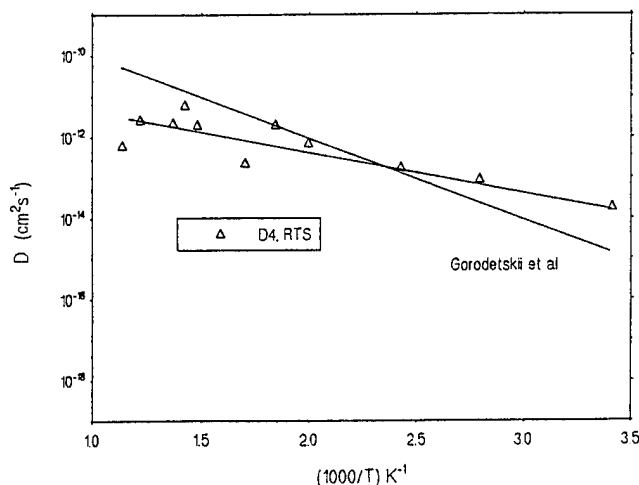
Fig. 6. An Arrhenius graph showing a comparison of the diffusivities D$_4$ with the results of Gorodetskii et al.

A recent measurement in epitaxial grown iodine doped MCT[11] layers gave a diffusion coefficient of 10^{-13} cm^2 s^{-1} at 430°C, which is in agreement with the results reported here.

ACKNOWLEDGMENTS

REFERENCES

1. E. Watson and D. Shaw, *J. Phys. C.* 16, 515 (1983).
2. E.A. Gorodetskii, G.A. Kachurin and C.S. Smirnov, *Diffuz Poluprov.* 72 (1967).
3. N. Aslam, E.D. Jones, T.C.Q. Noakes, J.B. Mullin and A.F.W. Willoughby, *J. Cryst. Growth.* 117, 249 (1992).
4. J. Malzbender, E.D. Jones, J.B. Mullin and N. Shaw, *J. Cryst. Growth,* to be published.
5. N.M. Stewart, E.D. Jones and J.B. Mullin, *J. Mat. Sci.* 3, 211 (1992).
6. E.D. Jones, J.C. Clark, J.B. Mullin and A.W. Brinkman, Proc. 6th Intl. Conf. on II-VI Compounds, to be published in *J. Cryst. Growth.*
7. E.D. Jones, J. Malzbender, J.B. Mullin and N. Shaw, Proc. 6th Intl. Conf. on II-VI Compounds, to be published in *J. Cryst. Growth.*
8. T. Shoi, H. Onabe and Y. Hiratate, *Nucl. Instr. Methods Phys. Res. A* 322, 324 (1992).
9. D. Shaw, *Semicond. Sci. Technol.* 7, 1230 (1992).
10. H. Tai and S. Hoi, *J. Jpn. Inst. Met.* 40, 722 (1976).
11. S. Murakami, T. Okamoto, K. Maruyama and H. Takigawa, *Appl. Phys. Lett.* 63, 899 (1993).

Diffusion in Mercury Cadmium Telluride—An Update

D. SHAW

Department of Applied Physics, University of Hull, Hull, HU6 7RX, UK

The various diffusion coefficients (self-diffusivity, chemical self-diffusivity compositional diffusivity, impurity diffusivity) are defined. The conditions required for the observation of a Kirkendall effect are described. There is good agreement in the results for Hg and for Cd self-diffusion. The evidence suggests that the self-diffusivity is largely independent of P_{Hg} above ~300°C but shows an increase as Hg saturation is approached (for both Hg and Cd). Good agreement is also found in the Arrhenius parameters describing the movement of the p to n conversion boundary. Modeling of this diffusion boundary does, however, raise problems which are discussed. The situation in compositional interdiffusion is more complex: above ~400°C, reasonable agreement exists between various workers for large x_{Hg} but not for small values; below 400°C, substantial disagreement is evident. In impurity diffusion exhibits both erfc and non-erfc profiles for reasons which are unclear. Good agreement is found between In diffusivity measurements at high In concentrations: at low concentrations, the diffusivity decreases dramatically. As diffusion yields erfc profiles with good agreement again being found: a notable feature is the P_{Hg} dependence of the As diffusivity. Where appropriate, diffusion models are discussed.

Key words: Diffusion, diffusivity, HgCdTe, impurities, interstitials, vacancies

INTRODUCTION

Atom diffusion is an important part of the science and technology of mercury cadmium telluride (MCT): it is directly exploited in the interdiffused multilayer process, in p to n type conversion and in dopant incorporation. An understanding of the relevant diffusion processes is obviously necessary if optimum results are to be achieved by diffusion anneals. Previous reviews of diffusion in MCT have been made.[1–3] This paper is concerned primarily with updating these earlier reviews. The existence of reliable diffusivity measurements is an essential prerequisite for a proper interpretation in terms of atomic events. In this context, reliability means not only quantitative accuracy but, more importantly, that the measured diffusivity is in fact the quantity that was intended to be measured (e.g. distinguishing volume diffusion from short-circuit path diffusion). Diffusion anneals

can take place under various conditions with different types of diffusion coefficient reflecting the different situations, and it is important to first define and describe these diffusion coefficients.

TYPES OF DIFFUSION COEFFICIENT INVOLVED IN MCT

Two distinct diffusion regimes can be recognized:
a) diffusion occurs without any net chemical fluxes; i.e. the material is chemically homogenous;
b) the material is chemically inhomogeneous so that diffusion gives rise to net chemical fluxes (we assume isothermal and single phase conditions).

In other words, regime (a) represents diffusion in conditions of chemical equilibrium and gives rise to self-diffusion coefficients in the case Hg, Cd, or Te diffusion and to isoconcentraton diffusion coefficients in the case of impurities. Regime (b) describes diffusion in conditions of chemical disequilibrium which arise during changes in nonstroichiometry (chemical

self-diffusion), changes in the Hg/Cd ratio (compositional interdiffusion or CID) and changes in impuirty doping levels (impurity diffusion). Ideally, diffusion in either regime occurs in single crystal material which is devoid of line or planar defects (i.e. single dislocations and subgrain boundaries). So far in MCT technology such defects (generically referred to as extended point defects or EPD) always occur and they provide rapid diffusion routes compared to volume diffusion in the surrounding lattice. It is important to understand and recognize the contribution of short-circuit path diffusion, via EPD, to a concentration profile obtained in a diffusion experiment.

Self-Diffusion

Because self-diffusion, by definition, does not involve net chemical fluxes, it can only be observed by 'tagging' the Hg, Cd, or Te atoms. This can be done by using a radiotracer or by using an enriched stable isotatope of the diffusion source. Self-diffusion, therefore, is measured by diffusion flow in an isotopic gradient so that, by Fick's first law of diffusion, the flux of tagged atoms, J^*, in one dimension is given by

$$J^* = -D^* \frac{\partial C^*}{\partial x} \qquad (1)$$

where C^* is the concentration of tagged atoms at position x and D^* is defined as the self-diffusion coefficient. It is commonly assumed that D^* is applicable to all isotopes of the particular element i.e. the effects of isotopic mass differences ($\sim 1\%$) are taken to be negligible. Experimental formats for self-diffusion measurements are based on one-dimensional diffusion into a semi-infinite sample from a thin surface film diffusion source or by arranging that the surface concentration, C_o^* of the tagged species does not change with time (i.e. an external phase provides essentially an infinite reservoir of tagged atoms). Gaussian and erfc concentraton profiles are obtained for the thin film and infinite source conditions respectively.[4]

It is generally accepted that atomic diffusion basically takes place via a single jump of an atom to a nearest neighbor site on the same sublattice. Such jumps occur by either:
- direct exchange of substitutional atoms occupying neighboring sites, or
- the involvement of lattice point defects (e.g.) vacancies, self-interstitials, di-vacancies.

The presence of point defects means that jumps between interstitial sites as well as between substitutional sites must be taken into account. If D^* represents a nondefect jump mechanism, it will be purely a function of temperature, T, and composition (x_{Cd}). On the other hand, for a defect based mechanism[4]

$$D^* = f_k D_k C_k \qquad (2)$$

where D_k is the defect diffusivity, C_k is the defect concentration (site fractions referred to the sublattice) and f_k is the correlation factor ($f_k = 0.78$ or 1, respec-

tively, for a single vacancy or interstitial mechanism). D^* now not only depends on T through D_k but also on C_k which in turn is a function of T and level of nonstoichiometry (controlled by the ambient Hg pressure, P_{Hg}). As an example, consider Hg self-diffusion by a V_{Hg}'' mechanism. Defect chemistry shows that $[V_{Hg}''] = K_V/p^2 P_{Hg}$ where K_V is a temperature dependent reaction constant and p is the free hole concentration. Equation (2) now becomes

$$D^* = (0.78 \, K_V/S) D_{V_{Hg}''}/p^2 P_{Hg} \qquad (3)$$

where S is the sublattice site concentration and $D_{V_{Hg}''}$ is the V_{Hg}'' diffusivity. If the MCT crystal is intrinsic then $p = p_i$ (the intrinsic hole concentration) and at a constant T, $D^* \propto P_{Hg}$. However, if the electroneutrality condition (charge balance) is $p = 2[V_{Hg}'']$, it readily follows that $D^* \propto P_{Hg}^{-1/3}$ at constant T. Details for other situations can be found in Ref. 4. If self-diffusion involves more than one mechanism (e.g. vacancy and interstitial), then the measured D^* is the sum of the separate component self-diffusivities and a single Gaussian or erfc profile is still observed.

Isoconcentration Diffusion

In an isoconcentration diffusion experiment, the mercury cadmium telluride sample would first be uniformly doped by impurity diffusion after which a second, but substantially shorter duration, anneal would follow under conditions identical to the first anneal, apart from a tagged impurity diffusion source replacing the original impurity source. The concentration profiles of the tagged impurity are erfc because of the need to use an 'infinite' impurity source. Investigations proceed by observing the effects of doping level, P_{Hg} and T.

Chemical Self-Diffusion

Following Guldi et al.,[5] we define the deviation from stoichiometry, Δ, by

$$\Delta = M_{tot} - Te_{tot} \qquad (4)$$

where M_{tot} and Te_{tot} are the total metal (Hg plus Cd) and total Te concentrations. Note that in chemical self-diffusion, the Hg/Cd ratio is constant: it is the M_{tot}/Te_{tot} ratio that is changing. Assuming that the dominant defects are single self-interstitials and vacancies on both sublattices then it is straightforward to show

$$\Delta = (M_i + V_{Te}) - (Te_i + V_M) \qquad (5)$$

where M_i and Te_i are the total metal and Te interstitial concentrations (i.e. all charge states), V_{Te} and V_M are the total metal and Te vacancy concentrations (i.e. all charge states). Given an MCT sample annealed at a certain P_{Hg} to give a uniform value of Δ which is then annealed again at the same temperature but different P_{Hg}, we can define a flux in Δ, J_Δ, in one dimension by[5]

$$J_\Delta = -D_\Delta \frac{\partial \Delta}{\partial x} \qquad (6)$$

where D_Δ is the chemical self-diffusion coefficient.

Fick's second law of diffusion, therefore, gives

$$\frac{\partial \Delta}{\Delta t} = \frac{\partial}{\partial x}\left(D_\Delta \frac{\partial \Delta}{\partial x}\right) \qquad (7)$$

Detailed analyses, which assume local equilibrium between defects, for specific defect models[5,6] show D_Δ to be a function of Δ which is why D_Δ must be regarded generally as Δ dependent and so must remain within the differential term in Eq. (7). D_Δ also depends on the individual defect diffusivities.[5,6] Solving Eq. (7) is only possible if D_Δ is either constant, in which case an analytic solution can be obtained, or is a known function of Δ and the appropriate defect diffusivities, when numerical integration can be carried out. Either route first requires identification of the defects in Eq. (5).

More importantly perhaps is the question of how Δ can be measured, as $\Delta \leq 10^{19}$ cm^{-3}.[7] If the defects in Eq. (5) are all singly ionized then from charge balance

$$\Delta = p\text{-}n \qquad (8)$$

alternatively if they are all doubly ionized then

$$\Delta = (p\text{-}n)/2 \qquad (9)$$

where n is the free electron concentration. Provided either of these ionization conditions is met then Δ can be measured via measurement of (p-n). Otherwise (p-n) can still be measured but while it will be related to Δ, the precise connection will be unclear.

Given that D_Δ is a function of Δ, it follows from Eq. (7) that Δ is a function solely of $x/\sqrt{t}$. This means that in a chemical self-diffusion anneal, the depth x after time t, for a particular value of Δ, satisfies $x/\sqrt{t} =$ constant i.e. $x^2 \propto t$. In particular for a p-n junction at depth x_j, $\Delta = 0$ and $x_j^2 \propto t$.

It is a natural step to relate D_Δ with the self-diffusivities but two factors need to be taken into account:

- D^* could be dominated by the defects $(V_{Hg}V_{Te})$ or (Hg_iV_{Hg}) which would make no contribution to D_Δ;
- D_Δ relates primarily to defect diffusivities D_k [Eq. (2)] whereas D^* is related to D_kC_k, a high D_k does not necessarily give a high D_kC_k (high D_kC_k terms will dominate D^*).

Compositional Interdiffusion

Consider a layer of HgTe joined to a layer of CdTe in the plane defined by x = 0 in the laboratory frame of reference. HgTe occupies the space < 0 and the layers are thick enough for them to equate to semi-infinite solids, i.e. the CID region is located around x ~ 0. Suppose also that inert markers are included at this interface, i.e. this marker plane defines the initial interface. At the annealing temperature, diffusional mixing of Hg and Cd on the metal sublattice will take place with net fluxes of Hg and Cd across the marker plane. Suppose further that Hg diffuses faster than Cd (which therefore requires a counter vacancy flow) so that the marker plane moves into the original HgTe layer. The velocity of the marker plane v in the laboratory frame is given by[8]

$$v = \left(D_{Hg} - D_{Cd}\right)\frac{\partial x_{Hg}}{\partial x} \qquad (10)$$

where D_{Hg} and D_{Cd} are the diffusivities at the marker plane. Referred also to the laboratory frame the intermixing of Hg and Cd can be characterized by a single diffusivity, the compositional interdiffusivity $\tilde{D}$, equal to[8]

$$\tilde{D} = D_{Hg}x_{Cd} + D_{Cd}x_{Hg} \qquad (11)$$

D_{Hg} and D_{Cd} are known as intrinsic diffusion coefficients. The displacement of the marker plane requires $D_{Hg} \neq D_{Cd}$ and is known as the Kirkendall effect. Although the discussion has centered on the marker plane (initially at x = 0), Eq. (10) and Eq. (11) are valid for any marker plane. It follows that $\tilde{D}$, D_{Hg}, and D_{Cd} are functions of x_{Hg} i.e. concentration dependent. Tang and Stevenson[9] also showed that Eq. (10) and Eq. (11) remain valid when the analysis takes specific account of the Te sublattice.

$\tilde{D}$ as a function of x_{Hg} can be determined experimentally from a complete CID profile;[10] D_{Hg} and D_{Cd} can only be obtained from combined measurements of $\tilde{D}$ and v, i.e. inert markers must be inserted throughout the CID region. The observation of a Kirkendall effect in HgTe/CdTe CID has been reported.[11,12] Tungsten wires[11] and micro-pores[12] were used as the inert markers. The 'inertness' of these markers has, however, been queried and the conclusion drawn that there is no real Kirkendall effect in MCT.[3] A consequence of this conclusion, from Eq. (10), is that $D_{Hg} = D_{Cd}$ and further that[9] $D_{Hg} = D_{Cd}$ at all x_{Hg}.

At the level of interest concerned with material/structure preparation knowledge of $\tilde{D}$ and its dependence on x_{Hg}, T and Δ is very important. Interest in the intrinsic diffusivities, D_{Hg} and D_{Cd}, is primarily theoretical through their relationships to D^*_{Hg} and D^*_{Cd} (self-diffusivities). These relationships are complex,[9] and it is a moot point, given the present experimental precision and accuracy for $\tilde{D}$, D^*_{Hg}, and D^*_{Cd}, whether useful conclusions can be arrived at.

Short-Circuit Path Diffusion

Attention has already been drawn to the need to take into account the effect of EPD on the penetration by diffusion of a diffusant into MCT. In essence, EPD provide a parallel diffusion path to volume diffusion. Palfrey[13] was first to recognize their possible influence on Hg self-diffusion profiles in MCT and more recent work has supported her interpretation.[14,15]

It appears that the most commonly encountered situation arises when there is no overlap between the outdiffusion zones of adjacent dislocations or grain boundaries. Theoretical modeling has been performed;[16,17] and although the detail is complex, the essential results can be simply described (see Ref. 14 for a fuller description). For single dislocations, the average planar concentration at depth x after time t is

$$C(x,t) = C_oF(s) + \pi C_o a^2 dQ(s) \qquad (12)$$

Table I. Arrhenius Parameters for D^*_{Hg} and D^*_{Cd} in MCT

	Ref.	Temp. (°C)	P_{Hg}	D_o (cm²s⁻¹)	Q(eV)
D^*_{Hg}	19	350–490	Varied	0.47*	1.51*
	20	350–500	Varied	0.28†	1.51†
	15	254–452	Saturation	3×10^{-3}	1.20
D^*_{Cd}	19	400–490	Varied	0.7	1.55
	20	350–500	Varied	0.057†	1.44†
	21	350–500	Varied [≤0.5P_{Hg}(sat)]	0.068	1.41
	21	230–500	Saturation	1.9×10^{-3}	1.15

*Chen[19] gave D_o = 0.99 cm²s⁻¹, Q_o = 1.50 eV, but these values give D^*_{Hg} about twice the measured ones. The parameters in the table were obtained by a least squares fit to Chen's graphical data.
†Tang and Stevenson[20] omitted data at 350°C in the calculation of their parameters for D^*_{Hg} and D^*_{Cd} (private communcation) because of a suspected break in the Arrhenius line below 400°C. The parameters in the table were obtained by least squares fitting to all their graphical data between 350 and 500°C inclusive.
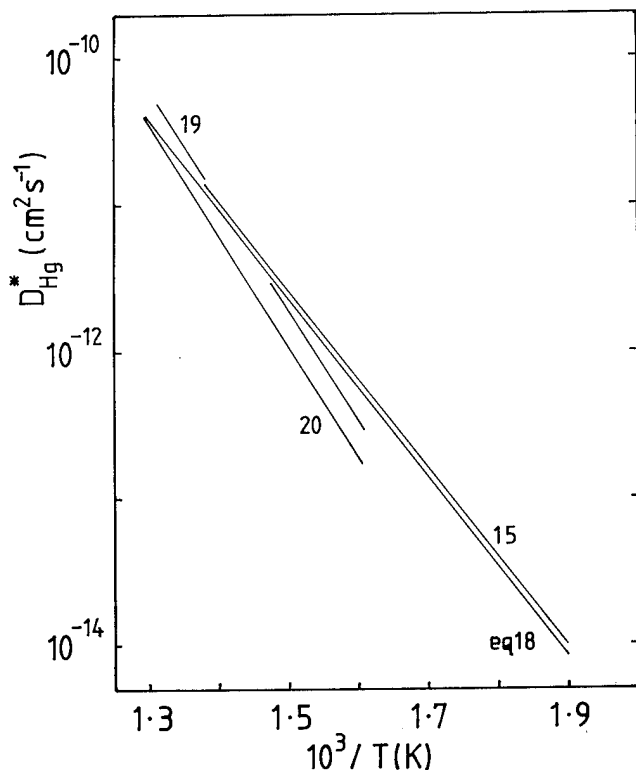
Fig. 1. Arrhenius plots for D^*_{Hg} in $Hg_{0.8}Cd_{0.2}$Te from Refs. 15,19, 20 calculated using Eq. (18) and parameters in Table I.

where s = x/2 $\sqrt{Dt}$, D is the volume diffusivity [D*, D_Δ, $\tilde{D}$, D(impurity)]: C_o is the surface concentration, a is the dislocaton pipe diameter, d is the dislocation density. F(s) is an erfc or Gaussian function depending on boundary conditions and represents volume diffusion. Q(s) is a complex function which provides a negligible contribution to Eq. (12) when s ≤ 2. When s ≥ 2, the Q(s) term becomes dominant in Eq. (12), so that for a constant surface concentration (erfc)
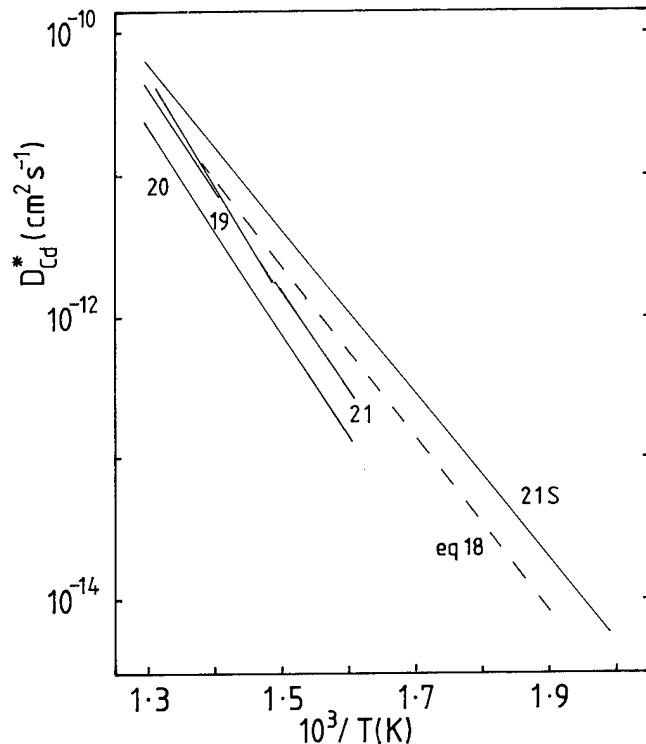
Fig. 2. Arrhenius plots for D^*_{Cd} in $Hg_{0.8}Cd_{0.2}$Te calculated using the parameters given in Table I. The S label against Ref. 21 denotes Hg saturation. Also included for comparison is a plot of D^*_{Hg} from Eq. (18).

$$C(x,t) \propto (Dt)^{0.92} \exp(-g_d x) \qquad (13)$$

or for the thin film case (Gaussian)

$$C(x,t) \propto (Dt)^{0.92}(\Delta_d-1)^{1/2} \exp(-g_d x) \qquad (14)$$

with

$$g_d \approx [(\Delta_d-1)a^2]^{-1/2} \qquad (15)$$

and $\Delta_d = D'_d/D$ where D'_d is the diffusivity in the dislocation pipe. For (sub) grain boundaries, two component profiles are again found[17] with volume diffusion again described by $C_oF(s)$ [as in Eq. (12)] but in the fast tail

$$C(x,t) \propto \exp(-g_{gb}x^{1.2}) \qquad (16)$$

where $g_{gb} = (0.78/D'_{gb} \delta)^{0.6}(4D/t)^{0.3}$. D'_{gb} is the diffusivity in the grain boundary whose width is δ. Equations (12) and (16) are valid provided d ≤ $(\pi Dt)^{-1}$ and the mean separation between layers is > 10 $\sqrt{Dt}$,[18] respectively.

Hg AND Cd SELF-DIFFUSION IN MCT

Measurements using radiotracers have been made of D^*_{Hg}[15,19,20] and of D^*_{Cd}[19–21] as functions of P_{Hg},[19–21] as well as at Hg saturation only,[15,21] within the temperature range 254–500°C. A notable feature is that in the Hg diffusion profiles[15,19,20] and in the Cd ones[19,20] the profiles comprised two sections, a 'slow' erfc first section followed by a 'fast' tail. Whereas Refs. 19 and 20 interpreted both sections in terms of volume diffusion processes, their profiles are classic illustrations of Eq. (12). In view of the later arguments and evi-

dence,[13–15] it is difficult to sustain the identification of the 'fast' components with a volume diffusion process, i.e. they should be identified with short circuit path diffusion. Consequently, we shall only consider the 'slow' diffusion data from Refs. 19 and 20. It was concluded from measurements between 350 and 500°C that D_{Hg}^* and D_{Cd}^* were independent of P_{Hg}.[19,20] Shaw,[21] however found a slightly different situation for D_{Cd}^*: at 500°C, D_{Cd}^* was independent of P_{Hg} but at 350 and 400°C, D_{Cd}^* showed no variation with P_{Hg} until $P_{Hg} \geq$ 0.5 P_{Hg}(sat.) when D_{Cd}^* increased sharply. At 280°C, Shaw further found $D_{Cd}^* \propto P_{Hg}^{0.52}$ for P_{Hg} between 4×10^{-4} and 0.2 atm. An equally good fit to these data at 280°C is provided by

$$D_{Cd}^* = 4.8 \times 10^{-14} P_{Hg}^{1/3} + 2.7 \times 10^{-13} P_{Hg}^{2/3} \text{ cm}^2\text{s}^{-1} \quad (17)$$

The Arrhenius parameters describing the results for D_{Hg}^* and D_{Cd}^* are presented in Table I. In addition least squares fitting of all the D_{Hg}^* results at Hg saturation from[15,19,20] yields for the range 254–500°C,

$$D_{Hg}^* = 3.8 \times 10^{-3} \exp(-1.22\text{eV}/kT) \text{ cm}^2\text{s}^{-1} \quad (18)$$

and is based on eight values from Refs. 19 and 20 and 13 from Ref. 15. Arrhenius plots of D_{Hg}^* and D_{Cd}^* using Table I results and Eq. (18) are shown in Fig. 1 and Fig. 2, respectively. Firstly, we can see that to within a factor of two, there is good agreement between Ref. 19 and Ref. 20 for D_{Hg}^* and also between Refs. 19–21 for D_{Cd}^* (using P_{Hg} independent D_{Cd}^* results from Ref. 21). Secondly, there does appear to be a small but significant difference, evident in both figures, between the plots at Hg saturation and the others. Recall that the parameters from Refs. 19 and 20 are based on assuming that the self-diffusivity is independent of P_{Hg} at a given temperature. Figures 1 and 2 indicate otherwise with the difference being more marked for D_{Cd}^*. Further support is provided by Eq. (18) which is virtually identical to the results of Ref. 15 despite the inclusion of data from Refs. 19 and 20. Summing up, it is suggested that above ~300°C, D_{Hg}^* and D_{Cd}^* at Hg saturation are greater than at lower pressures where the self-diffusivity is independent of P_{Hg}. As the temperature rises, the difference in the self-diffusivity between low P_{Hg} and P_{Hg}(sat.) decreases to virtually zero at ~500°C. Below 300°C, the limited evidence (D_{Cd}^* at 280°C) indicates that D_{Cd}^* and probably D_{Hg}^* become dependent on P_{Hg} across the whole pressure range [note Eq.(17)]. Equation 18 is also plotted in Fig. 2 from which it is clear that at Hg saturation D_{Hg}^* and D_{Cd}^* differ by less than a factor two between 254 and 500°C ($D_{Cd}^* > D_{Hg}^*$) whereas at lower P_{Hg}, $D_{Hg}^* > D_{Cd}^*$ by < 50%[19] or by less than a factor two.[20] It would be difficult to claim that these differences between D_{Hg} and D_{Cd} can be seen as established. A fair conclusion is that any differences are small and within a factor of two. The equality, or near equality, of D_{Hg}^* and D_{Cd}^* is consistent with the conclusion of Ref. 3 that there is no Kirkendall effect in MCT (see section on Composition Interdiffusion).

As to diffusion mechanisms the independence of D_{Hg}^* and D_{Cd}^* to P_{Hg} can be explained in terms of a nondefect mechanism or, depending on the electroneutrality condition, single vacancy, single interstitial, or defect complexes [e.g. interstitial/vacancy, divacancy $(V_{Hg}V_{Te})$]. A full discussion of appropriate defect mechanisms can be found in Ref. 21. Equally a mixture of all three types of mechanism could be operative. The argument that a $(V_{Hg}V_{Te})$ mechanism necessitates $D_{Hg}^* = D_{Te}^*$ is incorrect.[5] In Eq. (17), the simplest interpretation of the P_{Hg} relationships is that the first and second terms represent diffusion by $Cd_i^{\cdot}$ and $Cd_i^{\cdots}$, respectively, provided $p \propto P_{Hg}^{-1/3}$ (i.e. n $\propto$ $P_{Hg}^{1/3}$) which could arise through the electroneutrality condition $p = 2[V_{Hg}'']$.

Finally, it is important to record that Archer et al.[15,22] concluded that D_{Hg}^* was independent of the method of growth of the MCT material.

CHEMICAL SELF-DIFFUSION IN MCT

Measurement of D_Δ in MCT has been confined to determining x_j^2/t, where x_j is the p-n junction depth after time t during anneals in Hg vapor i.e. D_Δ at $\Delta = 0$.[23–29] Bulk[23–27] and LPE[28,29] samples were used. It was found that at Hg saturation x_j^2/t followed the Arrhenius relation[24–26]

$$x_j^2 / t = A \exp(-Q/kT) \quad (19)$$

The values of A and Q which were obtained are summarized in Table II. Very good agreement is apparent, particularly as x_j was determined by thermal probing[24,25] or by optical absorption.[26] Assuming that the conversion process is controlled purely by diffusion (which is justified by the $x_j^2 \propto$ t relationship) Schaake et al.[23] and Harman[30] have modeled the p → n conversion. Both assumed diffusion by Hg interstitials and vacancies. According to Ref. 23

$$x_j^2 / t = 2S\left(D_{Hg}^*(Hg) + D_{Hg}^*(Te)/f\right)/C_{XSTe} \quad (20)$$

or Ref. 30

$$x_j^2/t = \pi SD_{Hg}^*(Te)\left[fC_{XSTe}\left(1 + R/f\right)^2\right]^{-1} \quad (21)$$

where $D_{Hg}^*(Te)$ and $D_{Hg}^*(Hg)$ are the Hg self-diffusivities at Te and Hg saturation, respectively; f is the vacancy correlation factor (= 0.78), S is the concentration of cation sites (= 1.2×10^{22} cm^{-3}) and R = $D_{Hg}^*(Te)/D_{Hg}^*(Hg)$. C_{XSTe} is the total concentration of excess Te in the p-type region (inclusive of precipitates). $D_{Hg}^*(Hg)$ and $D_{Hg}^*(Te)$ were identified with Hg interstitials and Hg vacancies respectively.

Table II. Values of A and Q in Eq. (19) for MCT

Ref.	x_{Cd}	Temp. Range (°C)	A (cm²s⁻¹)	Q (eV)
24	0.19–0.30	240–370	0.51	0.97
25*	0.2	150–320	2.8	1.03
26	0.21–0.25	280–420	0.28	0.91

*Data for x_j^2 / t

Identifying D^*_{Hg}(Te) with D^*_{Hg} from Ref. 20 (Table I) and D^*_{Hg}(Hg) with Eq. (18) and by dividing the experimental values of x_j^2/t (using data from Ref. 25) (Table II) with model values from Eq. (20) and Eq. (21), we can obtain values of C_{XSTe} in the samples used in x_j^2/t measurements. The results are shown in Table III at the two temperatures 250 and 370°C which represent the validity limits of Eq. (18) and Eq. (19), respectively. Schaake et al.[23] also measured values of $(x_j^2 C_{XSTe}/t)$ at 225 and 270°C. These experimental values are compared in Table III with the model values calculated using Eq. (20) and Eq. (21). The diffusivities

Table III. Comparison of Schaake et al.[23] and Harman[30] Models with Experiment

Temp (°C)	C_{XSTe}(cm^{-3})	
	Schaake et al.	Harman
370	1.3×10^{18}	3.1×10^{17}
250	4.4×10^{17}	7.0×10^{16}

	$x_j^2 C_{XSTe}/t$ (cm^{-1}s^{-1})		
	Exper.[23]	Schaake et al. Model	Harman Model
270	8.6×10^8	5.2×10^8	9.2×10^7
225	8.2×10^7	4.6×10^7	5.8×10^6

have necessarily been extrapolated to 225°C, which is not unreasonable as Eq. (18) is the dominant term.

The values of C_{XSTe} so derived are in agreement with expected magnitudes.[23,25] However, in Eq. (20) and Eq. (21), C_{XSTe} would be expected to be constant in a given set of experiments, so that the activation energy for x_j^2/t [Q in Eq. (19)] should be 1.22–1.51 eV and not be significantly less. This difference in activation energies accounts for the fall in C_{XSTe} evident in Table III as the temperature falls. On the other hand, there is excellent agreement between experiment and the Schaake model for $(x_j^2 C_{XSTe}/t)$ at both 225 and 270°C. Support for the Schaake model[23] comes from the observation at 300°C that x_j^2/t varies as $P_{Hg}^{0.48}$:[24] this would be the D^*_{Hg}(Hg) term in Eq, (20) which also links up well with the dependence $D^*_{Cd} \propto P_{Hg}^{0.52}$ found at 280°C.[21]

A further problem arises from the results of Wienecke et al.[7] who carried out high temperature in situ Hall and resistivity measurements on Te saturated Hg$_{0.8}$Cd$_{0.2}$Te. They found native acceptor concentrations (V''_{Hg}) in excess of 1×10^{19} cm^{-3} between 300 and 600°C. The clear implication is that previous estimates of C_{XSTe} are at least an order of magnitude too low (see also Table III) which in turn means that the right hand sides of Eq. (20) and Eq. (21) are too small by at least a factor of ten. Given that these acceptor concentrations are correct, the only way to reconcile x_j^2/t with a faster diffusion process, than

Table IV. Summary of CID Parameters Defined by Eq. (11) and Eq. (22)

Ref.	Interface or Profiling Method*	Temp (°C)	x_{Cd}	Nonstoichiometry or Doping	D_0 (cm^{2}s^{-1})	Q (eV)
31	SV + LG	550				$1.49 + 0.51 x_{Cd} + 0.0017 P_{Hg}$
		600	0.1–0.9	$0 < P_{Hg}$ (atm) < 6	1	$1.42 + 0.62 x_{Cd} + 0.0098 P_{Hg}$
32	SV + LG	450–700	0.1–0.7	Te rich	$300\exp(-7.53 x_{Cd})$	1.92
33	SS + LG	690	0.3–0.9	Hg rich	1	$1.39 + 0.46 x_{Cd}$
34	SS + LG	470–590	0.3–1	Te rich	$2 \times 10^6 \exp(-8.16 x_{Cd})$	$1.42 - 0.32 x_{Cd}$
35	SS + LG	400–600	0–1	Te rich (>500°C) Hg rich (<450°C)	$315\exp(-8.06 x_{Cd})$ ($=315 \times 10^{-3.5 x_{Cd}}$)	1.93
36	SS	500–600	0.05–0.95	Te rich	1	$1.54 + 0.47 x_{Cd}$
				Hg rich	1	$1.60 + 0.41 x_{Cd}$
37,41	SS	400–600	0.1–0.9	Te rich	1	$1.54 + 0.46 x_{Cd}$
				Hg rich	1	$1.53 + 0.47 x_{Cd}$
38	HgTe/CdTe Superlattice (MBE)	200–220	0–1	Hg rich	1	$1.46 + 0.63 x_{Cd}$
		240		Hg rich	1	$1.45 + 0.49 x_{Cd}$
39,40	$x_{Cd} = 0.27/0.85$ MQW (MBE)	200–265	0.27–0.85	—	†$24\exp(-37.5 x_{Cd})$ †$2.5\exp(-37.5 x_{Cd})$	$1.82 - 1.50 x_{Cd}$ $1.79 - 1.50 x_{Cd}$
42	RBS	280–340	~1	Hg Saturation	1.25×10^3	2.0
43	Radiotracer	300–400	~1	Hg Saturation	1.7×10^{-2}	1.57
		100–300	~1	Hg Saturation	2.8×10^{-13}	0.27
44	PIXE	360–550	~1	Hg Saturation	6.6	1.91
45	Radiotracer	250–350	~0	Te rich	3.1×10^{-4}	0.66

*SV,SS denote solid/vapor, solid/solid interfaces, respectively; LG denotes layer growth during CID.
†The upper and lower entries refer respectively to positions in the stack which are near the middle and close to the substrate.

given by D_{Hg}^*, seems to be to invoke short circuit paths i.e. EPD.

COMPOSITIONAL INTERDIFFUSION

In common with $\tilde{D}$ in other systems, the experimental values for $\tilde{D}$ in MCT can be represented in the Arrhenius form

$$\tilde{D}(x_{Cd},T) = D_o(x_{Cd}) \exp(-Q(x_{Cd})/kT) \qquad (22)$$

where $D_o(x_{Cd})$ and $Q(x_{Cd})$ are exponential and linear functions of x_{Cd}, respectively. It turns out that while D_o and Q may both be functions of x_{Cd} equally satisfactory fits are obtained with D_o constant and Q dependent on x_{Cd} and vice versa. Most of the results for $\tilde{D}$ vs x_{Cd} have been obtained by CID across a single interface with the composition profile being determined by the electron microprobe technique.[31–37] Additionally, Auger electron spectroscopy and x-ray photoelectron spectroscopy have been used to gain better spatial resolution.[35] Compositional interdiffusion experiments have also been performed in superlattice structures[38] and multiple quantum wells.[39,40] In the case of Ref. 38, double crystal x-ray diffraction was used to monitor the interdiffusion. The nature of the technique means that what is observed is some average taken through the stack. By contrast, Kim et al.[39,40] developed the transmission electron microscopy technique to enable composition profiles across a single interface in their MQW stacks. In each case,[38–40] interpretation of the results was achieved by matching to simulated data based on an exponential variation of $\tilde{D}$ with x_{Cd} at a given temperature.

The parameters for $\tilde{D}$ which describe the results from Refs. 31–40 are summarized in Table IV. Points to note are that where $\tilde{D}$ has been obtained at a single temperature,[31,33,38] D_o has been taken as unity (following Ludington's analysis).[41] Ludington showed that Tang and Stevenson's Te-rich results[37] could be fitted to within 60% between 450 and 550°C by the parameters shown in Table IV for Refs. 37 and 41. To within a factor of two, the same parameters describe $\tilde{D}$ between 400 and 600°C. The parameters for the Hg-rich results from Ref. 37 have also been evaluated and are included in Table IV. Leute et al.[36] presented their results in graphical form ($\tilde{D}$ vs x_{Cd} at different temperatures). The parameters given in Table IV for Ref. 36 were derived from their graphs. The parameters given by Kim et al.[39,40] refer to ~300K: the parameters included in Table IV were derived from Fig. 4 of Ref. 39. It should be noted that the parameters recorded by Ref. 34 appear to contain errors as they yield values of $\tilde{D}$ many orders of magnitude greater than indicated by their CID profiles. Tang and Stevenson[37] measured $\tilde{D}$ between 300 and 600°C; but below 400°C, the variation of $\tilde{D}$ with x_{Cd} could not be fitted to a single exponential, the dependence on non-stoichiometry increased and the overall variation in $\tilde{D}$ with x_{Cd} decreased significantly.

Further points are: CID profiles reduce to a single profile when plotted against $x/\sqrt{t}$;[31] $\tilde{D}$ shows little dependence on nonstoichiometry, at least above

400°C;[31,36,37] $\tilde{D}$ increases with either donor (In) or acceptor (Ag) doping.[36]

When $x_{Cd} \to 1$, Eq. (11) tells us that $\tilde{D} \to D_{Hg}$ i.e. the diffusivity of Hg in CdTe. Similarly, for $x_{Cd} \to 0$, $\tilde{D} \to D_{Cd}$ i.e. the diffusivity of Cd in HgTe. These limiting values for $\tilde{D}$ can be directly measured by diffusion from a Hg[42–44] or Cd[45] ambient into CdTe or HgTe, respectively. The Arrhenius parameters obtained from such experiments are given in Table IV. The radio-tracer technique was used by Refs. 43 and 45 whereas profiling by Rutherford back-scattering (RBS)[42] and by proton induced x-ray emission[44] were alternative techniques also used. Jones et al.[43] found that their profiles consisted of two sections, designated slow and fast. Only the parameters for their slow components are given in Table IV as the situation is seen as very similar to that found for self-diffusion in MCT (see section on Hg and Cd Self-Diffusion in MCT).

In order to compare the various results for $\tilde{D}$ listed in Table IV, values of $\tilde{D}$ at $x_{Cd} = 0$ and 1 are shown as Arrhenius plots in Fig. 3 (omitting, however, Ref. 34). The pattern of data has a divide in the region 350–400°C. Above ~400°C, there is good agreement at $x_{Cd} = 0$ between Refs. 31–33, 35, 36, and 41 whereas at $x_{Cd} = 1$ two groups are evident with each group showing good agreement between its members i.e. Refs. 31, 32, 35, 36, and 41 and 33, 43, and 44). The difference in $\tilde{D}$ between these two groups is a factor between 10 and 100 and is clearly a substantial one. Possible explanations of this discrepancy can be found in Ref. 44, but it is still a problem requiring an answer. Below ~350°C, the results of Ref. 42 at $x_{Cd} = 1$ and of Ref. 45
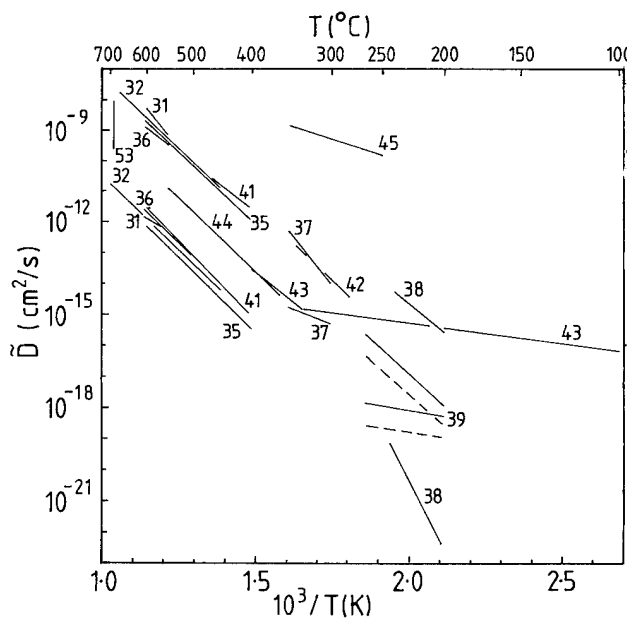
Fig. 3. Arrhenius plots of $\tilde{D}$ at $x_{Cd} = 0$ and 1 from Eq. (11) and the data given in Table IV (extrapolated where necessary). At 300 and 350°C, the $\tilde{D}$ values from Ref. 37 correspond to the maximum and minimum values found at $x_{Cd} = 0.1$ and 0.9, respectively. For Kim et al.,[39] the solid and broken lines denote positions in the middle and bottom (substrate) of the multi-layer stack. The plots for Ref. 31 correspond to $P_{Hg} = 1$ atm. As there is little difference in $\tilde{D}$ between Hg and Te-rich conditions in the results of Ref. 36 only the plots for Te rich conditions are shown.

Table V. Summary of Results Obtained for D_{In} in MCT from Fits to Erfc Distributions

Ref.	x_{Cd}	Temp. (°C)	Ambient Atm.	C_0^s (cm⁻³)	D_0^s (cm²s⁻¹)	Q^s (eV)	C_0^f (cm⁻³)	D_0^f (cm²s⁻¹)	Q^f eV
46	0.2	300–450	Hg Saturation	*6E18	1.5E-4	0.95	*2.5E18	2E-6	0.55
47	0.2	230–401	High P_{Hg}	4E19 to	†1.65E-3	1.17	—	—	—
			Low P_{Hg}	5E21	0.92	1.48	—	—	—
48	0.2	300–450	High P_{Hg}	1E20 to 1E21	4E-3	1.24	—	—	—
49	0.2(?)	250–400	Hg Saturation	4E15	2.2E-6	1.16	—	—	—
						D_{In}cm²s⁻¹			
50	0.22	225	Flowing Ar	2E21		4.3E-15			
51	0.22–025	380	High P_{Hg}	8E20		3.8E-13			
52	0.22	300	Capped	7E19		5E-14			
		350	Capped	7E19		3E-13			
53	0.22	400	Capped	7E19		8E13			

Note: Where a single erfc profile was observed, the parameters are entered under the 's' suffix. The 's' and 'f' suffixes refer to slow and fast erfc components. C_0 denotes the In surface concentration. *At 400°C; †Eq. (6) in Ref. 47 contains a misprint for D_0. The correct value is 1.65E-3, not 1.65E-2.
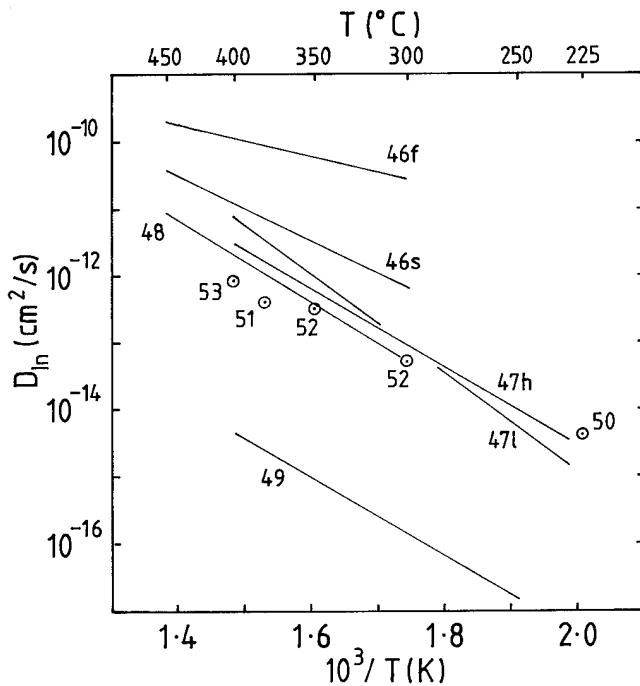
Fig. 4. Arrhenius plots of the results for D_{In} given in Table V. The 'h' and 'l' labels associated with Ref. 47 denote the high and low P_{Hg} conditions, respectively.

at x_{Cd} = 0 must be regarded as suspect. It is possible in Ref. 45 that the 40 MeV O⁵⁺ ions used for profiling also drive the Hg ions deeper into the sample.[44] At x_{Cd} = 0 the slopes of the plots for Refs. 37–39 are not too dissimilar from those above 400°C; however, below ~350°C, marked changes in the slopes for x_{Cd} = 1 are evident with Refs. 37, 39, and 43 finding substantial reductions whereas Ref. 38 found a substantial increase. In terms of magnitudes of $\tilde{D}$, the radiotracer results at x_{Cd} = 1[43] coincide with those for x_{Cd} = 0[38] at ~200°C, which seems an improbable situation. As a general conclusion for x_{Cd} = 0 below ~350°C, it seems that the data lie within a factor of ten of values

extraplated from the higher temperature measurements whereas for x_{Cd} = 1, below 350°C, the situation is quite uncertain.

IMPURITY DIFFUSION

Since the earlier review of impurity diffusion in MCT,[2] most interest has focused on In and As which are proving to be important dopants. This section will be confined to these impurities.

In Diffusion in MCT

The present situation is defined by work carried out since 1983.[46-53] Earlier work was considered in Ref. 47. This recent work is based on radiotracer[46,47] or SIMS[48-53] profiling of bulk[46,47] or epilayer (LPE,[48,51-53] MBE,[49] MOVPE[50]) samples using a variety of diffusion sources: evaporated layer,[46,50] electroplated layer,[47] vapor,[47,48,51] In-doped MBE layer,[49] In ion implant.[52,53] Generally, single erfc profiles were obtained, in some cases extending over nearly four orders of magnitude in In concentration. Gorshkov et al.[46] reported profiles consisting of two erfc sections: a slow and a fast component. Non-erfc profiles were also found[47,51,52] whose shapes indicated that D_{In} was concentration dependent, decreasing with falling In concentration. Gorshkov et al.[46] also found that D_{In} (slow) was independent of P_{Hg} at 300°C, a feature supported by Ref. 47 from measurements between 230 and 400°C; although a small variation may be present, it is commensurate with the experimental scatter. Isoconcentration experiments at 400°C gave single erfc profiles with diffusivities equal to D_{In} (slow).[46] This equality and the existence of a single erfc implies that the fast component seen by Ref. 46 is not due to short circuit path diffusion and reflects a volume mechanism where there is a departure from local defect equilibrium. The results from Refs. 46–53 are summarized in Table V and are shown also as Arrhenius plots in Fig. 4. To within a factor of ten, it is evident in Fig. 4 that there is agreement between all the data, apart

Table VI. Summary of D_{As} Data vs Temperature for MCT

Ref.	x_{Cd}	Temp. (°C)	Ambient Atm.	C_o(cm⁻³)	D_{As}(cm²s⁻¹)
56	0.18	400	As and Hg	2.5E18	*(8–11)E-14
57	0.2(?)	350	P_{Hg} = 0.8 atm	(2–4)E18	7.5E-15
			P_{Hg} = 0.52 atm	(2–4)E18	3.4E-13
			P_{Hg} = 0.16 atm	(2–4)E18	4.3E-12
†58	0.19–0.23	400	Hg Saturation	2E18	2.8E-14
			Hg Saturation	2E18	‡2.9E-14
		450	Hg Saturation	1.2E18	2.6E-13
			Hg Saturation	5E18	1.9E-13
			Hg Saturation	1E18	2.0E-13
49	0.2(?)	400	Hg Saturation	~8E17	3.0E-14,4.5E-14
		350	Hg Saturation	~8E17	3.0E-15
		250	Hg Saturation	~8E17	3.0E-17, 7.5E-17, 1.6E-16

Note: C_o denotes the As surface concentration.
*The lower and higher limits represent Gaussian and erfc fits, either of which gave equally good fits.
†The data listed were obtained with MOCVD layers. Very similar results were obtained with LPE material.[59]
‡Ref. 58 gives D_{As} = 1.9E-14 cm²s⁻¹ but a better fit is given by 2.9E-14cm²s⁻¹.

from Ref. 49 and the fast component of Ref. 46, with substantially closer agreement existing between Refs. 47, 48, 50, and 52. A striking aspect of Fig. 4 is the huge reduction in D_{In} observed by Myers et al.[49] We see from Table V that the In concentrations used by Ref. 49 are three to five orders of magnitude smaller than those employed by the other workers and it seems reasonable to seek an explanation for the disparity in D_{In} in terms of this concentration difference.

Diffusion models for D_{In} have already been described and discussed.[46,47] More recent models have also been put forward.[48,51,54] Vydyanath et al.[48] proposed the In is present largely as $(2In_{Hg}V_{Hg})^x$ with the electroneutrality condition

$$[\;In_{Hg}^{\cdot}\;] = [(In_{Hg}V_{Hg})']$$

and that $In_{Hg}^{\cdot}$ diffuses via a V_{Hg}'' mechanism. This model gives D_{In} independent of P_{Hg} but also inversely proportional to In_{tot} where In_{tot} is the total In concentration (see Appendix 1). This latter aspect of D_{In} explains neither the erfc profiles nor the increase in D_{In} with increasing In_{tot}, seen in the non-erfc profiles. Weck and Wandel[51] interpreted their profiles in terms of In interstitials, In_i, diffusing by the Frank Turnbull mechanism ($In_i + V_{Hg} \leftrightarrow In_{Hg}$) and by the kick-out mechanism ($In_i + Hg_{Hg}^x \leftrightarrow In_{Hg} + Hg_i$). These mechanisms both give rise to a dependence of D_{In} on P_{Hg} which does not seem to have been considered by Ref. 51. The model of Wong and Roedel[54] considers that In is present entirely as $In_{Hg}^{\cdot}$ and In_{Hg}^x with diffusion occurring via V_{Hg}'' or possibly V_{Hg}'. A weak dependence on P_{Hg} was claimed but it is unclear how this compared with experimental findings.[46,47] More importantly perhaps is their neglect of impurity banding at high In_{tot} which ensures that all the In is always fully ionized.[4] Their use of the mass action law between n and p is also invalid in degenerate material.[4] A model based on $In_{Hg}^{\cdot}$ and the singly ionized acceptor defect
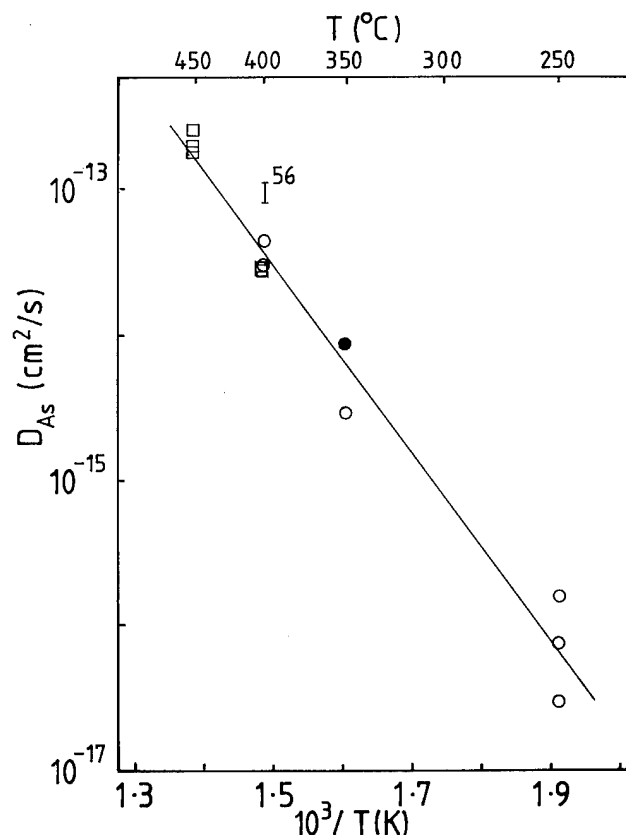
Fig. 5. Arrhenius plots of D_{As} at or near Hg saturation. Data from Table VI. Symbols: ● ;[57] □ ;[58] ○.[49] The solid line is a plot of Eq. (24).

pair $(In_{Hg}V_{Hg})'$ with diffusion via the defect pair is described in Appendix 1. This model provides erfc profiles, D_{In} independent of P_{Hg} at high In_{Tot}, a large reduction in D_{In} at low In_{Tot}, all of which are observed. It also predicts that D_{In} at low In_{Tot} varies as $P_{Hg}^{-1/3}$ or P_{Hg}^{-1} which can be tested by experiment. The problem of non-erfc profiles, however, still remains. As a first step, it would be valuable to be able to distinguish

between the conditions which lead to erfc profiles and those leading to non-erfc profiles.

Vydyanath et al.[48] based their diffusion model, in part, on the electrical properties measured at 77K of In doped samples quenched from temperatures between 400–600°C. The assumption was made that the defect situation at the anneal temperature was frozen in during the quench. This is an assumption which is not easy to justify because the quench cannot be instantaneous. If the sample cools at a linear rate α Ks^{-1} from an anneal temperature T_0 then the diffusion length, L, of In during the cooldown period is[55]

$$L = 2(D_{In}(T_0)/\beta)^{1/2} \qquad (23)$$

where $\beta = \alpha Q/kT_0$; $D_{In}(T_0)$ is D_{In} at the anneal temperature, and Q is the activation energy of D_{In}. Taking $\alpha = 30\ Ks^{-1}$ and parameters for D_{In} from Table V, we find $L \approx 0.04$ and 3 μm for $T_0 = 400$ and 600°C, respectively. These values compare with average In separations of 0.01 and 0.001 μm at In concentrations of 10^{18} and 10^{21} cm^{-3}. In other words, relative to the mean separation of the In defects, In is very mobile during the quench period.

As Diffusion in MCT

Measurements of D_{As} have been carried out solely in epitaxially grown material (LPE,[56,57,59] MOCVD,[58,59] MBE[49]), from anneals in the temperature range 250–450°C. Various As diffusion sources were utilized: vapor,[56] step-doped layers,[49,57] or As ion-implants.[58,59] Falconer et al.[56] used the radiotracer method with serial sectioning to obtain As diffusion profiles, whereas secondary ion mass spectroscopy profiling was employed in all the other cases. Diffusion anneals were performed under Hg saturation, apart from Ref. 56 where the presence of the As would reduce P_{Hg} in the ampoule. The dependence of D_{As} on P_{Hg} was also determined at 350°C.[57] In all cases, good single erfc profiles, extending up to three orders of magnitude in concentration, were found. Bubulac et al.[58,59] also found a deeper exponential tail to their erfc profiles, whose appearance was related to the EPD concentration. The values for D_{As} derived from the erfc profiles are listed in Table VI. Arrhenius plots for the data at or near Hg saturation are given in Fig. 5 and reveal a not unreasonable measure of consistency, particularly in view of the mixture of techniques used. A least squares fit of these data (excluding Ref. 56) to an Arrhenius relation yields (at Hg saturation)

$$D_{As} = 1.52 \times 10^{-4} \exp(-1.28\ eV/kT)\ cm^2s^{-1} \quad (24)$$

At 350°C, the results of Chandra et al.[57] show that D_{As} rises dramatically with reducing P_{Hg}. A least squares fit to their three measurements gives

$$D_{As} = (9 \overset{\times}{\underset{\div}{}} 5) \times 10^{-15}/P_{Hg}^{3.6\pm1.4}\ cm^2s^{-1} \qquad (25)$$

for P_{Hg} in atm.

Chandra et al.[57] proposed that As is incorporated as the singly ionized defects $As_{Hg}^{\cdot}$ and As_{Te}', with $[As_{Te}']$ $\gg [As_{Hg}^{\cdot}]$ and only $As_{Hg}^{\cdot}$ being mobile (diffusing by V_{Hg}''). Analysis similar to that given in Appendix 1 and

bearing in mind that the $As_{Hg}^{\cdot}$ diffusivity is $\propto [V_{Hg}'']$ shows that $D_{As} \propto P_{Hg}^{-3}$ for intrinsic conditions or for the electroneutrality conditions $p = [As_{Te}']$ or $p = 2 V_{Hg}''$]. In each case D_{As} is also independent of As concentration (i.e. erfc profiles).

A final point concerns the exponential tails observed by Bubulac et al.[58,59] which was attributed by them to enhanced volume diffusion of As in a region where there was no local defect equilibrium. It is interesting to note that all of the erfc plus tail profiles that they present are consistent with all of the features predicted by short circuit path diffusion[16,17] (see also section on Short-Circuit Path Diffusion). Using Eq. (13) and Eq. (15), with a = 5×10^{-8} cm, their profiles give $\Delta_d \approx 1.8 \times 10^6$ and 1×10^6, respectively, at 400 and 450°C. It appears that short circuit paths can provide an alternative explanation of the As tail.

CONCLUSIONS

Self-Diffusion

Good agreement exists on the experimental values for D_{Hg}^* and D_{Cd}^*. The evidence suggests that the self-diffusivity is greater at Hg saturation than at lower P_{Hg} where, above 300°C, it is largely independent of P_{Hg}. More work is needed below 300°C to establish and confirm how D_{Hg}^* and D_{Cd}^* vary with P_{Hg}. Above 300°C, no single diffusion mechanism can be identified, various possibilities exist. Below 300°C, there is clear, but limited, evidence for an interstitial mechanism. Measurement of D_{Hg}^* and D_{Cd}^* in doped extrinsic MCT would provide valuable information in elucidating self-diffusion mechanisms.

Chemical Self-Diffusion

There is good agreement between results on the movement of p-n junctions. Modeling of the conversion process, however, is a little uncertain as it may underestimate experimental conversion rates because of uncertainty in the true excess Te. Measurements of the in-situ electrical conductivity relaxation times following a step change in P_{Hg}, using the basic technique of Ref. 7, would be invaluable.

Compositional Interdiffusion

Above ~400°C, there is reasonable agreement between different workers at low x_{Cd}, but at high x_{Cd}, there is substantial disagreement for reasons that are not clear. Below ~400°C, the agreement is poor. There is a clear need for more careful experiments and analysis.

Impurity Diffusion

Quite good consistency exists between D_{In} results from erfc profiles obtained at high In concentrations. The remarkable drop in D_{In} found at low In concentrations can be accounted for in a way consistent with the high concentration D_{In}. There is, however, a real problem in explaining how and why non-erfc profiles arise. The situation for D_{As} probably represents the best overall position for a diffusant: there is both good

agreement between experimental data and between experiment and a diffusion model based on a mobile $As_{Hg}^{'}$ diffusing via Hg vacancies.

Influence of Growth Technique

It is worth noting that where direct comparisons have been made (e.g. $D^{*}(Hg)$ at Hg saturation and D_{In}) bulk and epilayer material yield essentially identical results.

REFERENCES

1. M. Brown and A.F.W. Willoughby, *J. Cryst. Growth* 59, 27 (1982).
2. D. Shaw, *J. Cryst. Growth* 86, 778 (1988).
3. D.A. Stevenson and M.F.S. Tang, *J. Vac. Sci. Technol. B* 9, 1615 (1991).
4. D. Shaw, *Atomic Diffusion in Semiconductors* ed. D. Shaw, (London: Plenum Press, 1973), Ch. 1.
5. R.L. Guldi, J.N. Walpole and R.H. Rediker, *J.Appl. Phys.* 44, 4896 (1971).
6. S.S. Chern and F.A. Kroger, *J. Sol. State Chem.* 14, 299 (1975).
7. M. Wienecke, M. Schenk and H. Berger, *Semicond. Sci. Technol.* 8, 299 (1993).
8. B. Tuck, *Introduction to Diffusion in Semiconductors*, (Stevenage: Peter Peregrinus, 1974), p. 116.
9. M.F.S. Tang and D.A. Stevenson, *J. Phys. Chem. Solids* 51, 563 (1990).
10. F.J.A. den Broeder, *Scripta Metall.* 3, 321 (1969).
11. V. Leute and W. Stratmann, *Zeit. Physik. Chemie.* 90, 172 (1974).
12. V.I. Ivanov-Omskii, K.E. Mironov and V.K. Ogorodnikov, *Phys. Stat. Solidi* (a) 60, 37 (1980).
13. H.D. Palfrey, *J. Cryst. Growth* 94, 778 (1989).
14. D. Shaw, *Semicond. Sci. Technol.* 7, 1230 (1992).
15. N.A. Archer, H.D. Palfrey and A.F.W. Willoughby, *J. Cryst. Growth* 117, 177 (1992).
16. A.D. LeClaire and A. Rabinovitch, *J. Phys. C: Solid State Phys.* 14, 3863 (1981); 15, 3455 (1982); 16, 2087 (1983).
17. A.D. LeClaire, Brit. *J. Appl. Phys.* 14, 351 (1963).
18. G.E. Murch and S.J. Rothman, *Diffusion and Defect Data 42*, 17 (1985).
19. J.S. Chen, PhD Thesis (University of Southern California, 1985).
20. M.F.S. Tang and D.A. Stevenson, *J. Vac. Sci. Technol.* A7, 544 (1989).
21. D. Shaw, *Phil. Mag. A* 53, 727 (1986).
22. N.A. Archer, H.D. Palfrey and A.F.W. Willoughby *J. Electron. Mater.* 22, 967 (1993).
23. H.F. Schaake, J.H. Tregilgas, J.D. Beck, M.A. Kinch and B.E. Gnade, *J. Vac. Sci. Technol. A* 3, 143 (1985).
24. N.V. Baranova, A.S. Tomson, N.P. Artamonov and A.V. Vanyukov, *Inorgan. Mater.* (USA) 12, 1751 (1976).
25. C.L. Jones, M.J.T. Quelch, P. Capper and J.J. Gosney, *J. Appl. Phys.* 53, 9080 (1982).
26. V.V. Bogoboyaschii, A.I. Elizarov, V.I. Ivanov-Omskii, V.R. Petrenko and V.A. Petoyakov, *Sov. Phys. Semicond.* 19, 505 (1985).
27. V.V. Bogoboyaschii, A.I. Elizarov, V.I. Ivanov-Omskii and V.A. Petoyakov, *Sov. Phys. Semicond.* 21, 888 (1987).
28. P. Koppel and K. Owens, *J. Appl. Phys.* 67, 6886 (1990).
29. D.T. Dutton, E. O'Keefe, P. Capper, C.L. Jones, S. Mugford and C. Ard, *Semicond. Sci. Technol.* 8, S266 (1993).
30. T.C. Harman, *J. Vac. Sci. Technol. A* 5, 3055 (1987).
31. L. Svob, Y. Marfaing, R. Triboulet, F. Bailly and G. Cohen-Solal, *J. Appl. Phys.* 46, 4251 (1975).
32. J.G. Fleming and D.A. Stevenson, *Phys. Stat.* Solidi (a), 105, 77 (1987).
33. V.I. Ivanov-Omskii, K.E. Mironov and V.K. Ogorodnikov, *Phys. Stat. Solidi*(a), 58, 543 (1980).
34. H. Takigawa, M. Yoshikawa, M. Ito and K. Maruyama, *Mater. Res. Soc. Symp. Proc.* 37, 97 (1985).
35. K. Zanio and T. Massopust, *J. Electron. Mater.* 15, 103 (1986).
36. V. Leute, H.M. Schmidtke, W. Stratmann and W. Winking, *Phys. Stat. Solidi* (a), 67, 183 (1981).
37. M.F.S. Tang and D.A. Stevenson, *Appl. Phys. Lett.* 50, 1272 (1987).
38. A. Tardot, A. Hamoudi, N. Magnea, P. Gentile and J.L. Pautrat, *Semicond. Sci. Technol.* 8, S276 (1993).
39. Y. Kim, A. Ourmazd, M. Bode and R.D. Feldman, *Phys. Rev. Lett.* 63, 636 (1989).
40. Y. Kim, A. Ourmazd and R.D. Feldman, *J. Vac. Sci. Technol. A* 8, 1116 (1990).
41. B.W. Ludington, *Mater. Res. Soc. Symp. Proc.* 90, 437 (1987).
42. K. Takita, K. Murakami, H. Otake, K. Masuda, S. Seki and H. Kudo, *Appl. Phys. Lett.* 44, 996 (1984); 47, 1119 (1985).
43. E.D. Jones, V. Thambipillai and J.B. Mullin, *J. Cryst. Growth* 118, 1 (1992).
44. J.H.C. Hogg, A. Bairstow, G.W. Matthews, D. Shaw and J.D. Stedman, *Mater. Sci. Engineering* B16, 195 (1993).
45. V.V. Belov, F.A. Zaitov and G.E. Popovyan, *Sov. Phys. Solid State* 11, 162 (1970).
46. A.V. Gorshkov, F.A. Zaitov, G.M. Shalyapina and S.B. Shangin, *Sov. Phys. Solid State* 25, 1532 (1983).
47. D. Shaw, *Phys. Stat. Solidi* (a), 89, 173 (1985).
48. H.R. Vydyanath, C.H. Hiner, S.R. Hampton and T.R. Krueger (unpublished work 1988).
49. T.H. Myers, K.A. Harris, R.W. Yanka, L.M. Mohnkern, R.J. Williams and G.K. Dudoff, *J. Vac. Sci. Technol.* B10, 1438 (1992).
50. H.D. Palfrey and A.F.W. Willoughby (private communication).
51. G. Weck and K. Wandel, European Workshop on II-VI Semiconductors, Aachen, 2–4 November 1992.
52. G.L. Destefanis, *J. Cryst. Growth* 86, 700 (1988).
53. L.O. Bubulac, *J. Cryst. Growth* 86, 723 (1988).
54. J. Wong and R.J. Roedel, *J. Vac. Sci. Technol.* A9, 2258 (1991).
55. G.M. Khattak, J.M. Majid, C.G. Scott and D. Shaw, *Solid State Commun.* 84, 1073 (1992).
56. J.E. Falconer, H.D. Palfrey and G.W. Blackmore, *J. Cryst. Growth* 100, 275 (1990).
57. D. Chandra, M.W. Goodwin and M.C. Chen and J.A. Dodge, *J. Electron. Mater.* 22, 1033 (1993).
58. L.O. Bubulac, D.D. Edwall and C.R. Viswanathan, *J. Vac. Sci. Technol. B* 9, 1695 (1991).
59. L.O. Bubulac and C.R. Viswanathan, *J. Cryst. Growth* 123, 555 (1992).
60. H.R. Vydyanath, *J. Vac. Sci. Technol. B* 9, 1716 (1991).
61. D. Shaw, *Semicond. Sci. Technol.* 9, 1729 (1994).

APPENDIX 1

As a variation and simplification of the Vydyanath et al. model[48] assume that In is incorporated as $In_{Hg}^{'}$ and $(In_{Hg}V_{Hg})' \equiv A'$. At high In concentrations, the electroneutrality condition is $[In_{Hg}^{'}] = [A']$ and the total In concentration is simply

$$In_{Tot} = [In_{Hg}^{*} In_{Hg}^{'}] + [A'] \qquad (A1)$$

Assuming that In diffusion is due to the mobile A' defect whose diffusivity is $D(A')$, then

$$D_{In} \frac{\partial In_{Tot}}{\partial x} = D(A') \frac{\partial [A']}{\partial x}$$

so that

$$D_{In} = D(A') \frac{\partial [A']}{\partial x} \qquad (A2)$$

At high In_{Tot}, $[In_{Hg}^{'}] = [A']$, so Eq. (A2) becomes

$$D_{In} = 0.5 D(A') \qquad (A3)$$

At low In_{Tot} ($\sim 10^{16}$ cm^{-3}), the electroneutrality condi-

tion can be taken as $p = 2[V''_{Hg}]$ and, if $[In_{Hg}^{\cdot}] \gg [A']$, use of the Law of Mass Action[60] and Eq. (A2) shows that

$$D_{In} = \frac{[A']}{In_{Tot}} D(A') \propto D(A')/P_{Hg}^{1/3} \qquad (A4)$$

Alternatively, at high P_{Hg} and low In_{Tot}, the sample may be intrinsic, in which case it is easy to show from Eq. (A2) that

$$D_{In} = \frac{[A']}{In_{Tot}} D(A') \propto D(A')/P_{Hg} \qquad (A5)$$

At high In_{Tot}, D_{In} [Eq. (A2)], is therefore independent of both P_{Hg} and In concentration ($\therefore$ erfc profiles) while at low In concentrations [Eq. (A3) and Eq. (A4)], D_{In} is again independent of concentration but should show an inverse dependence on $P_{Hg}^{1/3}$ or P_{Hg}. Equations (A1), (A2), and (A3) also show that D_{In} decreases by a factor $\sim [A']/In_{Tot}$ ($\ll 1$) in going from high to low In concentrations.

NOTE

A more recent and detailed analysis of D_{As} can be found in Ref. 61.

Variation of Arsenic Diffusion Coefficients in HgCdTe Alloys with Temperature and Hg Pressure: Tuning of p on n Double Layer Heterojunction Diode Properties

D. CHANDRA, M.W. GOODWIN, M.C. CHEN, and L.K. MAGEL

Central Research Laboratories, Texas Instruments Inc., Dallas, TX 75265

Arsenic diffusion coefficients were measured in HgCdTe alloy films at 375, 400, and 425°C. The diffusion coefficients displayed a strong dependence on Hg pressures at all three temperatures, increasing by 1000 x with decreasing Hg pressure. The Hg pressures employed were selected to span a portion of the single phase field at each temperature. These investigations added to the diffusion measurements at 350°C reported earlier. The behavior reported at all three temperatures generally resembled the behavior observed at 350°C. For example, at 375°C, the diffusion coefficient increased from 1.6×10^{-14} cm²/s for a Hg overpressure of ~1.25 atm, corresponding to the Hg saturated end of the phase field, to 3.2×10^{-12} cm²/s, when the Hg overpressure was decreased to 0.2 atm, at a point within the phase field, but still considerably removed from the Te-saturated end. For mercury pressure ranges generally within an order of magnitude from the Hg saturated end point, the transport behavior remained simple classical and the diffusion coefficients varied approximately as $\propto P_{He}^{-3}$ at all three temperatures. With continued decrease in the mercury pressure, the transport behavior still remained simple classical, but the dependence of the diffusion coefficients on mercury pressure became more complex, progressing from a P_{Hg}^{-3} dependence to a P_{Hg}^{-1} dependence. This transition was most apparent at 425°C. With additional decrease in the Hg pressure, the transport behavior became more complex and could no longer be described by a simple classical or a monocomponent concentration independent Fickian model. This range was not studied during the present investigations. Additional progress in tuning the positioning of the p/n junction for double layer heterojunction films was possible from the results obtained. This was demonstrated by comparing diode performances obtained on heterojunctions films subjected to seleccted anneal sequences.

Key words: As, diffusion, diode, HgCdTe, heterojunction, infrared detectors

INTRODUCTION

P on n double layer HgCdTe heterostructures with a mid wavelength infrared (MWIR) top layer can offer significant performance improvements in a HgCdTe photovoltaic detector under certain circumstances.[1,2] These heterostructures are particularly preferred over n on p structures when minority carrier lifetimes and mobilities and technological problems related to surface passivation control are considered.[2] Furthermore, at higher operating temperatures, diode leakage due to diffusion[3] is eliminated from the wide band gap region. A properly constructed heterojunction detector offers improved reverse breakdown charac-

teristics at very low temperatures and long detection wavelengths due to reduced tunneling.[1] In general, long wavelength infrared (LWIR) p on n HgCdTe photodiodes offering superior performances have been obtained by both molecular beam epitaxy (MBE)[4] and liquid phase epitaxy (LPE).[5] Though the upper limit of the n on p homojunction diodes has also been raised to comparable magnitudes recently,[6] the reproducibility of these performance levels is not known.

Optimization of the heterojunction performance depends critically on tuning dopant profiles with compositional variations. When the p/n junction resides too deeply within the compositional heterostructure, formation of valence band barriers to the photogenerated minority carriers across the junction cannot be avoided.[7] At the other extreme, if the
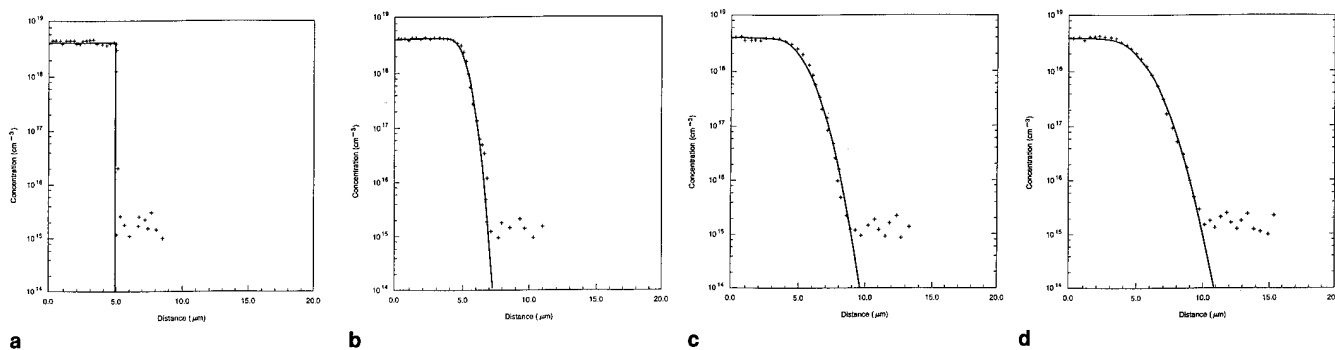
Fig. 1. (a) As-grown profile as described in the text; (b) distribution of arsenic after 1 h at 400°C; Hg overpressure: 0.61 atm; the solid line shows the best fit obtained assuming composition independent Fickian diffusion; (c) distribution of arsenic after 4 h at 400°C; Hg overpressure: 0.61 atm; the solid line shows the best fit obtained assuming composition independent Fickian diffusion; (d) distribution of arsenic after 6 h at 400°C; Hg overpressure: 0.61 atm; the solid line shows the best fit obtained assuming composition independent Fickian diffusion.

p/n junction is located deep within the long wavelength base layer, the beneficial effects of the wider energy gap in reducing generation-recombination and tunneling leakage currents are lost.[1] The optimum performance can presumably be obtained when the p/n junction is located such that the extent of the graded band gap region is narrower than the depletion region width.[7] Therefore, the dopant profiles establishing the location of the p/n junction have to be tuned. For p on n heterojunctions in HgCdTe, the dopant diffusion coefficient of relevance involves almost exclusively the acceptor impurity.[8] It is commonly arsenic.

EXPERIMENTAL PROCEDURES

The procedures followed during the present study were generally similar to the methods followed during an earlier study.[8] Arsenic doped, uniform thickness and specular HgCdTe films were grown on HgCdTe substrates by dipping Hg-rich LPE. The growth temperature ranged between 330 and 350°C, usually staying between 300 and 340°C for the overwhelming majority of the runs employed. The film thickness varied between 3 and 10 μm, with the majority falling between 4.5 and 9 μm. The substrate HgCdTe thickness ranged between 10 and 70 μm. Unlike the arsenic-doped cap layers, the base or the substrate layers were grown by dipping Te-rich LPE on CdZnTe. These substrate HgCdTe layers were either undoped or for double layer heterojunctions, doped with indium.

Diffusion annealing of sectioned pieces of these films was performed at selected temperatures under constant selected Hg partial pressures for desired time periods. The annealing scheme consisted of the following: The whole heterojunction film, approximately 2 × 3 cm in size, was sectioned into eight individual pieces. One of these pieces was held back as an 'as-grown' reference piece and not subjected to any further treatment. Each of the other seven pieces was subsequently annealed at a specific 'anneal' temperature under a constant Hg partial pressure within a sealed and closed ampoule in a multi-zone annealing furnace. Here the desired Hg partial pressure was obtained by maintaining the Hg reservoir at the required 'reservoir' temperature in the respective furnace zone. Note that the 'reservoir' temperature is different and lower than the specimen 'anneal' temperature. Each individual piece was subjected to only one specific set of diffusion annealing conditions—a specific temperature, a specific Hg partial pressure, a specific length of time. It was then not subjected to any additional anneal of any kind. At least seven different diffusion experiments were possible from each heterojunction film grown. Other details of these processes remained similar to the 'diffusion anneal' methods followed during the earlier investigation.[8] Approximately 72 heterojunction films were grown for these experiments.

The resulting As profiles were measured by secondary ion mass spectrometry (SIMS), using either Cs+ or O_2^+ primary ions, employing a Cameca 3f ion mass spectrometer (IMS). The compositional profile across the heterostructure was determined either by the [125]Te secondary electronegative ion yield during SIMS where a Cs+ primary ion beam was used or by directly determining Cd variation when O_2^+ primary ions were employed. The former method is based on the observation that a linear relationship exists between the ion yield and the Cd fraction.[9] These methods remained generally similar to procedures followed during the earlier investigations.[8] Limit of detectability of As ranged between 1 and 2×10^{15} cm^{-3}, though the precise limit depended on the sputtering rate.

A somewhat different annealing sequence was followed when the objective was to study diode performances. In this case, the specimens were subjected to two separate annealing treatments. The first consisted of a 'junction placement anneal' at >350°C where, unlike the conditions discussed above, the respective Hg partial pressures were not held fixed but varied in a controlled sequence. For most of the duration of this anneal, the mercury overpressures employed remained not only lower than the corresponding mercury-saturated limits by varying degrees, but were also far removed from the respective tellurium-saturated limits. During the final step, the mercury pressure employed was raised to equal the magnitude at the respective Hg saturated limit while the temperature was still maintained at >350°C. Other details of the process remained similar to the

Variation of As Diffusion Coefficients in HgCdTe Alloys with Temperature and
Hg Pressure: Tuning of p on n Double Layer Heterojunction Diode Properties

601

junction positioning anneal employed during the earlier investigation.[8] The second annealing treatment following the junction placement anneal consisted of anneals between 230 and 270°C under mercury-saturated conditions.

RESULTS AND DISCUSSIONS

Three anneal temperatures were investigated during the present investigations: 375, 400, and 425°C. At each of these temperatures, the diffusion anneals were performed at selected Hg partial pressures. At each selected partial pressure for each temperature, the reproducibility of the diffusion process was evaluated by performing individual anneal experiments for different time periods. A representative partial sequence can be observed in Fig. 1. Here the As profiles for four of the pieces sectioned from the same double layer film following specific annealing treatments are displayed. Figure 1a shows the as-grown profile; Fig. 1b the profile after 1 h at 400°C at a mercury overpressure of 0.61 atm; Fig. 1c the profile after 4 h at the same temperature and mercury overpressure with Fig. 1d showing the profile after 6 h at the same temperature and mercury overpressure. The solid lines in Figs. 1b, 1c, and 1d indicate the best fit possible assuming just composition independent Fickian or classical diffusion. Note that for the as-grown section (Fig. 1a), a virtual step profile in As was obtained, with negligible diffusion into the base layer, providing an ideal starting point for subsequent diffusion anneals. Furthermore, for the cap and base layer thicknesses employed during these investigations, the diffusion process can be very closely approximated by 'diffusion from an infinitely thick layer into an infinite body' since both of these layers are thick compared to the magnitudes of the diffusion coefficients encountered and the anneal times employed. The diffusion model essentially simplifies to:[8,10–12]

$$C(x,t) = \frac{C_0}{2} \cdot \mathrm{erfc}\left(\frac{x}{2\sqrt{Dt}}\right), \qquad (1)$$

where the initial concentrations are given by:

$$C(x, 0) = C_0 \text{ for } -\infty < x < 0$$

and $\qquad C(x, 0) = 0 \text{ for } 0 < x < \infty.$

Similar to the methods followed during the earlier investigations,[8] the best fits to the experimental profiles were obtained by allowing only the magnitudes of the diffusion coefficients to vary in the composition independent diffusion mechanism described above. As apparent from Fig. 1, the quality of the agreement between the experimental data and the predicted behavior is excellent almost to the SIMS detectability limit—1–2 × 10^{15} cm^{-3}. Hence each of these fits permits a measurement of the respective diffusion coefficient corresponding to the specific diffusion anneal experiment performed. These magnitudes differ slightly from experiment to experiment. For example, the respective magnitudes of the diffusion coefficients yielding the best fits with the experimental profile

results vary from 9.53×10^{-13} cm²/s for 1 h at 400°C (Fig. 1b) to 9.36×10^{-13} cm²/s for 4 h at 400°C (Fig. 1c) to 9.97×10^{-13} cm²/s for 6 h at 400°C (Fig. 1d). All these anneals were performed under a mercury overpressure of 0.61 atm. This partial pressure is within the phase field at this temperature and removed from both the Hg saturated limit (1.90 atm) and the Te saturated limit (7×10^{-3} atm).[13]

The overwhelming majority of the results collected during these investigations was obtained following the sequence and analysis described above. The results can be displayed by showing the diffusion coefficients estimated from each As concentration profiles obtained following specific anneal steps. Figure 2 shows the measured diffusion coefficients obtained during the present investigations at 375, 400, and 425°C as functions of the respective mercury overpressures. For each individual anneal temperature, the diffusion coefficients decreased with decreasing Hg pressure, approximately as $\propto 1/P_{Hg}^3$, where P_{Hg} is the respective Hg overpressure. This is similar to the dependence observed during the earlier investigation[8] at a lower temperature. The conditions employed during these measurements (ranging from incorporation of As in the cap layer during growth from a Hg-rich LPE melt, therefore under Hg-rich conditions, but at <350°C, to the performance of anneals at higher temperatures, but under precisely controlled Hg overpressures) need to be carefully considered in any comparison with literature results. A very large portion of the results reported in the literature was obtained under conditions fundamentally different from those followed during the present investigations. Among the few areas of convergence, where a comparative assessment is possible, lie the diffusion data obtained by other workers where the entire diffusion experiments were performed under Hg saturated conditions (these could be compared with diffusion coefficients obtained from the present investigations at the respective Hg-saturated limits). For each
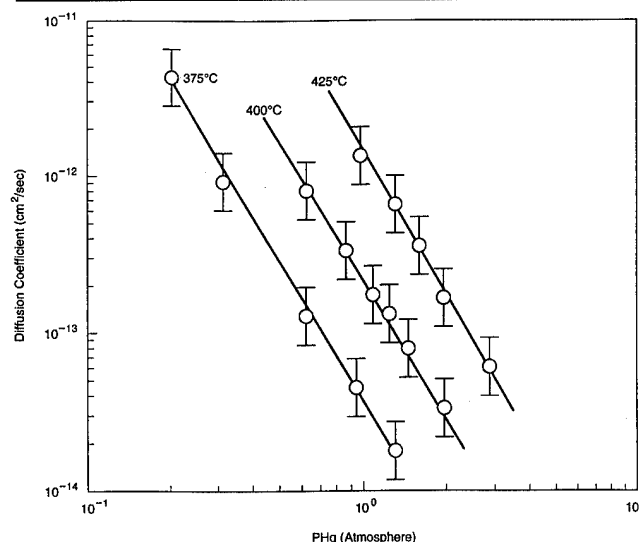

Fig. 2. Dependence of the diffusion coefficient of arsenic at 375, 400, and 425°C in mercury cadmium telluride on the Hg overpressure.

a   b   c
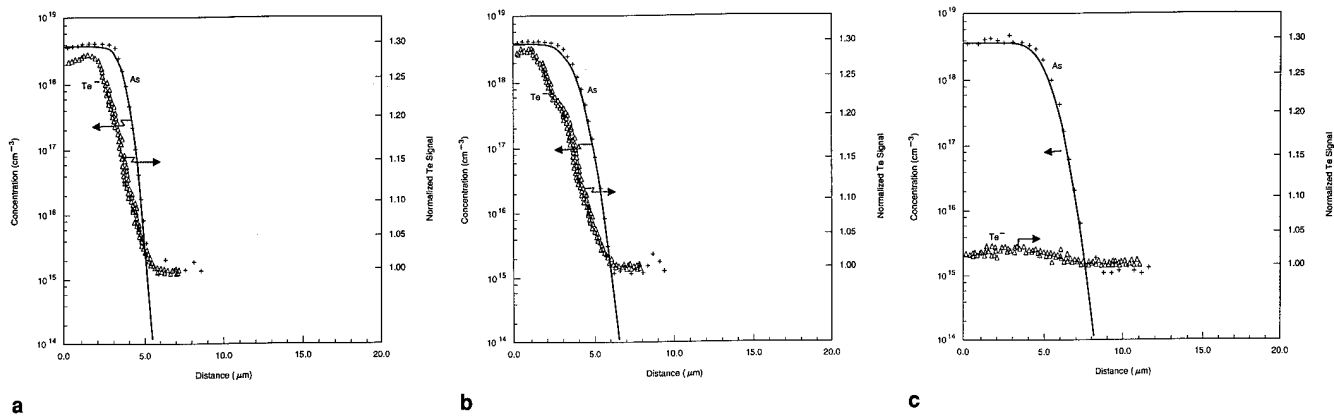
Fig. 3. (a) Arsenic concentration profile and composition profile after 2 h at 425°C; Hg overpressure: 1.51 atm; the solid line through the arsenic distribution shows the best fit obtained assuming concentration independent Fickian diffusion; (b) arsenic concentration profile and composition profile after 4.5 h at 425°C; Hg overpressure: 1.51 atm; the solid line through the arsenic distribution shows the best fit obtained assuming concentration independent Fickian diffusion; (c) arsenic concentration profile and composition profile after 5.5 h at 425°C; Hg overpressure: 1.51 atm; the solid line through the arsenic distribution shows the best fit obtained assuming concentration independent Fickian diffusion. Respective as-grown layer compositions as determined by electron microprobe are listed in Table I.

Table I. Results from the Profile Data in Fig. 3

Specimen Set in Fig.	(Temp. °C)	Mercury Overpressure (atm)	Cap Layer Composition (X_{CdTe})	Base Layer Composition (X_{CdTe})	Diffusion Coefficient (cm²/s)
a	425	1.51	0.284	0.222	3.82×10^{-13}
b	425	1.51	0.284	0.222	3.91×10^{-13}
c	425	1.51	0.227	0.224	3.79×10^{-13}

one of the temperature regimes studied during the present investigations, the highest Hg partial pressures employed corresponded to the respective Hg saturated limits. Diffusion coefficients measured at these limiting pressures from the results displayed in Fig. 2 agree well with results obtained by other workers under Hg saturated conditions.[14]

All measurements and analysis reported above correspond to double layer structures. The cap layer composition (the CdTe mole fraction in $Hg_{1-x}Cd_xTe$) can differ significantly from that of the base layer composition. This variation will lead to a compositional gradient, which in turn will result in a lattice parameter gradient, since no attempts were made during these investigations to lattice match the MWIR cap layers with LWIR base layers. The lattice parameter gradient will lead to the formation of misfit dislocations with a density proportional to the lattice constant gradient under the present conditions.[15,16] The latter in turn will be directly proportional to the compositional gradient in this case. For example, an uniform variation from a composition of x = 0.28 to a composition of x = 0.22 within a distance of 5 µm will lead to a misfit dislocation density of 5.7×10^6 cm⁻².[16] During the present investigations, attempts were made to assess the importance of these dislocations on the arsenic diffusion coefficients measured. Diffusion anneals were performed with several double layers where the composition of the cap layer was maintained very close to the composition of the base layers. These were then compared with diffusion anneals

performed on double layers where the two compositions differ significantly. Representative results from these experiments are displayed in Fig. 3. Figure 3a shows the arsenic concentration profile and the composition profile obtained on a double layer where the cap composition differs significantly from the base layer composition following a 2 h anneal at 425°C at a mercury overpressure of 1.51 atm. Determination of the compositional profile or the variation of the CdTe mole fraction as a function of depth, was determined, as discussed above, from a determination of the Te⁻ ion yield from SIMS results when using a Cs⁺ primary ion beam. A linear relationship exists between this ion yield and the Cd mole fraction.[8,9,17] The composition profile in Fig. 3a has been displayed after normalizing the Te⁻ signal obtained from the cap layer and the interdiffused region between the cap and the base layers with respect to the signal obtained from the base layer. The compositions of both the cap and the base layers were also determined independently from cross sections of the reference as-grown piece with quantitative x-ray analysis in a scanning electron microscope/electron probe microanalyzer (SEM/EPMA), which in turn were calibrated with reference bulk HgCdTe standards.[18] These results are displayed in Table I. Note that for the specimen displayed in Fig. 3a, the composition of the cap layer at a CdTe mole fraction of 0.284 ± 0.002 is significantly higher than the base layer composition at a CdTe mole fraction of 0.222 ± 0.002. Figure 3b shows the arsenic concentration profile and the composition profile measured in

Variation of As Diffusion Coefficients in HgCdTe Alloys with Temperature and
Hg Pressure: Tuning of p on n Double Layer Heterojunction Diode Properties

603

another piece from this same double layer structure following an anneal of 4.5 h at 425°C under the same mercury overpressure of 1.51 atm. Figure 3c shows the arsenic concentration profile and the composition profile from a separate double layer structure after an anneal of 5.5 h at 425°C under the same mercury overpressure of 1.51 atm. In this case, however, the composition of the cap layer differed little from that of the base layer (Table I). The solid lines displayed depict the best fits possible using the composition independent Fickian diffusion model described above [Eq. (1)], where the magnitude of the diffusion coefficient was the only parameter allowed to be varied in obtaining the fit. As discussed above, this method permits an estimation of the diffusion coefficient. The magnitudes of the estimated diffusion coefficients change very little for these fits to the experimental profiles—from 3.82×10^{-13} cm²/s for 2 h at 425°C (Fig. 3a), to 3.91×10^{-13} cm²/s for 4.5 h at 425°C (Fig. 3b), to 3.79×10^{-13} cm²/s for 5.5 h at 425°C (Fig. 3c). The first two magnitudes obtained for a double layer structure with significant compositional difference between the cap and the base layer (0.284 ± 0.002 vs 0.222 ± 0.002) differ little from the magnitude obtained for a double layer structure where the compositional difference between the cap and the base layer is virtually non-existent (0.227 ± 0.002 vs 0.224 ± 0.002). All these diffusion coefficients, as indicated (Table I), were estimated under a mercury overpressure of 1.51 atm, which is removed from both the Hg saturated limit (2.7 atm) and the Te saturated limit (1.2×10^{-2} atmosphere) at this temperature.[13] Even with more than 10 x decrease in the compositional gradient, the diffusion coefficient estimated is not influenced in any measurably significant manner. The expected misfit dislocation density, within limits, can be estimated reasonably reliably from the results and basic relationships provided by Szilagyi et. al.[16] The total compositional change displayed for all profiles in Fig. 3 occurs approximately over 2.5–3.5 μm. The predicted misfit dislocation density would vary from a lower limit of 6×10^6 to an upper limit of 2×10^7 cm⁻² for the profiles displayed in Figs. 3a and 3b, whereas it would vary from a lower limit of 0 (no misfit, hence no misfit dislocation density) to an upper limit of 5×10^5 cm⁻² for the profile displayed in Fig. 3c.[16] This very large variation in both the measured compositional variation and the expected misfit dislocation density do not appear to be influencing the estimated diffusion coefficients measured.

Diffusion coefficients were measured over a range of mercury pressures following these procedures. As indicated above, Fig. 2 shows the results obtained at 375, 400, and 425°C. With mercury pressures decreasing below the range displayed in Fig. 2, the arsenic diffusion behavior began to change. This is most apparent at 400 and 425°C, as displayed in Fig. 4. With mercury pressure decreasing from the mercury saturated limits, the relationship between the estimated diffusion coefficients and the mercury overpressures changed progressively from a $\sim 1/P_{Hg}^3$

type of dependence to an apparently simple $\sim 1/P_{Hg}$ type of dependence. At 400°C, the $1/P_{Hg}^3$ dependence is approximately followed between the Hg-saturated limit of 1.9 atm and ~0.5 atm, and then gradually transitioning to an approximately $1/P_{Hg}$ dependence between ~0.5 and ~0.2 atm. The $1/P_{Hg}$ dependence appears fully developed between ~0.2 and 0.06 atm. A basically similar trend is observed for 425°C, with the transition to the $1/P_{Hg}$ dependence apparently completed at the slightly higher pressure of ~0.4 atm. Here, too, the $1/P_{Hg}$ dependence appears fully developed between ~0.4 and 0.06 atm.

For the mercury pressure regimes displayed in Fig. 4, the diffusion behavior could still be described very well by a simple concentration independent Fickian diffusion model [Eq. (1)]. With continued decrease of the mercury overpressure below the limit displayed in Fig. 4, however, the concentration profiles could no longer be described by this simple model. Even for a partial pressure of 0.03 atm, the concentration profiles deviated significantly from the concentration independent model. These profiles resembled strongly the profile obtained at a mercury overpressure of 0.11 atm at 350°C and displayed earlier (Fig. 3 in Ref. 8). These correspond somewhat more appropriately to a multi-component diffusion behavior. Approximate general overpressure ranges below which the concentration profiles begin to deviate significantly from a simple concentration independent Fickian diffusion model can be determined from these results. When combined with trends observed during the earlier investigation,[8] the respective limits appear to decrease with increasing temperature (being at ~ 0.11 atm for 350°C[8] and decreasing to ~0.06 atm at 400 and 425°C as described above).

We now consider only the mercury partial pressure regimes where the diffusion behavior of arsenic can be well described by the simple concentration independent model [Eq. (1)]. These ranges are displayed in
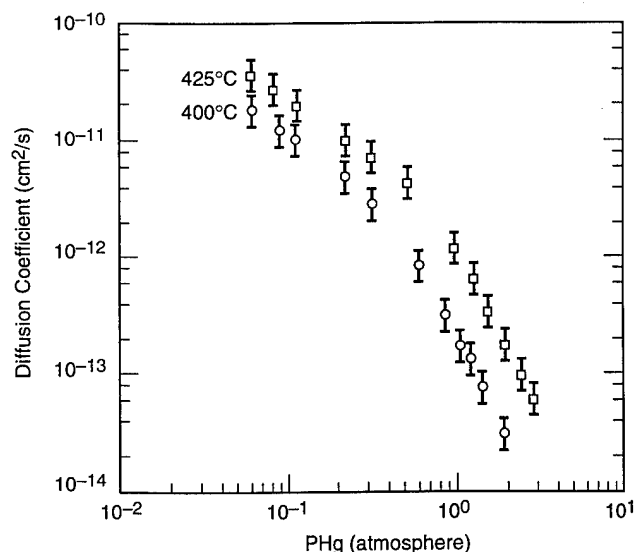

Fig. 4. Dependence of the diffusion coefficient of arsenic at 400 and 425°C in mercury cadmium telluride on the Hg overpressure.

Fig. 4. The behavior at mercury pressure regimes below the limits (~0.06 atm) displayed in Fig. 4 deviates from this simple model, as discussed above, and therefore will not be addressed during the present investigations.

Following the basic description of arsenic transport developed during the earlier investigation,[8] we make the reasonable simplifying assumptions:
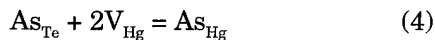
- As grown from the Hg-rich melt and therefore under Hg-saturated conditions, the arsenic atoms occupy sites in the chalcogen sublattice (As_{Te}). These are in equilibrium with both the Hg vacancies (V_{Hg}) and the Te vacancies (V_{Te}).

- Assuming only vacancy driven substitutional diffusion, arsenic will transport almost exclusively by employing vacancies in the metal sublattice, since $V_{Hg} \gg V_{Te}$. Correspondingly, only arsenic 'dissolved' in the metal sublattice will participate in the transport.

- Hence for the 'total' arsenic' which can reside either in the chalcogen or the metal sublattice sites, determined by the respective defect equilibria, the effective 'total' diffusion coefficient (D^T_{As}) can be postulated to be proportional to the vacancy driven substitutional diffusion coefficient active for arsenic on the metal sublattice sites (D^{Hg}_{As}), normalized by the concentration of the arsenic atoms on the metal sublattice sites (As_{Hg}).

Here $[As_{Hg}]$ is the concentration of the dominant mobile species. Similar cases have been analyzed by Stevenson[19] and Tuck.[20] Note that the nature of the diffusion mechanism considered here is purely vacancy driven substitutional diffusion (no other enhanced 'defect' driven diffusion coefficient, as postulated by some workers)[21] was invoked. Furthermore, existence of nonsubstitutional diffusion mechanisms (for example an interstitial diffusion component) was ignored.

The quasi-chemical or 'defect' equilibria reactions of relevance can be expressed as:

$$As_{Te} + V_{Hg} = As_{Hg} + V_{Te} \qquad (2)$$

$$V_{Te} + V_{Hg} = 0 \qquad (3)$$
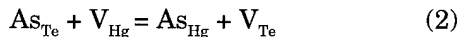
Adding Eq. (2) and Eq. (3) yields:

$$As_{Te} + 2V_{Hg} = As_{Hg} \qquad (4)$$

The respective equilibrium constant can be expressed as:

$$K_4 = \frac{\left[As_{Hg}\right]}{\left[As_{Te}\right]\left[V_{Hg}\right]^2} \qquad (5)$$

As assumed, initially the overwhelming majority of the arsenic atoms in the films as grown under Hg-saturated conditions would occupy sites in the chalcogen sublattice (As_{Te}). This can be expressed in terms of a simple inequality

$$[As_{Hg}] \ll [As_{Te}] \qquad (6)$$

Consider the mercury pressure regime near the Hg-saturated limit where this inequality is still valid. Since most of the arsenic will reside in the chalcogen sublattice, the concentration $[As_{Te}]$ will remain invariant within this regime. Combining Eq. (5) with the inequality [Eq. (6)], it is possible to express:

$$[As_{Hg}] \propto [V_{Hg}]^2 \qquad (7)$$

The 'total' arsenic diffusion coefficient (D^T_{As}) as discussed above, and similar to cases analyzed by other workers,[19,20] will be expressed by the vacancy driven substitutional diffusion coefficient for arsenic atoms on the metal sublattice sites (D^{Hg}_{As}) normalized by the concentration of arsenic atoms on the metal sublattice sites ($[As_{Hg}]$). This is equivalent to expressing:

$$D^T_{As} \propto [As_{Hg}] \cdot (D^{Hg}_{As}) \qquad (8)$$

where the relationship between the vacancy driven substitutional diffusion coefficient and the vacancy concentration can be expressed simply as:

$$D^{Hg}_{As} \propto [V_{Hg}] \qquad (9)$$

Equations (7), (8), and (9) can be combined to yield:

$$D^T_{As} \propto [V_{Hg}]^3 \qquad (10)$$

For the $Hg_{1-x}Cd_xTe$ alloys with $x \cong 0.2$, the vacancy concentration within the 150 to 655°C temperature range can be approximated as:[13,22]

$$\left[V_{Hg}\right] \propto \frac{1}{P_{Hg}} \qquad (11)$$

From Eq. (10) and (11):

$$D^T_{As} \propto P_{Hg}^{-3} \qquad (12)$$

Figure 2 depicts the mercury pressure regimes at 375, 400, and 425°C where this dependence is approximately obeyed. Consistent with the description above, the pressure ranges are close to the respective Hg-saturated limits at each temperature. Each pressure regime appears to be spread less than 10 x away from the Hg-saturated ends. Agreement between the experimental results and Eq. (12) also implies the validity of the inequality [Eq.(6)] within these pressure regimes.

With continued decrease in the mercury overpressure from these ranges, the inequality [Eq. (6)] will become progressively invalid. This can be directly observed from Eq. (5) where it is evident that the ratio $[As_{Hg}]/[As_{Te}]$ increases with the increasing Hg vacancy concentration as $\propto [V_{Hg}]^2$. Two limiting ranges will, therefore, be established:

- for low Hg vacancy concentrations or for high mercury overpressures, most of the arsenic will stay on the chalcogen sublattice and the behavior indicated by Eq. (12) will be observed;

- with continued increase in the Hg vacancy concentration or with decreasing mercury overpressure, however, a progressive transfer of arsenic to the metal sublattice will occur, leading to increasing $[As_{Hg}]$, until a stage is reached where

Variation of As Diffusion Coefficients in HgCdTe Alloys with Temperature and
Hg Pressure: Tuning of p on n Double Layer Heterojunction Diode Properties

605

$[As_{Hg}]$ will change relatively little with further increase in the Hg vacancy concentration or with decreasing mercury overpressure. For this limit, it is possible to approximate Eq. (8) as:

$$D^T_{As} \propto [As_{Hg}] \cdot [D^{Hg}_{As}] \propto [D^{Hg}_{As}] \qquad (13)$$

Combining Eqs. (13), (9), and (11) yields:

$$D^T_{As} \propto P_{Hg}^{-1} \qquad (14)$$

Figure 4 displays the dependence of measured diffusion coefficients at 400 and 425°C on mercury partial pressures, with both the limiting conditions distinguishable. For higher mercury overpressures, Eq. (12) appears to approximate the experimental dependence, but with decreasing Hg pressures Eq. (14) becomes clearly prevalent.

The progression from a P_{Hg}^{-3} dependence to a P_{Hg}^{-1} dependence with decreasing mercury overpressure is, therefore, consistent with the basic schematic description of arsenic transport developed above. An important requirement for the applicability of this scheme would be the validity of Eq. (11). As indicated above, results obtained by Vydyanath et al.[13,22] appear to strongly support this relationship for $Hg_{0.8}Cd_{0.2}Te$. The validity of this equation also means that the crystals would be intrinsic over the temperature and pressure ranges employed during these investigations. For $Hg_{1-x}Cd_xTe$ with $x \geq 0.4$ however, Eq. (11) may no longer be valid.[22] For these compositions, the dependence of arsenic diffusion coefficients on mercury partial pressures may, therefore, become more complex. During the present investigations, the highest magnitudes of x, even for the cap layers, remained much lower: ≤ 0.3. Within this range, as discussed above, the diffusion behavior appears to be independent of composition. Therefore, Eq. (11) appears to be valid over the whole range of compositions studied, leading in turn to the applicability of Eq. (12) and Eq. (14) over the regimes of high and low mercury overpressures respectively (Fig. 2 and Fig. 4).

Activity of arsenic: When grown from the Hg-rich nutrient melt by dipping LPE, arsenic is already 100% active as an acceptor. The arsenic atoms are located almost exclusively in the Te sublattice, equivalently described by the inequality [Eq. (6)]. No activation or site transfer anneal of any kind would be necessary for the exclusive purpose of restoring or attaining the activation of arsenic as an acceptor. However, when annealed under decreasing mercury pressures, progressive deactivation of arsenic must occur. This activity can subsequently be restored by mercury-saturated anneals.[8,21,23] For mercury-deficient anneals near the respective mercury-saturated ends, defined approximately by the inequality ([Eq. 6)] above, earlier results appeared to indicate the adequacy of mercury-saturated anneal at 270°C in restoring the activity of arsenic.[8] With continued decrease in the mercury overpressure, arsenic activation would also continue to decrease. Restoration of the activity may then require mercury-saturated anneals at increasingly higher temperatures.

During the present investigations, preliminary attempts were continued to assess the selectivity in locating the p-n junction with respect to the compositional profile available from the diffusion results displayed in Fig. 2 and Fig. 4. If the p-n junction is positioned such that the extent of the graded band gap region is wider than the depletion region width, a valence band barrier to the transport of minority carriers across the junction would form.[1] The height and width of the barrier depend on the compositional grading width, the difference in composition across the heterojunction (Δx), the p-n junction location relative to the heterojunction, and the n-side depletion width, which is related to the carrier concentration on the n-side and the junction voltage. Diodes exhibiting low quantum efficiencies with significant bias and temperature dependencies can be deemed to have barriers. Long wavelength infrared diodes displaying unusually large magnitudes of R_0A have also been associated with valence band barriers.[8] Valence band barriers have been observed in photodiodes when one or more of the above parameters lead to the location of the p-n junction such that the resulting n-side depletion width becomes narrower than the graded band gap region.[8,24] For VLWIR systems, for example, with base layer cutoffs >12 μm at 80K, valence band barriers have been observed for heterojunctions when the base layer dopant level and the compositional difference (Δx) at the heterojunction simultaneously exceeded 1.5×10^{15} cm^{-3} and 0.06, respectively.[24]

Once a barrier has been formed, it would be impossible to eliminate it by annealing under Hg-saturated conditions, since the compositional junction would always widen at a faster rate than the movement of the p-n junction.[8] The movement of the p-n junction is controlled almost exclusively by the transport coefficients of arsenic.[8] Preliminary results obtained during this investigation extend our earlier
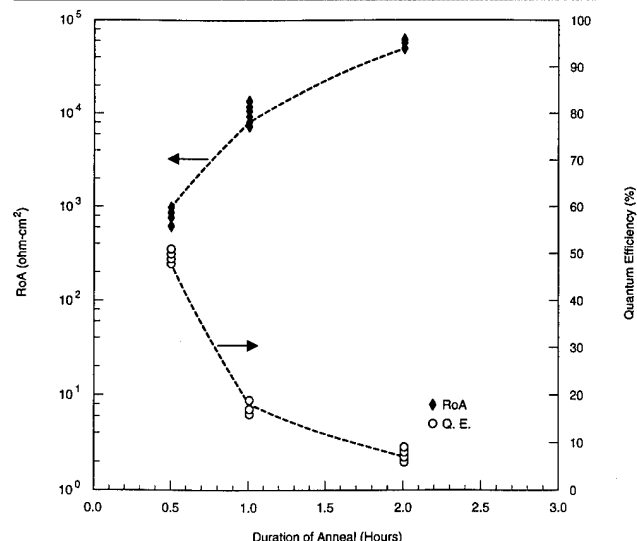

Fig. 5. Dependence of R_0A and quantum efficiency for double layer heterojunction specimens on the duration of anneal at 375°C under mercury-saturated conditions.

observations. Valence band barriers are introduced by mercury saturated anneals, but can be eliminated by suitable mercury deficient anneals. With decreasing mercury overpressures, compositional interdiffusion coefficients decrease,[25] exactly opposite to the trends for arsenic.

Figure 5 shows the progressive change in the magnitudes of R_0A and quantum efficiency for double layer heterojunction specimens annealed at 375°C under Hg-saturated conditions (mercury partial pressure at 1.27 atm) for 0.5, 1.0, and 2.0 h, respectively. All specimens were sectioned from the same large double layer film. Following each anneal, the individual specimens were stoichiometrically adjusted by a low temperature mercury saturated anneal at 250°C to reduce the Hg vacancy concentration below 5×10^{13} cm^{-3}. The R_0A increased steadily from between 600–1000 ohm-cm^2 to $>5 \times 10^4$ ohm-cm^2. Quantum efficiency continued to decrease with increasing duration of anneal at 375°C, falling from ~50% for the 0.5 h point to < 10% for the 2 h point.
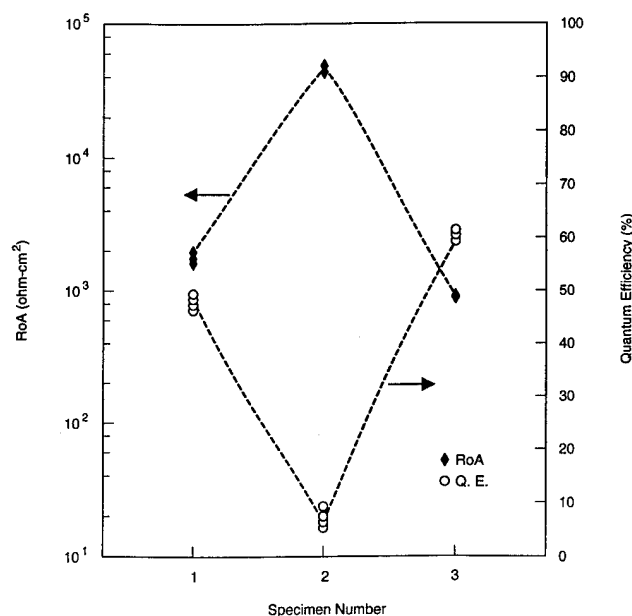

Fig. 6. Dependence of R_0A and quantum efficiency for three specimens sectioned from the same double layer heterojunction on selected annealing treatments as described in the text.

Figure 6 displays the corresponding results for double layer heterojunctions where one of the specimens was processed by the 'junction placement anneal' described above. This anneal was performed under mercury 'deficient' conditions or with mercury overpressures less than the mercury saturated limits for most of the duration of the anneal at temperatures >350 C. The mercury overpressures employed were varied sequentially during the duration of the anneal with the final step consisting of a mercury-saturated anneal. This last procedure restored the activity of arsenic. Figure 6 displays the R_0A and the quantum efficiency (QE) for three specimens sectioned from the same double layer film. Specimen 1 was not subjected to any junction placement anneal, but only to a low temperature (250°C) stoichiometric adjustment anneal under mercury-saturated condition for 24 h. Specimen 2 was subjected to a mercury-saturated anneal for 90 min at 375°C followed by the low temperature stoichiometric adjustment anneal. Specimen 3 was subjected to a 'junction placement anneal' followed by the low temperature mercury-saturated stoichiometric adjustment anneal. R_0A varied from between 1500 and 2000 ohm-cm^2 for specimen 1 to >42000 ohm-cm^2 for specimen 2 to between 850 and 900 ohm-cm^2 for specimen 3. Corresponding quantum efficiency measurements yielded ~48% for specimen 1, <10% for specimen 2, and ~60% for specimen 3. The base layer cutoff was measured at 9.94 µm at 80K. No anti-reflection coating was employed. For specimen 3, the quantum efficiency was also measured as a function of increasing reverse bias. No dependence was noted. Hence, it can be concluded that specimen 1, characteristic of the as-grown material, displayed a small valence band barrier, which subsequently increased upon annealing under mercury-saturated conditions at 375°C (specimen 2) but which was eliminated by the junction placement anneal (specimen 3).

Figure 7 shows the current-voltage (I-V) and dynamic impedance area-voltage (RA-V) behavior for three representative diodes from three different double layer heterojuction (DLHJ) films subjected to the junction placement anneal. The device dark currents are diffusion limited and the RA products reach magnitudes close to 1×10^5 ohm-cm^2 for an applied reverse bias between 40 and 60 mV even for a base layer cutoff
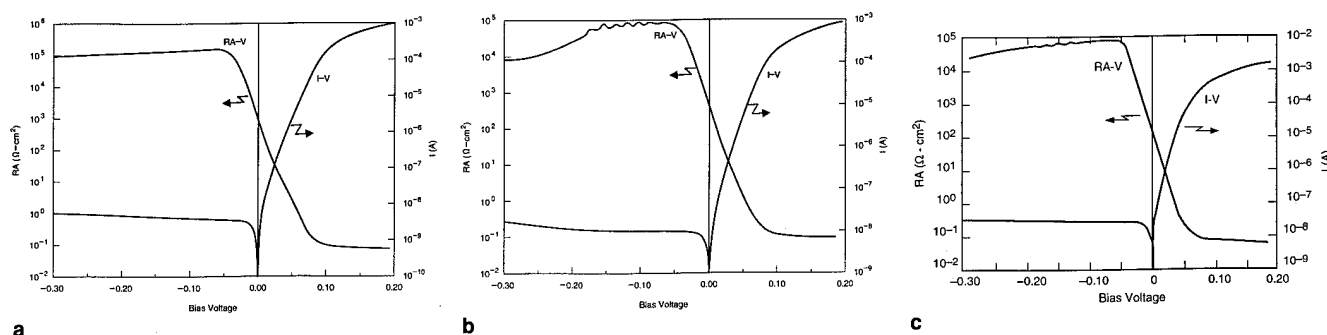

Fig. 7. (a) Typical RA-V and I-V characteristics for a test diode built on a 9.0 µm (at 78K) cutoff mercury cadmium telluride DLHJ film; (b) typical RA-V and I-V characteristics for a test diode built on a 9.5 µm (at 78K) cutoff mercury cadmium telluride DLHJ film; (c) typical RA-V and I-V characteristics for a test diode built on a 10.8 µm (at 78K) cutoff mercury cadmium telluride DLHJ film.
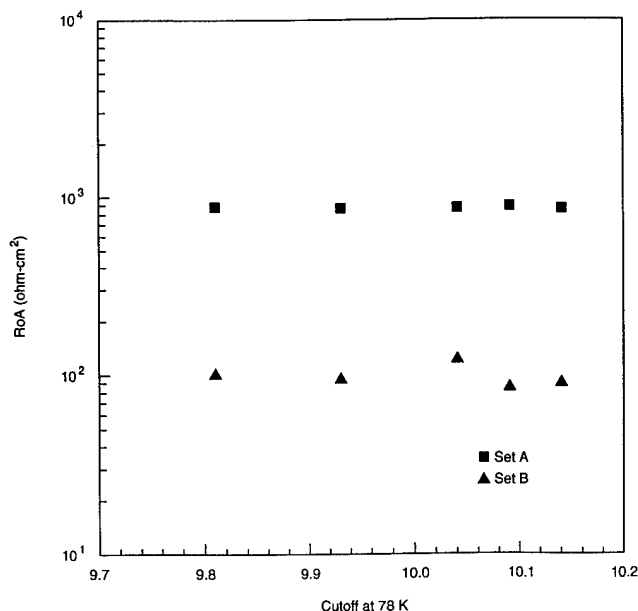
Variation of As Diffusion Coefficients in HgCdTe Alloys with Temperature and
Hg Pressure: Tuning of p on n Double Layer Heterojunction Diode Properties

607

Fig. 8. Dependence of R_0A for sets of sister specimens sectioned from five DLHJ films on selected annealing treatments as described in the text.

Fig. 9. R_0A products at 78K under 0° FOV for test diodes built on double layer films following anneals as described in the text; the solid line depicts an idealized performance behavior with a base layer dopant density of 3×10^{15} cm^{-3} and Auger-limited minority carrier lifetime.[4]

of 10.8 μm at 80K. The device leakage currents continued to be lower than 50 μA cm^{-2} at a reverse bias of 50 mV and independent of bias up to a reverse bias of 300 mV.

As indicated above, with decreasing mercury pressure, the compositional interdiffusion coefficients decrease,[25] opposite to the trend observed for arsenic as displayed in Fig. 2 and Fig. 4. Furthermore, the variation with Hg pressure is much weaker for interdiffusion coefficients compared to the strong dependence observed for arsenic. As a result, mercury-deficient anneals can include sequences beyond the 'junction positioning anneals' discussed above. When deliberately continued longer than optimum, these anneals can degrade the performance of a heterojunction. Figure 8 shows the R_0A products for two sets of five specimens each as a function of cutoff. The first set (A) consists of samples sectioned from five individual DLHJ films. The second set (B) consists of specimens sectioned from the same five heterojunction films. Set A was subjected to the optimum 'junction positioning anneal', whereas the sister samples in set B were subjected to a mercury-deficient anneal approximately 2 x longer. The R_0A magnitudes measured for diodes fabricated on set A specimens appear to be approximately 5 x superior. Hence, even when comparing performances on sister specimens sectioned from the same heterojunction film, thus eliminating film to film variation, tuning of mercury-deficient anneals will be important.

Figure 9 shows representative diode performances at 78K under 0° field of view (FOV) for double layer films with cutoffs between 9 and 13 μm subjected to optimum junction placement anneals. No valence band barriers were observed, as determined by the bias dependence of the quantum efficiency on selected films. The measured quantum efficiency varied be-
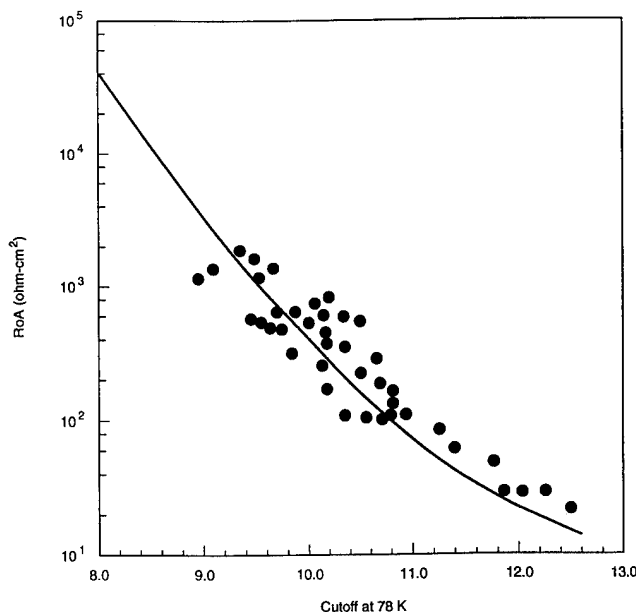
tween 55 and 60% from specimen to specimen, without the use of any anti-reflection coating, and remained invariant with increasing reverse bias. Use of mercury-deficient junction placement anneals has been extended to the near VLWIR (cutoff at ~11 μm) or VLWIR (cutoffs >12 μm) range during this investigation. Increasing incidence of valence band barriers within these ranges has been reported by other workers.[24]

CONCLUSION

When introduced during liquid phase epitaxy growth, arsenic diffusion behavior in mercury cadmium telluride remains concentration independent and simple classical for mercury overpressures near the mercury-saturated limits. The diffusion coefficients measured increase strongly with decreasing mercury pressures. The basic dependence on the mercury overpressures can be interpreted relatively simply and appears similar over a wide temperature range. The enhanced arsenic diffusion with decreasing mercury pressures can be successfully employed to tune double layer heterojunction performance parameters.

REFERENCES

1. K. Kosai and W.A. Radford, *J. Vac. Sci. Technol.* A8, 1254 (1990).
2. A. Rogalski and W. Larkowski, *Electron Techn.* 18, 55 (1985).
3. M.B. Reine, A.K. Sood and T.J. Tredwell, *Semiconductors and Semimetals,* ed. R.K. Willardson and A.C. Beer (New York: Academic, 1981), Vol. 18, Chap. 6, p. 207.
4. J.M. Arias, J.G. Pasko, M. Zandian, S.H. Shin, G.M. Williams, L.O. Bubulac, R.E. DeWames and W.E. Tennant, *J. Electron. Mater.* 22, 1049 (1993).
5. G.N. Pultz, P.W. Norton, E.E. Krueger and M.B. Reine, *J. Vac. Sci.Technol.* B9, 1724 (1991).
6. G. Destefanis and J.P. Chamonal, *J. Electron. Mater.* 22, 1027 (1993).

7. P.R. Bratt, *J. Vac. Sci. Technol.* A1, 1687 (1983).

8. D. Chandra, M.W. Goodwin, M.C. Chen and J.A. Dodge, *J. Electron. Mater.* 22, 1033 (1993).

9. L.O. Bubulac and C.R. Viswanathan, *Appl. Phys. Lett.* 60, 222 (1992).

10. W. Jost, *Diffusion in Solids, Liquids and Gases,* (New York: Academic, 1962).

11. B.l. Boltaks, *Diffusion in Semiconductors,* (New York: Academic, 1963).

12. S.K. Gandhi, *The Theory and Practice of Microelectronics,* (New York: John Wiley and Sons, 1968).

13. H.R. Vydyanath, *J. Electrochem. Soc.* 128, 2609 (1981).

14. T.H. Myers, K.A. Harris, R.W. Yanka, L.M. Mohnkern, R.J. Williams and G.K. Dudoff, *J. Vac. Sci. Technol. B* 10, 1438 (1992).

15. D. Chandra, J.H. Tregilgas and M.W. Goodwin, *J. Vac. Sci. Technol.* B9, 1852 (1991).

16. A. Szilagyi and M.N. Grimbergen, *J. Vac. Sci. Technol. A* 4, 2200 (1986).

17. L.O. Bubulac, D.D. Edwall, J.T. Cheung and C.R. Viswanathan, *J. Vac. Sci. Technol. B* 10, 1633 (1992).

18. T.M. Moore, *J. Vac. Sci. Technol. A* 1, 1651 (1983).

19. D.A. Stevenson, *Diffusion in the Chalcogenides of Zn, Cd and Pb, Atomic Diffusion in Semiconductors,* ed. D. Shaw, (New York: Plenum Press, 1973).

20. B. Tuck, *Atomic Diffusion in Semiconductors,* (Bristol: Adam Hilger, 1988).

21. L.O. Bubulac, D.D. Edwall and C.R. Viswanathan, *J. Vac. Sci. Technol. B* 9, 1695 (1991)

22. H.R. Vydyanath, *J. Vac. Sci. Technol. B* 9, 1716 (1991).

23. L.O. Bubulac, S.J.C. Irvine, E.R. Gertner, J. Bajaj, W.P. Lin and R. Zucca, Intl. Conf. on Narrow Gap Semiconductors, 19–23 July, 1992.

24. S.P. Tobin, E.E. Krueger, G.N. Pultz, M. Kestigian, K.-K. Wong and P.W. Norton, *J. Electron. Mater.* 22, 959 (1993).

25. M.-F.S. Tang and D.A. Stevenson, *J. Vac. Sci. Technol. A* 5, 3124 (1987).

Enhanced Arsenic Diffusion and Activation in HgCdTe

S.H. SHIN, J.M. ARIAS, M. ZANDIAN, J.G. PASKO, L.O. BUBULAC, and R.E. DE WAMES

Rockwell International Science Center, Thousand Oaks, CA 91360

Temperature and time dependent Hg-annealing studies for arsenic activation have been carried out on As-doped molecular beam epitaxy HgCdTe either *in situ* or by ion implantation to determine the extent of arsenic activation in the single layer. Enhanced As diffusion and activation in double layer heterostructures have also been investigated to further our understanding of the effects on zero bias resistance-area product (R_0A) and quantum efficiency. The results show that the arsenic activation anneal is limited by Hg self-diffusion into the HgCdTe epilayer. Using this arsenic activation process for either *in situ* doped arsenic or implanted arsenic, high performance p-on-n double layer heterostructure photodiodes have been demonstrated on both mesa and planar device structures.

Key words: As, diffusion, HgCdTe, infrared detectors

INTRODUCTION

The use of Group V elements (N, P, As, and Sb) as p-type dopants in HgCdTe heterojunction structures has led to a renewed interest in p-type doping studies by liquid phase epitaxy (LPE),[1] metalorganic vapor phase epitaxy (MOVPE),[2] and molecular beam epitaxy (MBE).[3,4] In the case of MBE-grown double layer heterojunction (DLHJ) devices, reliable and controllable high carrier concentration p-type doping is now key to meeting the technical needs for fabrication of long wavelength infrared (LWIR) focal plane arrays (FPAs). In this study, we have investigated As-doping of HgCdTe through the incorporation of arsenic during low temperature MBE growth and via ion implantation into DLHJ HgCdTe layers.

Previous attempts[3–5] at As-doping of HgCdTe by MBE resulted in n-type behavior, despite significant incorporation of As into these layers observed using secondary ion mass spectroscopy (SIMS), with As concentrations ranging from 1.4×10^{17} to 4.0×10^{18} cm^{-3}.

All as-grown samples exhibited n-type conductivity with electron concentrations measured by Hall effect ranging from 1.7×10^{15} to 2.2×10^{15} cm^{-3}. Hall mobility is closer to two orders of magnitude below that of In-doped n-type HgCdTe (i.e. 500–1100 vs ~1×10^5 cm^2/V.s).[5] The electron carrier concentration of as-grown arsenic doped n-type HgCdTe layers also increased with As flux for layers grown at the same temperature.[5] The arsenic is not electrically active and the material is highly resistive. Amphoteric behavior is a possible explanation for this behavior. The high resistivity due to low electron mobility of the as-grown layer indicates compensation of arsenic acceptors by arsenic donors. Another potential proposition is poor crystallinity of the layers due to arsenic precipitates[7] at growth temperatures below 160°C.

Last year, we reported the first p-type conversion of *in situ* As-doped MBE alloy HgCdTe.[5] The arsenic activation was achieved by post-growth thermal annealing above 425°C under saturated Hg partial pressure, followed by 250°C low temperature annealing under Hg-rich ambient. This result is consistent with the results observed on another Group V element,
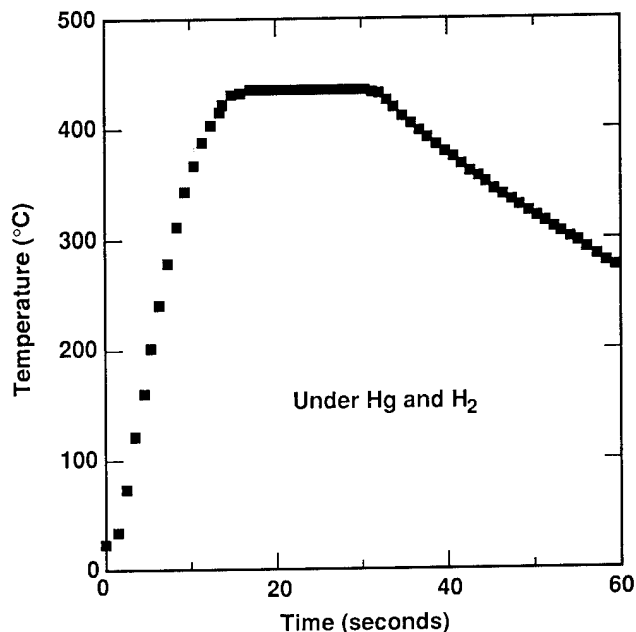
Fig. 1. A typical temperature-time profile used in the arsenic activation anneal experiments.

phosphorus-doped bulk HgCdTe by Vydyanath et al.[8] They observed that the hole concentration in the phosphorus doped samples increases with increasing partial pressure of Hg, in contrast to the behavior observed in undoped HgCdTe. They also suggested that phosphorus behaves amphoterically in HgCdTe, acting as a single acceptor occupying interstitial and Te lattice sites at high Hg pressure, and as a single donor occupying Hg lattice sites at low Hg pressure.

In this paper, we describe the effect of varying the Hg annealing conditions to shed more light on arsenic doping mechanisms in HgCdTe. The samples were grown by MBE at T <160°C for As-doped single layers, and at ~195°C for heterojunction double layers. In the case of DLHJ, arsenic was incorporated either during the low 160°C temperature MBE growth or post growth ion implantation process. The hole carrier concentrations have been measured as functions of Hg anneal temperature and time to determine the extent of arsenic activation in the As-doped HgCdTe single layers and compared to the SIMS profile analysis. Since high temperature Hg annealing also interdiffuses Cd and Hg at the heterojunction (HJ) interface, the effect of changing the Hg annealing processing conditions of p-on-n LWIR HgCdTe heterostructures has been studied to further our understanding of the effect on R_0A and quantum efficiency. Furthermore, specified conditions of the As activation anneal may result in an improvement in device performance, and may also provide further insight into the criteria of the optimum p/n junction in terms of cap layer thickness and composition when arsenic is used as the capping layer dopant.

EXPERIMENTAL

The open-tube annealing furnace used in these experiments was a vertical LPE furnace modified for

high temperature annealing, operating at hydrogen over pressures of up to 150 psi. Since a Hg anneal in a closed quartz ampoule above 410°C can degrade the HgCdTe sample, a high pressure open-tube annealing process has been developed for high temperature As activation as well as for diffusion. This annealing furnace has been described elsewhere.[6] After the high temperature annealing (400–570°C), the epilayers were n-type annealed at 250°C under a Hg environment to remove nonstoichiometric Hg vacancies induced by the high temperature annealing process. The epitaxial HgCdTe layers used for this study have been grown on (211) CdZnTe substrates in a Riber MBE system.[9]

Two techniques for arsenic doping in HgCdTe heterostructures have been explored:

- *in situ* arsenic doping during the HgCdTe cap layer growth by MBE, and
- planar p-on-n junction process of arsenic implantation into the HgCdTe DLHJ grown by MBE.

Molecular beam epitaxially grown LWIR HgCdTe was implanted with an As enrage of 300 KeV and a dose of 1×10^{14} cm^{-2}, and post implantation thermal annealing was carried out under various Hg partial pressures using high pressure conventional annealing or rapid thermal annealing. To determine the effects of arsenic activation temperature and time on detector R_0A and quantum efficiency, SIMS analysis of the arsenic profile and Dx values between base and cap layers were monitored.

A typical temperature-time profile used for the conventional activation anneal experiments is shown in Fig. 1. The heatup time is about 13 min. For 60 s short time annealing (rapid thermal anneal), the sample was kept in the cold zone during the initial heatup cycle until it reached the anneal temperature equilibrium, and then rapid thermal annealing was carried out for 60 s. The thermocouple used for monitoring the anneal temperature was a thin bare surface K-type thermocouple which is placed in a 1/4 inch ceramic tube with 1 mm wall thickness. The thermocouple tip always touches the ceramic wall for temperature monitoring. Since the ceramic tube sits in the 150 psi hydrogen and Hg vapor pressure, the thermocouple reaches the equilibrium quickly by convection of the Hg vapor and hydrogen gas rather than radiation heat transfer from the heater. Once the sample has been loaded into the quartz boat with the quartz cover placed on it, the ceramic tube is adjusted to the position of the sample. The thermocouple must be exactly in the same position every run. Equally importantly, the Hg weight and hydrogen over pressure must be constant each run to keep the thermal mass in the anneal tube the same.

A stop watch is started at the same time the furnace is turned on. From this point, the furnace temperature rises to the anneal temperature at 13 min from t = 0. At the end of the 13 min, the sample temperature is recorded. A typical temperature profile is shown in Fig. 1 for a target temperature set at 436°C. The sample temperature was held to within 0.5° of the

target. For rapid thermal annealing time of 60 s at a given equilibrium temperature, at t = 0 s from the start of lowering the sample, 5 s is needed to finish positioning the sample. After 60 s of annealing, another 5 s is needed to finish returning the sample to the starting temperature.

As Activation of As-doped MBE Alloy HgCdTe

Initial As activation measurements were performed on arsenic doped HgCdTe to determine the activation efficiency. These layers were grown at 160°C. The samples grown for As activation had alloy composition ranging from x = 0.26 to x = 0.30. The thickness of samples was typically about 4 μm. Secondary ion mass spectroscopy depth profile analysis in medium wavelength infrared (MWIR) HgCdTe (x = 0.268) layers for As concentration is shown in Fig. 2. The SIMS profile shows an arsenic concentration of 4.0 × 10^{18} cm^{-3} near the surface as shown in Fig. 2. The Hall carrier concentrations are shown as a line mark, with SIMS concentration measurements of As for the alloy HgCdTe shown for comparison. The Hall carrier concentration was measured after arsenic activation anneal at 436°C/10 min. The close agreement between the Hall measurements and SIMS average arsenic concentration indicates nearly 100% electri-

cal activity of the *in situ* arsenic in the HgCdTe layer after post-growth annealing. For the experiments of temperature and time dependence on the Hg annealing, the HgCdTe samples were annealed as a function of time at 436°C and as a function of temperature for 60 s by rapid thermal annealing. Both annealings were investigated under Hg and hydrogen overpressure to prevent surface degradation of HgCdTe epilayers. Typical Hall mobilities for these layers with concentration of 3.1 × 10^{16}–3.3 × 10^{18} cm^{-3} lie in the range of 8660–120 cm^2/V.s at 77K. Table I summarizes the electrical characteristics measured at 77K on these samples after high temperature Hg-anneal as a function of time and temperature.

The Hall carrier concentration vs annealing time for an *in situ* As-doped MWIR HgCdTe sample is shown in Fig. 3. This figure and Table I show that the n-type carrier concentration (as-grown MBE HgCdTe x = 0.268, n = 2.2e15 cm^{-3}, μ = 1,109 cm^2/V.s at 77K) initially increases sharply with increased anneal time

Table I. Time Dependence on Annealing Effects for a Given Temperature at 436° and Hall-Effect Data for *In Situ* As-Doped MWIR HgCdTe Alloy Layer

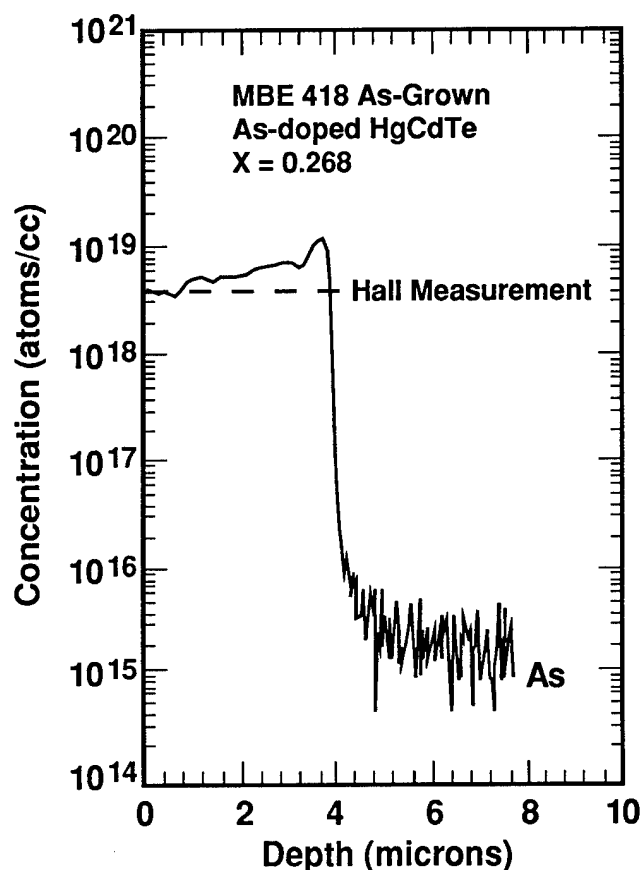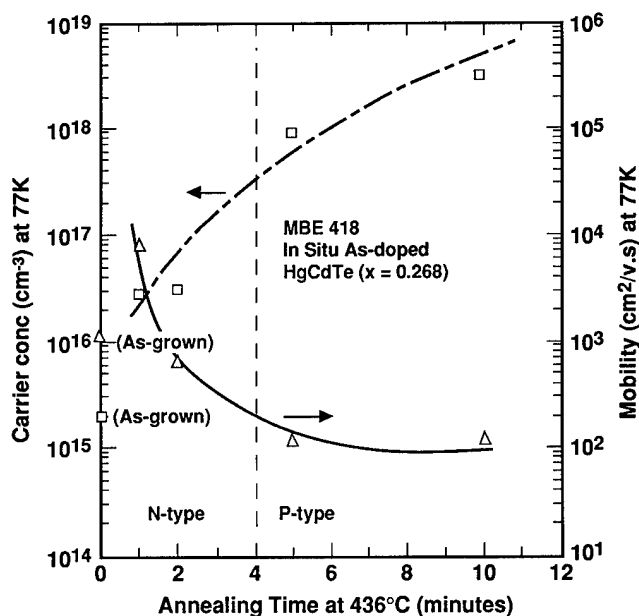| Anneal Condition (°C/min)	n/p	Resistivity (Ω-cm)	Conc. (cm^{-3})	Mobility (cm^2/V.s)	SIMS (cm^{-3})
As-Grown	n	2.56	2.2e15	1.10e3	4e18
436/1	n	0.023	3.1e16	8.66e3	
436/2	n	0.260	3.4e16	7.06e2	
436/5	p	0.051	9.7e17	1.25e2	
436/10	p	0.015	3.3e18	1.20e2	

Note: The HgCdTe epilayer is 4 μm thick.

Fig. 2. Secondary ion mass spectroscopy profile of arsenic concentration in an as-grown MWIR alloy HgCdTe layer. Arsenic concentration agrees closely with Hall carrier concentration after As activation anneal at 436°C for 10 min.
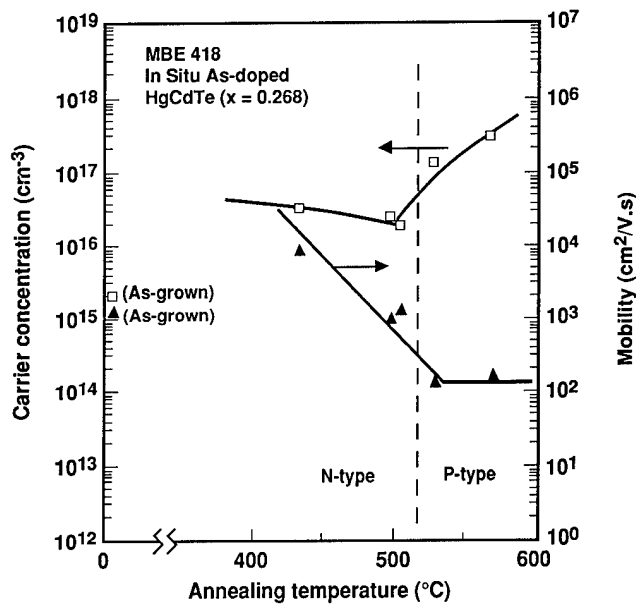

Fig. 3. Time dependence of arsenic activation at T = 436°C for an arsenic doped MBE HgCdTe layer with X = 0.268. Arsenic activation was carried out under saturated Hg partial pressure at 436°C for 1,2,5, and 10 min annealing, followed by low temperature Hg-anneal at 250°C for 20 h.

**Table II. Time Dependence on Annealing
Effects for 60 s Rapid Thermal Annealing and
Hall-Effect Data for *In Situ* As-Doped
MWIR HgCdTe Alloy Layer**

Anneal Cond. (°C)	Carrier Type (n/p)	Resistivity (Ω-cm)	Carrier Conc. (cm⁻³)	Mobility (cm² V.s)	SIMS (cm⁻³)
As-Grown	n	2.56	2.2e15	1.10e3	4.0e18
436	n	0.023	3.1e16	8.66e3	
500	n	0.274	2.4e16	9.57e2	
507	n	0.27	1.8e16	1.26e3	
530	p	0.37	1.3e17	1.32e2	
570	p	0.143	2.9e17	1.49e2	

Fig. 4. Temperature dependence of arsenic activation for an arsenic doped MBE HgCdTe layer with X = 0.268°C. Arsenic activation annealing was carried out for 60 s at 436, 500, 507, 530, and 570°C, followed by low temperature Hg-anneal at 250°C for 20 h.

for a given temperature of 436°C, and continues to increase until it converts to p-type due to arsenic activation after 436°C/5 min annealing. The time dependence of Hall carrier concentration indicates that hole carrier conduction overtakes the electron carrier conduction as the annealing time increases at 436°C. It ultimately converts to p-type. Meanwhile, the high electron mobility values decrease from 8.66×10^3 to 120 cm²/V.s, as the hole carrier dominates the transport property of the layer. For comparison purposes, the Hall carrier concentration vs temperature for rapid thermal annealing (Table II) of the same As-doped sample for 60 s is shown as well in Fig. 4. As the temperature increases from 436 to 570°C for a 60 s anneal, the n-type arsenic concentration decreases slightly to 507°C and then increases, but it did not convert to p-type completely. This suggests that Hg-annealing at 570°C for 60 s is not long enough to convert the 4 µm thick As-doped layer from n- to p-type.

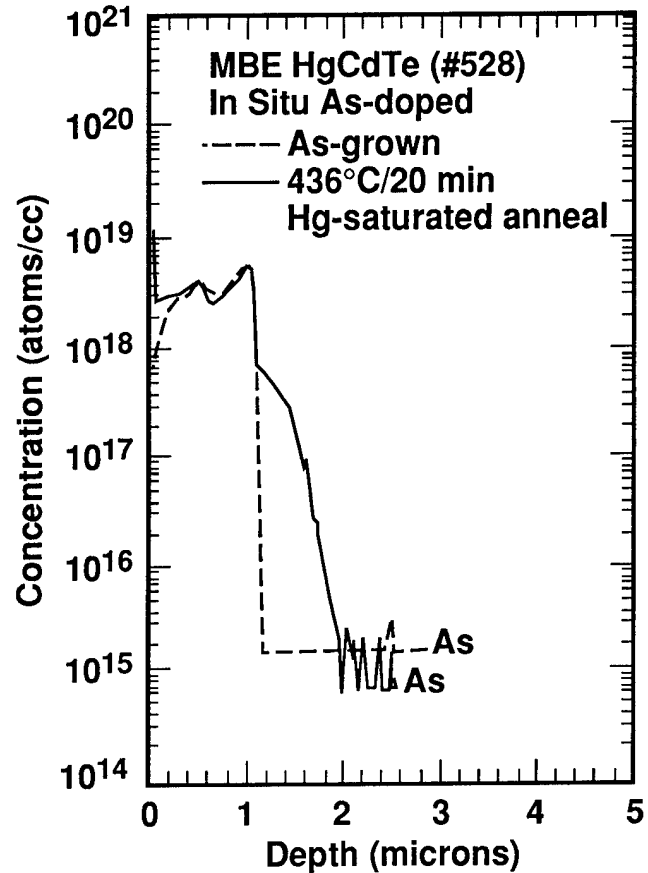The Hg penetration depth during the arsenic acti-

Fig. 5. Secondary ion mass spectroscopy depth profile for arsenic concentration of an *in situ* arsenic-doped cap layer and in the base layer for (a) arsenic in as-grown double layer (dotted line), and (b) arsenic after activation anneal (solid line).

vation anneal under high mercury partial pressure was calculated at 450°C, assuming that the Hg diffusion is the same in the As activation process as it is in the reported data of Zaitov[10] and Chen.[11] At 400°C and high mercury partial pressure, the Hg self-diffusion coefficient is reported in the range of 5×10^{-11}–7×10^{-10} cm²/s in undoped HgCdTe (x = 0.2) materials. At 450°C and high Hg partial pressure, the Hg self-diffusion constant is $D = 1.7 \times 10^{-10}$ cm⁻²/s in undoped HgCdTe (x = 0.2) materials and $D = 5.0 \times 10^{-10}$ when doped with indium.[10] Taking the expression for the penetration depth to be $L \sim (Dt)^{1/2}$ and the parameter $D_{Hg} = 5.0 \times 10^{-10}$ cm²/s, we calculated $L = 1.73 \times 10^{-4}$ cm for 1 min annealing at 450°C. This is in good agreement with the anneal time for arsenic activation as shown in Table I. The result of time dependent arsenic activation suggests that this activation is limited by Hg self-diffusion into the layer, which may be affected also by the impurity content. The diffusion time in the arsenic activation also indicates that at 450°C, 60 s arsenic activation should be long enough for the 1 µm capping layer for the DLHJ devices.

As Diffusion In Situ As-Doped DLHJ HgCdTe

In an experiment to investigate As diffusion during high temperature annealing, *in situ* grown As-doped double layer heterostructure layers were used. Sec-

ondary ion mass spectroscopy profiles of samples as-grown and after anneals at 436°C followed by 250°C low temperature annealing are shown in Fig. 5. In the *in situ* grown As-doped double layers, the epilayers show an acceptor peak level about 5×10^{18} cm^{-3} and a sharp drop to about 1.1 μm deep. After 436°C/20 min anneal for As activation, As diffused into the base layer to about 2.0 μm deep at the 2×10^{15} cm^{-3} In background level. Assuming a peak at 8×10^{17} cm^{-3} and erf As distribution, the diffusion coefficient of As into x = 0.22 HgCdTe at 436°C was estimated at 1.29×10^{-13} cm^2/s. This value is an experimental upper limit of the MBE HgCdTe epilayer since a few minutes of furnace rise time from 250°C of the annealing furnace were not included. After high temperature annealing at 436°C for 20 min, As diffused into the base layer about 0.8 μm deep; and a significant inter-diffusion occurs during annealing with the p/n junction located in the tail of the graded region, as shown in Fig. 5. Therefore, in the case of *in situ* grown DLHJ structure,[12] a p/n junction is formed in the graded region under optimum capping layer thickness and anneal temperature as discussed in the section on annealing effects on HgCdTe p$^+$-n junctions by arsenic implantation.

Enhanced Arsenic Diffusion

To understand the As diffusion and interdiffusion of heterostructures, we studied the effects of Hg partial pressures while keeping the HgCdTe wafer at

436°C. These samples were processed in a split-wafer experiment using the standard arsenic implantation with two different annealing procedures; one set of samples [Fig. 6(1)] was annealed at 436°C for 20 min in the standard saturated Hg pressure (~2 atm), followed by a 250°C anneal for 20 h.[4-6] The second set [Fig. 6(2) and Fig. 6(3)] of samples from the same wafers was subjected to a high temperature "enhanced diffusion" anneal consisting of 436°C for 10 min in lower Hg partial pressures (< 0.5 atm), followed by the standard low temperature annealing. The Hg partial pressure inside the anneal tube was estimated from the Hg-pressure vs temperature data. As shown in Fig. 6, the enhanced diffusion anneal,[13,14] which drives the arsenic deeper, takes advantage of the faster diffusion of arsenic dopants relative to Hg and Cd in HgCdTe under low Hg overpressure. The As profile was monitored in two sets of samples. The dopant profile for the unconventionally processed sample shows considerable dopant migration during 10 min of annealing, as compared to the dopant profile of the conventional anneal. In the case of the conventional process at 436°C/20 min anneal, the As profile appears to follow Fick's law, but deviations were observed for enhanced diffusion anneals under low Hg partial pressure. With decreasing Hg pressures, the As profiles show an additional rapid diffusion component, similar to shapes observed for Hg self-diffusion into HgCdTe at high temperatures.[11] At 436°C, for example, the diffusion coefficient increased
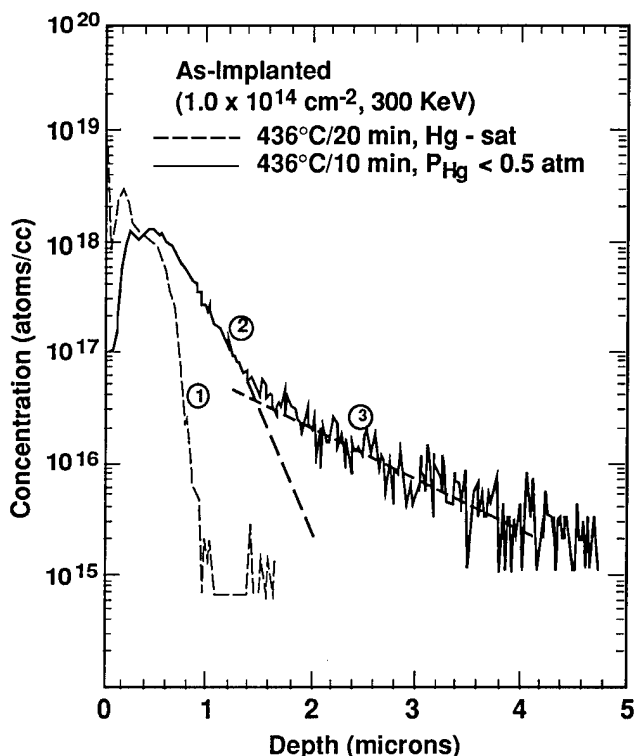

Fig. 6. Secondary ion mass spectroscopy profiles for arsenic concentration of an ion implanted as-doped HgCdTe for (1) arsenic after saturated Hg partial pressure anneal, and (2) and (3) arsenic after low Hg pressure anneal.
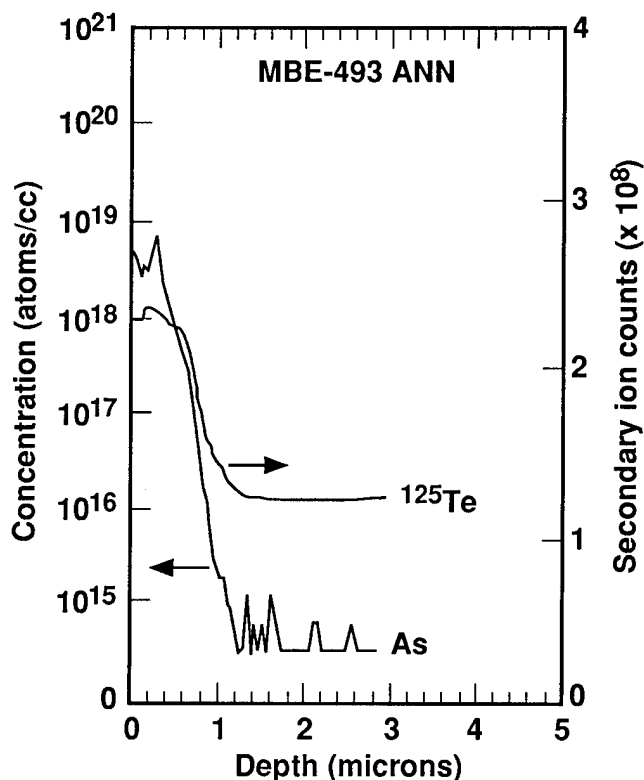

Fig. 7. Arsenic and ^{125}Te (Cd composition) SIMS profile for an MBE LWIR HgCdTe p-on-n HgCdTe device after arsenic activation anneal.
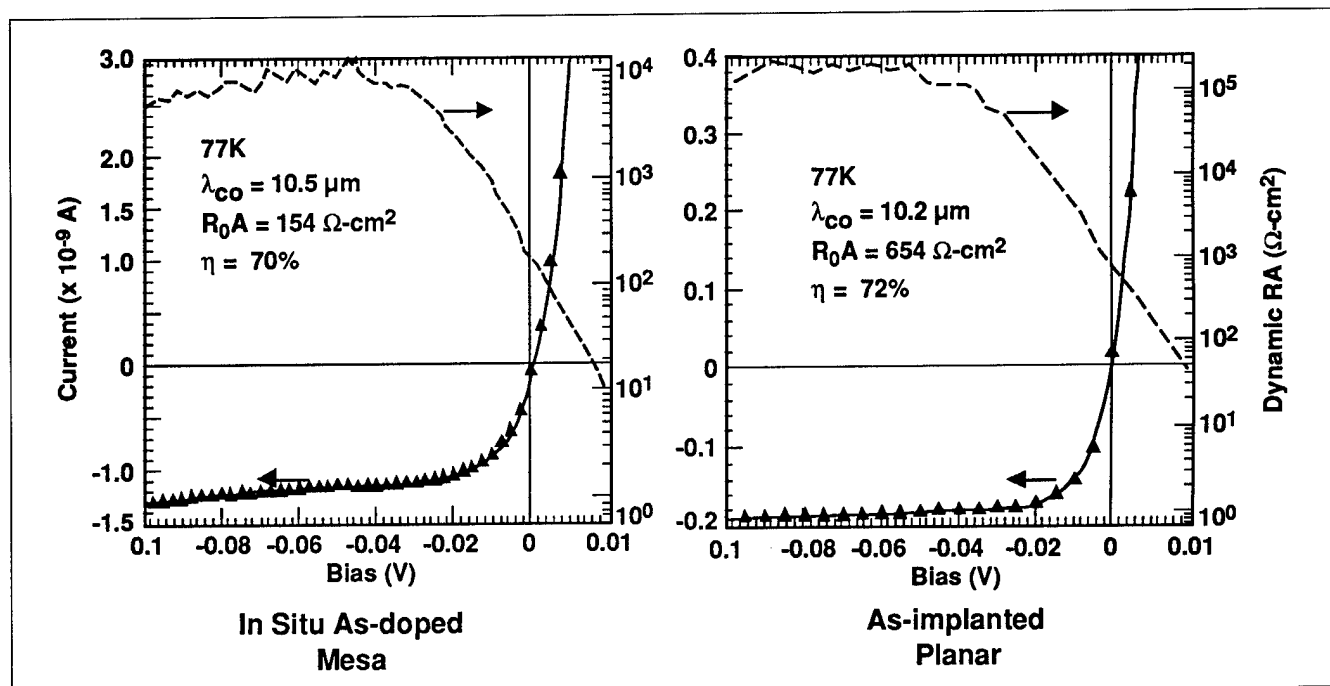
Fig. 8. Current-voltage characteristics of *in situ* as-doped and as-implanted LWIR HgCdTe photodiodes.

from a slow component, $D_1 = 2.1 \times 10^{-13}$ cm²/s for a saturated Hg pressure of 2 atm, to two diffusion coefficients; $D_1 = 1.7 \times 10^{-12}$ cm²/s and a fast component $D_2 = 1.35 \times 10^{-11}$ cm²/s, respectively, when the Hg pressure is decreased to < 0.5 atm. Both components are significantly influenced by the change in Hg pressure, with a more pronounced effect on the fast component, D_2. Since the Hg vacancy concentration is inversely proportional to the Hg partial pressure, the defects involved in the diffusion process could be Hg vacancies for the slow component, and other defects induced by high temperature annealing under low Hg-partial pressure for the fast component.

Annealing Effects On HgCdTe p⁺-n Junctions By Arsenic Implantation

Although the arsenic diffusion and *in situ* As-doping techniques have been used to fabricate high performance HgCdTe photovoltaic photodiodes, ion implantation also offers another advantage for the incorporation of dopants to fabricate planar p-on-n heterostructures. The experimental procedure used for As activation anneals was very similar to that of *in situ* As-doped layers. There is no difference in procedure, but the initial As position between *in situ* and ion-implanted As-doping can be quite different, resulting in either a homojunction or heterojunction. Figure 7 shows SIMS depth profiles for arsenic and [125]Te. The [125]Te profile has been proven to follow the HgCdTe alloy composition via matrix effects.[16] The [125]Te profile in Fig. 7 shows significant interdiffusion at the heterointerface after the first high temperature anneal step. The As diffusion profile implies a junction depth of about 1 μm based on a background indium concentration of 2×10^{15} cm⁻³.

The planar p⁺-n HgCdTe heterostructures, formed

by selective pocket diffusion of arsenic (As) deposited by ion implantation, show that they have high performance and that their dark currents are diffusion limited down to 52K.[4] This heterostructure requires good control over the junction location in addition to arsenic activation annealing in the range of 10^{17}–10^{18} cm⁻³. For diffusion limited diodes, the R_0A and quantum efficiency are directly related to the minority carrier diffusion length of the base n-type layer and the compositional grading, which is related to the cap layer composition (x), thickness, and arsenic doping levels. The ideal junction location is close to the center of the grading with optimal grading[14] of 0.3–0.8 μm width. Any lack of control of p/n junction formation will result in a barrier in the junction and poor quantum efficiency, in particular at low temperature below 77K.[15]

In Situ and Ion Implanted As-Doped MBE HgCdTe Photodiode

As materials growth and extrinsic n- and p-type doping techniques advance, of critical importance will be the properties of heterostructure interfaces and p/n junction locations. Therefore, the ultimate test of the materials is photodiode design and their performance. Both the *in situ* and ion-implanted p-on-n double layer heterostructure photodiodes fabricated with MBE HgCdTe using the annealing process described in this paper show well-behaved characteristics as shown in Fig. 8. The n-type base layer (x = 0.22) is 8–10 μm thick and doped with indium at the 2×10^{15} cm⁻³ level, while the wide bandgap capping layer (x ~ 0.28) is approximately 1 μm thick and undoped. Arsenic is either *in situ* doped during the growth or selectively implanted after double layer growth. The sample undergoes a 436°C anneal for 10 min under

saturated Hg partial pressure to activate the arsenic and a 250°C for 20 h anneal to annihilate Hg vacancies. Figure 8 shows current-voltage characteristics of typical *in situ* arsenic doped mesa and ion-implanted planar photodiodes at 77K for comparison, showing R_0A values of 154 and 654 ohm-cm^2 and cut-off wavelengths of 10.5 and 10.2 μm at 77K, respectively. The detailed analysis of the current-voltage characteristics of these diodes as a function of temperature shows that their dark currents are diffusion limited down to almost 50K.[4] Furthermore, these results show that the diode performance is affected by neither ion implantation damage nor arsenic diffusion sources after high temperature arsenic activation annealing.

CONCLUSION

In summary, we have investigated the arsenic activation of *in situ* As-doped single- and double-layer structures as a function of time and temperature. The time dependence of the As activation was determined from Hall measurements and shows an increase in the carrier concentrations, from $n = 2.2 \times 10^{15}$ cm^{-2} for as-grown n-type, $x = 0.268$ to $n = 3.4 \times 10^{16}$ cm^{-2} for 2 min anneal at 436°C; and to $p = 9.7 \times 10^{17}$ cm^{-2} for 436°C/5 min anneal; and then finally to $p = 3.3 \times 10^{18}$ for 10 min anneal at 436°C. The mobility, however, increases initially from 1.1×10^3 cm^2/V.s for as-grown n-type to 8.66×10^3 cm^2/V.s for n-type and drops to 120 cm^2/V.s for p-type. Diffusion calculations suggest that arsenic activation is limited by Hg self-diffusion for 4 μm thick HgCdTe epilayers. Enhanced arsenic diffusion for the DLHJ structures under Hg-deficient conditions also indicates that defect equilibrium strongly affects the As diffusion coefficient, resulting in deeper p/n junction as well as enhanced Cd out-diffusion near the surface.

We also found a dependence of diode characteristics on the annealing conditions of both *in situ* As-doped and As implanted HgCdTe DLHJ structures. We previously determined that the best diode characteristics with high R_0A and high quantum efficiency are obtained at 436°C/10 min, followed by low temperature anneal at 250°C for 20 h. However, sometimes the QE degraded as temperature decreased, particularly at 40K. This degradation may be due to Cd/Hg interdiffusion near the p/n junction location during the high temperature annealing.

REFERENCES

1. T. Tung, M.H. Kalisher, A.P. Stevens and P.E. Herning, *Mat. Res. Soc. Symp. Proc.* 90, 321 (1987).
2. L.O. Bubulac, S.J.C. Irvine, E.R. Gertner, J. Bajaj, W.P. Lin and R. Zucca, *Semicond. Sci. Technol.* 8, S270 (1993).
3. O.K. Wu, G.S. Kamath, W.A. Radford, P.R. Bratt and E.A. Pattern, *J. Vac. Sci. Technol. A* 8, 1034 (1990).
4. J.M. Arias, J.G. Pasko, M. Zandian, S.H. Shin, G.M. Williams, L.O. Bubulac, R.E. DeWames and W.E. Tennant, *Appl. Phys. Lett.* 62, 976 (1993).
5. J.P. Faurie, M. Boukerche, J. Reno, S. Sivananthan and C. Hsu, *J. Vac. Sci. Technol.* A3, 55 (1985).
6. S.H. Shin, J.M. Arias, M. Zandian, J.G. Pasko and R.E. DeWames, *J. Electron. Mater.* 22 (8), 1029 (1993).
7. A.C. Warren, J.M. Woodwall, J.L. Freeouf, D. Grischkowsky, D.T. McInturf, M.R. Mellock and N. Otsukam, *Appl. Phys, Lett.* 57 (13) 1331 (1990).
8. H.G. Vydyanath, R.C. Abbot and D.A. Nelson, *J. Appl. Phys,* 54, 1323 (1983).
9. J.M. Arias, S.H. Shin, J.G. Pasko, R.E. DeWames and E.R. Gertner, *J. Appl. Phys.* 65, 1747 (1989).
10. F.A. Zaitov, A.V. Gorshkov and G.M. Shalyapina, *Sov. Phys. Solid State,* 20, 927 (1978).
11. J.S. Chen, PhD Dissertation, University of Southern California (1985).
12. J. Arias, M. Zandian, J. Pasko, S.H. Shin, W. McLevige and R. DeWames, IRIS Specialty Group on Infrared Materials and Devices, NASA-Ames, CA, August 1992.
13. L.O. Bubulac, D.D. Edwall and C.R. Viswanathan, *J. Vac. Sci. Technol. B* 9, 1695 (1991).
14. D. Chandra, M.W. Goodwin, M.C. Chen and J.A. Dodge, Proc. 1992 MCT Workshop, to be published in the *J. Electron. Mater.* 22 (8) (1993).
15. K. Kosai and W.A. Radford, *J. Vac. Sci. Technol. A* 8, 1254 (1990).
16. L.O. Bubulac and C.R. Viswanathan, *Appl. Phys. Lett.* 60, 222 (1992).

P-Type Doping of Double Layer Mercury Cadmium Telluride for Junction Formation

L.O. BUBULAC, D.D. EDWALL, S.J.C. IRVINE, E.R. GERTNER, and
S.H. SHIN

Rockwell International Science Center, 1049 Camino Dos Rios, Thousand
Oaks, CA 91360

Extrinsic p-type doping of long wavelength infrared-HgCdTe double layer heterostructure for p-on-n device application requires good control of the p-type dopant, regardless of the doping technique. The approach is to place the electrical junction ahead of the compositional interface, thus avoiding quantum efficiency reduction. This research addresses the As and P doping of HgCdTe by an implant/diffusion process. The data demonstrates an enhanced atomic diffusion process for As and P from an ion implanted source, within the single phase domain, with a diffusion rate orders of magnitude higher than the rate under Hg-saturated conditions at the same temperature. This work also reveals a new phenomenon, namely, a transition in the enhanced diffusion of both As and P from an exponential to a Gaussian redistribution. This transition is controlled by temperature at a given P_{Hg}. Gaussian diffusion dominates at high temperatures, $T > 400°C$. The diffusion coefficient of the Gaussian mechanism decreases as the P_{Hg} increases, from $D_P \sim 2 \times 10^{-11}$ cm²/s at $P_{Hg} \sim 0.02$ atm to $D_P \sim 3 \times 10^{-14}$ cm²/s under Hg-saturated conditions (quartz ampoule) at 440°C. The difference in the diffusion coefficients between open tube and closed tube (quartz ampoule), under nominally Hg-saturated conditions, indicates that P_{Hg} is undersaturated regardless of the Hg-source proximity. The deviation of P_{Hg} from saturation is estimated from the annealing furnace temperature profile up to a maximum of 50%. Variation of the diffusion coefficient close to Hg saturation appears to be sharply dependent on the actual P_{Hg} value (example: $D_P \sim 1 \times 10^{-12}$ cm²/s in open-tube anneal vs $D_P \sim 3 \times 10^{-14}$ cm²/s in closed tube at nominally the same temperature, $T = 440°C$). Comparative anneals of As and P showed faster diffusion rates for P than for As in both mechanisms.

Key words: Annealing, diffusion, HgCdTe

INTRODUCTION

Extrinsic p-type doping of long wavelength HgCdTe has received a wide interest for double layer heterostructure p-on-n device applications.[1-4] This structure requires an electrical junction located deeper than the compositional junction to avoid the formation of any valence band barriers to the transport of the photogenerated minority carriers across the junction. This implies, besides a stable interface, a controlled behavior of p-type dopants in any thermal treatment following their introduction into the layer. One way to p-type dope HgCdTe is to diffuse As or P from an ion implanted source. Diffusion by a conventional technique (closed tube, Hg-saturated, $T > 400°C$) would require long anneal times, which cannot be used because the interdiffusion in the heterointerface is faster than the dopant diffusion. The range of Cd-Hg interdiffusion coefficients across the pseudobinary at 400°C are 2×10^{-12} cm²/s to 5×10^{-15} cm²/s[5] while the diffusion coefficients for As[6-8] and P,[9] are in the low 10^{-14} cm²/s range. On the other hand, the advantage of a heterostructure in decreasing leakage currents may be diminished if the compositional difference between the cap layer and the absorber layer is very small. An enhanced diffusion process can be applied to form p/n planar junctions, with the purpose of consistently locating the electrical junction beyond the graded
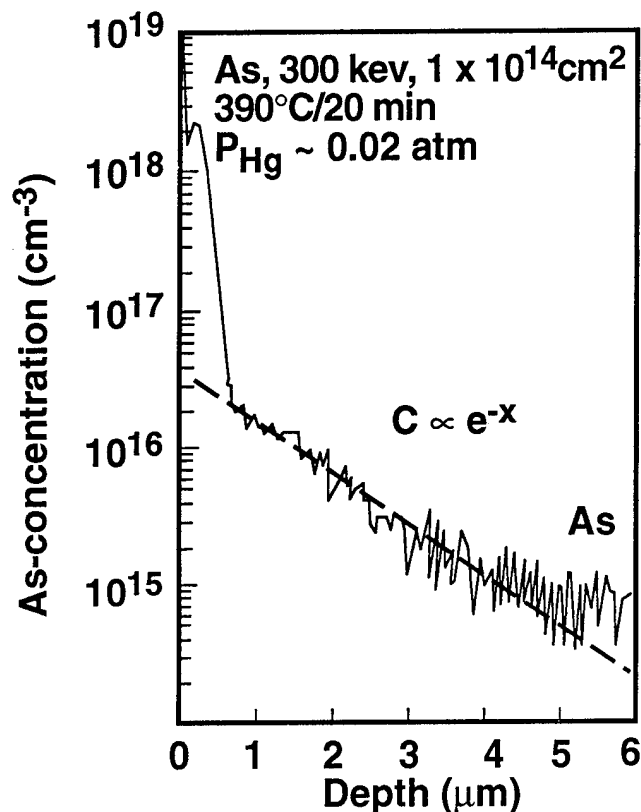
a
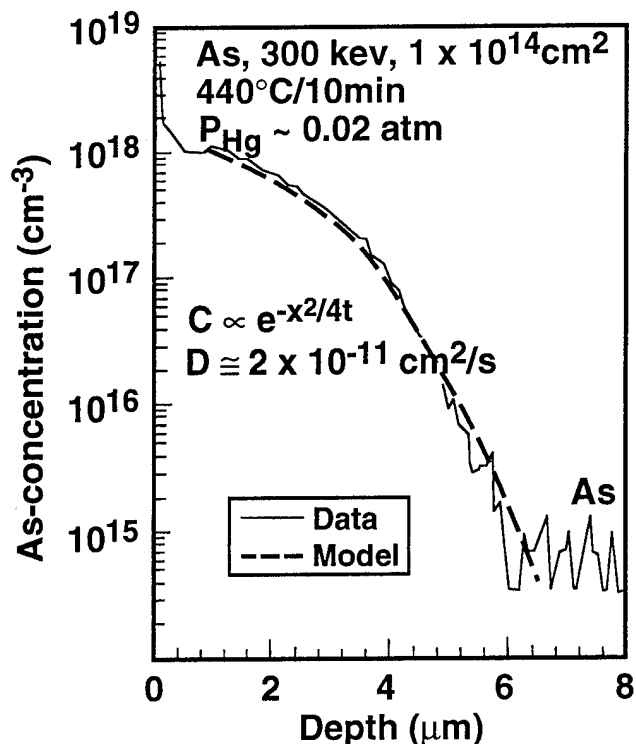
b

Fig. 1. As-redistribution (SIMS) in post-implant anneal in open-tube (MOCVD-reactor) at P_{Hg} ~0.02 atm (within the existence domain but close to Te-phase boundary) for MOCVD, double layer HgCdTe: (a) at 390°C for 20 min, and (b) at 440°C for 10 min.

region of the heterointerface. Fast As diffusion by an atomically enhanced mechanism, from an ion implanted source[2,7] as well as a grown sourc,[2,4] has been demonstrated.

This paper addresses the p-type doping of HgCdTe, in conjunction with p-on-n junction formation, by an implant/anneal process of As and P.[7,8,10] The objectives of this work are as follows:

- To control the p-type doping concentration for junction formation, by first identifying the different diffusion mechanisms that may occur. The material and fabrication parameters could be chosen to minimize or suppress the undesirable components and develop a reproducible diffusion process.
- To develop a junction formation method by which the electrical junction in a double layer HgCdTe structure would be consistently located beyond the graded region of the heterointerface.

EXPERIMENT

The material used for the initial experiments was a long wavelength infrared (LWIR) HgCdTe double layer structure, with an middle wavelength infrared (MWIR) cap layer, grown by metalorganic chemical vapor deposiont (MOCVD).[11] The initial anneals were also performed in the MOCVD reactor. The confirmation of the initial results and further supporting evidence were obtained using LWIR liquid phase epitaxy (LPE) single layer material grown from the Te-rich corner of the phase diagram.[12] The source for doping with As and P was ion implantation. The post implant annealing was performed in an open tube setup, in a modified LPE growth furnace with a high pressure of H_2, ~10 atm.[13] We chose the open tube annealing technique because it is more production-oriented. The anneal conditions were chosen within the single phase domain of the phase diagram. For reference, we used the conventional anneal in a closed tube (quartz ampoule). The P_{Hg} was estimated from P-T tables. The main analytical techniques employed were secondary ion mass spectrometry (SIMS)[14,15] for As and P concentration profiles and the electron beam induced current (EBIC) technique for junction depth determination. Whenever indicated, the value of the diffusion coefficient, D, refers only to the Gaussian component, and it was determined from a theoretical fit to the Gaussian model down to very low concentrations, ~10^{14}/cm^3.

As AND P DIFFUSION

P_{Hg} Close to Te-Phase Boundary

Annealing of As-ion implanted samples under a low partial pressure of Hg (P_{Hg} ~0.02 atm) with one atmosphere pressure of H_2, in an MOCVD reactor, has been shown[2] to yield an enhanced diffusion of As compared with the anneal in a saturated Hg overpressure in a closed tube (quartz ampoule) at the same temperature. The material on which this effect was observed was LWIR-MCT (double layer structure)

grown by MOCVD. Diffusion data up to 350°C has been published.[2]

This paper extends the experiments on As diffusion in undersaturated Hg pressure by using higher sample

temperatures, 400 and 440°C, and within experimental error, the same partial pressure of Hg; P_{Hg} ~0.02 atm. The material and the annealing technique were the same. Secondary ion mass spectrometry results on As redistribution are presented in Fig. 1a for 390°C
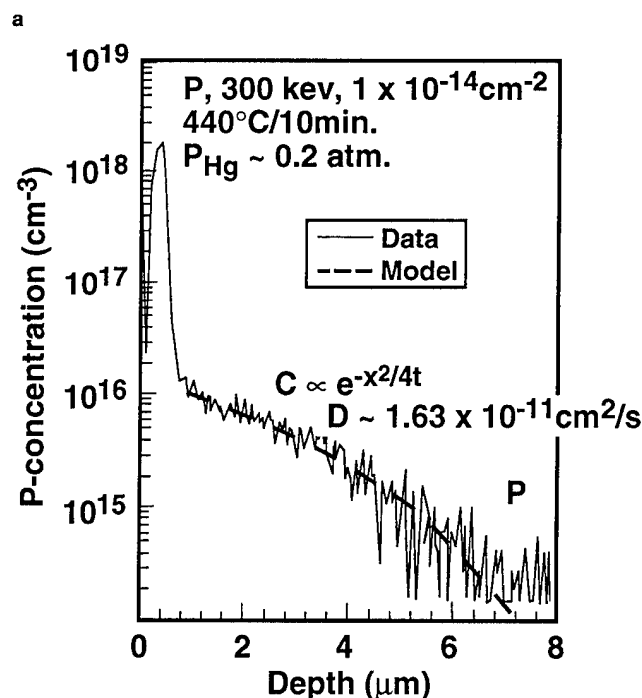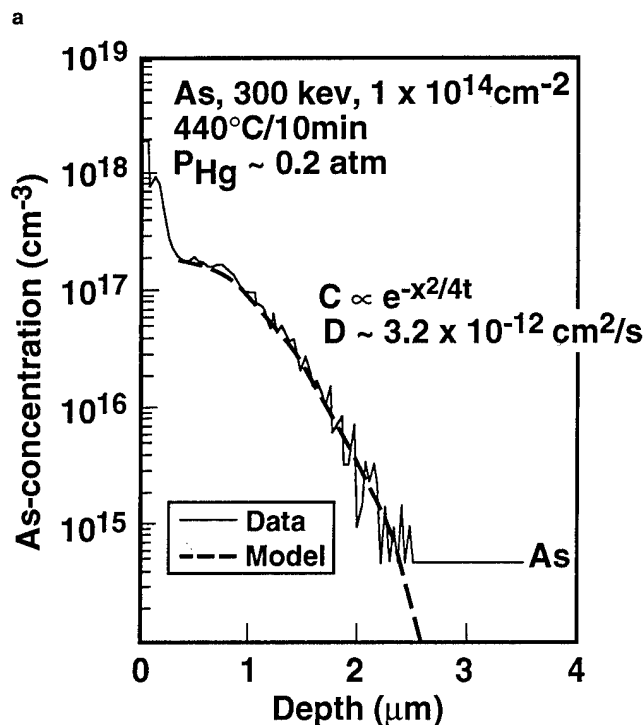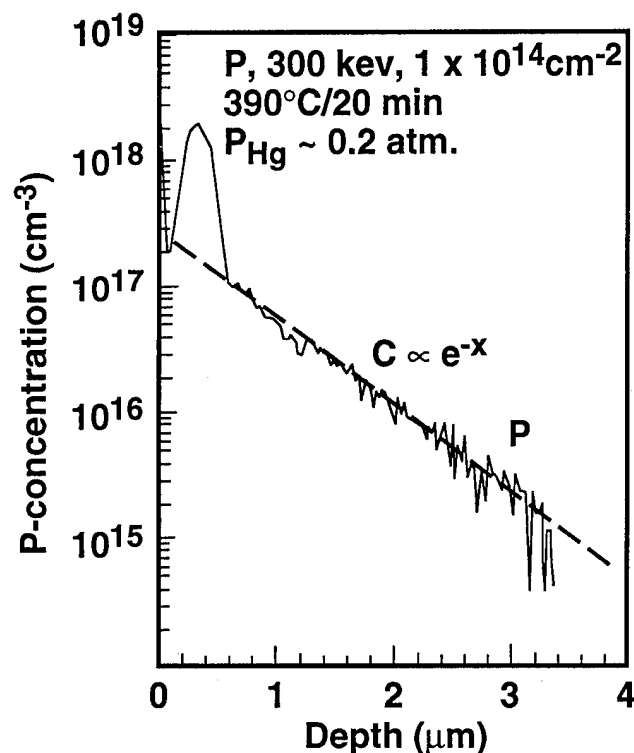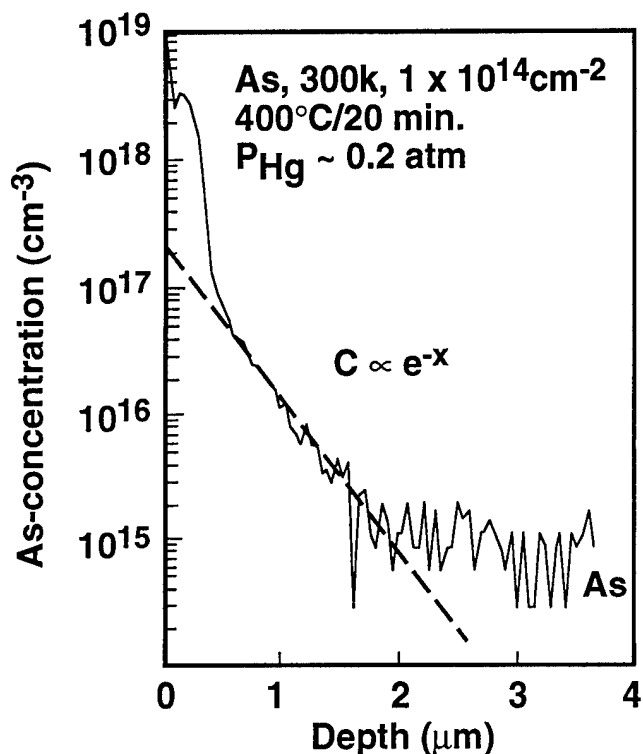

a

b

Fig. 2. As-redistribution (SIMS) in post-implant anneal in open-tube (MOCVD-reactor) at P_{Hg} ~0.2 atm (within the existence domain) for LPE, single layer HgCdTe: (a) at 400°C for 20 min, and (b) at 440°C for 10 min.

a

b

Fig. 3. P-redistribution (SIMS) in post-implant anneal in open-tube (MOCVD-reactor) at P_{Hg} ~0.2 atm (within the existence domain) for LPE, single layer HgCdTe: (a) at 390°C for 20 min. and (b) at 440°C for 10 min.

P, 50KeV, 1x10^{14} cm^{-2}
435°C/2.25 hrs
P$_{Hg}$ ~ 3 atm.

$C \propto e^{-x^2/4t}$
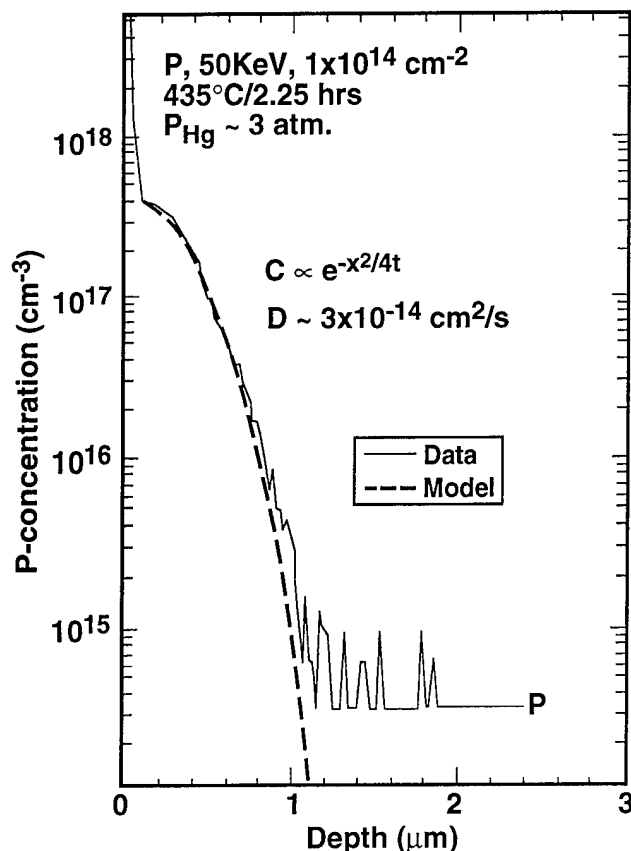
$D \sim 3 \times 10^{-14}$ cm^2/s

Data
Model

P

Fig. 4. P-redistribution (SIMS) in conventional anneal (closed tube; quartz ampoule) at saturated Hg-overpressure, (on Hg-phase boundary, P$_{Hg}$ ~3 atm) at 435°C for 2.25 h for LPE-single layer HgCdTe.

P, 300 KeV, 1x10^{14} cm^{-2}
440°C/2.25 hrs
P$_{Hg}$ ~ 3 atm.

$C \propto e^{-x^2/4t}$

$D \sim 3.7 \times 10^{-13}$ cm^2/s

Data
Model

n = 5 x 10^{14} cm^{-3} (Hall)

P

X$_j$ EBIC

Fig. 5. P-redistribution (SIMS) in open tube anneal (modified LPE furnace) at P$_{Hg}$ ~3 atm (close to Hg-phase boundary—sample placed as close to Hg source as possible) and 440°C for 2.25 h.

anneal and Fig. 1b for 440°C anneal. Although the diffusion at these elevated temperatures increased with temperature, the change in the type of diffusion was unexpected. The mechanism of the atomic enhanced diffusion switches from an exponential dependence of the concentration vs depth (C $\propto$ e^{-x}) to a Gaussian redistribution (C $\propto$ e$^{-x^2/4t}$). This result was confirmed on other samples with the same structure from a different wafer. The transition from exponential to Gaussian behavior was determined by temperature. Gaussian atomic diffusion appeared to predominate at high temperatures, T >400°C.

To avoid the potential complications of the double layer structure, such as a change in band gap, defects in the heterointerface, and high content of dislocations (etch pit density, EPD ~ low 10^7/cm^2), the diffusion behavior was investigated using low dislocation density (10^5 cm^2) LPE single layers. The experiments of Fig. 1 were repeated with P$_{Hg}$ approximately one order of magnitude higher, but still below the Hg rich phase boundary, ~0.2 atm., on LPE single layers using two different dopants, As and P. Both dopants were introduced in the layer via ion implantation at a fluence of 1 × 10^{14}/cm^2 with an energy of 300 KeV. Secondary ion mass spectrometry redistribution profiles for both As and P obtained at 400 and 440°C are shown in Fig. 2 and Fig. 3, respectively. These data confirm the previous results regardless of the differ-
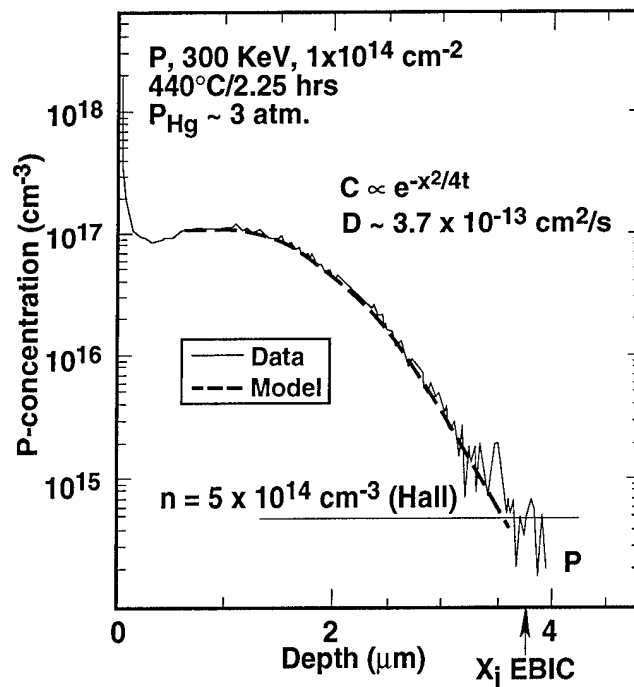
ence in the growth technique, the structural defect density of the material, and the implanted species. A transition in the diffusion mechanism occurs which is controlled by temperature. The exponential atomic diffusion predominates at 400°C and Gaussian atomic diffusion appears to predominate, or perhaps is initiated at high temperature, T >400°C

P$_{Hg}$ Close to Hg-Phase Boundary

Annealing at elevated PHg, close to the Hg-phase boundary was explored in parallel for As and P in an open tube apparatus.

Closed-Tube Anneal

For comparison to our open tube method, we have determined the P-diffusion coefficient using a conventional closed-tube anneal in saturated Hg vapor. Figure 4 shows results of P annealed in a quartz ampoule. The implant was performed at 50 KeV with a fluence of 1 × 10^{14}/cm^2. The post-implant anneal was performed at 435°C and the annealing time was long, 2.25 h, to minimize the initial effects of damage on the redistribution of the implanted species. Secondary ion mass spectrometry profiling showed Gaussian redistribution with a diffusion coefficient of D$_P$ = 3 × 10^{-14}/cm^2/s or less. These profiles, as expected, are similar to the profiles obtained previously for As, fitting well with the published data for the volume diffusion coefficient.[7]

Open-Tube Anneal

The closest condition to Hg-saturation in the open tube apparatus was with an anneal identical in temperature and time to that used for the closed tube

experiment (440°C, 2.25 h) but with the sample placed as close to the Hg source as possible. This aimed to obtain near saturated Hg vapor conditions in the open tube. The estimated P_{Hg} was ~3 atm. The SIMS results on P-concentration and compositional profiles are shown in Fig. 5 for an implant with 300KeV, and fluence of $1 \times 10^{14}/cm^2$.

The effect of the different implant energy from the closed tube experiment (Fig. 4) is negligible due to the long-term anneal. These data show a significant redistribution of P by a classical Gaussian mechanism, with a diffusion coefficient about an order of magnitude higher than the corresponding closed tube anneal, i.e., D ~3.7×10^{-13} cm²/s vs 3×10^{-14} cm²/s. There is a striking similarity of P-redistribution during this anneal with the previous Gaussian enhanced diffusion obtained at low P_{Hg} but at the same temperature (T > 400°C). This suggests that the P_{Hg} conditions are undersaturated regardless of the proximity of the Hg source, causing an enhanced Gaussian diffusion to occur. This also suggests that at very small variations of P_{Hg}, in the proximity of the saturation (closed tube vs open tube), the diffusion coefficient varies sharply with the actual value of P_{Hg}. The electrical activity of P in this anneal was determined to be p-type by using the EBIC technique through junction depth determination. The electrical junction was located, within experimental errors, where Hall-determined n-type background equaled the P-SIMS concentration profile, suggesting a high activation efficiency, ~100%.

We then compared As and P at different anneal conditions. To avoid variations in P_{Hg} from run to run, two samples were implanted under similar conditions (50 KeV and $10^{14}/cm^2$), one with As and another one with P and were annealed in the same open tube. P_{Hg} and anneal temperature were about the same as in the experiment shown in Fig. 5 (P_{Hg} ~3 atm, 430°C), but the annealing time was shorter, 10 min.

Secondary ion mass spectrometry data for the As and P redistribution are shown in Fig. 6a and Fig. 6b, respectively. No noticeable redistribution of As was observed (Fig. 6a), except for the initial fast redistribution in a shallow region due to the initially unannealed implant damage (which for As are heavier than for P). The As profile appears sharp at a depth of 0.8 µm. However, P showed a Gaussian redistribution with a diffusion coefficient of 1×10^{-12} cm²/s, confirming, within the experimental error, the previous result from Fig. 5. From this experiment, P appears to be a faster diffusant than As at high temperature (~430°C) and high (but not saturated) P_{Hg}.

Other experiments were performed at temperatures equal or less than 400°C and at lower P_{Hg}, to investigate the comparison of As and P in the atomic exponential regime. Results for As and P from anneals in low P_{Hg}, (~0.2 atm) and at 390°C for 10 min are shown in Fig. 7. Both As and P exhibit exponential extended components, and the diffusion rate for P was higher than for As. These results show that for the exponential enhanced diffusion, P is also faster than
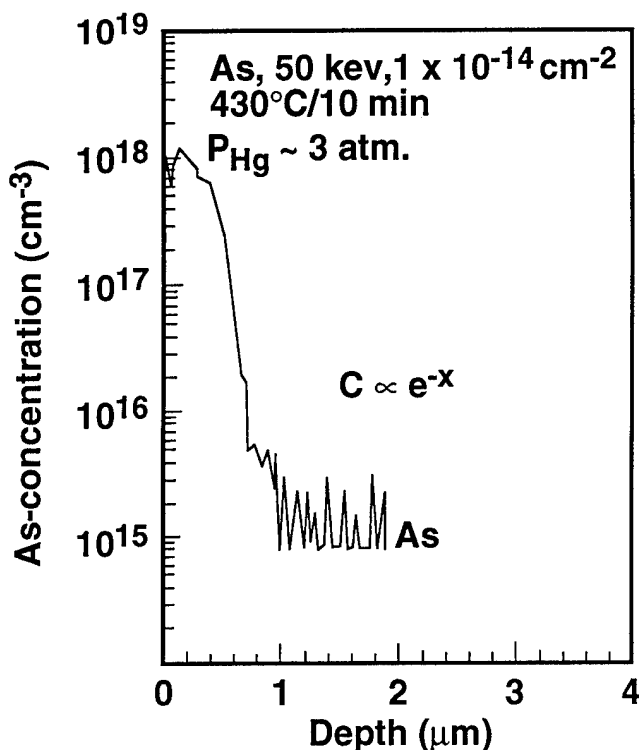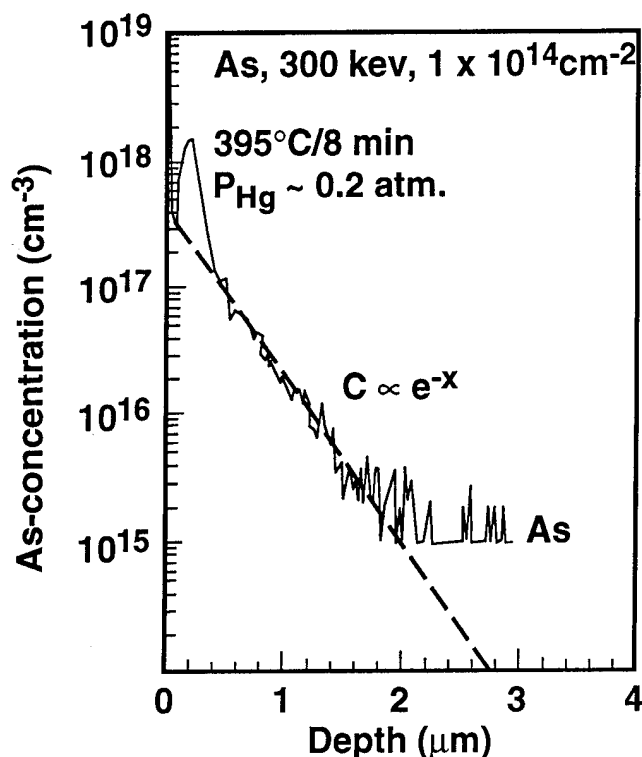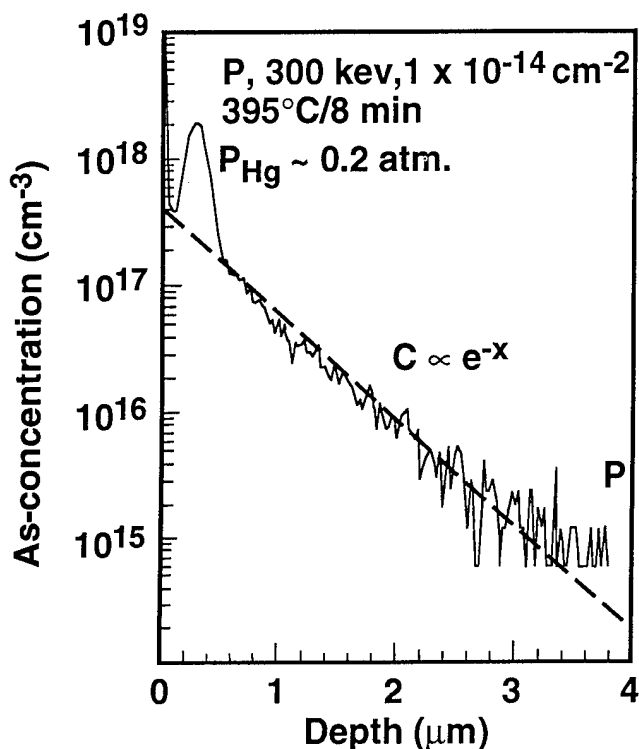

a
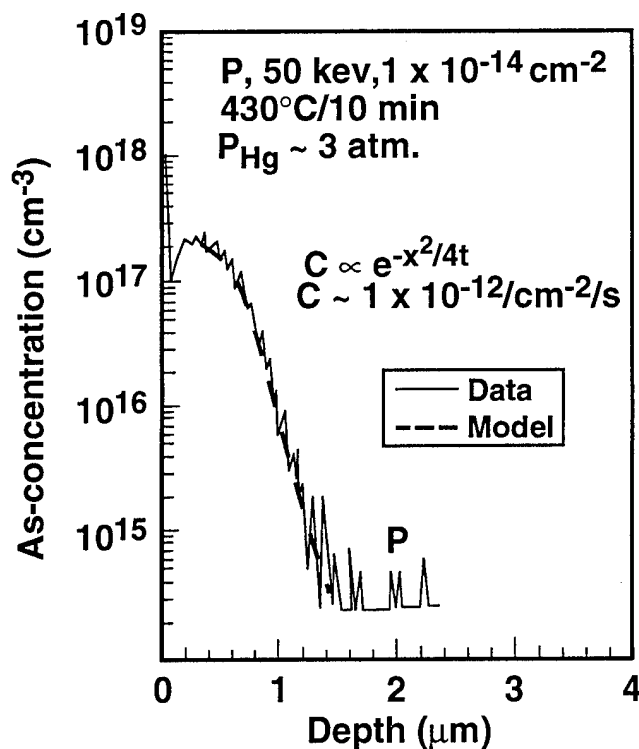
b

Fig. 6. Comparative redistribution profiles for As and P (SIMS) in open tube anneal at P_{Hg} ~3.0 atm (close to Hg-phase boundary—sample placed as close to Hg source as possible) and 430°C for 10 min: (a) for As, and (b) for P.

As; the diffusion depth (defined conventionally at a concentration of $1 \times 10^{15}/cm^3$) for P was ~3.5 vs ~2.0 μm for As.

a

b

Fig. 7. Comparative redistribution profiles for As and P (SIMS) in open tube anneal at ~0.2 atm and 395°C for 8 min: (a) for As, and (b) for P.

APPLICATION OF ENHANCED DIFFUSION TO JUNCTION FORMATION

The investigation of As and P behavior in a post-implant anneal reveals two kinds of methods that can be developed to place the p-on-n junctions deep into the layer, based on ion implantation and annealing in an open tube setup. Thus, each individual mechanism, exponential or Gaussian, or both in combination, can be used to obtain a desired profile compatible with the device double layer architecture and processing. An example is given in Fig. 8 for P-ion implanted in a single layer of LPE-grown MCT. The electrical junction is located on the SIMS redistribution profile (within experimental error) as determined by EBIC measurements. A significant observation is that in the experiment from Fig. 8, the initial uniform composition (single layer) is not changed (i.e., no significant Hg loss). (The material composition profile was determined by the Te-SIMS profiling technique developed in Ref. 10.) The surface decrease in Te^{125}-SIMS is shallow enough (<1000Å) to be explained by a SIMS surface effect. A low temperature Hg-vacancy anneal is performed at the end to reveal the n-type background and thus to form the extrinsic doped p-on-n junction.

DISCUSSION

The presented data demonstrate an enhanced atomic diffusion process for As and P in post-implant anneals in Hg-undersaturated conditions within the single phase solidus.

A transition in the atomic enhanced mechanism from exponential to Gaussian, within the single phase region, is revealed for both As and P. The transition appears to be controlled by temperature at any given P_{Hg}. The exponential atomic mechanism appears to predominate at T <400°C. The diffusion rate appears to be higher as the temperature increases. At T >400°C a transition is revealed in the diffusion mechanism, and the Gaussian redistribution profile predominates. The diffusion coefficient appears to decrease as the P_{Hg} increases; an example shows variations at ~440°C from D = 2×10^{-11} cm²/s at P_{Hg} ~0.02 atm to D = 3×10^{-14} cm²/s at Hg saturated conditions (conventional closed tube anneal, on the Hg-phase boundary). D should also increase with temperature at a given P_{Hg}, as suggested by the data from the saturated anneals.[7]

The nominally saturated open tube conditions for P_{Hg} are in fact undersaturated regardless of the proximity of the sample to the mercury source; thus D in the Gaussian diffusion obtained in the open tube anneal, with the sample as close as possible to the Hg source (Fig. 5), is more than one order of magnitude higher than D in the conventional saturated closed tube anneal (Fig. 4); D ~5×10^{-13} cm²/s vs D ~3×10^{-14} cm²/s.

The large difference in the diffusion coefficient of the two experiments, closed tube (Fig. 4) and open tube (Fig. 5), run in nominally similar conditions of

temperature and time, suggests that the diffusion coefficient of the Gaussian component decreases sharply as the P_{Hg} approaches the Hg-phase boundary. This implies that the associated p-type electrical activation may increase sharply, depending on site occupancy.

The experiments run on samples with various EPD (Fig. 1 and Fig. 2) show that the behavior of both components is independent of EPD for two orders of magnitude difference (from low 10^5 to low $10^7/cm^2$).

The number of atoms under the Gaussian enhanced profile in Fig. 1b (integrated dose is 1.3×10^{14} cm^{-2}) is close, within experimental error, to the number of implanted atoms (1×10^{14} cm^{-2}). This data suggests that implanted atoms undergo a site transfer under low P_{Hg} and that all the implanted atoms participate in enhanced Gaussian diffusion.

The electrical activation of p-type dopants appears to be dependent on the partial pressure of Hg. At one extreme of P_{Hg}, close to the Te-phase boundary (P_{Hg} ~0.02 atm), and at a low diffusion temperature, ~350°C, the electrical activation of p-type dopants in the predominant exponential redistribution is undetectable.[2] Therefore, the exponential component requires electrical activation to p-type by a separate site transfer, which is observed at T >415°C.[10] At the other extreme of P_{Hg} close to the Hg-phase boundary (high P_{Hg} but still undersaturated, ~3 atm) and at a high temperature, 430–450°C, the activation temperature of P in the predominant Gaussian redistribution appeared to be the same, within experimental error, as the diffusion temperature. The activation efficiency is ~100% at saturation conditions as observed at 440°C in the open tube anneal (Fig. 5) and at 400°C and at 450°C in closed tube.[10] Given the dependence of the activation efficiency on the P_{Hg} of column V elements[16] (higher as the Hg-overpressure approaches the Hg-phase boundary) the activation efficiency should be highest precisely on the phase boundary, and it should decrease as P_{Hg} decreases. The data imply that at slightly undersaturated conditions electrical activity may vary as much as the diffusion coefficient varies. Further work is needed to elucidate this point.

From the comparative anneals of As and P, P appears to have a faster diffusion rate in both exponential and Gaussian enhanced diffusion mechanisms.

Lack of stringent control of partial pressure of Hg (P_{Hg}) at any step in the annealing procedure may cause a great variance in the redistribution profiles of p-type dopants, regardless of the material defect structure.

As a consequence of this study, two atomic enhanced mechanisms can be used, individually or in combination, to diffuse As and P from an ion implanted source for p-on-n device applications. The choice of either mechanism for junction formation should depend on the device architecture. The final choice should be based on the device performance.

SUMMARY

We have revealed the existence of a transition in the atomic enhanced mechanism from exponential to Gaussian within the single phase region. The transition of the mechanism from exponential to Gaussian is controlled by temperature at any given P_{Hg}, T >400°C. The diffusion coefficient, D, of the Gaussian mechanism appears to be sharply dependent on P_{Hg} close to Hg-phase boundary (D_p~1×10^{-12} cm^2/s in open tube and D_p~3×10^{-14} cm^2/s in closed tube at nominally similar conditions of temperature and time, 440°C and 10 min). The electrical activation of As and P, ~100% at saturation, may also vary significantly with P_{Hg} close to the Hg-phase boundary. The P diffusion mechanisms appear to be faster than As in any atomic enhanced mechanism.

The transition process in the diffusion mechanism and the high sensitivity of the diffusion coefficient of the Gaussian component on P_{Hg} in the proximity of saturation can provide an explanation for the wide range of results for the dopant redistribution from any source. It is important to identify these phenomena in order to be able to control the atomic diffusion, and by that to control the device performance.
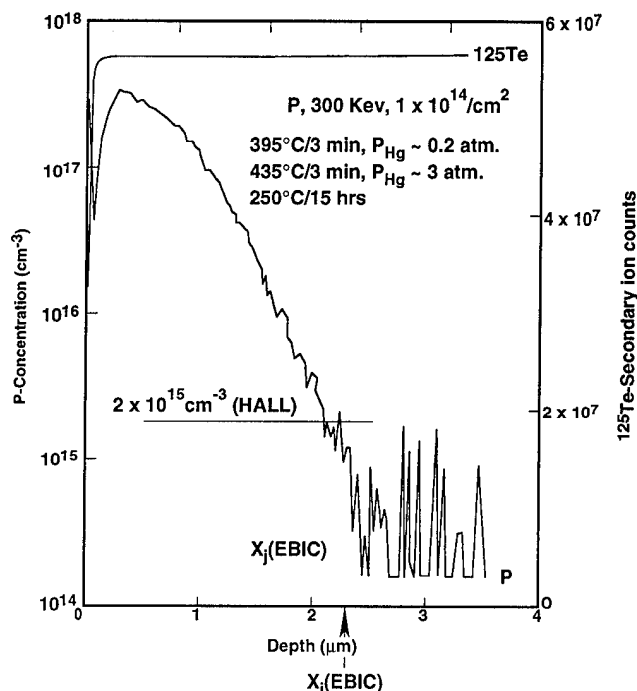
ACKNOWLEDGMENT

Fig. 8. P-redistribution profile (SIMS) in a combined atomic enhanced diffusion together with compositional profile (SIMS- [125]Te) and EBIC - determined junction depth: anneal at 385°C/3 min and ~0.2 atm, followed by an anneal at 435°C/6 min and ~3 atm and followed by an anneal at 250°C/15 h.

REFERENCES

1. T. Tung, M.H. Kalisher, A.P. Stevens and P.E. Herning, *Mat. Res. Soc. Symp. Proc.* 90, 321 (1987).
2. L.O. Bubulac, S.J.C. Irvine, E.R. Gertner, J. Bajaj, W.P. Lin and R. Zucca, *Semicond. Sci. Technol.* 8, S270 (1993).
3. J.M. Arias, J.G. Pasko, M. Zandian, S.H. Shin, G.M. Williams, L.O. Bubulac, R.E. DeWames and W.E. Tennant, *Appl. Phys. Lett.* 62, 976 (1993).
4. D. Chandra, M.W. Goodwin, M.C. Chen and J.A. Dodge, Proc. of the 1992 MCT Workshop, *J. Electron. Mater.* (8) (1993).
5. Mei-Fan S. Tang and David A. Stevenson, *Appl. Phys. Lett.* 50 (18), (4 May 1987).
6. J.E. Falconer and H.D. Palfrey, *J. Cryst. Growth* 100, 275 (1990) North Holland.
7. L.O. Bubulac, D.D. Edwall and C.R. Viswanathan, *J. Vac. Sci. Technol. B* 9 1695 (1991).
8. L.O. Bubulac and C.R. Viswanathan, J. Cryst. Growth 123, 555 (1992).
9. A.V. Gorshkov, F.A. Zaitov, S.B. Shangin, G.M. Shalyapina, I.N. Petrov and I.S. Asaturova, *Sov. Phys. Solid State* 26 (19), October (1984).
10. L.O. Bubulac, D.S. Lo, W.E. Tennant, D.D. Edwall, J.C. Chen, J. Ratusnik, J.C. Robinson and G. Bostrup, *Appl. Phys. Lett.* 50 (22), 1 June (1987).
11. S.J.C. Irvine, E.R. Gertner, L.O. Bubulac, R.V. Gil and D.D. Edwall, *Semicond. Sci. Technol.* 6 (1991) C15.
12. H.R. Vydynath, J.B. Parkinson, R.S. Stapp, C.L. Westmark and J. Bajaj, Mtg. IRIS Specialty Group on IR Detector, 1990.
13. S.H. Shin, J.M. Arias, M. Zandian, J.G. Pasko and R.E. DeWames, to be published in *J. Electron. Mater.* (1993).
14. R.J. Blattner and C.A. Evans, Jr., *Scanning Electron Microscopy / 1990 / IV-Sem. Inc.,* (Chicago: AMF O'Hare, 1990), p. 200.
15. L.O. Bubulac and C.R. Viswanathan, *Appl. Phys. Lett.* 60 (2), 13 January (1992).
16. H.G. Vydyanath, R.C. Abbot and D.A. Nelson, *L. Appl. Phys.* 54, 1323 (1983).

Annealing Experiments in Heavily Arsenic-Doped (Hg,Cd)Te

H.R. VYDYANATH and L.S. LICHTMANN

Aerojet Electronic Systems Division, P.O. Box 296, Azusa, CA 91702

S. SIVANANTHAN, P.S. WIJEWARNASURIYA, and J.P. FAURIE

University of Illinois at Chicago, Chicago, IL 60680

Arsenic doped molecular beam epitaxy (MBE) (Hg,Cd)Te films were grown on (Cd,Zn)Te substrates. The concentration of arsenic was varied from 5×10^{18} cm^{-3} to 1×10^{20} cm^{-3}. After the growth, the epitaxial layers were annealed at various partial pressures of Hg within the existence region of (Hg,Cd)Te at temperatures ranging from 400 to 500°C. Hall effect and resistivity measurements were carried out subsequent to the anneals. 77K hole concentration measurements indicate that for concentrations of arsenic $<10^{19}$ cm^{-3}, most of the arsenic is electrically active acting as acceptors interstitially and/or occupying Te lattice sites at the highest Hg pressures. At lower Hg pressures, particularly at annealing temperatures of 450°C and higher, compensation by arsenic centers acting as donors appears to set in and the hole concentration decreases with decrease in Hg pressure. These results indicate the amphoteric behavior of arsenic and its similarity to the behavior of phosphorus in (Hg,Cd)Te previously inferred by us. A qualitative model which requires the presence of arsenic occupying both interstitial and Te lattice sites along with formation of pairs of arsenic centers is conjectured.

Key words: Amphoteric, annealing, As, diffusion, HgCdTe, Hg partial pressure

INTRODUCTION

Recently, there has been an increased emphasis on replacing native acceptor defect doping with external acceptor dopants.[1] The reasons for this are twofold. First, it is possible—in principle at least—to increase the Shockley-Read-limited carrier lifetime using acceptor dopants whose energy levels are closer to the valence band edge. Secondly, with the recent success in the (Hg,Cd)Te heterojunction work[2-7] and particularly with the improved performance obtainable in p-on-n heterojunctions,[8,9] the acceptor dopant study has taken on an increasingly significant role. The only way one can fabricate p-on-n heterojunctions, is with the use of an acceptor dopant in the wider-band-gap layer and a donor dopant in the optically active layer and to reduce the native acceptor defect concentration well below the concentration of the dopants.

The large size of the group V elements and hence the low diffusivity of these elements are expected to result in stable and well controlled p-n junctions. In a detailed study of the mode of incorporation of phosphorus in bulk-grown $Hg_{0.8}Cd_{0.2}Te$, Vydyanath et al.[10] established the amphoteric behavior of phosphorus.

Also, electrical activity, solubility, and mode of incorporation of P, As, Sb and Bi were investigated in $Hg_{1-x}Cd_xTe$ layers grown by liquid phase epitaxy from Te-rich solutions.[11] Not surprisingly, these elements were found to be amphoteric in epitaxially grown (Hg,Cd)Te also.

The main objective of the current study is to study the incorporation mechanism of arsenic in (Hg,Cd)Te particularly at concentrations in excess of 10^{18} cm^{-3} since at lower concentrations, arsenic is well behaved with no self-compensation under Hg saturated conditions.[12]

Although our initial objective was to study the behavior of arsenic in (Hg,Cd)Te grown by different
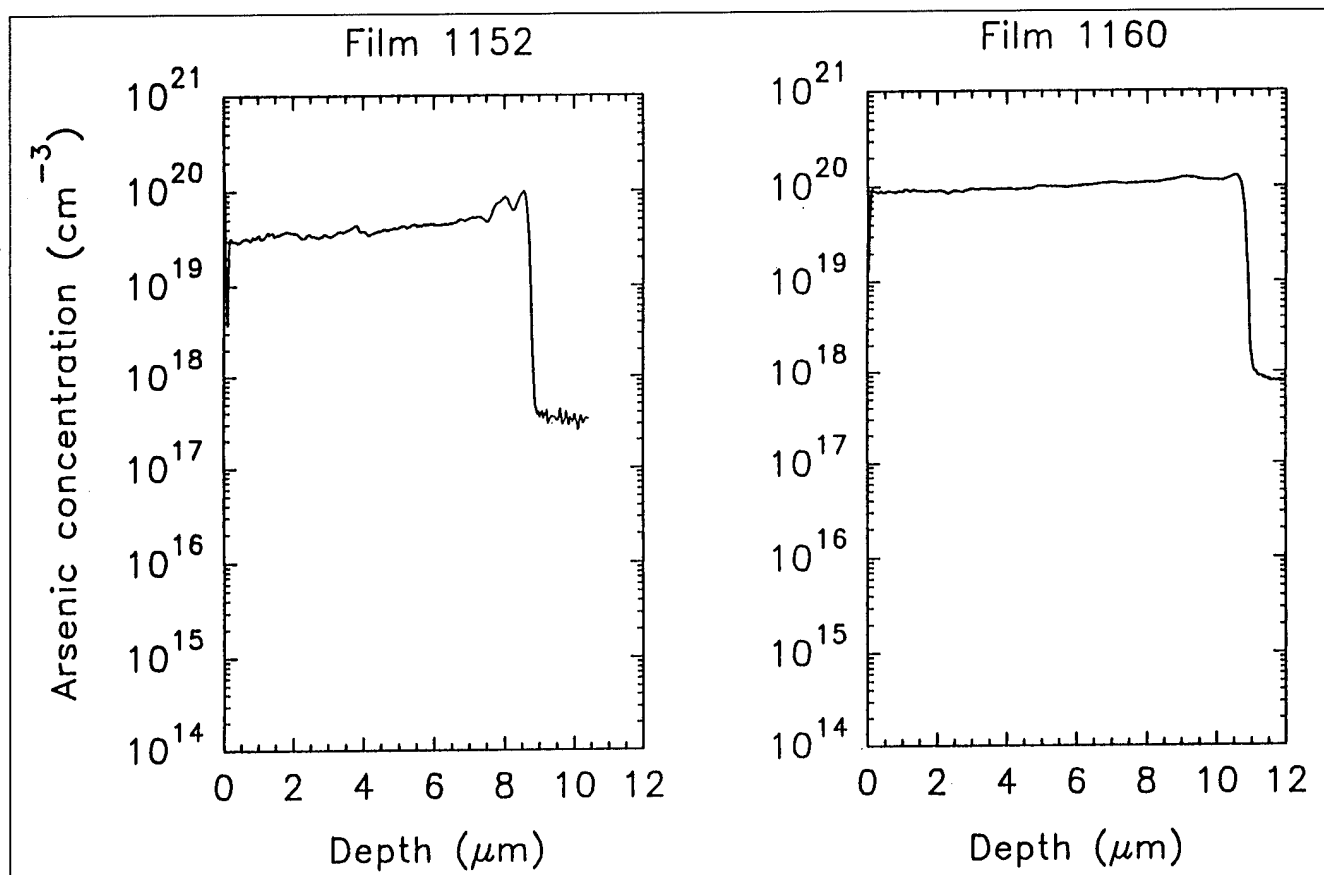
Fig. 1. Secondary ion mass spectroscopy analysis of the arsenic concentration in the MBE (Hg,Cd)Te films.

Table I. Summary of Composition, Thickness, and Arsenic Concentrations of the MBE Films Selected for the Study

Film #	X_{CdTe}	Thick. μm	As Conc., cm^{-3} (SIMS Data)
1150	0.23	10	5×10^{18}
1152	0.22	9.8	4×10^{19}
1159	0.21	12.6	1×10^{19}
1160	0.22	12	1×10^{20}

technologies, our choice had to be limited to molecular beam epitaxy (MBE) grown material for two reasons. First, we had no access to Hg-rich liquid phase epitaxy (LPE) growths which can result in high arsenic concentrations, and second, Te-rich LPE, which we have access to, in our laboratories does not result in high arsenic concentrations.[11]

Our motivation to study the equilibrium behavior of arsenic in (Hg,Cd)Te at concentrations in excess of 10^{18} cm^{-3} led us to perform annealing experiments at 400 to 500°C although in practice, MBE grown p-n junctions using arsenic are not expected to be exposed to these high temperatures. Annealing studies at temperatures below 400°C were not undertaken because of uncertainty in reaching equilibrium with regard to arsenic dopant defects at low temperatures.

In our study, $Hg_{1-x}Cd_xTe$ films with X = 0.21 to 0.23 and arsenic concentrations ranging from 10^{18} cm^{-3} to 10^{20} cm^{-3} were grown, via the MBE technique. These films were analyzed for the arsenic concentration via secondary ion mass spectroscopy (SIMS). The arsenic doped epitaxial films were equilibrated from 400° to 500°C in Hg atmospheres corresponding to stoichiometric conditions ranging from Hg-saturated to Te-saturated conditions. Subsequent to the anneals, the ampoules containing the samples were air cooled to room temperature. Hall effect and resistivity measurements were carried out on these samples to establish the variation of carrier concentration and carrier mobility as a function of the partial pressure of Hg and arsenic concentration at different temperatures.

Based on the information gathered from these data, it is clear that arsenic behaves amphoterically in MBE grown (Hg,Cd)Te similar to its behavior in LPE (Hg,Cd)Te[11] and that of phosphorus in bulk and LPE material.[10,11] At high concentrations of arsenic, larger than 10^{19} cm^{-3} and at annealing temperature of 450°C and above, the 77K hole concentration in the cooled crystals is less than the total arsenic concentration, suggesting that the crystals are well compensated particularly at low Hg pressures. The behavior of arsenic as an acceptor at high Hg pressures and as a donor at low Hg pressures is also deduced from the results.

FILM GROWTH AND ARSENIC ANALYSIS

All the (Hg,Cd)Te epitaxial layers were grown at University of Illinois at Chicago. The details of growth have already been published elsewhere[13-15] and will
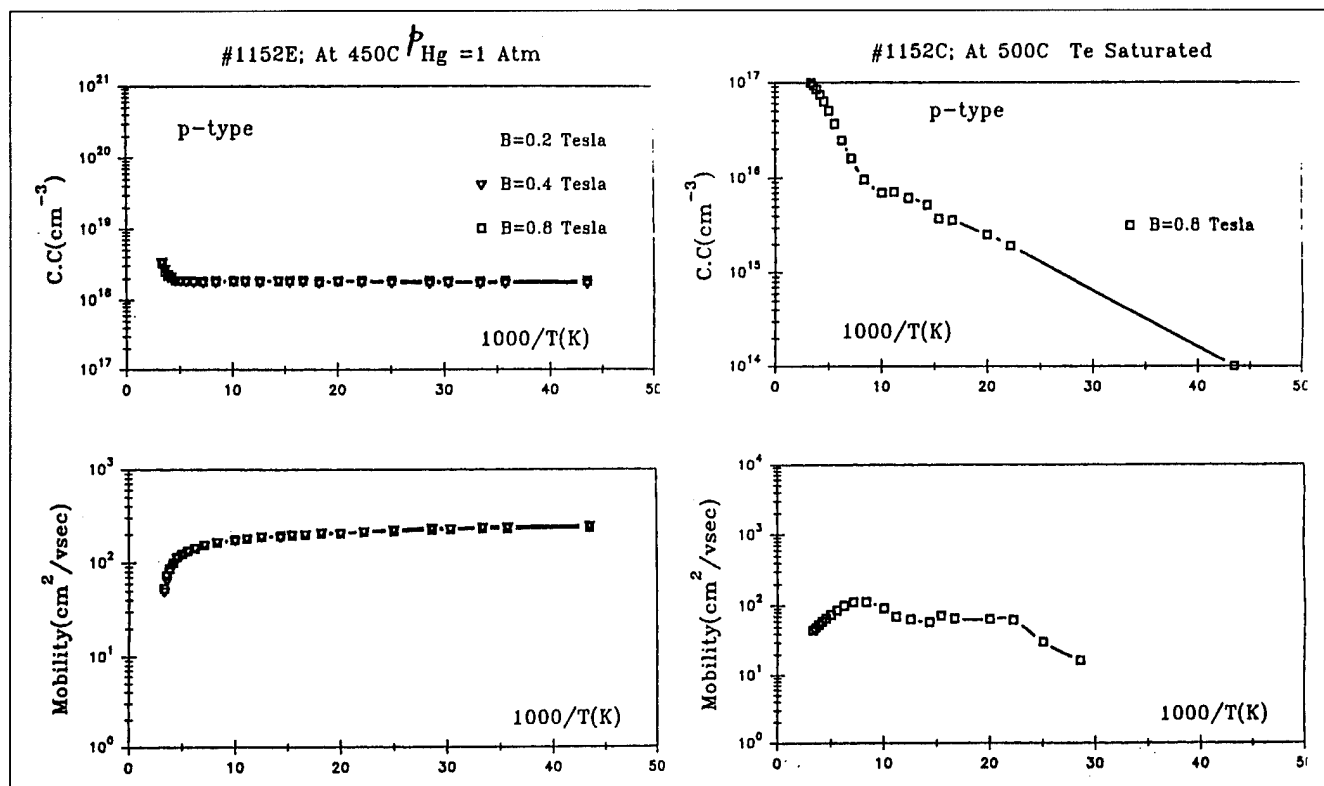
Fig. 2. Temperature dependence of the hole concentration and hole mobility in film 1152 containing 4×10^{19} cm^{-3} of arsenic.

not be repeated here. The composition of the Hg$_{1-x}$Cd$_x$Te layers in this work corresponds to X = 0.21 to X = 0.23. The arsenic concentration in the films was varied from 10^{18} cm^{-3} to 10^{20} cm^{-3}. The concentration of arsenic in the films was confirmed via SIMS analysis at Charles Evans Associates, Redwood City, CA. Table I summarizes the compositions and the arsenic concentrations in the films deduced from the SIMS analysis. Secondary ion mass spectroscopy analysis data of arsenic concentration for two of the samples as a function of depth into the film are shown in Fig. 1. From the results shown in the figure, the doping uniformity in the films appears to be satisfactory.

ELECTRICAL DATA

Figure 2 shows the p-type carrier concentration and carrier mobility measured as function of temperature from 30 to 300K at various magnetic fields for samples (of film 1152 with 3.0×10^{19} cm^{-3} arsenic) which turned p-type after annealing at different temperatures and partial pressures of Hg.

Figures 3 through 5 summarize the 77K hole concentration as a function of partial pressures of Hg at T = 400 to 500°C in films 1150, 1152, and 1160 with arsenic concentrations ranging from 5×10^{18} cm^{-3} to 1×10^{20} cm^{-3}.

Figure 6 presents the 77K hole mobility data as a function of the hole concentration for various arsenic doped samples annealed under different conditions; data for undoped crystals along with calculations based on impurity and lattice scattering[16,17] are also shown.
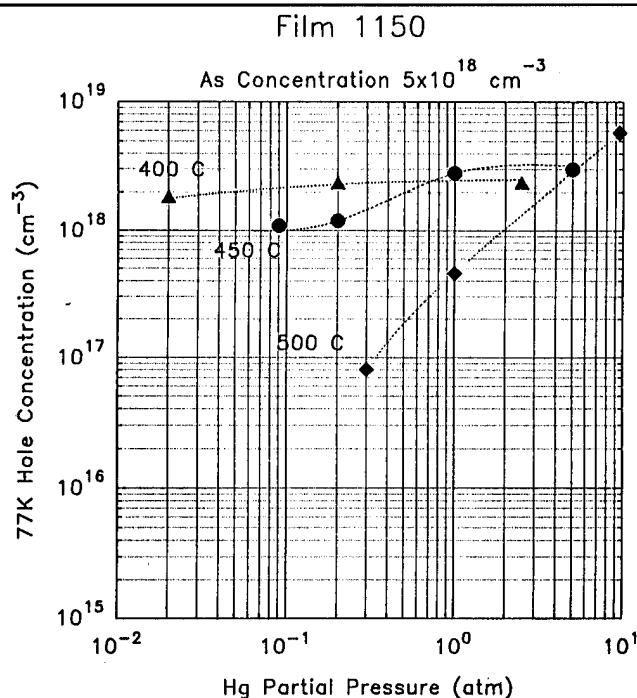

Fig. 3. 77K hole concentration as a function of the partial pressure of Hg for film 1150 containing 5×10^{18} cm^{-3} of arsenic subsequent to equilibration at 400 to 500°C.

DISCUSSION

Results of hole concentration as a function of temperature of measurement from 30 to 300K in samples of film 1152 with 4.0×10^{19} cm^{-3} indicate that all the electrically active arsenic is ionized at 77K in the
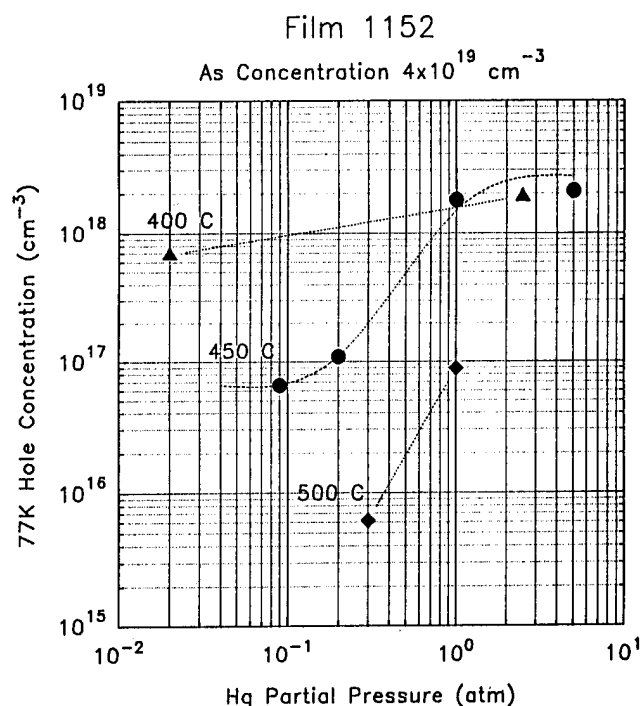
Film 1152

As Concentration 4×10^{19} cm^{-3}

Fig. 4. 77K hole concentration as a function of the partial pressure of Hg for film 1152 containing 4×10^{19} cm^{-3} of arsenic subsequent to equilibration at 400 to 500°C.

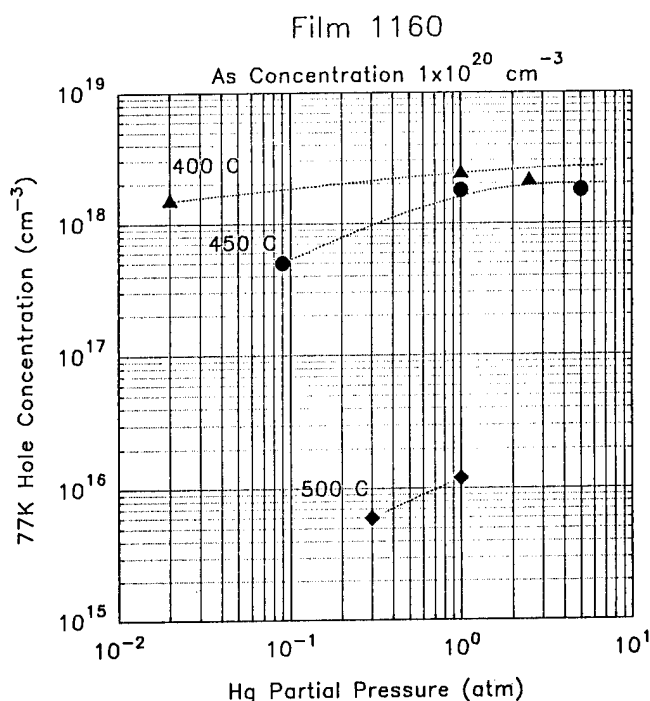## Film 1160

As Concentration 1×10^{20} cm^{-3}

Fig. 5. 77K hole concentration as a function of the partial pressure of Hg for film 1160 containing 1×10^{20} cm^{-3} of arsenic subsequent to equilibration at 400 to 500°C.

samples investigated and hence 77K hole concentration can be assumed to reflect the defect state in the crystals at the equilibration temperatures.

Results shown in Fig. 3 through Fig. 5 indicate that all the arsenic doped samples are p-type after anneals at T = 400 to 500°C throughout entire region of existence of (Hg,Cd)Te from Hg saturated to Te satu-
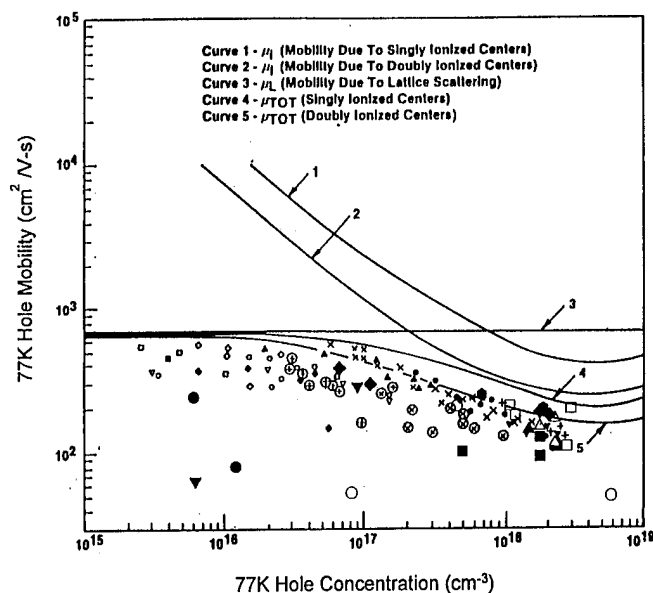

Fig. 6. 77K hole mobility as a function of 77K hole concentration in arsenic doped MBE films (large symbols), undoped LPE films[16,17] (small symbols) and calculated values assuming ionizing impurity scattering and lattice scattering.[16] MBE samples: ▲ 400°C, 10^{20} cm^{-3} As, ✦ 400°C 4×10^{19} cm^{-3} As, △ 400°C 5×10^{18} cm^{-3} As, ■ 450°C, 1×10^{20} cm^{-3} As, ◆ 450°C 4×10^{19} cm^{-3} As, ☐ 450°C, 5×10^{18} cm^{-3} As ● 500°C, 1×10^{20} cm^{-3} As, ▼ 500°C, 4×10^{19} cm^{-3} As, ○ 500°C, 5×10^{18} cm^{-3} As.

rated conditions. The values of Hg pressure for Te saturated conditions, at T = 400° to 500°C were taken from previously published work reported by one of us.[17] It is clear from the results shown in Fig. 3 that for film 1150 with a total arsenic concentration of ~5 × 10^{18} cm^{-3}, most of the arsenic is present in an electrically active form at 400 and 450°C with 1 to 3 × 10^{18} cm^{-3} hole concentration at 77K. At 500°C at Hg saturated conditions, film 1150 appears to yield one hole for every arsenic atom with no compensation. However, as the Hg pressure is decreased at 500°C, the 77K hole concentration decreases super linearly, indicating the onset of compensation from arsenic donor centers.

Results from Fig. 4 for film 1152 with a total arsenic concentration of 4 × 10^{19} cm^{-3} show the hole concentration to be much lower than the total arsenic concentration even at the highest Hg pressures, indicating the onset of compensation by arsenic donors even at the highest Hg pressures. At lower Hg pressures (just as with film 1150 with 5 × 10^{18} cm^{-3} arsenic) the hole concentration decreases super linearly with decrease in Hg pressure at 450 and 500°C.

Film 1160 with a total arsenic concentration of 1 × 10^{20} cm^{-3} shows a similar behavior to that of films 1150 and 1152. The 77K hole concentration in Sample 1160 (Fig. 5) is much lower than the total arsenic concentration at all temperatures and partial pressures of Hg with increasing compensation setting in at higher temperatures and lower pressures of Hg. In fact, at 500°C under Te-saturated conditions, the 77K hole concentration is only 6 × 10^{15} cm^{-3}, a negligible fraction of the total arsenic concentration in the sample.

It is clear from the results shown in Fig. 3 to Fig. 5 that the compensation by arsenic donor centers sets in at higher arsenic concentrations, lower Hg pressures, and higher temperatures of anneal. The 77K hole mobility in arsenic-doped samples appears to be similar to that of the undoped crystals except for samples annealed at 450 to 500°C under Te-rich conditions. It is possible that at the higher temperatures of anneal pair formation is less favored and isolated multiply ionized centers may become appreciable in concentration. Also at higher temperatures of anneal and lower Hg pressures, there is a much higher degree of compensation.

It is also to be noted that the hole concentration dependence on the temperature of measurement is much steeper for Sample 1152 annealed under tellurium-saturated conditions compared to that annealed under Hg-rich conditions (Fig. 2) indicating that the Fermi level in the Te-rich annealed samples is farther away from the valence band edge than in the Hg-rich annealed samples. This fact supports the notion that under Hg deficient conditions, compensating arsenic donors become appreciable in concentration making the crystals less p-type and the Fermi level to lie farther away from the valence band edge thus resulting in a larger free energy for complete electrical activation.

The 77K hole concentration results shown in Fig. 3 through Fig. 5 are replotted in Fig. 7 through Fig. 9 (for different concentrations of arsenic at a fixed annealing temperature in each figure). By displaying the results in this format, it is possible to present in the same figures, the values of the intrinsic carrier concentration and the hole concentration in undoped

(Hg,Cd)Te crystals at each temperature, arising from the presence of Hg vacancy native acceptor defects. The intrinsic carrier concentration and the hole concentration in the undoped crystals are derived from the mass action constants K_i and K''_{VHg} established previously in literature.[16,17]

From the results shown in Fig. 7 through Fig. 9, it

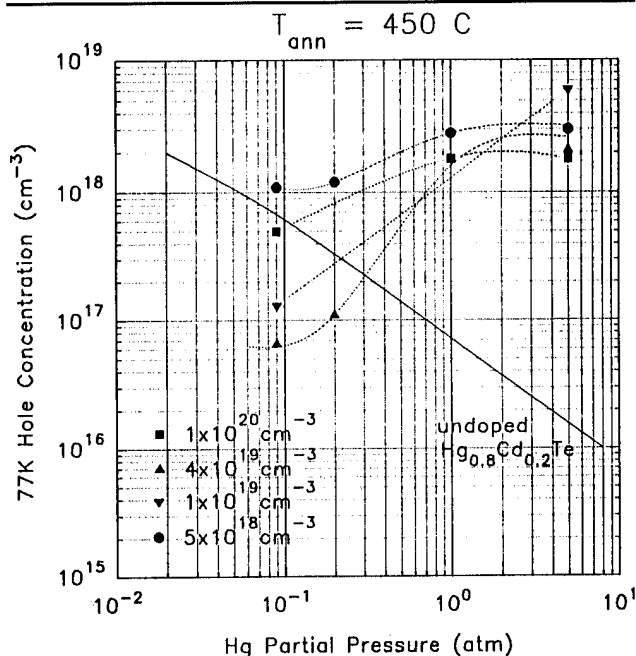

Fig. 8. 77K hole concentration as a function of the partial pressure of Hg for films doped with various As concentrations after annealing at T = 450°C; expected hole concentration for undoped crystals also shown.
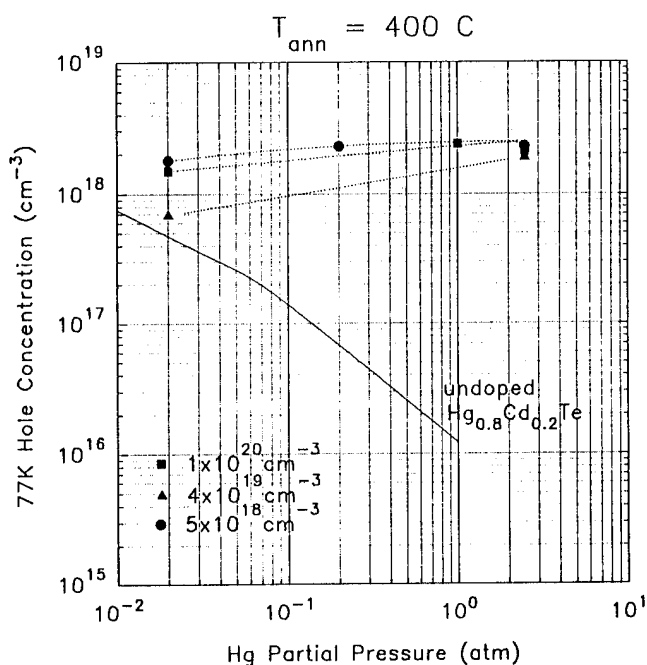

Fig. 7. 77K hole concentration as a function of the partial pressure of Hg for films doped with various As concentrations after annealing at T = 400°C; expected hole concentration for undoped crystals also shown.
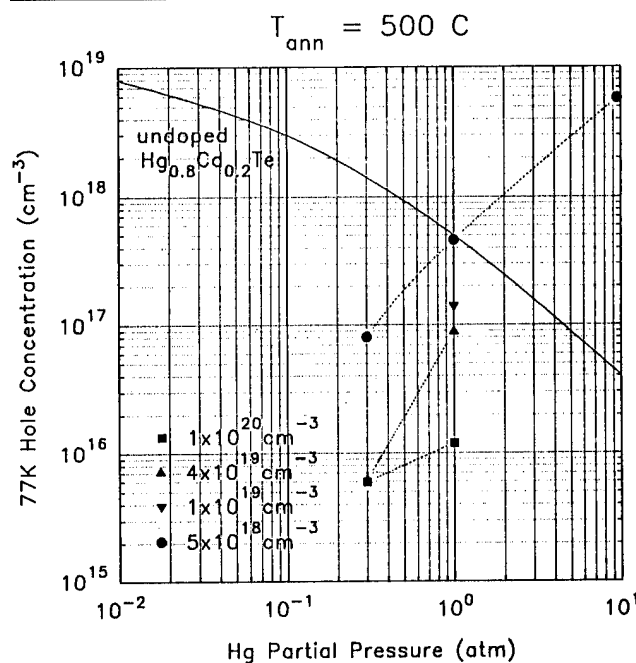

Fig. 9. 77K hole concentration as a function of the partial pressure of Hg for films doped with various As concentrations after annealing at T = 500°C; expected hole concentration for undoped crystals also shown.

Table II. Defect Formation Reactions, Mass-Action Relations, Electroneutrality Condition, and Arsenic Balance Equation

	Reaction	Mass-Action Relation
1.	$O \rightarrow e' + h^{\cdot}$	$K_i = [e'][h^{\cdot}]$
2.	$Hg_{Hg}^{x} \rightarrow V_{Hg}'' + 2h^{\cdot} + Hg(g)$	$K_{V_{Hg}''} = \left[V_{Hg}''\right][h^{\cdot}]^2 \, p_{Hg}$
3.	$As_i'' + As_{Hg}^{\cdot} \rightarrow (As_i As_{Hg})'$	$K_{p_{(As_i As_{Hg})'}} = \dfrac{\left[(As_i As_{Hg})'\right]}{\left[As_i''\right]\left[As_{Hg}^{\cdot}\right]}$
4.	$As_i' + As_{Hg}^{\cdot\cdot} \rightarrow (As_i As_{Hg})^{\cdot}$	$K_{p_{(As_i As_{Hg})'}} = \dfrac{\left[(As_i As_{Hg})^{\cdot}\right]}{\left[As_i'\right]\left[As_{Hg}^{\cdot\cdot}\right]}$
5.	$As_i' + Hg(g) \rightarrow As_{Te}' + Hg_{Hg}^{x}$	$K_{As_{Te}'} = \dfrac{\left[As_{Te}'\right]}{\left[As_i'\right] p_{Hg}}$
6.	$As_i' + 2h^{\cdot} + Hg_{Hg}^{x} \rightarrow As_{Hg}^{\cdot} + Hg(g)$	$K_{As_{Hg}^{\cdot}} = \dfrac{\left[As_{Hg}^{\cdot}\right] p_{Hg}}{\left[As_i'\right][h^{\cdot}]^2}$
7.	$2As_i' + Hg_{Hg}^{x} + h^{\cdot} \rightarrow (As_i As_{Hg})' + Hg(g)$	$K_{(As_i As_{Hg})'} = \dfrac{\left[(As_i As_{Hg})'\right] p_{Hg}}{\left[As_i'\right]^2 [h^{\cdot}]}$
8.	$2As_i' + Hg_{Hg}^{x} + 3h^{\cdot} \rightarrow (As_i As_{Hg})^{\cdot} + Hg(g)$	$K_{(As_i As_{Hg})^{\cdot}} = \dfrac{\left[(As_i As_{Hg})^{\cdot}\right] p_{Hg}}{\left[As_i'\right]^2 [h^{\cdot}]^3}$
9.	$As_{Hg}^{\cdot} + V_{Hg}'' \rightarrow (As_{Hg} V_{Hg})'$	$K_{p_{(As_{Hg} V_{Hg})'}} = \dfrac{\left[(As_{Hg} V_{Hg})'\right]}{\left[As_{Hg}^{\cdot}\right]\left[V_{Hg}''\right]}$
10.	$As_{Hg}^{\cdot\cdot} + V_{Hg}'' \rightarrow (As_{Hg} V_{Hg})^{\cdot}$	$K_{p_{(As_{Hg} V_{Hg})'}} = \dfrac{\left[(As_{Hg} V_{Hg})^{\cdot}\right]}{\left[As_{Hg}^{\cdot\cdot}\right]\left[V_{Hg}''\right]}$

Electroneutrality Condition:

$$[e'] + 2[V_{Hg}''] + [As_i'] + 2[As_i''] + [As_{Te}'] + [(As_i As_{Hg})'] + [(As_{Hg} V_{Hg})']$$

$$= [h^{\cdot}] + [As_{Hg}^{\cdot}] + 2[As_{Hg}^{\cdot\cdot}] + 3[As_{Hg}^{\cdot\cdot\cdot}] + [(As_i As_{Hg})^{\cdot}] + [(As_{Hg} V_{Hg})^{\cdot}]$$

Arsenic Balance Equation:

$$[As_i'] + [As_i''] + [As_{Te}'] + 2[(As_i As_{Hg})'] + [(As_{Hg} V_{Hg})'] + [As_{Hg}^{\cdot}] + [As_{Hg}^{\cdot\cdot}]$$

$$+ [As_{Hg}^{\cdot\cdot\cdot}] + [(As_i As_{Hg})^{\cdot}] + [(As_{Hg} V_{Hg})^{\cdot}] = [As_{Total}]$$

Table III. Variations of Defect Concentrations as a Function of p_{Hg} and/or Arsenic Concentrations for Various Approximations to the Electroneutrality Condition and Arsenic Balance Equation

Type of Defect and Approximation to the the Electroneutrality Condition and Arsenic Balance Equation	$[\ ]\ \alpha\ p_{Hg}^r\ [As_{Tot}]^s$	
	r	**s**
1. $[h^\cdot] \approx [As_i'] = [As_{Tot}]$	0	+1
$[e']$	0	−1
$[V_{Hg}'']$	−1	−2
$[As_i'']$	0	0
$[As_{Te}^\cdot]$	+1	+1
$[As_{Hg}^\cdot]$	−1	+3
$[As_{Hg}^{\cdot\cdot}]$	−1	+4
$[As_{Hg}^{\cdot\cdot\cdot}]$	−1	+5
$[(As_i As_{Hg})^\cdot]$	−1	+5
$[(As_i As_{Hg})']$	−1	+3
$[(As_{Hg} V_{Hg})']$	−2	+1
$[(As_{Hg} V_{Hg})^\cdot]$	−2	+3
2. $[h^\cdot] = [As_{Te}'] = [As_{Tot}]$	0	+1
$[e']$	0	−1
$[V_{Hg}'']$	−1	−2
$[As_i']$	−1	+1
$[As_i'']$	−1	0
$[As_{Hg}^\cdot]$	−2	+3
$[As_{Hg}^{\cdot\cdot}]$	−2	+4
$[As_{Hg}^{\cdot\cdot\cdot}]$	−2	+5
$[(As_i As_{Hg})^\cdot]$	−3	+5
$[(As_i As_{Hg})']$	−3	+3
$[(As_{Hg} V_{Hg})']$	−3	+1
$[(As_{Hg} V_{Hg})^\cdot]$	−3	+3
3. $(As_i As_{Hg})^\cdot] = [As_i'] = \dfrac{[As_{Tot}]}{3}$	0	+1
$[h^\cdot]$	+1/3	−1/3
$[e']$	−1/3	+1/3
$[V_{Hg}'']$	−5/3	+2/3
$[As_i'']$	−1/3	+4/3
$[As_{Hg}^\cdot]$	−1/3	+1/3
$[As_{Hg}^{\cdot\cdot}]$	0	0
$[As_{Hg}^{\cdot\cdot\cdot}]$	+1/3	−1/3
$[(As_i As_{Hg})^\cdot]$	0	+1
$[(As_i As_{Hg})']$	−2/3	+5/3
$[(As_{Hg} V_{Hg})']$	−2	+1
$[(As_{Hg} V_{Hg})^\cdot]$	−4/3	+1/3

is clear that at 400°C all the arsenic-doped samples with total arsenic in excess of 5×10^{18} cm^{-3} have higher hole concentration than in undoped crystals throughout the entire existence region of (Hg,Cd)Te. At 450°C, all the samples appear to be more p-type than the undoped crystals at partial pressures of Hg slightly higher than corresponding to Te-saturated conditions. At 500°C, samples 1152 and 1 160 with total arsenic concentration of 4×10^{19} cm^{-3} and 1×10^{20} cm^{-3}, respectively, have lower hole concentration than the

4. $\quad [(As_iAs_{Hg})^{\cdot}] = [As'_{Te}] = \dfrac{[As_{Tot}]}{3}$	0	+1
$[h^{\cdot}]$	+1	−1/3
$[e']$	−1	+1/3
$[V''_{Hg}]$	−3	+2/3
$[As'_i]$	−1	+1
$[As''_i]$	−2	+4/3
$[As^{\cdot}_{Hg}]$	0	+1/3
$[As^{\cdot\cdot}_{Hg}]$	+1	0
$[As^{\cdot\cdot\cdot}_{Hg}]$	+2	−1/3
$[(As_iAs_{Hg})^{\cdot}]$	0	+1
$[(As_iAs_{Hg})']$	−2	+5/3
$[(As_{Hg}V_{Hg})']$	−3	+1
$[(As_{Hg}V_{Hg})^{\cdot}]$	−1	+1/3
5. $\quad [(As_iAs_{Hg})'] = [(As_iAs_{Hg})^{\cdot}] = \dfrac{[As_{Tot}]}{4}$	0	+1
$[h^{\cdot}]$	0	0
$[e']$	0	0
$[V''_{Hg}]$	-1	0
$[As'_i]$	+1/2	+1/2
$[As''_i]$	+1/2	+1/2
$[As^{\cdot}_{Hg}]$	−1/2	+1/2
$[As^{\cdot\cdot}_{Hg}]$	−1/2	+1/2
$[As^{\cdot\cdot\cdot}_{Hg}]$	−1/2	+1/2
$[As'_{Te}]$	+1/2	+3/2
$[(As_{Hg}V_{Hg})']$	−3/2	+1/2
$[(As_{Hg}V_{Hg})^{\cdot}]$	−3/2	+1/2

undoped crystals at all partial pressures of Hg, and Sample 1150 with 5×10^{18} cm^{-3} of arsenic is more p-type than the undoped crystals at $p_{Hg}>1$ atm and less p-type at $p_{Hg}<1$ atm.

The results shown in Fig. 7 through Fig. 9 also indicate that the film 1150 containing 5×10^{18} cm^{-3} arsenic is more p-type at 77K than the film 1152 containing 4×10^{19} cm^{-3} arsenic at all Hg pressures

*The quasichemical approach pioneered by Kröger and Vink[18] forms the basis for our defect analysis. This approach has successfully predicted the defect situation in several II-VI[19-24] and IV-VI compounds.[25-27] A large number of other examples of the application of the approach can be found in Kröger's book.[28] The defect notations used in this paper are also from Ref.s 18 and 28, according to which the subscript denotes the lattice site occupied and superscript denotes the effective charge. Superscript cross x stands for a neutral charge, dash (-) for an effective negative charge and a dot (•) for an effective positive charge. Thus, As''$_i$ and As$^{\cdot\cdot}_{Hg}$ stand for As in interstitial and Hg lattices with a double negative effective charge and a double positive effective charge, respectively.

Square brackets ([ ]) denote concentration in terms of site fraction which is given by the ratio of number of defects, cm^{-3} to the total number of lattice sites, cm^{-3}. By this definition, $[Hg^x_{Hg}] = 1$ since most of the Hg lattice sites are occupied.

after anneals at 400–500°C. Film 1160 containing 1×10^{20} cm^{-3} arsenic appears to have hole concentration which is intermediate between those of films 1150 and 1152 containing 5×10^{18} cm^{-3} and 4×10^{19} cm^{-3} of As, respectively.

While attempting to find an explanation for the experimental results, the possibility of reaching solubility limit for arsenic particularly at the 10^{20} cm^{-3} concentration levels also needs to be considered.

Data in Fig. 6 indicate that the arsenic doped samples containing arsenic on the order of 4×10^{19} cm^{-3} to 10^{20} cm^{-3} but with hole concentration less than 10^{16} cm^{-3} show mobilities much lower than those in undoped samples with the same hole concentration but containing only Hg vacancies. Obviously the heavily arsenic doped samples are well self-compensated and the hole concentration is a negligible fraction of the total arsenic concentration in the samples.

A qualitative model which can explain the experimental results reported in this paper requires the dominance of arsenic in interstitial sites acting as singly ionized acceptors for concentrations of up to 2 to 5×10^{18} cm^{-3} at high Hg pressures. At higher arsenic concentrations, compensation by arsenic donor species sets in. The compensating donor species $(As_iAs_{Hg})^{\cdot}$

are deduced to be comprised of singly ionized arsenic in interstitial sites paired with doubly ionized arsenic on Hg lattice sites.

At still higher arsenic concentrations, we begin to see the dominance of arsenic acceptor species $(As_iAs_{Hg})'$ comprised of doubly ionized As in interstitial sites paired with singly ionized As on Hg lattice sites.

Figure 10 shows schematically, the dominance of the different arsenic species as a function of the partial pressure of Hg and arsenic concentration in the crystals at T = 400°C. This figure, referred to as the range boundary diagram, shows the dominant arsenic species in different ranges of electroneutrality approximation.* Thus, range 1 where $[h^\cdot] \approx [As'_i] \approx [As_{Tot}] >> [As'_{Te}], [e'], [V''_{Hg}]$ indicates that $h^\cdot$ and As'_i are comparable in concentration and are much higher in concentration compared to As'_{Te}, $As^\cdot_{Hg}$, e', V''_{Hg} etc., whereas in range 2 where $[As'_i] \approx [(As_iAs_{Hg})'] \approx [As_{Tot}]/2$, these two arsenic species are comparable in concentration and are higher in concentration compared to any other electrically active species such as e', $h^\cdot$, As'_{Te}, $As^\cdot_{Hg}$, V''_{Hg}, etc.

Table II shows the relevant defect formation reactions and mass action constants for the formation of defects shown in Fig. 10. Table III shows the variation of the various As species, native defect species, $[e']$ and $[h^\cdot]$ in forms of p^r_{Hg} $[As_{Tot}]^s$ when the electroneutrality condition and the As charge balance equation shown in Table II are approximated by only the dominant members.

Expressions for the range boundaries in Fig. 10 are obtained by equating expressions for the concentration of any one of the species in the two adjacent ranges and are summarized in Table IV in terms of the mass action constants defined in Table II, p_{Hg} and As_{Tot}.

In arriving at the qualitative model shown in Fig. 10, we have not included the results on film 1160 with arsenic concentration at 1×10^{20} cm^{-3}. The fact that this film shows hole concentration which is intermediate between that of films 1150 and 1152 containing arsenic concentrations of 5×10^{18} cm^{-3} and 4×10^{19} cm^{-3} cannot be explained by our model. We could come up with no satisfactory model which explains the data for film 1160. It is probable that at arsenic concentration of 10^{20} cm^{-3}, the solubility limit is reached at 400 to 500°C; presence of arsenic as second phase in the film may give rise to anomalous electrical data. Additionally, impurity band conduction may become an issue at such high arsenic concentrations. More work needs to be done to sort out these questions.

Excluding the data on film 1160 with arsenic concentrations of 10^{20} cm^{-3}, the data on films containing arsenic ranging from 10^{18} cm-3 to 4×10^{19} cm^{-3} can be qualitatively explained with the defect model shown in Fig. 10.

At arsenic concentrations below 5×10^{18} cm^{-3} at moderate to high Hg pressures the electroneutrality condition is dominated by arsenic present as acceptors in interstitial and Te lattice sites as denoted by ranges (2) and (1) in Fig. 10. The dependences of the various defects including electrons and holes at the

Table IV. Expressions for Range Boundaries of Figure 10

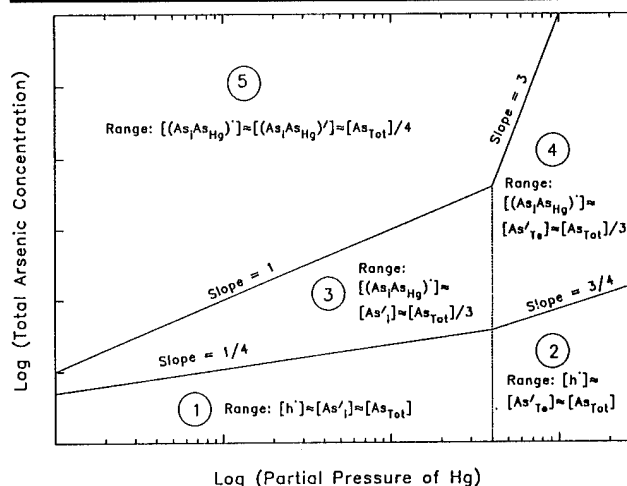| Range Boundary	Expression
1. $[As_{Tot}]_{3,1}$	$K_{(As_iAs_{Hg})'}^{1/4}\, p_{Hg}^{1/4}$
2. $[As_{Tot}]_{2,4}$	$\left(K_{As'_{Te}}^{1/2}\,\middle|\,K_{(As_iAs_{Hg})'}^{1/4}\right) p_{Hg}^{3/4}$
3. $[As_{Tot}]_{3,5}$	$\left(K_{(As_iAs_{Hg})'}^5\,\middle|\,K_{(As_iAs_{Hg})'}^3\right)^{1/2} p_{Hg}$
4. $[As_{Tot}]_{4,5}$	$\left(K_{As'_{Te}}^2\,\middle|\,K_{(As_iAs_{Hg})'}\right) p_{Hg}^3$
5. $(p_{Hg})_{1,2}$	$\left(K_{As'_{Te}}\right)^{-1}$
6. $(p_{Hg})_{3,4}$	$\left(K_{(As_iAs_{Hg})'}\,\middle|\,K_{As'_{Te}}\right)$

Log (Partial Pressure of Hg)

Fig. 10. Schematic range diagram for arsenic doped (Hg,Cd)Te showing dominance of different arsenic species at different concentrations of As and various partial pressures of Hg.

high temperature are shown in Table III. As the partial pressure of Hg is decreased, depending on the concentration of arsenic present in the crystals, one moves from range (2) to range (4) to range (3) or from range (2) to range (1) to range (3) (Fig. 10). In ranges (3) and (4), arsenic acceptor centers in interstitial and Te lattice sites (As'_i and As'_{Te}) are compensated by donor centers $(As_iAs_{Hg})^\cdot$ formed from the pairing of doubly positively ionized arsenic centers occupying Hg lattice sites $(As^{\cdot\cdot}_{Hg})$ with singly negatively ionized centers of arsenic in interstitial sites (As'_i). The defect formation reaction for these pairs is shown in Table II and the defect concentration dependences for ranges (3) and (4) are shown in Table III.

At very high arsenic concentrations and low Hg pressures, the samples are extremely heavily compensated with negatively ionized pairs $(As_iAs_{Hg})'$ com-

pensating the positively ionized pairs (As_iAs_{Hg}) (range (5), (Fig. 10). It is to be noted that the pairs $(As_iAs_{Hg})'$ are formed from As_i'' and As_{Hg}. Table I shows the defect formation reaction for these pairs and Table III shows the defect concentration dependence on partial pressure of Hg and total arsenic concentration for range (5).

As can be noted from Fig. 10, at low to moderate Hg pressures as the concentration of arsenic is increased, we move from range (1) to range (3) to range (5).

It is to be noted that the defect situation shown schematically in Fig. 10 holds good for all anneal temperatures in the current study, with the range boundary dependence on arsenic concentration and partial pressure of Hg as shown in the figure. However, the actual concentrations of arsenic and partial pressure of Hg at which the ranges will dominate will vary with temperature of anneal.

A complete defect model which quantitatively explains all the experimental data will have to consider the complete electroneutrality condition and the complete As balance equation similar to what was demonstrated by us previously for (Hg,Cd)Te doped with indium,[29] iodine[30] and phosphorus[10] and will be published elsewhere.[31]

SUMMARY

Variation of the 77K hole concentration on the partial pressure of Hg and total arsenic concentration, subsequent to equilibration at 400–500°C, confirms the amphoteric behavior of arsenic in heavily doped (Hg,Cd)Te samples. A tentative mechanism of incorporation is proposed which requires its presence in interstitial and Te lattice sites as isolated and paired species.

REFERENCES

1. C.E. Jones, K. James, J. Merz, R. Braunstein, M. Burd, M. Eetemadi, S. Hutton, and J. Drumheller, *J. Vac. Sci. Technol. A* 3, 131 (1985).
2. C.C. Wang, M. Chu, S.H. Shin, W.E. Tennant, J.T. Cheung, M. Lanir, A.H.B. Van der Wyck, G.M. Williams, L O. Bubulac and R.J. Eisel, *IEEE Trans. Electron Devices* ED-7, 154 (1980).
3. M. Lanir and K.J. Riley, *IEEE Trans. Electron Devices* ED-29, 274 (1982).
4. P.R. Bratt, *J. Vac. Sci. Technol.* A1, 1987 (1983).
5. P.S. Nayar, P.B. Ward, P.C. Colter, S.R. Hampton, J.W. Slawinski, L. Fishman, C.M. Callahan and H.R. Vydyanath, *Technical Digest IEDM* (San Francisco) 385 (1984).
6. R.A. Riedel, E.R. Gertner, D.D. Edwall and W.E. Tennant, *Appl. Phys. Lett.* 46, 64 (1985).
7. H.R. Vydyanath, P.B. Ward, S.R. Hampton, L. Fishman, J. Slawinski, C. Devaney, J. Ellsworth and T. Krueger, *Proc. SPIE* 686, 14 (1986).
8. W. Radford, private communication.
9. H.R. Vydyanath, P.B. Ward, S.R. Hampton, J.B. Parkinson and B. Klank, *Proc. SPIE* 1097, 110 (1989).
10. H.R. Vydyanath, R.C. Abbott and D.A. Nelson, *J. Appl. Phys.* 54, 1323 (1983).
11. H.R. Vydyanath, J.A. Ellsworth and C.M. Devaney, *J. Electron. Mater.* 16, 13 (1987).
12. T. Tung, *J. Cryst. Growth* 86 (1988).
13. J.P. Faurie, R. Sporken, S. Sivananthan and M.D. Lange, *J. Cryst. Growth* 111, 698 (1991).
14. R. Sporken, M.D. Lange, S. Sivananthan and J.P. Faurie, *Appl. Phys. Lett.* 59, 81 (1991)
15. J.P. Faurie, S. Sivananthan and P.S. Wijewarnasuriya, *Proc. SPIE* 1735, 141 (1992).
16. H.R. Vydyanath, *J. Electrochem. Soc.* 128, 2609 (1981).
17. H.R. Vydyanath and C.H. Hiner, *J. Appl. Phys.* 65, 3080 (1989).
18. F.A. Kröger and H.J. Vink, *Solid State Physics III*, ed. F. Seitz and D. Turnbull (New York: Academic, 1956), p. 307.
19. G.H. Hershman and F.A. Kröger, *J. Solid State Chem.* 2, 483 (1970).
20. V. Kumar and F.A. Kröger, *J. Solid State Chem.* 3, 387 (1971).
21. H.R. Vydyanath, S.S. Chern and F.A. Kröger, *J. Phys. Chem. Solids* 34, 1317 (1973).
22. H.R. Vydyanath and F.A. Kröger, *J. Phys. Chem. Solids* 36, 509 (1975).
23. D. De Nobel, *Philips Res. Rep.* 14, 361 (1959).
24. S.S. Chern, H.R. Vydyanath and F.A. Kröger, *J. Solid State Chem* 14, 33 (1975).
25. H.R. Vydyanath, *J. Appl. Phys.* 47, 4993 (1976).
26. H.R. Vydyanath, *J. Appl. Phys.* 47, 5003 (1976).
27. H.R. Vydyanath, *J. Appl. Phys.* 47, 5010 (1976).
28. F.A. Kröger, *The Chemistry of Imperfect Crystals* (Amsterdam: North Holland, 1974) Vol. 2, Chaps. 14–16.
29. H.R. Vydyanath, *J. Electrochem. Soc.* 128, 2619 (1981).
30. H.R. Vydyanath and K.A. Kröger, *J. Electron. Mater.* 11, 111 (1982).
31. H.R. Vydyanath, L.S. Lichtmann, S. Sivananthan, P.S. Wijewarnasuriya and J.P. Faurie (to be published).

Status and Application of HgCdTe Device Modeling

K. KOSAI

Santa Barbara Research Center, Goleta, CA 93117

In this article, device modeling refers to numerical simulation of semiconductor device physics to predict electrical behavior. The silicon integrated circuit industry provides the example for the use of technology computer-aided design to simulate wafer fabrication processes, and the electrical performance of devices and circuits. This paper first reviews semiconductor device modeling in general, then as applied in work supporting the development and analysis of HgCdTe infrared detectors. Example applications of one- and two-dimensional device modeling are simulation of a bias-selectable, integrated two-color detector, and two-dimensional effects on the spectral response of a HgCdTe detector with composition grading.

Key words: HgCdTe, infrared detectors, semiconductor device modeling

INTRODUCTION

Device Modeling in the Si Integrated Circuit Industry

Because of the complicated and expensive fabrication process, numerical simulation has become a critical tool for the development of silicon integrated circuits (IC).[1,2] The inherent two-dimensional (2D) nature of metal-oxide-silicon field-effect transistors, as well as their small scale and proximity in modern high-density ICs, require numerical modeling of the fabrication process and device behavior in two or three dimensions (3D). This modeling is known as technology computer-aided design (TCAD) in the silicon IC industry, and encompasses numerical simulation of wafer fabrication and device performance.[2] Examples of these models include SUPREM for silicon process modeling and PISCES for device.

The TCAD sequence in IC design is to simulate the fabrication process and use the resulting geometric dimensions and doping distributions to specify the input parameters to a device simulator. For a given device, the simulator generates a set of current-voltage characteristics that are fit to analytic expressions by parameter extraction. The analytic expressions, with parameters specific to a device and pro-

cess, are then used in a circuit simulator to analyze the affect of process variations on IC performance.

In the context of this paper, device modeling refers to computer-aided simulation of semiconductor device physics to predict electrical behavior. This is in contrast to the analytical device models that are intended to approximate device electrical characteristics in a computationally efficient manner for use in circuit simulators.

HgCdTe Detector Modeling

Major reasons for the development of $Hg_{1-x}Cd_xTe$ infrared (IR) detectors are the ability to tune the spectral response by adjusting the CdTe mole fraction x,[3] as well as the enhanced device performance made possible by heterojunctions.[4] The optimization of the heterojunction device requires careful engineering, because the composition grading at the p-n junction can interact with the doping profile to form a barrier to collection of photogenerated minority carriers.[4]

Initial research concentrated on the parameters affecting the height of the barrier and examined the equilibrium case of no diode bias or photocurrent.[5-7] Simulations using the HgCdTe detector model HET III, showed that the effects of a barrier on detector quantum efficiency were less than that predicted by the Boltzmann factor of $\exp(-E_B/kT)$, where E_B, is the height of the barrier, k, the Boltzmann constant, and

635

T, the temperature.[8]

In 1984–1987, the Materials Laboratory of the Air Force Wright Aeronautical Laboratories sponsored the Manufacturing Science Program for Enhanced Yield of HgCd Te Detector Arrays at the Santa Barbara Research Center (SBRC) of the Hughes Aircraft Company. The purpose of this program was to establish a science base for technologies considered critical to the manufacturing of photovoltaic HgCdTe detector arrays. A major task was to develop a device physics model for HgCdTe detectors with spatially varying composition.

The effort was a collaboration between SBRC and Professor R.W. Dutton of Stanford University. The approach was to enhance SEDAN III[9] and PISCES IIB,[10,11] the silicon device models developed by Professor Dutton's group, to allow simulation of graded composition HgCdTe devices. The results of this work are the one-dimensional (1D) detector model HET III, based on SEDAN III, and the 2D model SABIR, based on PISCES IIB. The source code for these models was delivered to the Air Force at the conclusion of the Manufacturing Science Program, and both HET III and SABIR are being used by a number of Department of Defense laboratories and contractors.

SEMICONDUCTOR DEVICE EQUATIONS

In the most general view, the physics of semiconductor devices are described by the Maxwell, Boltzmann transport, Schrödinger, and thermal diffusion equations. To be useful to the technologist developing a device or fabrication process, a device model must produce results in less than several hours when executing on workstation computers. This forces one to include the minimum amount of physics consistent with the desired accuracy and computational speed.

The most common approach is to assume isothermal conditions and ignore thermal diffusion. The Schrödinger equation is used only indirectly, and results in the effective mass approximation. Other simplifying assumptions include parabolic energy bands, and the neglect of most bands except the electron and hole bands at the fundamental energy gap. For the device model, the most important quantities from this treatment are the energy levels and densities of states used in carrier and impurity level statistics.

For most semiconductor devices, magnetic field effects are negligible, and only Poisson's equation is treated:

$$\nabla^2(\epsilon\psi) = -q(p\text{-}n + N_D^+ - N_A^-) - \rho_F. \quad (1)$$

The dependent variables in Eq. (1) are the electrostatic potential, ψ, and the electron and hole densities, n and p. Parameters are ϵ the static permittivity, N_D^+ and N_A^- the concentrations of ionized donors and acceptors, and ρ_F, any other fixed charge such as those at insulator interfaces, while q, is the elementary charge. This equation is highly nonlinear due to the coupling of the carrier densities with ψ through

their distribution functions.

The Boltzmann transport equation (BTE) describes the nonequilibrium distribution of carriers as a function of time and their position and velocity. It may be solved using Monte Carlo methods, but the usual approach is to derive simplified equations by the method of moments.[12] The zero order moment of the BTE gives the continuity equations for electrons and holes,

$$\frac{\partial n}{\partial t} = \frac{1}{q}\nabla \cdot \vec{J}_n - U(n), \frac{\partial p}{\partial t} = -\frac{1}{q}\nabla \cdot \vec{J}_p - U(p), \quad (2)$$

where $\vec{J}_n$ and $\vec{J}_p$ are the electron and hole current densities, and U(n) and U(p), the net electron and hole recombination rates. The moments of the carrier velocities give the drift-diffusion equations,

$$\vec{J}_n = qn\mu_n\vec{F} + q\nabla(D_n n), \vec{J}_p = qp\mu_p\vec{F} - q\nabla(D_p p), (3)$$

where μ_n and μ_p are the carrier mobilities, D_n and D_p, their diffusion coefficients, and $\vec{F}$, the electrostatic field. With the assumption that the electrostatic field is sufficiently low to ignore energy gain by the carriers, and the neglect of Joule heating, Eq. (1)–(3) form the most common set of equations used to describe semiconductor devices. Selberherr[13] reviews in detail the derivation, discretization and numerical solution of these equations.

The value of the electrostatic potential is arbitrary within a constant, and for homogeneous semiconductors, it is conventional to equate it to the intrinsic Fermi level.[13] For heterojunctions, it is more appropriate to identify the electrostatic potential with the local vacuum level,[9] and specify band alignments through the spatially dependent electron affinity, χ.[14]

Other differences between simulations of homogeneous and heterogeneous semiconductors are that the material parameters vary with positions, and the electric field, $\vec{F}=-\nabla\psi$, in Eq. (3) must be replaced by $\frac{1}{q}\nabla E_c$ or $\frac{1}{q}\nabla E_v$, the gradients of the conduction or valence band edges.[15] Besides χ, the position-dependent material parameters are the band gap energy, the permittivity, and the densities of states for electrons and holes. The mobilities, diffusion coefficients, and recombination rates are treated as position-dependent in both homogeneous and heterogeneous semiconductors, because they vary with doping, carrier concentration, or electric field. Mobility values are determined either through lookup tables, or analytic functions, while D_n and D_p are related to μ_n and μ_p by the Einstein relation.

SEDAN[9] and PISCES[10,11] numerically solve the device equations under steady-state and time-transient conditions for ψ, n, and p subject to several boundary conditions. These include steady-state or time-varying currents or voltages at electrical contacts, fixed carrier concentrations at ohmic contacts, and recombination velocities at surfaces, interfaces, or Schottky contacts.

Recombination rates include Shockley-Read-Hall,

$$c_{Tn}c_{Tp}\,(np - n_i^2\,)/(c_{Tn}[n + n_1\,] + c_{Tp}[\,p + p_1]) \quad (4)$$

$$n_1 = N_c e^{-(E_C - E_T)/kT}, \quad p_1 = N_v e^{-(E_T - E_V)/kT}, \quad (5)$$

radiative,

$$B(np - n_i^2\,), \quad (6)$$

and Auger,

$$(c_n n + c_p p)(np - n_i^2), \quad (7)$$

where c_{Tn}, c_{Tp}, B, c_n, and c_p are material or doping dependent parameters, N_C and N_V, the conduction and valence band densities of states, E_C and E_V the conduction and valence band energies, and E_T, the trap energy. In present versions, c_{Tn}, c_{Tp} may spatially vary with doping, but the radiative and Auger recombination coefficients are constants. Note that there is no explicit carrier lifetime in this formulation.

Derived quantities include the electrostatic field, currents and voltages at electrical contacts, energy bands, quasi-Fermi levels, current densities, and recombination rates. PISCES also allows lumped resistors and capacitors to be attached to contacts, and, after obtaining a solution, an optional perturbation analysis can derive the AC admittance between any two terminals.

As enhanced versions of SEDAN and PISCES, HET III and SABIR retain all the capabilities of their predecessors. SEDAN has heterojunction capabilities and can model silicon, GaAlAs, and HgCdTe devices. Additional capabilities of the HET III version in use at SBRC include:

- analytic expressions for specification of HgCdTe composition profiles
- specification of HgCdTe composition profiles through tabular data in files
- InSb material parameters
- ability to specify material parameters for a general semiconductor in the input file
- multiple semiconductor types in one simulation (abrupt heterojunctions only)
- photogeneration due to monochromatic radiation
- quantum efficiency as a function of wavelength at a fixed bias, or as a function of bias at a fixed wavelength for InSb and HgCdTe diodes
- band-to-band tunneling across InSb and graded-composition HgCdTe p-n junctions

After obtaining a solution, HET III calculates the band-to-band tunneling current in a HgCdTe or InSb diode by numerically integrating the expression given by Anderson.[16] The method accounts for varying HgCdTe composition across the p-n junction, but is limited to low currents because it not incorporated into the device equations.

SABIR is based on a 1985 version of PISCES IIB that is limited to homogeneous semiconductor materials. The major differences between the two are SABIR's ability to model graded-composition HgCdTe devices and the inclusion of photogeneration. The incident photon flux is normally incident, may be defined by an optical aperture and have a uniform or Gaussian intensity distribution in the lateral direction.

APPLICATIONS

At SBRC, we have used HET III and SABIR to understand the physics of devices, and as tools for the development and design of detectors and detector arrays. A partial list of applications includes:

- effects of cap composition and base doping on quantum efficiency of graded heterojunction HgCdTe detectors[8]
- design and development of a bias-selectable, integrated two-color detector
- analysis of high speed HgCdTe heterojunction bipolar junction transistor[17]
- physics of epitaxial CdTe passivation interface with HgCdTe
- optical area of gate-controlled InSb diodes
- effects of composition grading in HgCdTe photoconductors
- calculation of optical area, crosstalk, and line spread and modulation transfer functions of detector arrays.

HET III Applications

As previously mentioned in the introduction, an early application of HET III was a study of the quantum efficiency in heterojunction HgCdTe photovoltaic detectors.[8] One conclusion of the study was that in steady state a 4.5kT barrier degraded quantum efficiency by a factor of 0.5, which gives significantly less decrease than predicted by the Boltzmann factor, exp(–4.5) = 0.011. The explanation is that the rate of minority carrier holes escaping over a barrier of height E_B is proportional to $p_n \exp(-E_B/kT)$, where p_n is the minority carrier concentration in the n-type region. In the presence of steady state illumination, the barrier impedes collection of photogenerated holes and causes an increase in p_n over the same situation without a barrier. The exact value of the increase in p_n is dependent on the barrier height, the photon flux, minority carrier lifetime, and temperature.

An important device for the next generation of IR focal plane arrays is an integrated, dual-band photovoltaic detector.[18–22] In one variation, it consists of an n-p⁺-n structure in which one of the n-type layers is mid-wavelength IR (MWIR) absorbing, and the other, long wavelength IR (LWIR). The structure is vertically integrated by inverting the sequence of the p⁺ and n layers in an LWIR p⁺-on-n diode, and merging its p⁺ layer with that of the MWIR diode. The IR radiation is incident from the side with the MWIR detector, which absorbs the MWIR flux and transmits the LWIR. A similar structure has been fabricated in InGaAsP heterostructures for wavelengths in the 0.9–1.6 µm range.[23]

If electrical contact is made to all three layers, it is possible to detect simultaneously in two spectral bands.[23] A difficulty with this approach for IR focal
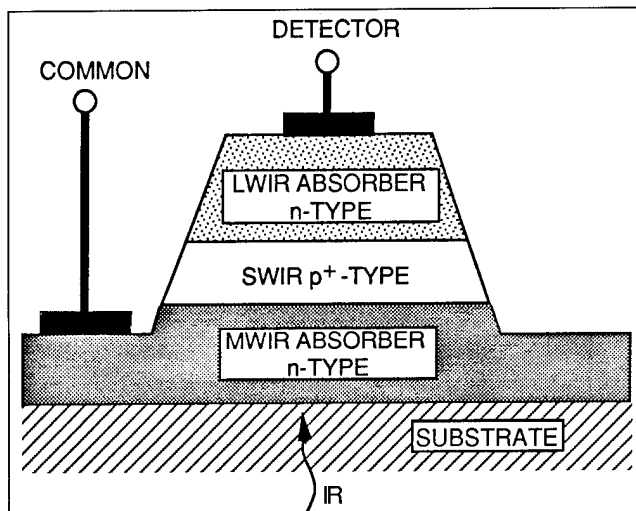
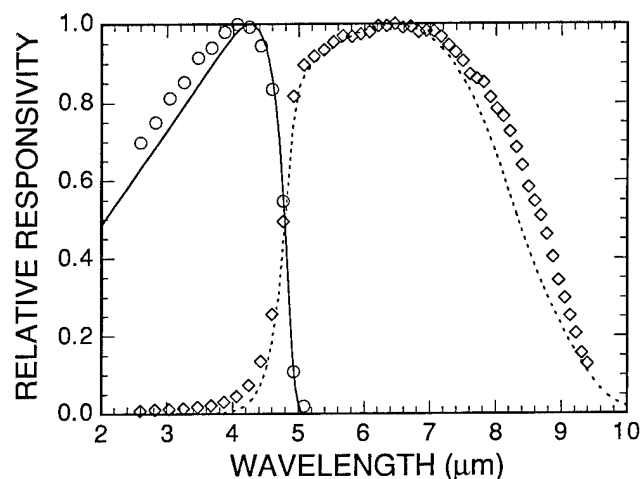Fig.1. Schematic cross section of bias-selectable, integrated two-color detector.

Fig. 2. Measured spectral responsivity (A/W), normalized to a peak value of 1, for a HgCdTe, two-color detector with zero (circles) and 200 mV (diamonds) bias applied to LWIR contact. Solid and dashed curves are calculated with HET III using experimentally measured composition and arsenic profiles.
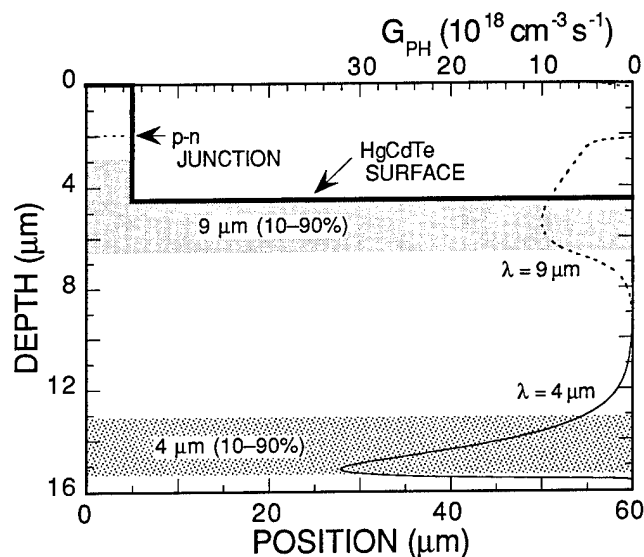

Fig. 3. Two-dimensional cross section of a backside-illuminated HgCdTe mesa diode with vertical composition profile shown in Fig. 4. The curves plotted along the right and top scales are the photogeneration rates at 4 and 9 μm with incident photon fluxes of 5×10^{15} cm^{-2} s^{-1}. The two shaded bands indicate the horizontal boundaries where 10 and 90 percent of the total photogeneration occurs at each wavelength.

plane arrays has been the requirement of at least two electrical contacts within each pixel, which can result in the optical area being significantly less than the unit cell. An alternative approach leaves the middle p$^+$ layer electrically floating, and detects either LWIR or MWIR radiation, depending on the polarity of the electrical bias applied between the contacts to the two n-type layers (Fig. 1). The polarity of device bias selects the detected wavelength band, because only the reverse-biased diode is optically active. Advantages of this approach are the need for only one electrical contact within each pixel and compatibility with existing readout integrated circuits.

Despite its apparent simplicity, the bias-selectable version requires carefull engineering to achieve good spectral selectivity. Unless suppressed by proper choice of doping and composition at the two p$^+$-n junctions, bipolar junction transistor gain can cause unwanted sensitivity to wavelengths outside the selected wave-length band.

Simple modeling of the Hg-Cd interdiffusion during liquid-phase-epitaxy growth and detector fabrication has been very useful in the development of the triple-layer structure. The HgCdTe growth and Hg-Cd interdiffusion calculations followed the method of Zanio and Massopust[24] and used the diffusion constants reported by Tang and Stevenson.[25] Together with HET III device modeling, the growth and interdiffusion modeling allowed rapid evaluation of the effects of various initial and final growth parameters for the top and middle-layers.

Figure 2 shows the relative spectral response of a two-color detector fabricated in layers from the second set of growths guided by the modeling. The growth parameters in the second set were slightly adjusted to account for the differences between the simulated and measured composition profile. The spectral response shows low MWIR response in the LWIR detection mode, the condition most susceptible to the undesirable effects of transistor gain. The HET III calculations, based on the measured composition and As doping profiles, are in good agreement with the experimental data.

SABIR Applications

We have used 2D device simulations with SABIR mostly for the analysis of optical area and crosstalk in detector arrays. Another application was in calculating the optical area of gated InSb diodes.

The diode cross section illustrated in Fig. 3, is an example that illustrates the use of SABIR to analyze 2D effects in the spectral response of detectors. The cross section represents the right half of a symmetric mesa diode centered about the left vertical axis. The original wafer surface is along the top axis, while the

heavy line represents the HgCdTe surface after formation of the mesa. The region in the box enclosed between depths of 0 and 4.5 µm and lateral positions of 5 and 60 µm is an insulator. The grown p⁺-n junction of the diode is located at a depth of 2 µm and is shown as the dashed line between the left vertical axis and the mesa sidewall.

The composition profile is constant in the horizontal direction for any given depth, while in the vertical direction, the composition varies as shown in Fig. 4. The two curves at the right of Fig. 3 are the photogeneration rates as a function of vertical depth for radiation incident from the bottom at wavelengths of 4 and 9 µm. The magnitudes of the photogeneration rates are given by the top horizontal axis.

Because of the composition grading in the HgCdTe, the photogeneration rate for the 4 µm wavelength peaks close to the bottom surface, while that for the 9 µm, near the top. The shaded areas at the top and bottom surfaces delineate the vertical depths between which 10 and 90 percent of the total photogeneration occurs for uniform lateral illumination at the two wavelengths. In the area to the right of the mesa, a significant fraction of the 9 µm radiation is not absorbed because of the HgCdTe removed to delineate the diode.

Two important effects determine the responsivity of the detector. The first is the fraction of the incident radiation absorbed, and the second is the optical area. One of the factors determining optical area is the amount of lateral collection, which is larger for minority carriers created closer to the back surface. For this reason, there will be enhanced detector response to shorter wavelengths. This effect, as well as the loss of LWIR absorbing HgCdTe due to the mesa delineation, results in a 2D calculation giving a shorter cutoff wavelength than a 1D. Figure 5 compares the relative spectral responsivity as calculated in 1D by HET III and 2D by SABIR.

FUTURE DIRECTIONS

The SBRC approach to HgCdTe device modeling, as established on the Manufacturing Science Program, has been to adapt and customize the silicon TCAD tools developed at Stanford University. Stanford has discontinued development of SEDAN and is concentrating on 2D and 3D device models. The next PISCES release should occur in the last quarter of 1993, and is expected to include new capabilities such as:

- heterostructures and multiple semiconductor types in a simulation
- hot carriers and lattice heating with separate temperatures for the lattice, electrons and holes, thermal diffusion in the lattice and energy transport by carriers
- an improved AC small-signal analysis technique that allows calculations into the 10^{14} Hz range
- mixed device and circuit modeling through an interface that allows circuit simulators to call PISCES directly.

From a user's perspective, PISCES is a state-of-the-art device modeling tool, but has limited plotting and visualization capabilities, and no support. It is distributed as Fortran and C source code, and, as a research vehicle, is not intended to meet the standards of commercial software. Two companies, Technology Modeling Associates (Palo Alto, CA) and Silvaco International (Santa Clara, CA), offer commercialized versions of PISCES with various proprietary enhancements. Source code for these versions is restricted to certain modules, making it difficult to modify. A third company, Dawn Technologies (Sunnyvale, CA), has developed a new 2D device model that is user-extensible and includes heterojunction capabilities, photogeneration with ray tracing, and a HgCdTe materials library.

The Santa Barbara Research Center hopes to upgrade SABIR by merging its modifications into the anticipated new version of PISCES. Needed improvements for the simulation of HgCdTe IR detectors and focal plane arrays include an optical source distributed in wavelength, optical ray tracing and reflection from interfaces, transport across abrupt hetero-
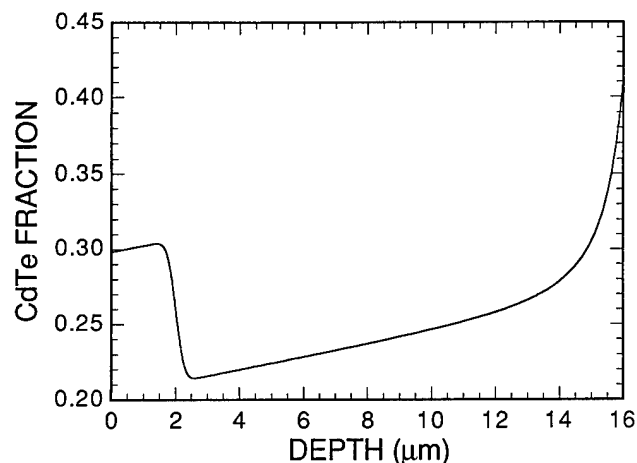

Fig. 4. HgCdTe composition profile used for calculations in Fig. 3 and Fig. 5.
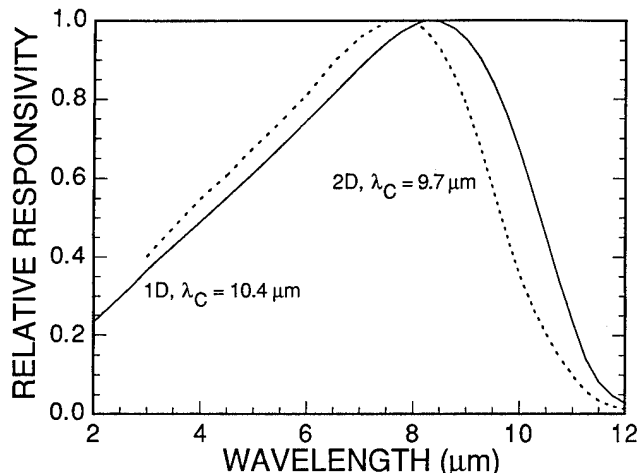

Fig. 5. Spectral responsivity (A/W), normalized to unity peak values, as calculated by HET III in 1D and SABIR in 2D.

junctions, and 2D tunneling. Desired HgCdTe-specific enhancements to SABIR include improved mobility models with dependences on composition, doping and temperature, calculation of the Auger and radiative recombination coefficients as spatially varying functions of composition, and the effects of nonparabolic bands. Advanced detector structures require the ability to model anisotropic transport, such as in quantum wells and superlattices, and may require calculation of quantum effects.

CONCLUSION

Numerical device modeling is necessary for the simulation of HgCdTe devices with spatially varying composition. The Santa Barbara Research Center has found the 1D and 2D device models, HET III, and SABIR, to be invaluable tools for the analysis and development of HgCdTe, InSb, and Si photodetectors. In these applications, the models are best suited for calculations that include photogeneration. It is difficult to calculate leakage currents and diode R_oA accurately due to numerical inaccuracies at small currents, as well as the sensitivity of actual devices to uncontrolled and unknown variables. Effects such as lateral collection, tunneling and impact ionization are also sensitive to variations in 3D.

In the past, development of HgCdTe models has heavily relied on SEDAN and PISCES, simulators originally developed for silicon devices. In recent years, developments such as Si-Ge and III-V heterostructures have resulted in the incorporation of heterojunctions into PISCES. Infrared detectors generally operate at low currents and electric fields, although there is interest in p-i-n devices operated at high reverse biases for high speed applications, as well as HgCdTe avalanche photodiodes in the 1.3–1.5 µm spectral region. The direction of the silicon IC industry is toward smaller device geometries, and higher electric fields and current densities, where hot carrier and energy transport effects become important. Consequently, the developments for silicon device models may diverge from the interests of the HgCdTe detector community.

HgCdTe device modeling is now a mature field and can no longer rely on developments intended for the silicon industry. There will be an increasing emphasis on capabilities specific to the needs and physics of HgCdTe-based devices. Finally, to be of maximum utility, device simulators must be used in conjunction with accurate process simulators. The latter are just becoming available and require fundamental understanding of the physics and chemistry of the HgCdTe material system.

ACKNOWLEDGMENTS

REFERENCES

1. R.W. Dutton and M.R. Pinto, *Pro. IEEE* 74, 1730 (1986).
2. R.W. Dutton and Z. Yu, *Technology CAD Computer Simulation of IC Processes and Devices* (Boston: Kluwer Academic Publishers, 1993).
3. P.W. Kruse, *Semiconductors and Semimetals*, eds. R.K. Willardson and A.C. Beer, (New York: Academic, 1981), Vol. 18, Chap. 1.
4. P.R. Bratt, *J. Vac. Sci. Technol. A* 1, 1687 (1983).
5. P. Migliorato and A.M. White, *Solid State Electronics* 26, 65 (1983).
6. P.R. Bratt and T.N. Casselman, *J. Vac. Sci. Technol. A* 3, 238 (1985).
7. F.L. Madrasz and F. Szmulowicz, *J. Appl. Phys.* 62, 3267 (1987); *J. Appl. Phys.* 64, 6373 (1988); *J. Appl. Phys.* 66, 3082 (1989).
8. K. Kosai and W.A. Radford, *J. Vac. Sci. Technol. A* 8, 1254, (1990).
9. Z. Yu and R.W. Dutton, *SEDAN III-A Generalized Electronic Material Device Analysis Program,* Integrated Circuits Laboratory, Stanford University, unpublished technical report (1985).
10. M.R. Pinto, C.S. Rafferty and R.W. Dutton, *PISCES II: Poisson and Continuity Equation Solver,* Stanford Electronics Laboratories, Stanford, University, unpublished technical report (1984).
11. M.R. Pinto, C.S. Rafferty, H.R. Yeager and R.W. Dutton, *PISCES II Supplementary Report,* Stanford Electronics Laboratories, Stanford University, unpublished technical report (1985).
12. K. Hess, *Advanced Theory of Semiconductor Devices,* (Englewood Cliffs, NJ: Prentice Hall, 1988).
13. S. Selberherr, *Analysis and Simulation of Semiconductor Devices* (New York: SpringerVerlag, 1984).
14. A.G. Milnes and D.L. Feucht, *Heterojunctions and Metal-Semiconductor Junctions* (New York: Academic, 1972), Chap. 1.
15. A. H. Marshak, *IEEE Trans. Electron Deuices* 36, 1764 (1989).
16. W.W. Anderson, *Infrared Physics* 17, 147 (1977).
17. M. Jack, G. Chapman, M. Kalisher, K. Kosai, J. Myrosznyk, W. Radford, M. Ray and O. K. Wu, *Models and Measurement of $Hg_{1-x}Cd_xTe$ Heterojunction Transistors,* Intl. Electron Devices Mtg., San Francisco, CA, December 9–12, 1990.
18. E.F. Schulte, U.S. Patent No. 5,113,076, *Two Terminal Multiband Infrared Radiation Detector,* May 12, 1992.
19. T.N. Casselman, D.T. Walsh, J.M. Myrosznyk, K. Kosai, W.A. Radford, E.F. Schulte and O.K. Wu, *An Integrated Multispectral IR Detector Structure,* 1990 U.S. Workshop on the Physics and Chemistry of Mercury Cadmium Telluride and Novel IR Detector Materials.
20. J.M. Arias, M. Zandian, G.M. Williams, E.R. Blazejewski, R.E. DeWames and J.G. Pasko, *J. Appl. Phys.* 70, 4620 (1991).
21. E.R. Blazejewski, J.M. Arias, G.M. Williams, W. McLevige, M. Zandian and J. Pasko, *J. Vac. Sci. Technol. B* 10, 1626 (1992).
22. T. Tung, L.V. DeArmond, R.F. Herald, P.E. Herning, M.H. Kalisher, D.A. Olson, R.F. Risser, A P. Stevens and S.J. Tighe, *Infrared Detectors: State of the Art,* SPIE Vol. 1735, 109 (1992).
23. J.C. Campbell, T.P. Lee, A.G. Dentai and C.A. Burrus, *Appl Phys. Lett.* 34, 401 (1979).
24. K. Zanio and T. Massopust, *J. Electron. Mater.* 15, 103 (1986).
25. M.F.S. Tang and D.A. Stevenson, *J. Vac. Sci. Technol. A* 5, 3124 (1987).

Transport Studies in Narrow-Gap Semiconductors Revisited

SRINIVASAN KRISHNAMURTHY and ARDEN SHER

SRI International, Menlo Park, CA 94025

Transport-related properties such as electron mobility, Hall coefficient, Fermi level, and energy gap are calculated with accurate analytical band structures, Fermi-Dirac statistics, and a full solution to the Boltzmann transport equation. These calculated values differ substantially from the ones obtained with parabolic or k·p generated band structure approximations for a $Hg_{0.78}Cd_{0.22}Te$ alloy. A new way to analyze absorption data to extract the temperature variation of the band gap is also explained.

Key words: Band gap, calculation of accurate band structures, electron mobility, Fermi level, Hall coefficient, HgCdTe

INTRODUCTION

Approximations such as parabolic band structures, Maxwell-Boltzmann (MB) statistics for electrons, and neglect of the gain term in the Boltzmann transport equation (BTE) (commonly known as collision time approximation) are often used to compare against and interpret experimental results. These approximations are often made to both elastic and inelastic scattering mechanisms. Even in large-gap materials, the constant effective mass approximation is valid only very near (within $\approx E_g/10$) to the band edge.[1,2] This approximation is particularly poor for narrow gap materials, and nonparabolic corrections calculated in the k·p formalism are often used.[3–5] Although this correction is substantial, it still differs considerably from our more accurately calculated band structures. However, our fit of these more accurate conduction bands to an analytical function makes many

results transparent and simplifies the calculations. As the Fermi energy can easily move into the conduction band of lightly doped small-gap materials, the form of the Boltzmann equation with Fermi-Dirac (FD) (instead of the usual MB) statistics must be used to obtain accurate transport coefficients.

In this paper, we report results from our study of absorption coefficients, Fermi energies, and Hall coefficients calculated with Fermi-Dirac statistics, accurate pseudopotential band structures fine tuned with tight-binding (TB) corrections, and the mobility with a full solution to the BTE.

BAND STRUCTURE

Quantitatively accurate band structures of most semiconductors[6–8] can be obtained using a minimum set of sp^3 orbitals in semi-empirical calculations. First, for each alloy constituent, empirical pseudopotential form factors are used to calculate a TB Hamiltonian, H in the minimum set. This H is then transformed into a zeroth order Hamiltonian H_0 in an orthonormal
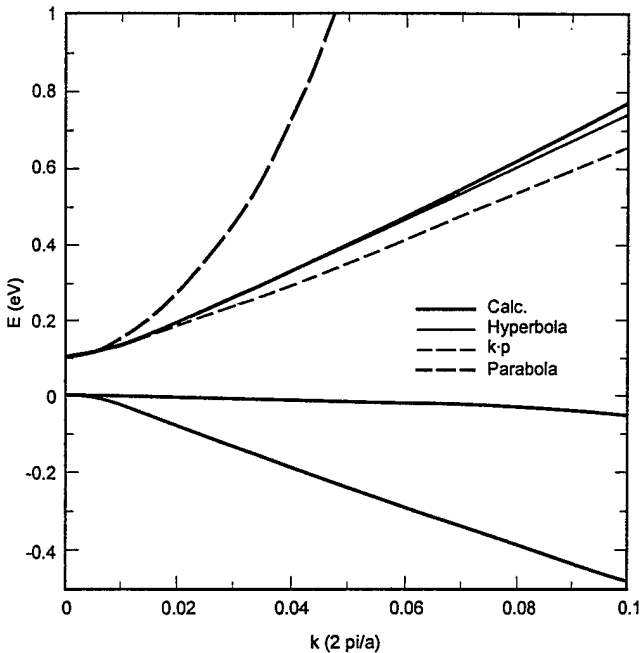
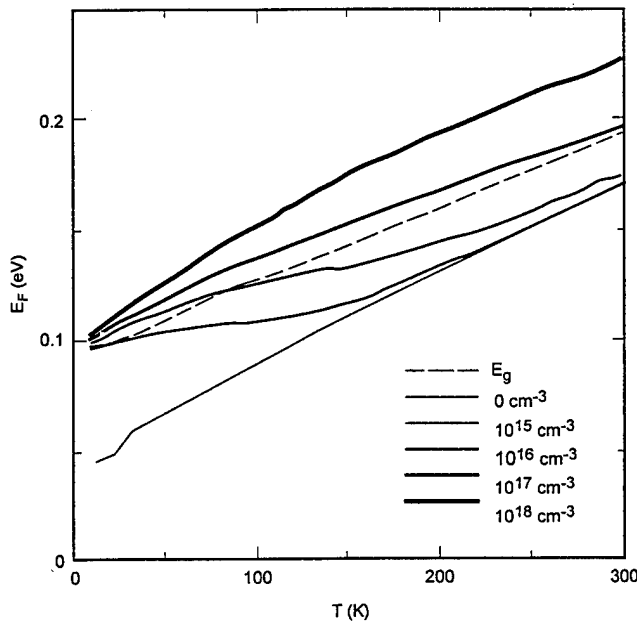Fig. 1. Our approximation to 77K electronic structure of $Hg_{0.78}Cd_{0.22}Te$.

Fig. 2. Fermi energy as a function of temperature:hyperbolic bands. The dashed (experimental) curve is from Ref. 10.

basis. Then a perturbative Hamiltonian having a first-neighbor TB form is added to H_0 to fine tune the band structure to fit the measured symmetry point energies. Because long-range interactions are included in this Hamiltonian, the measured band curvatures are correctly reproduced. This procedure is followed for both HgTe and CdTe, and then the alloy band structures are calculated in the coherent potential approximation.

We focus on the $Hg_{0.78}Cd_{0.22}Te$ alloy with band-gap energy ranging around 100 meV at low temperature for the studies reported here. We find that the calculated conduction band is replicated very well by a

hyperbola,

$$E_k = (\gamma k^2 + c^2)^{1/2} - c \qquad (1)$$

where γ and c are adjusted to fit the calculated band structure in the energy range of interest. When γ and c are treated as constants related to the band gap, E_g and the effective mass, this expression reduces to the same nonparabolic correction form obtained in the $k \cdot p$ method.[4] However, the numerical values of γ and c are not same as ours. For example, in the chosen case, γ and c are 48.3 and 0.058, respectively, whereas the corresponding $k \cdot p$ values are 36.0 and 0.05. The differences are found to be large enough to cause a noticeable change in the band structure and transport properties. The band structure calculated by diagonalizing the Hamiltonian is shown in Fig. 1 (thick line). We can see that the fitted hyperbola (thin line) agrees quite well up to an energy of 0.5 eV from the conduction band edge. Without loss of accuracy, in the studies considered here, Eq. (1) is used as the energy dispersion relation in transport expressions that follow. Also shown in Fig. 1 is the poor reproduction of the conduction band obtained with an effective mass approximation (long dashed line) and that with usual nonparabolic ($k \cdot p$) correction (short dashed line).

Two qualitative features of the band structure in Fig. 1 that impact transport properties should be noted. First, for energies $E - E_c$ greater than 50 meV where the shape of the conduction band is nearly linear in k the group velocity is nearly a constant independent of k. Then, the density of states (DOS) increases proportional to E rather than $E^{1/2}$ as in the case of parabolic bands. Clearly these features modify the transport properties of electrons occupying these states. As we will show in the following section, at the carrier concentration and temperatures often found in device structures, the Fermi level falls into the region where these features contribute to transport properties.

FERMI LEVEL

The calculation of the Fermi level, ϵ_F as a function temperature, T and doping concentration, n_D is required for all transport calculations. A knowledge of temperature-dependent gap $E_g(T)$ is essential to obtain accurate values of ϵ_F in narrow gap material. Ideally, the temperature dependence should be deduced by including electron-phonon terms and lattice dilation in the Hamiltonian from which the variation of Eg with T can be obtained. We have developed a general method to incorporate the phonon and alloy effects into the same CPA formalism,[9] but such an approach is not attempted here. Instead, we use the empirically deduced expression[10] given by

$$E_g = 0.0954 + 0.327T/1000 \qquad (2)$$

Although the gap has been fitted to a number of different analytical functions,[10–12] we chose the above expression simply to demonstrate the effects of various approximations. After obtaining trends, we in-

tend to repeat these calculations with a proper treatement by including the electron-phonon interaction Hamiltonian.

Here ϵ_F is calculated from the condition[13] that at a given T the number of electrons in the conduction band is the sum of electrons excited from the valence band and the donor levels. In this study, where the modifications caused by the band structures are being emphasized, the donor states are assumed to be located at the bottom of the conduction band.[14] The valence and conduction band DOS are calculated from our band structure. The valence band DOS yields an average hole effective mass of 0.65. The ϵ_F (relative to the valence band edge) as a function of T and n_D are given in Fig. 2. We found that the more accurate hyperbolic band is substantially different from parabolic-band generated values. The impact of these differences on the transport properties will be large when ϵ_F is located near the energy where the band changes its character from parabolic to linear. Also, when ϵ_F is near to or greater than E_g, the absorption cutoff wavelength is strongly influenced because the transition cannot take place to filled states. A proper account of this effect, called the Moss-Bernstein shift, must be included along with these accurate band structures. In addition, we note that the Fermi level and the measured band gap affect each other. The changes in the gap are accompanied by band curvature changes. The gap and the curvature change affect the Fermi energy, which in turn affects the apparent measured band gap. Hence, a proper interpretation of optical absorption to deduce the energy gap has to be done self-consistently to include both these effects.

ENERGY GAP

In order to emphasize the point that the measured value of E_g and its T dependence is sensitively dependent on the self-consistent determination of the band shapes and ϵ_F, we carried out a preliminary calculation of the absorption coefficient α. The absorption coefficient α is proportional to $k^2 \rho_c (1-f_c) \rho_v f_v$, where f is a k dependent FD distribution function, ρ is a k dependent DOS, and subscripts c, v represent conduction and valence band, respectively. The k^2 factor arises from the matrix elements that are in the expression for α. The temperature and energy-independent proportionality constant, which arises from the square of the overlap matrix element, is adjusted to agree with an experimental curve at 80K in the vicinity of a given value of $\alpha(\lambda)$ at wave length λ. A nearly linear dependence of $\log(\alpha)$ on λ was observed[15] for various T between 80 and 300K and Cd concentrations near 0.22.

Because the band edges are often broadened by impurity and phonon scattering (known as Urbach tails), the gap cannot simply be assigned to the energy corresponding to the apparent cutoff wavelength λ_{co} where these curves project to zero. The procedure used by many authors[11] is to assign λ_{co} to be the place where α is 500 cm^{-1} or 1000 cm^{-1}. The justification for this procedure is that the actual unbroadened shape of $\alpha(\lambda)$ is very sharp and if the Urbach tail ends at 500 cm^{-1} or 1000 cm^{-1}, then the corresponding λ at which this occurs will be close to the actual λ_{co}. In the spirit of this procedure, we adjust the proportionality constant to fit the $\log(\alpha)$ vs photon energy E curve at 80K. As seen from Fig. 3a, we find that this one constant fits nearly the entire curve at 80K. The constant is chosen such that the calculation and experiment agree very well in the vicinity of 500 cm^{-1}. There is little, if any, Urbach tail at this temperture. Once the constant is determined by this procedure, it is used for every temperature. At higher temperatures, the tails are present. We then artificially adjust the band gap
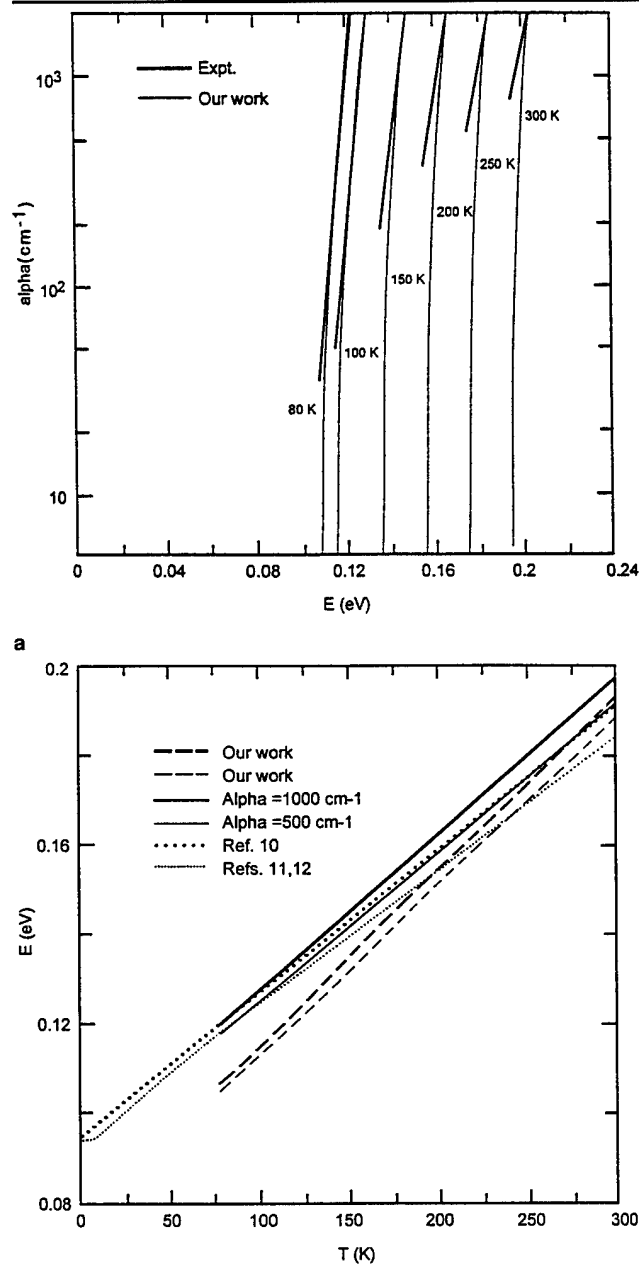

Fig. 3. (a) Absorption coefficient as function of photon energy; (b) energy gap as a function of temperature.
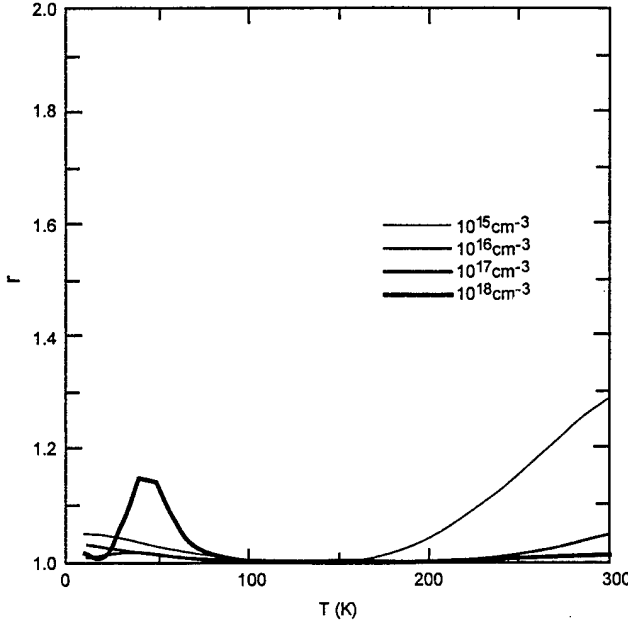
Fig. 4. Hall factor as a function of temperature: hyperbolic bands.

(with its corresponding band curvature) to mock the temperature variation by changing the Cd concentration until the calculated α curve fits a point on the experimental curve. In the course of this procedure, the Fermi energy also changes, which necessitates that the calculations be done iteratively until self-consistency is reached. The theoretical curve is then used to project the effective band gap. Fig. 3a displays the curves so obtained. The temperature variations of the energy gaps deduced in this way, with two different proportionality constants, are shown in Fig. 3b (dashed lines). Also shown in Fig. 3b (solid lines) for comparison are effective E_g vs T variations if values are taken from the data[15] corresponding to α at 500 cm^{-1} and at 1000 cm^{-1}. Also, the experimental energy gap and its temperature variation measured by different groups[10-12] are plotted (dotted lines) in Fig. 3b for comparison. It is clear that various experiments differ substantially from each other. Also note that our curves are lower than the ones that are normally deduced from the same experiments, and the variation in T is no longer linear. Once the proportionality constant is calculated from our band structures, the energy gap is expected to lie between the two dashed lines shown here. However, the gap at T = 0K predicted by our band structure method is in agreement with that of Refs. 10–12. The E_g(T) will start with a zero slope[12] and connect smoothly to our 80K value. A nonlinear variation of E_g at much lower T, however, has been observed in recent two-phonon experiments.[12] All these results emphasize the need for proper calculations of E_g(T), and α(T) so that more reliable device parameters can be established.

HALL COEFFICIENT

The carrier density, n in n-type material, is normally deduced from measurements of Hall coefficients R_H, given by r_e/en, by assuming the Hall factor

r_e is unity. If one uses a parabolic approximation for the conduction band and MB statistics, r_e, is approximately unity. We set out to examine the effect of removing these approximations using the correct band structures. It requires generalizing the BTE to include FD distribution functions, f(k). We start from

$$\frac{df(k)}{dt} =$$

$$\sum_{k'}\left[w(k,k')f(k')(1-f(k)) - w(k',k)f(k)(1-f(k'))\right] \quad (3)$$

The first term of the right side is the gain term and the second one is the loss term. As a consequence of general statistical mechanics arguments,[16] the ratio of transition probabilities is such that $w(k,k')\ e^{-\beta E_{k'}} = w(k',k)\ e^{-\beta E_k}$. In equilibrium, the left side of Eq. 3 is identically zero and f from Eq. 3 becomes the equilibrium FD distribution function f_0 given by

$$f_0(E_k) = \left(e^{\beta(E_k-\epsilon_F)} + 1\right)^{-1} \quad (4)$$

where β is $(k_B T)^{-1}$. In the presence of electric and magnetic fields,

$$\frac{df(k)}{dt} = \frac{\partial f(k)}{\partial t} + \nabla f(k) \cdot \frac{e}{\hbar}(E + v \times B) \quad (5)$$

In steady state, the $\partial f(k)/\partial t$ in Eq. (5) vanishes. In the small field regime, we can linearize f and write it as a sum of f_0 and a perturbation $f_1(k)$. Discarding the derivative of $f_1(k)$ and after some algebraic manipulation, Eq. (5) reduces to[17]

$$\nabla f_0(k) \cdot \frac{e}{\hbar}(E + v \times B) =$$

$$\sum_{k'}\left[W(k,k')f_1(k') - W(k',k)f_1(k)\right] \quad (6)$$

where the renormalized W and the usual transition probability per unit time w are related by

$$W(k,k') = w(k,k')\frac{(1-f_0(k))}{(1-f_0(k'))} \quad (7)$$

Note that for elastic scattering W and w are equal. However, for inelastic cases, the effect depends on whether the energies at k and k' are larger or smaller than ϵ_F. If both initial and final energies are larger (or smaller) than eF, then only a small correction to w is expected. However, if the initial state is above ϵ_F and the final state is below ϵ_F, then that scattering is suppressed.

In the collision time approximation, the gain term in Eq. (7) is neglected and the effective collision time, τ_k^F is

$$\left(\tau_k^F\right)^{-1} = \sum_{k'}W(k',k) \quad (8)$$

Using this collision time approximation, it is straight-forward to obtain the expression for r_e.

$$r_e = 3k_B T \left[\frac{\sum_k f_0 \sum_k k^2 \gamma_k^3 (\tau_k^F)^2 f_0 (1-f_0)}{\left(\sum_k k^2 \gamma_k^2 \tau_k^F f_0 (1-f_0) \right)^2} \right] \quad (9)$$

where $V_k E_k$ is $\gamma_k k$. The r_e value calculated from Eq. (9) with parabolic bands is approximately 1 for higher temperatures but shows considerable structure with a maximum value of about 2 at lower temperatures. However, when the more accurate hyperbolic band structure is used, the variation at low T is reduced to a maximum value of about 1.2, suggesting that re-ported intrinsic densities may be smaller in this temperature range by approximately 20%. The calcu-lated r_e with hyperbolic band structures are shown for various T and doping densities in Fig. 4. The effect of removing the collision time approximation and add-ing T dependence of band gap on the values of r_e still needs to be studied to extract correct carrier densities from Hall measurements. However, our tentative conclusion is that approximating r_e to be 1 is better than we had reason to expect.

DRIFT MOBILITY

The collision time approximation in the formalism developed above is removed, and a full solution to BTE with FD statistics[17] is used to calculate the mobility μ. The details of this generalization are being published elsewhere and only the results are summa-rized here.[17] This method is a generalization of the one to solve the Boltzmann equation with MB statistics.[18]

In Fig. 5, we compare the mobilities calculated in various approximations to experiments. The carrier concentration in the calculations was set equal to that used in the experimental value of $5 \times 10^{14} cm^{-3}$. Two experimental data sets taken on LPE material[19,20] are shown in Fig. 5 (dashed lines). The latest set exhibits higher mobilities for the same Cd content and carrier concentration and is presumably a better material. Also shown are the mobilities obtained from our hyperbolic band structure (thick solid line) and from the k·p band structure (thin solid line). For compari-son, the mobility obtained in the collision time approx-imation with our band structure (dotted line) is also shown in Fig. 5.

It is instructive to compare various curves in Fig. 5. All curves are calculated with the same scattering parameters. Only ionized impurity and LO phonon scattering are included. No correction due to compen-sation is included. First, our calculated mobilities are higher than those from the k·p band structure. The smaller γ deduced from the k·p method means that the DOS is larger, resulting in this lower mobility. How-ever, both curves predict a hump in the temperature variation of mobility near 40K, where phonon scatter-ing takes over from the impurity scattering, which dominates at lower temperatures. The full solution to BTE, in conjunction with the change in the Debye

screening length and phonon scattering, gives rise to this hump. Second, the collision time approximation does not produce this hump. We note that the mobility calculated with a collision time approximation grossly overestimates the scattering rate and wipes out this peak in the mobility. A smaller peak near 200K is due to changes in the Fermi energy.

Our predictions fall within ±25% of the latest ex-perimental values over the temperature range from 10 to 300K. Our calculated values are smaller at low T and larger at high T than experiments. As we demonstrated here, the electron mobility is a sensi-tive function of the shape of the band structure; we must await our better temperature-dependent band structures before improvements will be forthcoming. We have already shown from our preliminary studies of absorption coefficient that empirical gaps are as much as 20% too large. If detailed calculations verify these results, then impurity-dominated mobilities will increase at low T, and the small neglected scatter-ing mechanisms (alloy disorder, transverse optical and acoustic phonons) will decrease the mobility slightly at high T to bring the predictions into better agreement with experiments at all temperatures.

CONCLUSIONS

In this paper, we have studied the effect of various approximations on electron transport coefficients and on ways to extract physical parameters from experi-ments. We point out how the values interpreted from experiments depend crucially on various approxima-tions such as effective mass, MB statistics, and colli-sion time. The main results are:

- Approximating the Hall factor by unity over a wide range of carrier concentrations and tem-peratures is accurate for most applications. An error of about 30% is expected at high T and low carrier concentration ($10^{15} cm^{-3}$), and about 20%
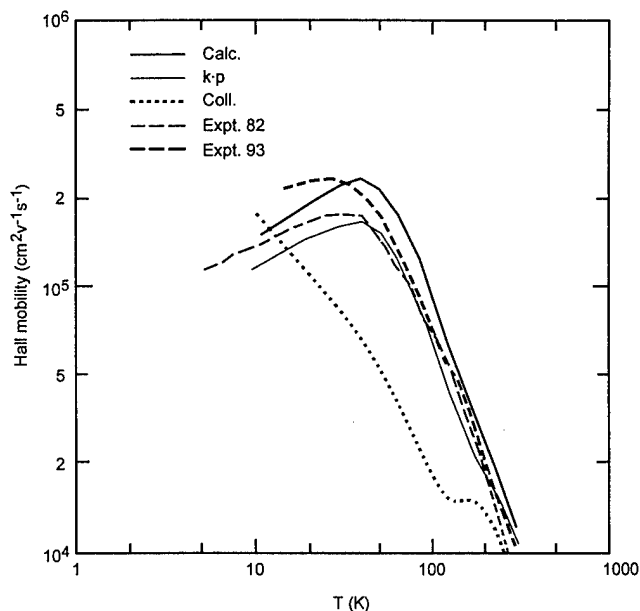
Fig. 5. Hall mobility as a function of T with various approximations.

is expected at low T and high carrier concentration (10^{18} cm^{-3}).

- The variation of the band gap with temperature for 22% Cd concentration is nonlinear and is faster at low temperature. The gap at low T is about 20 meV smaller than those usually quoted.
- The mobility calculated from a full solution to the BTE with FD statistics can explain the hump near 40K and is in good agreement with experiments. This result is obtained with no parameters in the theory adjusted to fit measured mobility data. Once the other scattering mechanisms such as acoustic and alloy disorder are included, the agreement is expected to be better.

ACKNOWLEDGMENT

REFERENCES

1. E.O. Kane, *J. Phys. Chem. Solids* 1, 249 (1957).
2. S. Krishnamurthy, A. Sher and A.-B. Chen, *J. Appl. Phys.* 61, 1475 (1987).
3. J.L. Schmidt, *J. Appl. Phys.* 41, 2876 (1970).
4. J.R. Meyer and F.J. Bartoli, *J. Vac. Sci. Technol.* 21, 237 (1982).
5. F.J. Bartoli, J.R. Meyer, R.E. Allen and C.A. Hoffman, *J. Vac. Sci. Technol.* 21, 241 (1982).
6. S. Krishnamurthy, A. Sher and A.-B. Chen, *Phys. Rev.* B 33, 1026 (1987).
7. A.-B. Chen and A. Sher, *Phys. Rev.* B 23, 5360 (1981).
8. M.A. Berding, S. Krishnamurthy, A. Sher and A.-B. Chen, *J. Vac. Sci. Technol.* A 5, 3014 (1987).
9. A.-B. Chen and A. Sher, *Phys. Rev.* B 5, 2897 (1972).
10. *Properties of HgCdTe,* J. Brice and P. Capper, eds., (New York: INSPEC, 1987) EMIS Data Review series No. 3, p. 103; and references cited therein.
11. G.L. Hansen, J.L. Schmidt and T.N. Casselman, *J. Appl. Phys.* 53, 7099 (1982).
12. D.G. Seiler, J.R. Lowney, C.L. Littler and M.R. Loloee, *J. Vac. Sci. Technol.* A 8, 1237 (1990).
13. S.M. Sze, *Physics of Semiconductor Devices* (New York: Wiley, 1981), p. 22.
14. See Ref. 17 for the case of donor level in the conduction band.
15. E. Finkman and Y. Nemirovsky, *J. Appl. Phys.* 50, 4356 (1979).
16. A. Sher and H. Primakoff, *Phys. Rev.* 119, 178 (1964).
17. S. Krishnamurthy and A. Sher, *J. Appl. Phys.* 75, 7904 (1994).
18. S. Krishnamurthy, A. Sher and A.-B. Chen, *Appl. Phys. Lett.* 55, 1003 (1989).
19. J. Bajaj, S.H. Shin, G. Bostrup and D.T. Cheung, *J. Vac. Sci. Technol.* 21, 244 (1982).
20. J Bajaj, private communication (1993).

Metalorganic Chemical Vapor Deposition CdTe Passivation of HgCdTe

Y. NEMIROVSKY, N. AMIR, and L. DJALOSHINSKI

Kidron Microelectronics Research Center, Department of Electrical Engineering, Technion, Haifa 32000, Israel

CdTe epilayers are grown by metalorganic chemical vapor deposition (MOCVD) on bulk HgCdTe crystals with x ~ 0.22 grown by the traveling heater method (THM). The THM HgCdTe substrates are (111) oriented and the CdTe is grown on the Te face. The metalorganic sources are DMCd and DETe, and the growth is performed at subatmospheric pressure. Ultraviolet (UV) photon-assisted hydrogen radicals pretreatment plays a dominant role in the electrical properties of the resulting heterostructures. The requirements of a good passivation for HgCdTe photodiodes vis-a-vis the passivation features of CdTe/HgCdTe heterostructures are discussed. The effect of valence band offset and interface charges on the band diagrams of p-isotype CdTe/HgCdTe heterostructures, for typical doping levels of the bulk HgCdTe substrates and the MOCVD grown CdTe, is presented. Electrical properties of the CdTe/HgCdTe passivation are determined by capacitance-voltage and current-voltage characteristics of metal-insulator-semiconductor test devices, where the MOCVD CdTe is the insulator. It is found that the HgCdTe surface is strongly inverted and the interface charge density is of the order of $10^{12} cm^{-2}$ when the CdTe epilayer is grown without the UV pretreatment. With the *in-situ* UV photon-assisted hydrogen radicals pretreatment, the HgCdTe surface is accumulated and the interface charge density is $-4 \cdot 10^{11} cm^{-2}$.

Key words: CdTe, HgCdTe, infrared detectors, metalorganic chemical vapor deposition (MOCVD), surface passivation

INTRODUCTION

Second generation infrared focal plane arrays based on HgCdTe photodiodes coupled to silicon signal processors, have led to increased interest in CdTe passivation.[1-3] Clearly, CdTe has become the preferred passivation technology for HgCdTe photodiodes, but the published work in the open literature addressing this passivation is rather limited (Refs. 4 and 5 and references therin).

The CdTe layers are deposited by different techniques (liquid phase epitaxy [LPE], molecular beam epitaxy [MBE], metalorganic chemical vapor depositon [MOCVD], hot wall epitaxy, sputtering, e-beam evaporation, and electrodeposition). In addition to the deposition process, there are several major issues that determine the passivation properties of the resulting

CdTe/HgCdTe heterostructures. These include the HgCdTe surface preparation and *in-situ* pretreatment, deposition-induced surface damage, interface charges, CdTe film stoichiometry, and electrical properties. Additional issues are related to adherence, step coverage, and thermal stability.[1,4]

The surface and interface pretreatments are a very important part of the MOCVD CdTe deposition technology. In principle, heterostructures that are grown in a single run in the well controlled environment of MOCVD (or MBE) systems should yield high quality interfaces with reduced interface charges. However, in the currently used device designs and architectures,[1] the CdTe passivation is deposited after the required processing steps. The HgCdTe surface is necessarily nonstoichiometric, contaminated (with foreign impurities and oxides) and damaged (in crystallinity). The chemical, structural, and electronic defects induce high density of fixed, fast, and slow

647

Table I. Requirements of a Good Passivation and Passivation Featurs of CdTe/HgCdTe Heterostructure

Requirements of a Good Passivation	Passivation Featurs of CdTe/HgCdTe
Interface Properties	
Surface Potential: near flat band	Band diagram depends on: CdTe and HgCdTe doping, valence band offset, interface charges and traps can be engineered to near flat band
Fixed, fast, slow states: low density	Determined by *in-situ* pretreatment
Surface Recombination Velocity: low	Barriers to electrons and holes are formed
Dielectric, Insulating, and Mechano-Chemical Propeties	
Good Insulator	Compensated or fully depleted
Excellent Adhesion	Similar chemistries
Chemical and Mechanical Stability	Lattice Matching (0.3%) Matching in thermal expansion Adequate mechanical hardness
Thermal Stability	Stable up to 150°C
Optically Transparent	Above 0.8 µm
Exhibits Radiation Hardening	High Z materials (48, 52), efficient absorber of high energy radiation
Deposition Technology	
Low Temperature Nondamaging	MOCVD, MBE, LPE, hot wall epitaxy Sputtering, evaporation, electrodeposition.

interface traps. Hence, an *in-situ* pretreatment that forms a reproducible and well-behaved hetero-interface, is a crucial part of the deposition process. Finally, it is important to develop a deposition process that will not introduce a deposition damage at the interface.

In this study, we grow CdTe epilayers (by the MOCVD growth technique) on bulk HgCdTe substrates and characterize the resulting interfaces. Metal-insulator-semiconductor test structures are processed and measured by capacitance-voltage and current-voltage characteristics. The ultraviolet (UV) photon-assisted hydrogen radicals pretreatment is studied and reported.[6,7]

THE REQUIREMENTS OF A GOOD PASSIVATION AND THE CORRESPONDING FEATURES OF CdTe/HgCdTe HETEROSTRUCTURE

The requirements of a good passivation for HgCdTe photodiodes and the passivation features of the CdTe/HgCdTe heterostructure are summarized in Table I. The required interface properties must be achieved without any compromise. These include: a well controlled and close to flat band surface potential and hence a low density of fixed surface charges to reduce tunneling currents (accumulated surfaces impose tunneling at the periphery of the junction and inverted surfaces impose tunneling to the substrate); a low density of fast and slow surface states to reduce low frequency noise currents; a low surface re-

combination velocity to reduce surface generated dark currents.

The required dielectric, insulation, and mechano-chemical properties are also highly stringent so that the passivation will be fully compatible with device processing, bonding and packaging, prolonged out-gassing, storage, and exposure to harsh environments. Finally, a low temperature nondamaging deposition technology is a must in the case of a passivation film for HgCdTe.

The major passivation features of the CdTe/HgCdTe heterostructure that are summarized in Table I indicate why CdTe has recently become the industry-favored passivation technology for HgCdTe photodiodes.[1] The calculated band diagram (and thus the surface potential at the HgCdTe side of the hetero-interface) depends on the valence band offset, doping levels of CdTe and HgCdTe, surface charges and traps at the hetero-interface and deep traps in the CdTe. Precise control of the electrical properties of the CdTe and the interface charges must be achieved to obtain the required interface properties. A low surface recombination velocity is readily achieved because potential barriers for electrons and holes are formed. In particular, the large conduction band offset forms a large barrier for electrons. The band diagram of CdTe/HgCdTe abrupt heterostructure is calculated and further evaluated in the following section.

CdTe is not hygroscopic (like ZnS), it is mechanically harder than HgCdTe, the heterostructure is nearly lattice matched (within 0.3%), the thermal coeffi-

cients of expansion of both materials are nearly the same and the chemistries are similar. Hence, CdTe films are negligibly stressed and adhesion is excellent (between CdTe and HgCdTe, CdTe, and subsequent metallization lines, CdTe and anti-reflection coatings for front-illuminated photodiodes). Chemical, mechanical, and thermal stability (up to 150°C) is reported. The high average atomic number of CdTe (Z_{Cd} = 48, Z_{Te} = 52) renders this material an efficient absorber of high energy radiation and efficient for radiation hardening.

A large number of low temperature deposition technologies are available for epitaxial CdTe (including MOCVD, MBE, LPE, hot wall epitaxy) as well as polycrystalline CdTe films (including e-beam evaporation, sputtering, electrodeposition).[4]

The preferred CdTe technology for passivation should be determined and tailored to the specific device design and architecture. The present study focuses on MOCVD CdTe because it is a dry process with high throughput and energetic species are not incorporated in the deposition process. The MOCVD process yields reproducible hetero-interfaces as well as CdTe epilayers which can be engineered to the exacting requirements discussed above. In addition, excellent step coverages are obtained and the morphology is mirror like. Surface recombination velocity of less than 5000 cm/s, obtained with MOCVD CdTe, is the lowest reported value for p-type long wavelength infrared (LWIR) HgCdTe.[5]

BAND DIAGRAM OF A CdTe/HgCdTe ABRUPT HETEROSTRUCTURE

Two equations govern the interface potentials in the two sides of the hetero-interface. These two equations enable us to calculate the total band bending (relative to the bulk) of each material, and thus the interface potentials of HgCdTe and CdTe (denoted by $\phi_{o,HgCdTe}$, $\phi_{o,CdTe}$, respectively).

The first equation is based on the lineup considerations of the bands of the two materials across the common Fermi level, as shown in Fig. 1.

$$E_{FV_{CdTe}} - E_{FV_{HgCdTe}} - \Delta E_V = q(\phi_{o,HgCdTe} - \phi_{o,CdTe}) \quad (1)$$

where ΔE_V is the valence band offset and $E_{FV_{CdTe}}$, $E_{FV_{HgCdTe}}$ are shown in Fig 1.

The second equation is based on the neutrality condition

$$Q_{CdTe}(\phi_{o,CdTe}) + Q_{HgCdTe}(\phi_{o,HgCdTe}) + q\sigma = 0 \quad (2)$$

where Q_{CdTe} and Q_{HgCdTe} are the total charge per unit area in the CdTe and HgCdTe, respectively and σ is the interface charge density.

These two charges can be expressed by the total band bending in each material (relative to the bulk of each material). Therefore, we have two equations and two variables, $\phi_{o,HgCdTe}$, $\phi_{o,CdTe}$, that can be obtained provided ΔE_V and σ are given. In practice, the valence band offset and the interface charges are not determined with the required accuracy. Measured values of the valence band offset ΔE_V range from 0 to 0.35 eV but there is more or less a consensus around 0.1 eV.[8,9] The interface charge density σ is partly fundamental (due to the difference in chemical bonding and 0.3% lattice mismatch across the hetero-interface) and partly technological (due to mechanical damage, nonstoichiometric surface, surface oxides and adsorbed impurities). It strongly depends on processing, pretreatment and deposition technology. Accordingly, σ can vary by several orders of magnitude.

Following the methodology previously developed for the calculation of a HgTe-CdTe abrupt heterostructure,[10,11] we present the calculated interface potentials of CdTe and HgCdTe, with ΔE_V and σ taken as parameters. This approach enables us to calculate the band diagram of the hetero-interface and to consider quantitatively the effects of ΔE_V and σ on the total band bending in each material. The detailed
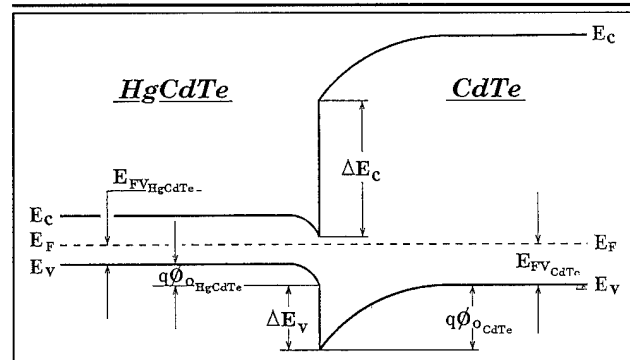
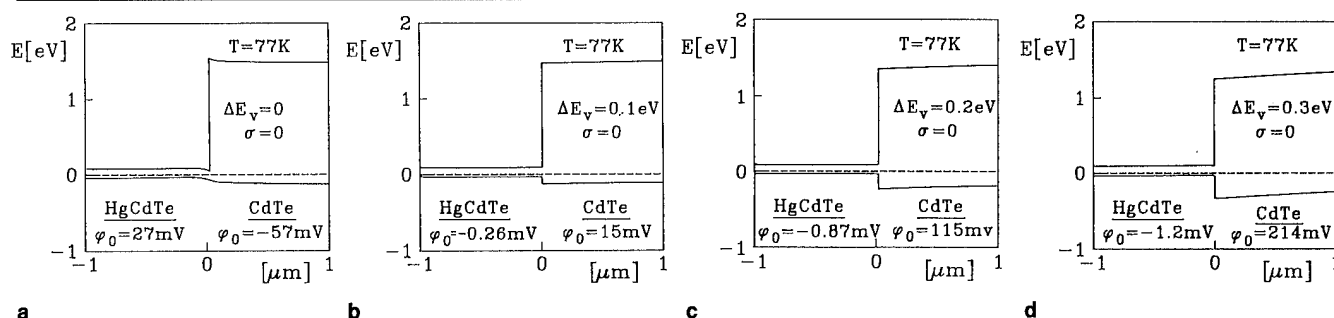Fig. 1. Schematic energy band diagram of an abrupt CdTe/HgCdTe heterostructure.

Fig. 2. Calculated band diagrams and surface potentials, (ϕ_o) at 77K, of p-CdTe ($N_a = 10^{13}$ cm^{-3} and $E_a = 0.15$ eV/p-HgCdTe (x = 0.225 and $N_a = 10^{16}$ cm^{-3}) heterostructures with the valence band offset as a parameter (a) $\Delta E_V = 0$; (b) $\Delta E_V = 0.1$ eV; (c) $\Delta E_V = 0.2$ eV; (d) $\Delta E_V = 0.3$ V. The interface charge density σ is taken as zero.

calculation of the band diagram of an abrupt CdTe-HgCdTe heterojunction are reported elsewhere.[12]

The calculated band diagram and the surface potentials of HgCdTe and CdTe, at 77K, with the valence band offset as a parameter, are shown in Fig. 2. The HgCdTe and CdTe doping levels and parameters are indicated in Fig. 2. We assume that the acceptor level of the MOCVD CdTe is 0.15 eV, corresponding to doubly ionized cadmium vacancy. The calculations take into account the freezeout in the CdTe as determined by the energy of the acceptor level. The interface charge density is assumed to be zero. In the wide range of the assumed valence band offset values (0–
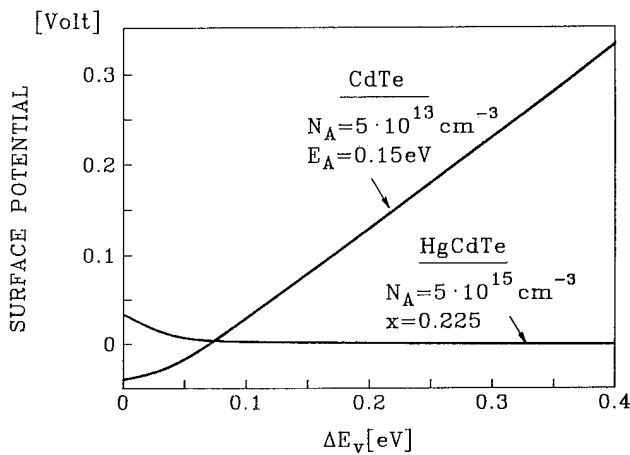
Fig. 3. The dependence of the calculated surface potentials of HgCdTe and CdTe, at 77K, upon the valence band offset. The interface charge density is taken as zero.

0.3 eV), the HgCdTe surface is practically at flat band. Only at zero offset, the surface is depleted and the band bending is 30 mV. The effect of the valence band offset on the surface potentials of HgCdTe and CdTe is exhibited in Fig. 3.

The band diagrams and surface potentials of CdTe and HgCdTe are hardly affected by varying the doping levels, as shown in Fig. 4. Depletion or close to flat band conditions are predicted, as long as the interface charge density is zero, even when the doping level of HgCdTe changes by an order of magnitude and the doping level of CdTe changes by two orders of magnitude. The drastic effect of the interface charges upon the band diagrams and surface potentials is shown in Fig. 5 and Fig. 6. Negative interface charges induce accumulation in the HgCdTe side while positive interface charges induce inversion. Figure 6 exhibits that interface charge density of the order of $5 \cdot 10^{11}$ cm^{-2} causes large deviations from flat band conditions.

The calculated band diagrams and surface potentials of Figs. 2–6 indicate that near flat band conditions can be obtained on p-type HgCdTe, provided that the electrical properties of the hetero-interface and the CdTe are carefully engineered and controlled. The theoretical and experimental uncertainty in the valence band offset introduces a variance in the surface potential of HgCdTe of the order of 30 mV. However, positive interface charges of even moderate density of the order of 10^{11} cm^{-2} induce strong inversion in p-type HgCdTe and strong accumulation in n-type HgCdTe and render the heterostructure use-
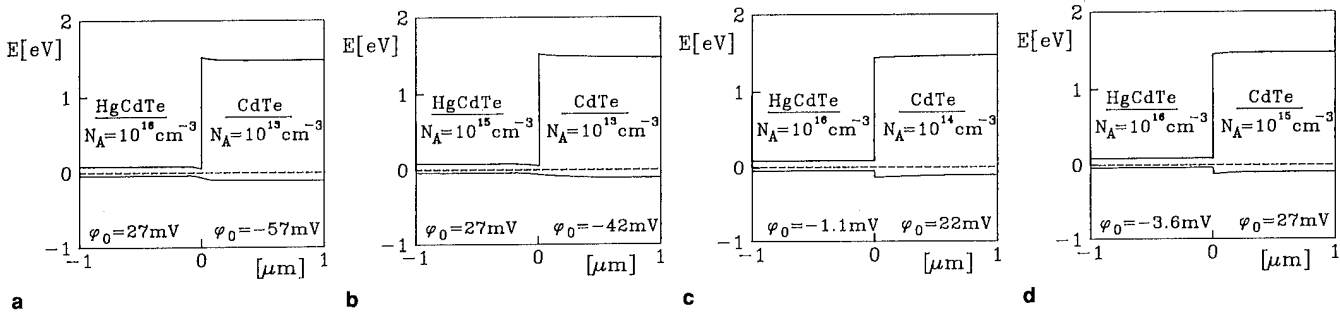

Fig. 4. Calculated band diagrams and surface potentials, (ϕ_o) at 77K, of p-CdTe/p-HgCdTe heterostructures for different doping levels of HgCdTe and acceptor concentrations in CdTe. (x = 0.225; E_A = 0.15 eV)(ΔE_V = 0; σ = 0) (a) HgCdTe: N_a = 10^{16} cm^{-3}, CdTe N_a = 10^{13} cm^{-3}; (b) HgCdTe: N_a = 10^{15} cm^{-3}, all other parameters are the same; (ΔE_V = 0.1 eV; σ =0) (c) CdTe: N_a = 10^{14} cm^{-3}; (d) CdTe: N_a = 10^{15} cm^{-3} and all other parameters are those of (c). The interface charge density σ is taken as zero and the valence band offset is either zero or 0.1 eV, as indicated.
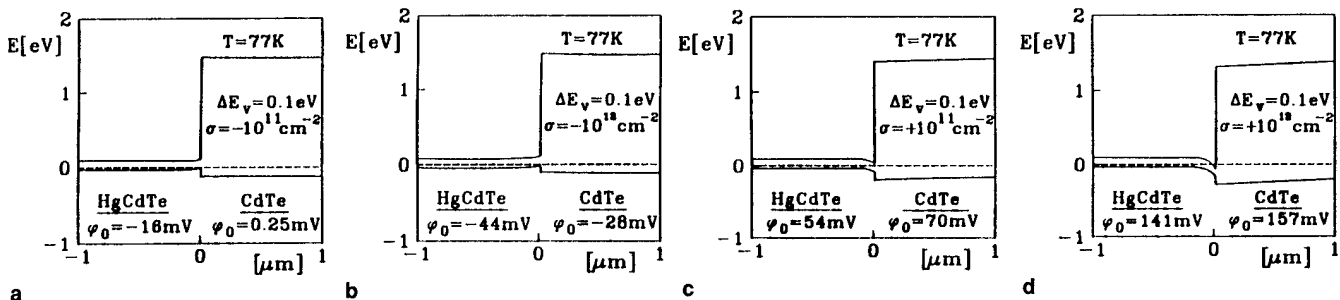

Fig. 5. Calculated band diagrams and surface potentials, at 77K, of p-CdTe (N_a = 10^{13} cm^{-3} and E_a = 0.15 eV)/p-HgCdTe (x = 0.225, N_A = 10^{16} cm^{-3}) heterostructures, for different interface charge densities: (a) σ = -10^{11} cm^{-2}; (b) σ = -10^{12} cm^{-2}; (c) σ = 10^{11} cm^{-2}; (d) σ = 10^{12} cm^{-2}. The valence band offset is taken as 0.1 eV.

less for passivation. Similarly, negative interface charges of the order of 10^{11} cm^{-2} induce accumulation in p-type HgCdTe and strong inversion in n-type HgCdTe. Hence, it can be concluded that the valence band offset and the exact values of the doping levels of CdTe and HgCdTe play a minor role in determining the exact values of the surface potentials. For the p-isotype heterostructure discussed here, close to flat band conditions are achieved for a wide range of doping levels and valence band offsets. However, the effect of the interface charge is drastic, and it is the most dominant parameter that controls the surface potentials.

MOCVD GROWTH OF CdTe ON HgCdTe

Substrates

Two types of (111) oriented ($\pm 2°$), bulk p-type $Hg_{1-x}Cd_xTe$ wafers ($x \cong 0.225$), were used in this study: single crystals grown by modified slush recrystallization and single crystals grown by traveling heated method (THM).[13,14] The electrical characteristics of typical wafers are: $N_a = 10^{16}$ cm^{-3}, $\mu_p \cong 600$ cm^{2}V^{-1} s^{-1} and $\tau_n \cong$ (5–20) ns, at 77K. The HgCdTe substrates were mechanically polished with 0.3 μm alumina powder and subsequently chemically etched for 30 s with 10% bromine in methanol solution. The CdTe epilayers were grown on the Te face of the $Hg_{1-x}Cd_xTe$ substrates and the face was determined with the Polisar etch.

MOCVD System and CdTe Growth Process

The MOCVD system was manufactured by Thomas Swan Inc., England, and has a horizontal quartz reactor. The graphite susceptor is heated with infrared lamps. The metalorganic sources, DETe and DMCd, supplied by Morton, are kept at 25°C. Palladium diffused hydrogen serves as the carrier gas. Growth runs, at 430°C, are performed at a subatmospheric pressure of 300 Torr and the total flow rate is 1.2 l/min. The partial pressures of DETe and DMCd in the reactor are 1 and 0.26 Torr, respectively.

The HgCdTe wafers are exposed to the following temperature cycle: the susceptor is heated to 430°C within 7 min. The susceptor temperature is stabilized at 430°C for additional 5 min. At 430°C, approximately 0.4 μm CdTe are grown in 3 min (the exact thickness depends on the pretreatment). After growth, the susceptor is cooled to 260°C in 6 min by flowing hydrogen (130 cc/min at 300 Torr) and after additional 15 min the susceptor temperature drops below 50°C. Under these conditions, 3000–5000Å CdTe are grown in 2.5–4 min. With the UV pretreatment described below, ~4000–6000Å are grown in 2.5–4 min. Mirror-like epilayers, with excellent morphology and no hillocks are observed on the Te face of (111) oriented substrates. The effect of the MOCVD growth parameters, including deposition temperature, duration, partial pressures of the metalorganic sources, and Hg and misorientation of HgCdTe substrates, will be reported elsewhere.[15]
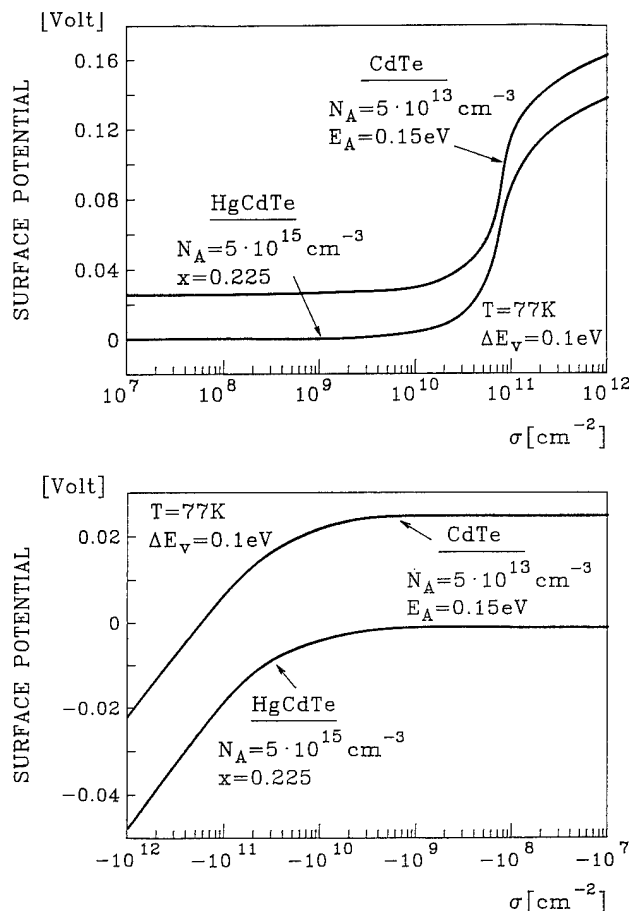

Fig. 6. The dependence of the calculated surface potentials of HgCdTe and CdTe, at 77K, upon the interface charge density: (a) positive charges, and (b) negative charges. The valence band offset is taken as 0.1 eV.

UV Photon Assisted Hydrogen Radicals Pretreatment

Ultraviolet radiation for an *in-situ* pretreatment prior to the growth of the epilayers is provided by a high pressure Hg lamp operating at 450 W, with a wide emission spectrum between 190 and 300 nm. In this pretreatment, the HgCdTe substrate, at 50°C, is irradiated by the UV lamp for 1 h while the reactor and the HgCdTe substrates are flushed in hydrogen, flowing at 250 cc/min, at a total pressure of 300 Torr. Prior to the subsequent growth of CdTe, the UV photons are shut off.

ELECTRICAL CHARACTERIZATION

MIS Test Devices

Metal-insulator-semiconductor devices were fabricated on p-type HgCdTe and used to characterize the electrical properties of the interface. The insulator of the MIS device consisted of the MOCVD grown CdTe epilayer, approximately 0.4 μm thick. The combination of evaporated titanium (500Å) and gold (1 μm) was used for bulk and gate metallization. The gate electrodes of ~500 μm diameter were evaporated
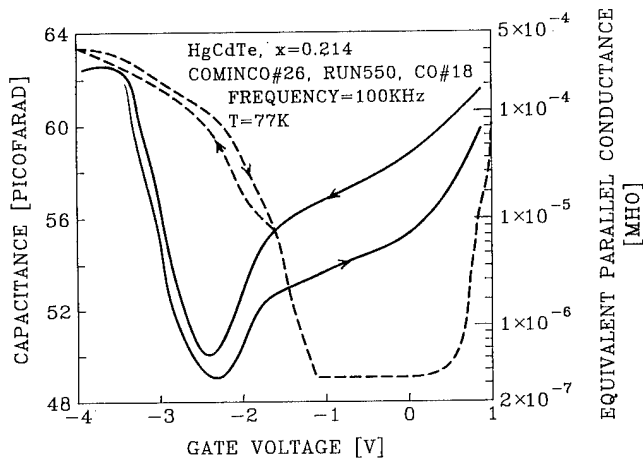
Fig. 7. Measured capacitance-voltage (solid line) and equivalent parallel conductance (dashed line) characteristics of MIS device that was not exposed to UV pretreatment. The measurement temperature is 77K and the measurement frequency is 100 kHz. Gate area is 0.002 cm².
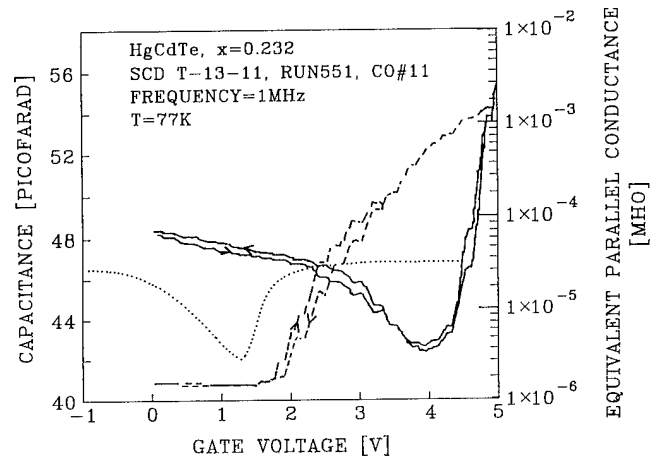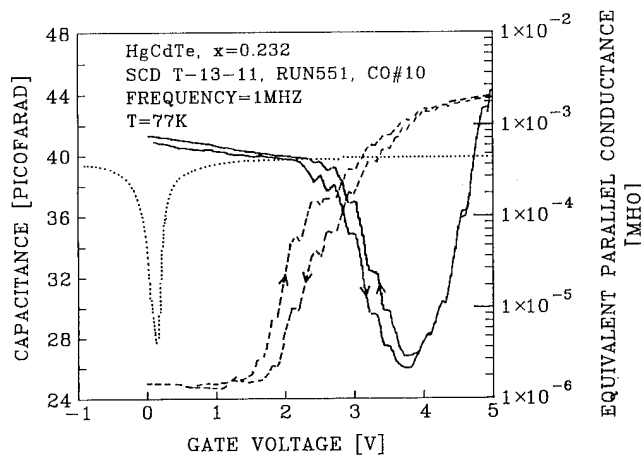

Fig. 8. Measured capacitance-voltage (solid line) and equivalent parallel conductance (dashed line) characteristics of MIS device that was exposed to UV pretreatment. The measurement temperature is 77K and the measurement frequence is 1 MHz. Gate area is 0.002 cm². Dotted line is the theoretical C-V curve.

through a metal mask and the bulk contact was evaporated on the rear side of the HgCdTe substrate. The devices were bonded and sealed with a cold shield at 77K, in a dewar. The devices were subject to annealing cycles in vacuum in the temperature range 70–140°C and were characterized repeatedly at several temperatures.

Capacitance and conductance were measured as a function of gate voltage, with frequency as a parameter, with an HP4192A impedance analyzer. The DC gate current was measured as a function of gate voltage with HP signal parameter analyzer. Simple MIS theory neglecting modifications due to the Kane model was applied for the analysis.

Capacitance-Voltage and Conductance-Voltage Characteristics

The surfaces of the CdTe/HgCdTe heterostructures are determined with measured capacitancevoltage and equivalent parallel conductance-voltage charac-

Fig. 9. Measured capacitance-voltage (solid line) and equivalent parallel conductance (dashed line) characteristics of MIS device that was exposed to UV pretreatment. The measurement temperature is 77K and the measurement frequence is 1 MHz. Gate area is 0.002 cm². Dotted line is the theoretical C-V curve.

teristics of MIS devices, as shown in Figs. 7–9.

The drastic effect of the positive interface charges, observed when the MOCVD CdTe is grown without an *in-situ* UV pretreatment, is shown in Fig. 7. At zero gate bias, the HgCdTe surface is inverted. The measured fiat band voltage is –3.3 V and the fixed interface charge density is $Q_{ss} = 6.4 \cdot 10^{11}$ cm⁻².

The C-V characteristic is analyzed with the following inputs:

Cinsulator (from Fig. 7) = 62 pF
Cminimum (from Fig. 7) = 49 pF
Gate area (measured) = $2 \cdot 10^{-3}$ cm²
Relative dielectric constant of CdTe = 10.6
Relative dielectric constant of HgCdTe = 18

The following MIS parameters are derived from simple MOS theory:

HgCdTe effective doping concentration = $9.7 \cdot 10^{15}$ cm⁻³
CdTe thickness = 3000Å
Flat band capacitance = 59 pF
Flat band voltage (from Fig. 7) = –3.3V

Metal-semiconductor (titanium-HgCdTe) work function difference $\Phi_{MS} = 0V$ based on: $\Phi_{MS} = \Phi_{MO} - (\Phi_S + E_g/2 + \phi_F)$ where the work functions of titanium and HgCdTe are $\Phi_{MO} = 4.3$ eV and $\Phi_S = 4.23$ eV, respectively.[16] From $V_{FB} = \Phi_{MS} - Q_{ss}/C_{OX}$, we obtain $Q_{ss} = 6.4 \cdot 10^{11}$ electrons/cm².

The interface is very stable with respect to temperature cycles. The devices were repeatedly annealed at temperatures up to 140°C, for 24 h at each cycle. The annealing temperature did not exceed 140°C because of the packaging glues and the experimental dewar and not because of even the slightest interface degradation.

Capacitance-voltage measurements on THM devices often yielded stronger inversion manifested by more negative flat band voltages (of the order of –5 V) and the calculated Q_{ss} is of the order of $1 \cdot 10^{12}$ cm⁻².

However, the same general features of the characteristic shown in Fig. 7 and the same high thermal stability were observed. These features include low frequency behavior with little dependence on measurement frequency (in the range of 100 kHz–1 MHz), and low equivalent parallel conductance ($3 \cdot 10^{-7}$ mho) around zero gate bias. The equivalent parallel conductance is measured in parallel to the capacitance.

The C-V characteristic of Fig. 7 exhibits correspondence between the calculated and measured characteristics and a small hysteresis at depletion. The apparent hysteresis around zero gate voltage may be attributed to variation in the response time of the minority carriers in inversion. However, C-V characteristics measured on different contacts exhibited a spread in the flat band voltage and hence in the fixed interface charge density, Q_{ss}. This is attributed to small variations in orientations of subgrains in the bulk substrates.[13,14]

The in-situ UV photon-assisted hydrogen radicals pretreatment exhibits a significant effect on the hetero-interface, as shown in Fig. 8. At zero gate bias, the HgCdTe surface is accumulated. The measured flat band voltage is +3 V and the fixed interface charge density is $Q_{ss} = -3.7 \cdot 10^{11}$ cm^{-2}. At zero gate bias, the equivalent parallel conductance is low and the insulator capacitance exhibits very small hysteresis. At depletion, the conductance increases by three orders of magnitude and 0.2–0.3 V hysteresis is observed, implying slow surface state density of $2.5 \cdot 10^{10}$ cm^{-2}. At strong inversion, the conductance saturates and the hysteresis disappears. The excellent thermal stability is again observed and the C-V and G-V characteristics do not exhibit any shifts even after repeated thermal cycles up to 140°C, where we stopped because of the experimental dewar.

The effective doping level derived from the minimum capacitance is $2 \cdot 10^{14}$ cm^{-3} and this is nearly two orders of magnitude lower than the original doping level of the HgCdTe substrate. Such a reduction in substrate doping level was previously observed during MOCVD growth of CdTe on CdTe substrates, after applying the UV pretreatment.[6] However, not all the MIS devices exhibited this behavior, as shown in Fig. 9. The characteristics of Fig. 9 are similar to those of Fig. 8: the HgCdTe surface is accumulated, the measured flat band voltage is 2.8 V and the fixed interface charge density is $Q_{ss} = -4.1 \cdot 10^{11}$ cm^{-2}. A small hysteresis is observed at depletion where the condutance increases. Again, excellent thermal stability is observed. Analysis of the doping level according to Cminimum yields a value close to the original doping level of the HgCdTe substrate. At this stage, it is not clear if this behavior is also related to different subgrains in the bulk substrates.

In summary, the interface properties of the p-isotype CdTe/HgCdTe heterostructure are very promising. Further optimization of the in-situ pretreatment is required to obtain near flat band conditions.

DC Gate Current-Voltage and Differential Resistance Characteristics

The DC gate current-voltage and differential resistance-voltage characteristics of two MIS devices, without and with UV pretreatment, are shown in Fig. 10 and Fig. 11. These curves demonstrate the insulation properties of the MOCVD CdTe at 77K. High values of dynamic resistance are observed at MIS devices grown with the UV pretreatment. The values are two orders of magnitude higher than those observed at MIS devices without UV pretreatment ($10^{11}\Omega$ in Fig. 11 compared to $10^{9}\Omega$ in Fig. 10).

The DC characteristics of Fig. 11 and the AC characteristics of Fig. 8 are measured on the same gate. The DC conductivity increases at positive gate volt-
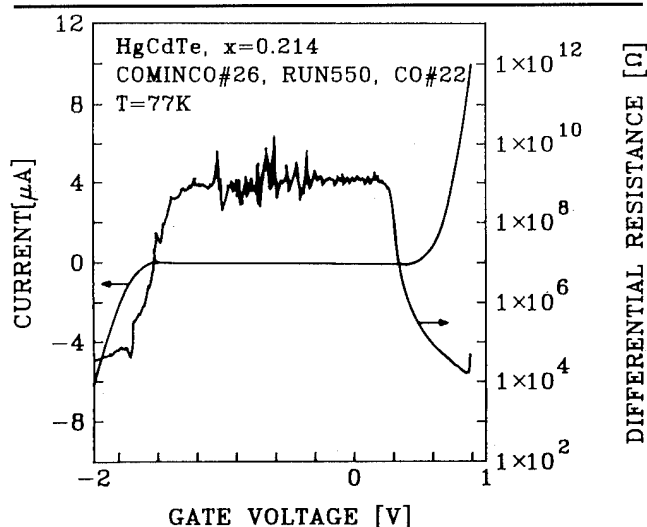

Fig. 10. Measured, at 77K, DC gate current-voltage and differential resistance-voltage characteristics of MIS device that was not exposed to UV pretreatment.
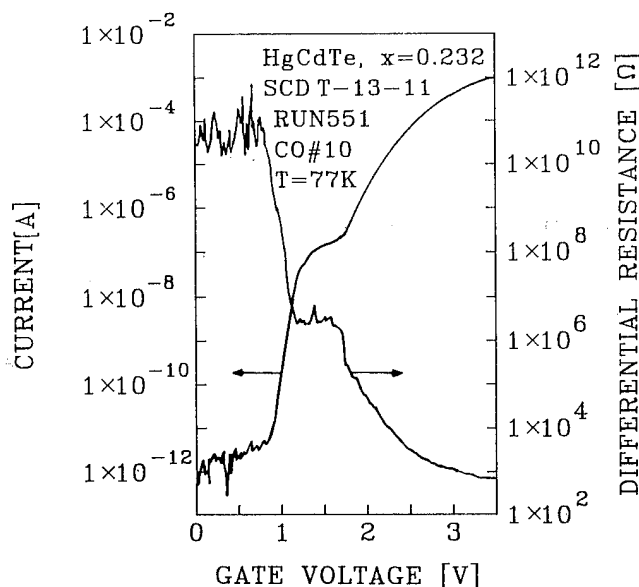

Fig. 11. Measured, at 77K, DC gate current-voltage and differential resistance-voltage characteristics of MIS device that was exposed to UV pretreatment.

ages inducing inversion due to tunneling between the n^+ inversion layer and the substrate (around 0.5 V gate voltage for the untreated device of Fig. 10 and around 3.5 V for the UV pretreated device of Fig. 11). The DC conductivity also increases at strong accumulation (–2V for the device of Fig. 10 and around –1 V for the device of Fig. 11).

The estimated dielectric breakdown field is of the order of 10^5V/cm.

SUMMARY AND CONCLUSION

This paper studies the passivation properties of MOCVD CdTe epilayers grown on the Te face of (111) oriented, bulk HgCdTe wafers. In general, the passivation properties of a specific technology are highly dependent on the orientation, the history, and the origin of the HgCdTe wafers. The present study indicates the potential passivation properties of MOCVD CdTe grown on p-type HgCdTe.

CdTe passivation of HgCdTe in general, and MOCVD CdTe in particular, has been hardly studied in the open literature.[17,18] Bulk HgCdTe wafers are used here since this is a well characterized and reproducible HgCdTe material and it was assumed that a new passivation should be characterized on an established rnaterial. Later on the results can be extended to HgCdTe of different sources and growth techniques. The (111) orientation corresponds to LPE HgCdTe epilayers currently used in production of focal plane arrays.

The study focuses on CdTe passivation that corresponds to the requirements of a wide range of device designs and architectures. Namely, the CdTe passivation is applied during an advanced stage of the processing of the devices and not necessarily as an integral part of the growth of the epilayers. The reported results indicate that MOCVD grown CdTe is a promising passivation technology, provided it is combined with appropriate HgCdTe surface and interface pretreatments. Otherwise, interface charges dominate the surface potential, imposing strong inversion on p-type substrates. With the reported UV photon-assisted hydrogen radicals pretreatment, accumulated interfaces are obtained on the p-type substrates.

It is believed that UV-induced heterogeneous dissociation of hydrogen, on the surface of the HgCdTe substrates, produces highly reactive hydrogen radicals.[6,7] The hydrogen radicals form volatile hydrides with Te atoms. In addition, the hydrogen radicals reduce native oxides that are formed on the surface and remove water molecules that are easily adsorbed on TeO_2 and on the polar surface of (111) HgCdTe. Possibly, additional volatile hydrides are formed of impurity atoms that reside on the HgCdTe surface after exposure to processing. The highly reactive nature of the hydrogen radicals and the photosensitized reaction at the surface, have the potential to form reproducible and controlled hetero-interfaces. The in-situ UV photon-assisted pretreatment should be optimized to obtain slightly accumulated or slightly depleted interfaces.

A carefully controlled growth process as well as interface and surface pretreatment tailored to the specific material is required in order to obtain near flat band conditions on p-type as well as on n-type material. The effect of the MOCVD growth parameters (deposition temperature, partial pressures of the metalorganic sources and partial pressure of Hg) in addition to UV photons and pretreatments will be reported elsewhere.[15] Studies of CdTe passivation and 1/f noise as well as CdTe passivation and gate controlled diodes are also essential before this promising technology can be fully assessed. Finally, it should be noted that MOCVD CdZnTe (Zn = 4%) epilayers can provide even superior passivation for $Hg_{1-x}Cd_xTe$ with $x \cong 0.22$, because of perfect lattice matching between the epilayer and substrate and because of the larger bandgap of CdZnTe.

ACKNOWLEDGMENT

REFERENCES

1. W.E. Tennant, C.A. Cockrum, J.B. Gilpin, M.A. Kinch, M.B. Reine and R.P. Ruth, J. Vac. Sci. Technol. B10, 1359 (1992).
2. P.H. Zimmermann, M.B. Reine, K. Spignese, K. Maschoff and J. Schrippa, J. Vac. Sci. Technol. A8, 1182 (1990).
3. S. Yuan, L. He, J. Yu, M. Yu, Y. Qiao and J. Zhu, Appl. Phys. Lett. 58, 914 (1990).
4. Y. Nemirovsky, N. Mainzer and E. Weiss, to be published in Narrow-Gap Cadmium-Based Components, ed. P. Copper, (EMIS/IEEE, 1994).
5. G. Sarusi, G. Cinader, A. Zemel, D. Eger and Y. Shapira, J. Appl. Phys. 71, 5070 (1992).
6. Y. Nemirovsky and A. Ruzin, J. Electron. Mater. 22 (8) 1, (1993).
7. J.T. Cheung, S.H. Shini, J.G. Pasko and R.E. DeWames, J. Vac. Sci. Technol. B10, 1538 (1992).
8. S.J. Chang, L.Y. Len, S.R. Forrest and C.E. Jones, Appl. Phys. Lett. 54, 1040 (1989).
9. J.P. Faune and Y. Guldner, Heterojunction Band Discontinuities, eds. F. Cappasso and G. Margaritando, ch. 7 (New York: North Holland, 1987).
10. L. Djaloshinski and Y. Nemirovsky, J. Appl. Phys. 73, 4473 (1993).
11. L. Djaloshinski and Y. Nemirovsky, submitted to J. Appl. Phys., 1993.
12. Y. Nemirovsky, L. Djaloshinski, D. Goren and N. Amir, submitted to J. Appl. Phys., 1994.
13. E. Weiss, E. Kedar and N. Mainzer, to be published J. Cryst. Growth, 1993.
14. E. Weiss, E. Kedar and N. Mainzer, to be published in MRS, Vol. 32, 1993.
15. N. Amir and Y. Nemirovsky, submitted to J. Crystal Growth, 1994.
16. Properties of Mercury Cadmium Telloride, EMIS data reviews series, ed. J. Brice and P. Capper, England (1987).
17. S.K. Ghandhi, K.K. Parat, H. Ehsani and I.B. Bhat, Appl. Phys. Lett. 58, 828 (1991).
18. D.W. Snyder, E.I. Ko, S. Mahajan and P.J. Sides, Mat. Res. Soc. Symp. Proc. Vol. 216, 41 (1991).

Investigation of Epitaxial P-p CdTe/Hg$_{0.775}$Cd$_{0.225}$Te Heterojunctions by Capacitance-Voltage Profiling

V. ARIEL, V. GARBER, and G. BAHIR

Department of Electrical Engineering, Technion, Haifa 32000, Israel

A. SHER and G. CINADER

Soreq NRC, Yavne 70600, Israel

We investigate the electrical properties of isotype P-p CdTe/Hg$_{0.775}$Cd$_{0.225}$Te heterojunctions grown *in situ* by the metalorganic chemical vapor deposition technique. The capacitance-voltage (C-V) characterization of Schottky barriers (SB) is used to study the apparent majority carrier distribution and the valence band discontinuity. The C-V characteristics of metal insulator semiconductor (MIS) devices were used to determine the interface charge density. A theoretical model suitable for analysis of graded heterojunctions was developed based on the numerical solution of Poisson's equation. The model includes an approximate description of the conduction band nonparabolicity and carrier degeneracy. We describe the procedures used in crystal growth and device fabrication for both SB and MIS structures. We demonstrated, on the basis of experimental measurements and theoretical analysis, that the valence band discontinuity in the devices studied here was 0.15 ± 0.05 eV and the fixed interface charge density was approximately $(3 \pm 1) \cdot 10^{10}$ cm^{-2}. Also, we observed a dependence of the C-V measurements on temperature which seems to be caused by either interface traps or carrier inversion at the CdTe/HgCdTe interface.

Key words: CdTe, HgCeTe, infrared detectors, metalorganic chemical vapor deposition (MOCVD), surface passivation

INTRODUCTION

Fundamental physical properties of HgCdTe make it the material of choice for infrared radiation detection.[1] It has been shown recently that CdTe can serve as a preferred passivation material for HgCdTe photodiodes.[1,2] Consequently, CdTe/HgCdTe heterojunctions have received increased attention.[2-4] Also, HgCdTe heterojunctions are used in advanced photodetector design.[5] The energy band discontinuity is an important technological parameter in heterojunction devices because it affects the energy band structure and electrical behavior of the devices.[5,6] The magnitude of the valence band discontinuity, ΔE_V, in CdTe/HgCdTe heterojunctions has been the subject of many theoretical and experimental investigations.[7] Nevertheless, there is no agreement about the exact value of ΔE_V, with reported values ranging from –0.1 to 0.5 eV.

The C-V profiling is a simple and accurate way of measuring the energy band discontinuities in isotype heterojunctions.[8] The approach is insensitive to compositional grading, as has been shown by Kroemer,[9] and therefore is suitable for studying HgCdTe heterojunctions where grading is usually present.[10,11] Recently, Chang et al.[7] applied C-V profiling to the HgCdTe layer grown by the liquid phase epitaxy on top of the CdTe substrate. These measurements showed a negative energy band discontinuity $\Delta E_V = (0.11 \pm 0.02)$ eV which is different from most experimental results in the literature.[7] In this work, we apply the C-V profiling technique to CdTe/HgCdTe heterojunctions grown by the metalorganic chemical vapor deposition (MOCVD) technique. Both the HgCdTe substrate and the CdTe cap layer were grown *in situ*, in single run, thus eliminating exposure of the heterointerface to ambient temperature.

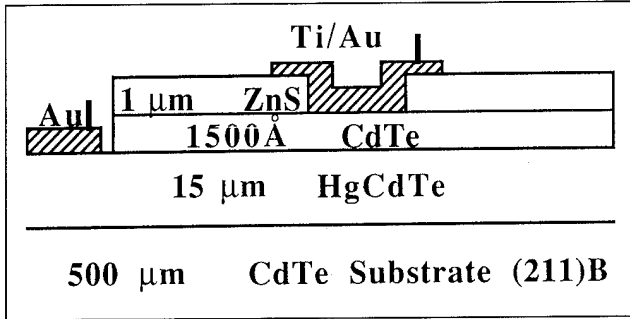First, we present a theoretical model needed for energy band calculation of CdTe/HgCdTe hetero-

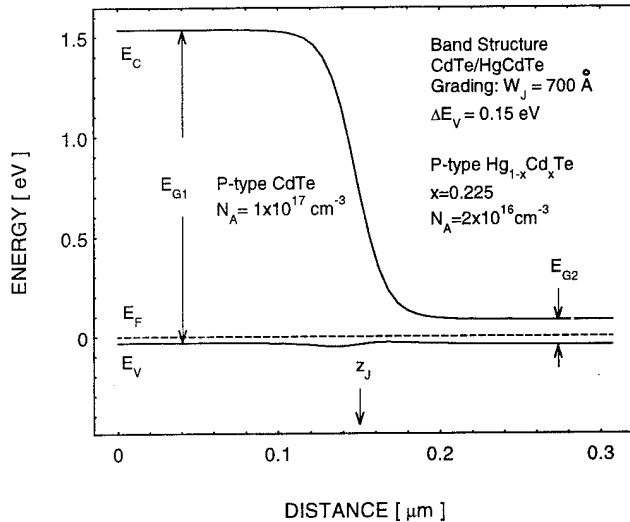Fig. 1. Schematic cross section of the Schottky barrier device used in this study.

Fig. 2. Calculated equilibrium energy-band diagram for CdTe/HgCdTe heterostructure.

junctions and for analysis of the experimental C-V data. Quantitative band diagrams for abrupt and graded junctions have been presented previously,[10,11] but they do not include conduction band nonparabolicity which has a significant effect in both CdTe and HgCdTe.[6,12] Then, we describe the MOCVD crystal growth and device preparation procedures. Finally, we use the Schottky barrier C-V profiling of the resulting CdTe/HgCdTe heterojunctions to determine ΔE_V.

THEORETICAL MODEL

In this section, a numerical solution of the one-dimensional Poisson's equation is discussed, suitable for simulation of the C-V characteristics of graded heterojunctions. The energy band structure of the device is needed for both qualitative and quantitative analysis of device behavior. A calculated energy band diagram of the CdTe/HgCdTe heterojunction is shown in Fig. 2. Epitaxially grown CdTe/HgCdTe heterojunctions usually have a graded interface between the two materials; consequently, solutions developed for abrupt heterojunctions may not lead to an accurate result. In particular, variation of the dielectric constant is a significant factor in CdTe/HgCdTe heterojunctions, which leads to Poisson's equation of the form

$$\frac{d^2\psi}{dz^2} = -\frac{\rho}{\varepsilon} - \frac{1}{\varepsilon}\frac{d\varepsilon}{dz}\frac{d\psi}{dz}. \qquad (1)$$

Here $\varepsilon(z)$ is the dielectric constant which varies with distance, ψ is the electrostatic potential, and ρ is the semiconductor charge concentration. Both electrons and holes must be included in the calculation because both accumulation and inversion may exist in the heterojunction. The contribution of shallow impurities and deep traps must also be considered, including the impurity freeze out effect. The semiconductor charge concentration can be written as

$$\rho = -q(p-n-N_A^- - N_{TA}^-) \qquad (2)$$

where n and p are electron and hole concentration, respectively, and N_A^- and N_{TA}^- are concentration of shallow and deep acceptor impurities. It is assumed in this work that $N_{TA} = 0.1N_A$ with the trap energy level located in the middle of the band gap.[6]

The cadmium mole fraction, x, is assumed to vary across the heterojunction as a complementary error function, with a characteristic junction width W_J

$$x(z) = x_1 - 0.5\,(x_1 - x_2)\mathrm{erfc}\left(\frac{z - z_J}{W_J}\right). \qquad (3)$$

Here z_J is the junction location which corresponds to the middle of the transition region; $x_1 = 1$ is the cadmium mole fraction of the CdTe layer, and $x_2 = 0.225$ is the cadmium mole fraction of the HgCdTe substrate (see Fig. 1). All device parameters that depend on cadmium composition vary along the device in accordance with Eq. (3); for example, the dielectric constant is assumed to vary as $\varepsilon = 20 - 9.4x$.[6] Also, an expression similar to Eq. (3) is used to describe grading of the impurity concentration.

To accurately model HgCdTe devices, carrier degeneracy and conduction band nonparabolicity must be treated.[6,12] Instead of calculating the nonparabolic Fermi-Dirac integral, which is a computationally demanding task,[6] the following approximation for the electron quasi-Fermi level, E_{FN}, can be used:[12]

$$(E_{FN} - E_C)/kT = \ln\left(\frac{n}{N_{C\alpha}}\right) + \frac{n}{N_{C\beta}}. \qquad (4)$$

Here, kT is the thermal voltage and E_C is the conduction band energy. $N_{C\alpha}$ and $N_{C\beta}$ are coefficients responsible for the description of degeneracy and nonparabolicity which depend on the band gap, electron effective mass, and temperature.[12] It has been shown that this approximation results in reasonable accuracy (absolute error in Fermi energy less than 10%) for E_{FN} up to 5 kT inside the conduction band.[12]

Because of a simple analytical form of approximation Eq. (4), Poisson's equation can be easily solved in one dimension using the finite differences

method and applying Newton's iterations.[13] The solution in the absence of the applied voltages results in the equilibrium carrier concentration, while the solution in the presence of the applied bias, assuming no current in the device, leads to a theoretical C-V characteristic which can be compared to experimental measurements.

The apparent majority carrier concentration, $\hat{p}$, can be determined from a C-V characteristic using the expressions

$$\hat{p}(z) = -\frac{C^3}{q\varepsilon}(dC/dV)^{-1},$$

$$z = \frac{\varepsilon}{C} \quad (5)$$

where C is the capacitance and V is the applied bias. The valence band discontinuity and the interface carrier density can be calculated from the apparent majority carrier distribution using the following integral relations[8]

$$\sigma_i = -\int_0^\infty \left(N_A^- + N_{AT}^- - \hat{p}\right)dz \quad (6)$$

$$\Delta E_V =$$

$$kT \ln\left[\frac{p_2/N_{V2}}{p_1/N_{V1}}\right] + \frac{q^2}{\varepsilon}\int_0^\infty \left(N_A^- + N_{AT}^- - \hat{p}\right)(z - z_J)dz \quad (7)$$

Here, q is the electron charge and N_V is the density of states in the valence band, which is assumed to be parabolic. Indices 1 and 2 in Eq. (7) refer to equilibrium parameters of CdTe and HgCdTe, respectively. Expressions (5), (6), and (7) were originally derived for abrupt heterojunctions with constant ε. Interestingly, these relations remain valid in the case of graded heterojunctions,[9] though all carrier densities must be scaled[14] in order to account for a nonuniform electric permittivity. It has been shown that such variable scaling does not affect the value of the integral Expressions (6), (7), and results in accurate values of the valence band discontinuity and the interface carrier density.[14]

CRYSTAL GROWTH AND DEVICE FABRICATION

We now describe the procedure used for device preparation in this work. The samples were grown on a (211)B CdTe substrate by the MOCVD technique in a horizontal reactor using interdiffused multilayer process (IMP).[15,16] The growth temperature was 360°C and the growth rates were 3.6 and 3 μm/h for the CdTe and HgTe, respectively. The structure of the sample is 10 μm of p-type HgCdTe (x = 0.225) covered by 1500–2000Å of CdTe grown *in situ* following the growth of the HgCdTe layer. Such a procedure avoids contamination of the CdTe/HgCdTe interface by exposure to the ambient atmosphere, which may lead to lower

interface charge density. Normally, a heat treatment was carried out for an additional 30 to 60 min at growth temperature in order to complete the homogenization of HgCdTe. The samples were Hg vacancy doped but we cannot reject the possibility of unintentional background doping with p-type impurities.

The thickness of the HgCdTe layer and the composition were derived from the transmission spectra. Secondary ion mass spectroscopy (SIMS), selective etching, and Auger spectroscopy measurements were used to determine the junction depth, which was approximately 2000Å, and junction grading, which varied in the range 300–800Å. The effective doping of the HgCdTe layer $N_A = 8 \cdot 10^{15} - 2 \cdot 10^{16}$ cm^{-3} was obtained from Hall measurements. The doping of CdTe was determined from Schottky barrier C-V measurements and varied in the range $N_A = 2 \cdot 10^{16} - 2 \cdot 10^{17}$ cm^{-3}. Carrier mobility in HgCdTe was determined from Hall measurements as $\mu = 500–600$ cm^2/V · s, and the life time was equal to several nanoseconds.

The surface morphology of the CdTe cap layer is mirror-like with no hillock-type defects of any kind. The HgCdTe layer, as well as the CdTe cap, were free of micro twins due to growth in (211)B orientation.[16] The crystal structure was checked by the double crystal difractometer.

Schottky barrier was formed on top of the CdTe layer by deposition of Ti/Au (see Fig. 1), while metal insulator semiconductor (MIS) capacitor was formed by deposition of 3500–4000Å of ZnS on top of the CdTe layer with Ti used as gate metallization. Ohmic contacts were obtained in both structures by etching of the CdTe layer followed by deposition of Au.

EXPERIMENTAL MEASUREMENTS AND DATA ANALYSIS

In this section, we describe the results of the experimental measurements and the procedure used for data analysis.

CV of Schottky Barrier
Ti/CdTe/Hg$_{1-x}$Cd$_x$Te
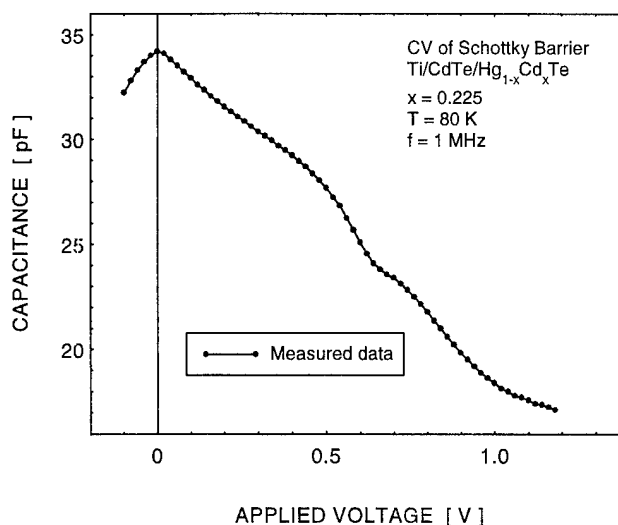
x = 0.225
T = 80 K
f = 1 MHz

Measured data

Fig. 3. A high frequency C-V characteristic of a Schottky barrier device, clearly showing the transition between CdTe and HgCdTe.
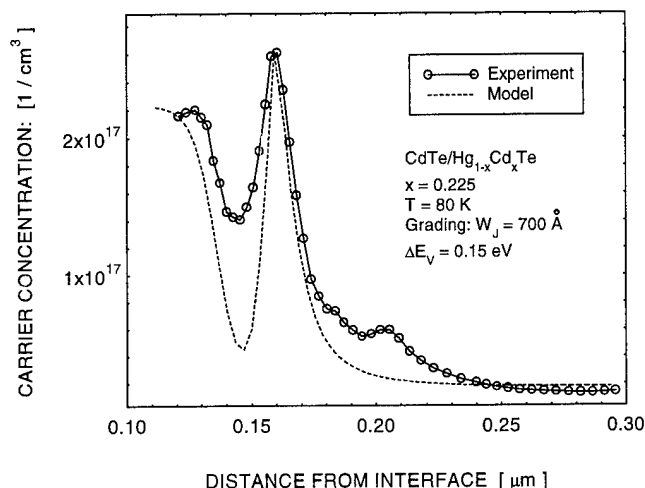
Fig. 4. A comparison of experimental and theoretical carrier concentration at the CdTe/HgCdTe interface. The experimental data was obtained from high-frequency C-V measurements of a Schottky barrier device, while the theoretical curve resulted from a numerical solution of Poisson's equation.
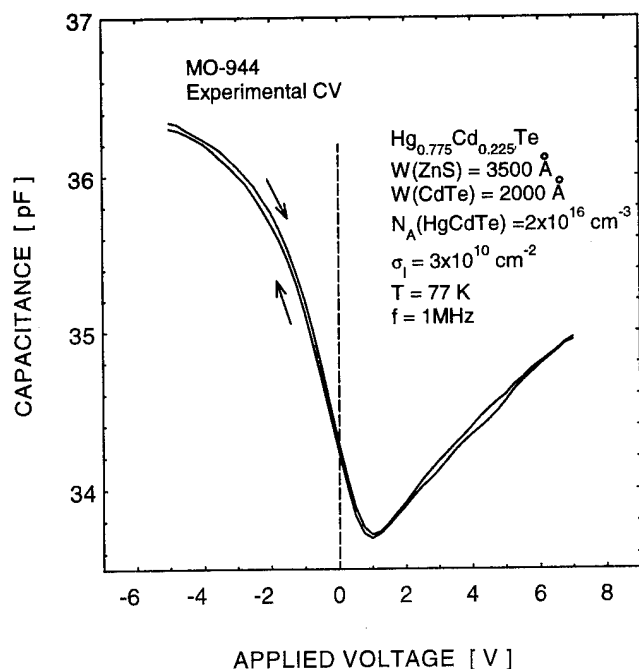

Fig. 5. The measured C-V characteristic of an MIS device. Note a very low hysteresis and the nearly flat band position of the C-V curve.

A number of devices from five different samples were studied here. The devices were mounted in a cryostat and the temperature was varied in the range of 70–150°K The C-V measurements were recorded with an HP4280A C-V plotter, for measurements at constant frequency of 1 MHz, and with an HP4192 impedance analyzer, for variable frequency measurements.

First, the C-V characteristics of SB devices were measured at high frequency in order to eliminate a contribution of minority carriers, which were assumed unable to follow the high frequency oscillations. We considered a measurement to be high frequency when there was no change in the C-V curve with the
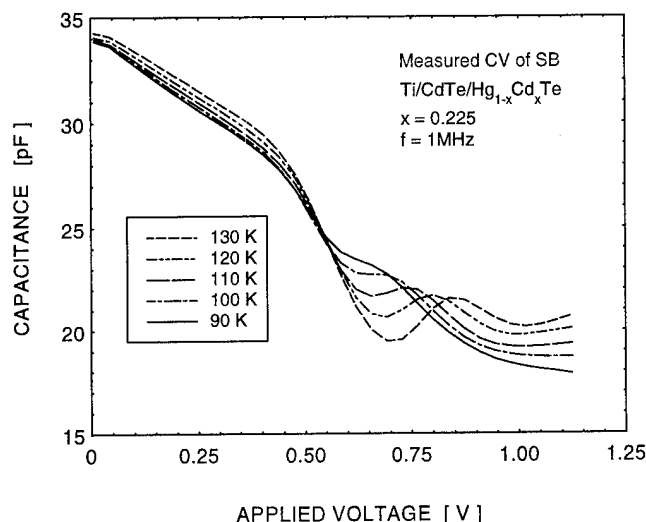
Fig. 6. Capacitance-voltage measurements of a Schottky barrier device at various temperatures.
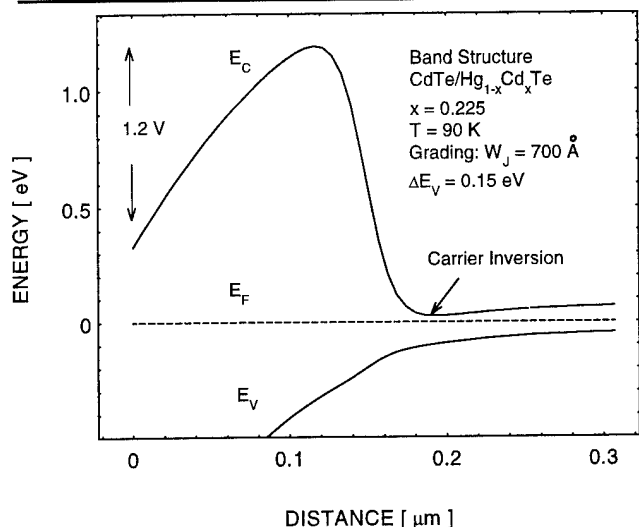
Fig. 7. Simulated energy bandbending in the presence of a reverse bias, demonstrating carrier inversion at the CdTe/HgCdTe interface.

increase in measurement frequency or lowering of temperature. In Fig. 3, we demonstrate a high frequency C-V curve of a heterojunction SB diode measured at a temperature of 80K and frequency of 1 MHz. As can be seen from Fig. 3, a clear transition from one material to another is observed, with the intermediate region due to the heterointerface. The apparent carrier concentration was reconstructed from the measured C-V data using Eq. (5). It was found that variations of the dielectric constant ($\varepsilon = 11\ \varepsilon_0$ for CdTe, $\varepsilon = 18\varepsilon_0$ for HgCdTe with x = 0.225, where ε_0 is the vacuum dielectric constant) are essential for a correct analysis of experimental data.[14] We calculated ΔE_V from Eq. (7) using the apparent carrier profile. Poisson's equation was solved in quasi-equilibrium and a theoretical carrier profile was obtained using information about the junction location and grading from the Auger and SIMS measurements. The value of the valence band discontinuity was adjusted in order to get the best agreement between the experi-

mental and theoretical carrier profiles, see Fig. 4. The preliminary results demonstrate a small positive ΔE_V = 0.15 ± 0.05 eV in agreement with the majority of other experimental investigations. The magnitude of the interface charge was then calculated with the help of Eq. (6) and using the assumed $\varepsilon(z)$ dependence. We found that the magnitude of σ_i obtained from Eq. (6) strongly depended on the assumed junction position, and an error of 100Å in the junction position led to an order-of-magnitude error in σ_i. This effect led to additional complications in the interpretation of C-V data since it was difficult to determine the precise junction location in the graded heterojunction. Consequently, we used C-V measurements of MIS devices to determine σ_i independently. In Fig. 5, we present a C-V measurement of an MIS device. As can be seen from the figure, practically no hysterisis is observed and the MIS capacitor is near the flat band. The value of the flat band voltage was used to calculate σ_i. Both SB and MIS measurements point to a relatively low fixed interface charge $\sigma_i = (3 \pm 1)\ 10^{10}$ cm^{-2}, assuming no contribution from charges at the ZnS/CdTe interface.

Measurements of Schottky barrier C-V characteristics at various temperatures demonstrated a strong temperature dependence for temperatures above 90K (Fig. 6). Temperature and frequency dependence of heterojunction C-V measurements were previously observed in GaInAs devices and were attributed to interface traps, caused by lattice mismatch at the heterojunction.[17] Another possible explanation is the presence of carrier inversion at CdTe/HgCdTe interface under a large reverse bias. A potential barrier is formed for minority electrons, because of a large conduction band discontinuity, causing carrier inversion at the CdTe/HgCdTe interface. In Fig. 7, we present a theoretical calculation of the energy band structure in the presence of reverse bias. As can be seen from the figure, the Fermi level approaches the conduction band in the vicinity of the interface, leading to a large concentration of minority electrons. Note that the measurements of ΔE_V described above were performed at low temperatures (T < 90K), where we expect the high frequency condition to hold with only majority carriers contributing to the measured capacitance.

CONCLUSIONS

In conclusion, we investigated MOCVD grown CdTe/HgCdTe heterojunctions by applying the C-V profil-

ing technique to Schottky barrier devices. A theoretical model was developed that includes the description of energy band nonparabolicity and carrier degeneracy which are essential for analysis of CdTe/HgCdTe heterojunctions. Using this model and applying the C-V profiling theory of graded heterojunctions, we determined the valence band discontinuity and the interface carrier density from experimental C-V measurements. It was shown that a small positive ΔE_V = 0.15 ± 0.05 eV was observed in agreement with the majority of published experimental data. Also, a relatively low interface charge density $\sigma_I = (3 \pm 1)\ 10^{10}$ cm^{-2} was extracted from both MIS and SB measurements.

ACKNOWLEDGMENTS

REFERENCES

1. Tennant, C.A. Cockrum, J.B. Gilpin, M.A. Kinch, M.B. Reine and R.P. Ruth, *J. Vac. Sci. Technol.* B 10 (4), 1359 (1992).
2. J.M. Arias, J.G. Pasko, M. Zandian, S.H. Shin, G.M Williams, L.O. Bubulac, R.E. De Wames and W.E. Tennant, *J. Electron. Mater.* 22 (8), 1049 (1993).
3. G. Sarusi, G. Cinader, A. Zemel, D. Eger and Y. Shapira, *J. Appl. Phys.* 71 (10), 5070 (1992).
4. Y. Nemirovsky, N. Amir and L. Djaloshinski, *J. Electron. Mater.* 24, 649 (1995).
5. K. Kosai and W.A. Radford, *J. Vac. Sci. Technol.* A8 (2), 1254 (1990).
6. F.L. Madarasz and F. Szmulowicz, *J. Appl. Phys.* 64 (11), 6373 (1988); F.L. Madarasz and F. Szmulowicz, *J. Appl. Phys.* 62 (8), 3267 (1987).
7. S.J. Chang, L.Y. Leu, S.R. Forrest and C.E. Jones, *Appl. Phys. Lett.* 54, 1040 (1989) and references therein.
8. H. Kroemer, W-Y. Chien, J.S. Harris and D.D. Edwall, *Appl. Phys. Lett.* 36, 95 (1980).
9. H. Kroemer, *Appl. Phys. Lett.* 46, 504 (1985).
10. P. Migliorato and A.M. White, *Sol.-State Electron.* 26, 65 (1983).
11. P.R. Bratt and T.N. Casselman, *J. Vac. Sci. Technol.* A3 (1), 238 (1985).
12. V. Ariel-Altschul, E. Finkman and G. Bahir, *IEEE Trans. Electron. Dev.* 39, 1312 (1992).
13. H.K. Gummel, *IEEE Trans. Electron. Dev.* 455 (1964).
14. D.I. Babic and H. Kroemer, *Sol.-State Electron.* 28, 1015 (1985).
15. S.K. Ghandhi, K.K. Parat, H. Ehsani and I.B. Bhat, *Appl. Phys. Lett.* 58 (8), 828 (1991).
16. G. Cinader, A Raizman and A. Sher, *J. Vac. Sci. Technol.* B 9 (3), 1634 (1991).
17. M. Ogura, M. Mizuta, K. Onaka and H. Kukimoto, *Jpn. J. Appl. Phys.* 22, 1502 (1983).

Metalorganic Chemical Vapor Deposition of HgCdTe for Photodiode Applications

P. MITRA, T.R. SCHIMERT, and F.C. CASE

Loral Vought Systems Corporation, P. O. Box 650003, Dallas, TX 75265

R. STARR, M.H. WEILER, M. KESTIGIAN, and M.B. REINE

Loral Infrared and Imaging Systems, Lexington, MA 02173

Metalorganic chemical vapor depositon (MOCVD) *in situ* growth of p-on-n junctions for long wavelength infrared (LWIR) and medium wavelength infrared (MWIR) photodiodes is reported. The interdiffused multilayer process was used for the growth of the HgCdTe junctions on CdTe and CdZnTe substrates. The n-type region was grown undoped while the p-type layer was arsenic doped using tertiarybutylarsine. Following a low temperature anneal in Hg vapor, carrier densities of $(0.2-2) \times 10^{15}$ cm^{-3} and mobilities of $(0.7-1.2) \times 10^5$ cm^2/V-s were obtained for n-type LWIR (x ~ 0.22) layers at 80K. Carrier lifetimes of these layers at 80 K are ~1–2 µs. For the p-type region arsenic doping was controlled in the range of $(1-20) \times 10^{16}$ cm^{-3}. Arsenic doping levels in the junctions were determined by calibrated secondary ion mass spectroscopy depth profile measurements. Composition and doping of the p-on-n heterojunctions could be independently controlled so that the electrical junction could be located deeper than the change in the composition. The graded composition region between the narrow and wide (x = 0.28–0.30) bandgap regions are 1–2 µm depending on the growth temperature. Backside-illuminated variable-area circular mesa photodiode arrays were fabricated on the grown junctions as well as on ion implanted n-on-p MWIR junctions. The spectral responses are classical in shape. Quantum efficiencies at 80K are 42–77% for devices without anti-reflection coating and with cutoff wavelengths of 4.8–11.0 µm. Quantum efficiencies are independent of reverse bias voltage and do not decrease strongly at lower temperatures indicating that valence band barrier effects are not present. 80K R_0A of 15.9 Ω-cm^2 was obtained for an array with 11.0 µm cutoff. Detailed measurements of the characteristics of the MOCVD *in situ* grown and implanted photodiodes are reported.

Key words: HgCdTe, infrared detectors, metalorganic chemical vapor deposition (MOCVD)

INTRODUCTION

Metalorganic chemical vapor deposition (MOCVD) of epitaxial HgCdTe offers the attractive opportunity to grow *in situ* structures for infrared detectors such as p-on-n or n-on-p junctions as well as more complex multilayer device architectures. In order to grow such structures, good control of composition as well as doping is essential. Furthermore, the individual p- and n-type layers must have electrical properties and carrier lifetimes consistent with theoretical ex-

pectations for HgCdTe with low defect density.

Considerable progress has been achieved in recent years in HgCdTe epitaxy by MOCVD using both interdiffused multilayer process (IMP)[1] and direct alloy growth (DAG). These include high composition and thickness uniformity,[2,3] high crystalline quality limited only by that of the substrates used,[4] the capability of *in situ* monitoring[5] as well as the ability to extrinsically dope the layers n-type[6–10] and p-type.[10–13] Fabrication of infrared photodiodes has been reported where the p-n junctions are formed by Hg diffusion,[14] arsenic ion implantation, diffusion and activation[1] or p-type LPE growth on n-type absorber layers.[8,15] How-

ever, progress in the *in situ* growth of p-n junctions by MOCVD and detailed characterization of the photodiodes has been very limited.[16,17] This is at least in part due to problems with p-type doping which has not been optimal. Junctions grown *in situ* offer the benefit of growing the photodiode structure in a single growth run over the laborious process of junction formation by ion implantation, dopant diffusion, and activation or by liquid phase epitaxy (LPE) growth of a p-type layer on an MOCVD grown n-type layer. Grown junctions also offer the most direct and straightforward route to more complex device structures such as the LWIR/MWIR p-n-N-P independently accessed back-to-back dual-band photodiodes, described elsewhere in these proceedings.[18]

In this paper MOCVD-IMP *in situ* growth of p-n junctions for long wave (8–12 μm) and medium wave (3–5 μm) infrared (LWIR and MWIR) photodiodes is described and their electrical and optical characteristics are reported. The n-type regions were grown undoped and rely on the background donors following a Hg anneal. The p-type regions were doped with arsenic using tertiarybutylarsine (TBAs). Although the primary emphasis of this paper is on *in situ* grown p-on-n junctions, the performance characteristics of a boron implanted MWIR photodiode array on vacancy doped p-type HgCdTe, is also described for the purpose of comparison. Since photodiode performance is strongly dependent on the properties of the individual n-type and p-type layers, junction doping and composition profiles, detailed epilayer and junction characterization is also reported.

MOCVD GROWTH

Metalorganic chemical vapor deposition of HgCdTe was performed using the interdiffused multilayer process where alternating layers of HgTe and CdTe are grown and subsequently allowed to interdiffuse to a homogeneous alloy composition. The total thickness of the CdTe-HgTe pairs in each cycle was ≤0.10 μm with the alloy composition determined by the relative thicknesses of the binaries. Growth was carried out in a horizontal geometry reactor built by Metals Research Semiconductors Ltd. at near atmospheric pressure. Growth temperature was in the range of 350–370°C. CdTe and lattice matched CdZnTe (4% nominal Zn content) substrates with orientations of (211)B and (100)4° misoriented toward the nearest <110> were used. An elemental Hg source heated to 250–255°C located in close proximity to the susceptor was used as the source of Hg vapor. The organometallic precursors used were dimethylcadmium and diisopropyltelluride at partial pressures of (1–3) × 10⁻³ atm. High purity palladium diffused hydrogen was used as the carrier gas. Substrate rotation, which in this reactor has resulted in extremely uniform layers with variation in alloy composition and thickness of ≤1% over 6 cm² wafer areas, was not used in the present work.

For arsenic doping TBAs was injected in the reactor only during the CdTe growth cycle at a II/VI ratio of

1.1–1.2 since it has higher incorporation efficiency under metal rich conditions.[11] A double dilution flow configuration was used for the TBAs bubbler, which enabled tight control of the dopant injection with partial pressures in the range 5×10^{-8}–1×10^{-5} atm. Under these conditions, arsenic incorporation in the HgCdTe could be controlled in the range of 2×10^{15}–$4 \times 10^{17} cm^{-3}$. The double dilution approach to arsenic doping is especially useful for controlling different dopant levels within a layer structure during a single growth run. The activation of arsenic as acceptors was found to be near 100% up to ~$2 \times 10^{17} cm^{-3}$ using secondary ion mass spectroscopy (SIMS). The accuracy of the SIMS calibration standard, however, was quoted to be within a factor of two at these doping levels. The n-type regions in the junctions were grown undoped. The LWIR p-on-n homojunctions were grown by switching on TBAs flow at a specific rate during the p-type layer growth, without changing the IMP cycle thicknesses. No change in the alloy composition was observed when TBAs was injected for doping levels <$1 \times 10^{17} cm^{-3}$. The p-on-n heterojunctions were grown similarly except that TBAs was injected a few steps prior to where the IMP cycle binary thickness ratio was altered for the wider bandgap cap layer. Arsenic doping in the p-on-n junctions was varied in the range $(0.2–2) \times 10^{17} cm^{-3}$. The epilayers were then annealed *in situ* at 350–390°C to complete the interdiffusion of the "binary" layers to homogeneous alloys. All of the HgCdTe epilayers were then subjected to a stoichiometric anneal at 230°C under Hg vapor to fill the Hg vacancies in the as-grown lattice. The thicknesses of the n-type and p-type layers are 10–15 μm and 1–3 μm, respectively.

CHARACTERIZATION

Alloy composition and epilayer thickness were determined from infrared transmission measurements at 300K. Carrier concentration and mobility were determined from Hall effect measurements of single homogeneous epilayers at 20–300K and magnetic field strengths in the range of 1.25 to 5.0 kG. Lifetime characterization was carried out primarily by transient millimeter wave reflectance (TMR) and in some cases by standard transient photoconductive decay. The details of the TMR lifetime test system have been described previously.[19] The noncontact TMR technique has been shown to yield results identical to PC decay over a wide range of lifetimes from ~5 ns to >10 μs. Laser irradiance was kept low to ensure that photo-excitation was in the low injection regime and the lifetime was insensitive to irradiance level. All of the films were tested unpassivated and were wet etched lightly in a Br-methanol solution just prior to the measurements.

Calibrated SIMS depth profiling was used to determine dopant concentration as well as composition profiles[20] in the heterostructures. All SIMS measurements were performed at Charles Evans & Associates, Redwood City, CA. Cs⁺ ion bombardment was used for measuring the dopant and ¹²⁵Te depth pro-

files. For heterostructures the alloy composition of the lower bandgap region was determined by Fourier transform infrared (FTIR) transmission which served as the calibration standard for determining the entire composition profile from the ^{125}Te signal intensity.

Variable area photodiode arrays[21] were fabricated using the grown p-on-n and implanted n-on-p junctions. The arrays consisted of 43 ZnS-passivated widely separated circular mesa photodiodes having radii in the 20–175 µm range. The arrays were bump interconnected to a circuit board and tested in the backside-illuminated configuration. No antireflection coating was used on the substrate surface. These photodiodes were characterized for I-V curves, zero bias resistance area product R_0A, quantum efficiency, effective lateral optical collection length, and spectral response.

CHARACTERIZATION RESULTS

Single Layer Films

As-grown, the undoped HgCdTe layers were well-behaved p-type, due to Hg vacancies, with hole concentrations dependent on the growth, temperature, and Hg partial pressure. Upon annealing under saturated Hg vapor at 235°C, the films converted to n-type with classical temperature dependence of Hall mobility and carrier concentration. Background carrier concentrations at 80K in the range $(3—20) \times 10^{14}$ cm^{-3} are observed in our MOCVD grown undoped n-type films with the variation most likely due to diffusion of substrate impurities into the HgCdTe during growth. For example, for substrates from a specific boule, variation in background concentration was significantly less, varying in the range $(3–8) \times 10^{14}$ cm^{-3}. 80K mobility of a large number of single layers with x = 0.19–0.32 for both (100)4° and (211)B oriented films is shown in Fig. 1. The thicknesses of the films were 10–

15 µm. The solid line is obtained from a fit to a large number of recent In doped $(1 \times 10^{15}$ cm$^{-3})$ LPE grown HgCdTe films.[22] The mobilities over a wide range of x values are shown to be independent of orientation and are similar to those for indium doped MOCVD[8] and close to state of the art In-doped LPE grown HgCdTe films for the corresponding x-values.

The temperature dependence of the transient lifetime on an n-type epilayer M209 with x = 0.24 is shown in Fig. 2. For M209, carrier concentration of 1.03×10^{15} cm^{-3} and mobility of 8.0×10^4 cm^2/V-s were measured at 80K. A calculation of the various recombination mechanisms show that Auger recombination is the dominant process governing lifetime in this case and the radiative recombination component is not significant. The Shockley-Read (S-R) component is also not significant as evidenced by the low Hg-vacancy and deep level acceptor densities used in the fit. The capture cross-sections used in the fit are the
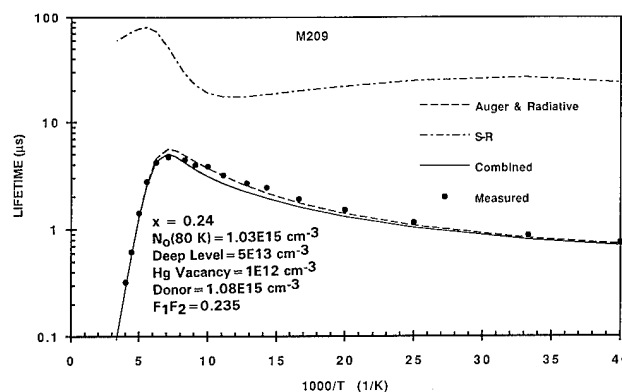
Fig. 2. Temperature dependence of lifetimes and modeling results of undoped n-type layers with x = 0.24.
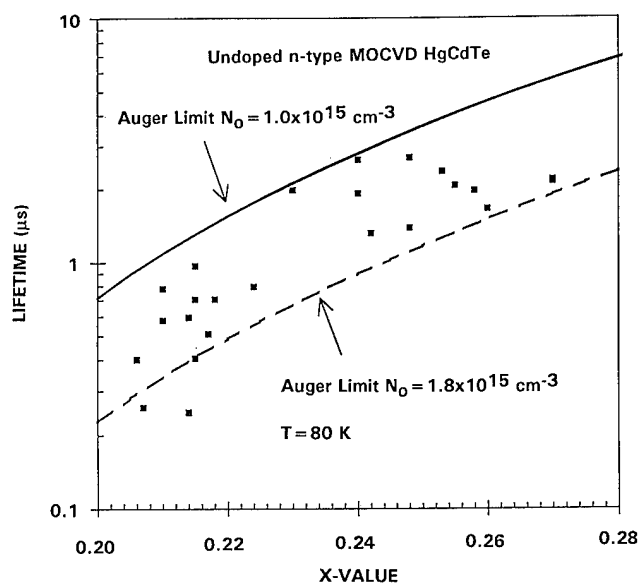
Fig. 3. The dependence of 80K lifetimes on composition in MOCVD grown undoped n-type HgCdTe. The solid and dotted lines are due to Auger + radiative recombination calculated for N_o values of 1.0×10^{15} and 1.8×10^{15} cm^{-3}, respectively, the limits of the 80K carrier concentration range of samples used in the plot.

Fig. 1. 80K mobility of MOCVD grown undoped n-type HgCdTe vs x-values for (100)4° and (211)B oriented films. The solid line is a fit to recent In-doped LPE data.
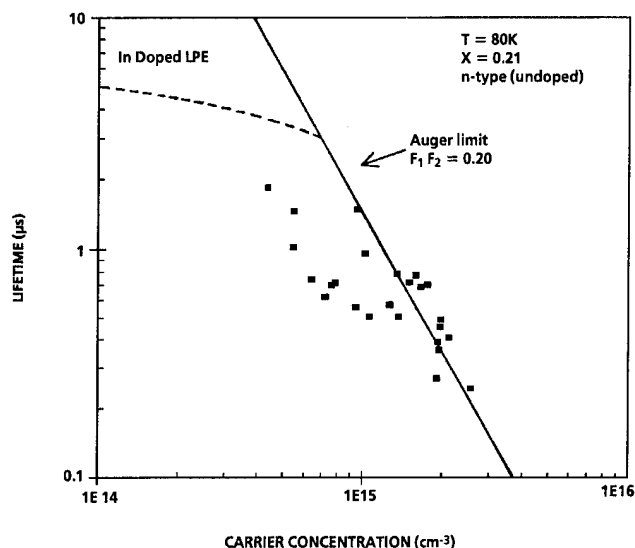
Fig. 4. 80K lifetimes of MOCVD undoped n-type x = 0.21 HgCdTe layers vs 80K carrier concentration. The solid line is the calculated Auger lifetime while the dotted line is the trend observed in In doped LPE films.
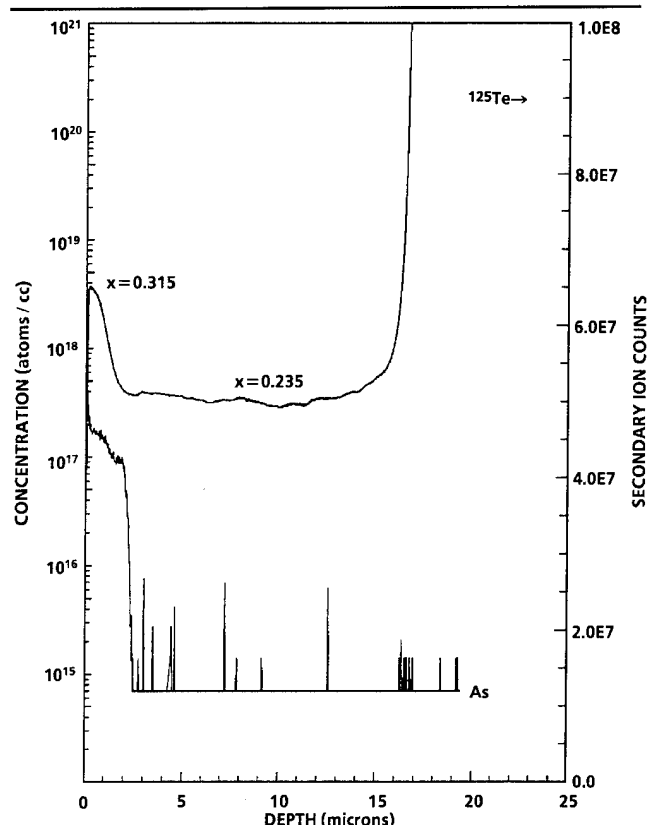

Fig. 5. SIMS depth profiles of composition and arsenic doping in an LWIR MOCVD grown p-on-n heterojunction.

same as used previously[23] to analyze vacancy doped p-type HgCdTe. The model is used, essentially unchanged, to describe S-R recombination in n-type HgCdTe by varying the Hg-vacancy and deep level densities. An Auger form factor $F_1F_2 = 0.235$ was assumed in the calculation and is consistent with that used in fitting the temperature dependence of lifetimes of several undoped n-type MOCVD HgCdTe

films grown in our laboratory.

The 80K lifetimes measured on several undoped n-type layers, with carrier concentrations of $(1-1.8) \times 10^{15}$ cm^{-3} and x-values in the range 0.20–0.28, are plotted in Fig. 3. The theoretical Auger + radiative lifetime calculations at 80K for the upper and lower limits of the electron concentrations are also shown. Most of the measured lifetimes fall within the calculated Auger limits demonstrating Auger limited lifetimes are attainable for undoped n-type HgCdTe grown by MOCVD for these alloy compositions and carrier concentrations. It should be noted that surface recombination effects have not been included in the present analysis. The lifetime results reported here on undoped n-type HgCdTe are similar to results reported on In-doped MOCVD grown[8,9,24] n-type films where Auger limited lifetimes have also been observed at electron concentrations $n_0 \geq 1 \times 10^{15}$ cm^{-3}

A plot of 80K lifetime vs carrier concentration for undoped, unpassivated x = 0.21 n-type films is shown in Fig. 4. For comparison, the Auger limit and the trend line for lifetimes reported for x = 0.21 In-doped LPE grown HgCdTe[25] are also shown. The plot shows Auger limited lifetime for the MOCVD HgCdTe with carrier concentration $\geq 1 \times 10^{15}$ cm^{-3}. At lower concentration the lifetime is S-R limited with somewhat shorter lifetimes than shown by the LPE trend line. For mid 10^{14} cm^{-3} carrier concentration, the lifetimes of the MOCVD layers is a factor of two lower than the LPE trend line.

The arsenic-doped p-type HgCdTe films show classical temperature dependence of Hall parameters. From the slope of the carrier concentration in the freezout region acceptor ionization energies in the range 6–10 meV were obtained for x = 0.30 arsenic-doped HgCdTe. Hole concentrations in these films were in the range of 3×10^{15} to 5×10^{16} cm^{-3}. Acceptor ionization energies of 6 meV have been reported for x = 0.30 arsenic-doped LPE HgCdTe.[26]

For MOCVD-IMP grown p-type films with x = 0.21 we have previously reported[27] that longer lifetimes were observed for arsenic-doped as compared to vacancy-doped HgCdTe. Similar results have been obtained for x = 0.30 arsenic doped layers. For low 10^{16} cm^{-3} hole concentration the lifetimes are 200–350 ns. These values are a factor of 2–5 lower than the radiative limit. Although these lifetime values are higher than previously reported in MOCVD arsenic doped HgCdTe,[28] they are nevertheless below the values observed in LPE arsenic doped HgCdTe where for x = 0.30 the lifetimes are at the radiative limit over a wide range of hole concentrations.[26] This difference in lifetime could be due to higher density of defects in arsenic-doped HgCdTe grown by MOCVD using TBAs.

Grown Junction Films

SIMS depth profiles of ^{125}Te signal intensity and arsenic provide a highly effective means of determining the composition and arsenic doping profiles in a grown junction. An example of a p-on-n heterojunction with x = 0.315 arsenic doped cap layer on an undoped

n-type LWIR (x = 0.235) layer grown on a CdTe(211)B substrate is shown in Fig. 5. To separate the electrical junction from the onset of the change in the alloy composition, TBAs was injected a few IMP cycles prior to changing conditions for the wider bandgap composition. Following growth, the structure was annealed *in situ* at 390°C. The change in the arsenic level from 1×10^{15} to 5×10^{16} cm^{-3} occurs over less than 0.5 μm resulting in a sharp rise before it levels off at 1×10^{17} cm^{-3}. The data show that arsenic doping and alloy composition can be independently controlled in MOCVD growth and demonstrates that heterojunctions without valence band barriers can be grown. The data also indicate that the arsenic is incorporated in the Te-sublattice since minimal diffusion has occured.

An example of a 32 μm thick MOCVD grown multilayer structure is shown in Fig. 6. This is a p-n-N-P LWIR/MWIR dual band detector structure[18] grown on an x = 0.42 arsenic doped buffer layer on CdTe(211)B. The p-on-n LWIR detector is a heterojunction grown on an n-on-p MWIR homojunction. The graded composition region in the heterostructure is ~1.5 μm. The growth of this structure demonstrates that arsenic doping can be controlled sufficiently to produce different doping levels during a single growth run enabling the growth of complex device architectures.

PHOTODIODE RESULTS AND DISCUSSION

We report data in this section for two different configurations of photodiodes fabricated from MOCVD-IMP HgCdTe films: ion implanted n-on-p MWIR homojunctions on Hg-vacancy doped p-type HgCdTe single layer films, and *in situ* grown LWIR p-on-n homojunctions and heterojunctions.

The characteristics of the variable-area arrays in each of these two configurations are summarized in Table I. All data in Table I are for a temperature of

80K. This table lists the film number, the substrate material and orientation, the array number, the average cutoff wavelength λ_{co} at 80K, the total variation (max-min) in percent of λ_{co} over the array, the R_oA at 80K of the best element of the array, the one-dimensional quantum efficiency QE(1D), and the optical collection length L_{OPT}. The latter two quantities were deduced from the dependence of quantum efficiency on junction area in the variable-area photodiode arrays.[21] The data in Table I show that the cutoff wavelength is generally quite uniform within each array, and reasonably uniform for arrays from the
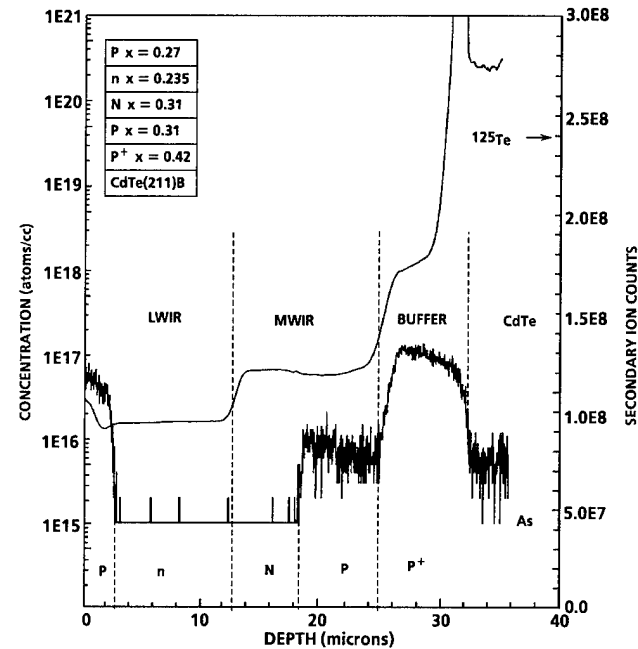
Fig. 6. SIMS depth profile of composition and arsenic doping in a p-n-N-P dual band detector structure grown on an x = 0.42 arsenic doped buffer layer.

Table I. Summary of MOCVD-Grown Photodiode Results

| Film	Device Configuration	Substrate	Array	λ_{co} (μm)	$\Delta\lambda_{co}$ (%)	R_oA (ohm-cm²)	QE (1D) (%)	L_{OPT} (μm)
177	Implant n-on-p	CdZnTe(100)4°→(110)	A	4.80	5.0	2.62×10^6	74	31
175	Grown p-on-n	CdZnTe(100)4°→(110)	A	6.36	3.4	9.01×10^3	67	28
			B	6.08	1.0	2.37×10^4	72	32
			C	6.11	2.1	9.64×10^3	71	29
			D	6.24	2.8	1.10×10^4	70	29
181A	Grown p-on-n	CdTe(100)2°→(110)	A	5.99	1.9	9.40×10^3	77	14
181BC	Grown p-on-n	CdZnTe(100)4°→(110)	B	5.10	2.3	3.80×10^4	42	18
193	Grown p-on-n	CdZn(211)Te	C	7.76	0.3	184	63	8
197	Grown p-on-n	CdTe(211)Te	B	7.74	1.5	336	52	9
			A1	7.76	1.1	213	59	10
209	Grown p-on-n	CdZnTe(211)Te	A1	9.10	1.9	142	55	17
			A2	8.68	2.5	374	46	24
211	Grown p-on-n	CdZnTe(211)Te	A1	11.03	7.2	15.0	47	10
			A2	10.96	1.5	15.9	49	9
257	Grown p-on-n	CdZnTe(100)4°→(110)	A1	8.94	1.8	33.6	62	13
264A	Grown p-on-n	CdTe(211)Te	A1	7.03	6.9	619	63	5
264B	Grown p-on-n	CdTe(211)Te	B2	8.36	0.5	93.4	68	5
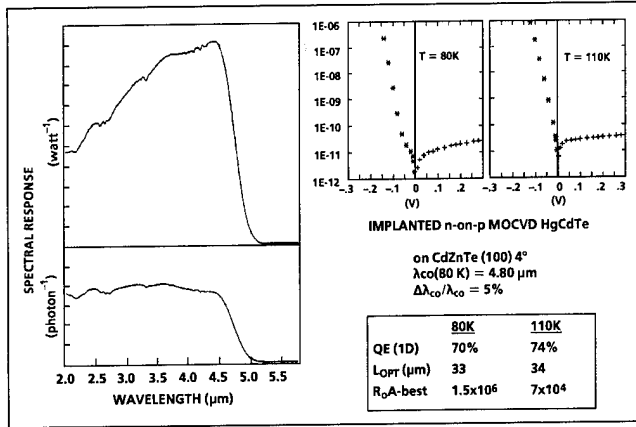
Fig. 7. Spectral response (80K) and I-V curves (80 and 110K) for an MWIR n-on-p implanted photodiode grown on (100)4° CdZnTe substrate.
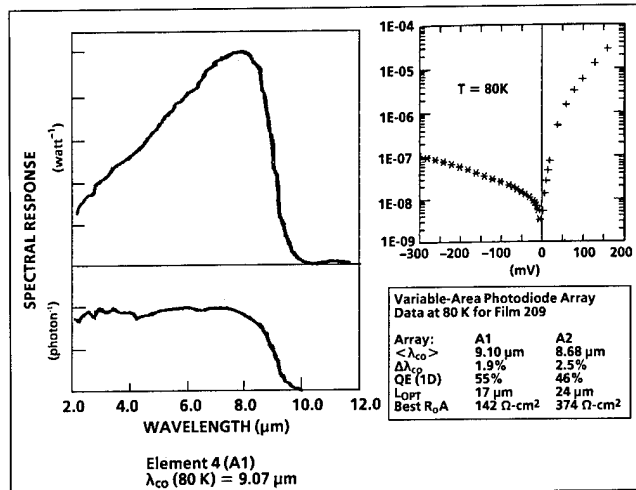

Fig. 8. 80K spectral response and I-V curves for an LWIR p-on-n MOCVD-IMP grown photodiode.
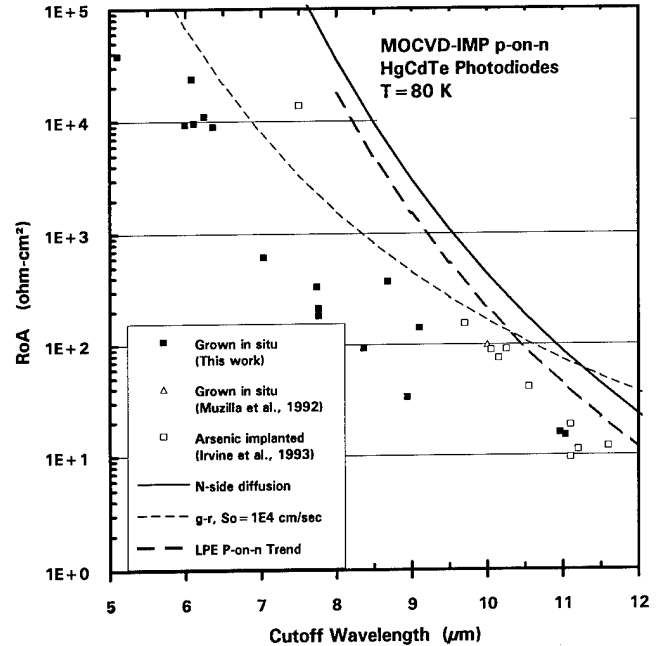

Fig. 9. R_0A data at 80 K for MOCVD *in situ* grown p-on-n junctions. The solid line is the calculated R_0A due to diffusion current from the n-layer only for a thickness of 15 μm and lifetime determined by the Auger mechanism. The dashed line is due to depletion layer g-r calculation with a surface recombination velocity of 1×10^4 cm/s.

same film, although no special measures were taken to optimize the lateral uniformity in the HgCdTe alloy composition over the film, such as rotation of the substrate during MOCVD growth.

Implanted n-on-p Photodiodes

The spectral response and I-V curves of one element of an MWIR n-on-p photodiode variable-area fabricated by boron ion implantation into Hg-vacancy doped p-type HgCdTe grown on a (100) CdZnTe substrate are shown in Fig. 7. This film was grown and interdiffused at a temperature of 350°C to provide a low concentration of Hg vacancy acceptors. Measurements on a section of this film gave an as-grown hole concentration of 3.75×10^{15} cm^{-3}, a mobility of 323 cm²/V-s, and a lifetime of 0.7 μsec, all measured at 80K. As shown in Fig. 7, the spectral response curve is classical in shape. The one-dimensional quantum efficiency values of 70% at 80K and 74% at 110K are close to the maximum of 80% expected with no anti-reflection coating. The best R_0A values measured for this array are 2.6×10^6 ohm-cm² at 80K and 2.5×10^5 ohm-cm² at 110K. This R_0A value at 110K is comparable to those of implanted n-on-p photodiodes formed in p-type Hg-

vacancy doped LPE films of the same cutoff wavelength.[29]

p-on-n *In Situ* Grown Photodiodes

The data for *in situ* grown p-on-n MOCVD photodiodes summarized in Table I demonstrate that good quantum efficiencies are achievable, especially when compared to the maximum quantum efficiency of 80% for the case here of no antireflection coating. The optical collection length values in Table I are generally consistent with the minority carrier diffusion lengths expected for n-type HgCdTe with doping in the $0.5–2 \times 10^{15}$ cm^{-3} range.

Spectral response and current-voltage (I-V) curves for a p-on-n photodiode grown *in situ* by MOCVD (film 209) is shown in Fig. 8. The data illustrate two general trends in all the LWIR p-on-n MOCVD photodiodes. The spectral response is usually classical in shape, with no sign of interface recombination effects. And the reverse bias I-V curves show strong evidence of defect-generated current, with rapid increases in current with increasing reverse bias voltage.

The R_0A data at 80K for the p-on-n *in situ* grown MOCVD junction arrays listed in Table I are plotted vs cutoff wavelength in Fig. 9. For comparison, the state-of-the-art R_0A values for p-on-n LPE two-layer heterojunctions are indicated by the heavy dashed line. One can see that the MOCVD grown junction data for a cutoff wavelength of 11 μm (Film 211) are within a factor of four of the LPE trend line. The solid line in Fig. 9 is the calculated R_0A due to diffusion current from the n-layer only, for a thickness of 15 μm and a lifetime determined by the Auger-1 mechanism. The dashed line is the calculated R_0A product due to

depletion layer g-r current, for doping levels of 1×10^{15} and 1×10^{16} cm^{-3} on the n-side and p-side, respectively, and for a depleted surface recombination velocity S_0 of 1×10^4 cm/s. The calculated g-r limited R_0A values increase proportionally to the assumed value for S_0. For typical LPE p-on-n heterojunction photodiodes, S_0 is typically 1×10^3 cm/s or less. Figure 9 indicates that these *in situ* grown MOCVD p-on-n junctions have S_0 values above 1×10^4 cm/s.

There are no published data in the literature for *in situ* grown p-on-n or n-on-p HgCdTe junctions by MOCVD-IMP that we can compare our data to. However, in unpublished work, Muzilla et al. reported[17] R_0A products at 80K greater than 100 ohm-cm^2 and quantum efficiencies of 30–65 % (with anti-reflection coating) for 64×64 backside-illuminated arrays of mesa photodiodes with CdTe passivation and cutoff wavelengths of 10.0 µm, grown *in situ* by MOCVD-IMP onto GaAs substrates. This value is shown by the triangle data point in Fig. 9 and is comparable to our best R_0A data. Irvine et al.[1] reported data for arsenic implanted p-on-n HgCdTe junctions formed in indium-doped n-type heterostructures grown by MOCVD-IMP onto GaAs substrates. Their data are quoted for a temperature of 77K and approach the n-side diffusion current theory for a donor doping of 3×10^{15} cm^{-3}. We have scaled their best data points from 77 to 80K, with the assumption that the best R_0A data were limited by only n-side diffusion current that varies as $\exp(E_G/kT)$, where $E_G = 1.24/\lambda_{CO}$. This scaling amounts to about a factor of two reduction in their quoted R_0A values for 77K. The best R_0A data from Fig. 8 of Ref.1 scaled in this way are plotted in Fig. 9. It is significant that all three sets of data are comparable at the long wavelength region around 11 µm.

DISCUSSION

An important feature which emerges from the characteristics of the *in situ* grown MOCVD p-on-n junctions is that the reverse-bias I-V curves, as well as the R_0A products, are dominated by defect-generated current mechanisms. These include not only conventional g-r current, but also tunneling-like reverse currents that increase rapidly with reverse bias voltage.

It is possible that intentional donor doping will improve junction quality, since the donor concentration can then be precisely controlled in the desired $(1-2) \times 10^{15}$ cm^{-3} range. The good quality of the implanted n-on-p junction reported here attests to the high quality of the undoped p-type MOCVD-IMP film. And the near-diffusion limited quality of the arsenic implanted/activated/diffused planar devices formed in indium-doped MOCVD-IMP grown LWIR heterostructures reported by Irvine et al.[1] is also encouraging. Both these observations taken together suggest that some fraction of the defects in our *in situ* grown MOCVD junctions may reside within the arsenic doped region itself, and that the present *in situ* arsenic doping with TBAs is not optimal.

Etch pit density (EPD) measurements with an etchant described by Hahnert and Schenk[30] indicate values in the range 5×10^5–1×10^7 cm^{-2}. In general, higher EPD values were obtained for HgCdTe films grown on CdTe than on CdZnTe. Only limited correlation, however, has been observed between the EPD values and photodiode quality. Clearly additional studies are required to catalog and determine the nature of the dominant defects in MOCVD grown junctions that are responsible for limiting the R_0A products and the reverse bias I-V curves, and methods need to be developed for their reduction.

CONCLUSIONS

MOCVD *in situ* growth of p-on-n HgCdTe junction photodiodes and of p-n-N-P-P$^+$ multilayer films has been demonstrated with the IMP technique. The electrical properties and carrier lifetimes of the background-doped n-type layers were shown to be close to those obtained in indium-doped LPE HgCdTe. Controlled *in situ* arsenic doping was achieved over the range of $(0.2-20) \times 10^{16}$ cm^{-3}. The arsenic profiles could be controlled such that different doping levels with sharp transitions were obtained during a single growth run. The control of alloy composition and arsenic doping was demonstrated by the growth of multilayer p-n-N-P-P$^+$ films. Graded composition regions in the heterostructures are 1.5 µm wide. Medium wavelength IR n-on-p photodiodes formed by boron implantation into Hg-vacancy p-type MOCVD films have characteristics at 110K comparable to those of implanted junctions in LPE HgCdTe films. The LWIR *in situ* grown p-on-n junctions exhibit classical spectral responses and high quantum efficiencies, but the reverse-bias I-V curves and the R_0A products at 80K are typically limited at present by defect-generated current mechanisms. Nevertheless, these data demonstrate the exciting potential that MOCVD-IMP holds for *in situ* growth of advanced HgCdTe multilayer devices.

ACKNOWLEDGMENTS

REFERENCES

1. S.J.C. Irvine, J. Bajaj and L.O. Bubulac, *Mater. Res. Soc. Symp. Proc. 299*, 99 (1994).
2. D.D. Edwall, *J. Electron. Mater.* 22, 847 (1993).
3. S. Murakami, Y. Sakachi, H. Nishino, T. Saito, K. Shinohara and H. Takigawa, *J. Vac. Sci. Technol.* B10, 1380 (1992).

4. M.J. Bevan, N.J. Doyle, J. Greggi and D. Snyder, *J. Vac. Sci. Technol.* A8, 1049 (1990).

5. J. Bajaj, S.J.C. Irvine, H.O. Sankur and S.A. Svoronos, *J. Electron. Mater.* 22, 899 (1993).

6. S.K. Ghandhi, N.R. Taskar, K.K. Parat and I.B. Bhat, *Appl. Phys. Lett.* 57, 252 (1990).

7. J.S. Gough, M.R. Houlton, S.J.C. Irvine, N. Shaw, M.L. Young and M.G. Astles, *J. Vac. Sci. Technol.* B9, 1687 (1991).

8. R. Korenstein, P.H. Hallock, D.L. Lee, E. Sullivan, R.W. Gedridge, Jr. and K.T. Higa, *J. Electron. Mater.* 22, 853 (1993).

9. S.J.C. Irvine, J. Bajaj, L.O. Bubulac, W.P. Lin, R.W. Gedridge, Jr. and K.T. Higa, *J. Electron. Mater.* 22, 859 (1993).

10. C.D. Maxey, I.G. Gale, J.B. Clegg and P.A.C. Whiffin, *Semicond. Sci. Technol.* 8, S183 (1993).

11. P. Capper, C.D. Maxey, P.A.C. Whiffin and B.C. Easton, *J. Cryst. Growth* 97, 833 (1989).

12. N.R. Taskar, I.B. Bhat, K.K. Parat, S.K. Ghandhi and G.J. Scilla, *J. Vac. Sci. Technol.* B9, 1687 (1991).

13. D.D. Edwall, L.O. Bubulac and E.R. Gertner, *J. Vac. Sci. Technol.* B10, 1423 (1992).

14. L.M. Smith, C.F. Byrne, D. Patel, P. Knowles, J. Thompson, G.T. Jenkin, T. Nguyen Duy, A. Durand and M. Bourdillot, *J. Cryst. Growth* 107, 605 (1991).

15. S. Oguz, D.L. Lee, R.J. Olson Jr. and E. Sullivan, *J. Cryst. Growth* 124, 664 (1992).

16. S. Oguz, R.J. Olson, Jr., D.L. Lee, L.T. Specht and V.G. Kreismanis, *SPIE Proc.* 1307, 560 (1990).

17. M.S. Muzilla, K. Tanala, E.C. Whitcomb, D.E. Molyneux, G.B. Beil, D.D. Edwall and E.R. Gertner, Rockwell International Corp. unpublished work (1992).

18. M.B. Reine, P.W. Norton, R. Starr, M.H. Weiler, M. Kestigian, B.L. Musicant, P. Mitra, T. Schimert, F.C. Case, I.B. Bhat, H. Ehsani and V. Rao, *J. Electron. Mater.* 24, XXX (1995).

19. A.J. Brouns, T.R. Schimert, P. Mitra, F.C. Case, S.L. Barnes and Y.L. Tyan, *Semicond. Sci. Technol.* 8, 928 (1993).

20. L.O. Bubulac and C.R. Viswanathan, *Appl. Phys. Lett.* 60, 222 (1992).

21. M.B. Reine, K.R. Maschhoff, S.P. Tobin, P.W. Norton, J.A. Mroczkowski and E.E. Krueger, *Semicond. Sci. Technol.* 8, 788 (1993).

22. S.P. Tobin, Loral Infrared & Imaging Systems, private communication.

23. Y.L. Tyan, T.R. Schimert and L.T. Claiborne, *J. Vac. Sci. Technol.* B10, 1560 (1992).

24. R. Zucca, D.D. Edwall, J.S. Chen, S.L. Johnson, C.R. Younger, *J. Vac. Sci. Technol.* B9, 1823 (1991).

25. G.N. Pultz, P.W. Norton, E.E. Krueger and M.B. Reine, *J. Vac. Sci. Technol.* B9, 1724 (1991).

26. T. Tung, M.H. Kalisher, A.P. Stevens and P.E. Herning, *Mat. Res. Soc. Symp. Proc.* 90, 321 (1987).

27. P. Mitra, T.R. Schimert, Y.L. Tyan, A.J. Brouns and F.C. Case, *Matl. Res. Soc. Symp Proc.* 299, 155 (1994).

28. C.D. Maxey, P. Capper, P.A.C. Whiffen, B.C. Easton, I. Gale, J.B. Clegg, A. Harker and C.L. Jones, *J. Cryst. Growth* 101, 300 (1990).

29. P.H. Zimmerman, Loral Infared & Imaging Systems, private communication.

30. I. Hahnert and M. Schenk, *J. Cryst. Growth* 101, 251 (1990).

Independently Accessed Back-to-Back HgCdTe Photodiodes: A New Dual-Band Infrared Detector

M.B. REINE, P.W. NORTON, R. STARR, M.H. WEILER, M. KESTIGIAN, and B.L. MUSICANT

Loral Infrared & Imaging Systems, Lexington, MA 02173

P. MITRA, T. SCHIMERT, and F.C. CASE

Loral Vought Systems Corporation, Dallas, TX 75265

I.B. BHAT, H. EHSANI, and V. RAO

Rensselaer Polytechnic Institute, Troy, NY 12180

We report the first data for a new two-color HgCdTe infrared detector for use in large dual-band infrared focal plane arrays (IRFPAs). Referred to as the independently accessed back-to-back photodiode structure, this novel dual-band HgCdTe detector provides independent electrical access to each of two spatially collocated back-to-back HgCdTe photodiodes so that true simultaneous and independent detection of medium wavelength (MW, 3–5 μm) and long wavelength (LW, 8–12 μm) infrared radiation can be accomplished. This new dual-band detector is directly compatible with standard backside-illuminated bump-interconnected hybrid HgCdTe IRFPA technology. It is capable of high fill factor, and allows high quantum efficiency and BLIP sensitivity to be realized in both the MW and LW photodiodes. We report data that demonstrate experimentally the key features of this new dual-band detector. These arrays have a unit cell size of $100 \times 100 \, \mu m^2$, and were fabricated from a four-layer p-n-N-P HgCdTe film grown *in situ* by metalorganic chemical vapor deposition on a CdZnTe substrate. At 80K, the MW detector cutoff wavelength is 4.5 μm and the LW detector cutoff wavelength is 8.0 μm. Spectral crosstalk is less than 3%. Data confirm that the MW and LW photodiodes are electrically and radiometrically independent.

Key words: Dual-band detectors, focal plane arrays, HgCdTe, infrared detectors, metalorganic chemical vapor deposition (MOCVD)

INTRODUCTION

There has always been a keen interest in two-color infrared detectors for many applications. For semiconductor quantum detectors, one of the most attractive two-color configurations is the stacked arrangement in which the shorter wavelength detector is placed optically ahead of the longer wavelength detector. The first detector absorbs only the shorter wavelength radiation and transmits the longer wavelength radiation to the second detector. This arrangement guarantees precise and fixed optical registration of

the two detectors. The first HgCdTe two-color detectors of this type were photoconductors, with one detector epoxied directly on top of a second detector.[1]

The trend today in infrared detection is toward large two-dimensional mosaic arrays of HgCdTe photodiodes that are electronically multiplexed.[2] These are generally referred to as infrared focal plane arrays (IRFPAs). The most common architecture for HgCdTe IRFPAs is the hybrid arrangement illustrated in Fig. 1, consisting of a backside-illuminated HgCdTe photodiode array that is interconnected to a silicon array of input circuits and multiplexers by a matrix of metal bumps, with one bump per unit cell connecting an individual photodiode to its input cir-
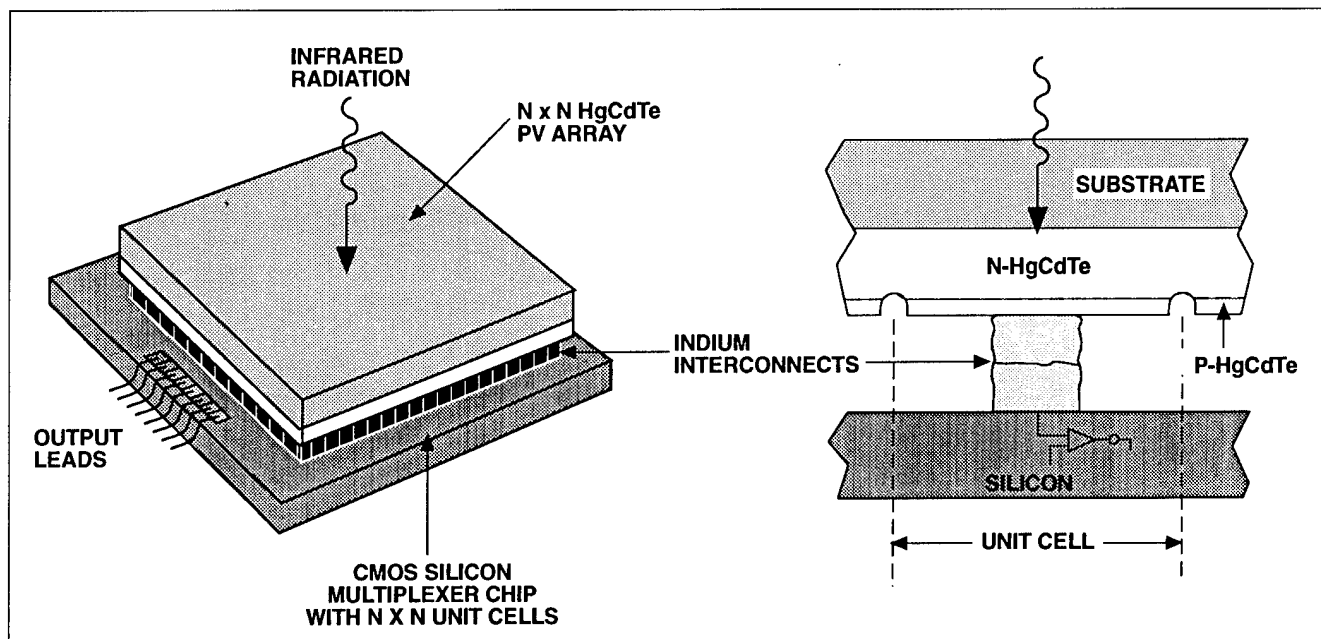
Fig. 1. Two-dimensional hybrid IRFPAs consisting of a backside-illuminated array of HgCdTe photodiodes interconnected by metal bumps to a silicon multiplexer chip.

cuit and preamplifier. The unit cell size is typically $50 \times 50\ \mu m^2$ to $100 \times 100\ \mu m^2$. The unit cell area in the silicon chip beneath each detector typically contains a low-noise preamplifier, a bias circuit for the photodiode, and an integrating capacitor. The HgCdTe photodiode array is usually grown epitaxially onto an infrared-transparent substrate such as CdTe, CdZnTe, sapphire, GaAs, or silicon. The highest performance HgCdTe photodiodes today are in the P-on-n heterojunction configuration and are grown by two-layer liquid phase epitaxy onto CdTe or CdZnTe.[3–5] (In this paper, we use the convention that an upper case P or N denotes the layer of wider energy band gap.)

There is great interest in extending the capability of such IRFPAs to detect two separate spectral bands such as the MW 3–5 μm and LW 8–12 μm bands for a variety of applications. Of course this can be done with single-color IRFPAs using beam splitters or filter wheels, but this adds considerable complexity which may be prohibitive for nonlaboratory applications where size and weight are at a premium. Hence, there is a need for a HgCdTe detector that can provide separate responses to different wavelengths and at the same time be incorporated into the staring IRFPA architecture shown in Fig. 1.

One such two-color HgCdTe detector that has been recently reported is the bias-selectable back-to-back photodiode.[6,7] This device is formed by sequentially growing two HgCdTe photovoltaic detectors epitaxially to form an n-P-N structure. These n-P-N devices were grown by a combination of sequential liquid phase epitaxy (LPE) and molecular beam epitaxy (MBE)[6] and by in situ MBE.[7] While the bias-selectable two-color detector affords perfect spatial collocation of the two detectors, it has the inherent drawback of not allowing temporal simultaneity of detection. Ei-

ther one or the other photodiode is functioning, depending on the bias polarity applied across the back-to-back pair. Other problems with the bias-selectable device are that it does not allow independent selection of the optimum bias voltage for each photodiode, and that there can be substantial medium wavelength (MW) crosstalk in the long wavelength (LW) detector due to injection from the floating forward-biased MW photodiode into the LW photodiode. Kosai[8] has reported that this crosstalk can be prevented by adjusting the energy band profile of the middle p-type layer, but this may add considerable complexity to the LPE growth of this device.

We have developed and demonstrated a new two-color HgCdTe infrared detector that is applicable to large MW/LW dual-band IRFPAs and which overcomes the problems of the bias-selectable device. This new two-color HgCdTe detector provides independent electrical access to each of two spatially collocated back-to-back photodiodes so that true simultaneous and independent detection and integration of MW and LW photocurrents is accomplished. Simultaneous detection of both wavelength bands is important for many dual-band IRFPA applications, such as the case of tracking rapidly moving objects, and provides a factor-of-two in efficiency for a staring IRFPA. The independent electrical access also allows bias voltages for the LW and MW photodiodes to be selected independently to optimize the performances of the individual MW and LW detectors and their readout circuits. Furthermore, independent electrical access eliminates the spectral crosstalk problem because neither junction is electrically floating.

The following section describes the operation and key features of this new dual-band detector. The section on experimental techniques briefly describes

the p-n-N-P metalorganic chemical vapor deposition (MOCVD) HgCdTe film growth and describes the fabrication of the dual-band detectors. The section on dual-band detector characterization data presents electrical and radiometric data on three arrays of p-n-N-P dualband detectors.

DEVICE CONCEPT

The independently accessed back-to-back photodiode dual-band detector is shown in cross section in Fig. 2. It is a p-n-N-P structure formed by four HgCdTe layers grown sequentially onto a CdZnTe substrate. It operates in the backside-illuminated mode with infrared radiation incident on the substrate surface. Figure 2 shows a single unit cell that can be replicated in two dimensions to form a backside-illuminated hybrid dual-band IRFPA.

A two-layer N-on-P MW homojunction is first grown *in situ* onto a CdZnTe substrate, followed by the *in situ* growth of a p-on-n two-layer LW homojunction. An isotype n-N heterojunction forms at the interface between the LW and MW n-type layers, which forms an ohmic connection so that the LW and MW photodiodes are in a back-to-back configuration. This isotype heterojunction performs another critical role in that it prevents LW photogenerated minority carriers (holes) from diffusing to and being collected by the MW junction, as is illustrated in the band diagram of Fig. 3.

This dual-band detector uses two bumps per unit cell for electrical, mechanical, and thermal interconnection to the silicon readout electronics chip. One bump contacts only the p-type region of the LW

photodiode. The other bump contacts the n-type region of the LW photodiode, and therefore also the n-type region of the MW photodiode, through an over-the-edge metalization. The p-type regions of all the MW photodiodes in the dual-band array are electrically connected and are accessed at the edge of the array through a common array ground contact. The LW photodiode is accessed directly through the two bumps, while the MW photodiode is accessed through the contact to the n-type region and the array ground. All bumps are identical and are on the same plane, which is necessary for high interconnect yield in large hybrid IRFPAs.

The MW and LW photocurrents obtained from this new dual-band detector are completely independent. Figure 2 shows two current-mode preamplifiers connected to the MW and LW photodiodes in such a way as to provide independent MW and LW output signals. The separate flows of the LW and MW photocurrents guarantee that the MW and LW output signals are independent.

The MW and LW junctions in this device are within diffusion lengths of each other. While the n-N isotype heterojunction barrier prevents injection of minority carriers from the LW junction to the MW junction, such injection from the MW to the LW is possible. This could lead to spectral crosstalk in the LW response spectrum, as in the case of the simple bias-selectable device. However, the independent electrical access prevents this from happening by fixing the bias voltage of each junction, so that neither is electrically floating.
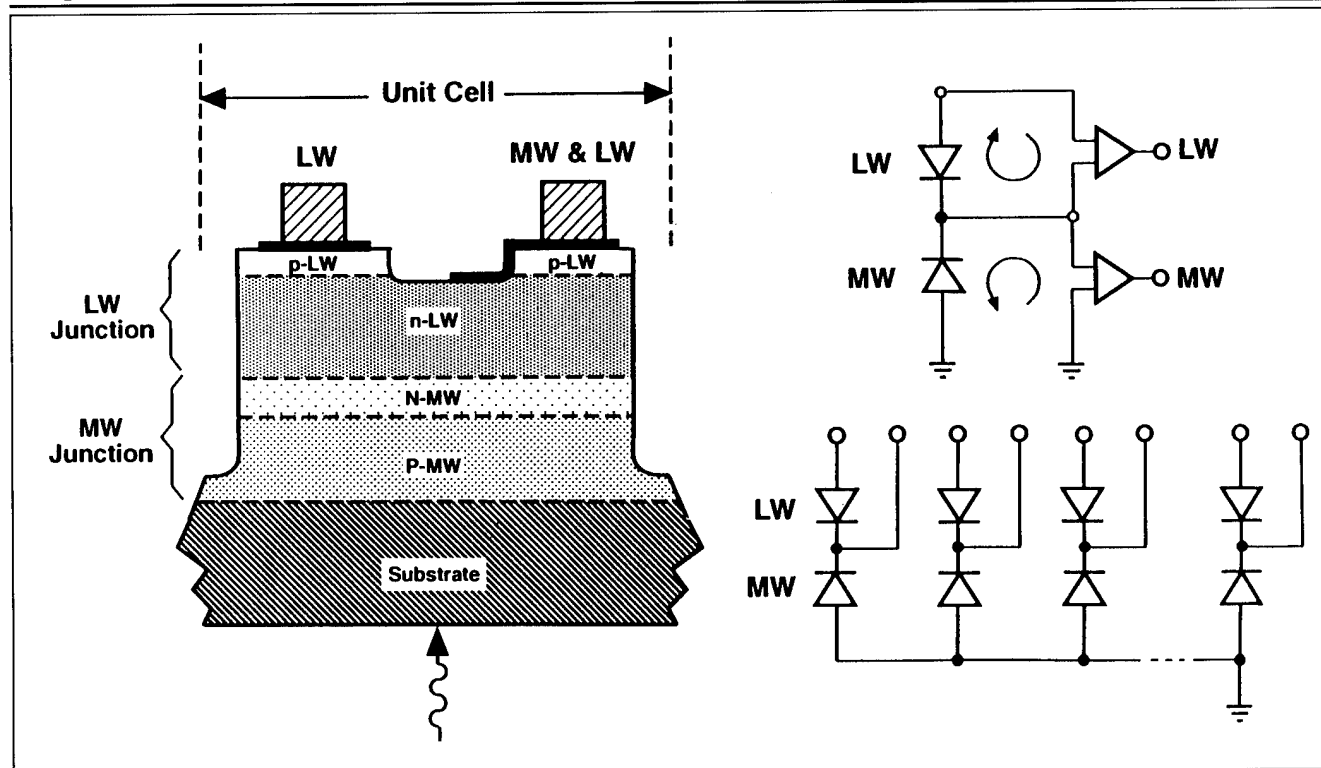
The use of a grown p-on-n junction for the LW

Fig. 2. Cross section of the independently accessed back-to-back HgCdTe photodiode dual-band detector.

Reine, Norton, Starr, Weiler, Kestigian, Musicant,
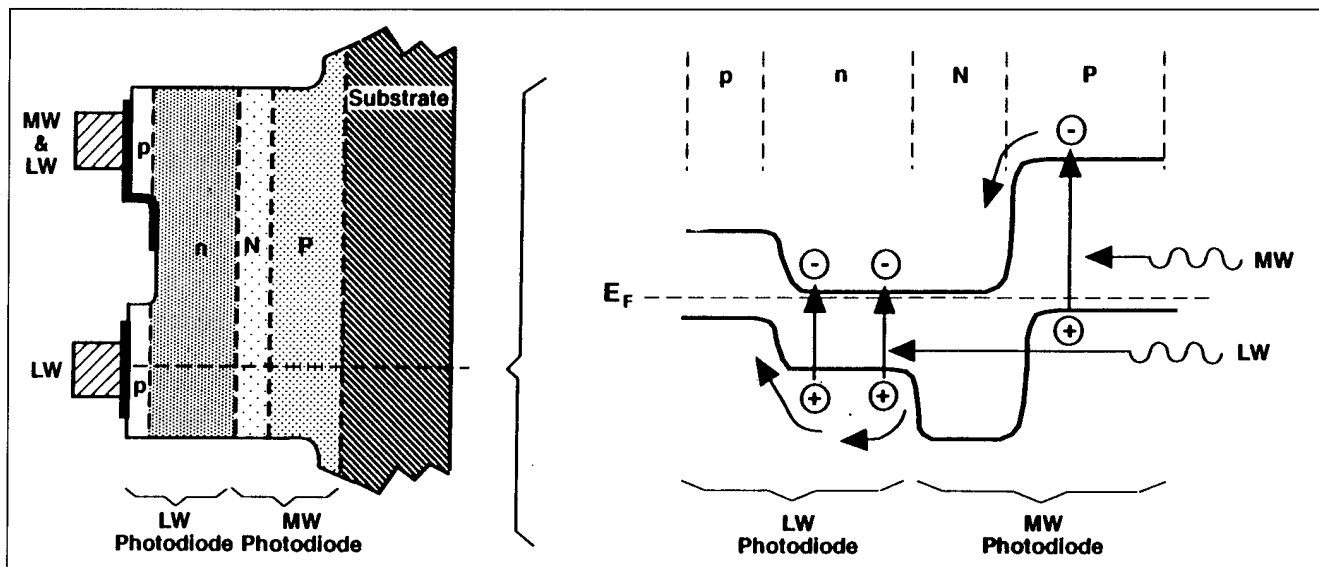Mitra, Schimert, Case, Bhat, Ehsani, and Rao

Fig. 3. Energy band diagram of the independently accessed back-to-back HgCdTe photodiode dual-band detector, along a line passing through the LW p-on-n junction.
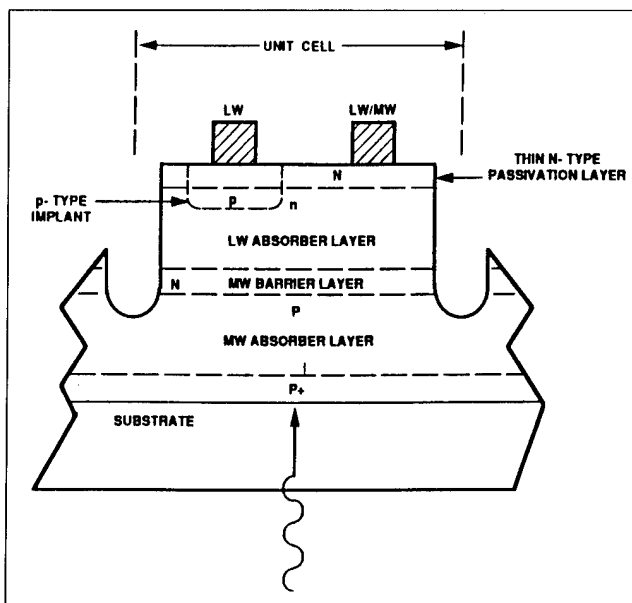

Fig. 4. Alternative approach for forming the LW photodiode in the new dual-band detector.

photodiode in this new dual-band detector is simple and takes advantage of the capabilities of *in situ* multilayer HgCdTe growth by vapor phase epitaxy. The mesa photodiode that lies beneath the n-side contact bump is shorted by the over-the-edge contact metal, and hence the photocurrent due to excess carriers collected by this junction is shorted. This results in a small dead area in the LW detector. The size of the dead area will depend on the dimensions of the unit cell, of the LW mesa, and of the contacts, but it should be able to be kept below 25% of the total area. We elected to use the grown p-on-n junction and the mesa geometry for the first demonstration of this new detector.

An alternative approach for forming the LW photodiode in this new dual-band detector is the planar ion implanted configuration shown in Fig. 4. This approach retains the key feature of having both bumps on the same level, with the added benefit that LW photocarriers generated beneath the n-side contact will laterally diffuse to the planar p-on-n junction and contribute to the photocurrent. This approach requires one less layer to be grown, but adds an arsenic implant step and an activation anneal step. A fourth layer of wider gap can be added during growth to assist in control of surface leakage current in the LW planar junction.

A noteworthy feature of this new dual-band detector is that the common contact for all detectors in an array is the MW p-type region, whereas the common contact between the MW and LW photodiodes in each dual-band detector is the contact to the n-type layers. This distinction is illustrated in the diagrams in Fig. 2. This difference between the array common contact and the common contact between MW and LW photodiodes presents certain interesting, although by no means unsurmountable, challenges for the input circuits that must connect to the dual-band detectors in a dual-band hybrid IRFPA, and which must maintain the simultaneity and independence of the MW and LW photocurrents during integration and multiplexing. Such a dual-band input circuit has been devised and recently demonstrated at Loral Infrared & Imaging Systems and will be the subject of a future paper.[9]

EXPERIMENTAL

MOCVD HgCdTe Multilayer Film Growth

As part of the development of this new device, multilayer HgCdTe films were grown *in situ* by MOCVD onto CdTe or CdZnTe substrates by two different methods: the interdiffused multilayer process[10] (IMP) at Loral Vought Systems Corporation (LVSC) in Dallas, TX, and the direct alloy growth[11]

(DAG) method at Rensselaer Polytechnic Institute
(RPI) in Troy, New York. Three types of multilayer
films were grown: p-n-N-P structures for dual-band
detectors, along with p-on-n and P-on-n LW single
homojunctions and heterojunctions, and n-on-p MW
single homojunctions. The single junction films were
grown as companions to the p-n-N-P films for growth
calibration purposes as well as to assess the quality of
the individual junctions that make up the p-n-N-P
dual-band detector. In both the IMP and DAG MOCVD
films, p-type doping was achieved by introducing
arsenic at levels of 5×10^{15} to 2×10^{17} cm^{-3} from a
tertiarybutyl-arsine (TBAs) source, while n-type dop-
ing was due to unintentional background donors at
levels of 0.5–1.5×10^{15} cm^{-3}. Other details of the
MOCVD growth methods and data on the grown p-on-
n and n-on-p single junctions are contained in Refs. 10
and 11.

Secondary ion mass spectroscopy (SIMS) data for a
four-layer p-n-N-P dual-band MOCVD HgCdTe film
grown *in situ* by the IMP method onto a CdZnTe(211)B
substrate are shown in Fig. 5. The arsenic profiles are
well defined and have abrupt fall-offs. The $Hg_{1-x}Cd_xTe$
alloy composition profiles, determined from the ^{125}Te
secondary ion signal intensity,[12] are uniform within
the MW and LW layers, which are separated by a
compositionally graded interdiffused region about 1
μm thick. It turns out that a compositionally graded
region of this thickness is actually desirable to avoid
the formation of a depletion region at the n-N isotype
heterojunction interface.

Device Fabrication

The three arrays for which data are presented in
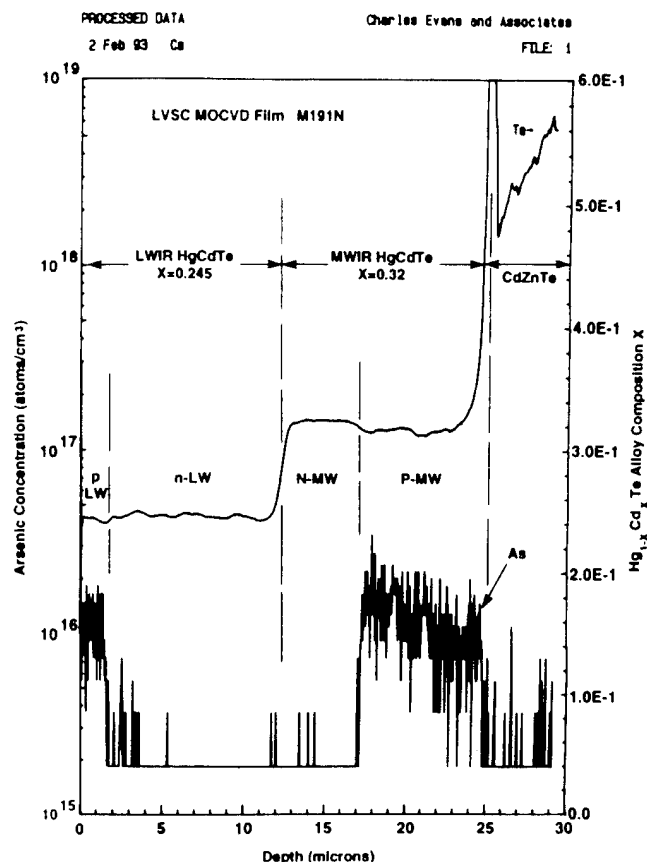
Fig. 5. Secondary ion mass spectroscopy profiles of $Hg_{1-x}Cd_xTe$ alloy
composition x and arsenic concentration for four-layer p-n-N-P dual-
band film M191N grown by IMP MOCVD onto a CdZnTe(211)B
substrate at Loral Vought Systems Corporation. This film was used to
fabricate the dual-band detectors for which data are presented in this
paper.
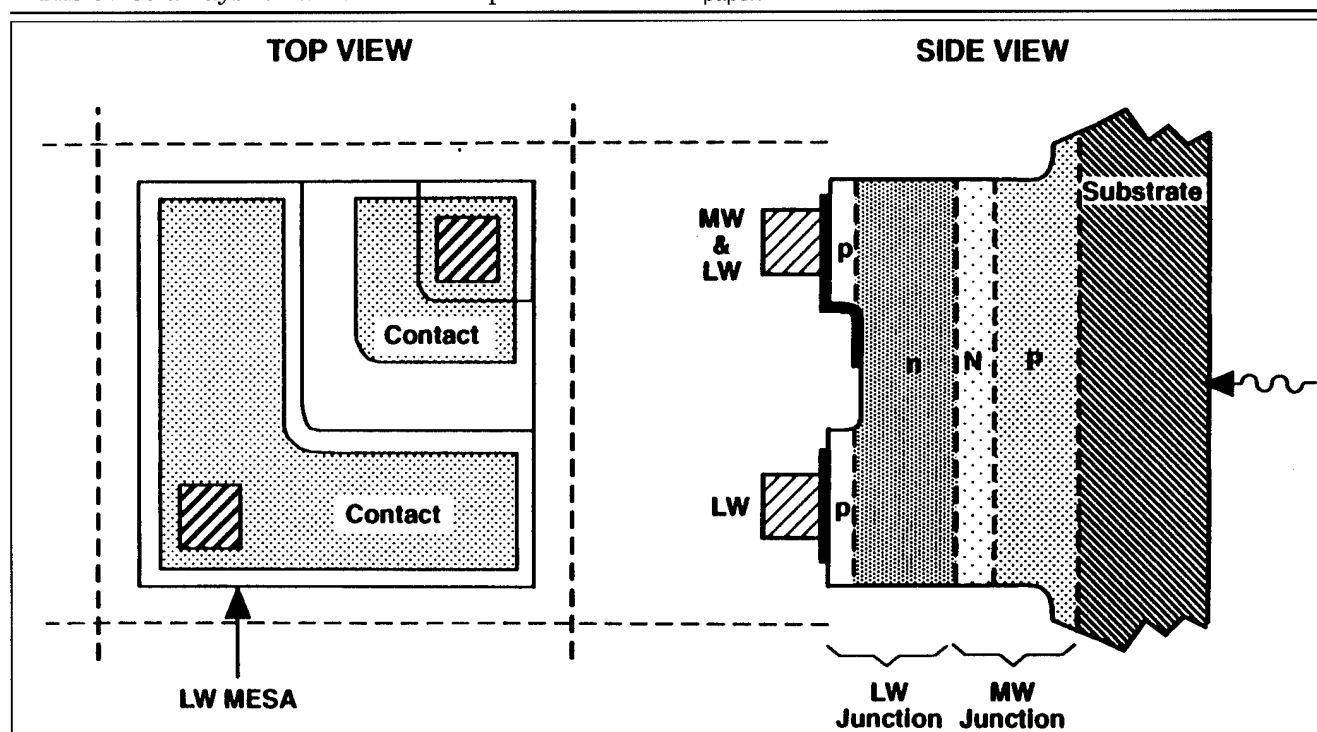
Fig. 6. Cross section and top view of the independently accessed back-to-back HgCdTe photodiode dual-band detector.
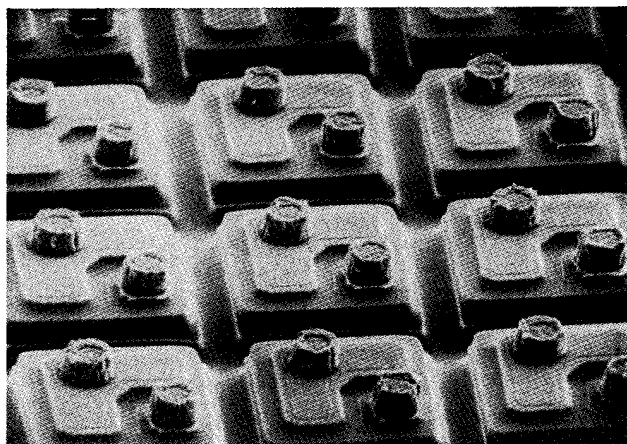
Fig. 7. Scanning electron microscope photos of 100 × 100 μm² dual-band detectors, defined by wet chemical etching in a four-layer p-n-N-P dual-band film grown by IMP MOCVD onto a CdZnTe(211)B substrate at Loral Vought Systems Corporation. This film had characteristics nearly identical to those of Film M191N of Fig. 4.
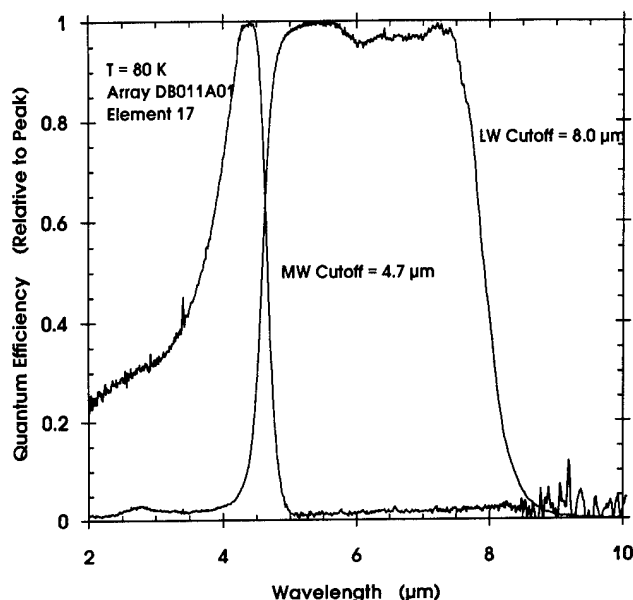

Fig. 8. Low spectral crosstalk (less than 3%) demonstrated by relative spectral response data at 80K for the MW and LW photodiodes in a dual-band detector fabricated from p-n-N-P Film M191N.

this paper were all fabricated from p-n-N-P MOCVD HgCdTe Film M191N, for which SIMS data were given in Fig. 5. The arrays were processed with conventional photolithographic and wet etching techniques, and no anti-reflection coating was used. The arrays were hybridized through bump interconnects to sapphire fanout boards and mounted into 120 pin grid array flat packs. They were tested in the back-side-illuminated configuration. The dual-band detector arrays reported here had unit cell dimensions of 100×100 μm² and were in an 8×8 format, but only two adjacent rows of eight elements from each array were electrically connected through the fanout board.

A top view of the dual-band detector geometry used for these first arrays is shown in Fig. 6. This can be compared with the scanning electron microscopy

(SEM) photo of an actual array shown in Fig. 7. The unit cell area is 100 × 100 μm². The "L-shaped" LW mesa photodiode is clearly evident, as is the common n-side contact with its over-the-edge metallization. Wet chemical etching was used to define the "L-shaped" LW mesa photodiode, as well as to define the larger mesa that delineates the MW photodiode. The etch depth for the LW photodiode mesa is about 2–3 μm, while the etch depth for the MW mesa is about 17–19 μm. The width of the etched region forming the MW mesa is about 25 μm, which corresponds to a fill factor of 60% relative to the 100 × 100 μm² unit cell area. This wide spacing between MW mesas is due to the isotropic behavior of wet etching. We will use dry etching for these devices in the near future, which will result in significantly larger fill factors and will allow smaller unit cell areas.

DUAL-BAND DETECTOR CHARACTERIZATION DATA

In this section, we present characterization data for independently accessed back-to-back photodiode dual-band test arrays. These data constitute the first reported demonstration of this new dual-band detector.

Relative quantum efficiency data vs wavelength for the MW and LW photodiodes in a p-n-N-P dual-band detector (Element 17 of Array DB011-A1) at 80K are shown in Fig. 8. The cutoff of the MW detector and the cuton of the LW detector occur at the same wavelength, indicating that the MW detector acts as a bandpass filter for the LW detector. The LW response spectrum is otherwise classical in shape, being independent of wavelength, with a cutoff wavelength of 8.0 μm. The MW response spectrum, however, has a distinct fall-off at shorter wavelengths, which we believe is due to recombination at the film-substrate interface or to a short diffusion length in the p-type MW layer. This is consistent with the low quantum efficiency of 14% for the MW photodiodes (see Fig. 12). We are addressing this issue by lowering the acceptor doping in this layer to the mid-10^{15} cm^{-3} range to increase the diffusion length, and we are including in the MOCVD growth sequence a wide-gap p-type $Hg_{1-x}Cd_xTe$ (x ≈0.4) buffer layer between the CdZnTe substrate and the p-type MW layer to isolate the MW p-type absorber layer from the film-substrate interface region.

Low spectral crosstalk, less than 1–3%, is indeed well demonstrated by the spectral response data in Fig. 8. It should be noted that the MW response is only 1–3 percent at wavelengths beyond 5 μm, but this is an artifact of the spectral measurement apparatus and conditions. The response of the LW detector is also about 1–3 % at wavelengths less than 4 μm. This we believe is due to MW radiation that is transmitted through the thin MW p-type layer at the bottom of the deeply etched regions delineating the MW mesa and that subsequently scatters into the LW detector. This effect will be eliminated by the narrower etched regions and the better etch depth control that dry

etching will provide.

The 80K cutoff wavelengths for the MW and LW photodiodes in three dual-band detector arrays tested were quite uniform, both within an array and from array to array on the film, as shown in Table I. The variations in MW and LW cutoff wavelengths over the three arrays were 0.05 and 0.26 μm, respectively, which demonstrates the uniformity of alloy composition and film thickness achievable with IMP MOCVD growth of HgCdTe.

Current-voltage (I-V) curves for the MW and LW photodiodes in a p-n-N-P dual-band detector (Element 22 of Array DB011-A1) at 80K are shown in Fig. 9. The diode polarities are as expected for the p-n-N-P configuration. There is significant leakage current at reverse bias voltage, and it is clear that this same leakage current mechanism also limits the R_0A products of both photodiodes. We attribute this leakage mechanism to defects in the MOCVD films. The R_0A values in Fig. 9 were calculated for the physical MW mesa area of 77×77 μm². In addition, the I-V curves of each photodiode in a p-n-N-P dual-band detector were determined experimentally to be independent of

the bias voltage on the other photodiode. The I-V curves shown in Fig. 9 for the MW and LW photodiodes each remained unchanged when measured with the other detector at bias voltages of −100 and −40 mV reverse bias, zero bias, and 20 mV forward bias.

Spot scan data for the MW and LW photodiodes in a p-n-N-P dual-band detector (Element 31 in Array DB011-C1) at 80K are shown in Fig. 10. The responses of both photodiodes were measured in the same scan. A focused 1000K blackbody provided at spot size of about 50 μm. The spot profile was not

Table I. Cutoff Wavelengths at 80K for the MW and LW Photodiodes in the Three p-n-N-P HgCdTe Dual-Band Arrays from IMP MOCVD Film M191N

Dual Band Array	Cutoff Wavelength at 80K (μm)	
	MW	LW
A-1	4.68	7.97–7.98
A-2	4.68	8.10–8.15
C-1	4.63–4.68	7.82-8.08

$\lambda_{co} = 4.5$ μm

$R_0 = 4.4 \times 10^9$ ohm

$R_0A = 2.6 \times 10^5$ ohm-cm²

$\lambda_{co} = 8.0$ μm

$R_0 = 1.3 \times 10^7$ ohm

$R_0A = 778$ ohm-cm²
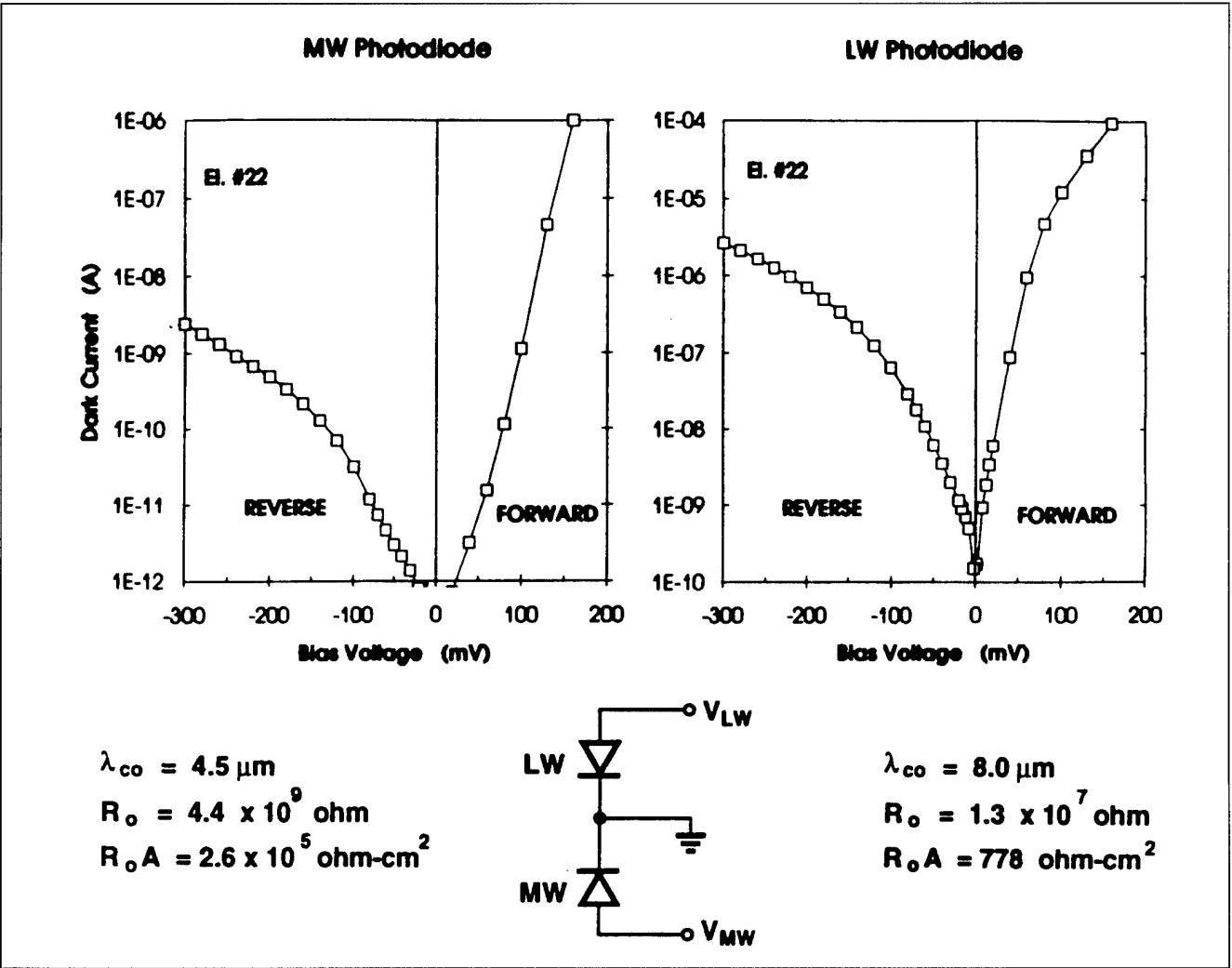
Fig. 9. Current-voltage curves and associated data for the MW and LW photodiodes in a p-n-N-P HgCdTe dual-band detector at 80K.

deconvolved from the data of Fig. 10. Both the MW and LW photodiodes are well defined and collocated. The 50% widths obtained from these scans are 79 μm for the LW photodiode and 81 μm for the MW photodiode, which are quite close to the actual mesa dimension of 77 μm.
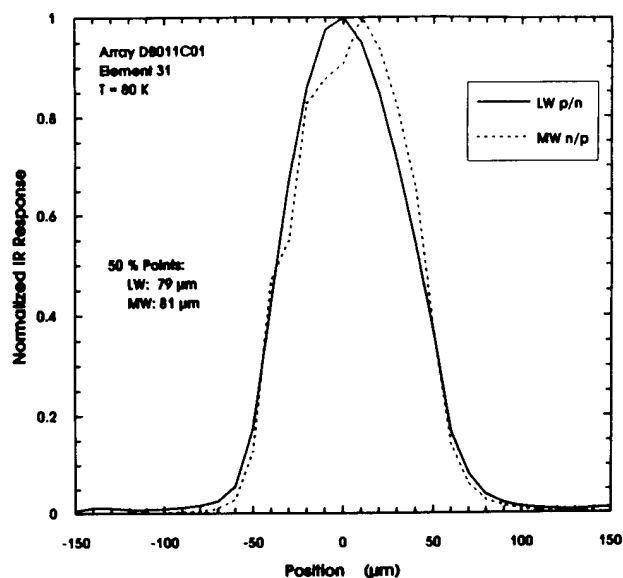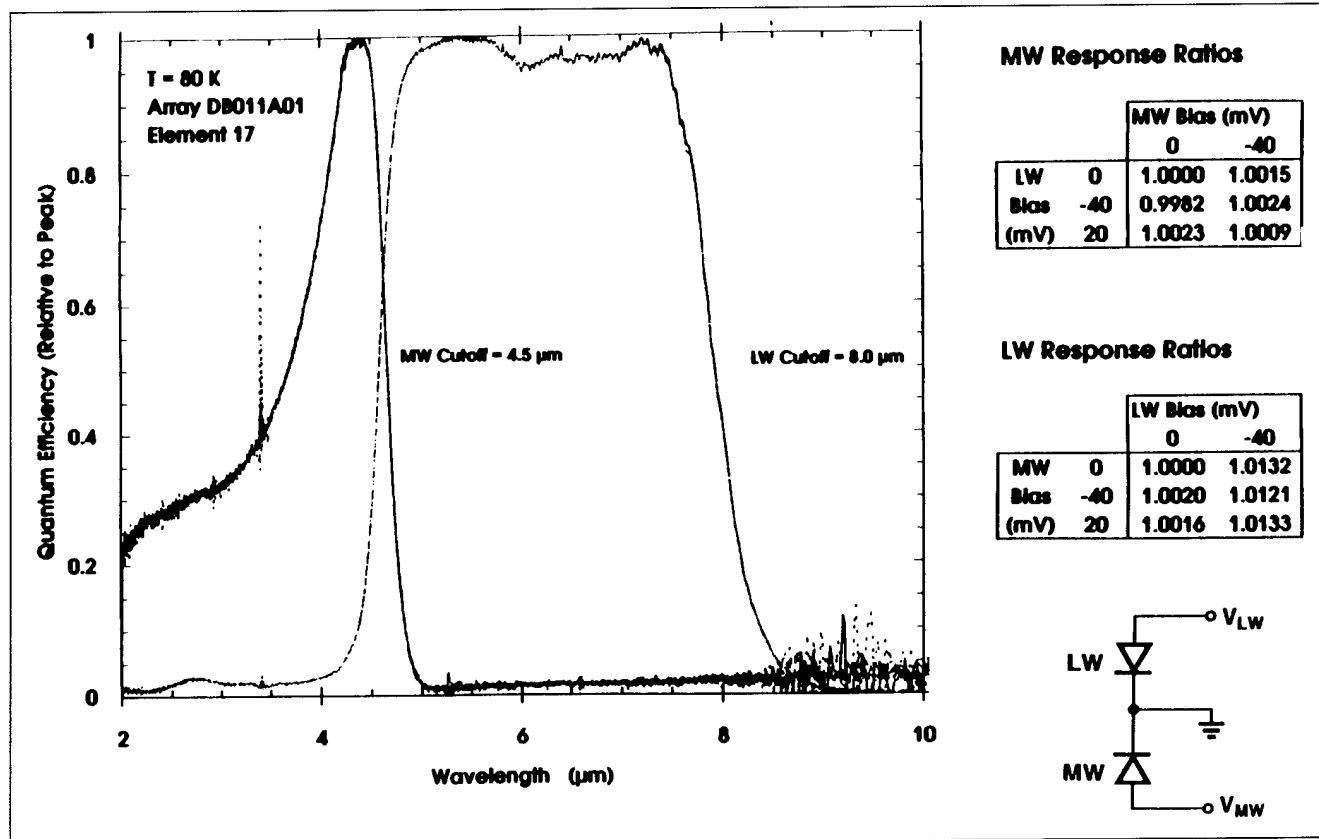

Fig. 10. Spot scan data for the MW and LW photodiodes in a p-n-N-P dual-band detector at 80K. Both the MW and LW signals were measured during the same scan.

Data were taken to confirm that the MW and LW photodiodes were electrically and radiometrically independent. The relative quantum efficiency vs wavelength curves in Fig. 11 for the MW and LW photodiodes of a dual-band detector at 80K (Element 17 of Array DB011-A1) are actually superpositions of six separate curves measured for six combinations of bias voltage on the two photodiodes. The MW photoresponse spectrum was measured for the MW photodiode at zero bias and at –40 mV reverse bias, with the LW photodiode bias set at –40 mV reverse bias, zero bias, and 20 mV forward bias. Similarly, the LW photoresponse spectrum was measured for the corresponding opposite set of bias voltage combinations. As can be seen in Fig. 11, the shapes of the response spectra for both the MW and LW photodiodes are independent of the bias voltage on either photodiode. The absolute magnitudes of the photoresponses of the MW and LW photodiodes are also independent of the bias voltage combinations. This is shown in the data in Fig. 11 for the ratios of the peak photoresponse with various bias voltage combinations to the peak photoresponse for zero bias on both photodiodes. These ratios are unity to within experimental error, except for a 1% increase in the LW photoresponse when the LW photodiode is reverse biased to –40 mV, which may be due to an increase in the collection volume resulting from the wider depletion width. All these data confirm that the infrared photoresponses of the MW and LW photo-

Fig. 11. Spectral response data for the MW and LW photodiodes in a p-n-N-P dual-band detector at 80K. Both the MW and LW response curves are actually overlays of six different curves measured for six combinations of bias voltage on the MW and LW photodiodes.

diodes in a p-n-N-P dual-band detector are indepen-
dent of the bias voltage on either photodiode.

Summary plots of the R_0A product and quantum
efficiency data at 80K for three arrays of p-n-N-P
dual-band detectors from Film M191N are shown in
Fig. 12. Each array was in a 2 × 8 format with 16
possible dual-band detectors. Figure 12 includes only
data for those dual-band detectors in which both the
MW and LW photodiodes were not open or not other-
wise defective. The R_0A and quantum efficiency val-
ues were calculated with the MW mesa area of (77
μm)^2 . There was no anti-reflection coating on these
arrays, so the maximum possible quantum efficiency
is 80%. In light of these conditions, and given that
approximately 25% of the LW photogenerated carri-
ers are captured by the shorted p-n junction that lies
in the corner of the unit cell beneath the common n-
side contact, the LW quantum efficiencies of just less
than 40% are quite respectable. The low MW quan-
tum efficiencies, around 14%, together with the peaked
behavior of the MW spectral response in Fig. 8 and
Fig. 11, lead to our conclusion that the p-type MW
layer has too short a diffusion length, or that there is
recombination at the film-substrate interface.

The MW R_0A values in Fig. 12 are uniform from
element-to-element and range between 1×10^5 and
3×10^5 ohm-cm^2. The LW R_0A values are less uniform
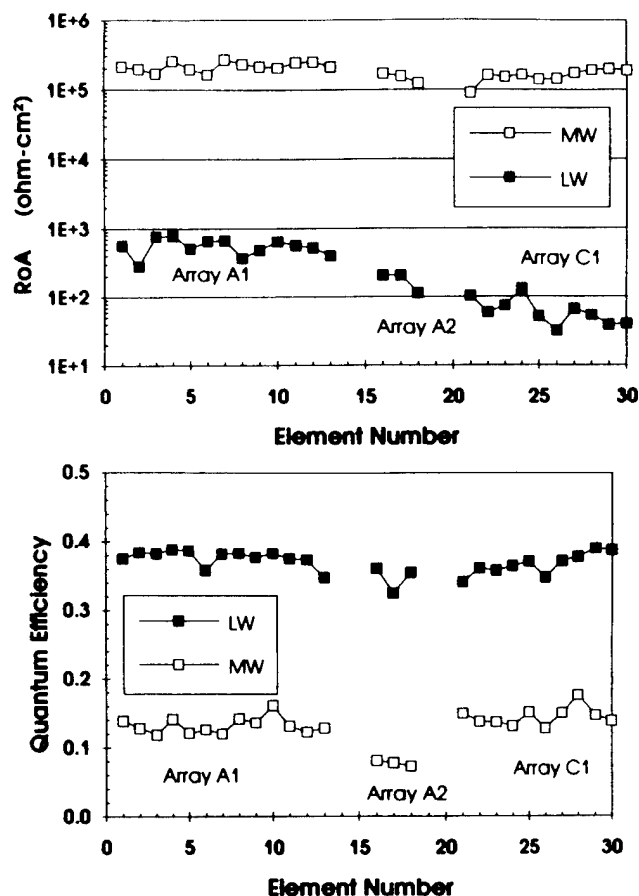
from element-to-element and show a definite varia-
tion from array to array, which we suspect is due to a
long-range variation in defect density over the film
area.

Figure 13 compares the R_0A data for the best LW p-
on-n photodiodes in the p-n-N-P dual-band detectors
to the conventional theoretical limits[13] for R_0A in p-on-
n HgCdTe photodiodes, to the state-of-the-art for P-
on-n LPE heterojunctions, and to "best-element" R_0A
data for two-layer p-on-n HgCdTe photodiodes grown
in situ by MOCVD by both the IMP and DAG tech-
niques. The solid line in Fig. 13 is the calculated R_0A
due to diffusion current from the n-layer only, for a
thickness of 15 μm and a lifetime determined by the
Auger-1 mechanism. The dashed line is the calcu-
lated R_0A product due to depletion layer g-r current,
for doping levels of 1×10^{15} and 1×10^{16} cm^{-3} on the n-
side and p-side, respectively, and for a depleted sur-
face recombination velocity S_0 of 1×10^4 cm/s. The
heavy dashed line is the trend line for P-on-n LPE
heterojunctions from Ref. 14. The solid square data
points in Fig. 13 are for the best LW photodiode
elements from the three dual-band arrays (see Fig.
12).

The data points represented by the open symbols in
Fig. 13 are "best-element" R_0A at 80K data for back-
side-illuminated variable-area arrays of circular mesa
p-on-n photodiodes, fabricated from MOCVD p-on-n
films grown *in situ* recently by IMP at LVSC and by
DAG at RPI. These R_0A data are taken from Refs. 10
and 11 and are listed in Table II, along with other
characteristics of each film and array: the film num-
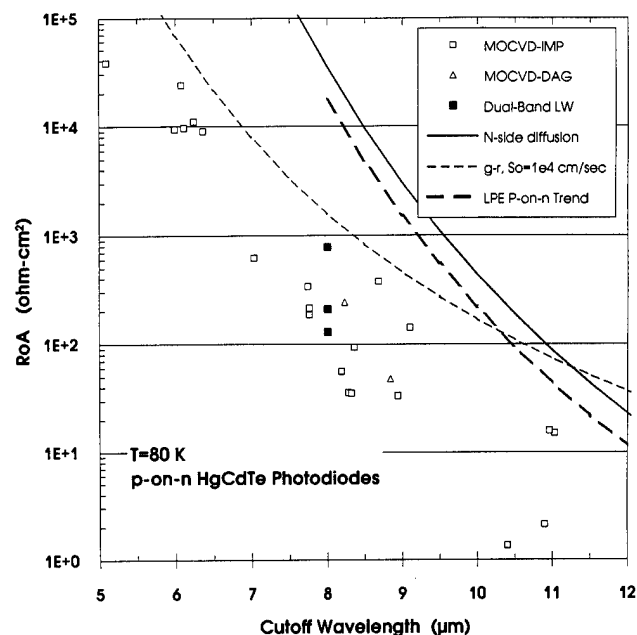ber, the MOCVD method (IMP or DAG), the substrate

Fig. 12. R_0A and quantum efficiency data for three arrays of p-n-N-P
dual-band detectors fabricated from LVSC Film M19IN. R_0A and
quantum efficiency were calculated with the MW mesa area of (77 μm)^2 .

Fig. 13. Comparison of R_0A data at 80K for p-on-n HgCdTe photo-
diodes grown *in situ* by MOCVD with P-on-n LPE heterojunction trend.
Open squares are IMP single junction data from Ref. 10, open
triangles are DAG single junction data from Ref. 11, and solid squares
are the best LW junctions in the three p-n-N-P dual-band arrays grown
by IMP. The LPE trend is from Ref. 14.

Table II. Data at 80K on Variable-Area p-on-n HgCdTe Photodiode Arrays Fabricated from p-on-n Films Grown *In Situ* by IMP and DAG MOCVD[10,11]

Film	Method	Substrate	Array	λ_{co}(μm)	$\Delta\lambda_{co}$ (%)	R_0A (ohm-cm²)	QE(1D) (%)	L_{OPT} (μm)
175	IMP	CdZnTe(100)4°→(110)	A	6.36	3.4	9.01×10^3	67	28
			B	6.08	1.0	2.37×10^4	72	32
			C	6.11	2.1	9.64×10^3	71	29
			D	6.24	2.8	1.10×10^4	70	29
181A	IMP	CdTe(100)2°→(110)	A	5.99	1.9	9.40×10^3	77	14
181BC	IMP	CdZnTe(100)4°→(110)	B	5.10	2.3	3.80×10^4	42	18
193	IMP	CdZnTe(211)Te	C	7.76	0.3	184	63	8
197	IMP	CdZnTe(211)Te	B	7.74	1.5	336	52	9
			A1	7.76	1.1	213	59	10
209	IMP	CdZnTe(211)Te	A1	9.10	1.9	142	55	17
			A2	8.68	2.5	374	46	24
211	IMP	CdZnTe(211)Te	A1	11.03	7.2	15.0	47	10
			A2	10.96	1.5	15.9	49	9
257	IMP	CdZnTe(100)4°→(110)	A1	8.94	1.8	33.6	62	13
264	IMP	CdTe(211)Te	A1	7.03	6.9	619	63	5
			B2	8.36	0.5	93.4	68	5
535-1	DAG	CdTe(100)4°→(111)B	B	8.23	5.7	241	41	16
535-2	DAG	CdTe(100)4°→(111)B	B	8.84	1.6	48	51	23

material and orientation, the array number, the average cutoff wavelength λ_{co} at 80K, the percent variation of λ_{co} over the array, the R_0A at 80K of the best element of the array, the one-dimensional quantum efficiency QE(1D), and the optical collection length L_{OPT}. The latter two quantities were extracted from the dependence of quantum efficiency on junction area in the variable-area photodiode arrays, as described in Ref. 14. The data in Table II show that cutoff wavelength is quite uniform across these arrays, that quantum efficiencies are reasonably high for devices with no anti-reflection coating, and the L_{OPT} values are as expected for the n-type base layers. The best R_0A values, however, are generally low compared to the LPE state-of-the-art, which we ascribe to defects in the MOCVD films.

Figure 13 shows that the LW photodiodes in the dual-band detectors have R_0A values comparable to or better than those of the single grown junctions listed in Table II. Efforts are underway to isolate and identify the defects responsible for these low R_0A products in grown MOCVD junctions, and we expect that these efforts will lead to improved quality in MOCVD grown junctions.

It should be noted that the triangle data points in Fig. 13 are for p-on-n homojunctions from two DAG MOCVD films (535-1 and 535-2). These R_0A values are significantly higher that the only previously reported p-on-n HgCdTe junctions grown *in situ* by DAG MOCVD by the Raytheon group,[15] who quoted an R_0A value of 50 ohm-cm² at 77K for a cutoff wavelength of 8.1 μm.

CONCLUSIONS

We have demonstrated for the first time a new dual-band HgCdTe detector with unique benefits: simultaneous and independent MW and LW detection, independent biasing of the MW and LW photodiodes, and

compatibility with high-density backside-illuminated hybrid HgCdTe IRFPA technology. We have implemented this new device with four-layer p-n-N-P MOCVD films qrown *in situ* on lattice-matched substrates. We have presented data on p-n-N-P dual-band detectors that confirm the electrical and radiometric independence of the MW and LW photodiodes in this new dual-band detector structure. These results demonstrate the utility of multilayer vapor phase epitaxial growth methods for HgCdTe, and we hope these results will stimulate the rapid development of HgCdTe vapor phase epitaxy.

REFERENCES

1. H. Halpert and B.L. Musicant, *Appl. Optics* 11, 2157 (1972).
2. D.A. Scribner, M.R. Kruer and J.M. Killiany, *Proc. IEEE* 79, 66 (1991).
3. T. Tung, M.H. Kalisher, A.P. Stevens and P.E. Herning, *Mat. Res. Soc. Symp. Proc.* 90, 321 (1987).
4. C.C. Wang, *J. Vac. Sci. Technol. B* 9, 1740 (1991).
5. G.N. Pultz, P.W. Norton, E.E. Krueger and M.B. Reine, *J. Vac. Sci. Technol. B* 9, 1724 (1991).
6. T.N. Casselman, D.T. Walsh, J.M. Myrosznyk, K. Kosai, W.A. Radford, E.F. Schultz and O.K. Wu, *Ext. Abs. 1990 U.S. Workshop on the Physics and Chemistry of Mercury Cadmium Telluride,* San Francisco, California, October 2–4, 1990.
7. E.R. Blazejewski, J.M. Arias, G.M. Williams, W. McLevige,

M. Zandian and J. Pasko, *J. Vac. Sci. Technol. B* 10, 1626 (1992).

8. K. Kosai, *J. Electron. Mater.* 24, 635 (1995).

9. A. Hairston, F. Jaworski, P. Kimball and R. Edwards, Loral Infrared & Imaging Systems, private communication.

10. P. Mitra, T.R. Schimert, F.C. Case, R. Starr, M.H. Weiler, M. Kestigian and M. B. Reine, *J. Electron. Mater.* 24, 663 (1995).

11. V. Rao, H. Ehsani, I. Bhat, M. Kestigian, R. Starr, M. H. Weiler and M. B. Reine, *J. Electron. Mater.* 24, 437 (1995).

12. L.O. Bubulac and C.R. Viswanathan, *Appl. Phys. Lett.* 60, 222 (1992)

13. M.B. Reine, T.J. Tredwell and A.K. Sood, *Semiconductors and Semimetals*, eds. R. K. Willardson and A. C. Beer, Vol. 18 (New York: Academic Press, 1981).

14. M.B. Reine, K.R. Maschhoff, S.P. Tobin, P.W. Norton, J.A. Mroczkowski and E.E. Krueger, *Semicond. Sci. and Technol.* 8, 788 (1993).

15. S. Oguz, R.J. Olson, Jr., D.L. Lee, L.T. Specht and V.G. Kreismanis, *Proc. SPIE* 1307, 560 (1990).

Room Temperature Characterization of $Hg_{1-x}Cd_xTe$ P-on-n Heterostructure Photodiodes

M. ZANDIAN, J.G. PASKO, J.M. ARIAS, R.E. DE WAMES, and S.H. SHIN

Rockwell International Science Center, Thousand Oaks, CA 91360

Measurements of 77K R_oA and 300K reverse bias dynamic impedance (R_dA) products at one volt reverse bias has been carried out to assess the degree of correlation of this figure of merit. Planar P-on-n heterostructures were grown on near lattice-matched CdZnTe substrates with $Hg_{1-x}Cd_xTe$ (0.20< x <0.30) by molecular beam epitaxy. These devices were passivated with CdTe and doped with indium and arsenic as n- and p-type dopants, respectively. Current-voltage characteristic of these devices exhibit thermally generated dark currents at small and modest reverse bias. We have observed that R_oA values of these long wavelength infrared P-on-n heterostructure photodiodes at 77K correlate with room temperature R_dA values. Diode arrays with high room temperature R_dA values at one volt reverse bias also have high R_oA values at 77K. Similarly, low R_dA values at room temperature indicate poor performance at 77K where deviation from diffusion current occurs at reverse bias of 0.2 to 1 volt at room temperature. The results presented here, for a small samples of devices, demonstrate that room temperature measurements of current-voltage characteristics to evaluate $Hg_{1-x}Cd_xTe$ (0.22< x <0.28) diode performance and array uniformity at lower temperatures can be used. This provides an acceptable criteria for further study at lower temperatures.

Key words: Current-voltage characteristics, HgCdTe, infrared detectors

INTRODUCTION

$Hg_{1-x}Cd_xTe$ is used extensively to fabricate mid- and long-wavelength infrared (LWIR) photodiodes and focal plane arrays (FPAs) primarily due to relative ease to grow from single epitaxial layers to complex heterostructures across the wide spectral range of 1 to 14 μm without the severe lattice matching constraints usually found with other semiconductor alloys.[1] During the past several years, we have seen significant advances in the performance of long-wavelength infrared p-on-n HgCdTe double layer photodiodes. But, characterization of LWIR $Hg_{0.78}Cd_{0.22}Te$ photovoltaic devices and FPAs requires testing at every step which is expensive and time-consuming. The benefit of a pre-screening before incurring costs at later stages improves yield and reduces costs. However, pre-screening for further tests at low temperature, does not

replace low temperature testing.

One of the major sources of dark currents in $Hg_{1-x}Cd_xTe$ has been found in Ref. 11 as surface generation current from surface states where surface and interface states act as g-r centers. Therefore, the R_oA product limited by surface/interface generation varies with temperature as n_i^{-1}. To observe excess dark currents in a diffusion limited region at room temperature, we have examined the dynamic impedance R_d at sufficiently high reverse bias (0 to 1 volt) where diffusion and g-r type currents are comparable. The possibility that excess dark currents observed at room temperature in reverse bias of diodes used in our study dominate the current voltage (I-V) characteristics at zero bias for low performance devices when the sample is cooled to 77K is reported here. Measurements to assess the degree of correlation between R_oA product values at 77K and room temperature R_dA product values at one volt reverse bias for several $Hg_{1-x}Cd_xTe$ arrays has been carried out.

a

b
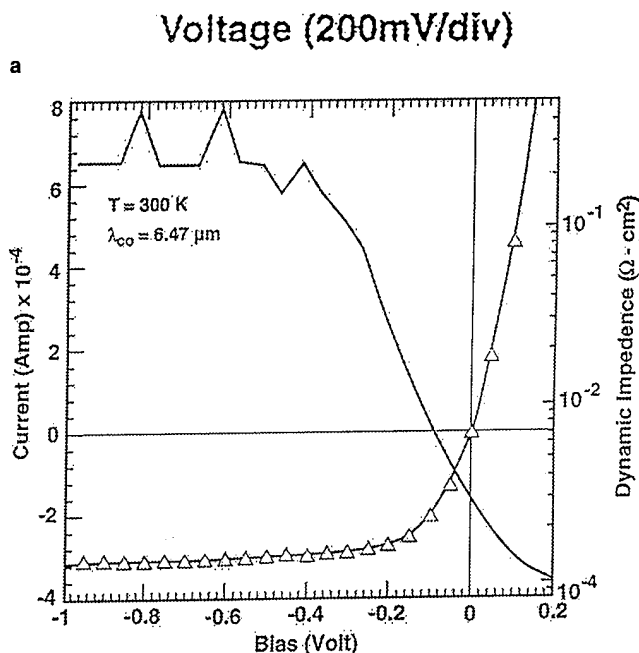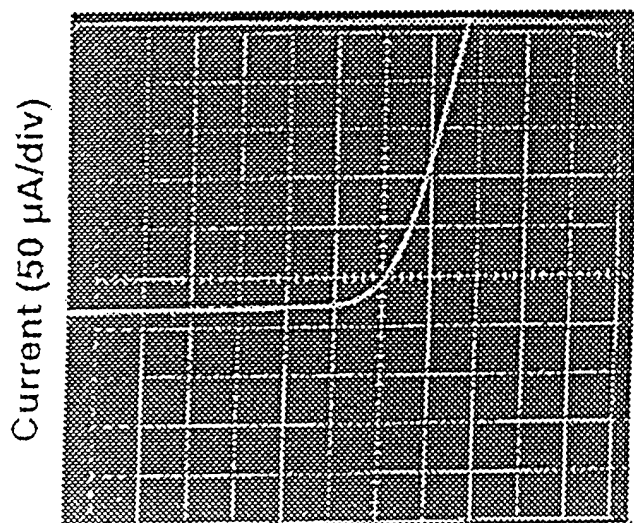
Fig. 1. Detail I-V characteristic of an MBE $Hg_{0.773}Cd_{0.227}Te$ planar photodiode (No. 508) at 300K. Note the dynamic impedance of the device is increasing to 0.27 Ω-cm² at (1V) reverse bias. The cutoff wavelength for this device is 10 μm at 77K and has an area 9 × 10⁻⁶ cm².
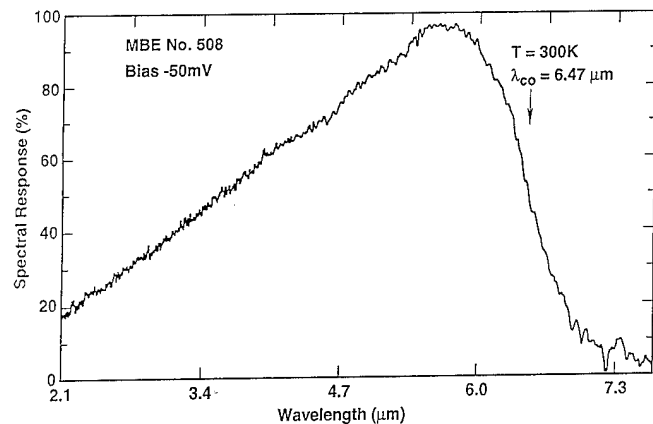

Fig. 2. Relative spectral response of MBE HgCdTe planar photodiode (No. 508) at 300K. The cutoff wavelength of the device at room temperature corresponds to absorbing layer with x = 0.227.
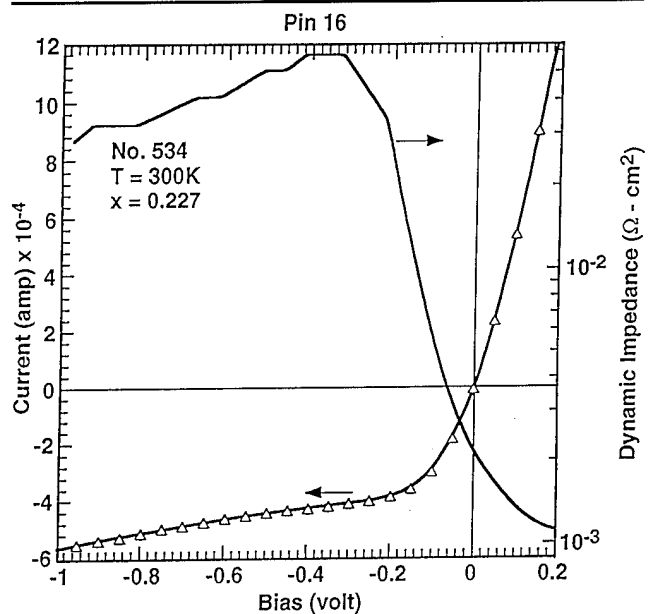

Fig. 3. Detail I-V characteristic of an MBE $Hg_{0.773}Cd_{0.227}Te$ planar photodiode (No. 534) at 300K. Note the dynamic impedance of the device is decreasing between 0.3 to 1 volt reverse bias. The cutoff wavelength for this device is 10.0 μm at 77K with R_oA value of 0.22 Ω-cm² and has an area 9 × 10⁻⁶ cm².

We have observed that diode arrays with high room temperature R_dA values at one volt reverse bias also have high R_oA values at 77K. Similarly, low R_dA values at room temperature indicate poor performance at 77K where deviation from diffusion current occurs at reverse bias of 0.2 to 1 volt at room temperature.

In the next section, we discuss our experiments and present our results in the Results and Discussion section. Concluding remarks are also presented.

EXPERIMENT

The p-on-n heterostructures were grown in a RIBER 2300 molecular beam epitaxy (MBE) system. A detailed discussion of MBE HgCdTe growth procedures and device fabrication used here can be found in Refs. 5 and 6. The epilayers were grown on near lattice-matched $Cd_{0.96}Zn_{0.04}Te$ substrates to minimize the dislocation density in HgCdTe epilayer. The (211)B orientation was chosen since we have obtained excellent surface morphology and high performance photodiodes on epitaxial layers grown on this orientation.[4,6,8,9] This structure consists of a 12 μm thick indium-doped (2 × 10¹⁵ cm⁻³) $Hg_{0.773}Cd_{0.227}Te$ LWIR absorbing layer followed by the growth of a 1 μm thick undoped $Hg_{0.7}Cd_{0.3}Te$ layer and a final 1000Å thick CdTe layer. The formation of planar photodiodes was achieved by first selectively implanting arsenic through windows made on a mask of photoresist/ZnS and then diffusing the arsenic by annealing through the cap layer into the narrow gap base layer. A schematic of the device structure can be found in Ref. 6.

RESULTS AND DISCUSSION

Figure 1a is a current-voltage characteristic of a typical MBE $Hg_{0.773}Cd_{0.227}Te$ planar photodiode at 300K. Dark currents at small and modest reverse bias voltage region are thermally generated for high performance devices, in good agreement with predicted theoretical values assuming minority carrier diffusion length of HgCdTe of similar composition and intrinsic carrier concentration for n-type layer at 300K. As illustrated in Fig. 1b, the dynamic impedance of this high performance device continues to increase to 0.27 Ω-cm^2 for modest bias voltages. No degradation in device performance at room temperature and 77K was observed when 2.5 volts reverse bias was applied at 300K. The I-V characteristics were measured up to 40°C, where at this temperature the series resistance becomes the limiting factor in measurement of R_dA.

The spectral response was measured with a Nicolet Fourier transform infrared spectrometer, the 50% spectral wavelength cutoff (λ_{co}) was used to determine the energy gap of HgCdTe. The 300K spectral response for these devices was broadband, with λ_{co} of 6.47 μm (x = 0.227), as illustrated in Fig. 2. This λ_{co} value is consistent with the narrow gap layer cutoff value of 6.40 μm (x = 0.229) calculated from the absorption edge of the room temperature infrared transmission spectra using the Hansen, Schmit, and Casselman equation.[7] 300K I-V characteristic of a low performance LWIR (x = 0.227) device is presented in Fig. 3, showing decrease in reverse bias dynamic impedance between 0.3 to 1 volt. 300K reverse bias R_dA value for this device is 2.6×10^{-2} Ω-cm^2 at one volt and 77K I-V characteristic was poor with R_oA value of 2.2×10^{-1} Ω-cm^2.

Several studies have been reported on the low temperature properties of LWIR photodiodes, where at high reverse bias the dynamic impedence was observed to decrease with a negative coefficient of current component.[2-4] Studying R_d at sufficiently high reverse bias and high temperatures where the R_oA varies with temperature as n_i^{-1} provides information on which component of dark current plays the major role in limiting the diode operation.[10] We report on a correlation of LWIR array uniformity and performance at 77K on voltage dependence of dynamic impedance (R_d) at 300K. This behavior is illustrated in Fig. 4, where results on R_oA product at 77K vs room temperature R_dA product at one volt reverse bias for several miniarrays with different absorbing layer compositions is shown. Both room temperature and 77K measurements were performed with no illumination for a nominal junction area of 30 × 30 μm^2. Note the dependence of dynamic impedance on bandgap of materials with upper limit R_oA values at 77K which is consistent for R_oA calculations based on an ideal diode equation using $n_D-n_A = 3 \times 10^{15}$ cm^{-3} and Auger-limited minority carrier lifetime. As shown in Fig. 4, higher R_dA values at room temperature seems to indicate also higher R_oA values at 77K. This suggests that current fluctuation at high reverse bias is still controlled by localized electrically active flaws and imperfections. No major variation from this behavior is seen except one sample (x = 0.220) which exhibited low R_dA products at room temperature but R_oA values at 77K was comparable to values for high performance arrays. However, quantum efficiency for this sample in contrast to quantum efficiency values for other arrays used in this study was low at 77K. Formation of electrical junction in wide bandgap cap layer could explain measured higher R_oA product and low quantum efficiency at 77K for this array. We have not yet attempted to analyze these results further; however, standard techniques to assess whether surface or bulk features are the limiting dark currents for low performance arrays provide good insight into understanding the dominant currents limiting R_oA at various temperature regions.

SUMMARY

In summary, we have demonstrated room temperature I-V characterization of $Hg_{1-x}Cd_xTe$ (0.22<x<0.28) devices. The device structure is planar P-on-n heterostructure grown by MBE, the p and n layers doped with arsenic and indium, respectively. Thermally generated dark currents dominate the I-V characteristic of these devices at 300K. Diode arrays with high room temperature R_dA values at one volt reverse bias also have high R_oA at 77K. Similarly, low R_dA values at room temperature indicate poor performance at 77K where deviation from diffusion currents occurs at reverse bias of 0.2 to 1 volt at 300K. The results presented here, for a small samples of devices demonstrate that room temperature measurements of I-V characteristics to evaluate $Hg_{1-x}Cd_xTe$ (0.22<x<0.28) diode performance and array uniformity at lower temperatures can be used. This provides an acceptable criteria for further study at lower temperatures.
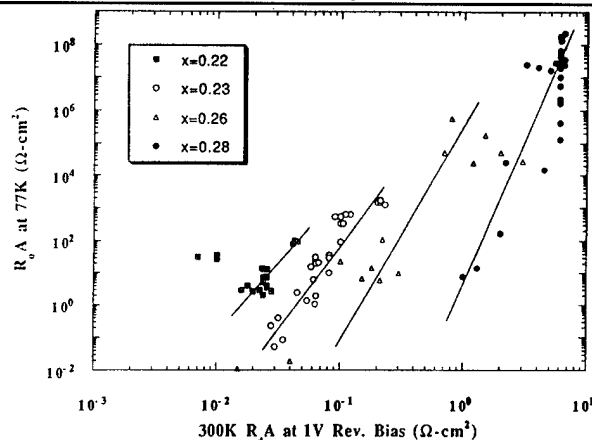
Fig. 4. R_oA at 77K vs 300K R_oA at 1V reverse bias for several miniarrays with 77K cutoff wavelength of 5.8, 6.8, 10, and 11 μm. The continuous line is a visual aid.

REFERENCES

1. P.R. Norton, *Optical Engineering* 30 (11), 1649 (1991).
2. R.E. DeWames, J.G. Pasko, E.S. Yao, A.H.B. Vanderwyck and G.M. Williams, *J. Vac. Sci. Technol.* A6 (4), 2655 (1988).
3. H.J. Hovel, *Semiconductor and Semi-Metals,* eds. R.K. Willardson and A.C. Beer (New York: Academic, 1975), Vol. II.
4. J.M. Wong, *IEEE Trans. Electron Dev.* 27 (1), 48 (1980).
5. J.M. Arias, M. Zandian, R. Zucca and R.E. DeWames, *Appl. Phys. Lett.* 58, 2806 (1991).
6. J.M. Arias, J.G. Pasko, M. Zandian, S.H. Shin, G.M. Williams, L.O. Bubulac, R.E. DeWames and W.E. Tennant, *J. Electron. Mater.* 22 (8), 1049 (1993).
7. G.L. Hansen, J.L. Schmit and T.N. Casselman, *J. Appl. Phys.* 53, 7099 (1982).
8. M. Zandian, J.M. Arias, R. Zucca, R.V. Gil and S.H. Shin, *Appl. Phys. Lett.* 59, 1022 (1991).
9. J.M. Arias, M. Zandian, G.M. Williams, E.R. Blazejewski, R.E. DeWames and J.G. Pasko, *J. Appl. Phys.* 70, 4620 (1991).
10. E. Placzek Popko and J.M. Pawlikowski, *J. Cryst. Growth* 72, 485 (1985).
11. M.B. Reine, A.K. Sood and T.J. Tredwell, *Semiconductors and Semimetals,* Vol. 18, eds. R.K. Willardson and A.C. Beer (New York: Academic Press, 1981), p. 201.

Reflectance and Photoreflectance for *In-Situ* Monitoring of the Molecular Beam Epitaxial Growth of CdTe and Hg-Based Materials

ZHONGHAI YU, M.A. MATTSON, and T.H. MYERS

Department of Physics, West Virginia University, Morgantown, WV 26507

K.A. HARRIS,* R.W. YANKA, and L.M. MOHNKERN

Martin Marietta Electronics Laboratory, Syracuse, NY 13221

L.C. LEW YAN VOON and L.R. RAM-MOHAN

Department of Physics, Worcester Polytechnic Institute, Worcester, MA 01609

R.G. BENZ II, B.K WAGNER, and C.J. SUMMERS

Physical Sciences Laboratory, Georgia Tech Research Institute, Atlanta, GA 30332

Epitaxial growth of Hg-based semiconductors by molecular beam epitaxy (MBE) and metalorganic MBE (MOMBE) has progressed sufficiently to shift emphasis to the control of factors limiting the yield of both materials and devices. This paper reports on an *ex-situ* study to evaluate the suitability of reflectance and photoreflectance (PR) as *in-situ* characterization techniques for the growth of CdTe and HgCdTe. Photoreflectance yields information about CdTe layers, with largest utility for doped and multi-layer structures. However, caution must be taken in interpretation of the spectra since the near-bandedge PR spectra consists of multiple transitions and the E_1 transition energy is very sensitive to the sample history. Photoreflectance appears to be of limited utility for HgCdTe single layer growth with x<0.4. However, reflectance measurements of the E_1 peak can be used to determine composition in HgCdTe single layers with an accuracy $\Delta x = \pm 0.01$, which can be useful for growth control. A tight binding model was used to calculate the E_1 peak energy as a function of bandgap for HgCdTe and HgTe/CdTe superlattices. Comparisons are made with experimental observations. Surface interdiffusion in HgTe-CdTe superlattices was probed using reflectance measurements.

Key words: HgCdTe, *in-situ* characterization, molecular beam epitaxy (MBE), metalorganic molecular beam epitaxy (MOMBE), reflectance, photoreflectance

INTRODUCTION

Significant progress has been made in the growth of HgCdTe alloy and HgTe/CdTe superlattice (SL) epitaxial layers by molecular beam epitaxy (MBE) and metalorganic MBE (MOMBE). High quality HgCdTe and HgTe/CdTe SL with properties suitable for infrared (IR) detector fabrication have been demonstrated.[1,2] Emphasis has shifted to evaluating and controlling critical factors during growth that limit the yield of both materials and devices.

Photoreflectance (PR) spectroscopy is a powerful tool for characterization of semiconductor materials and quantum well structures. Photoreflectance signals are observed at elevated temperatures in III-V semiconductors,[3] indicating that PR may be suitable as an *in-situ* monitoring technique during growth. Reflectance spectroscopy has been used for many years as a standard characterization technique for semiconductors. This *ex-situ* study assesses the utility of reflectance and PR as *in-situ* growth characterizations for CdTe and Hg-based MBE. Efforts concentrated on two key areas. The first area was an assess-
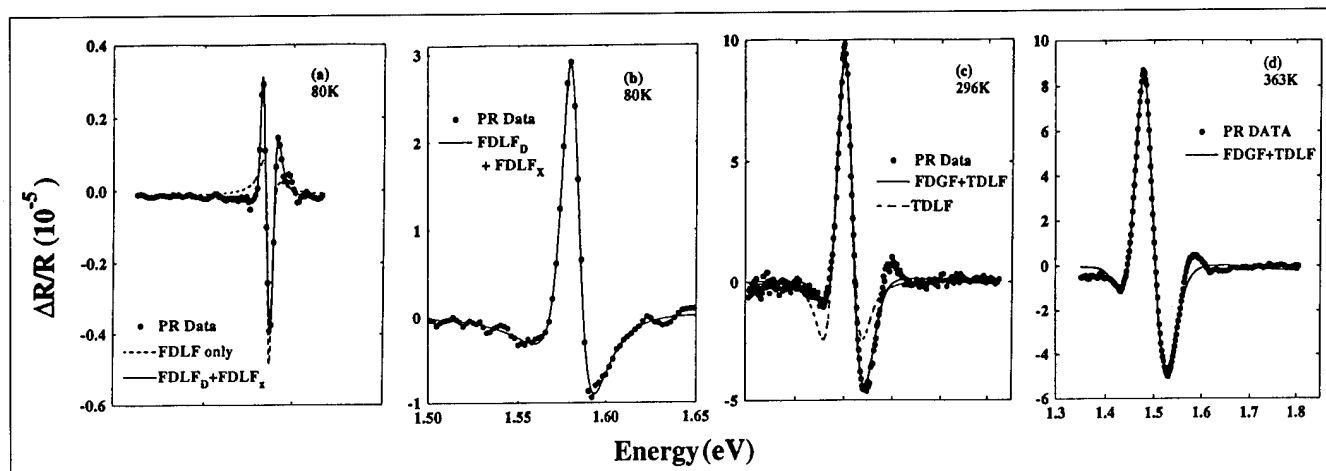
Fig. 1. Photoreflectance of CdTe. Plot (a) represents an 80K spectrum representative of undoped CdTe while plots (b), (c), and (d) are representative of iodine doped CdTe at 80, 296, and 363K, respectively.
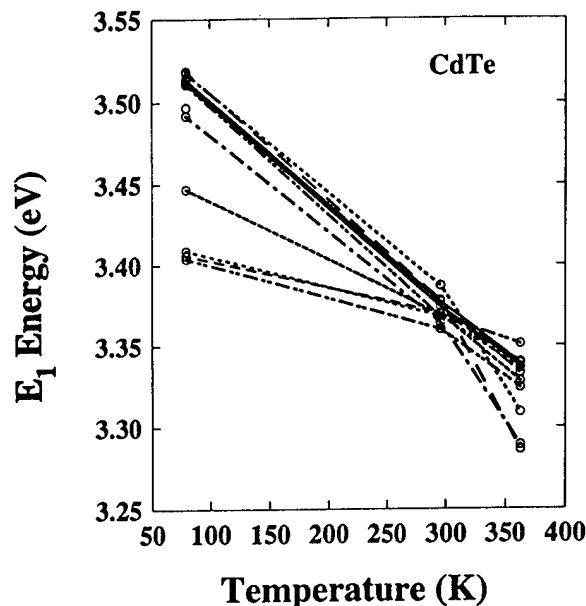

Fig. 2. E_1 transition energies of CdTe measured by photoreflectance. A wide spread in the transition energies was observed.

ment of the accuracy with which reflectance and PR measurements can determine composition during growth, allowing small corrections to be made in alloy composition or SL layer thicknesses thereby improving reproducibility. Second, a determination was made whether these techniques can provide an independent measure of the growth temperature, a very critical parameter in Hg-based MBE.

EXPERIMENTAL

During this study, PR and reflectance measurements were made on bulk and thin film CdTe, single layers of HgCdTe grown by MBE and MOMBE, and HgTe/CdTe superlattices. II-VI, Inc. (Saxonburg, PA) provided samples of undoped bulk (100) and (211)-oriented CdTe. The surface of the bulk CdTe was chemically polished with Br:methanol using a technique developed for MBE growth. An undoped (211)B CdTe/ (211)B GaAs layer, a (211)B HgCdTe/CdTe layer, and

six (211)B HgTe/CdTe superlattices grown by MBE were provided by Martin Marietta Electronics Laboratory. Four iodine doped (100) CdTe/CdTe layers and two (211)B HgCdTe/CdTe layers grown by metalorganic MBE were provided by the Physical Sciences Laboratory at Georgia Tech Research Institute. The epilayers were high quality as determined by transmission electron diffraction (TEM), Hall effect and double crystal x-ray diffraction measurements.

The CdTe samples exhibited significant photoluminescence (PL) during the PR measurements. To minimize the effect of the PL, a "sweeping" PR technique similar to that described by Shen et al.[4] was used. Light passing from a tungsten lamp through a 1/4-meter monochromator served as the probe source. The modulating light was provided by passing the 514 nm line of an argon ion laser through an acousto-optic modulator operating at 200 Hz. The power density at the sample ranged between 1 to 5 mW/cm². The reflected light was directed into a photomultiplier tube, with the resultant signal being deconvoluted into ac and dc signals using a lock-in amplifier and dc voltmeter for subsequent acquisition and analysis. A narrow bandwidth active bandpass filter was placed before the lock-in to further reduce noise. The minimum detectable $\Delta R/R$ was ~5 × 10^{-8}. All operations were under computer control. The samples were mounted in a simple dewar system for PR measurements, and data was taken at 80, 296, and 363K. Reflectance measurements were made at room temperature using an Olis-14 dual beam spectrophotometer. The measured reflectance was referenced to a calibrated sapphire window.

CdTe

Photoreflectance measurements in CdTe were made for near bandedge transitions and for the E_1 transition. Two distinctly different types of near-bandedge PR spectra were measured at 80K, as shown in Fig. 1. The relatively weak spectrum shown in Fig. 1a was representative of all undoped low carrier concentra-

tion samples and represents a superposition of a free exciton transition and a donor-hole transition.[5] In contrast, as illustrated by Fig. 1b, the iodine-doped layers and the undoped (100) bulk CdTe sample exhibited a strong signal dominated by the transition identified as the donor-hole transition. The fit to the PR spectra for doped samples was significantly improved if the excitonic transition was also included. The only fixed parameter in the least-squares fitting procedure was the choice of a first derivative of a Lorentzian as the functional form (FDLF) for the fit as appropriate for confined systems such as excitons and donors at low temperature.[6] Other choices for the functional form did not result in an adequate fit to the data. Both types of spectra indicated an exciton energy of 1.586±0.002 eV and donor-hole transition energy of 1.581±0.002 eV which implies an 80K bandgap of 1.596±0.002 eV.

Interestingly, only the samples exhibiting the strong donor-hole PR signal at 80K had a measurable PR signal at 296 and 363K. The PR signal at higher temperatures, as shown in Figs. 1c and 1d, consisted of a superposition of both excitonic and direct band-to-band transitions at 1.504±0.002 eV and 1.514±0.002 eV at 296K and 1.483±0.002 eV and 1.493±0.002 eV at 363K, respectively. This analysis is discussed in more detail in another paper presented at this workshop[7] and is consistent with the results of a recent photoluminescence study[8] indicating that excitons play a significant role at room temperature. The multiple transitions complicate interpretation and give an inherent uncertainty of up to 7 meV in any analysis of the spectra assuming only a single transition. For example, assuming only the third derivative of a Lorentzian functional form (TDLF) appropriate for band-to band transitions results in a bandgap energy of 1.507 eV. As shown in Fig. 1c, use of only a TDLF resulted in a poor fit to the data on both sides of the main figure. A significantly better single transition fit is obtained when the first derivative Gaussian function (FDGF) suitable for excitonic transitions[6] at high temperatures is also included. The multiple transition fits also yield values for the bandgap more consistent with previous electroreflectance and photoluminescence measurements.[8-11] If the near-bandedge PR signal for CdZnTe consists of similar multiple transitions, this could lead to an uncertainty in x-value of about 1%. It is also important to note that both in the as-grown samples and the chemically polished substrates, the only samples which exhibited a measurable high temperature PR signal also had an appreciable donor-hole signal at 80K. Thus, an appreciable room-temperature or above PR signal may be a signature of high levels of impurities in the substrates. This latter effect warrants more investigation.

The E_1 transition was also measured, and appeared to consist of a single, narrow transition. The PR spectrum was thus analyzed in the conventional fashion for the E_1 transition, as a third derivative of a Lorentzian function appropriate for a two-dimen-

sional transition. The surprizing results obtained for E_1 are displayed in Fig. 3. This figure shows the measured E_1 energy as a function of temperature for 13 samples. A very broad range of energies was observed at 80K, with the spread in energies becoming less pronounced as the temperature was raised. However, a distinct spread in the measured E_1 energies remained up to 363K. As discussed in more detail in another paper at this workshop,[7] the E_1 energy depends on many factors related to the sample's history. Certainly, this observation of a wide variation for E_1 in the current diverse set of samples allows a better understanding of the spread in reported E_1 values for CdTe reported in the literature, a spread which has been much larger than can be explained by the inherent precision of the measurements themselves.[9,12,13] Unfortunately, this spread limits the utility of this measurement for determining growth parameters such as substrate temperature. The samples which exhibited the least bowing in the E_1 energy as a function of temperature still had a slope at high temperatures that ranged form 0.54 to 0.62 meV/K. Without *a priori* knowledge of this slope for a given substrate, this uncertainty limits an independent determination of the substrate temperature to about ±10°C. Thus, while PR measurement of the E_1 energy in CdTe can be used as a general diagnostic of surface temperature, it appears that other techniques, such as the observation of Te-condensation by reflection high energy electron diffraction (RHEED) reported by Rajavel et al.[14] provide a better independent determination of substrate temperature. However, since the E_1 energy depends on the sample's growth param-
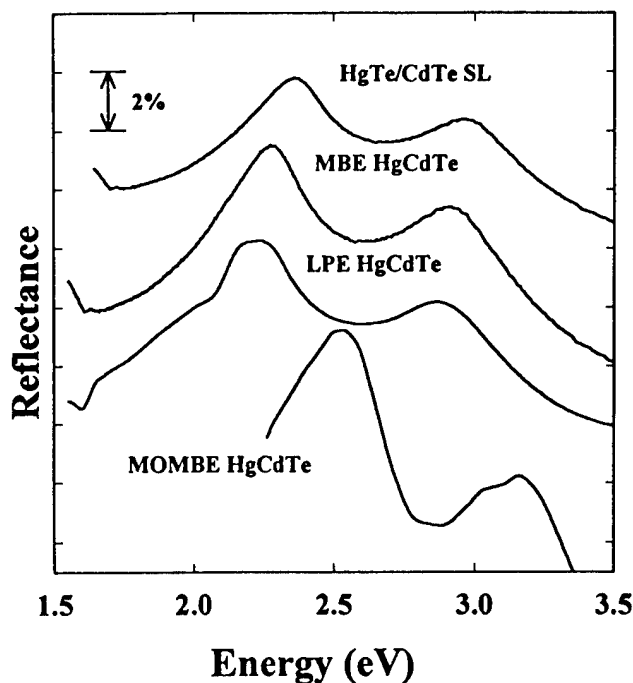

Fig. 3. Reflectance spectra from HgCdTe grown by MBE, MOMBE, and LPE and a spectrum from a HgTe/CdTe SL. The MBE and LPE samples have a nominal x-value of 0.22, while the MOMBE sample has a nominal x-value of 0.43.

Table I. Parameters Used in the ETBM Calculation

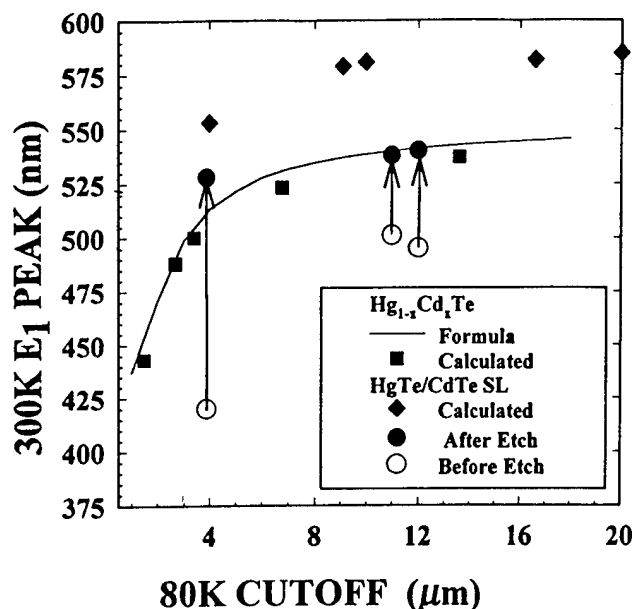|	77K	300K
E_0(HgTe)	–0.271 eV	–0.167 eV
E_1(HgTe)	2.21 eV	2.12 eV
E_0(CdTe)	1.596 eV	1.529 eV
E_1(CdTe)	3.44 eV	3.31 eV

Fig. 4. E_1 transition energy as a function of cutoff wavelength for HgCdTe and HgTe/CdTe SL. Experimental measurements are compared to results predicted by ETBM calculations. For HgCdTe, the ETBM calculations are compared to the formula by Raccah[16] based on electrolyte electroreflectance measurements.

eters, E_1 energies can be determined that correspond to the desired materials properties. Thus, the E_1 energy can serve as a process check. Deviation from this point during growth would indicate deviation from the desired characteristics.

A strong PR signal was easily observed in all of the doped CdTe layers. Variations in the PR signal with doping concentration and other growth parameters are discussed in another paper in this proceedings.[7] However, in all cases, the magnitude was virtually unchanged in going from 296 to 363K. This indicates that PR measurements in doped layers should be quite feasible at the growth temperatures. When proper interpretation is given to the spectra, PR will be a useful tool for investigating doped single layers and multi-layer structures based on CdTe.

HgCdTe AND HgTe/CdTe SUPERLATTICES

A photoreflectance signal was *not* observed for any of the HgCdTe single layers or HgTe/CdTe superlattices at room temperature or above, to the measurement limit of our system. This is consistent with earlier measurements of PR in undoped HgCdTe[13,15] which reported quite small signals at 80K. Only undoped layers with bandgaps corresponding to wavelengths larger than 4 μm were inves-

tigated. Highly doped multi-layer structures or single layers of shorter wavelength were not investigated. It is conceivable that either shorter wavelengths or the presence of strong electric fields at the junction/interfaces in doped structures will yield a PR signal during growth. However, the current result indicates that PR will be of limited value for the growth of undoped and single layers of Hg-based materials for long wave IR applications.

The E_1 transition can also be observed in reflectance measurements. Reflectance measurements made at room temperature as a function of energy for three samples of HgCdTe are compared in Fig. 2. The relatively sharp spectra from the MBE and MOMBE samples allowed a reproducible determination of the peak position to within ±0.5 nm, which corresponds to ±3 meV at these wavelengths. Shown for comparison is the reflectance spectrum obtained from a liquid phase epitaxy (LPE) sample. The relatively broad E_1 peak measured for this particular sample was representative of that measured for many samples from various sources and indicates a spread in x-value over the 1 cm linear dimension of our reflectance beam, precluding accurate peak determination. Thus, reflectance measurement also provides a measure of sample uniformity. By using expressions such as that given by Raccah et al.[16] which experimentally relate the E_1 energy at room temperature to x-value, the x-value can be determined to ±0.01. While this is not the accuracy desired in final control of cutoff wavelength, it is certainly accurate enough to serve as a coarse process check. The next step needed to fully implement this measurement during growth is an accurate determination of the shift in E_1 energy with temperature for HgCdTe. Again, as with the E_1 transition in CdTe, measurement of the E_1 reflectance peak in HgCdTe may best serve as an indicator of when growth has deviated from the desired conditions.

HgTe/CdTe SL continue to be of interest.[2] A calculation of the E_1 energy vs bandgap by Ritze et al.[17] for HgTe/CdTe SL suggested that, for 10 to 12 μm cutoff, measurement of the E_1 energy may be a better predictor of bandgap for the SL than for the equivalent alloy. The initial measurements of the E_1 peak position for several SL also supported a more pronounced variation of the E_1 energy with bandgap than is found for HgCdTe. Thus, a more detailed study of the E_1 transition in HgTe/CdTe SL was undertaken using reflectance measurements.

An empirical tight-binding method (ETBM), which has been described in detail elsewhere,[18] was used to calculate E_1 as a function of bandgap energy. For the present calculations, the parameters listed in Table I were used. Calculations were first made for the E_1 energy as a function of bandgap for the alloy, HgCdTe. As shown in Fig. 4, excellent agreement was found between the results of this calculation and the experimentally measured values of E_1 for HgCdTe. The values were obtained by linear interpolation of the tight-binding parameters of the constituents which corresponds to the virtual crystal approximation.

Deviation between experiment and theory away from the endpoints can thus be understood since this approach leads to practically no bowing in the E_0 and E_1 energies.

A valence band offset of -350 meV was assumed between HgTe and CdTe for the SL calculations. The barrier layers were taken to be $Hg_{0.1}Cd_{0.9}Te$ in order to reflect the actual composition in the samples. The calculations were done for the (100) growth direction assuming growth on a CdTe substrate. Strain effects are included by fitting the bulk energy shift and splitting of the HgTe to the respective a and b deformation potentials. For example, $dE_0/dP = 12.$meV/kbar[19] and $E_{1h}-E_{hh} = 22$ meV[20] for a CdTe substrate. Since the calculations were to be compared to samples grown in the (211) direction, first order corrections were made to the bandgap energies based on k·p calculations. The calculated results are summarized in Table II and compared with that for HgCdTe in Fig. 4. The trend in E_1 as a function of cutoff wavelength is very similar to that observed for HgCdTe, exhibiting essentially the same curvature.

Also shown in Fig. 4 are measured values of E_1 determined for the HgTe/CdTe SL using reflectance. It can be seen that the initial values for the SL disagree quite significantly with the predicted values. It was noticed that the measured E_1 values corresponded closely to that expected for the resulting HgCdTe if the layers were completely interdiffused. However, an interpretation of complete interdiffusion strongly conflicted with IR photoluminescence and TEM measurements made on the same SL.

The SL were then etched in a sequence of steps using a Br-methanol solution. About 0.25 μm was removed per step, and reflectance measurements were repeated after each etch step. The absorption coefficient of a HgTe/CdTe SL has values greater than 5×10^4 cm^{-1} at the E_1 energy.[21] Thus, the reflectance measurement samples a depth approximately equal to the etch step. The E_1 peak initially shifted quite dramatically toward longer wavelength with etch depth and then remained stable at a fixed wavelength after removal of about 0.5 μm. This effect was observed on all the superlattices and can be interpreted as interdiffusion of the SL at the front surface. The interdiffusion is not caused by the sample temperature during growth, or the SL would exhibit more severe interdiffusion near the substrate. Indeed, comparison of front-side and through the substrate photoluminescence indicates little change in bandgap throughout a relatively thick SL,[2] indicating minimal interdiffusion in the initial layers grown. Evidence of significant interdiffusion has not been observed in as-grown SL by transmission electron microscopy.

A detailed study of HgTe/CdTe SL interdiffusion by Kim et al.[22] has indicated that a significantly higher interdiffusion coefficient occurs near the surface of a SL as compared to the bulk, most likely due to surface generation of defects or vacancies. This effect was measured in SL annealed at elevated temperatures without an equilibrium Hg overpressure. It is con-

ceivable that similar conditions, deviating from equilibrium, occur during cooldown after growth. If the interdiffusion is indeed an artifact of the growth cooldown conditions, suitable changes can eliminate the problem. It should be noted that the rapid change in bandgap implied by the dramatic change in E_1 with etch depth would not show up in a PL measurement, and so was not detected. Indeed, the measurement of the E_1 reflectance peak has proven to be a useful tool for evaluating surface interdiffusion in HgTe/CdTe SL. One SL has been selected to monitor for an extended period of time to look for surface interdiffusion at room temperature.

A typical reflectance spectrum for a HgTe/CdTe SL after etching was shown in Fig. 3. This is the first report of E_1 and $E_1 + \Delta_1$ transition energies for HgTe/CdTe SL that are different from that observed for HgTe.[17,23] Values of E_1 measured for the etched SL are included in Fig. 4 as a function of measured SL cutoff wavelength. Interestingly, the values agree quite closely with that observed for HgCdTe. This result indicates that using measurements of the E_1 peak to determine the cutoff wavelength is possible for HgTe/CdTe SL. However, if a trend can be inferred from three points, the E_1 peak of the HgTe/CdTe SL exhibits less variation with wavelength than found for HgCdTe.

CONCLUSION

This paper reports on an evaluation of the suitability of reflectance and photoreflectance as *in-situ* characterization techniques for the growth of Hg-based materials. Photoreflectance can yield information about CdTe layers, with largest utility for doped and multi-layer structures. However, caution must be taken in interpretation of the spectra. The near-bandedge PR spectra appears to consist of multiple transitions while the E_1 transition energy is very sensitive to the sample history. The latter precludes using measurement of the E_1 transition energy to determine sample temperature without prior knowledge of the sample.

Photoreflectance appears to be of limited utility for

Table II. Calculated and Measured Values of E_0 and E_1 for Various HgTe/CdTe SL

Layer HgTe (Å)	Thick. CdTe (Å)	Calculated E_0 @ 80K (μm)	Calculated E_1 @ 296K (nm)	Measured E_0 @ 80K (μm)	Measured E_1 @ 296K (nm)
39	36	9.1	579	—	—
42	45	11.3	581	11.5	540
48	26	20.0	585	—	—
49*	26*	—	—	11	538
45	26	16.6	582	—	—
19	23	4.0	553	—	—
19	24	—	—	3.9	528

*These layer thicknesses were not measured directly, but inferred from growth conditions.

Hg-based alloy and single layer growth. However, reflectance measurements of the E_1 peak can be used to determine composition in HgCdTe single layers with an accuracy $\Delta x = \pm 0.01$, which is useful for growth control. For precise process control, however, the higher precision obtainable with ellipsometry or wavelength difference spectroscopy is desirable. A tight binding model was used to calculate the E_1 peak energy as a function of bandgap for HgCdTe and HgTe/CdTe superlattices. The SL were found to have essentially the same E_1 energy at a given cut-off wavelength as HgCdTe. Surface interdiffusion in HgTe-CdTe superlattices was probed using reflectance measurements.

ACKNOWLEDGMENTS

REFERENCES

1. J.M. Arias, J.G. Pasko, M. Zandian, S.H. Shin, G.M. Williams, L.O. Bubulac, R.E. DeWames and W.E. Tennant, *J. Electron. Mater.* (1993).
2. R.W. Yanka, K.A. Harris, L.M. Mohnkern, A.R. Reisinger and T.H. Myers, *J. Electron. Mater.* (1993).
3. H. Shen, *SPIE Proc.: Modulation Spectroscopy,* 1286, 125 (1990).
4. H. Shen and M. Dutta, *Appl. Phys. Lett.* 57, 587 (1990).
5. Zhonghai Yu, S.G. Hofer, N.C. Giles, T.H. Myers, D. Rajavel and C.J Summers, submitted to *Phys. Rev. B.*
6. A recent review of photoreflectance pertinent to confined systems can be found by O.J. Glembocki and B.V. Shanabrook, *Semiconductors and Semimetals,* vol. 36, (New York: Academic Press, 1992).
7. N.C. Giles, Jaesun Lee, T.H. Myers, Zhonghai Yu, R.G. Benz, II, B.J. Wagner and C.J. Summers, *J. Electron. Mater.* (24), 693 (1995).
8. Jaesun Lee, N.C. Giles, D. Rajavel, and C.J. Summers, *Phys. Rev. B* 49, 1668 (1994).
9. W.S. Enloe, J.C. Parker, J. Vespoli, T.H. Myers, R.L. Harper and J.F. Schetzina, *J. Appl. Phys.* 61, 2005 (1987).
10. C. Vasquez-Lopez, H. Navarro, Raul Aceves, M.C. Vargas and Cornelius A. Menezes, *J. Appl. Phys.* 58, 2066 (1985).
11. P.M. Arnirtharaj, F.H. Pollak, J.R. Waterman and P.R. Boyd, *Appl. Phys. Lett.* 41, 860 (1982).
12. A. Ksendov, F.H. Pollak and O.K. Wu, *Sol. State Comm.* 70, 963 (1989).
13. P.M. Amirtharaj, J.H. Dinan, J.J. Kennedy, P.R. Boyd and O.J. Glembocki, *J. Vac. Sci. Technol.* A4, 2028 (1986).
14. D. Rajavel, F. Mueller, J.D. Benson, B.K. Wagner, R.G. Benz, II and C.J. Summers, *J. Vac. Sci. Technol.* A8, 1002 (1990).
15. A. Ksendzov, F.H. Pollack, P. M. Amirtharaj and J.A. Wilson, *J. Cryst. Growth* 86, 586 (1988).
16. P.M. Raccah, *J. Vac. Sci. Tech.* A1, 1587 (1983).
17. M. Ritze, R. Enderlein, D. Schikora, O. Goede and W. Heimbrodt, *Supperlattices and Microstructures* 9, 351 (1991).
18. Lok C. Lew Yan Voon, L.R. Ram-Mohan, H. Luo and J.K. Furdyna, *Phys. Rev.* B47, 6585 (1993).
19. H.H. Cheong, J.H. Burnett, W. Paul, P.M. Young, Y. Lansari and J.F. Schetzina, *Semicon. Sci. Technol.* 8, S58 (1993).
20. Schulman and Chang, *Phys. Rev.* B33, 2594 (1986).
21. T.H. Myers, J.R. Meyer and C.A Hoffman, *Quantum Wells and Superlattices for Long-Wavelength Infrared Detectors* (Boston, MA: Artech House, Inc, 1993).
22. Y. Kim, A. Ourmazd and R.D. Feldman, *J. Vac. Sci. Technol.* A8, 1116 (1990).
23. P.P. Chow and D. Johnson, *J. Vac. Sci. Tech.* A3, 67 (1983).

Optical Properties of Undoped and Iodine-Doped CdTe

N.C. GILES, JAESUN LEE, T.H. MYERS, and ZHONGHAI YU

Department of Physics, West Virginia University, Morgantown, WV 26506

B.K. WAGNER, R.G. BENZ II, and C.J. SUMMERS

EOEML, Quantum Microstructures Laboratory

Georgia Tech Research Institute, Atlanta, GA 30332

A comprehensive study of the properties of undoped and iodine-doped CdTe structures by photoluminescence (PL) and photoreflectance (PR) is reported. Undoped bulk CdTe and iodine-doped CdTe layers grown by metalorganic molecular beam epitaxy on (100)-oriented CdTe and (211)B-oriented GaAs substrates with electron concentrations ranging from 10^{14} to mid- 10^{18} cm^{-3} were included in this study. Lineshape modeling of 80K PL and PR spectra indicated the presence of both free exciton and donor-hole transitions at the higher doping levels. Strong PL and PR signals were also observed at room temperature. If only a single transition is considered for the analysis of the 300K spectra, the PL emission peak and the PR transition energy both exhibit a strong dependence on electron concentration for doped layers. However, lineshape modeling of the room-temperature spectra indicated the presence of multiple transitions consisting of free exciton and direct band-to-band transitions. The use of two transitions resulted in a constant value of bandgap over the entire range of conductivities studied. A strong correlation remained between the broadening of the PR and PL spectra and excess carrier concentration $N_D - N_A$. In addition, the E_1 transition energy measured by PR was found to vary dramatically with growth conditions.

Key words: CdTe, metalorganic molecular beam epitaxy (MOMBE), photoluminescence, photoreflectance

INTRODUCTION

Efficient n-type doping of CdTe has been accomplished using iodine as an anion dopant.[1,2] Bright photoluminescence (PL) at low temperatures was obtained from a series of CdTe:I samples exhibiting room-temperature electron concentrations of ~1×10^{17} cm^{-3}.[3] In the prior PL study, the shallow donor nature of substitutional I_{Te} was verified. Photoreflectance (PR) measurements were also previously reported for the same set of samples.[4] The PL and PR spectroscopy studies have been extended in the present paper to include a series of samples displaying a wider range of conductivities.

CdTe:I epilayers were grown by MOMBE on (100)-oriented CdTe and (211)B-oriented GaAs substrates at Georgia Tech. Electron concentrations ranged from 10^{14} to mid 10^{18} cm^{-3} at room temperature. Ethyliodide was used as the gas source for the dopant precursor. The films were grown at substrate temperatures ranging from 170 to 250°C using CdTe as the source material. Excess Cd was provided from a separate Cd source for various layers. A summary of layer parameters is given in Table I. A two micron CdTe buffer layer was grown on the GaAs substrates prior to deposition of the two lightly doped epilayers (A9307 and A9309). The thicknesses of the doped regions only are included in Table I. Hall effect, x-ray diffraction, PL, and PR measurements indicated that the epilayers were of high quality. Undoped bulk samples were included in our study for comparison. Photoluminescence measurements were recorded from the
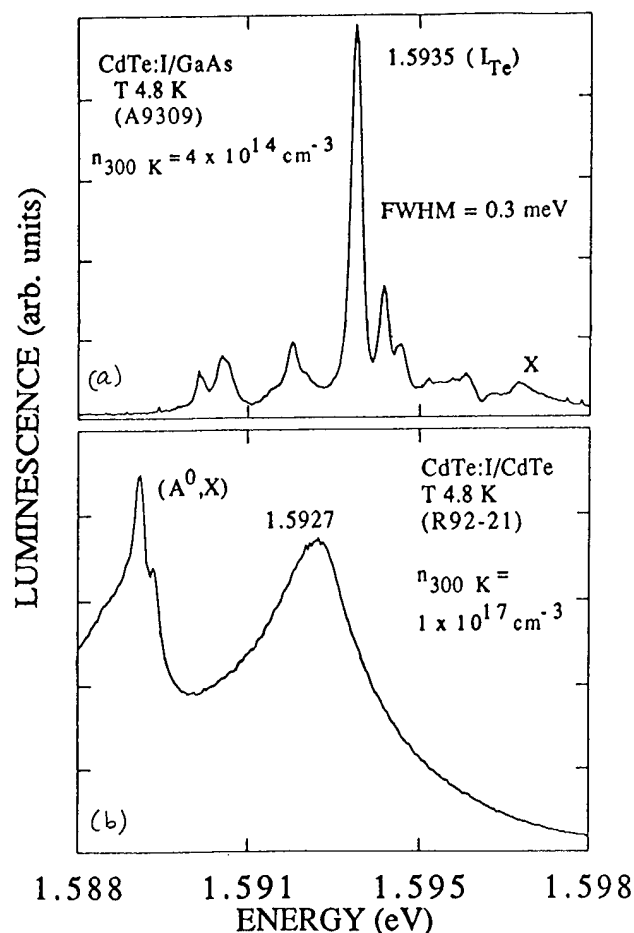
Fig. 1. Representative 4.8K PL spectra recorded under 500 mW/cm² excitation (argon ion laser, 514.5 nm) from (a) low-doped epilayer grown on a GaAs substrate showing (D⁰, X) at 1.5935 eV, and (b) heavily doped CdTe:I grown on bulk CdTe substrate.
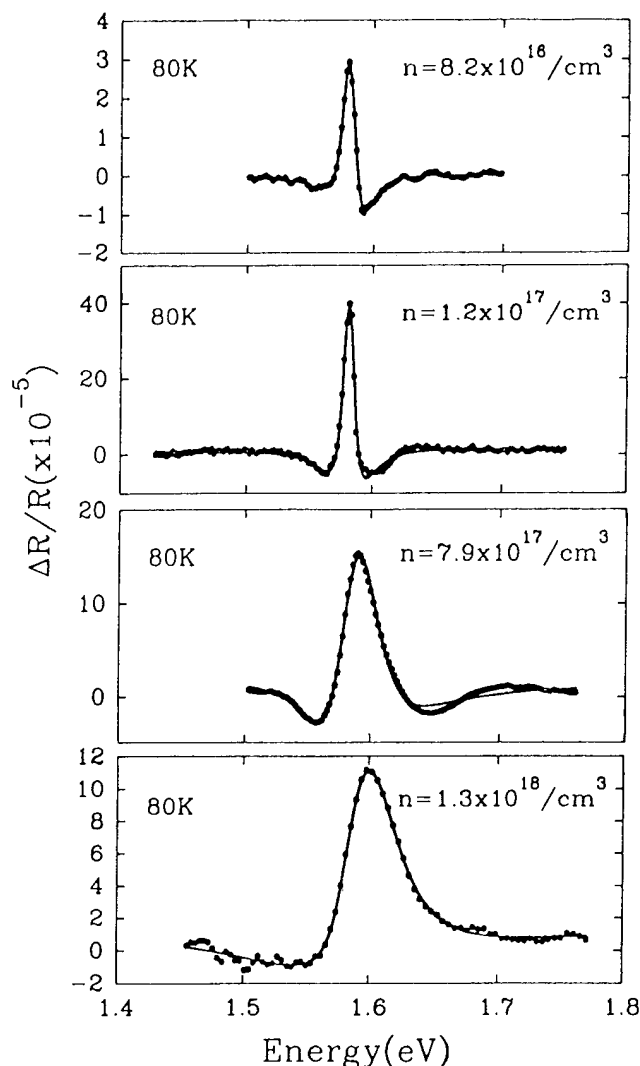

Fig. 2. Photoreflectance at 80K from CdTe:I/CdTe epilayers with varying carrier concentrations. A two-transition fit using two FDLF (solid line) reproduces the PR data (dots) very well. The two transitions are the iodine donor-hole transition at ~1.582 eV and the free exciton at ~1.588 eV.

samples at 4.8, 80K, and room temperature (~300K). Photoreflectance data was taken at 80, 296, and 363K. The PL[3] and PR[4] experimental setups have been described elsewhere.

Representative liquid-helium temperature PL spectra recorded from the iodine-doped epilayers are shown in Fig. 1 for emission immediately below the bandgap energy. The luminescence was excited using an incident power density of 500 mW/cm². Figure 1a is the emission recorded from the lowest doped epilayer which had a room-temperature excess electron concentration, $N_D - N_A$, of 4.4×10^{14} cm⁻³. Sharp bound-exciton lines were observed with the dominant emission corresponding to donor-bound exciton recombination (D⁰,X) at 1.5935 eV, consistent with the shallow donor nature of I_{Te}.[3] The free-exciton recombination, which normally is seen at 1.5954 eV in bulk or homoepitaxially grown CdTe, was observed at 1.5966 eV in Fig. 1a. This increase in free-exciton emission energy of 1.2 meV is believed to be related to residual strain due to the thermal expansion mismatch between the CdTe epilayer and the GaAs substrate upon cooling to 4.8K.

An estimate of the I_{Te} donor ionization energy E_D can be made from the (D⁰,X) emission energy in the

lowest doped CdTe:I epilayer once the strain-shift in the X emission is taken into account. Fluorine (E_D = 13.71 meV) and chlorine (E_D = 14.48 meV) donors in bulk CdTe produce bound exciton lines at 1.59314 and 1.59296 eV, respectively.[5] After subtracting the 1.2 meV shift due to strain in our CdTe/GaAs epilayer, the normalized energy for the iodine (D⁰,X) is 1.5923 eV, resulting in an estimate of the iodine E_D in the range from 14.5–15 meV. Thus, a consistent decrease in bound exciton emission energy (and increase in E_D) is predicted with increasing atomic number for these halogen species.

The PL spectrum from a more heavily doped epilayer grown on a CdTe substrate is shown in Fig. 1b. The broad donor-related PL band is centered around 1.5927 eV. Note that the (D⁰,X) line cannot be clearly resolved in this case but is consistent with a 14.5–15 meV value for E_D. Acceptor-bound exciton (A⁰,X) emission was also detected at 1.589 eV. As reported earlier,[3] the (A⁰,X) emission lines can be separately resolved in

high resolution scans as transitions due to Cu (1.5895 eV), Ag (1.5885 eV), and Li and/or Na (1.5892 eV) acceptor impurities in the CdTe:I/CdTe epilayers. Figure 1a shows that Cu contamination is absent when GaAs substrates are used. Our study indicates that diffusion of acceptor impurities from II-VI substrates into the epilayer during growth remains a problem.

Both PR and PL measurements were made at 80K. Two types of PR spectra were observed which differed by about a factor of ten in signal strength, as discussed elsewhere.[4] The weaker signal was only obtained from low-doped samples (n ≤ 1 × 10^15 cm^-3) and clearly consisted of the superposition of two transitions with energies at 1.582 and 1.588 eV. The mechanisms underlying the two transitions were determined through a comparison with the PL spectrum of the same CdTe taken at 78K. The PL spectrum consisted of two peaks with maxima near 1.581 and 1.589 eV. By tracking CdTe PL edge emission peaks from 1.6K to higher temperatures, Giles[6] has shown that the peak at 1.589 eV corresponds to a free-exciton transition, while the emission at 1.581 eV is associated with a donor-hole transition. Thus, the two overlapping PR signals are due to donor-hole and free-exciton transitions with energies of about 1.582 eV (donor) and 1.588 eV (exciton).

At 80K, the edge PL emission from the more heavily iodine-doped samples broadened to a single bright peak occurring at about 1.581 eV, varying only slightly with doping concentration. This emission occurs significantly below the 80K bandgap of CdTe (~1.598 eV). A similar result was observed for the PR measurements. Photoreflectance spectra from samples with different doping levels are shown in Fig. 2. Analysis of the 80K PR lineshape assumed only the first derivative of a Lorentzian function (FDLF), appropriate for confined systems such as excitons at low temperatures.[7] While the dielectric function of an impurity-band transition has been described by a more complex dielectric function,[8] the PR signal in Fig. 2 was adequately fit using a FDLF for extracting transition energies. A two-transition analysis was performed where both exciton and donor transitions were considered based on the results obtained for the less heavily doped samples. The PR spectra of the more heavily doped samples was dominated by the donor-hole transition with a relative contribution about ten times larger than that of the exciton contribution. Lightly doped or undoped samples exhibited contributions from donors and excitons at comparable intensities.

Figure 2 shows the results of the two-transition lineshape fits to the 80K PR spectra for the heavily doped CdTe:I samples. In all cases, the two-transition least-squares fit (solid line) provided for almost complete reproduction of the PR data (dots). The donor-hole transition occurred at 1.581 ± 0.001 eV for all doping levels and is consistent with the PL measurements. The energy difference between the two transition energies (exciton and donor) was consistently

found to be 5 meV ± 1 meV. Since the ground state energy of the exciton is 10 meV, this indicates a donor energy E_D of ~15 meV, which is consistent with the liquid helium temperature PL measurement. Note also in Fig. 2 that the PR transition broadens with increasing carrier concentration. Broadening of comparable magnitude was observed in the PL spectra.

Bright PL at room temperature was observed from the CdTe:I samples. As reported previously,[9] the signal intensity from the CdTe:I epilayers with n = 1 × 10^17 cm^-3 was ~1000 times larger than that obtained from a piece of bulk CdTe normally used as a PL standard. In the present study, the magnitude of the 300K PL signal increased with increasing doping level. Both the position of the PL peak and the full-width-at-half-maximum (FWHM) of the emission peak were found to depend on carrier concentration, as shown in Fig. 3 (solid dots). Note the shift in PL emission peak energy from 1.507 to 1.523 eV. However, the origin of the peak shift cannot be understood in terms of a single band-to-band transition. Even for the highest doping level, the PL emission peak energy is still too low to be attributed to conduction band valence band (e, h) recombination. The 300K bandgap of CdTe is about 1.513 eV, and the (e, h) emission should peak about 1/2 kT higher in energy.[9,10]

Room-temperature PR spectra taken near the band edge also indicated a strong dependence on electron
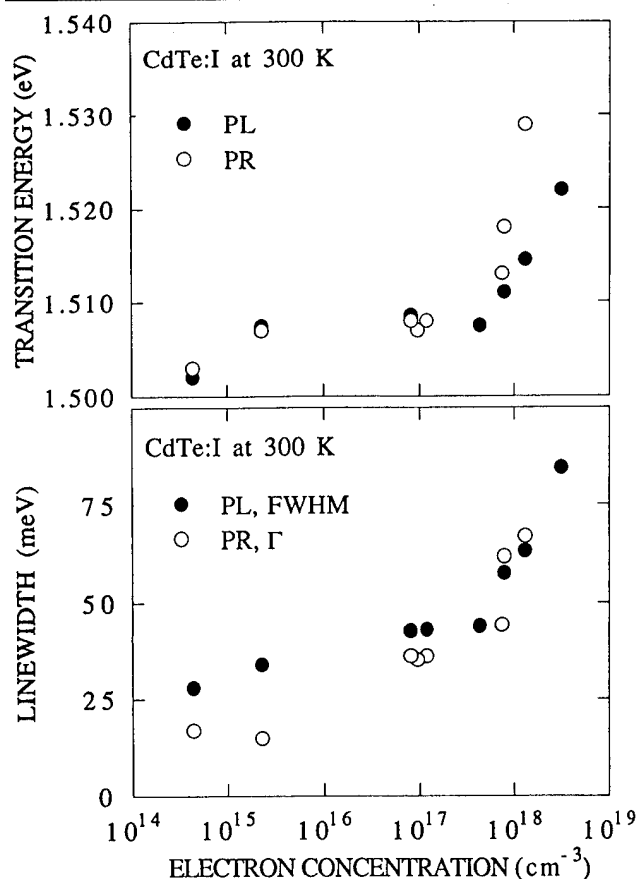
Fig. 3. Apparent transition energy and linewidth of PL and PR measurements as a function of carrier concentration in iodine-doped CdTe.
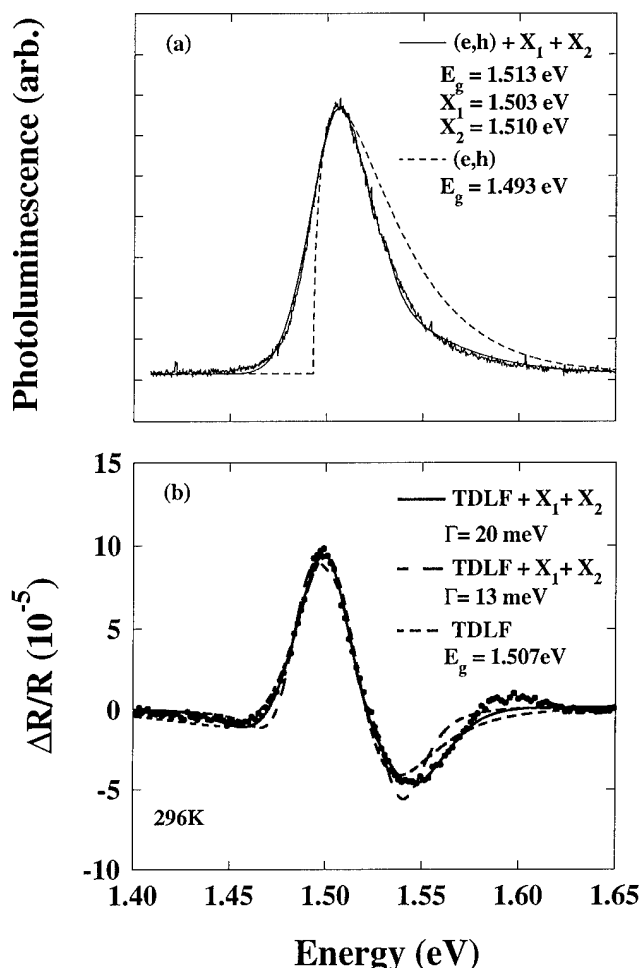
Fig. 4. Room-temperature (a) PL and (b) PR spectra for an iodine-doped CdTe epilayer ($n = 1 \times 10^{17}$ cm^{-3}). In (a), a single (e, h) transition gave a poor fit (dashed line), while agreement was obtained when excitonic contributions were included (dashed line). In (b), the PR data was not reproduced using a single (e, h) transition (heavy dashed line). An improved fit was obtained when excitonic contributions were included (dashed line), and the broadening parameter was increased to 20 meV (solid line).

Fig. 5. Correlation of the E_1 energy with (a) sample growth temperature, and (b) electron mobility.

concentration for heavily doped CdTe:I layers. Generally, the signals increased in strength with increasing doping. Interestingly, room-temperature PR signals were not observed in undoped bulk CdTe samples and were very weak in the low-doped epilayers. Thus, a strong room temperature PR signal may be a signal of impurities in CdTe. Fitting the measured PR data with a single third derivative Lorentzian function (TDLF) suitable for direct band-to-band transitions resulted in the transition energies and broadening parameters shown in Fig. 3 (open circles). While these energies are consistent with the PL peak positions, they again do not reflect the accepted bandgap of CdTe.

Figure 4 shows the PR and PL spectra from a heavily doped CdTe:I epilayer taken at room temperature. The PL spectrum shown in Fig. 4a consisted of a broad single peak centered at about 1.507 eV. A fit assuming that the PL emission is composed primarily of (e, h) recombination is shown by the dashed line in Fig. 4a. The fit to the data is poor and a bandgap of

1.493 eV is obtained which is far below the accepted value of 1.513 eV for CdTe at 300K. As discussed below, the 1.493 eV energy also disagrees significantly with the PR result. By including recombination bands due to the ground X_1 ($n = 1$) and first excited state X_2 ($n = 2$) of the free exciton, the PL emission curve was reproduced quite accurately (solid line).

A TDLF fit to the PR spectrum in Fig. 4b yields a transition energy of 1.507 eV. Note that the TDLF lineshape yields a poor fit to the data. Based on the PL results above, the PR data was analyzed using a combination of band-to-band transition (TDLF) and the first derivative functional forms appropriate for a Gaussian absorption profile (FDGF) expected for excitonic transitions at room temperature.[7] While not correct when excitonic contributions are significant, as in quantum well structures or at low temperatures, earlier PL studies[9] indicate that CdTe at room temperature is in a regime where both effects are comparable. Both the ground state and the first excited state of the exciton were used. The values obtained from the PL analysis for the transition energies ($E_g = 1.513$ eV, $X_1 = 1.503$ eV, and $X_2 = 1.5105$ eV) and the PL broadening parameter of the exciton transitions ($\Gamma =$

13 meV) were used as fixed parameters for this analysis. The fitting consisted primarily of determining the relative contribution of each transition. The result of this fit is also shown in Fig. 4b and resulted in an improvement over that obtained from a single band-to-band transition alone. By allowing the broadening parameter to vary, the PR data could be exactly reproduced with $\Gamma = 20$ meV. In both cases, the relative contribution of the (e, h):X_1:X_2 transitions was 1:1:1.5. The remarkable agreement between PL, which probes the imaginary part of the dielectric function, and PR, which probes the real part, clearly indicates that excitonic contributions to both signals are important at room temperature.

When both band-to-band and excitonic transitions were considered, all of the PR spectra could be accurately reproduced using a single value of the bandgap energy regardless of carrier concentration. This analysis yielded a 296K bandgap energy of 1.514 ± 0.002 eV for CdTe. The apparent shift in the transition energy for the PR and PL spectra shown in Fig. 3 reflects the varying contributions from the (e, h) and X transitions. Excitonic contributions were comparable to (e, h) transitions for low doping, while higher doping increased the relative (e, h) contribution.

One use of PR is to determine alloy composition through measurement of the bandgap. The present analysis indicates that the near-band-edge signal in CdTe consists of at least two overlapping transitions. Different surface preparations, crystal quality, or doping levels may affect the relative contribution of each transition, resulting in a shifting of the transition energy obtained by assuming only one transition. Such a shift was observed in the study by Vazquez-Lopez et al.[11] for PR of CdTe. Thus, PR analysis for room-temperature bandgap determination relying on only one transition has an inherent uncertainty of as much as 7 meV in CdTe and care must be exercised in the use of such an analysis. Such an uncertainty, for example, would result in an absolute error in x of

about 1% in $Cd_{1-x}Zn_xTe$.[12]

The E_1 transition in CdTe was also measured by PR and appeared to consist of a single, narrow transition in each sample. The PR spectrum was thus analyzed in the conventional fashion for the E_1 transition, as a third derivative of a Lorentzian function appropriate for a two-dimensional transition. The E_1 energy for 13 samples was measured as a function of temperature. A very broad range of energies, differing by as much as ~100 meV was observed at 80K. The spread in energies became less pronounced as the temperature was raised; however, a distinct spread in the measured E_1 energies remained up to 363K. This spread in energy was much larger than expected from the width of the transition (~40 meV) and did not appear to be the result of multiple transitions. The E_1 energy does appear to be related to the sample's characteristics and growth history. As shown in Fig. 5a, a distinct trend in E_1 energy measured at 363K occurs with growth temperature. The E_1 energy depends on more than just the growth temperature. As shown in the figure, a different growth rate resulted in a shift in the E_1 energy from the expected value. A correlation also apparently exists between the 80K E_1 energy and electron mobility, as shown in Fig. 5b.

It should be noted that discrepancies exist for the value of the E_1 energy in the literature for CdTe. Most studies have involved a single sample and the variation in the values of E_1 between the studies is larger than expected from the inherent precision of the measurement techniques. This study, with its variety of samples, reproduces most of the values reported for E_1. Indeed, the E_1 energy appears to be unique to each sample of CdTe depending on its prior history.

SUMMARY

Photoluminescence measurements made at liquid helium temperatures allowed determination of the iodine donor ionization energy E_D to be 14.5–15 meV. Photoreflectance and PL spectra taken at 80K in-

Table I. Growth Conditions, Room Temperature Electron Concentrations and Mobilities, and X-Ray Diffraction (Selected Samples Only) FWHM for the CdTe:I Epilayers Included in This Study

Sample	Growth Temp. (°C)	Cd (Torr) × 10⁻⁷	Thickness (μm)	n at 300K × 10¹⁵ (cm⁻³)	μ at 300K (cm²/V·s)	X-ray (FWHM arc-s)
R91-8	230	4.0	3.5	3100	461	100
R91-35	230	0.7	3.8	1300	577	—
R91-3	230	3.5	3.4	790	585	80
R91-12	230	4.0	2.0	750	573	—
R91-2	230	3.5	2.8	440	560	100
R91-24	170	0.4	2.0	130	789	50
R91-21	210	0.4	1.9	120	795	40
R91-9	230	0	2.4	110	767	100
R91-22	250	4.0	2.1	96	732	50
R91-25	190	0.4	2.4	93	789	60
R91-13	230	3.2	1.7	82	629	60
A9307	250	0	12.6	2.3	580	—
A9309	250	0	12.6	0.44	280	—

Beam equivalent pressures for excess Cd source included.

dicated the presence of both excitonic and donor related transitions. At the higher doping levels, both PR and PL measurements are dominated by the donor-hole transition occurring at 1.581 eV. The relative broadness of the transition correlated with carrier concentration. At 300K, the near-edge PL emission peak energy and PR transition energy both exhibited a strong dependence on electron concentration for doped layers if only a single band-to-band transition is considered for the PL and PR spectra measured. However, detailed lineshape modeling of room-temperature PL and PR spectra reveals that a strong excitonic component remains, even though the exciton binding energy in CdTe (10 meV) is only about 1/3 of $k_B T$ at room temperature. The best fit to the data is obtained using multiple transitions consisting of the free exciton (X_1 and X_2) and a direct band-to-band transition. This analysis indicates a constant value of bandgap over the entire range of conductivities studied. The relative strengths of the transitions differ according to doping concentration and film quality. The emission peak shift is due to the varying relative strength of excitonic recombination as compared to free electron-hole recombination.

ACKNOWLEDGMENTS

REFERENCES

1. D. Rajavel and C.J. Summers, *Appl. Phys. Lett.* 60, 2231 (1992).
2. D. Rajavel, B.K. Wagner, R.G. Benz II, A. Conte, K. Maruyama, C.J. Summers and J.D. Benson, *J. Vac. Sci. Technol. B* 10, 1432 (1992).
3. N.C. Giles, Jaesun Lee, D. Rajavel and C.J. Summers, *J. Appl. Physics* 73, 4541 (1993).
4. Zhonghai Yu, M.A. Mattson, T.H. Myers, K.A. Harris, R.W. Yanka, L.M. Mohnkern, L.C. Lew Yan Voon, L.R. Ram-Mohan, R.G. Benz II, B.K. Wagner and C.J. Summers, *J. Electron. Mater.* 24, 687 (1995).
5. J.M. Francou, K. Saminadayar and J.L. Pautrat, *Phys. Rev. B* 41, 12035 (1990).
6. N.C. Giles, Ph.D. Thesis, Physics, North Carolina State University (1987); and N.C. Giles, K.A. Bowers, R.L. Harper, Jr., S. Hwang and J.F. Schetzina, *J. Crystal Growth* 101, 67 (1990).
7. A recent review pertinent to confined systems can be found by O.J. Glembocki and B.V. Shanabrook, *Semiconductors and Semimetals,* vol. 36 (New York: Academic Press, 1992).
8. D.M. Eagles, *J. Phys. Chem. Solids* 16, 76 (1960).
9. Jaesun Lee, N.C. Giles, D. Rajavel and C.J. Summers, *Phys. Rev. B* 49, 1668 (1994).
10. A review of radiative emission lineshapes for common luminescence processes can be found in H. Barry Bebb and E.W. Williams, *Semiconductors and Semimetals,* vol. 8 (New York: Academic Press, 1972).
11. C. Vasquez-Lopez, H. Navarro, Raul Aceves, M.C. Vargas and Cornelius A. Menezes, *J. Appl. Phys.* 58, 2066 (1985).
12. A conservative variation of Eg with $Cd_{1-x}Zn_xTe$ composition was obtained using expressions in: D.J. Olego, J.P. Faurie, S. Sivananthan and P.M. Raccah, *Appl. Phys. Lett.* 47, 1172 (1985); and T.M. Razykov, *Thin Solid Films* 164, 301 (1988).

A Comparison of Techniques for Nondestructive Composition Measurements in CdZnTe Substrates

S.P. TOBIN, J.P. TOWER, and P.W. NORTON

Loral Infrared & Imaging Systems, Lexington, MA 02173

D. CHANDLER-HOROWITZ and P.M. AMIRTHARAJ

National Institute of Standards and Technology, Gaithersburg, MD 20899

V.C. LOPES, W. M. DUNCAN, and A.J. SYLLAIOS

Texas Instruments, Dallas, TX 75265

C.K. ARD

II-VI, Inc., Saxonburg, PA 16056

N.C. GILES and JAESUN LEE

West Virginia University, Morgantown, WV 26506

R. BALASUBRAMANIAN and A.B. BOLLONG

Johnson Matthey Electronics, Spokane, WA 99216

T.W. STEINER and M.L.W. THEWALT

Simon Fraser University, Burnaby, BC, Canada

D.K. BOWEN

University of Warwick, Coventry CV4 7AL, U.K.

B.K. TANNER

University of Durham, Durham DH3 ILE, U.K.

We report an overview and a comparison of nondestructive optical techniques for determining alloy composition x in $Cd_{1-x}Zn_xTe$ substrates for HgCdTe epitaxy. The methods for single-point measurements include a new x-ray diffraction technique for precision lattice parameter measurements using a standard high-resolution diffractometer, room-temperature photoreflectance, and low-temperature photoluminescence. We compare measurements on the same set of samples by all three techniques. Comparisons of precision and accuracy, with a discussion of the strengths and weaknesses of different techniques, are presented. In addition, a new photoluminescence excitation technique for full-wafer imaging of composition variations is described.

Key words: CdZnTe, HgCdTe, lattice constant, nondestructive measurements, photoluminescence, photoreflectance

INTRODUCTION

This paper presents an overview and comparison of nondestructive optical techniques for determining alloy composition x in $Cd_{1-x}Zn_xTe$ substrates for HgCdTe epitaxy. Monitoring and controlling the sub-

strate alloy composition is required to achieve lattice matching with epitaxial layers. In addition, composition contours reflect the history of the melt-solid interface and thus provide insight into the crystal growth process.

Previous workers have used a variety of techniques to characterize the alloy composition of CdZnTe boules and substrates. The lattice parameter from x-ray

698

Tobin, Tower, Norton, Chandler-Horowitz, Amirtharaj, Lopes, Duncan, Syllaios,
Ard, Giles, Lee, Balasubramanian, Bollong, Steiner, Thewalt, Bowen, and Tanner
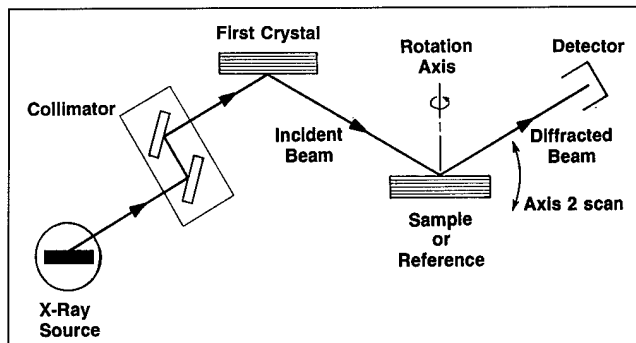
Fig. 1. High-resolution x-ray diffractometer used for lattice parameter measurements. The diffractometer plane (plane of the diagram) contains the x-ray path and the sample rotation axis. All crystal surfaces and Axis 2 are normal to the diffraction plane.

diffraction has been widely used.[1-5] For example, Muhlberg et al.[4] determined a Zn segregation coefficient of 1.6 by measuring the lattice parameter down the length of vertical Bridgman crystals. Duncan et al.[2] applied the low-temperature photoluminescence (PL) technique to CdZnTe substrate composition measurements. The position of the acceptor bound exciton peak was correlated to precision lattice parameter measurements of alloy composition. Compositions were calculated using the Magnea et al.[6] calibration of PL bandgap to alloy composition measured by x-ray fluorescence. Johnson et al.[5] correlated two nondestructive optical measurements, the room temperature transmission edge and 77K PL edge, to x-ray lattice parameters. The 77K photoreflectance technique was used by Kennedy et al.[3] to measure alloy composition by correlating 77K bandgap to lattice parameter and atomic absorption composition. Azoulay et al.[7] used electron microprobe mapping of boule cross sections to infer melt-solid interface shapes during growth.

In this work, we compare compositions measured by x-ray diffraction, photoluminescence, and photoreflectance. In contrast to previous work, which generally used single-crystal x-ray diffraction methods (Bond method or powder diffraction), we describe a new method using a standard double-crystal diffractometer and a silicon reference wafer. Our photoluminescence measurements follow the technique of Duncan et al. We have also used room-temperature photoreflectance, which is easier to implement than the previous 77K technique, yet still quite accurate.

EXPERIMENTAL

Sample Description

All samples were cut from single-crystal regions of

boules with nominal composition $Cd_{0.96}Zn_{0.04}Te$. Samples were obtained from five unseeded crystals produced by each of three different laboratories. Vertical Bridgman crystals were grown at Johnson Matthey and II-VI, Inc., while horizontal Bridgman crystals were grown at Texas Instruments. All starting materials were six 9s pure or better. Etch pit densities varied from $(0.5-3.0) \times 10^5$ cm^{-2}. Most of the samples were 2 cm $\times$ 2 cm $\times$ 1 mm in size. Sample surfaces were prepared by different methods including mechanical polishing, hydroplane polishing, and diamond point turning. All wafers were oriented (111) and measurements were made on the Te face.

Lattice Parameter Measurements

The new x-ray technique for lattice parameter measurements uses a standard high-resolution diffractometer and a single crystal silicon reference wafer to determine the absolute Bragg angle of the CdZnTe substrate.[8,9] In this technique, a sample rotation stage is used to eliminate the effects of sample misorientation on Bragg angle determination. Measurements were made at Loral on a Bede Model 200 diffractometer,* equipped with a Si (022) channel-cut collimator (CCC), a Si (111) monochromator crystal on the first axis, and a 100 mm XY sample translation stage incorporating 360 degree rotation about the specimen surface nonnal. The apparatus is shown in Fig. 1. The CCC and monochromator were set to the maximum of the CuKα_1 Bragg peak. The x-ray beam size was 2.0 × 0.5 mm. Details of the measurements can be found in Ref. 9; an abbreviated method follows:

1. A Si (100) reference wafer and CdZnTe (111) test sample were mounted side by side on the translation stage.
2. The Si reference wafer was scanned on Axis 2 to locate the 004 Bragg peak.
3. The specimen rotation technique[10] was used to position the diffracting vector of the Si reference in the diffractometer plane; the Axis 2 position of the diffraction peak was then measured.
4. The specimen holder was rotated 180 degrees about an axis normal to its surface (parallel to the diffractometer plane); the Axis 2 position of the diffraction peak was again measured.
5. The mean of the two Si peak positions (θ_1) was calculated.
6. Using the XY translation stage, the CdZnTe specimen crystal was moved into the beam.
7. Steps 2–5 were repeated with the CdZnTe specimen replacing the Si reference; a 333 reflection was used.
8. The mean of the two CdZnTe peak positions (θ_2) was calculated.

The two mean values correspond to the real Bragg angles plus an undetermined, but identical, diffractometer offset angle (standard high-resolution diffractometers measure relative, not absolute angles). Substitution of these two values into the Bragg equation

$$\lambda = 2\, d_{ref} \sin \theta_{ref} = 2\, d_{spec} \sin \theta_{spec} \qquad (1)$$

gives the lattice spacing of the specimen, d_{spec}. We assumed a value of 5.431020Å for the lattice parameter of Si, d_{ref}, and 1.540562Å for the CuKα_1 wavelength (used only to calculate θ_{ref}) The difference $\theta_1 - \theta_{ref}$ gives the diffractometer offset angle, which when subtracted from θ_2 yields θ_{spec}. A small correction must then be made for the effect of refraction, with the measured Bragg peaks being displaced from the kinematical Bragg positions given by Eq. (1). This reduces $\theta_{spec} - \theta_{ref}$ by 3.2 arc-s. Once d_{spec} is known, the $Cd_{1-x}Zn_xTe$ alloy composition x is then determined by a linear interpolation between the lattice parameters of CdTe (6.4812Å) and ZnTe[11] (6.1026Å). We note that an x value of 0.000 ± 0.001 was measured for a sample of pure CdTe by this technique. Our measured lattice parameter of 6.4812 ± 0.0004Å is in very good agreement with the most widely accepted value of 6.4809 ± 0.0005Å due to Williams et al.[12] We have used our value to calculate the Zn fraction, but the difference is within the error of 0.1% in Zn concentration determined by the rotary stage.

Photoreflectance

Photoreflectance[13] (PR) is a contactless and nondestructive type of electric field modulation spectroscopy. The modulation of the optical constants (or reflectivity, R) is caused by the induced photovoltage and resultant variation in the built-in field in the surface region of a semiconductor produced by an intense laser pump beam. The PR spectrum is obtained by using a weak probe beam. The modulation ΔR in R of the probe beam is small ($<10^{-4}$ R) but can easily be observed using phase-locked amplification. Measurements of $\Delta R/R$ with photon energy yield sharp derivative-like spectral features that result in precise and accurate determinations of the photon energies associated with interband transitions. The oscillatory line shapes are well understood and are described by the following equation:[13]

$$\Delta R/R = Re(A\, e^{i\Theta}\, [E - E_g - i\Gamma]^n) \qquad (2)$$

where E_g denotes the transition energy and Γ the phenomenological broadening; A and Θ are the intensity and the phase factors, and n was fixed at 1/2, the appropriate value for transitions across the direct gap in a zinc-blende semiconductor. The measured line shapes were fit using a nonlinear regression procedure to extract accurate values of the transition (band gap) energy.

Photoreflectance measurements were performed at the National Institute of Standards and Technology with a standard PR setup[13] consisting of an Ar$^+$ 488 nm line laser as the pump, a quartz-halogen bulb and double grating spectrometer as the probe source, and a silicon detector. Samples were measured at room temperature. The incident beam had a spot size on the sample of about 2–3 mm. Spectral scans were from 770–850 nm with increments of 0.5 nm for samples with x about 0.05. The variation in the direct gap with x was easily observed. Typical data for two samples are shown in Fig. 2, where a difference in x of 0.007 resulted in a shift in photon energy of 0.0040 eV. The precision of the measurement is about ten times better than this shift.

Photoluminescence

Liquid helium PL measurements were made at Texas Instruments (TI), West Virginia University (WVU), and Simon Fraser University (SFU). Relevant features of the different experimental setups are summarized in Table I.

Figure 3 shows the near-band-edge liquid helium photoluminescence spectrum of a high-quality CdZnTe substrate measured at WVU. Similar spectra were
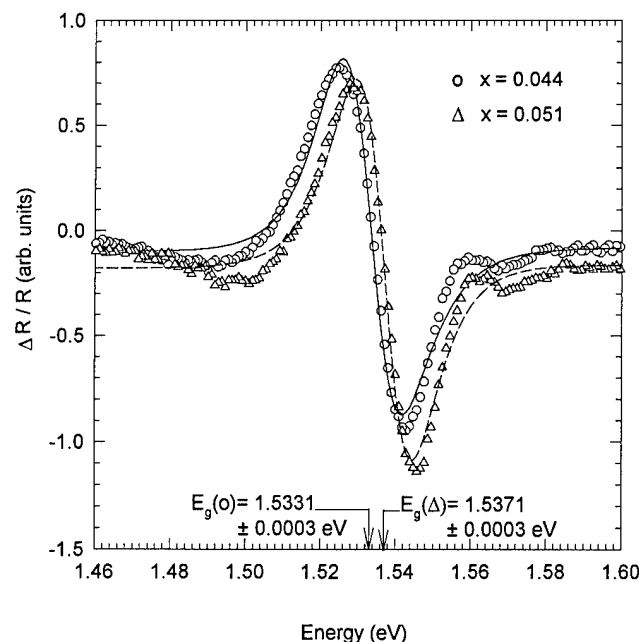
Fig. 2. Room temperature PR spectra of two $Cd_{1-x}Zn_xTe$ substrates.

Table I. Summary of Photoluminescence Instruments Used in This Study

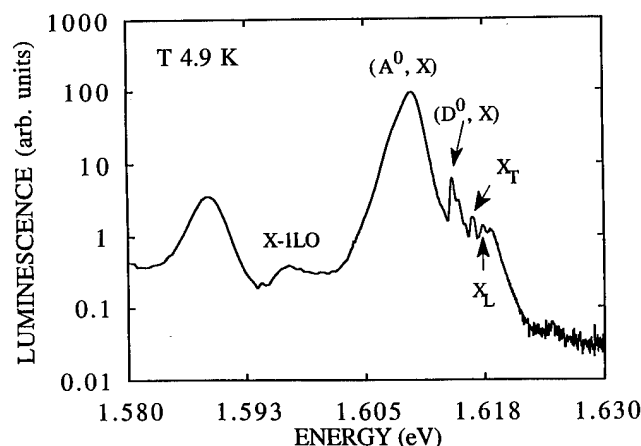| Laboratory	TI	WVU	SFU
Excitation Source	Ar, 515 nm	Ar, 515 nm	Ar, 515 nm
Excitation Power	0.2 W/cm², 6 mW	0.3 W/cm², 0.4 mW	1 W/cm², 20 mW
Spectrometer	Interferometer	0.64 m Monochrom.	Interferometer
Detector	77 K Ge pin	Photomultiplier	Si APD
Max. sample size	1 cm²	3.8 cm dia	5 cm dia

Tobin, Tower, Norton, Chandler-Horowitz, Amirtharaj, Lopes, Duncan, Syllaios, Ard, Giles, Lee, Balasubramanian, Bollong, Steiner, Thewalt, Bowen, and Tanner

Fig. 3. Near band edge photoluminescence spectrum of a CdZnTe substrate. Note the logarithmic luminescence intensity scale.
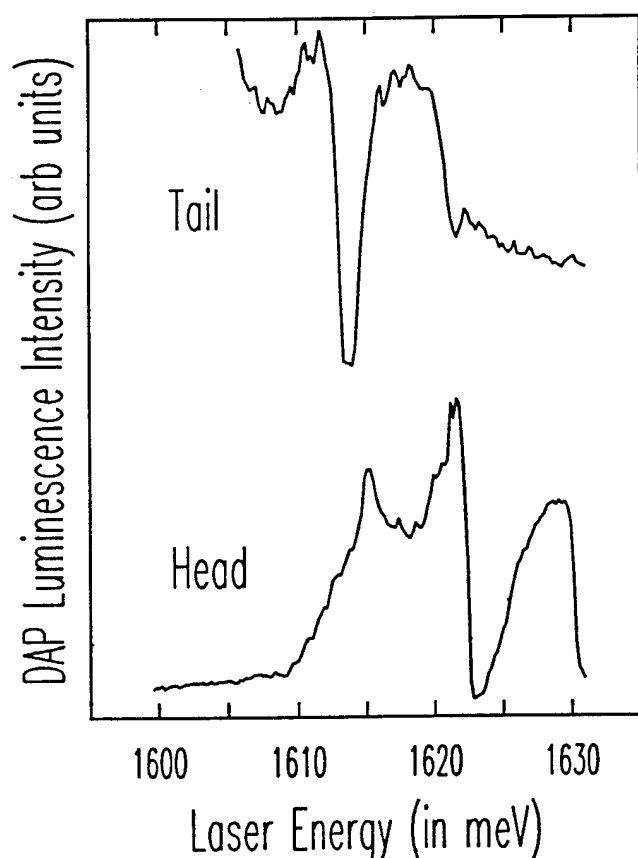
CdZnTe PLE Spectra

Fig. 4. PLE spectra from two CdZnTe samples with different compositions from the same vertical Bridgman boule. Head and tail refer to the first and last to freeze portions of the boule.

eV) and the first phonon replica of the free exciton (X-1LO, 1.596 eV) are also indicated. The mean free exciton energy is taken as 10 meV below E_g. Other peaks in the spectrum were not used for composition determination and are not discussed here.

At TI, the alloy composition x was determined from the low-temperature PL spectrum using the procedure of Duncan et al.[2] In this procedure, the band gap is determined by a 16 meV offset from the position of the acceptor bound exciton peak, usually the strongest near-bandgap peak. The composition is then determined using the Magnea et al. expression relating PL bandgap to composition.[6] Estimated precision in low-temperature PL data is 0.0002 in x, limited by spectrometer energy resolution.[2] Absolute accuracy is limited by composition calibration to about 0.002.[2] At WVU, the energy gap was determined by a 10 meV shift from the free exciton energy. The exciton energy was observed directly on the highest quality samples and inferred from the position of the LO phonon replica (21 meV shift) in less perfect samples. This method was expected to be somewhat more accurate than the acceptor bound exciton energy, which could depend on the identity of the unintentional and unknown acceptor species. The Magnea et al. expression was again used to determine composition.

At SFU, the CdZnTe PL spectrum was directly compared to that of a high-purity CdTe reference sample. The difference in energy of the donor bound exciton peaks was used to measure the energy gap difference. The advantage of the donor over the acceptor bound exciton peak is that it is narrower, allowing more accurate energy determination, and varies less in energy with different dopant atoms. For samples with no measurable (D^0,X) peak, the difference in (A^0,X) peaks was used. For comparison with measurements made by the other groups, the Duncan method was used. The precision of the SFU composition measurement is estimated to be 0.0001 in x, limited by the accuracy in peak position determination (60 μeV) due to alloy broadening of the donor bound exciton peak. The instrument resolution is a factor of 50 better.

In addition to single-point composition measurements, composition images were also produced at SFU. The SFU technique made use of photoluminescence excitation (PLE) spectroscopy.[14] In a PLE spectrum, the intensity of the donor-acceptor pair (DAP) luminescence is plotted as a function of tunable laser excitation energy. There is a sharp minimum in this spectrum at an energy slightly below the band gap due to polariton absorption (Fig. 4). Figure 5 shows the method used to obtain a PLE image. A CCD camera images the back-side DAP photoluminescence of the wafer fully front-side-illuminated by a tunable Ti-sapphire laser. A holographic filter rejects the near-band-edge exciton luminescence and the probe beam. Being deeper in the band gap, the DAP luminescence passes through the substrate and filter. Successive images are recorded as the laser is scanned in energy (typically 70 steps),

measured at the other laboratories. The dominant peak is the acceptor bound exciton (A^0,X) at 1.6099 eV; this peak is assumed to be 16 meV below E_g. The donor bound exciton (D^0,X), a narrower but weaker peak, appears at 1.6142 eV. The transverse and longitudinal free exciton peaks $(X_T$ and X_L, 1.6163 and 1.6174

giving a PLE spectrum at each pixel. The energy of the minimum, obtained by a parabolic fit to the spectrum, is then converted to a band gap and composition at each pixel. Scanning of the wafer is not required, and the entire wafer can be imaged in approximately 20 min. The advantage of PLE spectroscopy over PL band gap measurements is that the spectral position of the minimum in the PLE spectrum is an intrinsic property of the crystal and is dependent only on the band gap and temperature. Its position does not depend on the type and concentration of the impurities. Also, the position of the PL intensity dip is independent of the overall intensity at that pixel. It is not necessary to normalize the PL intensity or maintain uniform illumination across the entire wafer. Wafers up to 10 cm in diameter can be imaged in a special optical cryostat with relatively rapid (15 min) sample exchange. A closed cycle refrigerator maintains the samples at less than 20K. The precision of the measurements reported here is estimated to be 0.0002 in x, limited by the wavelength step interval of the tunable laser and the signal to noise ratio.

RESULTS

Lattice Parameter Measurements

A typical data set for the four rocking curves of a
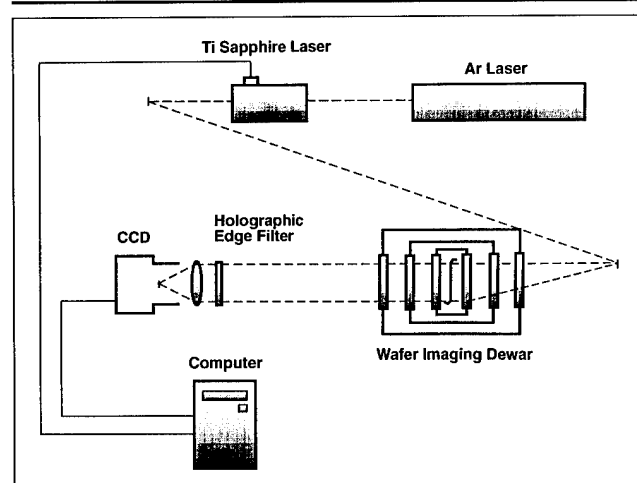
Fig. 5. PLE apparatus used for full-wafer composition imaging.

CdZnTe substrate lattice parameter measurement is shown in Table II. Typical rocking curve full width at half maximum (FWHM) values were 13 arc-s for Si (equipment limited) and 15–30 arc-s for CdZnTe.

The data give $\theta_{spec} - \theta_{ref} = 3.70883$ degrees when 3.2 arc-s is subtracted to allow for the effect of the different refractive indices of Si and CdZnTe. Thus, the specimen Bragg angle $\theta_{spec} = 38.27236$ degrees and we find $d_s = 1.24359$Å, giving a lattice parameter of 6.46189Å and y = 0.052.

Lattice parameter measurements for several CdZnTe substrates with different compositions are given in Table III.

Photoreflectance Results

Room temperature bandgap energies were mea-
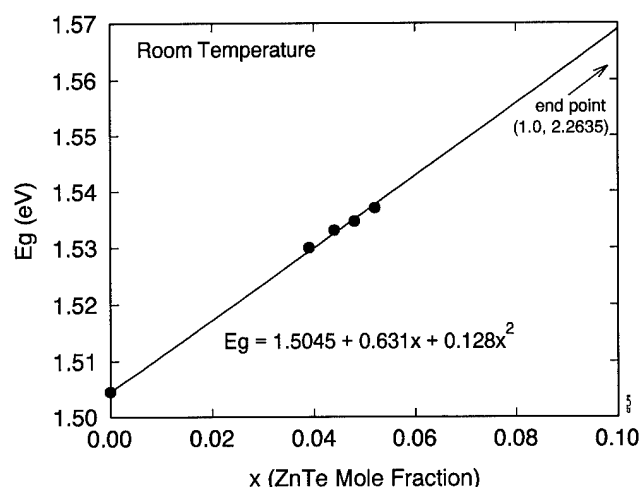
Fig. 6. Calibration curve for CdZnTe composition measurements by room temperature photoreflectance.

Table II. X-ray Data from a Representative CdZnTe Substrate Lattice Parameter Measurement

	Si		CdZnTe		
	0°	180°	0°	180°	Units
Rotation	70	250	266.5	86.5	deg
Axis 2	−80	1916	15166	13380	sec
Mean θ	918		14273		sec

Table III. Comparison of CdZnTe Composition x Measured by Different Techniques Using Existing PR and PL Calibrations from the Literature

Sample	Lattice Param. (Å)	PR Eg 300 K (eV)	PL Eg[†] 4.8 K (eV)	PL Eg* 4.2 K (eV)	x			
					Lattice	PR	PL[†]	PL*
A	6.4647	1.5331	1.6302	1.6295, 1.6306	0.044	0.046	0.049	0.047, 0.049
B	6.4633	1.5347	1.6304	1.6343	0.048	0.049	0.049	0.056
C	6.4618	1.5371	1.6342	1.6320, 1.6306	0.052	0.053	0.056	0.049, 0.052

[†]Measured at WVU.*Measured at TI on adjacent areas from the same slices.
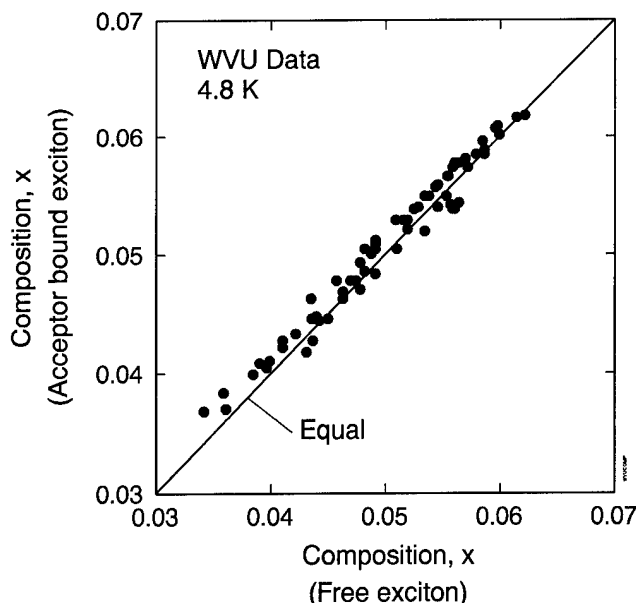
Fig. 7. Comparison of compositions determined by acceptor bound exciton and free exciton energy in low-temperature PL spectra.

Fig. 9. Relationship between PL energy gap and composition determined by lattice parameter measurements.
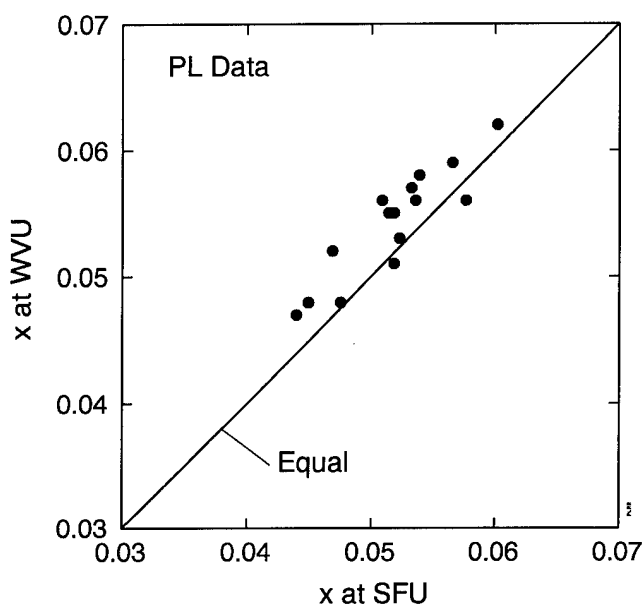

Fig. 8. Results of inter-laboratory comparison of composition measurements by low temperature PL.

sured for the same set of samples used for lattice parameter measurements. Care was taken to avoid spatial nonuniformities by making both types of measurements at the centers of the polished 2 × 2 cm samples. The results are listed in Table III. Photoreflectance compositions in Table III were determined from a previous correlation of 77K PR bandgap and composition (measured by lattice parameter and atomic absorption),[3] with the band gap shifted down by 75 meV from 77 to 300K. The agreement between independent composition measurements by lattice parameter and PR is very good, within 0.002 in x. A new room temperature PR calibration curve based on the lattice parameter composition measurements of this study was constructed, as shown in Fig. 6. Using

this curve, composition may be measured to within 0.001 by room-temperature photoreflectance.

Photoluminescence Results

The results of alloy composition determination by the free exciton method were in good agreement with the bound exciton method, as shown in Fig. 7. For a set of 69 samples, the largest discrepancy in x was 0.0028, with an average difference of 0.00063 and a standard deviation of 0.0011. For comparison, a range in calculated x of 0.001 is expected based on the range of reported acceptor energies for different acceptors (0.6 meV).

A round-robin experiment was conducted in which the same set of samples was measured at WVU and SFU. (Due to experimental sample size limitations, measurements at TI were made on a closely related set of samples.) The results are summarized in Fig. 8. For a set of 15 samples, the compositions agreed within 0.005 in x, with the average discrepancy being 0.0024. The offset in x between the two laboratories corresponds to about 1 meV in PL peak position. These differences cannot be explained entirely by composition variations within samples, which averaged 0.0008 in x for three-point measurements spaced 5 mm apart. The reason for the small discrepancy is still being investigated.

Table III compares compositions measured by PL to those measured by lattice parameter and PR on the same samples. The method of Ref. 2 was used to determine x in the table. It should be noted that PL measurements at TI were not made on the same samples as the others, but rather on nearby areas from the same slices from the boules. Because of Zn segregation effects in the ingots, some variation of composition is expected between different areas. It can be seen in Table III that the PL results are slightly

higher, by 0.003 on average, than the lattice parameter compositions.

Figure 9 shows the relationship between PL energy gaps determined from the acceptor bound exciton peak and compositions measured by lattice parameters on the same samples. Photoluminescence measurements from two different laboratories are shown; they are in relatively good agreement. A linear least-squares fit is shown through all of our data. The energy gaps are slightly higher than those predicted by the Magnea expression, in agreement with the earlier data of Duncan, also shown in the figure. For a given PL bandgap, the Magnea expression gives an x value approximately 0.004 higher than our results. Also shown in the figure is the expression of Olego et al.[15] translated to a 4.2K temperature. Our data fall below this curve, although generally within the reported error of ±5.5 meV in E_g.

Table IV compares compositions measured by the three methods using the new PR and PL calibration curves from this work. For measurements on the same samples, the agreement in x is within 0.001 for two of the samples and 0.003 for the third. This is an improvement over the results from Table III, using previous calibration curves from the literature, where the differences were up to 0.005.

Application to Composition Mapping

Because the segregation coefficient of Zn in CdZnTe is greater than one, the Zn content of the crystal decreases as solidification proceeds. This fact can be used to map the solidification front by mapping contours of Zn content in the crystal. Valuable information on the growth process has been obtained in this way.

Figure 10 shows a Zn composition contour map of a cross section of a vertical Bridgman crystal cut parallel to the growth axis. This map was generated at SFU by PLE imaging. The composition decreases in the growth direction by 0.008 over a distance of 7.5 cm. The fact that the concentration contours are not symmetrical relative to the growth axis may indicate some temperature asymmetry in the furnace.

Figure 11 shows another composition map at the first-to-freeze end of a vertical Bridgman ingot. It indicates a complex nucleation process initiated at the bottom left. Similar measurements have also been made for crystals grown by the horizontal Bridgman process, with some surprising results.[16]

DISCUSSION

Comparison of Methods

All three methods (x-ray lattice parameter,

Table IV. Comparison of CdZnTe Composition x Measured by Different Techniques with New PR and PL Calibrations

		x		
Sample	Lattice	PR	PL ^	PL *
A	0.044	0.045	0.044	0.043, 0.045
B	0.048	0.047	0.045	0.052
C	0.052	0.051	0.052	0.048, 0.045

^Measured at WVU. *Measured at TI on adjacent areas from the same slices.
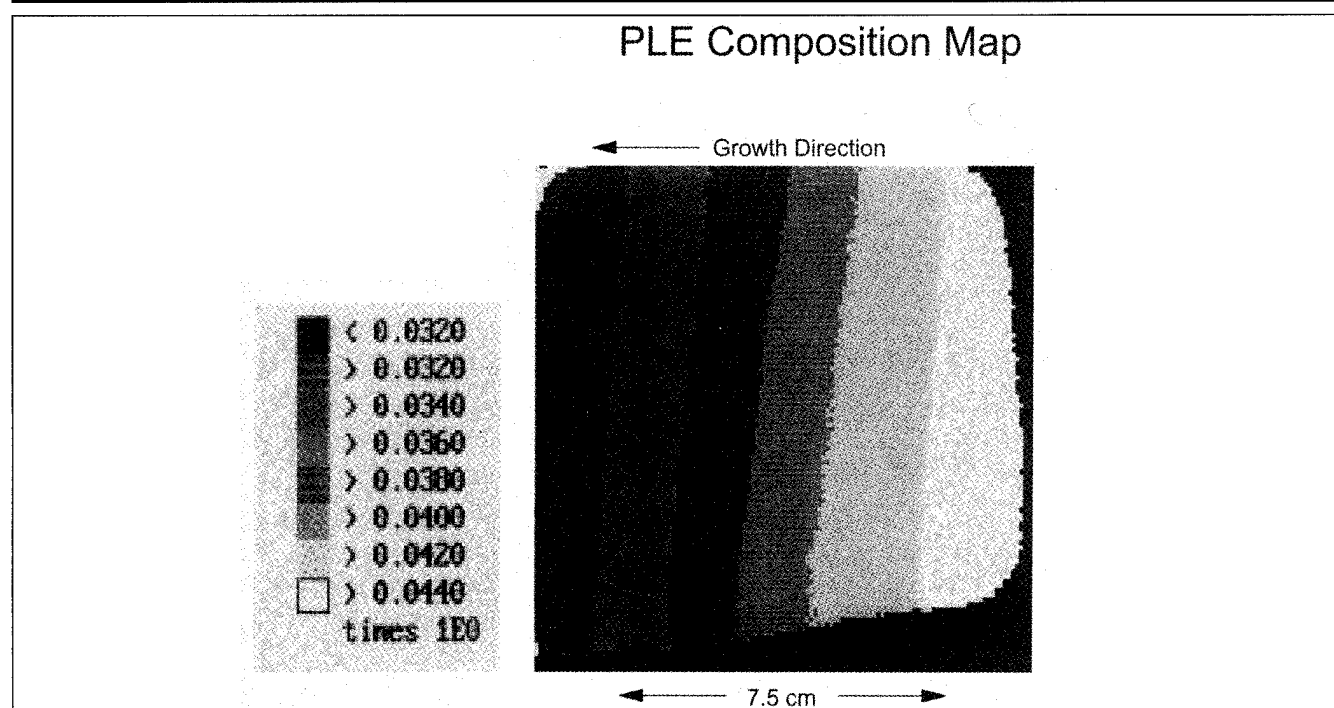
Fig. 10. Composition image of an axial slice through a vertical Bridgman ingot. The slice is 7.5 cm in its largest dimension. The total composition difference across the slice in the growth direction (right to left) is 0.008.

704

Tobin, Tower, Norton, Chandler-Horowitz, Amirtharaj, Lopes, Duncan, Syllaios,
Ard, Giles, Lee, Balasubramanian, Bollong, Steiner, Thewalt, Bowen, and Tanner
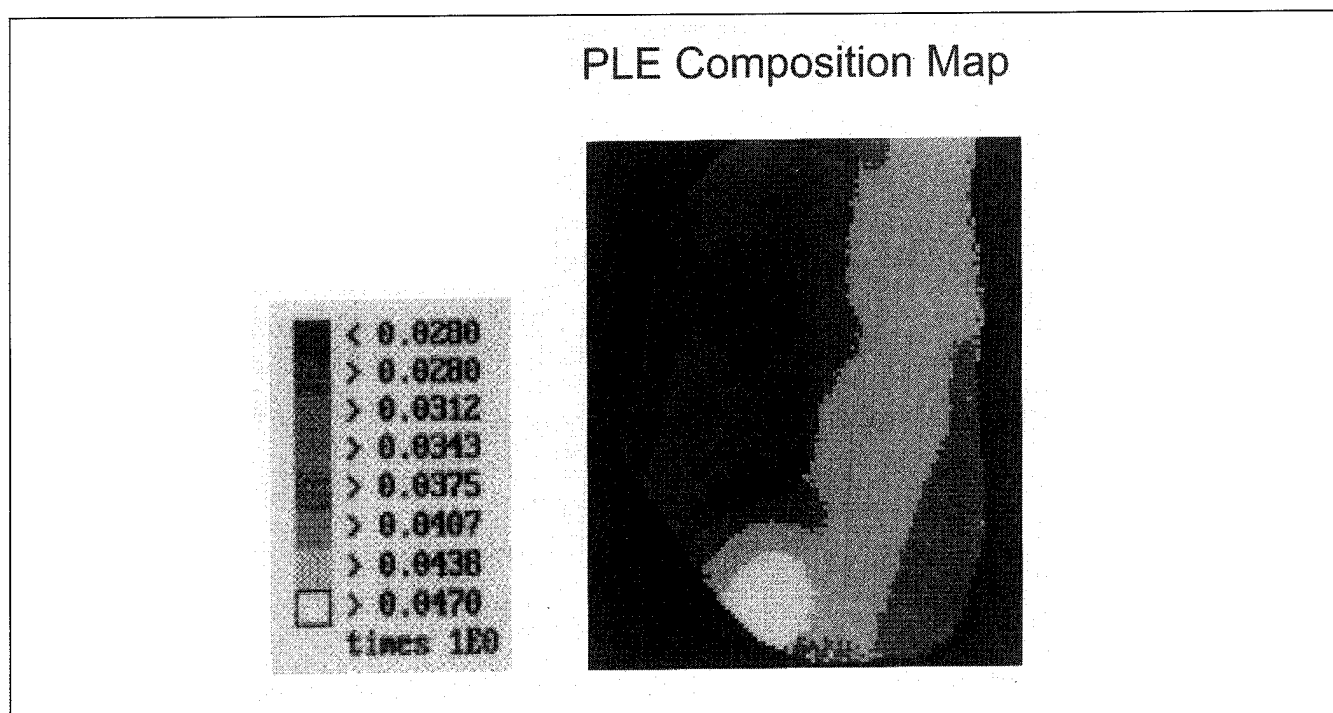
PLE Composition Map

Fig. 11. Composition image of an axial slice through the first-to-freeze end of a vertical Bridgman ingot. The growth direction was bottom to top. Asymmetric nucleation of the crystal is evident.

photoreflectance, low-temperature photolumines-cence) are capable of accurate measurement of alloy compositions with accuracies in the ±0.001 range. They are all near-surface measurements, with sampling depths ranging from submicrometer with PR to about one micrometer for PL and a few micrometers for x-ray diffraction. Etching studies using PL have shown that luminescence intensity can be strongly affected by surface preparation. Residual lattice damage from mechanical polishing or diamond point turning gives rise to deep levels and reduces the intensity of exciton peaks used to determine composition. However, the peak energies are not affected. Residual surface damage also broadens the x-ray rocking curves used for lattice parameter measurements, introducing some additional uncertainty in peak positions. Insofar as damage affects the band structure, it is also expected to degrade the results of PR measurements. Consequently, to obtain the highest accuracy with these techniques, a damage-free surface preparation method is required. For our samples, a free etch in 2% Br in methanol to a depth of about five micrometers was found to provide such a surface.

Comparing methods, the lattice parameter measurement has the advantages of being the most direct measurement of alloy composition and of being performed at room temperature with widely available equipment. It is somewhat time consuming because four rocking curve measurements and multiple sample rotations are required. This limits its usefulness in composition mapping. It is restricted to single-crystal materials of known orientation with sharp rocking curves. This should not be a significant limitation with state-of-the-art substrates. However, we did encounter anomalous results with some samples when x-ray measurements were made across sub-grain boundaries.

Photoreflectance is an attractive technique for wafer screening purposes because it is performed at room temperature and is relatively rapid (a few minutes per sample). Point-by-point mapping is possible. Spatial resolution is about 1 mm at present, but this could be reduced with lenses. There is an excellent correlation to lattice parameter measurements.

Low-temperature photoluminescence has the advantage of providing accurate composition measurements as well as information on defects and impurities. Peak identification at 4.2K is relatively straightforward, at least for the excitonic lines used for composition measurements. The precision of composition measurements can be significantly better than with the other techniques. Spatial resolution can be excellent; PL can be used to provide detailed maps of composition and defects at scales down to a few micrometers. The experimental inconvenience associated with liquid helium measurements can be avoided with special equipment employing closed-cycle He refrigerators, such as the PLE dewar used in this work. We note that previous work has shown that photoluminescence measurements at room temperature, while possible, have poorer composition resolution[2] and can suffer from very low luminescence intensity. Although not explored in this study, 77K PL measurements represent a reasonable compromise with good reported composition accuracy of ±0.0019 and amenability to large-area mapping.[5]

The round-robin comparison of PL composition measurements revealed an offset of about 0.002 in x, corresponding to a peak shift of 1 meV, between two laboratories. Although small, this difference is sig-

nificantly larger than the precision of the measurements. The reason for the discrepancy is still under investigation.

The photoluminescence excitation imaging technique is the best available method for rapidly obtaining composition images. It has a precision comparable to photoluminescence and should be insensitive to impurity effects.

CONCLUSIONS

We have identified three nondestructive optical techniques (x-ray lattice parameter, room-temperature photoreflectance, and low-temperature photoluminescence) capable of high accuracy (± 0.001 in x) composition measurements in $Cd_{1-x}Zn_xTe$ substrates. This is the first time that two of the techniques, lattice parameter using a standard high-resolution diffractometer and room-temperature photoreflectance, have been used for this purpose. There is a very good correlation between lattice parameter measurements and optical bandgap measurements by PR and PL. For room temperature photoreflectance, we have determined the relationship

$$E_g = 1.5045 + 0.631 \times + 0.128 \, x^2 \qquad (3)$$

valid for $x \approx 0.05$ and the CdTe and ZnTe endpoints. For 4.2K photoluminescence, we have determined the relationship

$$E_g = 1.6058 + 0.546 \, x \qquad (4)$$

valid from x = 0.03 to x = 0.06.

A round-robin comparison of PL composition measurements at different laboratories has shown relatively good agreement, with an average difference of 0.002 in x (1 meV in peak position).

A new direct imaging technique using photoluminescence excitation has been developed for composition imaging. It provides rapid composition uniformnity measurements of substrates. Composition maps of CdZnTe boule cross sections have given new insights into the crystallization processes of horizontal and vertical Bridgman crystals.

ACKNOWLEDGMENTS

REFERENCES

1. S.L. Bell and S. Sen, *J. Vac. Sci. Technol. A* 3, 112 (1985).
2. W.M. Duncan, R.J. Koestner, J.H. Tregilgas, H.-Y. Liu and M.-C. Chen, *Mat. Res. Soc. Symp. Proc.* 161, 39 (1990).
3. J.J. Kennedy, P. Amirtharaj, P.R. Boyd, S.P. Qadri, R.C. Dobbyn and G.G. Long, *J. Cryst. Growth* 86, 93 (1988).
4. M. Muhlberg, P. Rudolph, C. Genzel, B. Wermke and U. Becker, *J. Cryst. Growth* 101, 275 (1990).
5. S.M. Johnson, S. Sen, W.H. Konkel and M.H. Kalisher, *J. Vac. Sci. Technol. B* 9, 1897 (1991).
6. N. Magnea, F. Dal'bo, J.L.Pautrat, A. Million, L. DiCioccio and G. Feuillet, *Mat. Res. Soc. Symp. Proc.* 90, 455 (1987).
7. M. Azoulay, A. Raizman, G. Gafni and M. Roth, *J. Cryst. Growth* 101, 256 (1990).
8. D.K. Bowen and B.K. Tanner, to be published in *J. Appl. Cryst.*
9. D.K. Bowen, B.K. Tanner, J.M. Hudson, I. Pape, N. Loxley and S. Tobin, to be published in *Adv. X-ray Analysis* 37 (1994).
10. B.K. Tanner, C. Xi and D.K. Bowen, *Mat. Res. Soc. Symp. Proc.* 69, 191 (1986).
11. H.J. Holland and K. Beck, *J. Appl. Phys.* 39, 3498 (1968).
12. M.G. Williams, R.D. Tomlinson and M.J. Hanpshire, *Sol. State Comm.* 7, 1831 (1969).
13. F.H. Pollack and H. Shen, to be published in *Mater. Sci. and Micro.*
14. T.W. Steiner, M.L.W. Thewalt, R. Balasubramanian and B. Bollong, presented at Defect Recognition and Image Processing in Semiconductors (DRIP5), Santander, Spain, Sept.6–10,1993 (to be published).
15. D.J. Olego, J.P. Faurie, S. Sivanathan and P.M. Racccah, *Appl. Phys. Lett.* 47, 1172 (1985).
16. P.-K. Liao, G. Westphal, H.F. Schaake, B.E. Dean, G.T. Neugebauer, C.K. Ard, 1993 HgCdTe Workshop.

Investigation of Monolayer Roughness in HgTe-CdTe Superlattices

J.R. MEYER

Code 5612, Naval Research Laboratory, Washington, DC 20375

K.A. HARRIS,* R.W. YANKA, L.M. MOHNKERN, and A.R. REISINGER

Martin Marietta Electronics Laboratory, Syracuse, NY 13221

J.F. EGLER, K. MAHALINGAM, and N. OTSUKA

School of Materials Engineering, Purdue University, West Lafayette, IN 47907

Infrared photoluminescence (PL) measurements were performed on (211)-oriented superlattices with energy gaps in the range 110–495 meV. Most of the samples with thinner HgTe quantum wells displayed two PL peaks separated by $\Delta\hbar\omega \cong 30$–65 meV (which generally increased with decreasing well thickness). Both peak energies (E_p) sometimes varied gradually with location on the surface, and in one case three peaks of approximately equal spacing were observed in some locations. The data are consistent with a model which assumes the presence of randomly distributed islands having well thicknesses varying by approximately one monolayer. We find that $\Delta\hbar\omega$ and the variations of the spectra with temperature agree well with calculations based on this simple model.

Key words: HgTe-CdTe superlattices, photoluminescence, molecular beam epitaxy (MBE), quantum wells

INTRODUCTION

This paper reports a comprehensive experimental and theoretical investigation of infrared photolumiscence (IRPL) in HgTe-CdTe superlattices. By correlating results for a large number of samples with a broad range of layer thicknesses and energy gaps, we are able to probe the fundamental nature of the IRPL peaks due to monolayer fluctuations of the quantum well thickness. These are indicative of exceptional growth quality, since they imply the existence of large lateral islands over which the average layer thickness is smooth to within one monolayer (ML). In only two previous studies of HgTeCdTe and $Hg_{1-x}Cd_xTe$-CdTe, superlattices with multiple peaks have been reported near the band edge,[1,2] and in both cases the energy splittings were far too large to be

associated with ML fluctuations (they agreed with calculated energy differences between the heavy and light valence bands). While an earlier report of PL data from one of the present samples attributed the second peak to bound-exciton transitions,[3] we now believe that interpretation to be incorrect. Monte Carlo (MC) simulations are found to be consistent with this interpretation of the IRPL data.

EXPERIMENTAL

The HgTe-HgCdTe superlattices were deposited directly onto [211]B CdTe substrates by photon-assisted molecular beam epitaxy (PAMBE).[4] The substrate temperature was maintained at 170°C during growth. The $Hg_{1-x}Cd_xTe$ barrier compositions x were $\cong 0.9$ due to a continuous Hg overpressure during growth. Well and barrier thicknesses (d_w and d_B) for the superlattices, were determined from a correlation of the growth rate, the total thickness, and comparison of the PL energy gap to theory.[5] Transmission

Meyer, Harris, Yanka, Mohnkern, Reisinger, Egler, Mahalingam, and Otsuka

Table I. Well and Barrier Thickness, PL Peak Energy, FWHM, and Double-Peak Energy Separation for 17 [211]-Oriented HgTe-Hg$_{0.10}$Cd$_{0.90}$Te Superlattices

Growth No.	d_w (Å)	d_{B} (Å)	E_p (77K) (meV)	FWHM (77K) (meV)	ΔE (meV)
617	36	51	159	16	—
619	42	50	110	28	—
632	36	39	133	25	14
637	14	65	495	26	60
650	40	42	122	45	—
741	22	60	325	27	37
749	34	32	145	37	—
751	35	50	161	17	—
764	37	33	117	21	—
788	19	24	320	19	55
790	35	30	127	37	—
832	16	35	429	19	50
833	15	41	470	45	—
840	24	41	275	40	—
862	22	25	262	28	31
866	34	36	150	38	—
881	33	53	188	30	18
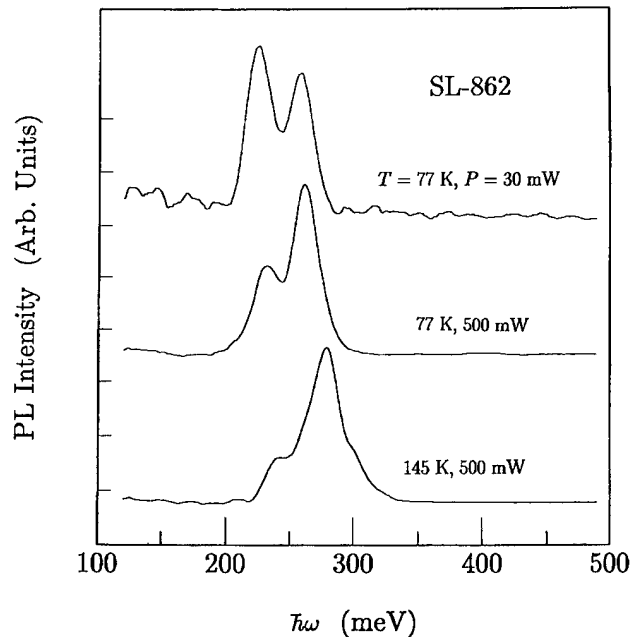
Fig. 1. Experimental PL spectra showing the double peak for SL-862 at 77K (two pump powers) and 145K.

electron microscopy cross-sectional measurements were performed at Purdue University on several of the superlattices studied which confirmed the well and barrier thickness measurments.

Infrared PL measurements were carried out at Martin Marietta using an apparatus described previously. Detailed theoretical modeling of the PL line shapes was carried out at Naval Research Laboratory using techniques described previously.[6,7] Molecular beam epitaxial growth kinetics for this material sys-

tem were studied by Monte Carlo simulations at Purdue University.

RESULTS AND DISCUSSION

All of the HgTe-CdTe superlattice samples studied emitted PL, which is not surprising since recombination lifetimes for a number of these superlattices were in the 100 ns to 20 μs range.[3,8] Table I summarizes the experimental PL peak energies (E_p) and full widths at half maximum (FWHM) for all samples, as well as double-peak energy splittings (ΔE) for those seven which displayed clearly resolvable multiple peaks. While the other ten superlattices exhibited only a single peak, that feature contained a shoulder or other substructure suggesting that the PL in fact consisted of poorly resolved multiple contributions. Double peaks were observed in both n- and p-doped samples, as well as in undoped superlattices.

Typical IRPL spectra displaying the clearly resolved double peaks are illustrated in Fig. 1 for SL-862. Data are shown at 77 and 145K for the maximum pump power (P) of 500 mW and at 77K for a much lower P (30 mW). The two peaks separated by 30 meV are seen to have similar line shapes and FWHM (28 meV). Note that whereas the lower-energy peak is more intense at the lower temperature and pump power, the higher energy peak becomes dominant once the temperature is increased to 145K.

We carried out detailed theoretical modeling of the PL line shapes in order to determine whether some aspect of the band structure could account for the presence of prominent double peaks with the observed properties. It is well known that the complicated free carrier dispersion relations in HgTeCdTe superlattices lead to multiple peaks in both the magneto-transmission spectra (e.g., double hole cyclotron resonance)[6] and the "mobility spectra" from the conductivity tensor (e.g. due to "mass broadening" and the extremely nonparabolic hole mass).[7] However, our calculations demonstrate that these phenomena have a relatively weak effect on the PL line shape. Whereas the magneto-optical and magneto-transport data are quite sensitive to variations in the electron and hole masses individually, the density of states which governs the photoluminescence depends only on the reduced electron-hole mass ($m_r^{-1} \equiv m_n^{-1} + m_p^{-1}$). Thus, even a very strong variation in the hole mass shifts m_r and the PL intensity by no more than a factor of two. While the model based on nonfluctuating layer thicknesses sometimes produces a shoulder due to contributions from different regions of the miniband or a very weak second feature due to transitions involving the light hole band, we find that those mechanisms fail completely to account for the energy splittings, intensity ratios, and layer-thickness dependences of the observed multiple peaks.

It has been recently shown that in the case of GaAs-Al$_x$Ga$_{1-x}$As heterostructures, monolayer fluctuations in the quantum well thickness can lead to well-resolved multiple peaks in the excitonic PL.[9–15] The observation of double peaks in the present spectra

(e.g., Fig. 1) may similarly be attributed to the coexistence of extended islands having a given average d_w with other islands whose average thickness differs by approximately 1 ML. This model accounts for the near equality of the observed FWHM for the two peaks, as well as for the temperature shift of the intensity ratio. While the lower-energy PL line dominates at low temperatures because the electron and hole wavefunctions are localized in the islands with thicker quantum wells, the higher-energy line gains intensity with increasing temperature as carriers are thermally excited into the islands with thinner d_w.

The strongest evidence for this interpretation is that it accurately accounts for both the magnitude and the energy-gap dependence of the splitting energy. The filled circles in Fig. 2 plot the experimental variation of ΔE with E_p (higher-energy line) for the seven superlattices displaying well-resolved double peaks. Apart from one anomalous point, the dependence is seen to be quite systematic. Using an eight-band transfer-matrix algorithm (k·p) which explicitly accounts for the growth orientation,[5] we have calculated the expected shift of E_p resulting from a 1 ML fluctuation[16] of d_w (assuming d_B = 30Å) in a [211] HgTe-Hg$_{0.1}$Cd$_{0.9}$Te superlattice. The result is given by the dashed curve in Fig. 2. We find that to lowest order, this calculation without adjustable parameters accounts quite well for both the magnitude and the layer-thickness dependence of the observed ΔE. Furthermore, it should be noted that the multiple-peak splittings reported for GaAs-Al$_x$Ga$_{1-x}$As heterostructures typically corresponded to 0.6–1.2 ML rather than precisely 1 ML.[11,12,15] The solid curve in Fig. 3 indicates that if the fluctuation magnitude is taken to be 1.5 ML, the data are reproduced almost exactly.

The experimental observation of monolayer thickness fluctuations in the PL data is indicative of high quality growth, since it implies that the islands over which the average quantum well thickness maintains monolayer smoothness must be quite large. Neighboring islands contribute separately to the photoluminescence only if their diameter is larger than the electron and hole wavefunctions. Comparison with estimates for either the exciton diameter or the de Broglie wavelength yields that the island size in the present structures must exceed 5000–1000Å.[17] However, it should be emphasized that the interfaces are known to remain microrough on the atomic scale, i.e., the implied "smoothness" pertains only to a constant average layer thickness within a given island.[11,12,15,18]

These conclusions from our PL data should be considered in the context of earlier magneto-transport determinations of Λ, the interface roughness correlation length (which may be taken as roughly equivalent to the island diameter).[19,20] By fitting a phenomenological model for interface roughness scattering to experimental electron mobilities in HgTe-CdTe superlattices with thin quantum wells, Λ ≅ 300Å was obtained for a series of [100]-oriented (PAMBE) samples[7] and[21] Λ ≅ 200Å for a series of [211]-oriented (nonphoto-assisted growth) superlattices.[13]

The discussion of the previous paragraph implies that these Λ are somewhat smaller than the minimum required for the observation of multiple PL peaks, and
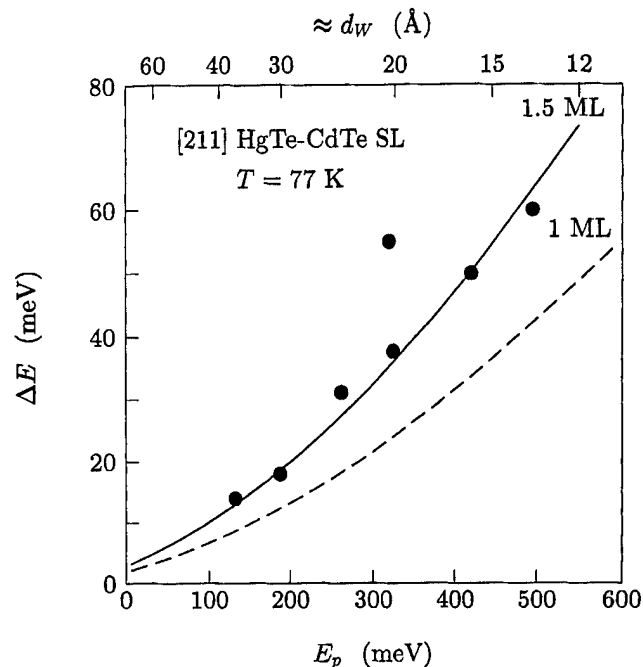
Fig. 2. Double-peak splitting vs PL energy gap (higher-energy peak). The curves are theoretical, assuming well-width fluctuations of one monolayer (1.32Å, dashed curve) and 1.5 monolayers (1.85Å, solid curve). The barrier thickness in the calculation is 30Å, for which the top scale gives the well thickness corresponding to the energy gap in the bottom scale.
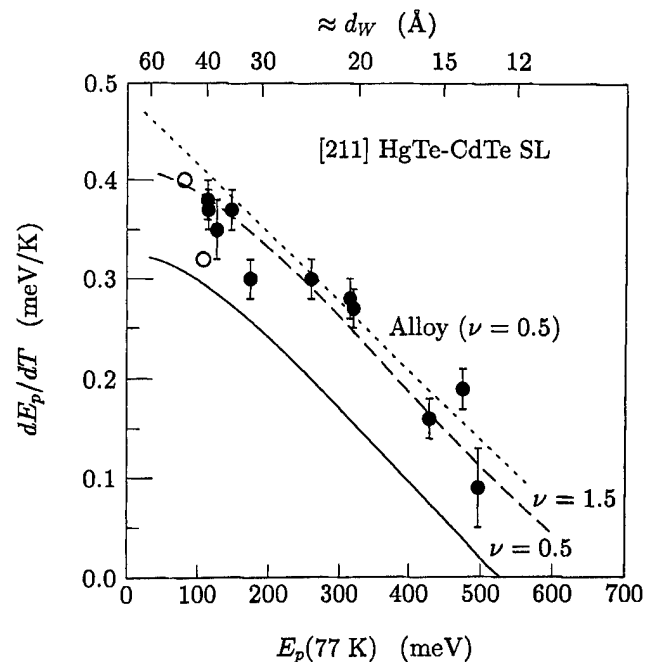
Fig. 3. Experimental (points) and theoretical (assuming D_B = 30Å and ν as indicated on the curves) temperature coefficients for the superlattice PL energy gap vs peak eneergy at 77K. The filled points are from the present work, while the open points are from the previous study of Baukus et al.[21,22] Also shown as the dotted curve is the analogous dependence for the Hg$_{1-x}$Cd$_x$Te alloy.[26] All results represent an average over the temperature range 77–300K.

in fact such features due to ML thickness fluctuations have never been observed in materials fabricated under the growth conditions employed in Refs. 5 and 13.

Further information about the nature of the islands is provided by scanning E_p as a function of lateral position. For SL-862, spectra were obtained at a grid of 41 different locations on the surface of the 2×2 cm^2 wafer. Although the relative intensities varied from point to point, double peaks were observed at most positions, and both energies shifted smoothly with translation of either in-plane coordinate. Data acquired for coarser grids on several of the other samples similarly indicated gradual shifts of the peak energies with location on the surface. Since abrupt rather than gradual variations should have been obtained if the net layer thicknesses change only in sudden jumps as on moves from island to island, these observations imply that the discrete steps of $\cong 1.5$ ML occur at only one of the two interfaces of each quantum well,[12] i.e. either HgTe-on-CdTe or CdTe-on-HgTe but not both. Recent reflection high energy electron diffraction (RHEED) data by Myers et al.[22] indicate that for [211] growth it is the HgTe-on-CdTe interface which is smoother. One also expects that a lateral variation in the flux rate should lead to transition regions in which islands with three different layer thicknesses coexist in relatively close proximity. Spectra for SL-637 confirm that while either one or two PL peaks are observed at most positions on the wafer, a third peak occasionally emerges as the surface is scanned.

Having identified the origin of the multiple peaks in the spectra for some of the samples, we now consider in more detail the implications of the PL results for all 17 superlattices. We begin by noting that the 77K values of the FWHM from Table I show little apparent correlation with E_p or layer thickness. The spectra as a function of T (down to 10K in some cases) generally yielded a zero-temperature extrapolation FWHM$_0$ in the range 9–18 meV. These are somewhat narrower than previous low-temperature values of 18–110 meV,[1,2 23–26] and the FWHM of 10 meV obtained earlier[3] for SL-632 at 4.5K is, to our knowledge, the narrowest ever reported for a Hg-based superlattice. The nonthermal contribution to the observed linewidth is probably due primarily to broadening of the conduction and valence extrema by potential fluctuations.[25,27] One obvious source of these fluctuations is the presence of monolayer roughness (on a lateral scale smaller than the exciton diameter and de Broglie wavelength) at one of the two interfaces for each quantum well (RHEED results imply that it is the CdTe-on-HgTe interface which is rougher).[20] Broadening is also expected due to fluctuations in the alloy composition of the barrier layers. The band structure calculations indicate that fluctuations on the order of $\Delta x_B \cong \pm 0.05$ would account for a significant fraction of the observed FWHM$_0$.

We next consider the related issue of how E_p and the energy gap E_g vary with temperature. It is well-known that dE_g/dT is positive for HgTe and negative

for CdTe, with a cross-over at $x \cong 0.5$. In lowest order, one may expect the superlattice to mimic HgTe, since the baseline for the confinement-induced energy levels is $E_g(T)$ in the quantum well material. However, a more detailed calculation indicates that when d_w is very thin, the net temperature coefficient in the superlattice becomes quite sensitive to dE_g/dT in the barrier layers. This is evident from both experimental and theoretical results for dE_p/dT in Fig. 3, which illustrates that the decrease of the temperature coefficient with increasing energy gap is just as rapid in the superlattice as it is in the Hg$_{1-x}$Cd$_x$Te alloy[28] (dotted curve). The data are taken from spectra at T between 77 and 300K for 11 of the present samples (filled points), along with two superlattices studied previously by Baukus, et al.[23,24] (open points). Theoretical dependences were obtained using temperature-dependent energy gaps from the orientation-dependent transfer-matrix algorithm, where we have employed the relation

$$E_p(T) = E_g(T) + \nu k_B T.$$

The solid curve in the figure represents $\nu = 1/2$, which is appropriate for momentum-conserving band-to-band transitions when nonthermal broadening mechanisms are ignored. Since the calculation employs no adjustable parameters, the agreement with experiment should be considered relatively good.

However, the dashed curve in Fig. 3 indicates that the theory and experiment come into much better agreement over the entire range of energy gaps if $\nu = 0.5$ is replaced by $\nu \cong 1.5$. Many previous studies of temperature-dependent PL in Hg-based superlattices and alloys have similarly found that dE_p/dT is equivalent to $dE_g/dT + \nu$, with $E_g(T)$ determined independently, only when $1 < \nu < 6$ is employed.[23–25,27–34] This finding is often interpreted[29–32] as implying that momentum is not conserved in the radiative transitions, since theory then yields $\nu = 2$.[30] However, that interpretation is inconsistent with other aspects of the data, particularly the magnitude of ν_{FWHM}, the temperature coefficient of the FWHM. Ravid and Zussman have pointed out that while $\nu_{FWHM} \cong 1.8$ is expected for momentum-conserving processes, a much larger value of $\nu_{FWHM} \cong 3.4$ is predicted for non-k-conservation.[35] Our spectra yield $1.1 < \nu_{FWHM} < 1.8$, which is far to small to be explained within the nonconservation-of-momentum hypothesis, and nearly all previous PL data at higher temperatures similarly imply $\nu_{FWHM} \ll 3.4$.[23–25,32,34] It should be noted that Hunter and McGill limited their original discussion of the possible importance of this mechanism in Hg$_{1-x}$Cd$_x$Te to the low temperature regime (T $\leq$ 30K), for which an electron-hole droplet like model was invoked.[30] The earlier theory of Lasher and Stern for non-k-conserving transitions in GaAs was similarly restricted to low temperatures, since it was based on processes involving localized states in the tails of the bands.[36] Those authors specifically argued that momentum should be conserved at higher temperatures, since most of the carriers then occupy nonlocalized

states well above the band extrema. Previous attributions of $\nu > 0.5$ at $T \geq 77K$ to nonconservation of momentum therefore seem physically unreasonable. A more likely interpretation is that the observed value of ν results from broadening of the density of states by potential fluctuations.[25] At lower temperatures, for which the electrons and holes preferentially occupy states in the tails of the fluctuations, PL can occur at energies below the average band gap. However, as k_BT approaches the magnitude of the fluctuations the PL energy becomes more representative of the average E_g, hence E_p displays an anomalously large temperature shift between the two regions. To account for the discrepancy between theory (with $\nu = 0.5$) and experiment in Fig. 3, the additional energy shift between 77 and 300K must be approximately 15–20 meV, i.e. of the same order as the nonthermal broadening of the PL line.

Monte Carlo simulations were performed in order to examine the growth process of HgTe-CdTe superlattices in the [211] direction. We used a model based on the simple cubic structure. We compared bond energies of atoms in respective configurations, i.e. kink, step, and terrace sites. Simulations were tried using the zinc-blende structure but it was found that those simulations consumed too much CPU time to obtain meaningful results because of the very weak bonds of HgTe and, hence, fast migrations and fast evaporations of Hg atoms. This method, although not as sophisticated to that which uses the zinc-blende structure, is justified because of the uncertainty of many parameters required for modeling of atomic processes in the zinc-blende structure. The details of this approach will be published elsewhere.[37]

The implications of the MC simulation results suggest that the HgTe surface prior to the growth of the CdTe layer is the rough interface which gives a gradual variation of E_p with position, while the smoother CdTe surface yields abrupt monolayer jumps, and hence gives rise to the multiple peaks in the PL spectra. This result is consistent with the recent RHEED observations.[22] The MC results also imply that if the growth of the HgTe layers were sufficiently slow or higher substrate temperatures were used, this would lead to the surface having a stationary roughness only a fraction of one monolayer in height.

SUMMARY

We have experimentally and theoretically investigated the PL properties of HgTe-CdTe superlattices with a broad range of energy gaps. A sizable fraction of the samples display clearly resolved double PL peaks due to monolayer fluctuations in the quantum well thickness. The systematic variation of peak splitting with energy gap is reproduced by [211] band structure calculations if the thickness fluctuations are taken to have units of 1.5 ML. These results confirm that the superlattice growth quality achievable by PAMBE is quite high, and that at least one interface for each quantum well has monolayer average smoothness over island dimensions exceeding

500Å. Data for dE_p/dT as a function of E_p have been compared with the theoretical temperature shift of the energy gap. The relatively modest discrepancy has been attributed to the influence of potential fluctuations rather than to nonconservation of momentum as in several previous works.

Monte Carlo simulations of the kinetic growth processes of HgTe-CdTe superlattices show that the HgTe-on-CdTe interfaces are much smoother than the CdTe-on-HgTe interfaces which is consistent with the IRPL data interpretation. Recent RHEED oscillation data are in agreement with the MC results. The results also suggest that the MBE growth of HgTe-CdTe superlattices can be further improved by slowing the HgTe growth rate.

REFERENCES

1. T.H. Myers, R.W. Yanka, K.A. Harris, A.R. Reisinger, J. Han, S. Hwang, Z. Yang, N.C. Giles, J.W. Cook, Jr., J.F. Schetzina, R.W. Green and S. McDevitt, *J. Vac. Sci Technol. A* 7, 300 (1989).
2. E. Monterrat, L. Ulmer, R. Mallard, N. Magnea, J.L. Pautrat and H. Mariette, *J. Appl. Phys.* 71, 1774 (1992).
3. K.A. Harris, R.W. Yanka, L.M. Mohnkern, A.R. Reisinger, T.H. Myers, Z. Yang, Z. Yu, S. Hwang and J.F. Schetzina, *J. Vac. Sci. Technol. B* 10, 1574 (1992).
4. K.A. Harris, T.H. Myers, R.W. Yanka, L.M. Mohnkern and N. Otsuka, *J. Vac. Sci. Technol. B* 9, 1752 (1991).
5. C.A. Hoffman, J.R. Meyer, R.J. Wagner, F.J. Bartoli, X. Chu, J.P. Faurie, L.R. Ram-Mohan and H. Xie, *J. Vac. Sci. Technol. A* 8, 1200 (1990).
6. J.R. Meyer, C.A. Hoffman, R.J. Wagner and F.J. Bartoli, *Phys. Rev. B* 43, 14715 (1991).
7. C.A. Hoffman, J.R. Meyer, F.J. Bartoli, J.W. Han, J.W. Cook, Jr., J.F. Schetzina and J.N. Schulman, *Phys. Rev. B* 39, 5208 (1989).
8. A.R. Reisinger, K.A. Harris, T.H. Myers, R.W. Yanka, L.M. Mohnkern and C.A. Hoffman, *Appl. Phys. Lett.* 61, 699 (1992).
9. B. Deveaud, J.Y. Emery, A. Chomette, B. Lambert and M. Baudet, *Appl. Phys. Lett.* 45, 1078 (1984).
10. M. Tanaka and H. Sakaki, *Superlatt. Microstruct.* 4, 237 (1988).
11. C.A. Warwick, W.Y. Jan, A. Ourmazd and T.D. Harris, *Appl. Phys. Lett.* 56, 2666 (1990).
12. D. Gammon, B.V. Shanabrook and D.S. Katzer, *Appl. Phys. Lett.* 57, 2710 (1990).
13. R.F. Kopf, E.F. Schubert, T.D. Harris and R.S. Becker, *Appl. Phys. Lett.* 58, 631 (1991).
14. A. Ourmazd, D.W. Tatlor, J. Cunningham and C.W. Tu, *Phys. Rev. Lett.* 62, 933 (1989).
15. C.A. Warwick and R.F. Kopf, *Appl. Phys. Lett.* 60, 386 (1992).
16. Monolayer planes along the [211] axis are more closely spaced (1 ML–> $a/2\sqrt{6} \cong 1.32$ Å) but contain fewer atoms than those along the [100] axis; there are six monolayers per unit cell.
17. We expect the island dimensions to be elongated, since atomic diffusions along the two in-plane axes are inequivalent in

[211] growth.

18. Y. Kim, A. Ourmazd, M. Bode and R.D. Feldman, *Phys. Rev. Lett.* 63, 636 (1989).

19. J.R. Meyer, D.J. Arnold, C.A. Hoffman and F.J. Bartoli, *Appl. Phys. Lett.* 58, 2523 (1991).

20. J.R. Meyer, D.J. Arnold, C.A. Hoffman, F.J. Bartoli and L.R. Ram-Mohan, *Phys. Rev. B* 46, 4139 (1992).

21. Although Ref. 20 derived $\Lambda = 80$ A for the [211] sample, that result was invalidly based on the use of the [100] monolayer thickness for both orientations.

22. T.H. Myers, R.G. Benz, II, B.K. Wagner and C.J. Summers, private communication.

23. J.P. Baukus, A.T. Hunter, O.J. Marsh, C.E. Jones, G.Y. Wu, S.R. Hetzler, T.C. McGill and J.P. Faurie, *J. Vac. Sci. Technol. A* 4, 2110 (1986).

24. J.P. Baukus, A.T. Hunter, J.N. Schulman and J.P. Faurie, *J. Appl. Phys.* 64, 283 (1988).

25. C.L. Cesar, M.N. Islam, R.D. Feldman, R. Spitzer, R.F. Austin, A.E. DiGiovanni, J. Shah and J. Orenstein, *Appl. Phys. Lett.* 54, 745 (1989).

26. M.M. Kraus, M.M. Regnet, C.R. Becker, R.N. Bicknell-Tassius and G. Landwehr, *J. Appl. Phys.* 71, 5610 (1992).

27. E. Monterrat, L. Ulmer, N. Magnea, H. Mariette, J.L. Pautrat, K. Kheng and F. Fuchs, *J. Appl. Phys.* 71, 1774 (1992).

28. M.H. Weiler, *Semiconductors and Semimetals,* Vol. 16, eds. R.K. Willardson and A.C. Beer (New York: Academic Press, 1981), p. 119.

29. D. Schikora, J.W. Tomm, K. Rakkenus and M. Pesa, *Phys. Stat. Sol.* (A) 118, K123 (1990).

30. A.T. Hunter and T.C. McGill, *J. Appl. Phys.* 52, 5779 (1981).

31. P. Gille, K.H. Herrmann, N. Puhlmann, M. Schenk, J.W. Tomm and L. Werner, *J. Cryst. Growth* 86, 593 (1988).

32. A. Ravid and A. Zussman, *J. Appl. Phys.* 67, 4260 (1990).

33. F. Fuchs and P. Koidl, *Semicond. Sci. Technol.* 6, C71 (1991).

34. P. Bochut, G. Destefanis, J.P. Chamonal, A. Million, B. Pelliciari and J. Piaguet, *J. Vac. Sci. Technol. B* 9, 1794 (1991).

35. A. Ravid and A. Zussman, *J. Appl. Phys.* 73, 3979 (1993).

36. G. Lasher and F. Stern, *Phys. Rev. A* 133, 553 (1973).

37. J.F. Egler, N. Otsuka and K. Mahalingam, to be published in *J. Appl. Phys.*

Journal of Electronic Materials
Author Instructions

General Purpose

The *Journal of Electronic Materials (JEM)* is published by the Electronic Materials Committee of The Minerals, Metals & Materials Society (TMS) and the Electron Devices Society of the Institute of Electrical and Electronics Engineers. *Journal of Electronic Materials* regularly reports on the science and technology of electronic materials, while examining new applications for semiconductors, magnetic alloys, insulators, and optical and display materials. The journal welcomes articles on methods for preparing and evaluating the chemical, physical, and electronic properties of these materials. Specific areas of interest are electronic memory and logic structures, magnetic-optical recording media, superlattices, packaging, detectors, emitters, metallization technology, superconductors, and low thermal-budget processing. The journal also selectively publishes invited and contributed review papers on topics of current interest to enable individuals in the field of electronics to keep abreast of activities in areas peripheral to their own. Further, *JEM* publishes papers from the annual conference sponsored by the TMS Electronic Materials Committee. It is the journal's editorial intent that the published papers be of interest to nonspecialists and specialists in the field of the particular contribution.

Review Process

Papers for *JEM* are reviewed by two qualified referees to determine suitability. The editor's decision to accept or reject a paper, based on referees' comments, is final. Send three copies of the manuscript key-stroked, double-spaced on 22×28 cm (8.5×11 in.) paper to the appropriate section or associate editor (see inside front cover). Alternatively, a paper/review/letter can be submitted directly to the editor (see inside front cover), who will assign the manuscript to appropriate section or associate editor (obviously the latter procedure takes longer). Papers dealing with subjects not identified with any particular section or associate editor should be sent to Theodore C. Harman. For letters only, fax one copy to G.B. Stringfellow (801/581-4816), followed simultaneously with two hard copies (one of which includes glossy prints or equivalent). Priority mail is recommended for shortened publication times. The initial submission should state that the contribution is for the Letters section. Authors will be notified when their manuscripts have been accepted for publication.

Stylistic Guidelines

All manuscripts should adhere to the following guidelines:

1. The manuscript, written in English, must be double-spaced throughout, key-stroked on one side of the paper only. Good quality office machine copy is acceptable.
2. Number all pages in sequence.
3. Key-stroke title of article and abstract on a separate first page.
4. The work's significance and its relation to the work of others should be detailed in the Introduction. Major assumptions should be stated and procedures adequately outlined.
5. Key-stroke references, figure captions, and tables on separate pages.
6. Key-stroke references in the style used by technical publications. References should be cited in the text by Arabic numerals as superscripts. Each individual reference should include the names of all the authors, the standard abbreviated name of the journal [see *World List of Scientific Periodicals,* 4th ed. (1960), Butterworths, London], the volume number, the initial page number, and the year of publication in parentheses. For books, the city of publication and the publisher should be given.
7. Use only those figures that are necessary to illustrate the meaning of the text. The text must include a citation of each figure. Original figures must be India Ink line drawings or black-and-white, high-contrast, glossy prints. (Color photographs or photocopies are not acceptable.) Original glossy prints should be submitted along with two sets of copies for the review and should be no larger than 22×28 cm (8.5×11 in.).
8. Measurements should be given metrically.
9. Submit: (a) the original manuscript and artwork, and (b) two single-sided photocopies of the manuscript and artwork.
10. Each submitted letter (up to six typewritten pages and up to four figures and/or tables) should be accompanied with an abstract of 100 words or less, a key words line, and a transfer of copyright form. The initial submission should state that the contribution is for the Letters section.

Copyright

Submission is a representation that the manuscript has not been published previously and is not currently under consideration for publication elsewhere. A statement transferring copyright from the authors (or their employers, if they hold copyright) to TMS will be required before the manuscript can be accepted for publication. A suitable form for copyright transfer is printed in the back of every January issue and is available from the editor's office and TMS.

Galley Process

Authors will be given the opportunity to review the typeset version of their manuscript. This review should be solely dedicated to detecting typographical errors. Editorial changes and corrections are not to be made at this time. To meet production deadline, a rapid turnaround of these proofs is necessary.

Page Charges and Reprints

Journal of Electronic Materials, like many other scientific and technical journals, depends on author page charges for a significant part of its support. Therefore, a charge of $110 per printed page is levied for all papers published. One hundred reprints will be supplied without additional charge for every paper on which the payment of these charges is authorized. It is expected that each author or sponsoring institution will contribute fairly to the support of *JEM* through payment of the page charges. However, authors may request a waiver of all or part of the page charges by sending a written request to *JEM.* Instructions and forms regarding page charges, waivers, and reprints will be forwarded from the TMS business office. These and any other special matters related to page charges should be referred to the *JEM* Circulation Department, TMS, 420 Commonwealth Drive, Warrendale, PA 15086; (412) 776-9080; fax (412) 776-3770.

TRANSFER OF COPYRIGHT

To be signed by the author or, in the case of multiple authorship, by at least one of the authors who agrees to inform the others, or, in case of a work made for hire, by the employer. The signed statement must be received by the editor before the manuscript can be accepted for publication.

Copyright to the article by _____

Submitted under the title _____
is hereby transferred to The Minerals, Metals & Materials Society, Inc. effective if and when the article is accepted for publication in

JOURNAL OF ELECTRONIC MATERIALS

For authors who are employees of the United States Government, the transfer of copyright is understood to be effective only to the extent that such copyright is transferable.

The authors explicitly reserve the following rights:

All proprietary rights other than copyright, such as patent rights.

The right to use all or part of this article in future works of their own, such as lectures, reviews, textbooks, or reprint books.

The right to make copies for the authors' own teaching use.

The right to use figures and tables in future publications, provided explicit acknowledgment is made of their initial appearance in this journal.

_____   _____
Signature   Signature

_____   _____
Name (print)   Name (print)

_____   _____
Title, if not Author   Title, if not Author

_____   _____
Date   Date

MATERIALS WEEK '95

Cleveland, Ohio
29 October—2 November 1995

A joint presentation of
ASM International
and
The Minerals, Metals & Materials Society (TMS)
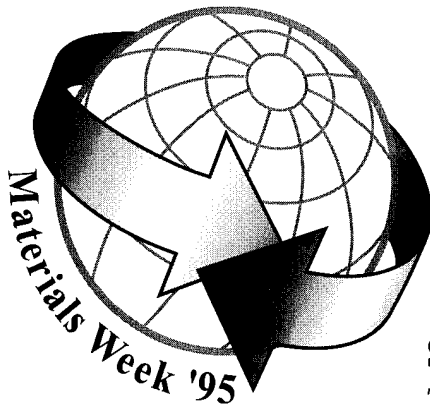
Spotlighting...
The Role of Materials in Global Competitiveness

More than 200 technical sessions will provide you with a comprehensive update of technological and economic developments from the global advanced materials community. A total of nearly 1,000 individual presentations will address issues of importance in research and development, materials selection, processing, design and manufacturing, testing, quality control, waste minimization, and recycling.

Featuring:
* Special Cleveland regional programming developed by local chapters to focus on the technical and developmental needs specific to the area.
  * *One-day registration fees will be available for the regional programming.*

* An opportunity to attend nearly 20 technical sessions programmed by ASM's Surface Engineering Division, TMS's Surface Modification and Coatings Technology Committee, and the Cleveland Regional Programming Task Force that will address today's hot topics in materials coatings, tribological materials, and heat treating.

* A presentation of interest to all who are involved in the transportation industry by ASM's Highway/Off-Highway Vehicle Division: Partnership for Next-Generation Vehicle (PNGV).

* A birthday celebration and symposium in honor of Professor James C.M. Li's contributions to the study of intermetallics, microstructure effects, fatigue and fracture, and composites.

* The 1995 Materials Exposition—an exhibit of products, processes, and services to fulfill the needs of the modern engineered materials field.

Plan now to join more than 4,000 of your colleagues at Materials Week '95 as they prepare for an important role in the future of the materials profession.

For more information, please contact:ASM's Member Services Center at 1-800-336-5152, ext. 703, fax: (216) 338-4634, e-mail: MemServ@po.asm-intl.org; or TMS Meeting Services at (412) 776-9000, ext. 232, fax: (412) 776-3770, e-mail: karl@tms.org.

ASM
INTERNATIONAL ®
The Materials Information Society

TMS OnLine
Minerals • Metals • Materials

Complete Materials Week '95 information is also available through TMS OnLine [modem: (412) 776-2040; Internet: online.tms.org for telnet or http://www.tms.org for World Wide Web].

TMS
Minerals • Metals • Materials

AUTHOR INDEX